Solar Absorption Cooling

Proefschrift

ter verkrijging van de graad van doctor
aan de Technische Universiteit Delft,
op gezag van de Rector Magnificus prof. dr. ir. J. T. Fokkema,
voorzitter van het College voor Promoties,
in het openbaar de verdedigen op dinsdag 18 September 2007 om 15.00 uur
door

Dong-Seon KIM

Master of Mechanical Engineering, Korea University, Seoul
geboren te Yesan, Zuid Korea

Dit manuscript is goedgekeurd door de promotor:
Prof. ir. H. van der Ree

Toegevoegd promotor:
Dr. ir. C. A. Infante Ferreira

Samenstelling promotiecommissie:
Rector Magnificus, voorzitter
Prof. ir. H. van der Ree, Technische Universiteit Delft, promotor
Dr. ir. C. A. Infante Ferreira, Technische Universiteit Delft, toegevoegd promotor
Prof. dr. P.D. Iedema, Universiteit van Amsterdam
Prof. dr.-ing. F. Ziegler, Technische Universität Berlin
Prof. dr.-ing. J. Gross, Technische Universiteit Delft
Prof. dr. ir. R.J.C. van Zolingen, Technische Universiteit Eindhoven
Dr. B. Bach, arsenal research
Prof. dr. G.J. Witkamp, Technische Universiteit Delft, reservelid

Dit onderzoek is gedeelterijk gefinancierd door Novem in het kader van het BSE-NEO programma.

ISBN 978-90-9022181-6

To my supportive wife Soo Min
and
my beloved family in Korea

Contents

Summary

Solar Absorption Cooling

Dong-Seon Kim

As the world concerns more and more on global climate changes and depleting energy resources, solar cooling technology receives increasing interests from the public as an environment-friendly and sustainable alternative. The coincidence of solar intensity and cooling demand has long been inspiring people to invent a machine that cools when the sun shines. It motivated the first solar cooling machine of the history dating back to as early as late 19th century and the numerous machines that followed. In the past, the public interest in solar cooling was in perfect synchrony with energy price (remember the oil crisis in seventies) and it will probably be the same in the future. As soon as energy price goes down so that a solar cooling system becomes no longer financially beneficial, public interest would vanish instantly as was witnessed in the past. Fortunately, prospect of solar cooling is better in the future as regards to the economic and political environment. With conventional energy resources being closer to depletion, effort to exploit alternative energy sources is not only limited to refrigeration industry but has become a general phenomenon across the whole industry. There are currently much stronger economic and political drives to promote solar cooling technology in the market. However, making a competitive solar cooling machine for the market still remains a challenge to the academic and industrial communities. In an effort to meet this challenge, this thesis reports the research activities carried out to form the basis for the development of a new solar cooling machine, which the author hopes would bring the solar cooling technology one more step closer to our daily lives.

This thesis consists of 8 chapters, each of which is dedicated for the description of a specific part of the research activities that will lead to the development of a new solar-driven absorption chiller. The followings are brief summaries of the chapters.

The first aim of **Chapter 1** is to give an overview of the state-of-the-art of the different technologies that are available to deliver refrigeration from solar energy. Unlike most review articles that were limited to solar thermal, especially sorption cooling technologies, this chapter is intended to give a broader overview including solar electric, thermomechanical, sorption and also some newly emerging technologies. The second aim is to compare the potential of these different technologies in delivering competitive sustainable solutions. The current commercial status of different solar cooling technologies may be quickly viewed in a comparison of the initial costs of various cooling systems. From the review of various solar cooling technologies, it was concluded that solar electric and thermomechanical technologies are currently not competitive with solar thermal technology in terms of initial cost. Among different thermally driven refrigeration technologies, absorption cooling is found the most cost-effective for solar cooling applications. Desiccant cooling can be a good solution for the applications where good indoor air quality is essential. But in general, high initial cost is likely to limit its application to large facilities. Adsorption and ejector cooling technologies are not favorable because of small power density and low COP. It was also concluded that the direction of future R&D would better be focused on low temperature-driven and air-cooled absorption technologies. It is because firstly, initial cost can be lowered significantly for a

low-temperature system and secondly, there is only a limited number of air-cooled machines in the market for the applications where a wet cooling tower should be avoided.

In **Chapter 2**, various absorption chillers are evaluated in terms of dynamic performance using a modular dynamic simulation model that has been developed to facilitate the simulation of a large number of different solar absorption cooling systems. The approach adopted in Chapter 2 is different from previous studies in several aspects. Firstly, unlike quasi-steady state models, all components in a solar cooling system were modeled with differential equations to take into account all thermal masses. Secondly, while most of the previous works assumed equilibrium between bulk working fluids, the absorption chiller models in Chapter 2 were developed to take account of the influences of non-equilibrium conditions by considering finite mass transfer rates in sorption processes. Finally, a modular approach has been taken to promote quick and efficient modeling and simulation of a large number of complex systems. Solar collectors have been modeled with the recent information about 209 solar collectors from 120 companies active in the European market and four different types of absorption chiller models have been developed using modular components. In total, 26 water-cooled and 19 air-cooled solar air conditioning systems have been simulated for two summer months in Milan and Naples in Italy. To summarize the simulation results, the single- and the half-effect LiBr/H2O chillers were found advantageous for minimizing initial cost for water- and air-cooled solar air conditioning systems, respectively. It was recommended that the half-effect LiBr-water absorption chiller should be developed to realize a low-cost air-cooled solar absorption air conditioning system.

In **Chapter 3**, a LiBr-water absorption chiller is designed based on one of the half-effect absorption cycles considered in Chapter 2. Firstly, several chiller configurations have been evaluated in terms of practicality and a direct heat-coupled parallel-flow design has been selected. Secondly, the chiller has been modeled with effectiveness method and simulated for cycle design. Finally, all components have been designed according to the cycle design result. It was found that most of the components should be built with extended (or enhanced) heat transfer surfaces to realize the original designs within the given physical dimension. For lack of resources, the final designs have been prepared with smooth heat transfer surfaces giving up the compactness and high power density of the original designs. The influences of this design change are analyzed in Chapters 5 and 7.

Chapter 4 presents a newly developed Gibbs energy equation for aqueous LiBr solution, from which other thermodynamic properties of the solution can be directly derived. Aqueous LiBr solution has been used for a long time in absorption refrigeration industry thanks to its excellent performance as an absorbent and for the same reason, it was chosen again for the half-effect absorption chiller proposed in this thesis. The study presented in this Chapter has been motivated by the need of an accurate thermodynamic study covering wide ranges of conditions observed from the fact that the thermodynamic properties of the solution are well established in the working domain of the conventional machines but not in the domain of unconventional cycles. The Gibbs energy equation developed in this Chapter is valid for the solutions in the concentration range from 0 to 70 wt% and the temperature range from 0 to 210 ^{o}C. An osmotic coefficient equation was developed to accurately reproduce the original solution density and the equilibrium vapour pressure from the literature. The solution enthalpy calculated from the Gibbs energy equation is consistent with the experimental differential heat of dilution and heat capacity data taken from the literature. The approach adopted in this Chapter has proved high flexibility and accuracy for describing electrolyte solutions over wide working ranges by allowing all relevant parameters to be systematically expressed in a single Gibbs energy equation that can be readily expandable to other thermodynamic property equations. Being able to describe the solution properties from pure solvent to the highly concentrated solutions near crystallization limits at temperatures from freezing points to 210 ^{o}C, the model developed in this Chapter provides a consistent and reliable basis for simulation and analysis of LiBr absorption systems.

In **Chapter 5**, a steady-state model is presented for simulation of the proposed half-effect LiBr-water absorption chiller. In the model development, special attention has been paid to the accurate modeling of the transport phenomena at the vapor-liquid interfaces of falling film flows and the transformation of governing equations for easy and quick solution. A falling film heat exchanger has been modeled with one-dimensional elementary control volumes in a non-uniform grid system taking into account the heat and mass transfer resistances at vapor-liquid interface and bulk film flow, which enabled more accurate prediction of temperature and concentration profiles in the falling film. Modified governing equations based on mathematical and thermodynamic principles promoted quick and stable convergence of solution saving great time and effort in simulation process. Simulation results show that COP and cooling capacity of the final chiller design would be less than the original design goals due to the reduction of heat transfer areas from the original design. The reduced heat transfer area in an internal heat exchanger, which is a large-diameter vertical tube with falling film flows on both sides, turned out to be the main reason for this reduced performance. The biggest uncertainty in the simulation results lies in the accuracy of the empirical correlations used for the falling film flows in the system. This subject is discussed in more detail in Chapters 6 and 7.

Chapter 6 is dedicated for the investigation of the heat and mass transfer in falling film flows. Literature has been analyzed focusing on the experiments with falling film flows in the small flow rate range near and below minimum wetting rate. Various tubular falling film heat exchangers were found in many articles but plate-type heat exchangers were rare. Experimental data for the tubular falling film heat exchangers were found highly inconsistent for LiBr-water solutions without surfactant in the small flow rate range, which was believed to be the result of strong surface tension effect. The experimental study presented in this Chapter has been motivated by the lack of experimental data on vertical plate falling film heat exchangers, which are indispensable for predicting the performance of an internal heat exchanger and therefore the behavior of the whole system. The experimental setup used in the experiments had an absorber consisting of a copper plate heat exchanger mounted inside a large glass tube so that not only the measurement of working conditions but also observation of the flow patterns on the plate was possible during the experiments. In total, 134 experiments were carried out with four different working fluids and two different heat transfer surfaces. The results are presented in various forms including heat and mass transfer rates, fluxes, coefficients and the correlations of appropriate non-dimensional numbers. The observations made during the tests are also discussed in relation to the reported heat and mass transfer coefficients and it is also attempted to explain the experimental results by comparing with the results of previous studies.

Chapter 7 describes the fabrication and test results of a half-effect LiBr-water chiller setup that has been constructed according to the final design in Chapter 3. In the beginning, several problems detected in preliminary tests and the corrective measures are described. The setup was tested under various operating conditions and the results are discussed in detail. In spite of many problems, the behavior of the setup could be well understood from the analysis of the test results. The analysis suggested that the poor performance of mid-pressure evaporator was the main reason for the small cooling capacity of the setup and the leaking refrigerant from low-pressure evaporator was responsible for the low COP, which was also verified by the simulation model developed in Chapter 5. At the end of the Chapter, several recommendations are made regarding the improvement of the setup.

Finally, **Chapter 8** gives overall conclusions and recommendations regarding the research activities reported in this thesis. The recommendations are given focusing on what has been missing or was insufficient in the course of research hoping for a follow-up research in the near future.

Samenvatting

Zongedreven Absorptie Koeling

Dong-Seon Kim

Gezien dat de wereld zich meer en meer zorgen maakt om globale klimaatsveranderingen, krijgen zongedreven koeltechnologieën toenemende publieksinteresse als milieu vriendelijke en duurzame alternatieven. De gelijktijdigheid van zonnestraling en koelvraag heeft sinds lang geleden mensen geïnspireerd om een machine uit te uitvinden die koelt als de zon schijnt. Het heeft de eerste zongedreven koelmachine reeds in de 19de eeuw tot stand gebracht en een groot aantal machines is hierna geïntroduceerd. In het verleden was de publieke belangstelling voor zongedreven koelmachines synchroon aan de energieprijs (denk aan de olie crisis in de 70 jaren) en zo zal het blijven in de toekomst. Als de energieprijs daalt zodat de zongedreven koelsystemen niet meer financieel aantrekkelijk zijn, vervaagt de publieke belangstelling zoals in het verleden is gebeurd. Gelukkig zijn de perspectieven van zongedreven koeling in de toekomst beter voor wat betreft economische en politieke randvoorwaarden. Met het einde van de conventionele energiebronnen in zicht, worden initiatieven ondernomen om alternatieve energiebronnen te gebruiken niet alleen door de koude industrie maar ook door de gehele industrie. Er zijn op het moment veel sterkere economische en politieke drijfveren om zongedreven koeltechnologie te stimuleren. Hoe dan ook, de ontwikkeling van een concurrerende zongedreven koelmachine voor de markt is nog steeds een uitdaging voor de academische en industriële gemeenschappen. In een poging om de uitdaging aan te gaan, rapporteert dit proefschrift over de onderzoeksactiviteiten die ondernomen worden om een basis te vormen voor de ontwikkeling van een nieuw zongedreven koelmachine, die, naar de verwachting van de auteur, zongedreven koeling dichterbij het dagelijkse leven zal brengen.

Dit proefschrift bestaat uit 8 hoofdstukken, elk gewijd aan de beschrijving van een specifiek deel van de onderzoeksactiviteiten die zullen leiden tot de ontwikkeling van een nieuw zongedreven absorptie koelmachine. In het vervolg een korte samenvatting van de inhoud van de verschillende hoofdstukken.

Het eerste doel van **Hoofdstuk 1** is een overzicht te geven van de stand-van-zaken van de verschillende technologieën die beschikbaar zijn om koeling uit zonne-energie te leveren. In tegenstelling met de meeste overzichtsartikelen die alleen zonthermische systemen beschouwen en vooral sorptie koeltechnologieën, is dit hoofdstuk opgezet om een breder overzicht te geven inclusief zonelektrisch, thermomechanisch, sorptie en ook enkele recentelijk opgekomen technologieën. Het tweede doel is om het potentieel van deze verschillende technologieën te vergelijken voor wat betreft het mogelijk maken van competitieve duurzame oplossingen. Het huidige commerciële stadium van de verschillende koeltechnologieën kan snel beoordeeld worden aan de hand van de investeringskosten van de verschillende systemen. Uit het overzicht van alternatieve koeltechnologieën, was geconcludeerd dat, voor wat betreft investeringskosten, zonelektrische en thermomechanische technologieën niet concurrerend zijn ten opzichte van zonthermische technologieën. Tussen de verschillende thermisch gedreven koeltechnologieën, absorptie koeling is het meeste kost effectief voor zongedreven koeltoepassingen. Desiccante koeling kan een goede oplossing zijn voor toepassingen met hoge binnenlucht kwaliteitseisen. Maar over het algemeen, beperken de hoge investeringskosten toepassing tot systemen met grote capaciteit. Adsorptie en ejecteur koeltechnologieën zijn minder aantrekkelijk door hun lage vermogensdichtheid en lage COP. Er is ook geconcludeerd dat toekomstige R&D inspanningen best gefocusseerd kunnen worden op lage temperatuur aangedreven en lucht gekoelde absorptie technologieën. Dit omdat de investeringskosten van lage temperatuur systemen aanzienlijk gereduceerd kunnen worden en omdat er geen lucht gekoelde machine beschikbaar is in de markt voor de toepassingen waar een koeltoren minder geschikt is.

In **Hoofdstuk 2** worden verschillende absorptie koelmachines geëvalueerd voor wat betreft hun dynamische prestaties. Hiervoor wordt een dynamisch simulatie model toegepast dat ontwikkeld is om de simulatie van een groot aantal verschillende zongedreven koelsystemen te vereenvoudigen. De benadering gekozen in Hoofdstuk 2 is, in een aantal opzichten, verschillend van gangbare oplossingen. Ten eerste, in tegenstelling met quasi statische modellen, zijn alle componenten gemodelleerd met differentiale vergelijkingen om rekening te houden met hun thermische massa's. Ten tweede, in tegenstelling met andere studies waar evenwicht tussen bulk werkmedia wordt verondersteld, zijn de absorptiekoelmachine modellen van Hoofdstuk 2 ontwikkeld om rekening te houden met het effect van niet-evenwicht toestanden. Hierbij is eindige stofoverdracht transport beschouwd gedurende de sorptie processen. Als laatste, is er gekozen voor een modulaire aanpak om een snelle en efficiente modellering en simulatie van een groot aantal complexe systemen mogelijk te maken. Zonnecollectoren zijn gemodelleerd op basis van recente informatie over 209 zonnecollectoren van 120 bedrijven die opereren in de Europese markt. De modulaire componenten zijn gebruikt om vier verschillende typen absorptie koelmachines samen te stellen. In totaal zijn 26 watergekoelde en 19 luchtgekoelde zongedreven absorptiekoelmachines gesimuleerd voor twee zomermaanden in Milaan en Napels in Italië. Om de simulatieresultaten samen te vatten, de eentraps en de half-effect LiBr/H_2O absorptiekoelmachines blijken gunstig om de investeringskosten te reduceren, respectievelijk voor water- en luchtgekoelde systemen. Het is aanbevolen om half-effect LiBr/H_2O absorptiekoelmachines te ontwikkelen om zo te komen tot lage kosten luchtgekoelde zonnegedreven absorptie koelmachines.

In **Hoofdstuk 3** wordt een LiBr-water absorptiekoelmachine ontworpen op basis van een van de half-effect absorptie kringprocessen beschouwd in hoofdstuk 2. Ten eerste, zijn verschillende configuraties geëvalueerd in termen van praktische uitvoeringsmogelijkheden. Hieruit is een direct gekoppelde parallel stroom ontwerp geselecteerd. Ten tweede is de absorptiekoelmachine gemodelleerd gebruik makend van de effectiviteitmethode en gesimuleerd ten behoeve van het kringproces ontwerp. Ten laatste zijn alle componenten ontwerpen in overeenstemming met het kringproces ontwerp. Er is geconcludeerd dat het grootste gedeelte van de componenten gebouwd zou moeten worden met vergrote warmteoverdracht oppervlak om zo de originele ontwerpen te kunnen construeren binnen de gegeven fysieke afmetingen. Door begrotingsbeperkingen zijn uiteindelijk alle ontwerpen geconstrueerd met gladde warmtewisseling oppervlakte, afstand nemend van de compactheid en hoge vermogensdichtheid van de originele ontwerpen. De effecten van deze ontwerpmodificaties worden geanalyseerd in hoofdstukken 5 en 7.

Hoofdstuk 4 presenteert een nieuw ontwikkelde Gibbs energie vergelijking voor LiBr-water oplossingen waaruit andere thermodynamische eigenschappen van de oplossingen afgeleid kunnen worden. Door zijn excellente eigenschappen, worden LiBr-water oplossingen sinds lang door de absorptie koelindustrie toegepast. Dat is ook de reden voor zijn toepassing in de half-effect absorptiekoelmachine die in dit proefschrift wordt onderzocht. De studie in dit hoofdstuk is het gevolg van de behoefte van een nauwkeurige thermodynamische studie dat grote toestand gebieden omvat. De thermodynamische eigenschappen zijn goed gedefinieerd in het werkgebied van conventionele machines maar niet in het werkgebied van niet conventionele kringprocessen. De Gibbs energie vergelijking ontwikkeld in dit hoofdstuk is geldig voor oplossingen in het concentratiebereik van 0 tot 70 gewichtsprocent en in het temperatuurbereik van 0 tot 210°C. Een osmotische coëfficiënt vergelijking is ontwikkeld om literatuur soortelijke gewicht en evenwicht dampspanning nauwkeurig te voorspellen. De oplossing enthalpie berekend vanuit de Gibbs energie vergelijking is consistent met experimentele waarden van de oplossing- en soortelijke warmte. De gekozen aanpak is flexibel en nauwkeurig om elektrolytische oplossingen te beschrijven over grote werkgebieden omdat alle relevante parameters systematisch kunnen worden uitgedrukt in een eenvoudige Gibbs energie vergelijking. Deze vergelijking is eenvoudig te converteren naar andere vergelijkingen voor thermodynamische eigenschappen. Het model ontwikkeld in hoofdstuk 4 kan de eigenschappen van de oplossing beschrijven vanaf zuiver oplosmiddel tot zeer hoog geconcentreerde oplossingen dicht bij de kristallisatie grens en vanaf de vriespunten tot 210°C. Hiermee vormt het een consistente en betrouwbare basis voor simulatie en analyse van LiBr-water absorptie systemen.

In **Hoofstuk 5** wordt een statisch model gepresenteerd voor simulatie van de onderzochte half-effect LiBr-water absorptie koelmachine. In de modelontwikkeling is speciaal aandacht besteed aan de modellering van de overdrachtsprocessen aan de dampvloeistof interface van vallende film stromingen en aan de transformatie van de heersende vergelijkingen ten behoeve van snelle en eenvoudige oplossing. Een vallende film warmtewisselaar is gemodelleerd met eendimensionaal controle volumes in een niet uniforme rooster, rekening houdend met warmte en stofoverdracht weerstanden aan de dampvloeistof interface. Hiermee kunnen temperatuur en concentratie in de vallende film nauwkeurig worden voorspeld. De, op mathematische en thermodynamische principes gebaseerde, gemodificeerde stelsel vergelijkingen maakt snelle en stabiele convergentie mogelijk en bespaart hiermee aanzienlijke oplossingstijd en simulatie inspanning. Simulatie resultaten laten zien dat de COP en koelvermogen van het uiteindelijke experimentele koelmachine ontwerp kleiner zijn dan de oorspronkelijke doelstelling door de reductie van de werkelijke warmtewisseling oppervlakte ten opzichte van het oorspronkelijke ontwerp. De oppervlakte reductie van de interne warmte- en stofwisselaar blijkt de voornaamste oorzaak van de verslechtering van de prestaties. Deze warmtewisselaar is een verticale buis met een groot diameter met vallende film stromen aan beide zijden. De grootste onzekerheid in de simulatie resultaten wordt veroorzaakt door de empirische correlaties die gebruikt worden voor de vallende films. Dit onderwerp wordt in meer detail besproken in hoofdstukken 6 en 7.

Hoofdstuk 6 wordt gewijd aan warmte- en stofoverdracht in vallende film stromen. Er wordt een overzicht gegeven van de literatuur met speciaal aandacht voor experimenten met vallende film stromingen met stromen in de buurt van de minimum bevochtiging grens. Er zijn een aantal studies geïdentificeerd over vallende filmen om pijpen maar een zeer beperkte hoeveelheid voor vallende film stromen in plaat warmtewisselaars. De experimentele gegevens voor vallende films van LiBr-water oplossingen om pijpen, waarbij geen capillaire actieve stoffen zijn toegepast, blijken zeer inconsistent voor stromen in de buurt van de minimum bevochtiging grens. Dit wordt toegekend aan sterke oppervlakte spanning invloeden. Het experimentele onderzoek gerapporteerd in dit hoofdstuk wordt gemotiveerd door het gebrek aan experimentele gegevens voor vallende films aan vertikale platen. Dergelijke gegevens zijn essentieel voor de voorspelling van de prestaties van de interne warmtewisselaar met vallende films aan beide zijden. De experimentele opstelling gebruikt voor deze experimenten had een absorber die bestond uit een koperen plaat warmtewisselaar gemonteerd binnen een glazen pijp met een grote diameter zodat naast de experimenten die verricht konden worden ook de stromingspatronen zichtbaar waren gedurende de experimenten. In totaal zijn 134 experimenten verricht met vier verschillende werkmedia en twee verschillende oppervlakten. De resultaten zijn op verschillende manieren gepresenteerd inclusief warmte en stof overdracht coëfficiënten, stromen en dimensieloos correlaties. De visualisaties verkregen gedurende de experimenten worden ook besproken in relatie met de gerapporteerde warmte en stof overdrachtscoëfficiënten. De resultaten worden ook besproken aan de hand van een vergelijking met voorgaande studies.

Hoofdstuk 7 beschrijft de fabricage en experimentele resultaten verkregen met de half-effect LiBr-water absorptie test opstelling. De opstelling is opgebouwd in overeenstemming met het eind ontwerp besproken in hoofdstuk 3. Eerst worden inleidend experimenten beschreven waarmee problemen en oplossingen zijn geïdentificeerd. De opstelling is getest onder verschillende werkomstandigheden en de resultaten worden gedetailleerd besproken. Het gedrag van de opstelling kon verklaard worden uit de analyse van de test resultaten. De analyse suggereert dat de slechte prestaties van tussendruk verdamper de hoofdoorzaak van het beperkte koelvermogen van de opstelling was. De lekkage van koudemiddel vanuit de lagedruk verdamper zorgde voor een lage COP. Het model ontwikkeld in hoofdstuk 5 is ingezet om bovenstaande invloeden te kwantificeren. Aan het eind van het hoofdstuk worden aanbevelingen gedaan om de opstelling te verbeteren.

Hoofdstuk 8 geeft de algemene conclusies en aanbevelingen voor wat betreft het onderzoek gerapporteerd in dit proefschrift. De aanbevelingen focusseren op de punten waarin dit onderzoek onvolledig is, in de hoop dat vervolg onderzoek antwoorden daarop kan vinden.

1 Introduction

1.1 Solar cooling in a warming globe

Since the beginning of the last century, average global temperature has risen by about 0.6 K according to UN Intergovernmental Panel on Climate Change (IPCC). It is also warned that the temperature may further increase by 1.4 to 4.5 K until 2100 (Climate Change 2001, 2001). As signs of the warming, warm winter days, extreme summer heat waves, melting of glaciers and sea level rise have been reported from many countries.

Although there are natural parameters that may have contributed to the warming, there exists a general consensus that the climate changes observed in the last 50 years are most likely due to human activities. Having realized the seriousness of the situation, the world community decided to take initiatives to stop the process. One of such efforts is Kyoto Protocol, an international treaty on global warming that came into force as of 16 Feb 2005, the idea of which is concisely explained by United Nations Environment Programme (UNEP) as:

"The Kyoto Protocol is a legally binding agreement under which industrialized countries will reduce their collective emissions of greenhouse gases by 5.2% compared to the year 1990 … The goal is to lower overall emissions from six greenhouse gases - carbon dioxide, methane, nitrous oxide, sulfur hexafluoride, HFCs, and PFCs- calculated as an average over the five-year period of 2008-12. National targets range from 8% reductions for the European Union and some others to 7% for the US, 6% for Japan, 0% for Russia, and permitted increases of 8% for Australia and 10% for Iceland."

In order to meet the imposed target, each country in Annex I, a group of industrialized countries, is supposed to cut down the production and the use of greenhouse gases in its territory. Especially regarding the reduction of carbon dioxide, being an inevitable byproduct of industrial activities, industries should improve facilities and processes to achieve the goals.

HVAC industry is one of those hardest hit by the effect of the protocol. In Europe, use of HFC-134a will be banned for the air conditioning units in new cars starting from 1 Jan 2009. And inspection and/or monitoring are required for all stationary HFC-based refrigeration, air conditioning, heat pump units and fire protection systems for the safe containment of HFCs. Besides, regarding the energy efficiency of various products including HVAC systems, European Commission adopted a framework directive "Directive for Eco-design requirements for energy-using products" in 2003, aiming at the huge energy saving potential in private households and buildings sectors.

Reduction of energy consumption for cooling, however, cannot be relied solely on the improvement of efficiency. Although significant achievements have been made in the improvement of air conditioning efficiency in the past, the energy consumption for cooling has continued to rise due to the cooling demand that is increasing even faster. In Europe, number of residential air conditioning units had increased 7 times in 10 years to reach 0.018 unit per household in 2000 (Cool Appliances, 2003). A recent European project (EECCAC, 2003) predicted 400% increase of cooling demand in Europe from 1990 to 2020 estimating energy consumption for cooling to increase from 186 to 412 PJ and CO_2 production from 18,073 to 40,103 kiloton.

This increase in cooling demand puts enormous strains on existing power grids, threatening national security of stable energy supply. The Italian blackout on 26 June 2003, for example, was caused by an extreme increase of electricity demand for cooling combined with a reduction of the production capacity of large-scale power plants due to scarcity of cooling water. And the large number deceased people during the heat wave in France in the same year were also due to the failure of existing power plants in supplying enough electricity for cooling demand.

Reduction in the use of synthetic refrigerants and the production of CO_2 provides a new opportunity for solar cooling. Considering that cooling demand increases with the intensity of solar radiation, solar cooling has been considered as a logical solution. The history of solar cooling dates back to as early as 1878 when the French mathematician Augustin Mouchot demonstrated his solar engine with the absorption cooling machine of Edmond Carré to produce ice at the World Exhibition in Paris (Thévenot, 1979). The public was amazed by the apparent paradox of producing ice from sunlight. In late 19th century, some pioneering scientists like Mouchot seriously tried to exploit solar energy as an alternative energy to coal, the most popular fuel at the time, anticipating its sources would be exhausted soon by the huge consumption of the fast-growing industry (Smith, 1995). But as energy prices went down with diversifying energy sources and developing transportation technologies, the idea of using solar energy became less attractive.

It was not until the 1970s that solar cooling received great interests again from the public, when the world suffered from the oil crisis that had been initiated by Arab members of OPEC from political motivations. The world realized that they could no longer depend on cheap oil price and began to look for alternatives. Industries tried to reduce energy consumptions by improving energy efficiency on one hand and diversifying energy sources on the other. There were many projects for development or demonstration of solar cooling technologies and solar cooling continued to be an important issue in the 1980s (Lamp and Ziegler, 1998).

It has been almost 130 years since the first demonstration of solar cooling. Fossil fuel resources are closer to their exhaustion as the early pioneers had anticipated in 19th century. Only change they did not expect was that this planet has warmed up significantly in the mean time only to worsen the situation. Fortunately, a variety of solar cooling technologies has been developed and many of them are available in the market at much cheaper prices than ever.

The first aim of this chapter is to give an overview of the state-of-the-art of the different technologies that are available to deliver refrigeration from solar energy. Unlike most review articles that were limited to solar thermal, especially sorption cooling technologies (Lamp and Ziegler, 1998; Li and Sumathy, 2000; Grossman, 2002), this chapter is intended to give a broader overview including solar electric, thermomechanical, sorption and also some newly emerging technologies. The second aim is to compare the potential of these different technologies in delivering competitive sustainable solutions. The current commercial status of different solar cooling technologies may be quickly viewed in a comparison of the initial costs of various cooling systems. Finally, an introduction is given to the topics discussed in the following chapters.

1.2 Solar electric cooling

A solar electric cooling system consists mainly of photovoltaic panels and an electrical cooling device.

Since the first discovery of photoelectric effect by the French physicist, Antoine-Cesar Becquerel in 1839, photovoltaic or solar cell technology has been dramatically improved in both performance and price. Modern solar cells are basically semiconductors whose efficiency and cost vary widely depending on the material and the manufacturing methods they are made from. Most of the solar cells commercially available in the present market are made from silicon as shown in Fig. 1.1.

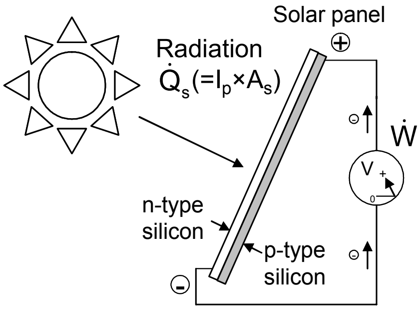

Figure 1.1 Schematic diagram of a solar photovoltaic panel

In Eq. (1.1), efficiency of a solar electric panel is defined by the ratio of power $\dot{W}$ (kW) to the product of solar cell or panel surface area A_s (m^2) and the direct irradiation of solar beam I_p (kW/m^2). I_p=1 kW/m^2 is commonly used for the calculation of nominal efficiency.

$$\eta_{sol-pow} = \frac{\dot{W}}{I_p \times A_s} = \frac{\dot{W}}{\dot{Q}_s} \tag{1.1}$$

Although higher efficiencies are reported from laboratories, a high-performance solar electric panel sold in the market yields about 15% efficiency under the midday sun in a clear day. An evaluation study on building-integrated solar electric panels reported the highest average overall efficiency of 10.3% (Fanney et al, 2001).

Price of a solar electric panel varies widely in the market. For example, retail price of a solar electric panel in Germany varies between €3 to €7 (Solar Rechner, 2005) per Wp (peak Watt), i.e. production of 1W under 1 kW/m^2 of solar radiation.

The biggest advantage of using solar electric panels for cooling would be the simple construction and high overall efficiency when combined with a conventional vapour compression air-conditioner. A schematic diagram of such a system is given in Fig. 1.2.

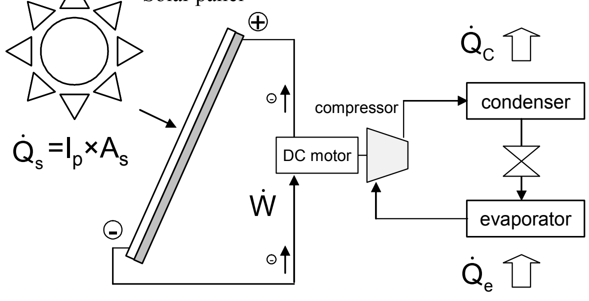

Figure 1.2 Schematic diagram of a solar electric compression air-conditioner

In Fig. 1.2, the power $\dot{W}$ is consumed by the mechanical compressor to produce the cooling power $\dot{Q}$. The efficiency of refrigeration machine is defined as the cooling power $\dot{Q}$ divided by $\dot{W}$ as in Eq. (1.2).

$$\eta_{pow-cool} = \frac{\dot{Q}_e}{\dot{W}} \tag{1.2}$$

Combination of the two efficiencies in Eq. (1.1) and Eq. (1.2) gives the solar-to-cooling or the overall efficiency of a solar electric cooling system as in Eq. (1.3).

$$\eta_{sol-cool} = \eta_{sol-pow} \times \eta_{pow-cool} = \frac{\dot{Q}_e}{\dot{Q}_s} \tag{1.3}$$

COP (Coefficient of Performance) is an alternative term to efficiency commonly used in refrigeration field.

Considering that the COP of a well-designed air-cooled vapour compression air-conditioner is in the range of 3 to 4, when it is combined with solar electric panels with 10% efficiency, the system will produce cooling at an overall efficiency between 30 and 40%.

Solar electric vapour compression cooling systems are rare and only a few systems are found in literature. Several solar electric cooling systems were developed at ILK Dresden ranging from an ice maker to a telecommunication post (Rudischer et al, 2005). All systems were designed for autonomous operation and packaged in standard containers. Cooling COPs of the vapour compression machines in those systems ranged from 1.1 to 3.3 for different evaporator temperatures between -5 and 15^{o}C and the condenser temperatures between 45 and 61^{o}C. Mono-crystalline PV modules and variable-speed compressors were used with batteries or generators as a backup.

There are several challenges in the broader commercialization of this type of systems:

Firstly, the systems should be equipped with some means to cope with the varying electricity production rate with time, e.g. electric battery, mixed use of solar- and grid electricity or a variable-capacity compressor and so on.

Secondly, high-efficiency air-conditioners based on environment-friendly refrigerants should be available in the market.

Finally, the price of a solar electric panel should be further decreased to compete with other solar cooling technologies.

Until today, the biggest problem with solar electric cooling is the high price of a solar electric panel. If a 10%-efficiency solar electric panel is combined with a vapour compression air conditioner with 3.0 COP, the overall efficiency will be 30%. Assuming the unit price of the solar electric panel is €5/Wp, the solar electric panel alone would cost €1,667 to produce 333 W electricity for 1kW cooling. This is about twice the cost for the solar thermal collectors needed to drive a water-cooled single-effect LiBr chiller with 0.7 COP in Grossman (2002).

Besides vapour compression cooling, some other types of electric cooling technologies can also be used in combination with solar electric panels.

Thermoelectric cooling uses Peltier effect first discovered by the French physicist Jean Charles Athanase Peltier in 1834. Modern thermoelectric elements are made of semiconducting materials such as bismuth telluride and antimony telluride alloys (Bi_2Te_3 and Sb_2Te_3). Since they have neither moving parts nor refrigerant and can be made very small, they have been used in electronic chip cooling, portable refrigerators and in space applications like satellite and space ships where physical size of a cooling system is extremely limited. COP of this system is currently very low, ranging from 0.3 to 0.6. Small thermoelectric air-conditioners with a few hundred watts capacity are available in the market.

A Stirling refrigerator can be connected to solar electric panels to provide cooling. Although an ideal Stirling cycle should work as efficiently as Carnot cycle, COPs of the Stirling refrigerators developed until now are lower than those of vapour compression counterparts. Ewert et al (1998) reported the test results of a small (maximum cooling capacity below 100W) free-piston Stirling refrigerator in a COP-temperature lift diagram. The COP decreased approximately from 1.6 to 0.8 while temperature lift (air-to-air) was varied from 13 to 33K with ambient temperature ranged from 23 to 28^{o}C. Berchovitz et al (1999) reported the COP of a similar machine (nominal capacity 40W), which decreased from 1.65 to 1.17 with the decreasing cold-side temperature from -1.4 to -19.1 while hot-side temperature was maintained between 28.4 and 30.3^{o}C . There are many practical difficulties in developing an efficient Stirling refrigerator or air-conditioner. Major problems are low COP and limited power density due to the poor heat transfer between working fluids (mostly helium) and the ambient (Kribus, 2002). For this reason, only a small Stirling refrigerator, where surface-to-volume ratio is relatively large, has competitiveness against small domestic vapour compression refrigerators.

Electrically-driven thermoacoustic refrigeration machine is another option for solar cooling. Its thermodynamic cycle resembles a series of Brayton cycles grouped together. Until now, the efficiencies of thermoacoustic cooling systems are lower than those of vapour compression systems. Poese et al (2004) reported the performance of a refrigeration system with a cooling capacity of 119W designed for 200-liter ice cream cabinet. The system yielded a COP of 0.81 with the heat transfer fluid temperatures in ambient (heat rejection) and cold (heat removal) heat exchangers at 33.9^{o}C and -24.6^{o}C respectively. These performance figures are comparable to those of the small Stirling refrigerators described above. Fischer and Labinov (2000) mentioned an on-going project at that time, which intended to develop a 10kW air conditioning system expecting COP of 2.0 with ambient temperature at 35^{o}C. But since then, no further information about this project could be found in literature. A thermoacoustic system has a very simple construction with no moving parts, which could provide higher reliability than a Stirling system. But as is the case with a Stirling system, cooling power density is low and no machine has been reported with a reasonably large capacity for air conditioning.

Magnetic cooling, which has long been used in cryogenics, is also a possibility. Magnetocaloric effect was discovered by Emil Warburg, a German physicist in 1881, who observed a piece of metal placed near a strong magnet was warmed up. Later this principle was reversely used to cool down objects at very low temperatures in cryogenics. Presently several groups of researchers are working on this technology for refrigeration and air conditioning. Recently, a few permanent-magnet room-temperature magnetic refrigeration systems have been developed (Gschneider, 2001; Shir et al, 2005). Gschneider (2001) demonstrated an overall COP of 3.0 with a rotary magnetic refrigerator/freezer, which compares favourably with conventional refrigerators. Although this technology has a potential of outperforming conventional vapour compression technology, the cost of magnetic material is prohibitively expensive [$1,830/kW cooling, gadolinium without processing cost - Fischer and Labinov (2000)] for practical application.

1.3 Solar thermal cooling

Solar thermal systems use solar heat rather than solar electricity to produce cooling effect. Solar thermal collectors convert sunlight into heat and this heat in turn drives a heat-driven refrigeration machine.

Solar collectors are available in different types and in a wide range of efficiency. Depending on its optical design, a solar collector can be classified into concentrating or non-concentrating type collector.

History of the concentrating type solar collector dates back to the time of Archimedes and his “burning mirror”, when he allegedly used bronze mirrors to focus sunlight to burn Roman ships in 3rd century B.C. The same type of solar collector was used to heat up Augustin Mouchot’s solar engine in the Paris World Exhibition 1878. Concentrating solar collectors are used to get a high temperature by using a large curved mirror to direct sunlight to a small absorber, through which a heat transfer fluid is pumped to catch the heat. Because they work best with direct solar rays, they are commonly equipped with tracking devices to follow the movement of the sun.

Non-concentrating type collectors do not have a reflective surface for concentrating sunlight. The world's first solar collector of this type is attributed to the Swiss scientist Horace de Saussure for his invention of “solar hot box” in 1760s. He made a wooden box with a glass plate covering its top. He put the box under the sun to let the sunlight penetrate the glass cover to warm up the inside. He realized that it might have important practical applications as it was small, inexpensive and easy to make. This hot solar box has become the prototype for the solar water heaters since late 19th century (Butti and Perlin, 1980). A non-concentrating solar collector has an absorber, which is usually a black-painted metal plate with a flow path for heat transfer fluid, encased with a glass cover and insulation material.

Regardless of the collector type, the absorber surface can be coated with a selective material that has a high absorption for the solar spectrum and low emittance for infrared radiation. The space between absorber and glass cover can also be evacuated to minimize heat loss.

Because concentrating type collectors normally have tracking devices, their investment and running costs are high. For this reason, they have been used mostly in high-temperature applications for power or process heat generation. But some stationary CPC (Compound Parabolic Concentrator) collectors are available for solar heating and cooling at reasonable prices.

Non-concentrating type collectors are dominant in the solar collector market. Among them, flat-plate solar collectors are the most common, which consist of a metallic absorber and an insulated casing topped with glass plate(s). Evacuated collectors have less heat loss and perform better at high temperatures. Evacuated collectors are typically made in a glass tube design, i.e. a metallic absorber inserted in an evacuated glass tube, to withstand the pressure difference between the vacuum and the atmosphere. Fig. 1.3 shows schematic diagrams of these two collectors.

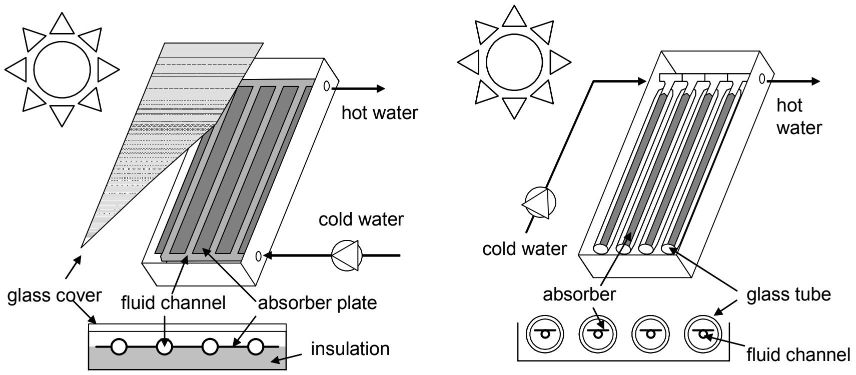

(a) Flat-plate type (b) Evacuated tube type

Figure 1.3 Schematic diagrams of non-concentrating solar collectors

A solar collector provides heat to the "heat engine" or "thermal compressor" in a heat-driven refrigeration machine. The efficiency of a solar collector is primarily determined by its working temperature. At a higher working temperature, the collector looses more heat to ambient and delivers less heat. On the other hand, the heat engine or thermal compressor generally works more efficiently with a higher temperature. A solar thermal system is designed in consideration of these two opposing trends.

1.3.1 *Thermo-mechanical cooling*

In a solar thermo-mechanical cooling system, a heat engine converts solar heat to mechanical power, which in turn drives a mechanical compressor of a vapour compression refrigeration machine. A schematic diagram of such a cooling system is shown in Fig. 1.4.

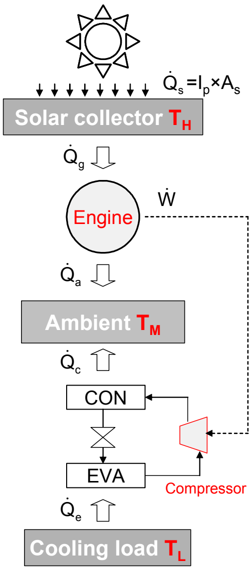

Figure 1.4 Solar thermo-mechanical cooling system

In the figure, a solar collector receives solar radiation $\dot{Q}_s$ [product of the surface area, A_s (m^2), and the solar radiation perpendicular to the surface I_p (kW/m^2), see Eq. (1.4)] from the sun and supplies $\dot{Q}_g$ to a heat engine at the temperature T_H. The ratio of supply heat $\dot{Q}_g$ to the radiation $\dot{Q}_s$ is defined as the thermal efficiency of a solar thermal collector, $\eta_{sol\text{-}heat}$.

$$\eta_{sol-heat} = \frac{\dot{Q}_g}{I_p \times A_s} = \frac{\dot{Q}_g}{\dot{Q}_s} \tag{1.4}$$

$\eta_{sol\text{-}heat}$ would be 1.0 if the solar collector is a perfectly insulated black body. In reality, $\eta_{sol\text{-}heat}$ is less than 1 due to optical and thermal losses.

A heat engine produces mechanical power $\dot{W}$ and rejects heat $\dot{Q}_a$ to ambient at temperature T_M. The efficiency of engine, $\eta_{heat\text{-}pow}$ is defined as the power produced per heat input $\dot{Q}_g$ in Eq. (1.5).

$$\eta_{heat-pow} = \frac{\dot{W}}{\dot{Q}_g} \tag{1.5}$$

The mechanical power $\dot{W}$ in turn drives the compressor in a refrigeration machine to remove heat $\dot{Q}_e$ from the cooling load at temperature T_L. Waste heat $\dot{Q}_c$, which is equal to the sum of $\dot{Q}_e$ and $\dot{W}$, is rejected to ambient at the temperature T_M. Efficiency of the refrigeration machine is the same as in Eq. (1.2).

Then the overall efficiency of a solar thermo-mechanical cooling system is given by the three efficiencies in Eq. (1.4), (1.5) and (1.2) as follows.

$$\eta_{sol-cool} = \eta_{sol-heat} \times \eta_{heat-pow} \times \eta_{pow-cool} = \frac{\dot{Q}_e}{\dot{Q}_s} \tag{1.6}$$

The maximum efficiencies of the real engine and refrigeration machine are limited by those of Carnot cycles working at the same temperatures. The efficiency of a Carnot power cycle working between T_H and T_M is given by

$$\eta_{heat-pow}^{id} = \frac{T_H - T_M}{T_H} \tag{1.7}$$

and the efficiency of a Carnot refrigeration cycle working between T_M and T_L is given by

$$\eta_{pow-cool}^{id} = \frac{T_L}{T_M - T_L} \tag{1.8}$$

The product of the two Carnot efficiencies in Eq. (1.7) and (1.8) gives the efficiency of an ideal heat-driven refrigeration machine working between the three temperatures as

$$\eta_{heat-cool}^{id} = \eta_{heat-pow}^{id} \times \eta_{pow-cool}^{id} = \frac{T_L}{T_H}\left(\frac{T_H - T_M}{T_M - T_L}\right) \tag{1.9}$$

, which limits the maximum efficiency achievable with any real heat-driven refrigeration machine working between the same temperatures.

In a solar thermo-mechanical system, the efficiency of a heat engine is of particular interest. Because the heat source temperature T_H varies in different projects, the performance of a real engine is often compared to that of a Carnot cycle working at the same temperatures. The ratio of real efficiency to Carnot efficiency is called “second law efficiency”. This is a measure of how closely a real machine operates to an ideal machine.

For solar power generation, Rankine and Stirling power engines have been popularly considered.

Solar Rankine systems were actively investigated in the 1970s and 80s when the world was suffering from high oil price. Prigmore and Barber (1975) designed a water-cooled organic Rankine cycle based on R-113 to produce turbine shaft work with 11.5% efficiency (58% second law efficiency) from 101.7 ^{o}C water from solar collectors. The turbine work could be used either to drive an electric generator or a R-12 refrigerant compressor. When 50% solar collector efficiency is assumed, the solar-to-power efficiency would have been 5.8%.

With higher heat source temperature, higher engine efficiency can be achieved. In early 1980s, the Coolidge Solar Irrigation project demonstrated a trough ORC (Organic Rankine Cycle) solar power plant in US. The system used a trough type concentrating collector and a toluene Rankine power cycle. A peak heat-to-power efficiency of 24% (57% second law efficiency) was attained with the maximum heat transfer fluid temperature of 268^{o}C (Larson, 1983). Higher power generation efficiency was reported from a large-scale solar power generation system. The Solar One demonstration plant operated between 1982 and 1988 in the west Mojave Desert of California and was equipped with a 35%-efficient (58% second law efficiency) Rankine power generation system driven by 516^{o}C superheated steam from a tower-mounted receiver on which solar radiation was focused by thousands of sun-tracking mirrors on the ground (Stein and Geyer, 2001).

If a 24%-efficient Rankine cycle working at 268^{o}C heat is connected to a state-of-the-art trough collector of today, e.g. EuroTrough from Geyer et al (2002) has an efficiency of 67% at this temperature, the system would yield about the same efficiency as a high-performance solar electric panel (c.a. 16%) in the market.

Rankine cycles are also often used in combined generation systems. Oliveira et al (2002) reported test results of a small hot water-driven tri-generation system based on a Rankine-ejector cycle. This system produced the maximum of 1.5kW electricity and 5kW cooling. The average cooling COP was about 0.3 and the efficiency of the Rankine cycle was between 3% and 4% (15-20% second law efficiency) with 95^{o}C hot water and 20^{o}C heat sink.

Stirling engines have also been actively studied for power generation from the sun. Stirling engines are well known for their silent and low-temperature operability. But also they can operate at a very high temperature as well at which a Rankine engine cannot. Although Stirling cycle efficiency approaches that of a Carnot engine in theory, efficienciesH of Stirling engines in the past were reported in the range of 55 to 88% of second law efficiency (Reader and Hooper, 1983). The high performance of a Stirling engine was successfully demonstrated in several solar dish power programs in US, where the highest heat-to-electricity efficiency of 41% (≈ 57% of second law efficiency) was reported (Stein and Diver, 1994). Its success in this particular solar application is attributed to its high-temperature operability (gas temperature above 700^{o}C) and relatively simple design. Stirling engines have hardly been reported for the application to solar cooling. The reasons may be firstly, the maximum capacity of a Stirling engine is practically limited by the fact that its efficiency decreases with increasing capacity, i.e. decreasing surface-to-volume ratio, and secondly, a Stirling cycle is not as versatile as a Rankine cycle for being integrated into various hybrid systems for improved efficiency or multi-functionality.

In order for a solar thermo-mechanical cooling system to be competitive, the combination of a solar collector and a heat engine should be at least comparable to a solar electric panel in terms of price.

Assuming that a 60%-Carnot-efficient engine works with 150^{o}C heat source and 28^{o}C heat sink, the heat-to-power efficiency of this engine will be 17%. Among non-concentrating type solar collectors, only some evacuated tube type collectors can operate efficiently at 150^{o}C. A high performance evacuated tube collector working with 60% efficiency at 150^{o}C is available at the price of €771/m^2 [Sydney SK-6, Henning (2004)]. If this collector is combined with the heat engine, its solar-to-power efficiency would be 10%. Per 1m^2 of the solar collector, 100W of work will be produced under 1kW/m^2 solar radiation. Therefore the collector price per produced work is €7.71/Watt. This is rather high compared to the price of a solar electric panel in the current market [€3-7/Wp, Solar Rechner (2005)]. And it does not even include the cost of the heat engine.

A solar thermo-mechanical cooling system is likely more expensive than a solar electric cooling system. But these days, the merit of producing power, heat and cooling from a single system makes it often considered for the development of combined distributed generation systems.

1.3.2 Sorption cooling

Sorption cooling uses physical or chemical attraction between a pair of substances to produce cooling effect. Sorption is a collective term for the process in which one substance takes up or holds another. The reverse process is called desorption or often as generation. Both processes are irreversible and commonly accompanied by the exchange of heat with environment. Cooling effect is achieved by properly arranging these processes. Since the primary energy involved in these processes is heat rather than work, a sorption cooling system has a unique capability of transforming thermal energy directly into cooling power.

Among the pair of substances, the substance with lower boiling temperature is called sorbate and the other is called sorbent. Heat is generated while the sorbent absorbs the sorbate, which plays the role of refrigerant. Reversely, heat should be added to the sorbent to separate the refrigerant.

Fig. 1.5 shows a schematic diagram of a closed sorption system. In the figure, the component where sorption takes place is denoted as absorber and the one where desorption takes place is denoted as generator.

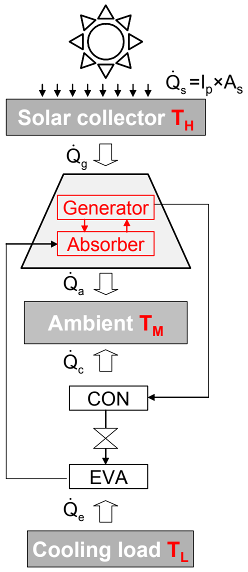

Figure 1.5 Solar sorption cooling system

The generator receives heat $\dot{Q}_g$ from the solar collector to regenerate the sorbent that has absorbed the refrigerant in the absorber. The refrigerant vapour generated in this process condenses in the condenser rejecting the condensation heat $\dot{Q}_c$ to ambient.

The regenerated sorbent from the generator is sent back to the absorber, where the sorbent absorbs the refrigerant vapour from the evaporator rejecting the sorption heat $\dot{Q}_a$ to ambient. In the evaporator, the liquefied refrigerant from the condenser evaporates removing the heat $\dot{Q}_e$ from the cooling load.

In an adsorption system, each of the adsorbent beds alternates generator and absorber function due to the difficulty of transporting its solid sorbent from one to another.

The combination of a generator and an absorber is equivalent to that of a heat engine and a compressor in Fig. 1.4. For this reason, the combination is often referred to as thermal compressor.

Due to the ambiguity in defining engine and compressor functions in a sorption cooling machine, a single heat-to-cooling efficiency in Eq. (1.10) is used, which can be defined for any heat-driven cooling machine.

$$\eta_{heat-cool} = \frac{\dot{Q}_e}{\dot{Q}_g} \qquad (1.10)$$

This efficiency of a heat-driven cooling machine, which is more commonly called COP, is often compared with the ideal efficiency in Eq. (1.9) to measure how the system efficiency deviates from ideal efficiency.

Sorption processes are called in different names depending on type of the sorbent and also on whether it takes place in an open or a closed environment.

Absorption refers to a sorption process where a liquid or solid sorbent absorbs refrigerant molecules into its inside and changes physically and/or chemically in the process.

Adsorption, on the other hand, involves a solid sorbent that attracts refrigerant molecules onto its surface by physical or chemical force and does not change its form in the process. When a chemical reaction takes place between adsorbent and refrigerant, it is particularly called chemical adsorption or chemisorption.

Desiccation refers to a sorption process where a sorbent, i.e. a desiccant, absorbs the moisture from humid air. This process is employed in an open sorption cycle, which is more commonly called desiccant cycle. Open sorption cycles are classified into either liquid or solid desiccant cycles depending on phase of the desiccant used.

1.3.2.1 Absorption

Invention of absorption refrigeration machine is attributed to Edmond Carré, who built a water-sulfuric acid machine in 1850 (Niebergall, 1981). His machine was also used in the first solar cooling machine demonstrated by Augustin Mouchot at the Paris World Exhibition in 1878 (Thévenot, 1979).

Absorption refrigeration has been most frequently adopted for solar cooling for several reasons.

First of all, it requires very low or no electric input. A famous example is the heat-driven ammonia diffusion refrigerator manufactured by Electrolux for the first time in 1925 based on Swedish students, Carl G. Munters and Baltzar von Platen. The machine worked very quietly and completely without electricity. It had been distributed to millions of homes worldwide until 1950s. This type of refrigerator is still being produced for hotel mini-bars and caravans. Another example is a self-circulating LiBr-water chiller, the concept of which was originally suggested by Edmund Altenkirch (Stephan, 1983). This system has no moving part inside the absorption unit as illustrated in Fig. 1.6.

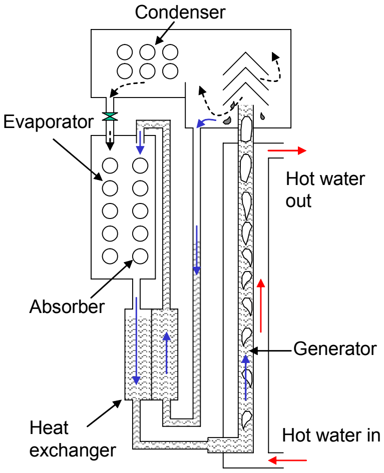

Figure 1.6 Self-circulating LiBr-water absorption chiller

LiBr solution is supplied from an absorber to the bottom of the generator by gravity, where it is heated by hot water. The solution boils and is driven upwards by the buoyancy of the generated steam bubbles. At the top of the generator, the heavy solution is separated from the steam and flows further to an absorber at a high position. From the bottom of the absorber, the solution flows back to the generator.

Yazaki, a Japanese manufacturer, produces such a self-circulating LiBr-water chiller with 35 kW cooling capacity, which consumes only 210 W of electricity for chilled water circulation (Yazaki Energy Systems Inc., 2005).

Secondly, for the same capacity, the physical dimension of an absorption machine is smaller than for solid sorption machines due to the high heat transfer coefficient of the liquid sorbent, i.e. absorbent. Besides, the fluidity of the absorbent gives greater flexibility in realizing a more compact and/or efficient machine.

Finally and perhaps the most importantly, because absorption refrigeration had already established its position in refrigeration industry, the well developed sorption community supported its application in solar cooling by providing expertise in operation and manufacturing.

Single-effect LiBr-water chiller, the most popular machine in solar cooling for its low-temperature operability, has been incorporated in numerous studies including the following demonstration projects.

A research group started a series of researches on solar absorption cooling by designing and optimizing solar heating and cooling systems for several locations (Löf and Tybout, 1974). One of their conclusions was that a combined heating and cooling system was more economical than a heating alone system in most locations. A solar house with a combined cooling and heating system based on a single-effect LiBr-water chiller was investigated in a university campus (Ward and Löf, 1975; Ward et al, 1979)

Hattem and Dato (1981) installed a solar absorption cooling system at EU Joint Research Center in Ispra, Italy, which consisted of a 4.6kW LiBr-water chiller and 36m^2 flat plate collectors. They reported theoretical and experimental results were in good agreement and the measured seasonal average of the chiller COP and the overall cooling efficiency were 0.54 and 9.6% respectively.

Al-Karaghouli et al (1991) reported the operation results of a solar cooling system installed at the Solar Energy Research Center in Iraq, which was considered the largest solar cooling system at the time. The system was equipped with two 60 ton LiBr-water chillers, 1577 evacuated tube collectors and various backup systems. They reported daily average collector efficiency of 49%, chiller COP 0.62 and solar fraction of 60.4%.

Best and Ortega (1999) summarized the results of Sonntlan Mexicali Solar Cooling project from 1983 to 1986 in Mexico. The solar cooling system included six single-family houses, 316 m^2 flat plate collectors, 30m^3 heat storage, a 90kW ARKLA-WFB 300 Solaire LiBr-water chiller and a 200 kW cooling tower. After a series of improvements on the solar collector system, the system managed to deliver enough cooling power that improved the yearly solar fraction up to 75%. COP of the absorption chiller varied from 0.53 to 0.73 when hot water was provided at the temperatures between 75 to 95 ^{o}C.

Izquierdo et al (2005) reported the performance of a LiBr-water chiller with 35kW nominal cooling capacity driven by hot water from 49.9m^2 flat plate collectors installed at a typical Spanish house in Madrid. Since the solar system was originally designed for 10 kW cooling capacity, the absorption chiller operated far away from its nominal working condition and yielded the maximum cooling capacity of only 7.5kW at the average COP of 0.34.

Due to lack of small-capacity LiBr chillers (<35kW) in the market, some small single-effect LiBr-water chillers have been developed recently and are currently under field test.

Storkenmaier et al (2003) reported the development of a 10kW water-cooled single-effect LiBr-water chiller. The machine is reported capable of producing 15^{o}C chilled water from 85^{o}C hot water with the COP 0.74 being cooled by cooling water at 27^{o}C. The design chilled water temperature was set rather high at 15^{o}C for the use of chilled ceilings. The cooling capacity was reported to vary between 40 to 160% of the nominal capacity with the hot water temperature increasing from 56 to 105^{o}C. The design is currently being improved for launching in the market in 2007 by the German company Phönix.

Safarik et al (2005) presented the performance data of a recently developed water-cooled single-effect LiBr-water chiller. The machine produced about 16kW cooling at 15^{o}C at the COP 0.75 with 90^{o}C hot water and 32^{o}C cooling water. With 27^{o}C cooling water, COP increased to 0.8 and 80^{o}C hot water was enough to produce the same cooling capacity. This machine is currently being field-tested in various locations in Europe by the German company EAW.

Double-effect LiBr-water machines were also used in a few solar cooling projects. Due to the requirement of a high driving temperature (ca. 150^{o}C), in most cases, the hot water from solar collectors was fed to the low-temperature generator of a double-effect machine (Ishibashi, 1979; Lamp and Ziegler, 1998). This system has a merit of alternatively operating the system in a single-effect cycle with solar heat or in a double-effect cycle with the heat from fuel combustion so that it can achieve a high seasonal efficiency.

It is also possible to drive a double-effect machine solely with solar heat when a concentrating solar collector is used. Lokurlu and Müller (2005) reported a system installed at a hotel in Turkey, which consisted of a steam-driven double-effect machine, a trough type parabolic solar collector and a backup steam boiler. The trough collector with 180m^2 aperture area heated pressurized water up to 180^{o}C and this water in turn generated 144^{o}C steam (4bar) for a 140kW double-effect LiBr-water chiller.

Ammonia absorption machines have also been popular. Although not as popular as LiBr machines, they have been used for various applications, mostly where a LiBr-water machine was not deemed suitable, e.g. refrigeration, air-cooled or heat pump operation.

Several studies were reported of the solar intermittent ammonia absorption refrigerators (Trombe and Foex, 1957; Chinnappa, 1961; Paassen, 1987). An intermittent ammonia absorption cycle can make an effective solar refrigerator that would be particularly appreciated in developing countries because it requires no power other than heat and guarantees a long life without any trouble. But in this application, absorption technology seems to have been overwhelmed by the adsorption counterpart. Hardly any study on an intermittent absorption refrigerator has been reported since early 1990.

The ammonia diffusion cycle of the early heat-driven domestic refrigerators has also found its place in solar cooling. Because the diffusion cycle needs no moving part, it makes a fully autonomous system when combined with solar collectors (Gutiérrez, 1988; Kunze, 2000; Jakob et al, 2003). According to Jakob et al (2003), recent development activities on solar DAR (Diffusion Absorption Refrigerator) in Europe cover cooling capacities between 16W and 2.5kW and cycle COPs between 0.2 and 0.5.

For development of continuous solar-driven refrigerators or heat pumps, single-effect ammonia machines have been the most frequently considered (Shiran et al, 1982; McLinden and Klein, 1983; Alvares and Trepp, 1987; Best, 1991; ARTISC, 2003).

Demonstrations with solar ammonia absorption machines were relatively rare. Recently, an ammonia absorption refrigeration system has been demonstrated at a winery in Graz, Austria (SACE Evaluation report, 2003). The system consists of a 10kW water-cooled ammonia-water absorption chiller, 100m^2 flat collectors and a 40kW wood chip boiler as a backup heater. The system was designed to maintain a wine storage at 10 to 12^{o}C.

Richter and Safarik (2005) introduced two small solar-driven water-cooled ammonia absorption cooling plants operating in Germany. One air conditioning system produced 15kW cooling at 3^{o}C driven by 95^{o}C hot water and the other produced 20kW at -6^{o}C driven by hot water at 100^{o}C. In both cases, COP was about 0.54.

Other than introduced above, numerous studies have been reported including various absorption cycles (Chinnappa and Martin, 1976; Sofrata et al, 1981; Alizadeh, 2000; Göktun and Er, 2001) and different working pairs (Sawada et al, 1994; Romero et al, 2001; Arivazhagan et al, 2005) and so on.

To summarize, current absorption technology can provide various absorption machines with COPs ranging from 0.3 to 1.2. Choice of an absorption cooling machine is primarily dependent on the performance of the solar collector to be used.

For solar collectors capable of efficiently working at around 150^{o}C, double effect LiBr-water chillers with COPs around 1.2 are available for air-conditioning. For refrigeration, ammonia-water GAX chillers with COPs around 0.8 can be considered. Heat transfer medium can be either a liquid with a high boiling temperature or steam. A high-performance evacuated tube or a concentrating type collector can be considered. According to Collector Catalogue 2004 (2004), a 40%-efficient evacuated tube collector at this temperature level costs €600-€700/m^2 (gross area).

For less expensive collectors working at around 90^{o}C, a single-effect LiBr-water or an ammonia-water absorption machine with a COP between 0.6 and 0.8 can be considered. Price of a solar collector varies widely in this temperature range. The price of a 50%-efficient collector at 90^{o}C ranges between €300 and €600/m^2.

1.3.2.2 Adsorption

Strictly speaking, physical adsorption is different from chemical adsorption in the aspect that physical adsorption does not involve any change in chemical composition nor in phase in the process. Although this distinction is often ignored in refrigeration field, physical and chemical adsorption technologies are separately presented.

Physical adsorption

Adsorbents like zeolite, silica gel, activated carbon and alumina are physical adsorbents having highly porous structures with surface-volume ratios in the order of several hundreds. They have numerous micro-pores that can selectively catch and hold certain types of substances, i.e. adsorbates. When they are saturated with the adsorbates, they can be regenerated simply by being heated. For their efficient separation and regeneration capabilities, they have been actively used in various separation processes.

Its capability of removing a gaseous substance makes an adsorbent useful for refrigeration. If an adsorbent and a refrigerant are contained in the same vessel, the adsorbent would maintain the pressure by adsorbing the evaporating refrigerant. The process is, however, intermittent because the adsorbent must be regenerated when it is saturated. For this reason, multiple adsorbent beds are required for continuous operation.

Some early adsorption refrigeration machines of 1920-1930s are briefly described in Niebergall (1981) including the SO_2-silica gel refrigerator of Safety Car Heating & Lighting Co for the transportation of ice on railways in USA and a methyl alcohol-activated carbon refrigerator of Amundsen Refrigerator Co. in Norway.

Like the other heat-driven refrigeration technologies, the oil crisis in the 1970s renewed the interest in adsorption technology. Pioneering work of Tchernev (1978) is said to have inspired many studies that followed (Wang and Oliveira, 2005).

Many studies on intermittent solar adsorption ice maker or refrigerators have been reported. Employed working pairs included activated carbon and methanol or ammonia (Pons and Guilleminot, 1986; Wang et al, 1997; Wang et al, 2000; Critoph, 2002) and silica gel-water (Grenier et al, 1988; Hildbrand et al, 2004). Except for a few indirect system (e.g. Wang et al, 2000), most of the solar adsorption refrigerators had solar collector-integrated adsorbers so that the adsorbent could be directly exposed to sunlight for higher efficiency. For this reason, performance of such a system has been usually reported in terms of solar-to-cooling or solar COP, i.e. cooling power divided by solar input. Current solar adsorption technology can provide a daily ice production of 4 to 7 kg per unit square meters of solar collector with a solar-to-cooling COP between 0.1 and 0.15 (Wang and Oliveira, 2005).

Recently, several small-capacity adsorption chillers have been developed for solar air-conditioning (Saha et al, 2001; Nuñez et al, 2004; Liu et al, 2005), which were all based on the working pair of silica gel-water. Cooling capacities were reported between 3.2 and 3.6 kW with reasonable evaporator temperatures. COPs ranged from 0.2 to 0.6 with heating temperatures varied from 55 to 95^{o}C. Unlike the more common single-staged double-bed systems, Saha et al (2001) developed a double-staged four-bed cycle machine to use very low driving temperatures. The machine produced 3.2kW cooling with COP of 0.36 from 55^{o}C hot water.

Presently, there are two major manufactures of adsorption chillers, namely Nishiyodo, Mayekawa and Takeshima (Saman et al, 2004). Their machines are all based on silica gel-water with cooling capacities between 70 and 350kW. Nishiyodo is know to have introduced the first machine of this kind in 1986 (Wang and Oliveira, 2005). According to the manufacture's specification (HIJC USA Inc., 2005), Nishiyodo's ADCM1-025 produces 72kW cooling from 90^{o}C hot water with COP of 0.66 when 29^{o}C cooling water is supplied. The operation weight of this model is 5.5 ton and the dimension is 2.4×3.6×1.8m^3, which give mass-basis and volumetric specific cooling powers (SCP) of 13W/kg and 4.6kW/m^3 respectively. Performance of this adsorption chiller is comparable to that of a commercially available single-effect LiBr-water absorption chiller. For example, WFC-SC20 from Yazaki produces 70kW cooling from 88^{o}C hot water with COP 0.7 when cooling water temperature is 31^{o}C (Yazaki Energy Systems Inc., 2005). Its operation weight is 1.2 ton and the dimension is 2×1.1×1.3m^3, which give 58W/kg and 24.5kW/m^3 as mass-basis and volumetric SCPs respectively. By comparison of SCPs, the adsorption chiller is 4.6 times heavier and 5.4 times bulkier than the absorption chiller. This comparison clearly shows one major problem associated with adsorption technology, i.e. low cooling power density.

Because of poor heat transfer characteristics and limited capacity of an adsorbent, an adsorption chiller is likely bulkier than an absorption chiller for the same capacity. Although an adsorption chiller has an advantage of operating with a wider range of heating temperature, the drawbacks due to low SCP significantly prevents this technology from its wider promotion. For a high SCP, various ideas have been tried including the use of extended surfaces such as plate-fin heat exchangers (Liu et al, 2005; Boer at al, 2005), adsorbent-coated heat exchangers (Talter and Erdem-Şenatalar, 2000; Wojcik et al, 2001), consolidated composite adsorbents (Tamainot-Telto and Critoph, 1997; Poyelle et al, 1999; Wang et al, 2004) and so on.

There also have been efforts to increase the COP. Multi-bed regenerative cycle uses the adsorption heat of one adsorber to heat another adsorber in regeneration phase by selectively circulating the heat transfer medium (Tchernev and Emerson, 1988; Pons and Poyelle, 1999; Wade et al, 1990).

Tchernev and Emerson (1988) developed a gas-fired double-bed regenerative zeolite-water system and reported a cooling COP of 1.2 and a heating COP of 1.8. In this system, a heat transfer fluid (oil) heated up to 204^{o}C by a gas boiler was circulated between two zeolite containers for regeneration. The COP varied from 1.5 to 0.9 when ambient temperature was increased from 27 to 38^{o}C for a constant SCP at 36W/kg. COP went down from 1.2 to 0.7 when its SCP was tripled to108W/kg.

Pons and Poyelle (1999) analyzed different types of advanced adsorption cycles based on zeolite-water and activated carbon-methanol. COPs of the cycles were estimated between 0.55 and 0.92 for water-cooled air-conditioning with the heat source temperatures ranging 140 to 230^{o}C.

As in absorption cycles, it is possible to reuse condensation or adsorption heats of one cycle for the regeneration of the other by staging or cascading (Douss and Meunier, 1989; Schawe, 2001; Akahira et al, 2005). In a typical cascading cycle, an adsorbent with high adsorption temperature of a so-called topping cycle is reused to drive a bottoming cycle with a low-temperature adsorbent. Douss and Meunier (1989) used zeolite-water in the topping cycle and active carbon-methanol for the bottoming cycle. COP was reported as 1.06 and SCP was 37W/kg of adsorbent.

Adsorption chillers seem to be comparable with absorption chillers in terms of maximum achievable COP. But their cooling power densities are much lower. For a high SCP, a research trend is to develop composite adsorbents to include chemical salts, which makes the distinction between physical and chemical adsorption meaningless.

To summarize, adsorption technology may be competitive in large solar cooling systems where its low power density is not a problem. But for small- or medium size solar cooling systems, it tends to be too bulky and expensive (Saman et al, 2004).

Chemical adsorption

The first idea of chemical absorption cooling dates back to as early as 1823, when Michael Faraday, the most influential scientist in the field of electricity, observed ammonia was absorbed by silver chloride and calcium chloride in his experimental setup for gas liquefaction.

Chemical adsorption or chemisorption is characterized by the strong chemical bond between the adsorbate and the adsorbent. Therefore it is more difficult to reverse and thus requires more energy to remove the adsorbed molecules than in a physical adsorption. Adsorption capacity is also much larger. Besides, unlike physical adsorption, chemical adsorption is a monovariant process. That is, once pressure is fixed, the reaction temperature is automatically determined.

The most commonly used chemical adsorbent has been calcium chloride ($CaCl_2$) in solar cooling applications. Calcium chloride adsorbs ammonia to produce $CaCl_2{\cdot}8NH_3$ as a product and it is also capable of absorbing water to produce $CaCl_2{\cdot}6H_2O$. This adsorbent expands significantly during the process and thus requires a room for the expansion in an adsorber design (Wang et al, 2004). It has also been used together with other physical adsorbents including some silicates (Tokarev et al, 2002; Restuccia et al, 2004).

Tokarev et al (2002) developed a composite material by impregnating calcium chloride in MCM-41 (a silicate) matrix, which has the maximum water absorption capacity of 0.75g per gram of dry adsorbent. Simulation results suggested that a COP of 0.7 was achievable with condenser and generation temperatures at 40^oC and 110^oC respectively.

Restuccia et al (2004) developed a chiller based on a similar composite and reported COP 0.6 at the condenser temperature of 35^oC and the generation temperature between 85 and 95^oC.

Increase of COP can also be realized by recycling adsorption heat between multiple numbers of adsorbers. Neveu and Castaing (1993) proposed an ammonia cycle with two different metallic salt beds. The first bed was filled with $MnCl_2$ and the second with $NiCl_2$. Heat was supplied only to the first bed and the second bed was heated by the adsorption heat from the first one. COP was expected to be 0.6 for 40^oC condenser and -10^oC evaporator temperature. They also predicted COP of 0.7 would be possible if $SrCl_2$ and $FeCl_2$ were used.

For its stability and less corrosiveness at high temperatures, a chemical adsorption cycle was also considered for a topping cycle in hybrid cascading cycles. Cerkvenik et al (1999) proposed a sorption cascading cycle for a COP of 1.8. The system consisted of a bottoming double-effect LiBr-water absorption cycle and a topping CaO-water chemical adsorption cycle. They also considered other salts like MgO, SrO and BaO and mentioned that new methods of salt preparation was in development for the use of MgO in the topping cycle. This multi-effect cycle requires, however, a very high heating temperature, which makes its application more attractive to fuel-fired cooling.

Because physical adsorbents lack cooling power and chemical adsorbent have relatively high reaction temperatures, chemical and physical adsorbents are often mixed together in various compositions to create a new composite adsorbent with desirable properties.

Metal hydride cooling, which is another branch of chemical adsorption cooling, is different from the others in the aspect that it uses hydrogen as a refrigerant. Since the first discovery of the absorption of hydrogen into palladium metal by Phil T. Graham in 1866, metal hydride systems have been studied mostly for hydrogen storage. But as more interest is given to hydrogen as the fuel of the future, the interest in metal hydride cooling systems is also increasing for their integration into hydrogen-fuelled systems.

In a basic two-bed cooling system, one bed is filled with a high-temperature hydride and the other is filled with a low-temperature hydride. In recharge mode, the high temperature bed is heated to release hydrogen while the low temperature bed is cooled to absorb the hydrogen. When the high temperature bed is cooled in cooling mode, hydrogen is released from the low temperature bed creating cooling effect by absorbing heat.

The research issues on metal hydride cooling are basically the same as the other adsorption technologies including the enhancement of specific cooling capacity and heat transfer in the beds. These issues are more important for a metal hydride system in the respect that no component in the system can take advantage of the high heat transfer coefficient from the phase change of the refrigerant. Driving temperature of a single-stage system starts from as low as 80^oC depending on the hydride and the heat rejection temperature. COPs of single-stage systems are in the vicinity of 0.5 (Gopal and Murthy, 1995; Hovland, 2002).

1.3.2.3 Desiccant cooling

Open sorption cooling is more commonly called desiccant cooling because sorbent is used to dehumidify air. In a basic desiccant cooling system, the cooling effect is produced by evaporative cooling, i.e. by evaporating water in a dry air flow. But desiccant cooling does not only refer to the desiccant-assisted evaporative cooling but to the other systems where desiccant dehumidification is adopted.

Evaporative cooling is a very efficient cooling method because, when dry air is available, it needs only a small amount of power to circulate water and air. But, in a humid environment, an evaporative cooler does not perform satisfactorily because humid air cannot induce enough evaporation of water. In a basic desiccant cycle, i.e. in a desiccant-assisted evaporative cooling system to be more precise, a desiccant dehumidifier supplies dry air to an evaporative cooler regardless of the climate conditions at the expense of heat input to the desiccant for regeneration.

Various desiccants are available in liquid or solid phases. Since desiccation is a sorption process of selectively removing the moisture from humid air, basically all water absorbing sorbents can be used as a desiccant. Examples are silica gel, activated alumina, zeolite, LiCl, LiBr and so on. Some metallic salts that are soluble in water can be used as liquid desiccants in the form of aqueous solutions.

History of liquid desiccant cooling dates back to 1930s when Kathabar Inc. is known to have produced the first LiCl system. This company has been continuously developing several LiCl dehumidification systems until today. Due to the high corrosiveness of LiCl solution, various construction materials have been considered and currently, one of their models is being fabricated out of fiber reinforced plastic.

In a liquid desiccant cooling system, the liquid desiccant circulates between an absorber and a regenerator in the same way as in an absorption system. A recuperative heat exchanger can be used between the absorber and the regenerator for an increased COP. Main difference is that the equilibrium temperature of a liquid desiccant is determined not by the total pressure but by the partial pressure of water in the humid air to which the solution is exposed to.

A typical liquid desiccant system is shown in Fig. 1.7.

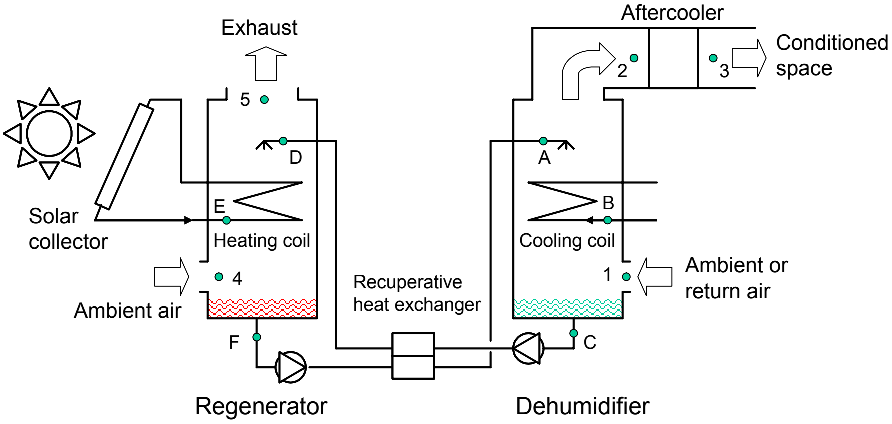

Figure 1.7 A liquid desiccant cooling system with solar collector

In the dehumidifier in Fig. 1.7, a concentrated solution is sprayed at point A over the cooling coil at point B while ambient or return air at point 1 is blown across the stream. The solution absorbs moisture from the air and it is simultaneously cooled down by the cooling coil. The results of this process are the cool dry air at point 2 and the diluted solution at point C. Depending on the cooling load of the conditioned space, an aftercooler further cools down this air stream.

In the regenerator, the diluted solution from the dehumidifier is sprayed over the heating coil at point E that is connected to solar collectors and the ambient air at point 4 is blown across the solution stream. Some water is taken away from the diluted solution by the air while the solution is being heated by the heating coil. The resulting concentrated solution is collected at point F and hot humid air is rejected to the ambient at point 5.

A recuperative heat exchanger preheats the cool diluted solution from the dehumidifier using the waste heat of the hot concentrated solution from the regenerator, resulting in a higher COP.

On the other hand, a solid desiccant cooling system is quite different in its construction mainly due to its non-fluid desiccant. The first solid desiccant system was patented by N.A. Pennington in 1955 (Pennington, 1955). His invention consisted of two revolving wheel structures, i.e. a desiccant wheel and a heat exchange wheel, with an air heater in-between and two direct evaporative coolers for the two air streams from and to the conditioned space. Until today, this design remains popularly commercialized in the market. Unlike its liquid counterpart, there is no risk of corrosion because solid desiccants exert much less corrosiveness on metal surfaces and also because they are commonly packed in honeycomb-shaped plastic structures.

Fig. 1.8 shows an example of solar-driven solid desiccant cooling system. The system has two slowly revolving wheels and several other components between the two air streams from and to a conditioned space. The return air from the conditioned space first goes through a direct evaporative cooler and enters the heat exchange wheel with a reduced temperature (A→B). It cools down a segment of the heat exchange wheel which it passes through (B→C). This resulting warm and humid air stream is further heated to an elevated temperature by the solar heat in the heating coil (C→D). The resulting hot and humid air regenerates the desiccant wheel and it is rejected to the ambient (D→E).

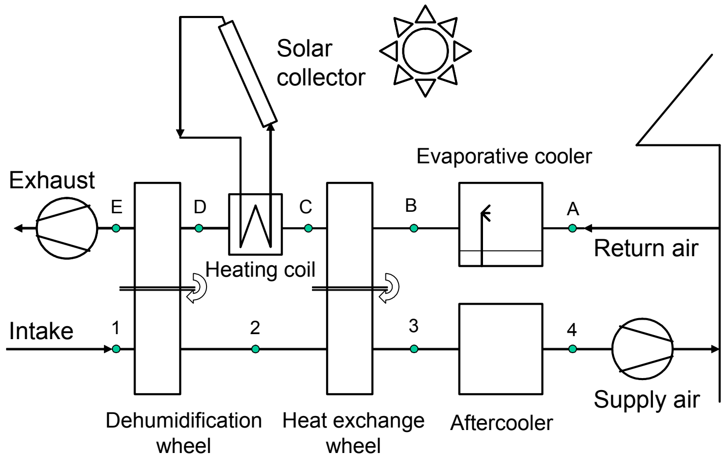

Figure 1.8 A solid desiccant cooling system with solar collector

On the other side, fresh air from the ambient enters the regenerated part of desiccant wheel (1→2). Dry and hot air comes out of the wheel as the result of dehumidification. This air is cooled down by the heat exchange wheel to a certain temperature (2→3). Depending on the temperature level, it is directly supplied to the conditioned space or further cooled in an aftercooler (3→4).

If no aftercooler is used, cooling effect is created only by the heat exchange wheel, which was previously cooled by the humid return air at point B on the other side. The temperature at point 3, i.e. T_3, cannot be lower than T_B, which in turn is a function of the return air condition at point A. If the return air at point A is not dry, T_3 cannot be lowered enough for cooling. For this reason, use of an aftercooler is common. Depending on the required temperature, a direct or indirect evaporative cooler or a cooling coil from a compression or an absorption chiller can be used.

From a thermodynamic point of view, the dehumidification process is not much different from a closed sorption process. Neglecting the enthalpy changes in the air flow, the same heat will be required to remove 1kg of water from a sorbent regardless it is in a closed vessel or it is in a humid air stream. Therefore, in principle, the COP of a desiccant system should be similar to its closed counterpart. For example, COP of 0.7 was said achievable with a solid desiccant cooling system under "normal" operating conditions (Henning, 2004). Similar COPs were also reported for liquid dehumidifiers (Matsushita et al, 2005). But in practice, COP varies widely depending on operating conditions.

In a very dry region, an evaporative cooler alone may be able to meet the whole cooling demand for air-conditioning. In this case, energy is consumed only for circulation of water and air, leading to a very high cooling COP. This high COP is the result of the free supply of water, which must be generated at the expense of extra heat input in a closed sorption system. Therefore, when there is not much need of dehumidification, a desiccant-assisted evaporative cooling system operates closely to a pure evaporative cooler and a very high COP can be achieved. In a humid climate, on the contrary, its performance would be very poor.

Influence of the local climate conditions on the performance of a desiccant-assisted evaporative cooling system was investigated by Eicker et al (2001). The authors presented the simulation results of a system based on solar air collectors in four different climates including Jakarta (Indonesia), Phoenix (Arizona, US), Seville (Spain) and Stuttgart (Germany) ranging from tropical to moderate European climates. The highest COP of 4.04 was reported for Jakarta followed by 1.12 for Seville, 1.02 for Phoenix and 0.57 for Stuttgart. The highest COP in Jakarta is mainly due to the operation mode in which the system operated 88% of time. In this mode, due to the high humidity in the conditioned space, the system operated without using the direct evaporative cooler on the supply air side and produced virtually no cooling power. In total, the system met only 1% of the total cooling demand. In other systems, however, this percentage was 78% in Seville, 75% in Phoenix and 89% in Stuttgart.

Nevertheless, desiccant dehumidification can be a very efficient option when there is a substantial latent cooling load. In a conventional refrigeration system, air is cooled down near to its dew temperature for moisture removal and reheated to a comfortable temperature before being supplied. Because desiccant dehumidification does not need this super-cooling and reheat processes, it can provide dry air more efficiently. Besides, desiccant dehumidification process is known to kill airborne viruses and bacteria cleaning the supply air of biological contamination (Kovak et al, 1997). For the advantages in producing a large amount of quality air, desiccant-assisted cooling systems become more and more popular in commercial and public buildings with large ventilation needs such as supermarkets, theaters, hospitals, hotels, schools and so on.

Since evaporative coolers cannot operate efficiently for all applications, combinations of desiccant dehumidification and other types of refrigeration methods are increasingly being considered. For example, when desiccant dehumidification is combined with a conventional or an absorption chiller, a smaller chiller can be used than otherwise needed. And also there is a potential of higher overall efficiency by using the waste heat from the chillers for desiccant regeneration (Fathalah and Aly, 1996; Tsay et al, 2005).

A desiccant cooling system is actually a complete HVAC system which has ventilation, humidity and temperature control devices in a ductwork. Therefore it is inappropriate to compare a desiccant cooling system with such components as chillers. Nevertheless, desiccant dehumidification offers, at least, a more efficient humidity control than the other technologies. When there is a large ventilation or dehumidification demand, solar-driven desiccant dehumidification can be a very good option.

1.4 Other technologies

Some other cooling technologies that were not mentioned in the previous sections are briefly introduced in this section. They are either relatively underdeveloped or a combination of the other existing technologies.

Electrochemical cooling is a new concept, which uses the thermal effects of the reversible electrochemical reactions such as in a reversible electrochemical cell. This new cooling concept is based on the idea that a reversible electrochemical cell that releases heat when voltage is applied would absorb heat when the voltage is reversed (Gerlach and Newell, 2003). This technology is very young and currently being investigated for its technical feasibility.

Ejector cooling is a century-old technology based on a jet vacuum pump which has been more commonly called (vapour jet) ejector. In early 20th century, when steam was more abundant than electricity, this technology was used for air conditioning of trains and large buildings (Garris et al, 1998). As is the case for the other heat-driven technologies, the potential of using low-temperature heat and natural refrigerants renewed interest in this technology in the 1970s. With a generator temperature between 85 and 95°C, most of the maximum COPs reported are in the range of 0.2 to 0.33 for a condenser temperature between 28 and 32°C (Murthy et al, 1991; Nguyen et al, 2001; Alexis and Karayiannis, 2005). Although Balaras et al (2007) reported a much higher COP of 0.85 for a pilot steam ejector plant, this relatively high performance was only possible with a heat source temperature at 200°C. Although the simple construction of an ejector system is a great advantage, its COP makes it difficult to compete with the other heat-driven technologies. There were some pessimistic opinions regarding the potential of performance improvement. Garris et al (1998) and Fischer and Labinov (2000) considered it unlikely that COP could be improved to a competitive level due to the inevitable energy dissipation in the working mechanism of conventional ejectors.

Various kinds of combined or hybrid systems have also been investigated. By selectively combining different technologies, creation of new functions or enhancement of performance was intended.

By combining mechanical vapour compression and sorption cooling technologies, new systems have been created such as compression-absorption (Herold et al, 1991; Ayala et al, 1998; Swinney et al, 2001; Fukuta et al, 2002) and compression-adsorption systems (Sward and LeVan, 1999; Bedbak and Gopal, 2004), which could yield higher overall COP for the applications where electric- and thermal energy sources are simultaneously available.

Some modified or hybrid Rankine power cycles have also been proposed for geothermal and solar applications. Use of absorption fluids as a new working fluid in a Rankine cycle or combined Rankine-absorption cycles was suggested for high-efficiency power (Kouremenous et al, 1991; Jawahar and Kumar, 1994). In spite of these efforts, the investment cost of a modified Rankine or any other heat engine-based solar power system is not likely to be lower than that of an equivalent photovoltaic system. For example, Kouremenous et al (1991) estimated 25% increase in efficiency with their new power cycle in comparison with a conventional steam Rankine cycle. This would enable 20% reduction in the solar collector area that would be required for a steam Rankine system for the same capacity. But even if the cost of solar thermal collectors can be lower than that of solar electric panels for an equivalent photovoltaic system, the total cost would still be higher with the solar thermal power system when the cost of a heat engine is added. For this reason, modified or hybrid Rankine cycles have been used mostly in multi-generation applications (Xu et al, 2000; Oliveira et al, 2002), where the versatility of producing power, heating and cooling from a single system can justify an increased investment cost.

Some modifications have been proposed to absorption cycles for the improvement of overall performance or process efficiency. Some examples are the integration of ejectors and membranes.

Use of vapour jet ejectors has been proposed to improve the performance of absorption cycles (Sun et al, 1996; Rogdakis and Alexis, 2002, Sözen and Özalp, 2005). In a typical ejector-absorption cycle, the high-pressure vapour from a generator drives an ejector to pump up some of the refrigerant vapour from an evaporator directly to a condenser. A positive result is a reduced circulation ratio, i.e. less solution flows for the same cooling capacity, which would lead to an increased COP. A negative result is an increased generator temperature due to the raised generator pressure. Although substantial performance improvement may be possible, it is questionable whether it can justify the increased generator temperature in solar applications. Rogdakis and Alexis (2002), for example, reported that COP ranged between 1.1 and 1.36 for a NH_3/H_2O ejector-absorption cycle with a condenser temperature between 25.9 and 30.6°C, absorber between 48.6 and 59.1°C, evaporator between -1.1 and 7.7°C and the generator temperature fixed at 237°C.

Liquid jet ejectors were also used in absorption cycles to boost or to lower the pressure of a component (Kumar et al, 1993; Jelinek et al, 2002, Levy et al, 2004). Since this type of ejector is driven by a liquid jet, the pressure differential that it creates in an absorption cycle is not as large as that of a vapour jet ejector. When an ejector is placed between condenser and generator, for example, the condenser pressure is raised while the generator pressure is lowered. This will lower the generator temperature and thus improve the performance of a solar absorption cooling system. But this cannot be done without extra input of energy because a mechanical pump should provide the power for the driving liquid jet. However, a similar effect can also be achieved when an ejector is placed between evaporator and absorber. In this case, the ejector pumps the refrigerant vapour from the evaporator to the absorber, which consequently raises the absorber pressure. This raised absorber pressure makes it possible to use less concentrated solution in the absorber and consequently in the generator, which effectively lowers the generator temperature. In some absorption systems where the difference between system pressures is large, the ejector can be driven by the high-pressure solution from a generator with no need of extra energy input. Use of a liquid jet ejector in an absorption cycle is desirable if it is driven by a free energy source such as the liquefied refrigerant from a condenser or the solution from a generator. The ejector, in this case, plays as a recovery device for the work that would otherwise be lost.

Use of membranes has been proposed for the separation processes in absorption cycles. Riffat and Su (2001) proposed the use of reverse osmosis membranes in a centrifuge for separating water from aqueous LiBr solution. For the same purpose, Fahmy et al (2002) and Riffat et al (2004) investigated the potential use of pervaporation process, which is another membrane separation process that extracts a solvent from a mixture by letting the solvent preferentially permeate through a permeation membrane and then evaporate. Membrane separation technology could be an alternative to the distillation process commonly used in classic absorption systems. But until now, no membrane-integrated absorption system has been demonstrated.

Although not so many as absorption counterparts, some hybrid adsorption systems were also investigated. Zhang and Wang (2002) predicted 10% increase in COP by using an ejector in a solar-driven adsorption system. Chua et al (2003) reported simulation results of a miniature electro-adsorption chiller, which is a combined adsorption and thermoelectric cooling device. Their simulation predicted that the system COP could be as high as 0.9 with the minimum evaporator and condenser temperatures at around 11 and 35°C respectively. Thanks to the relatively high efficiency and the ease of miniaturization, this system may found its application in electronics cooling.

1.5 Affordable solar cooling

There is no doubt that solar cooling is an environment-friendly alternative to the conventional cooling technology. Several solar cooling technologies are considered mature and actively promoted in the market. Every year, increasing numbers of new solar cooling facilities are reported from many countries. But the scale is still very small. Until today, the total cooling capacity of the solar air conditioning systems in Europe is only 6MW (Nick-Leptin, 2005).

A solar cooling system is not what one can just pick up at a shop and install at his or her house. Setting up a solar cooling system requires a good planning and a substantial amount of skillful labor. Besides, for a large facility, optimization of the system is often necessary accompanied by system monitoring for an extended period. All in all, a solar cooling system is much more expensive than a conventional system. Especially when there is no existing solar system, the cost of new solar collectors or panels would overwhelm the whole project budget. Therefore, a solar cooling system is expected to deliver enough benefit that could justify all the extra efforts and investment.

Solar cooling definitely saves a substantial amount of primary energy use. This reduces the generation of carbon dioxide and levels off the peak electricity demand in mid summer, which is an important benefit for the environment and the national economics. But when it comes to financial benefit, the situation is not so encouraging. Although it varies depending on various parameters including local energy prices and operating conditions, financial benefit is often only marginal. In many cases, the capital cost associated with high initial investment tends to negate the benefit from solar operation, resulting in a very long payback time. For example, Henning (2004) compared different solar sorption cooling systems for an office building in Madrid, Spain. Although the amount varied among the systems, the annual cost of a solar cooling system was always higher than a conventional cooling system. Therefore solar cooling should be hardly attractive to an individual person, if there were no incentives for it. In this respect, political and financial supports from the government play an important role for the promotion of solar cooling technologies in the private sector.

As described in the previous sections, various solar cooling technologies are already available in the market. Although each technology has its own positive and negative aspects, high initial cost is a common problem. For its broader distribution, first of all, a solar cooling system should be available at a reasonable price.

Although differing in technical maturity and commercial status, the various solar cooling technologies discussed in the previous sections are compared in terms of performance and initial cost in Fig. 1.9.

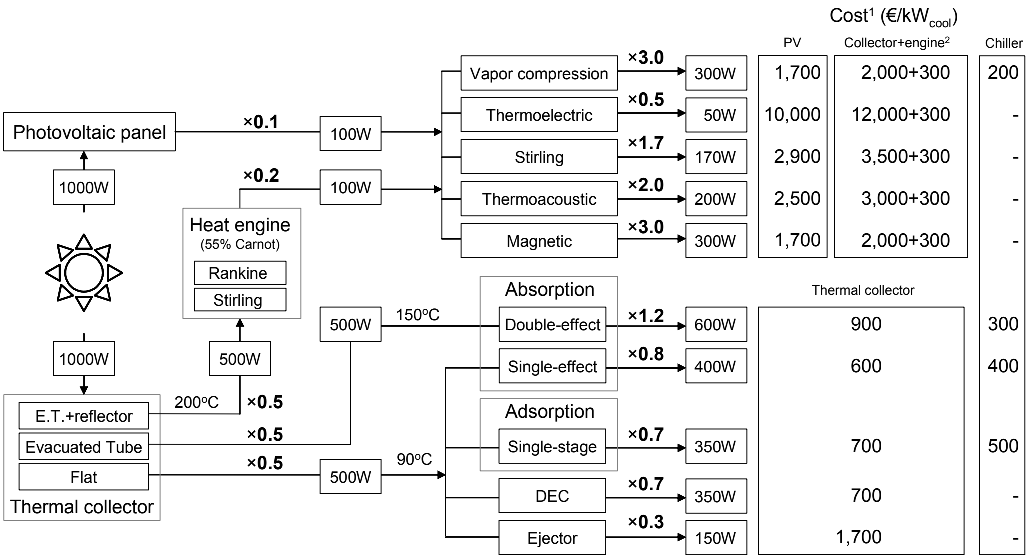

1. Based on retail prices without installation, rounded off below €100
2. 150% of a vapor compression chiller cost

Figure 1.9 Performance and cost of various solar cooling systems

Since the existing chillers based on these technologies differ widely in cooling capacity ranging from a few tens to several mega watts, the efficiencies and the unit cost values assumed in Fig. 1.9 are those of the smallest machines available from the different cooling technologies.

For example, COP of a vapour compression chiller is assumed at 3.0, which is valid only for a small air-cooled air conditioner with a cooling capacity of a few kilowatts, though a much higher COP above 5 is often reported for large centrifugal machines with cooling capacities of hundreds of kilowatts.

Solar electric systems are assumed to be equipped with 10%-efficient solar photovoltaic panels with a unit price at €5/Wp (Solar Rechner, 2005). This solar electric panel converts a solar radiation of 1,000W/m^2 into 100W of electricity and the various electric chillers transform this electric energy into the cooling powers of different magnitudes according to the specified chiller COPs. As shown in the figure, only magnetic chiller is comparable to vapour compression chiller in terms of solar electric panel cost. Although chiller cost is not given for the other electric cooling technologies, no other electric cooling technology is currently competitive with compression cooling technology in terms of total cost.

In order to generate the same amount of electricity, a thermomechanical system needs a high temperature solar thermal collector and a heat engine. In Fig. 1.9, the efficiency of a solar collector is assumed 50% at 200^{o}C and that of a heat engine is assumed 20% (56% second law efficiency). Among non-tracking solar collectors, a Sydney type collector [evacuated tubes with cylindrical absorbers and CPC concentrators, ca. €600/m^2 (Collector Catalogue 2004, 2004)] may satisfy this application. Although a tracking solar collector may better suit this application, use of a tracking collector is excluded to provide a common basis for the comparison with the solar thermal systems where non-tracking low-temperature solar collectors are commonly used. As shown in Fig. 1.9, the cost for a thermomechanical system is far larger than that of an equivalent solar electric system even without the engine cost. Although it is possible to cut down the cost as is done in large-scale solar power stations, a solar thermomecahncial system is not likely to be cheaper than a solar electric system in terms of operation cost.

Among the solar thermal systems in Fig. 1.9, a double-effect LiBr-water absorption chiller requires the highest driving temperature at 150°C. A 50%-efficient evacuated tube collector at this temperature would cost approximately €550/m^2 (Collector Catalogue 2004, 2004) and a double-effect LiBr-water chiller costs ca. €300/kW$_{cooling}$ (Peritsch, 2006). All the rest of the thermally-driven chillers are equipped with a 50%-efficient flat collector at 90°C, which costs ca. €250/m^2 (Collector Catalogue 2004, 2004). The cost of a single-effect LiBr-water absorption chiller is estimated at ca. €400/kW$_{cooling}$ (Peritsch, 2006) and that of a single-stage adsorption chiller is estimated at about €500/kW$_{cooling}$ (Weeda, 2002).

Although an ejector chiller would cost less than the other sorption chillers, its low COP would cost more for solar collectors. A desiccant system would also cost more than the other sorption systems due to the need of handling large quantities of air and water. The double-effect LiBr-water absorption and the single-stage adsorption systems are comparable in terms of total cost as at ca. €1,200/kW$_{cooling}$. The total cost of a single-effect LiBr-water absorption system is estimated as the lowest at ca. €1,000/kW$_{cooling}$.

Although Fig. 1.9 is based on ideal assumptions, it is clear that solar electric and thermomechanical systems are more expensive than solar thermal systems. Besides, these technologies are not compatible with the biggest solar infrastructure existing today, i.e. solar heating systems. Therefore, for solar cooling applications in general, these technologies are not advantageous.

Among the sorption cooling technologies, desiccant cooling can be a good solution for the applications where good indoor air quality is essential. But in general, high initial cost is likely to limit its application to large facilities.

Absorption and adsorption cooling technologies are comparable in terms of performance. But presently, an adsorption chiller is more expensive than an absorption chiller. The low power density of an adsorbent tends to increase the price of an adsorption machine by requiring bigger components for the same capacity. Much R&D effort will be necessary for raising its power density to a competitive level.

Although it may be available at the lowest cost as shown in Fig. 1.9, current solar absorption cooling technology is not likely to deliver much financial benefit. This was commonly shown in Henning (2004) and Balaras et al (2007), where the annual cost of a solar system was always higher than that of a conventional (electric compression) system. The main reason is the high initial cost of a solar system, of which the largest portion is usually taken up by solar collectors. For the reduction of initial cost, an absorption chiller should be made to work with less or cheaper solar collectors. That is, either the chiller's COP should be increased or its driving temperature should be lowered. Considering the numerous efforts carried out in the past, it is unlikely that significant cost reduction can be achieved by merely improving the existing chillers. It would require development of new thermodynamic cycles and/or working fluids.

Regarding the direction of future R&D in solar cooling, it would better be focused on low temperature sorption systems. It is because firstly, the cost of a solar collector system tends to increase with working temperature more rapidly than the COP of a sorption machine does.

And secondly, high temperature-driven chillers would not be compatible with the existing solar heating systems which were originally designed to produce domestic hot water.

Another important subject in the future R&D is the development of air-cooled machines. Currently, there is at least one air-cooled machine for solar cooling in the market. Its performance, however, seems to become unsatisfactory for ambient temperatures above 35^{o}C A wet cooling tower is unfavorable in most of the small applications where regular maintenance work is impossible or in the arid regions where water is scarce.

1.6 Outline of this thesis

The following chapters are devoted to the description of research work that has been carried out regarding the development of a solar-driven air-cooled absorption chiller for solar air conditioning.

In Chapter 2, various absorption chillers are evaluated in view of application to solar air conditioning. Energetic and economic performances of the chillers are evaluated using realistic dynamic models in combination with different working fluids and solar collectors. From the results, development of a half-effect LiBr-water absorption chiller is proposed for its energetic and economic merits.

In Chapter 3, a LiBr-water absorption chiller is designed based on a half-effect LiBr-water absorption cycle with a low generator temperature. The design results suggest that extended heat transfer surfaces should be used in most of the components in order to secure the target cooling capacity within an acceptable physical dimension.

Chapter 4 presents the thermophysical property database developed for the working fluids involved in the selected absorption cycle. Existing correlations for the thermodynamic properties of aqueous LiBr solution are critically reviewed. Observing the discrepancies between the existing correlations and the lack of an accurate wide-ranging correlation, an improved correlation is newly developed. Physical properties of all working fluids are collected from literature and presented in mathematical forms.

Heat and mass transfer processes in falling film flows are modeled in Chapter 5. The results are incorporated in component models for simulation. Governing equations are modified to promote quick and stable solution using mathematical and thermodynamic principles. Some simulation results are presented and discussed.

Chapter 6 introduces experimental results obtained from the falling film flow setup which was designed to measure average heat and mass transfer coefficients of falling film flows over vertical plates. Measured heat and mass transfer coefficients are presented for different fluids and heat transfer surfaces.

Chapter 7 describes the fabrication and test results of a chiller setup. Several aspects of actual design and fabrication process are discussed. Trial operations, identified problems and the following countermeasures are also discussed in detail. Finally, analysis and discussion of test results are followed by conclusions and recommendations.

Nomenclature

A	area, m^2
COP	coefficient of performance
I_p	solar radiation normal to collector surface, W/m^2
$\dot{Q}$	heat transfer rate, kW
T_H	temperature of high-temperature heat source, K
T_L	temperature of low-temperature heat source, K
T_M	temperature of low-temperature heat sink, K
$\dot{W}$	mechanical power, kW

Greek symbols

η	efficiency

Super- and subscripts

id	ideal
a	absorber
c	condenser
cool	cooling
e	evaporator
g	generator
heat	driving heat
pow	mechanical power
s, sol	solar radiation, solar collector

References

Al-Karaghouli, A., Abood, I., Al-Hamdani, N.I., 1991, The solar energy research center building thermal performance evaluation during the summer season, Energy Conversion and Management, Vol. 32, pp. 409-417

Akahira, A., Amanul Alam, K.C., Hamamoto, Y., Akisawa, A., Kashiwagi, T, 2005, Mass recovery four-bed adsorption refrigeration cycle with energy cascading, Applied Thermal Eng., Vol. 25, pp. 1764-1778

Alexis, G.K., Karayiannis, E.K., 2005, A solar ejector cooling system using refrigerant R134a in the Athens area, Renewable Energy, Vol. 30, pp. 1457-1469

Alizadeh, S., 2000, Multi-pressure absorption cycles in solar refrigeration: a technical and economical study, Solar Energy, Vol. 69, pp.37-44

Alvares, S.G., Trepp, Ch., 1987, Simulation of a solar driven aua-ammonia absorption refrigeration system Part2: viability for milk cooling at remote Brazilian dairy farms, Int. J. Refrigeration, Vol. 10, pp. 70-76

Arivazhagan, S., Murugesan, S.N., Saravanan, R., Renganarayanan, S., 2005, Simulation studies on R134a-DMAC based half effect absorption cold storage systems, Energy Conversion and Management, Vol. 46, pp. 1703-1713

ARTISC, 2003, Refrigeration, heating and air-conditioning using an absorption refrigeration system heated by transparently insulated solar collectors, EU project, Fifth Framework Program, CRAFT/70436/1999

Ayala, R., Heard, C.L., Holland, F.A., 1998, Ammonia/Lithium nitrate absorption/ compression refrigeration cycle. Part II. Experimental, Applied Thermal Engineering, Vol. 18, pp. 661-670

Balaras, C.A., Grossman, G., Henning, H.M., Infante Ferreira, C.A., Podesser, E., Wang, L., Wiemken, E., 2007, Solar air conditioning in Europe-an overview, Renewable and Sustainable Energy Reviews, Vol. 11, pp. 299-314

Bedbak, S.S, Gopal, M.R., 2004, Performance analysis of a compressor driven metal hydride cooling system, Int. J. Hydrogen Energy, Vol. 30, pp. 1127-1137

Berchovitz, D.M., McEntee, J., Welty, S., 1999, Design and testing of a 40W free-piston Stirling cycle cooling unit, Proc. of 20th International Congress of Refrigeration, Sydney, Austrailia

Best, R., 1991, Experimental studies on the operating characteristics of an ammonia-water absorption system for cooling, Chem. Eng. Research & Design, Vol. 69, pp. 153-160

Best, R., Ortega, N., 1999, Solar refrigeration and cooling, Renewable Energy, Vol. 16, pp. 685-690

Boer, R. de, Smeding, S.F., Grisel, R.J.H., 2005, Development and testing of a sorbent filled heat exchanger for use in compact solid sorption cooling systems, Proc. of International Sorption Heat Pump conf., Denver, USA

Butti, K. and Perlin, J., 1980, A golden Thread: 2500 Years of Solar Architecture and Technology, Cheshire Books, Palo Alto, ISBN 0-442-24005-8

Cerkvenik, B., Satzger, P., Ziegler, F., Poredoš, A., 1999, High efficient sorption cycles using CaO/H_2O and $LiBr/H_2O$ for gas cooling, Proc. of 3rd ASME/RAES Renewable and Advanced Energy Systems for the 21st Century Conference, Hawaii, USA

Chinnappa, J., 1961, experimental study of the intermittent absorption refrigeration cycle employing the refrigerant-absorbent systems of ammonia-water and ammonia-lithium nitrate, Solar Energy, Vol. 5, pp. 1-18

Chinnappa, J.C.V., Martin, H.V., 1976, Dual-mode operation by solar energy of an ammonia-water two-stage cycle: A comparative study, Solar Energy, Vol. 18, pp. 337-342

Chua, H.T., Gordon, J.M., Ng., K.C., Chakraborty, A., 2003, The electro-adsorption chiller: a miniaturized cooling cycle with application to microelectronics, Proc. of International Conference of Refrigeration, Washington, DC USA

Climate Change 2001, 2001, The Scientific Basis, Third Assessment Report, UN Intergovernmental Panel on Climate Change, Cambridge University Press, ISBN 0521 01495 6

Cool Appliances, 2003, Policy Strategies for Energy Efficient Homes, publication of IEA, ISBN 92-64-19661-7

Collector Catalogue 2004, 2004, Institut fur Solartechnik SPF, Rapperswil, Switzerland

Critoph, R.E., 2002, Carbon-ammonia systems-previous experience, current projects and challenges for the future, Proc. of Int. Sorption Heat Pump conf., Shanghai, China

Douss, N., Meunier, F., 1989, Experimental study of cascading adsorption cycles, Chem. Eng. Science, Vol. 44, pp. 225-235

EECCAC, 2003, Energy Efficiency and Certification of Central Air Conditioners–Final report, Vol 1., Armines, France

Eicker, U., Hofker, G., Lomas, K., Eppel, H., 2001, Desiccant cooling with solar energy, Proc. of 2001 CIBSE National Conference, London, UK

Ewert, M.K., Agrella, M, DeMonbrun, D., Frahm, J., Bergeron, D.J, Berchowitz, D. , 1998, Experimental Evaluation of a Solar PV Refrigerator with Thermoelectric, Stirling, and vapour Compression Heat Pumps, Proc. ASES Solar 98 Conference, Albuquerque, USA

Fahmy, A., Mewes, D., Ohlrogge, K., 2002, Novel pervaporation technology using absorption refrigeration for vapour removal, AIChE Journal, Vol. 48, pp. 2518-2523

Fanney, A.H., Dougherty, B.P., Davis, M.W., 2001, Measured performance of building integrated photovoltaic panels, J. Solar Energy Eng., Vol. 123, pp. 187-193

Fathalah, K., Aly, S.E., 1996, Study of a waste heat driven modified packed desiccant bed dehumidifier, Energy Conversion and Management, Vol. 37, pp. 457-471

Fischer, S., Labinov, S., 2000, Not-in-kind technologies for residential and commercial unitary equipment, Project report ORNL/CON-477, Oak Ridge National Laboratory, US DOE DE-AC05-96OR22464

Fukuta, M., Yanagisawa, T., Iwata, H., Tada, K., 2002, Performance of compression/absorption hybrid refrigeration cycle with propane/mineral oil combination, Int. J. Refrigeration, Vol. 25, pp. 907-915

Garris, C.A., Hong, W.J., Mavriplis, C., Shipman, J., 1998, A new thermally driven refrigeration system with environmental benefits, Proc. of 33rd Intersociety Engineering Conference on Energy Conversion, Colorado Springs, USA

Gerlach, D.W., Newell, T.A., 2003, Direct electrochemical method for cooling and refrigeration, Proc. of International Conference of Refrigeration, Washington, DC USA

Geyer, M., Lüpfert, E., Nava, P., Osuna, R., Esteban, A., Schiel, W., Schweitzer, A., Zarza, E., 2002, EuroTrough-a new parabolic trough collector family for cost efficient solar power generation, Proc. of 11th SolarPACES International Symposium on Concentrated Solar Power and Chemical Energy Technologies, Zurich, Switzerland

Gopal, M.R., Murthy, S.S., 1995, Performance of a metal hydride cooling system, Int. J. Refrigeration, Vol. 18, pp. 413-420

Göktun, S., Er, I.D., 2001, The optimum performance of a solar-assisted combined absorption-vapor compression system for air conditioning and space heating, Solar Energy, Vol. 71, pp. 213-216

Grenier, Ph., Guilleminot, J.J., Meunier, F., Pons, M., 1988, Solar powered solid adsorption cold store, J. Solar Energy Eng., Trans. ASME, Vol. 110, pp. 192-197

Grossman, G., 2002, Solar-powered systems for cooling, dehumidification and air-conditioning, Solar Energy, Vol. 72, pp. 53-62

Gschneider, Jr. K., 2001, Magnetic refrigerators/freezers and air conditioners, Proc. of Domotechnica Appliance Engineering, Köln, Germany

Gutiérrez, F., 1988, Behaviour of a household absorption-diffusion refrigerator adapted to autonomous solar operation, Solar Energy, Vol. 40, pp. 17-23

Hattem, D.V., Dato, P.A., 1981, Description of an active solar cooling system, using a LiBr-H2O absorption machine, Energy and Buildings, Vol. 3, pp. 169-196

Henning, H.M., 2004, Solar-assisted air-conditioning handbook in buildings: A handbook for planners, Springer-Verlag Wien, ISBN 3-211-00647-8

Herold, K.E., Howe, L.A., Radermacher, R., 1991, Analysis of a hybrid compression-absorption cycle using lithium bromide and water as the working fluid, Int. J. Refrigeration, Vol. 14, pp. 264-272

HIJC USA Inc., 2005, Performance table at http://www.adsorptionchiller.bigstep.com, the last access on 07 Dec. 2006

Hildbrand, C., Dind, Ph., Pons, M., Buchter, F., 2004, A new solar powered adsorption refrigerator with high performance, Solar Energy, Vol. 77, pp. 311-318

Hovland, V., 2002, Integrated cabin and fuel cell system thermal management with a metal hydride heat pump, Pro. 8th Int. Symp. on Metal-Hydrogen Systems, Annecy, France

Ishibashi, T., 1979, The operation results of the Yazaki experimental solar house, Silver Jubilee Congress of ISES, Atlanta, USA

Izquierdo, M., Syed, A., Rodriguez, P., Maidment, G., Missenden, J., Lecuona, A., Tozer, R., 2005, A novel experimental investigation of a solar cooling system in Madrid, Int. J. Refrigeration, Vol. 28, pp. 859-871

Jakob, U., Eicker, U., Taki, A.H., Cook, M.J., 2003, Development of an optimized solar driven diffusion-absorption cooling machine, Proc. of ISES Solar World Congress 2003, Göteborg, Sweden

Jawahar, N., Kumar, S., 1994, Absorption heat-pump regeneration in a Rankine steam cycle, Heat Recovery Systems and CHP, Vol. 14, pp. 599-612

Jelinek, M., Levy, A., Borde, I., 2002, Performance of a triple-pressure-level absorption cycle with R125-N, N'-dimethylethylurea, Applied Energy, Vol. 71, pp. 171-189

Kouremenous, D.A., Rogdakis, E.D., Anotonopoulos, K.A., 1991, Anticipated thermal efficiency of solar driven NH_3/H_2O absorption work producing units, Energy Conversion and Management, Vol. 31, pp. 111-119

Kovak, B., Heimann, R., Hammel, J., 1997, The sanitizing effects of desiccant-based cooling, ASHRAE Journal, April 1997, pp. 60-64

Kribus, A., 2002, Thermal integral micro-cogeneration systems for solar and conventional use, Journal of Solar Energy Engineering, Vol. 124, pp189-197

Kumar, S., Prévost, M., Bugarel, R., 1993, Experimental studies of a three-pressure absorption refrigeration cycle, Int. J. Refrigeration, Vol. 16, pp. 31-39

Kunze, G., 2000, Efficient solar cooling with an improved ammonia-absorption system, Renewable Energy World, Vol. 3, pp. 111-112

Lamp, P. and Ziegler, F., 1998, European research on solar-assisted air conditioning, Int. J. Refrigeration, Vol. 21, pp.89-99

Larson, D., 1983, Final report of the Coolidge solar irrigation project, Sandia National Laboratory report, SAND83-7125, Albuquerque, New Mexico, USA

Levy, A., Jelinek, M., Borde, I., Ziegler, F., 2004, Performance of an advanced absorption cycle with R125 and different absorbents, Energy, Vol. 29, pp. 2501-2515

Li, Z.F., Sumathy, K., 2000, Technology development in the solar absorption air-conditioning systems, Renewable and Sustainable Energy Reviews, Vol. 4, pp. 267-293

Liu, Y.L., Wang, R.Z., Xia, Z.Z., 2005, Experimental study on a continuous adsorption water chiller with novel design, Int. J. Refrigeration, Vol. 28, pp. 218-230

Löf, G.O.G., Tybout, R.A., 1974, The design and cost of optimized systems for residential heating and cooling by solar energy, Solar Energy, Vol. 16, pp. 9-18

Lokurlu, A., Müller, G., 2005, Experiences with the worldwide first solar cooling system based on trough collectors combined with double effect absorption chillers, Proc. of International Conference Solar Air-conditioning, Bad Staffelstein, Germany

Matsushita, S., Yamaguchi, S., Saito, K., Kawai, S., Hongo, K., Inagaki, K., 2005, Performance evaluation of open type absorption dehumidifier using LiCl solution as liquid desiccant, Proc. of International Sorption Heat Pump Conference, Denver, USA

McLinden, M.O., Klein, S.A., 1983, simulation of an absorption heat pump solar heating and cooling system, Solar Energy, Vol. 31, pp. 473, 482

Murthy, S.S., Balasubramanian, R., Murthy, M.V.K., 1991, experiments on vapour jet refrigeration system suitable for solar energy applications, Renewable Energy, Vol. 1, pp. 757-768

Neveu, P., Castaing, J., 1993, Solid-gas chemical heat pumps: field of application and performance of the internal heat of reaction recovery process, Heat recovery Systems & CHP, Vol. 13, pp. 233-251

Nick-Leptin, J., 2005, Political framework for research and development in the field of renewable energies, Proc. of International Conference Solar Air conditioning, Bad Staffelstein, Germany

Niebergall, W., 1981, Sorptions-Kaltemaschinen, Handbuch der Kaltetechnik; Bd. 7, Springer-Verlag, Berlin

Nuñez, T., Mittelbach, W., Henning, H.M., 2004, Development of an adsorption chiller and heat pump for domestic heating and air-conditioning applications, Proc. of Int. conf. on Heat Powered Cycles, Cyprus

Nguyen, V.M., Riffat, S.B., Doherty, P.S., 2001, Development of a solar-powered passive ejector cooling system, Applied Thermal Engineering, Vol. 21, pp. 157-168

Oliveira, A.C., Afonso, C., Matos, J., Riffat, S., Nguyen, M., Doherty, P., 2002, A combined heat and power system for buildings driven by solar energy and gas, Applied Thermal Engineering, Vol. 22, pp.587-593

Paassen, J.P. van, 1987, Solar powered refrigeration by means of an ammonia-water intermittent absorption cycle, Delft University of Technology, Laboratory of Refrigeration and Indoor Climate Technology, Report no. K127, ISBN 90-370-0013-4

Pennington, N.A., 1955, Humidity changer for air conditioning, U.S. Patent No. 2700537

Peritsch, M., 2006, Supermärkte als Energiezentralen, Publikation Energiesysteme der Zukunft, Federal Ministry of Transport, Innovation and Technology, Austria, http://www.energiesystemederzukunft.at/publikationen/, the last access on 07 Dec. 2006

Poese, M.E., Smith, R.W., Garrett, S.L., van Gerwen, R., Gosselin, P., 2004, Thermoacoustic refrigeration for ice cream sales, Proc. of 6th Gustav Lorentzen Natural Working Fluids Conference, Glasgow, Scotland

Pons, M., Guilleminot, J.J., 1986, Design of experimental solar-powered, solid-adsorption ice maker, J. Solar Energy Eng., Trans. ASME, Vol. 108, pp. 332-337

Pons, M., Poyelle, F., 1999, Adsorptive machines with advanced cycles for heat pumping or cooling applications, Int. J. Refrigeration, Vol. 22, pp. 27-37

Poyelle, F., Guilleminot, J.J., Meunier, F., 1999, Experimental tests and predictive model of an adsorptive air conditioning unit, Ind. & Eng. Chem. Research, Vol. 38, pp. 298-309

Prigmore, D. and Barber, R.,1975, Cooling with the sun's heat Design considerations and test data for a Rankine cycle prototype, Solar Energy, Vol.17, pp. 185-192

Reader, G.T., Hooper C., 1983, Stirling engines, Cambridge University Press, London, pp.247-248

Restuccia, G., Freni, G., Vasta, S., Aristov, Y., 2004, Selective water sorbent for solid sorption chiller: experimental results and modeling, Int. J. Refrigeration, Vol. 27., pp. 284-293

Richter, L., Safarik, M., 2005, Solar cooling with Ammonia water absorption chillers, Proc. of International Conference Solar Air conditioning, Bad Staffelstein, Germany

Riffat, S.B., Su, Y.H., 2001, Analysis of using centrifugal reverse osmosis in absorption refrigeration systems, Proc. of 2001 CIBSE National Conference, London, UK

Riffat, S.B., Wu, S., Bol, B., 2004, Pervaporation membrane process for vapour absorption system, Int. J. Refrigeration, Vol. 27, pp. 604-611

Rogdakis, D., Alexis, G.K., 2002, Performance of characteristics of two combined ejector-absorption cycles, Applied Thermal Engineering, vol. 22, pp. 97-106

Romero, R.J., Rivera, W., Pilatowsky, I., Best, R., 2001, Comparison of the modeling of a solar absorption system for simultaneous cooling and heating operating with an aqueous ternary hydroxide and with water/lithium bromide, Solar Energy Materials and Solar Cells, Vol. 70, pp. 301-308

Rudischer, R., Waschull, J., Hernschier, W., Friebe, C., 2005, Available solar cooling applications for different purposes, Proc. of International Conference Solar Air conditioning, Bad Staffelstein, Germany

SACE, 2003, Solar Air conditioning in Europe: Evaluation Report, EC project NNE5/2001/25

Safarik, M., Richter, L., Mockel, F., Kretschmar, S., 2005, Performance data of a small capacity absorption chiller, Proc. of International Conference Solar Air-conditioning, Bad Staffelstein, Germany

Saha, B.B., Akisawa, A., Kashiwagi, T., 2001, Solar/waste heat driven two-stage adsorption chiller: the prototype, Renewable Energy, Vol. 23, pp. 93-101

Saman, W., Krause, M., Vajen, K., 2004, Solar Cooling Technologies: Current Status and Recent Developments, Proc. of 42nd ANZSES Conference Solar 2004, Perth, Australia

Sawada, N., Tanaka, T., Mashimoto, K., 1994, Development of organic working fluid and application to absorption systems, Proc. of Absorption Heat Pump conference, AES-Vol.31, ASME, New Orleans, USA

Schawe, D., 2001, Theoretical and experimental investigations of an adsorption heat pump with heat transfer between two adsobers, Ph.D. dissertation, University of Stuttgart

Shir, F., Mavriplis, C., Bennett, L.H., Torre, E.D., 2005, Analysis of room temperature magnetic regenerative refrigeration, Int. J. Refrigeration, Vol. 28, pp. 616-627

Shiran, Y., Shitzer, A., Degani, D., 1982, Computerized design and economic evaluation of an aqua-ammonia solar operated absorption system, Solar Energy, vol. 29, pp. 43-54

Smith, C., 1995, Revisiting solar power's past (history of solar power projects), MIT's Technology Review-01/07/1995

Sofrata, H., Khoshaim, B., Nasser, A., Megahed, M., 1981, A solar-powered LiBr dual cycle, Applied Energy, Vol. 9, pp. 185-191

Solar Rechner, http://www.solarrechner.de/module.htm, the last access on 07 Dec. 2006

Sözen, A., Özalp, M., 2005, Solar-driven ejector-absorption cooling system, Applied Energy, Vol. 80, pp. 97-113

Stein, W.B., Diver, R.B., 1994, A compendium of solar dish/Stirling technology, Sandia National Laboratory report, SAND93-7026, Albuquerque, New Mexico, USA, http://www.osti.gov/energycitations/servlets/purl/10130410-xiVU1V/native/10130410.pdf , the last access on 07 Dec. 2006

Stein, W.B., Geyer, M., 2001, Power from the sun, Chapter 12, pp. 25-27, http://www.powerfromthesun.net/chapter12/Chapter12new.htm, the last access on 07 Dec. 2006

Stephan, K., 1983, History of absorption heat pumps and working pair developments in Europe, Int. J. Refrigeration, Vol. 6, pp. 160-166

Storkenmaier, F., Harm, M., Schweigler, C., Ziegler, F., Albers, J., Kohlenbach, P., Sengewald, T., 2003, Small-capacity water/LiBr absorption chiller for solar cooling and waste-heat driven cooling, Proc. of International Congress of Refrigeration, Washington D.C., USA

Sun, D.W., Eames, I.W., Aphornratana, S., 1996, Evaluation of a novel combined ejector-absorption refrigeration cycle-I: compute simulation, Int. J. Refrigeration, Vol. 19, pp. 172-180

Sward, B.K., LeVan, M.D., 1999, Examination of the performance of a compressor-drive adsorption cooling cycle, Applied Thermal Engineering, vol. 19, pp. 1-20

Swinney, J., Jones, W.E., Wilson, J.A., 2001, A novel hybrid absorption-compression refrigeration cycle, Int. J. Refrigeration, Vol. 24, pp. 208-219

Talter, M., Erdem-Şenatalar, A., 2000, Effects of metal mass on the performance of adsorption heat pumps utilizing zeolite 4A coatings on heat exchanger tubes, Int. J. Refrigeration, Vol. 23, pp. 260-268

Tamainot-Telto, Z., Critoph, R.E., 1997, Adsorption refrigerator using monolithic carbon ammonia pair, Int. J. Refrigeration, Vol. 20, pp. 146-155

Tchernev, D.I., 1978, Solar Energy Application of Natural Zeolites, Natural zeolite, occurence, properties and use, Oxford: Pergamon Press, pp.479-486

Tchernev, D.I., Emerson, D.T., 1988, High-efficiency regenerative zeolite heat pump, ASHRAE Trans., Vol. 94, pp. 2024-2032

Thévenot, R., 1979, A history of refrigeration throughout the world, Int. Inst. Refrigeration, Paris

Tokarev, T., Gordeeva, L., Romannikov, V, Glaznev, I., Aristov, Y., 2002, New composite sorbent $CaCl_2$ in mesopores for sorption cooling/heating, Int. J. Thermal Sciences, Vol. 41, pp. 470-474

Trombe, F., Foex, M., 1957, The production of cold by means of solar radiation, Solar Energy, Vol. 1, pp. 51-52

Tsay, Y.S., Kato, S., Ooka, R., Koganei, M., Shoda, N., 2005, Study on the applicability of combining desiccant cooling system with heat pump in hot and humid climate, Proc. of 2005 World Sustainable Building Conference in Tokyo, Tokyo, Japan

Wade, L., Sywulka, P., Hattar, M., Alvarez, J., 1990, High efficiency sorption refrigerator design, Advances in Cryogenic Eng., Vol. 35, pp. 1375-1382

Wang, L.W., Wang, R.Z, Wu, J.Y., Wang, K., 2004, Compound adsorbent for adsorption ice maker on fishing boats, Int. J. Refrigeration, Vol. 27, pp. 401-408

Wang, R.Z., Jia, J.P., Zhu, Y.H., Teng, Y., Wu, J.Y., Cheng, J., 1997, Study on a new solid adsorption refrigeration pair: active carbon fibre-methanol, ASME J. Solar Energy Eng., Vol. 119, pp. 214-219

Wang, R.Z., Li., M., Xu, Y.X., Wu, J.Y., 2000, An energy efficient hybrid system of solar powered water heater and adsorption ice maker, Solar Energy, Vol. 68, pp.189-195

Wang, R.Z., Oliveira, R.G., 2005, Adsorption refrigeration-an efficient way to make good use of waste heat and solar energy, Proc. International Sorption Heat Pump conference, Denver, USA

Ward, D.S. and Löf, G.O.G., 1975, Design and construction of a residential solar heating and cooling system, Solar Energy, Vol. 17, pp. 13-20

Ward, D.S., Duff, W.S., Ward, J.C., Löf, G.O.G., 1979, Integration of evacuated tubular solar collectors with lithium bromide absorption cooling systems, Solar Energy, Vol. 22, pp. 335-341

Weeda, M., 2002, Combined cold, heat and power generation; Techno-economic assessment of integrated fuel cell and sorption heat pump systems, Energy Research Centre of the Netherlands, Project report ECN-C-02-074

Wojcik, A.M.W., Jansen, J.C., Maschmeyer, Th., 2001, Regarding pressure in the adsorber of an adsorption heat pump with thin synthesized zeolite layers on heat exchangers, Microporous Mesoporous Materials, Vol. 43, pp. 313-317

Xu, F., Goswami, D.Y., Bhagwat, S.S., 2000, A combined power/cooling cycle, Energy, vol. 25, pp. 233-246

Yazaki Energy Systems Inc., 2005, Specifications of water-fired chillers and chiller-heaters at http://www.yazakienergy.com/waterfiredspecifications.htm, the last access on 07 Dec. 2006

Zhang, X.J., Wang, R.Z., 2002, A new combined adsorption–ejector refrigeration and heating hybrid system powered by solar energy, Applied Thermal Engineering, Vol. 22, pp. 1245-1258

2 Evaluation of solar absorption cooling systems[1]

From the variety of solar collectors and absorption chillers, various solar absorption cooling systems can be considered for solar air conditioning. Although, in principle, all of them may serve for the purpose, they will not be equal in energetic and financial performance. A system must be thoroughly evaluated before final selection. Evaluation of a solar cooling system is generally not easy because there are many parameters to consider, most of which are time-dependent. The evaluation criterion is, however, simple. The best system must be the one that would bring the maximum benefit out of the minimum investment. For a fair evaluation, different systems should be compared in a common realistic environment. Dynamic simulation would be one of such environments.

Prediction of dynamic performance is particularly important for solar thermal systems considering the fact that solar energy is transient in nature and economics of a solar system is critically dependent on its effective use. Therefore dynamic simulation has been an indispensable part of many research works where various solar thermal systems were evaluated.

Zhuo (1995)'s literature survey on the previous works on dynamic modeling of absorption systems revealed that early works were focused on the performance of whole solar cooling systems using quasi-steady state models (Stuart and Sheridan, 1977; Anand et al, 1982; McLinden and Klein, 1983; Kaushik et al, 1985; Alvares and Trepp, 1987). In these works, only storage tanks were modeled with differential equations and other components were modeled with steady state equations, which is a typically adopted approach in TRNSYS. Zhuo (1995) also classified the previous works into two groups depending on the detail of a model, i.e. lumped and distributed parameter models, and pointed out that most of the works were based on lumped parameter models with two exceptions (Butz and Stephan, 1989; Sano et al, 1991).

Some other works not mentioned in Zhuo (1995) include modeling of a periodically operating ammonia-water heat pump (Jeong, 1990), a solar ammonia-water absorption cooling system with refrigerant storage (Kaushik et al, 1991) and more recent works on hot water-driven LiBr-water absorption heat pump and chillers (Jeong et al, 1998; Bina et al, 2005; Kohlenbach and Ziegler, 2006; Fu et al, 2006).

As will be presented in the following sections, the approach adopted in the present study is different from that of quasi-steady state models from the fact that all components in a solar cooling system were modeled with differential equations. In a small solar cooling system, storage is even neglected or thermal capacities of other components are not small enough to be neglected. And since the main purpose of present study is to evaluate different types of absorption chillers in terms of dynamic performance, quasi-steady state modeling is not acceptable.

Distributed parameter model such as Butz and Stephan (1989) requires excessive computing time for the time scale to be simulated in the present study. For comparison of different systems in terms of seasonal performance, lumped parameter model was thought sufficient and models were developed accordingly. The present approach is different from others in the aspect that while most of the previous works assumed equilibrium between bulk working

---

[1] Parts of this Chapter have been published in Kim and Machielsen, 2002a and 2002b.

fluids, the absorption chiller models in this study were developed to take account of the influences of non-equilibrium conditions by considering finite mass transfer rates in sorption processes.

Another aspect worth mentioning about the present work is that a “modular” approach has been taken when modeling a system. This approach has been preferred considering the large number of absorption chillers and working fluids to be modeled for the present purpose. Writing an individual program for each of different systems is a time-consuming and redundant job especially when those systems are only different combinations of common components. In the present study, the “common components” were developed in a flexible way so that they can be shared among different systems. In this respect, the approach taken by this study is similar to that of Fu et al (2006).

In the following, beginning with a general description of solar collectors and absorption chillers, modeling details and simulation results are given in the following sections.

2.1 Basic components in solar absorption cooling

Two basic components of a solar absorption cooling system, solar collector and absorption chiller, are discussed below to give an overview of the state of the art of solar absorption cooling technology.

2.1.1 Solar collectors

Currently, several types of solar collectors are available in the market ranging from a simple unglazed plastic solar collector for swimming pools to a sophisticated evacuated tube collector that could even be used for the production of high-temperature steam.

Collector Catalogue 2004 (2004), published by Institute für Solartechnik SPF at Rapperswil in Switzerland, provides information about 209 solar collectors from 120 companies active in the European market. Although there are many other parameters that determine the characteristics of a solar collector, two values are of particular interest to system designers, namely efficiency and price.

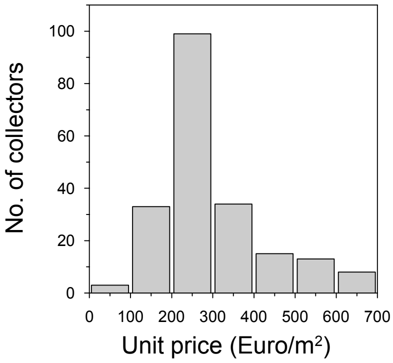

Figure 2.1 Price of solar collectors in European market

Fig. 2.1 shows the price distribution of the solar collectors listed in the catalogue. In the figure, it is clearly shown that most of the collectors are in the price range from 200 to 300 Euro/m^2.

Regarding the type of a solar collector, most of collectors below 400 Euro/m^2 are flat plate collectors and the others are evacuated tube collectors with or without optical concentrators.

The efficiencies of the solar collectors are rather scattered. That is, large deviations in efficiency are found between the solar collectors with comparable prices. Therefore any absolute price from the catalogue cannot be used with high reliability. Only the general trend of efficiency against the price could be extracted from the catalogue.

Static efficiency of a solar collector, which was previously defined by Eq. (1.4) in Ch.1, is commonly described by

$$\eta_{col} \equiv \frac{\dot{Q}_{col}}{I_p \times A_{col}} = \eta_\circ - c_1 T_r - c_2 T_r^2 I_p \qquad \text{where } T_r \equiv (T_{htm,avg} - T_{amb})/I_p \tag{2.1}$$

where the reduced temperature, T_r is the temperature difference between the heat transfer medium in the solar collector and the ambient air divided by the solar radiation, which can be considered as the driving potential of the solar collector's heat loss to the ambient.

The first term η_o on the right side of Eq. (2.1) represents the optical efficiency of a solar collector. The second term gives the combined conductive and convective heat losses. The last term can be understood as a correction term to represent the non-linear characteristic of a solar collector in high operating temperature range due to radiation heat loss. Among the three constants η_o, c_1 and c_2, only c_1 is subject to change in the presence of wind. Collector Catalogue 2004 (2004) provides these constants for many solar collectors under standard test conditions. Fig. 2.2 shows these constants against the solar collector price.

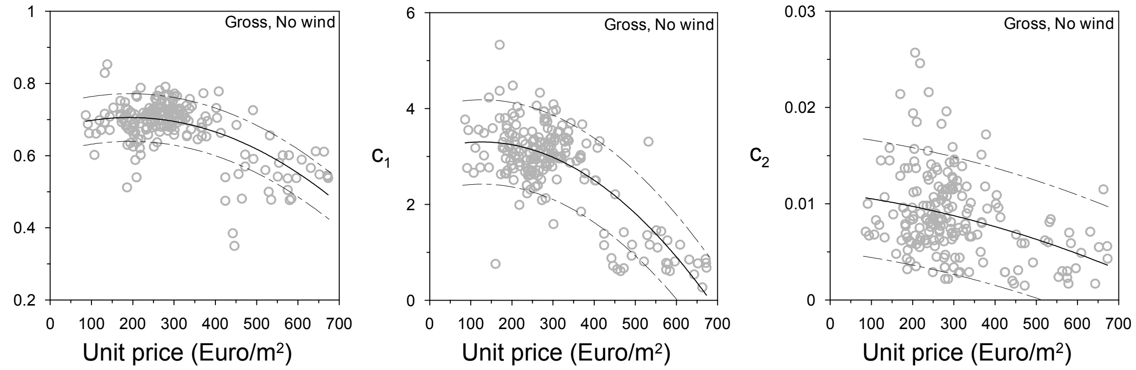

(a) η_o (b) c_1 (c) c_2

Figure 2.2 Variation of the constants in Eq. (2.1) against the collector price

The data in Fig. 2.2 are based on the gross efficiency of a solar collector, i.e. A_{col} in Eq. (2.1) is the gross surface area, measured under no wind condition.

Although c_2 has the least influence on the efficiency among the three constants, it is not negligible when the working temperature is high.

In Fig. 2.2a, the maximum optical efficiency is as high as 0.8 for the collectors in the low price range but it is only 0.6 for those in the high price range. Since this η_o is not based on the absorber surface area but on the gross surface area of a collector, this does not mean that more expensive collectors have poorer optical performance but means that expensive solar collectors like evacuated tube type collectors have a relatively small absorber surface area within the same gross dimension.

A large amount of heat can be lost from a solar collector via conduction and convection to ambient depending on its insulation. And this insulation performance varies widely with collector price, which is shown in terms of the coefficient c_1 in Fig. 2.2b. A good evacuated solar collector has a very small c_1, several times smaller than that of a cheap flat plate collector.

Using the data in Fig. 2.2, the constants in Eq. (2.1) are described as a function of the collector price by

$$\eta_o=0.671(\pm 0.066)+3.565\times 10^{-4}\omega-9.266\times 10^{-7}\omega^2 \quad (2.2a)$$

$$c_1=3.971(\pm 0.88)-1.665\times 10^{-3}\omega-5.695\times 10^{-6}\omega^2 \quad (2.2b)$$

$$c_2=1.182(\pm 0.61)\times 10^{-2}-6.572\times 10^{-6}\omega-7.684\times 10^{-9}\omega^2 \quad (2.2c)$$

where ω is the unit collector price in Euro/m^2 of gross area. The values between parentheses are standard deviations, which are also shown as dotted lines in Fig. 2.2.

Using Eq. (2.1) and (2.2), efficiency curves are shown for some differently priced collectors in Fig. 2.3.

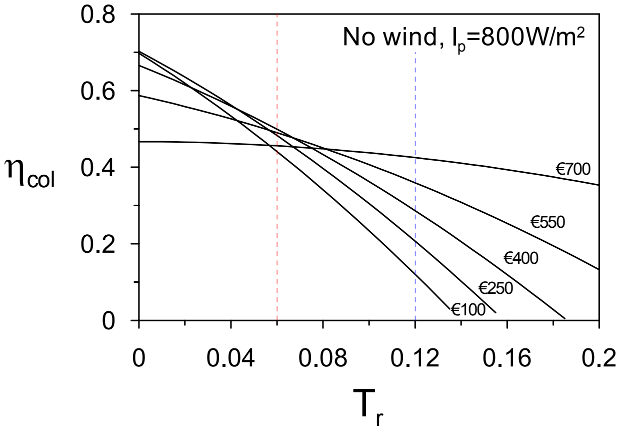

Figure 2.3 Collector efficiency vs. reduced temperature with collector price as parameter

In Fig. 2.3, one can see that efficiencies of different solar collectors are not much different at around T_r=0.06. The maximum deviation between the different efficiency values is only 6% at this point (i.e. $44\leq\eta_{col}\leq 50\%$). This means that, when the ambient temperature is 32°C and the solar intensity is 800W/m^2, all solar collectors can produce 80°C hot water within the efficiency range of 47±3% regardless of the price.

In Fig. 2.3, it can also be seen that expensive collectors like evacuated tube type collectors outperform flat plate collectors only when T_r is large, i.e. when either the working temperature is high or the intensity of solar radiation is low.

Eqs. (2.1) and (2.2) can be used to represent the performance-vs.-price characteristic of a typical solar collector available in the European market, which can be used as a common platform for the evaluation of different solar cooling systems.

2.1.2 Absorption chillers

The largest portion of the present absorption chiller market is taken by direct-fired machines with capacities larger than, at least, 35 kW. Recent R&D effort in the field of direct-fired machines is mainly focused on the development of high-efficiency machines by raising the working temperatures (Garimella et al, 1997; Stitou et al, 2000) or hybridization (Kim et al, 2002; Worek et al, 2003) of absorption cycles.

On the other hand, the market for indirect-fired chillers, i.e. water- or steam-fired machines, is relatively small and much of recent R&D activities are focused on the development of absorption chillers for small-scale residential and commercial applications. Currently, several small absorption chillers are already in or close to the market. Table 2.1 lists some small absorption chillers available in the market.

Table 2.1 Small-capacity absorption chillers (cooling capacity smaller than 35kW)

Cycle type	Working pair	Manufacturer	Country	Qe(kW)	Cooling medium	Heating medium	Min. driving T(oC)	Cooling COP[5]
SE[1]	$LiBr-H_2O$	Phoenix	Germany	10	water	Hot water	90-100	0.74
		EAW	Germany	15				0.7
		Yazaki	Japan	35				0.71
		Rotartica	Spain	11				0.67
	$LiCl-H_2O$	ClimateWell AB	Sweden	7				0.7
	NH_3-H_2O	Pink	Austria	10				0.6
DE[2]	$LiBr-H_2O$	Rinnai	Japan	5	water	Gas-fired	150-170[4]	1.2-1.3
GAX[3]	NH_3-H_2O	Robur	Italy	18	air		160-180[4]	0.8-0.9
		Cooling technologies	USA	17				

1. SE: Single-Effect absorption cycle; 2. DE: Double-Effect absorption cycle; 3. GAX: Generator Absorber eXchange absorption cycle; 4. Equivalent steam or hot water temperatures; 5. Estimated cooling COP based on net heat input to the system

Among the chillers in Table 2.1, only the single-effect chillers are suitable for solar cooling. The particular double-effect and GAX chillers are all direct-fired. Nevertheless they can also be made steam- or water-fired and their minimum driving temperatures in Table 2.1 are the equivalent steam or hot water temperatures in that case.

Currently, all single-effect absorption chillers in the market are water-cooled and they require a driving temperature in the range between 90 and $100^{o}C$ for a COP between 0.6 and 0.74.

No indirect-fired double-effect chiller has been reported in this small capacity range. The particular double-effect chiller in the table is a water-cooled, city gas-fired machine and yields a cooling COP of about 1.2. It would require approximately $160^{o}C$ steam or pressurized hot water to drive an equivalent indirect-fired machine.

The GAX chiller is another high-efficiency option but none is currently available for solar cooling in the market. Both GAX chillers in the table are air-cooled gas-fired machines mainly used in large houses or in small commercial buildings. Cooling COP is about 0.8 and it would require approximately $170^{o}C$ steam or pressurized hot water to drive an equivalent indirect-fired machine.

Until now, virtually all absorption chillers use either water or ammonia as a refrigerant. In general, a water absorption chiller yields higher COP than an ammonia chiller at the same driving temperature. This is because the latent heat of water is larger than of ammonia and thus requires less circulation of the absorbent in the absorption cycle. But water absorption cycles are not without shortcomings. Due to the risk of crystallization of absorbents, no air-cooled water absorption chiller has been successfully developed until now. Besides, there is also no water absorption refrigerator because water freezes at 0^{o}C. These are the applications where ammonia chillers are dominating. Although its COP is lower, an ammonia chiller can be made for refrigeration and for air-cooled operation.

Currently, in the field of solar absorption cooling, water-cooled single-effect chillers are dominant. The reason becomes clear when the driving temperature is considered. The driving temperature of a single-effect water-cooled absorption chiller is between 90-100 ^{o}C in Table 2.1, which is close to but below the boiling temperature of water. Then the driving temperature of an air-cooled single-effect absorption chiller would certainly be beyond 100^{o}C not to mention the other types of high-temperature absorption chillers. An absorption chiller with a driving temperature higher than 100^{o}C is unfavorable for some reasons. Firstly, it needs expensive high-temperature solar collectors. Secondly, the whole solar collector circuit (piping, storage, pumps, valves and etc.) needs to be pressurized to prevent water from boiling unless it uses less volatile heat transfer media like glycol solutions or oils at the expense of high auxiliary power consumption and environmental disfavour. Nevertheless, because a high temperature chiller has a potential to compensate for these disadvantages with better performance, use of a high-temperature chiller should not be abandoned without a proper analysis.

Disadvantages of water-cooled systems have also to be pointed out. A water-cooled system is inevitably accompanied by high initial and operation costs concerning the use of a cooling tower. And besides, the open water network becomes an ideal place for the growths of bacteria that could cause various diseases.

Regarding the initial cost of a water-cooled system, for example, a cooling tower for 10kW cooling capacity alone costs approximately €2,000-2,500 (Schweigler et al, 2005), which is €200-250 per $kW_{cooling}$. This is a substantial figure considering that a single-effect LiBr-water absorption chiller costs €400~1,000/$kW_{cooling}$ depending on capacity (Arsenal Research, 2005). That is, the cost of a cooling tower alone is expected to be as much as 20-25% of an absorption chiller.

Water consumption is also not negligible. According to a recent survey of European solar cooling systems (SACE, 2003), the average water consumption of water-cooled solar cooling systems in Europe is 5.3kg/kWh cooling. This is a huge waste considering that the evaporation of only 1.4 kg water is enough to provide an equivalent cooling effect.

Although a cooling tower may be the only practical solution for high-intensity applications like multi-storey office buildings and hotels, it is not desirable for less demanding applications like medium-size houses or small offices, which small absorption chillers are aiming at.

Various solar absorption cooling systems will be evaluated in the following sections in view of all the aspects discussed above. Before proceeding further, the working principles of various absorption cycles are briefly explained in the following subsections.

2.1.2.1 Single-effect cycle

The single-effect (SE) cycle is the simplest absorption cycle, having only a minimum number of components. The biggest advantage of the SE cycle is its simplicity. As is shown in Fig. 2.4, a SE chiller consists of five main components, namely generator (GEN), absorber (ABS), condenser (CON), evaporator (EVA) and a solution heat exchanger (SHX).

Heat recovery is realized only by a single-phase solution heat exchanger (SHX) located between generator and absorber. For systems where it is acceptable, another single-phase refrigerant heat exchanger (RHX) can also be used between the liquefied refrigerant from condenser and the refrigerant vapour from evaporator to increase the subcooling of liquefied refrigerant before entering the evaporator thus reducing the loss of refrigerant due to flashing.

The COP of a SE chiller ranges from 0.6 to 0.8. The driving temperatures are in the range of 90 to 100°C for a water cooled system and those of air-cooled systems need to be roughly 30K higher.

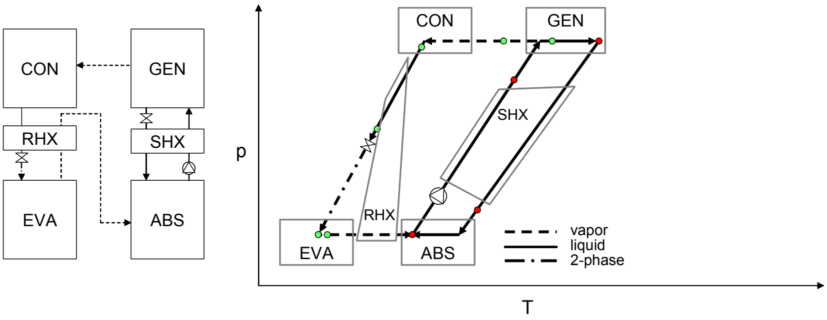

Figure 2.4 Block and P-T-x diagram of single-effect absorption cycle

2.1.2.2 Double-effect cycle

Fig. 2.5 shows a double-effect absorption cycle.

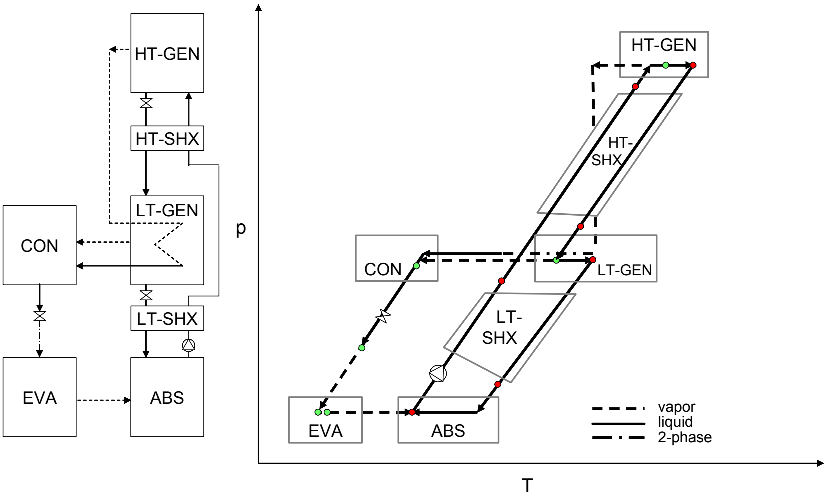

Figure 2.5 Block and P-T-x diagram of double-effect absorption cycle

It is basically a SE cycle with an extra generator (high-temperature generator, HT-GEN in Fig. 2.5) and another heat exchanger (HT-SHX) between the two generators. The extra generator is designed to operate at such a high pressure that its refrigerant vapour condenses at a temperature which is high enough to boil the solution in the generator of the SE absorption cycle (low-temperature generator, LT-GEN). The result is an increased COP.

The particular double-effect cycle in Fig. 2.5 is a serial flow type, which means that the whole solution from the absorber goes through the two generators in series. In a parallel-flow double-effect cycle, after the LT-HEX one part of the solution flows to the HT-GEN and the other flows to the LT-GEN.

Since the HT-GEN operates at a high pressure, this cycle is not practical for a refrigerant with a low boiling temperature like ammonia. The highest pressure in a double-effect LiBr-water cycle approaches atmospheric pressure.

The COP of a typical water-cooled double-effect LiBr-water chiller ranges between 1.2-1.3 and the driving temperature is in the range of 150-170°C.

2.1.2.3 Half-effect cycle

Although no half-effect absorption chiller is listed in Table 2.1, this cycle is included here because it is promising for application to solar absorption cooling as suggested by Kim and Machielsen (2002b)

Fig. 2.6 shows one of the low-temperature cycles known by such names as "two-stage" or "half-effect" absorption cycles.

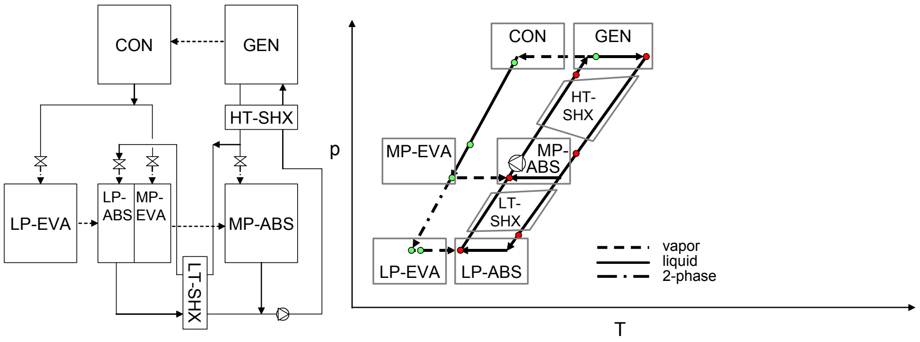

Figure 2.6 Block and P-T-x diagram of heat-coupled parallel-flow half-effect cycle

Among the different names, "half-effect" is preferred because "two-stage" is a very general term that would even encompass a double-effect cycle.

The name, half-effect has been given in line with the ideas of "single-" and "double-effect" cycles because this cycle has roughly half of a single-effect cycle's COP.

Among various half-effect cycles, the cycle in Fig. 2.6 can best be characterized by the heat-coupled absorber (LP-ABS)-evaporator (MP-EVA) configuration. This is the reason why it has been named "heat-coupled".

The cycle has a single generator (GEN in Fig. 2.6) and condenser (CON) but two evaporators (LP- and MP-EVA), two absorbers (LP- and MP-ABS) and two solution heat exchangers (LT- and HT-SHX). The functions of the generator and condenser are the same as in other cycles. The liquefied refrigerant from the condenser is split into two flows and distributed to LP-EVA (low-pressure evaporator) and MP-EVA (mid-pressure evaporator). Among the two absorbers, LP-ABS (low-pressure absorber) is in thermal contact, i.e. "heat-coupled", with MP-EVA as shown in the block diagram, which means that the evaporating refrigerant in MP-EVA cools down the LP-ABS. In this configuration, refrigeration effect is attained only in LP-EVA and the removed heat from the cold heat source is transferred firstly by mass transfer (i.e. absorption of vapor) from LP-EVA to LP-ABS, by heat conduction from LP-ABS to MP-EVA, then again by mass transfer from MP-EVA to MP-ABS where it is finally rejected to the environment.

The biggest advantage with this cycle in solar cooling application is that the generator temperature is significantly lower than for the other cycles. Disadvantages are firstly, complicated system configuration and secondly, a reduced COP.

The name "parallel-flow" has been used to differentiate the cycle presented in Fig. 2.6 from another half-effect cycle. As shown in Fig. 2.6, all solution first flows to the generator and it is then split to proceed to the two absorbers in parallel. However this solution flow can also be configured to flow through the two absorbers in series as shown in Fig. 2.7a.

Another example of half-effect cycle is shown in Fig. 2.7b. This cycle is a combination of two single-effect cycles where the absorber of one cycle is "mass-coupled" to the generator of the other.

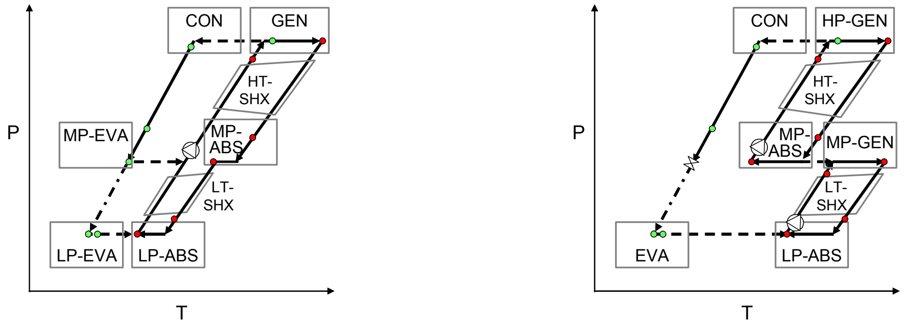

(a) heat-coupled serial-flow (b) mass-coupled

Figure 2.7 Other half-effect cycles

The COP of a half-effect cycle ranges between 0.3 and 0.4. Typical driving temperatures for water-cooled half-effect cycles are in the range of 60 to 70^{o}C. Air-cooled cycles would require driving temperatures about 30K higher than this temperature level.

2.1.2.4 GAX cycle

This cycle has been named after one of its components, which is the generator-absorber heat exchanger (GAX in Fig. 2.8).

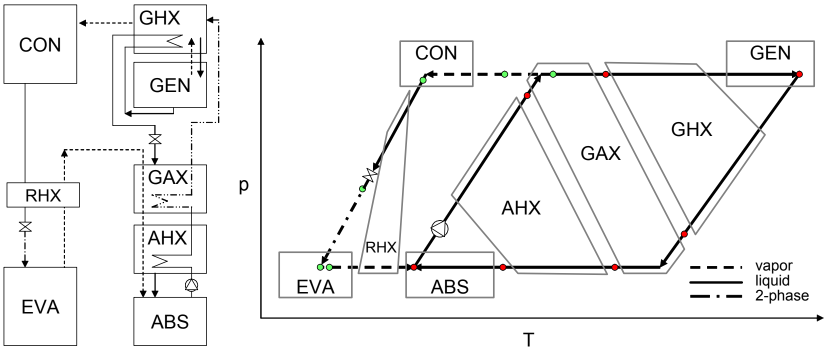

Figure 2.8 Block and P-T-x diagram of double-effect absorption cycle

As shown in Fig. 2.8, this cycle operates in a wide temperature range. After the generation process is finished in the generator (GEN in Fig. 2.8), the solution temperature has reached a very high level. This high-temperature solution is reused to boil off extra refrigerant from the colder solution first in the generator heat exchanger (GHX) and then in the GAX. Difference between GHX and GAX is that GAX has two-phase flows on both sides, i.e. generation in the cold side and absorption in the hot side. Thanks to this heat recovery, extra refrigerant is generated resulting in a higher COP.

There is another heat exchanger called absorber heat exchanger (AHX) between GAX and an ordinary absorber at the bottom, which is cooled by the coldest solution in the cycle. When there is no GAX or GAX is not working properly due to low driving temperatures, the GAX cycle becomes an AHX cycle working at a lower temperature level and its COP decreases.

Because GAX cycles require a working fluid that is stable in a wide temperature range, aqueous ammonia solution is typically used. In a NH_3-H_2O GAX cycle, the role of the rectifier is very important because the refrigerant vapour leaving the high-temperature generator has a low purity.

Another interesting characteristic of the GAX cycle is that its COP increases continuously as the driving temperature increases, which is quite different from the other absorption cycles where the COP is more or less constant over the entire operating temperature range.

For example, Fig. 2.9 shows a COP vs. generator temperature curve quoted from Kim and Machielsen (2002a). Since the GAX cycle in Fig. 2.9 operates as an AHX cycle in the lower temperature range, its COP continuously follows the COP of the AHX and the GAX cycles in Fig. 2.9 in the corresponding temperature range.

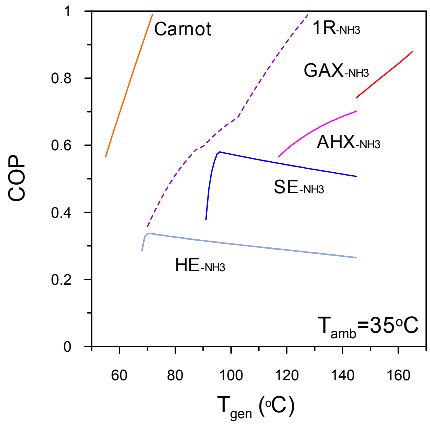

Figure 2.9 COP of various NH_3-H_2O cycles (Kim and Machielsen, 2002a)

2.2 Dynamic models

Considering the number of systems to be evaluated, it has been decided to take a modular approach in modeling a system, which is similar to that of Grossman and Michelson (1985). As can be concluded from the previous section, although different in configuration, absorption chillers have common components such as generator, absorber, condenser and evaporator. Therefore, if models for such components are written in such a way that they can be used for different systems, much effort and time can be saved that would otherwise be needed for writing a new program for each system. Very recently, this approach has also been taken by Fu et al (2006), where a dynamic model library was developed for simulation of absorption systems for Dymola, which is a simulation software providing a complete environment for dynamic model development. Their purpose was to reduce the development time for system modeling by "object-oriented" modeling.

Another aspect worth mentioning in the present modeling approach is that the component models have been developed for minimal computing time. Governing equations and property correlations were simplified within acceptable error ranges. Considering that dynamic simulation in solar engineering is often intended for the evaluation of the seasonal or annual performance of a system, short computing time is an important practical advantage.

In the following Sections, dynamic models will be developed for the different system components. The derivation of some of the equations reported here requires consultation of Chapter 5 and of Appendix C.

2.2.1 Solar collector

As described in Section 2.1.1, static performance of a solar collector can be described by the three constants in Eq. (2.1), namely η_o, c_1 and c_2. Beside these parameters, a dynamic model takes into account the influences of the thermal masses of the solar collector and of the heat transfer medium inside.

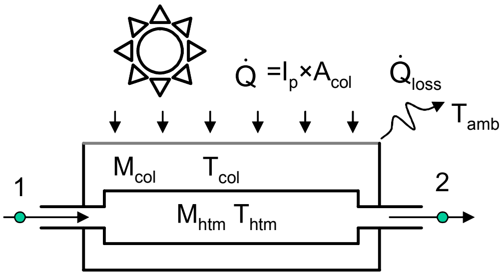

Figure 2.10 Schematic diagram of solar collector

First of all, it is assumed that the temperature of the heat transfer medium inside the collector and that of the surrounding structure, i.e. the body of the solar collector, vary at the same rate in time, i.e. $dT_{col}/dt = dT_{htm}/dt$. That is, there is no time delay in the heat transfer between heat transfer medium and solar collector body. It is further assumed that the mass of heat transfer medium inside the collector is constant.

Then an energy balance equation for the whole solar collector in Fig. 2.10 gives a time derivative of the heat transfer medium temperature T_{htm} as

$$\frac{dT_{htm}}{dt}=\frac{1}{M_{htm}C_p^{htm}+M_{col}C_p^{col}}\times \left[\dot{m}_{01}C_p^{htm}\left(T_{01}-T_{02}\right)+\eta_o I_p A_{col}-c_1 A_{col}\left(T_{htm}-T_{amb}\right)-c_2 A_{col}\left(T_{htm}-T_{amb}\right)^2\right] \tag{2.3}$$

For simulation purposes, T_{02} is set equal to T_{htm}, which assumes that the mass of heat transfer medium inside is so large that the condition at the outlet is not influenced by that of the incoming medium. This is equivalent to the so-called "upwind scheme" in computational fluid dynamics.

The constants η_o, c_1 and c_2 in Eq. (2.3) are given in Eq. (2.2) as functions of the collector price.

2.2.2 Generator

Fig. 2.11 is a schematic diagram of a falling film type generator. Rich solution (state1 in Fig. 2.11) is distributed onto the heat exchanger where the heat transfer medium is passing through (5→6). The generated vapour flows out (4) and the poor solution flows down (2) to the bottom of the generator.

The generator model includes two control volumes. One is for the heat exchanger section and the other for the solution at the bottom. The generator model does not include a vapour model. Such model will be treated separately in a pressure vessel model that will follow. Therefore, the conditions of the exiting vapour flow at state 4 in Fig. 2.11 represent the average conditions of the vapour generated in the generator at a certain time step.

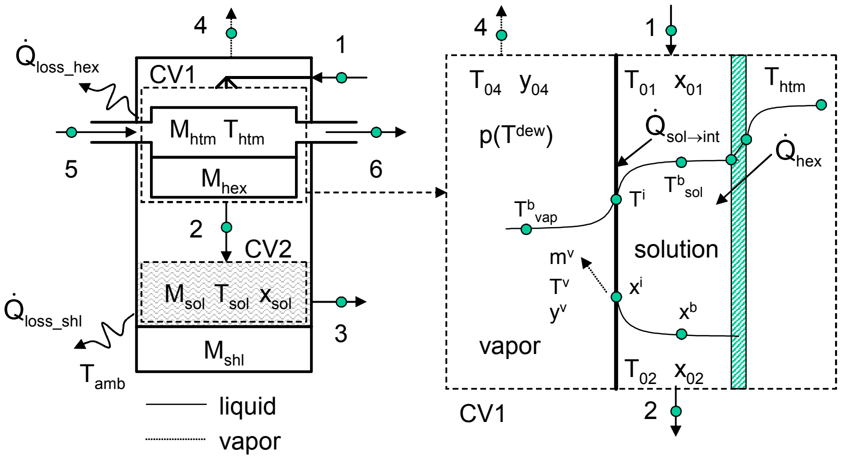

Figure 2.11 Schematic diagram of the generator

In the heat exchanger control volume (CV1 in Fig. 2.11), the mass of the falling film on the surface of the heat exchanger is negligibly small compared with that of the heat transfer medium inside it. The mass of liquid film can thus be neglected and consequently heat and mass transfer on the falling film side are assumed to take place instantaneously.

The mass of the heat transfer medium inside the heat exchanger is assumed constant, so that the energy balance equation over the heat exchanger gives the time derivative of heat transfer medium temperature T_{htm} as

$$\frac{dT_{htm}}{dt} = \frac{1}{M_{htm}C_p^{htm} + M_{hex}C_p^{hex}} \times \left[\dot{m}_{05}C_p^{htm}\left(T_{05} - T_{06}\right) - \dot{Q}_{hex} - \dot{Q}_{loss\_hex} \right] \tag{2.4}$$

Like in the solar collector model, the temperature gradient of heat transfer medium and that of the surrounding structure, the generator heat exchanger in this case, are assumed to be identical in Eq. (2.4). This assumption has been made for all following components and thus it will not be repeatedly explained from here on.

$\dot{Q}_{hex}$ and $\dot{Q}_{loss\_hex}$ in Eq. (2.4) are the heat transfer rate from the heat transfer medium to the falling film and the heat loss from the heat transfer medium to the environment, respectively:

$$\dot{Q}_{hex} = \left(UA\right)_{hex}\left(T_{htm} - T_{sol,avg}^{b}\right) \tag{2.5}$$

$$\dot{Q}_{loss\_hex} = \left(UA\right)_{loss\_hex}\left(T_{htm} - T_{amb}\right) \tag{2.6}$$

Accurate determination of $\dot{Q}_{hex}$ in Eq. (2.5) requires a detailed model as described in Section 5.2 in Ch. 5. Since the purpose of the present dynamic simulation does not require such an elaborate model, the falling film model in Ch. 5 has been simplified as follows.

In the following, the heat transfer between vapour and solution and the mass transfer resistance in the vapour phase are neglected.

Since the heat transfer between vapour and solution is neglected, the heat transfer rate from bulk solution to interface, $\dot{Q}_{sol\to int}$ is equal to the product of vapour flow rate, $\dot{m}_{04}$ and heat of desorption, Δh_{des}, as in

$$\dot{m}_{04}\Delta h_{des} - \dot{Q}_{sol\to int} = \dot{m}_{04}\Delta h_{des} - \left(\alpha A\right)_{sol\to int}\left(T_{sol}^{b} - T^{i}\right)_{avg} = 0 \tag{2.7}$$

where $\alpha_{sol\to int}$ is the heat transfer coefficient between bulk solution and interface and T^{b}_{sol} and T^{i} are the bulk solution and interface temperature respectively.

Assuming the vapour and solution are in equilibrium at the interface, T^{i} is equal to the equilibrium temperature T^{*} for the corresponding solution concentration x^{i} and the pressure p, i.e. $T^{i}=T^{*}(p,x^{i})$.

Assuming that mass transfer takes place between bulk solution and the interface only by diffusion (see Appendix D1 and Section 5.2 in Ch. 5 for a combined convection-diffusion model), mass balance for the absorbent at the interface gives $\dot{m}_{04}$ in terms of the concentration difference across the liquid film as

$$\dot{m}_{04} - \rho KA\left(x^{i} - x^{b}\right)_{avg} = 0 \tag{2.8}$$

where K is the mass transfer coefficient between bulk solution and interface.

Introducing Eq. (C1.6) from Appendix C1 for T^i in Eq. (2.7) gives

$$T^i \equiv \left(\frac{\partial T}{\partial x}\right) x^i + T_{x00} \tag{2.9}$$

where T_{x00} is the intercept on the temperature axis of the linear approximation of an equilibrium curve in the T-x domain.

Combining Eq. (2.7) and (2.8) gives a new expression for $\dot{m}_{04}$ as

$$\dot{m}_{04} = \left[\frac{1}{\rho K}\left(\frac{\partial T}{\partial x}\right) + \frac{\Delta h_{des}}{\alpha}\right]^{-1} A \left[T^b_{sol,avg} - \left(\frac{\partial T}{\partial x}\right) x^b_{avg} - T_{x00}\right] \tag{2.10}$$

where the average temperature and concentration are defined by

$$T^b_{sol,avg} \equiv (1-F)\times T_{01} + F\times T_{02} \tag{2.11}$$

$$x^b_{avg} \equiv (1-F)\times x_{01} + F\times x_{02} \tag{2.12}$$

where F is a weight factor, which has been set at 0.5.

The average bulk solution temperature defined by Eq. (2.11) causes a large error when the temperature of the incoming solution (T_{01}) is far away from its equilibrium temperature (T^*_{01}) because the temperature and concentration profiles are not fully developed at the inlet of the heat exchanger. This is clearly illustrated in Fig. 5.6 in Ch. 5, where the solution is shown to experience a radical change as soon as it enters the generator.

A possible solution is to use an equilibrium temperature T^*_{01} instead of T_{01} in Eq. (2.11). Then inserting Eq. (2.11) and (2.12) into Eq. (2.10) and rearranging it gives

$$\dot{m}_{04} = C_1 T_{02} + C_2 x_{02} + C_3 \tag{2.13}$$

where the constants are defined by

$C_1 \equiv F\left[\frac{1}{\rho K}\left(\frac{\partial T}{\partial x}\right) + \frac{\Delta h_{des}}{\alpha}\right]^{-1} A$, $C_2 \equiv -C_1\times(\partial T/\partial x)$ and $C_3 \equiv [(1-F)(C_1 T^*_{01} + C_2 x_{01}) - C_1\times T_{x00}]/F$.

By Eq. (2.13), for the given inlet conditions, the vapour generation rate $\dot{m}_{04}$ is now described in terms of the bulk solution temperature T_{02} and the concentration x_{02} at the outlet of the heat exchanger.

On the other hand, neglecting the heat transfer between vapour and solution and using Eq. (5.40) from Ch.5, an overall energy balance equation for the falling film can be written as

$$\Sigma\dot{Q} = \dot{m}_{01} C^l_p (T_{02} - T_{01}) + \dot{m}_{04}\left[a_{x=x_{01}} h^{fg} + C^v_p (T_{04} - T^*_{01}) + C^l_p (T^*_{02} - T_{02})\right] - \dot{Q}_{hex} = 0 \tag{2.14}$$

where $a_{x=x01}$ is the gradient of the equilibrium curve, $\partial(1/T^{dew})/\partial(1/T)$, at $x=x_{01}$ as defined in Appendix C2 and T_{04} is the temperature of vapour that leaves the generator.

Neglecting the superheat of solution leaving the heat exchanger, i.e. letting $T^*_{02}=T_{02}$ in Eq. (2.14), and inserting Eq. (2.5) into Eq. (2.14) gives

$$\dot{m}_{01}C_p^l\left(T_{02}-T_{01}\right)+\dot{m}_{04}\left[a_{x=x_{01}}h^{fg}+C_p^v\left(T_{04}-T_{01}^*\right)\right]-\left(UA\right)_{hex}\left(T_{htm}-T_{sol,avg}^b\right)=0 \qquad (2.15)$$

Then, inserting Eq. (2.11) and (2.13) into (2.15) and rearranging it for T_{02} gives

$$T_{02}=-\left(\frac{D_2}{D_1}\right)x_{02}-\frac{D_3}{D_1} \qquad (2.16)$$

where the new constants are defined by

$$D_1\equiv\dot{m}_{01}C_p^l+C_1\left[a_{x=x_{01}}h^{fg}+C_p^v\left(T_{04}-T_{01}^*\right)\right]+F\left(UA\right),$$
$$D_2\equiv C_2\left[a_{x=x_{01}}h^{fg}+C_p^v\left(T_{04}-T_{01}^*\right)\right]\text{ and}$$
$$D_3\equiv-\dot{m}_{01}C_p^lT_{01}+C_3\left[a_{x=x_{01}}h^{fg}+C_p^v\left(T_{04}-T_{01}^*\right)\right]+\left(UA\right)\left[\left(1-F\right)T_{01}^*-T_{htm}\right].$$

Finally, replacing T_{02} in Eq. (2.13) with Eq. (2.16) and inserting it into the following mass balance equation for absorbent

$$\Sigma\dot{m}=\dot{m}_{01}x_{01}-\dot{m}_{02}x_{02}-\dot{m}_{04}y_{04}=\dot{m}_{01}\left(x_{01}-x_{02}\right)+\dot{m}_{04}\left(x_{02}-y_{04}\right)=0 \qquad (2.17)$$

gives a quadratic equation for x_{02} as

$$E_1x_{02}^2+E_2x_{02}+E_3=0 \qquad (2.18)$$

where $E_1\equiv C_2-C_1D_2/D_1$, $E_2\equiv(C_3-C_1D_3/D_1)(1-y_{04})-\dot{m}_{01}$ and $E_3\equiv\dot{m}_{01}x_{01}-y_{04}(C_3-C_1D_3/D_1)$. y_{04} is the absorbent concentration in the exiting vapor, which is not zero for the systems where the absorbent is volatile as in a NH_3-H_2O system.

For solution, Eq. (2.18) is first solved for x_{02} and then $\dot{m}_{04}$ and T_{02} are calculated using Eq. (2.17) and (2.16), respectively. And then heat transfer rates can be calculated by Eq. (2.5) and (2.6) for the determination of the time derivative in Eq. (2.4).

Although the falling film model described above gives a larger error than the falling model in Ch. 5, it is simpler and quick to solve, which is particularly favourable for dynamic simulation.

For the solution in the control volume at the bottom (CV2 in Fig. 2.11), the following equations were derived.

Total solution mass balance;

$$\frac{dM_{sol}}{dt}=\dot{m}_{02}-\dot{m}_{03} \qquad (2.19)$$

Absorbent mass balance;

$$\frac{d\left(M_{sol}x_{sol}\right)}{dt}=\dot{m}_{02}x_{02}-\dot{m}_{03}x_{03} \tag{2.20}$$

Energy balance;

$$\begin{aligned}\frac{dT_{sol}}{dt}=&\frac{1}{M_{sol}C_p^l+M_{shl}C_p^{shl}}\\&\times\left[\dot{m}_{02}h_{02}^l-\dot{m}_{03}h_{03}^l-h_{sol}^l\frac{dM_{sol}}{dt}-M_{sol}\left(\frac{\partial h_{sol}^l}{\partial x}\right)\frac{dx_{sol}}{dt}-\dot{Q}_{loss\_shl}\right]\end{aligned} \tag{2.21}$$

where the heat loss from the solution to environment $\dot{Q}_{loss\_shl}$ is defined by

$$\dot{Q}_{loss\_shl}=\left(UA\right)_{loss\_shl}\left(T_{sol}-T_{amb}\right) \tag{2.22}$$

2.2.3 Absorber

The absorber model is different from the generator model only from the fact that the condition of incoming vapour is independent from the conditions of solution inside the absorber as explained in Appendix C2. Therefore the generator model can also be used for the absorber only with minor modifications regarding the properties of the vapour involved.

2.2.4 Condenser

Fig. 2.12 shows a schematic diagram of the condenser.

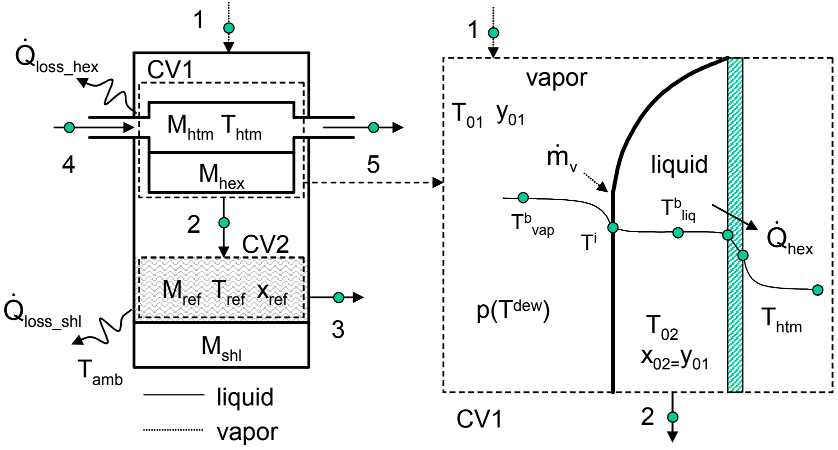

Figure 2.12 Schematic diagram of the condenser

The condenser model consists of a heat exchanger control volume and a liquid control volume at the bottom. Like for the generator model, the thermal mass of condensed refrigerant in the heat exchanger is neglected.

Assuming the mass of heat transfer medium inside the heat exchanger is constant, an energy balance equation over the heat exchanger gives the time derivative of heat transfer medium temperature T_{htm} as

$$\frac{dT_{htm}}{dt} = \frac{1}{M_{htm}C_p^{htm} + M_{hex}C_p^{hex}} \times \left[\dot{m}_{04}C_p^{htm}\left(T_{04} - T_{05}\right) + \dot{Q}_{hex} - \dot{Q}_{loss\_hex} \right] \tag{2.23}$$

where $\dot{Q}_{loss\_hex}$ is defined by Eq. (2.6) and $\dot{Q}_{hex}$, the heat transfer from the condensing refrigerant to the heat transfer medium, is defined by

$$\dot{Q}_{hex} = \left(UA\right)_{hex}\left(T_{avg}^{i} - T_{htm}\right) \tag{2.24}$$

where T^i is the equilibrium temperature of refrigerant at the vapor-liquid interface. This temperature is equal to the corresponding dew temperature T^{dew} when the refrigerant is pure. When the refrigerant is not pure, an average interface temperature should be used instead. In the present condenser model, in order to avoid complexities in relation to the modeling of the condensation of mixtures, the following assumptions have been made.

- Heat and mass transfer resistances in liquid film are negligible
  → Bulk liquid is assumed saturated anywhere in the heat exchanger.

- Condensation temperature is uniform at the boiling point of refrigerant.
  → The average condensation temperature $T^i_{avg}=T^*(p, x_{02})$.

Potential errors by the assumptions above are not significant for pure refrigerants. However, for non-azeotropic refrigerants such as ammonia-water mixture, particularly the second assumption would cause underestimation of the heat transfer rate between the condensate and the heat transfer medium.

Then Eq. (2.24) becomes

$$\dot{Q}_{hex} = \left(UA\right)_{hex}\left(T_{02}^{*} - T_{htm}\right) \tag{2.25}$$

where $T^*_{02}= T_{02}=T^*(p, x_{02})$.

The condensation rate $\dot{m}_{01}$ is calculated by

$$\dot{m}_{01} = \frac{Q_{hex}}{h^{fg}} \tag{2.26}$$

And because all the vapour entering the heat exchanger control volume is condensed, the absorbent mass balance equation gives

$$x_{02} = y_{01} \tag{2.27}$$

For the liquid control volume at the bottom (CV2 in Fig. 2.12), the following equations were derived.

Total refrigerant mass balance:

$$\frac{dM_{ref}}{dt} = \dot{m}_{02} - \dot{m}_{03} \tag{2.28}$$

Absorbent mass balance:

$$\frac{d\left(M_{ref}x_{ref}\right)}{dt} = \dot{m}_{02}x_{02} - \dot{m}_{03}x_{03} \tag{2.29}$$

Energy balance:

$$\begin{aligned}\frac{dT_{ref}}{dt} = {} & \frac{1}{M_{ref}C_p^l + M_{shl}C_p^{shl}} \\ & \times\left[\dot{m}_{02}h_{02}^l - \dot{m}_{03}h_{03}^l - h_{ref}^l\frac{dM_{ref}}{dt} - M_{ref}\left(\frac{\partial h_{ref}^l}{\partial x}\right)\frac{dx_{ref}}{dt} - \dot{Q}_{loss\_shl}\right]\end{aligned} \tag{2.30}$$

where the heat loss from the refrigerant to environment $\dot{Q}_{loss\_shl}$ is defined in the same way as in Eq. (2.22).

2.2.5 *Evaporator*

Although basically the same, the evaporator model is different from the generator model in a few aspects, which were intended for simpler and quicker solution of the equation set. In this section, only the differences are explained.

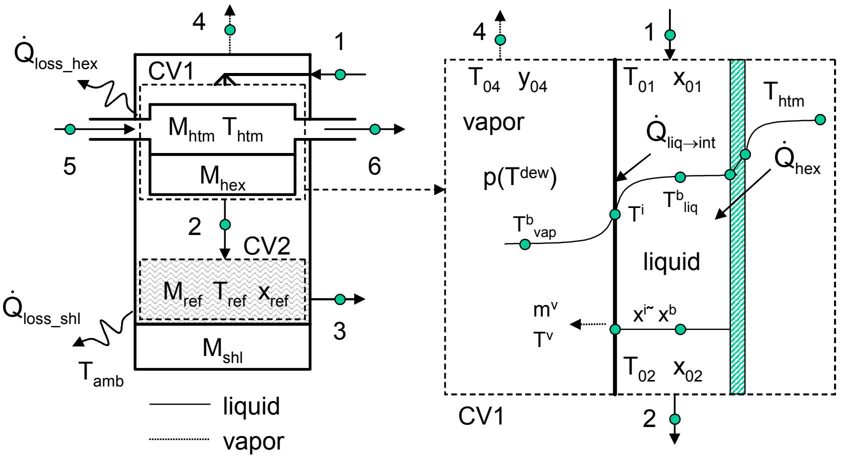

Figure 2.13 Schematic diagram of the evaporator

The biggest difference from the generator model is that the mass transfer resistance is neglected in the evaporator. This assumption would introduce an error only for non-azeotropic systems and it is negligibly small when the purity of a refrigerant is high.

Having neglected the mass transfer resistance in the liquid film, the average interface temperature T^i_{avg} is given by

$$T^i_{avg} = \left(\frac{\partial T}{\partial x}\right) x^b_{avg} + T_{x00} \tag{2.31}$$

Note that x^i_{avg} in Eq. (2.9) is replaced by x^b_{avg}. In order to simplify the solution process, the average bulk concentration x^b_{avg} in Eq. (2.31) has been defined by the following equation.

$$x^b_{avg} \equiv (1-F)\times(x_{01})_{t=t} + F\times(x_{02})_{t=t-\Delta t} \tag{2.32}$$

Note that Eq. (2.32) is different from its counterpart in the generator model, i.e. Eq. (2.12). In Eq. (2.32), x_{02} is not the value from the present time step but the one from the previous. By using the previous value of x_{02}, the mathematic system of equations for the evaporator has one less unknown than the generator model. By this approximation, the solution procedure and computing time was greatly reduced. Errors from this approximation are negligible for a small time step.

Assuming that $T_{04}=T_{01}$ in Eq. (2.15) and using Eq. (2.7), (2.11) and (2.31), Eq. (2.15) gives T_{02} as

$$T_{02} = G_1 T_{01} + G_2 T_{htm} + G_3 \tag{2.33}$$

where the constants are defined by

$$G_1 \equiv \frac{\dot{m}_{01}C^l_p - \left[G_0(\alpha A)_{liq\to int} + (UA)_{hex}\right](1-F)}{\dot{m}_{01}C^l_p + \left[G_0(\alpha A)_{liq\to int} + (UA)_{hex}\right]F}, \quad G_2 \equiv \frac{(UA)_{hex}}{\dot{m}_{01}C^l_p + \left[G_0(\alpha A)_{liq\to int} + (UA)_{hex}\right]F} \text{ and}$$

$$G_3 \equiv \frac{(\alpha A)_{liq\to int}\left[(\partial T/\partial x)x^b_{avg} + T_{x00}\right]}{\dot{m}_{01}C^l_p + \left[G_0(\alpha A)_{liq\to int} + (UA)_{hex}\right]F}$$

wherein $G_0 \equiv a_{x=x_{01}} h^{fg} / \Delta h_{des}$, which is 1.0 for a pure refrigerant.

For solution, Eq. (2.33) is first calculated for T_{02} and then $\dot{Q}_{hex}$ is determined by Eq. (2.5) and (2.11). Then the evaporation rate $\dot{m}_{04}$ is given by Eq. (2.7).

For a non-azeotropic refrigerant, at the end of the iteration step, x_{02} is calculated by the following equation from mass conservation

$$x_{02} = \frac{\dot{m}_{01}x_{01} - \dot{m}_{04}y_{04}}{\dot{m}_{01} - \dot{m}_{04}} \tag{2.34}$$

where y_{04} is the concentration of absorbent in the exiting vapour flow.

2.2.6 Generator-Condenser

This component is a steam-fired generator, similar to the generators encountered in steam-driven absorption chillers and in double-effect absorption chillers.

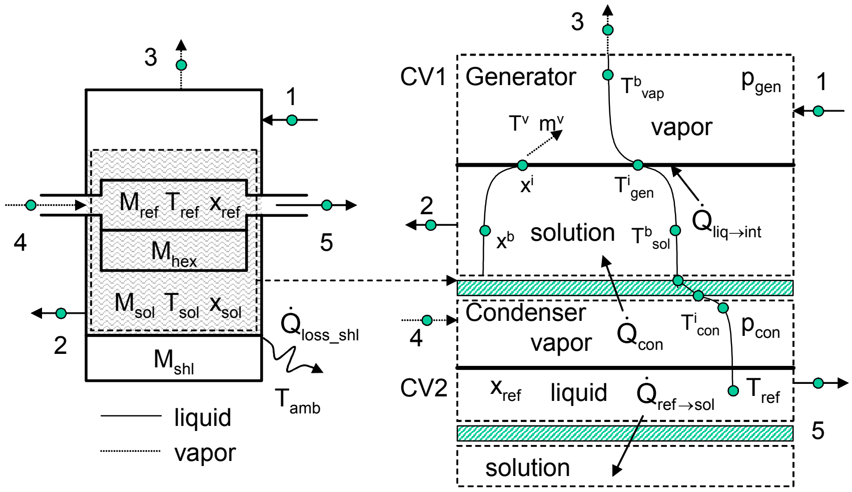

Figure 2.14 Schematic diagram of the generator-condenser

In this model, it is assumed that a heat exchanger is immersed in a mass of solution and steam is condensed inside the heat exchanger. The model consists of two control volumes as shown in Fig. 2.14. Again, there is no vapour control volume in this model.

To begin with, the two control volumes are linked by condensation heat transfer $\dot{Q}_{con}$ defined by

$$\dot{Q}_{con} = (UA)_{con} \left(T^i_{con} - T^b_{sol}\right)_{avg} \tag{2.35}$$

where T^i_{con} and T^b_{sol} are the vapor-liquid interface temperature in the condenser and the bulk solution temperature in the generator respectively.

And there is another sensible heat transfer from the bulk liquid refrigerant and the bulk solution at the bottom of condenser, $\dot{Q}_{ref\rightarrow sol}$ defined by

$$\dot{Q}_{ref\rightarrow sol} = (UA)_{ref\rightarrow sol} \left(T^b_{ref} - T^b_{sol}\right)_{avg} \tag{2.36}$$

Assuming that there is no pressure loss and no heat transfer resistance in the condensate film in the condenser, i.e. $T^i_{con}=T^{dew}(p_{con})$, and the bulk solution temperature is uniform around the condenser at $T^b_{sol,avg}=T_{sol}$, Eq. (2.35) becomes

$$\dot{Q}_{con} = (UA)_{con} \left(T^{dew}_{con} - T_{sol}\right) \tag{2.37}$$

The amount of condensation $\dot{m}_{04}$ is calculated by

$$\dot{m}_{04} = \frac{\dot{Q}_{con}}{h^{fg}} \tag{2.38}$$

Therefore for the liquid at the bottom of the condenser, the following equations are derived.

Total refrigerant mass balance:

$$\frac{dM_{ref}}{dt} = \dot{m}_{04} - \dot{m}_{05} \tag{2.39}$$

Energy balance:

$$\begin{aligned}\frac{dT_{ref}}{dt} &= \frac{1}{M_{ref}C_p^l + M_{hex}C_p^{hex}} \\ &\quad \times \left[\dot{m}_{04}h_{04}^{*l} - \dot{m}_{05}h_{05}^l - h_{ref}^l \frac{dM_{ref}}{dt} - M_{ref}\left(\frac{\partial h_{ref}^l}{\partial x}\right)\frac{dx_{ref}}{dt} - \dot{Q}_{ref \to sol} \right]\end{aligned} \tag{2.40}$$

where h_{04}^{*l} is the enthalpy of saturated condensate

On the other hand, for the generator control volume, i.e. CV1, the following equations are derived.

Assuming Eq. (2.10) holds also in this case, the amount of generated vapour is described by

$$\dot{m}_{03} = \left[\frac{1}{\rho K}\left(\frac{\partial T}{\partial x}\right) + \frac{\Delta h_{des}}{\alpha} \right]^{-1} A \left[T_{sol} - \left(\frac{\partial T}{\partial x}\right) x_{sol} - T_{x00} \right] \tag{2.41}$$

For the bulk of solution, the following equations are derived:

Total solution mass balance:

$$\frac{dM_{sol}}{dt} = \dot{m}_{01} - \dot{m}_{02} - \dot{m}_{03} \tag{2.42}$$

Absorbent mass balance:

$$\frac{d\left(M_{sol}x_{sol}\right)}{dt} = \dot{m}_{01}x_{01} - \dot{m}_{02}x_{02} - \dot{m}_{03}y_{03} \tag{2.43}$$

Energy balance:

$$\begin{aligned}\frac{dT_{sol}}{dt} &= \frac{1}{M_{sol}C_p^l + M_{shl}C_p^{shl}} \\ &\quad \times \left[\dot{m}_{01}h_{01}^l - \dot{m}_{02}h_{02}^l - \dot{m}_{03}h_{03}^v - h_{sol}^l \frac{dM_{sol}}{dt} - M_{sol}\left(\frac{\partial h_{sol}^l}{\partial x}\right)\frac{dx_{sol}}{dt} - \dot{Q}_{loss\_shl} \right]\end{aligned} \tag{2.44}$$

where h_{03}^{v} is the enthalpy of the generated vapour and $\dot{Q}_{loss\_shl}$ is defined by Eq. (2.22)

2.2.7 Generator-Absorber

This component is used in GAX chillers, where absorption heat is used to generate extra refrigerant vapour for high efficiency. It has been modeled as a falling film type heat exchanger where absorption takes place in the falling film on the outer surface of the heat exchanger causing the solution inside to boil as shown in Fig. 2.15.

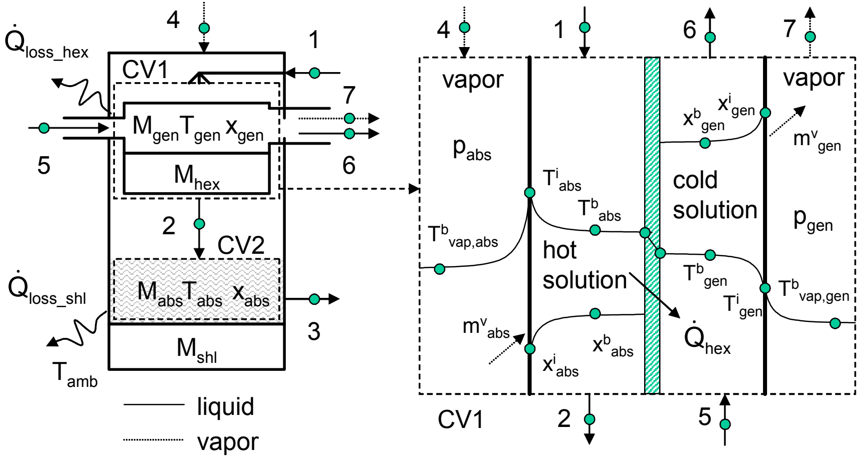

Figure 2.15 Schematic diagram of the generator-absorber

Thermal mass of the falling film is neglected and the bulk solution temperature is assumed uniform in the generator. These assumptions make this component model to be a mere combination of the generator part of the generator-condenser model in Section 2.2.6 and the falling film part of the generator in Section 2.2.2. Therefore Eqs. (2.41)~(2.44) apply to the generator side of CV1 and all the solution equations in Section 2.2.2 apply to the absorption side.

2.2.8 Absorber-Evaporator

In this component, the vapor-absorbing solution on one side is cooled down by the evaporating refrigerant on the other. This component is found in the heat-coupled half-effect absorption chillers introduced in Section 2.1.2.3, where part of the refrigerant flow is used to cool down an absorber to allow for a lower generator temperature.

The present model consists of three control volumes as shown in Fig. 2.16. Control volume 1 (CV1) contains a thin heat exchanging wall with two falling films on both sides. After the two falling films exchange heat in CV1, the solution enters CV2 and the refrigerant enters CV3 which are thermally separated from each other.

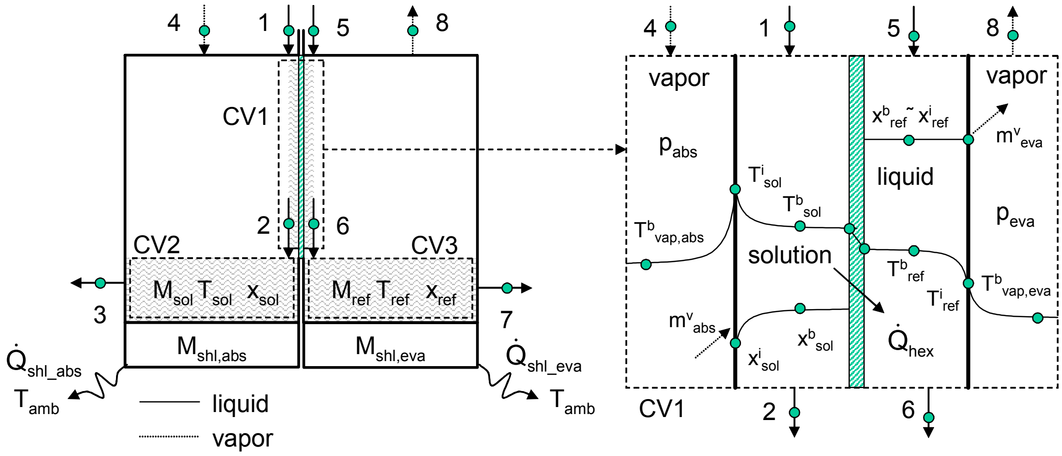

Figure 2.16 Schematic diagram of the absorber-evaporator

The thermal masses of the heat exchanger wall and of the two falling films in CV1 are all neglected and heat and mass transfer are assumed to take place instantaneously. Besides, the mass transfer resistance in the refrigerant film has been neglected.

From these assumptions, the heat and mass transfer model in CV1 becomes a combination of the falling film part of the evaporator in Section 2.2.5 and that of the generator in Section 2.2.2 with a modification of the definition of heat transfer rate between the two falling film flows.

The heat transfer rate between the absorber and evaporator $\dot{Q}_{hex}$ is defined by

$$\dot{Q}_{hex} = (UA)_{hex}\left(T^b_{sol} - T^b_{ref}\right)_{avg} \tag{2.45}$$

Then, according to Eq. (2.33), the bulk temperature of refrigerant at the outlet of CV1, i.e. T_{06}, is given by

$$T_{06} = G_1 T_{05} + G_2 T^b_{sol,avg} + G_3 \tag{2.46}$$

where the indexes in G_1, G_2 and G_3 in Eq. (2.33) are changed accordingly.

Inserting Eq. (2.46) into the following definition of average bulk refrigerant temperature and rearranging gives

$$\begin{aligned} T^b_{ref,avg} &\equiv (1-f)\times T_{05} + f\times T_{06} \\ &= \left[(1-f) + fG_1\right]\times T_{05} + fG_2 \times T^b_{sol,avg} + fG_3 \end{aligned} \tag{2.47}$$

where *f* is a weight factor, which has been set at 0.5 for simulation purposes.

Replacing T_{htm} in (2.5) with $T^b_{ref,avg}$ of Eq. (2.47) and using the same derivation process as from Eq. (2.5) to Eq. (2.16) in Section 2.2.2 gives the bulk temperature of the solution at the outlet of CV1, T_{02}, as

$$T_{02} = -\left(\frac{D_2}{D_1}\right)x_{02} - \frac{D_3}{D_1} \tag{2.48}$$

where

$$D_1 \equiv \dot{m}_{01}C_p^l + C_1\left[a_{x=x_{01}}h^{fg} + C_p^v\left(T_{04} - T_{01}^*\right)\right] + \left(UA\right)_{hex}F\left(1 - fG_2\right),$$

$$D_2 \equiv C_2\left[a_{x=x_{01}}h^{fg} + C_p^v\left(T_{04} - T_{01}^*\right)\right] \text{ and}$$

$$D_3 \equiv -\dot{m}_{01}C_p^l T_{01} + C_3\left[a_{x=x_{01}}h^{fg} + C_p^v\left(T_{04} - T_{01}^*\right)\right]$$
$$+\left(UA\right)_{hex}\left[\left(1-F\right)\left(1-fG_2\right)T_{01}^* - \left[\left(1-f\right) + fG_1\right]T_{05} - fG_3\right].$$

The rest of the solution procedure is the same as in Section 2.2.2.

Equations for CV2 and CV3 are basically the same as those of the generator model and they are not repeated.

2.2.9 *Rectifier*

For those systems where volatile absorbents are used, the refrigerant vapour generated by a generator has always a certain amount of absorbent in it. Because this refrigerant impurity increases the evaporator temperature, a rectifier is normally used to remove the absorbent from the refrigerant vapor.

A rectifier, which is also called distillation column, is basically a heat exchanger that partially condenses refrigerant vapor. Since an impure vapour has a dew temperature higher than the boiling (final condensation) temperature, when it passes through a cold heat exchanger surface, the less volatile component, i.e. the absorbent, is condensed on the surface resulting in an increased purity of the bulk vapor.

Fig. 2.17 shows a schematic diagram of the rectifier.

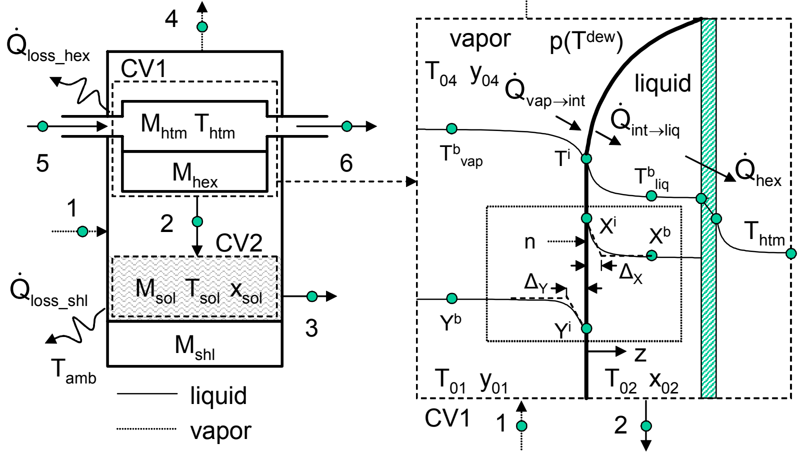

Figure 2.17 Schematic diagram of the rectifier

All the previous models assumed that the mass transfer resistance is negligible in the vapour phase. This assumption should be avoided in a realistic rectifier model because that is one of the main characteristics of a rectifier.

A rectifier model has been developed using the analysis summarized in Appendix D1. However it has been abandoned because the formulation and solution process were too complicated and time consuming.

Instead, the following simpler model has been used in the simulation. The model consists of two control volumes, one for the heat exchanger where the refrigerant vapour is partly condensed (CV1 in Fig. 2.17) and the other for the condensate at the bottom (CV2).

Regarding the mass transfer in the vapour phase in CV1, the model depends on rectification efficiency η_{rec}, which is defined by

$$\eta_{rec} = \frac{y_{04} - y_{01}}{y_{04}^{id} - y_{01}} \tag{2.49}$$

where y_{04}^{id} is an ideal absorbent concentration in the exiting vapor, which has been set to zero. Therefore, in the extreme case of $\eta_{rec}=1$, the exiting vapour is pure refrigerant. In simulation, η_{rec} has been set to an arbitrary value between from 0.9 to 0.95 for a reasonable purity level in the condenser.

Neglecting the heat transfer resistance in the liquid film, the overall energy balance for the liquid film in CV1 is expressed by

$$\Sigma\dot{Q} = \dot{m}_{02} h^{fg} + \dot{Q}_{vap\to int} - \dot{Q}_{hex} = 0 \tag{2.50}$$

where $h^{fg} \equiv h^{v} - h^{l}_{02}$ and the heat transfer rates $\dot{Q}_{vap\to int}$ and $\dot{Q}_{hex}$ are defined by

$$\dot{Q}_{vap\to int} = \left(\alpha A\right)_{vap\to int} \left(T_{vap}^{b} - T^{i}\right)_{avg} \tag{2.51}$$

$$\dot{Q}_{hex} = \left(UA\right)_{hex} \left(T^{i} - T_{htm}\right)_{avg} \tag{2.52}$$

where the average of vapour and interface temperatures are defined by

$$T_{vap,avg}^{b} = \left(1-F\right) \times T_{04} + F \times T_{01} \tag{2.53}$$

$$T_{avg}^{i} = \left(1-F\right) \times T_{04}^{i} + F \times T_{02}^{i} \tag{2.54}$$

Regarding the interface temperatures in Eq. (2.54), the following assumptions have been made:

T^{i}_{02} is the interface temperature of the solution at its bulk concentration x_{02}. Assuming $x^{i}_{02} \approx x_{02}$, i.e. neglecting mass transfer resistance in liquid film, Eq. (2.9) gives

$$T_{02}^{i} \equiv \left(\frac{\partial T}{\partial x}\right) x_{02} + T_{x00} \tag{2.55}$$

T^{i}_{04} is the interface temperature of the film at the top, where condensation just started. The interface concentration at this location may be assumed to be in equilibrium with the bulk vapour concentration, i.e. $y^{i}_{04} \approx y^{b}_{04}$. Similar to Eq. (2.9), the equilibrium vapour and liquid concentrations may be expressed by a linear approximation for a small concentration range as

$$y^{i} \equiv \left(\frac{\partial y}{\partial x}\right) x^{i} + y_{00} \tag{2.56}$$

which is also suggested by Keizer (1982).

Then, using Eq. (2.9) and (2.56), T^{i}_{04} can be expressed as

$$T_{04}^{i} \equiv \left(\frac{\partial T}{\partial x}\right)\left(\frac{\partial y}{\partial x}\right)^{-1} \left(y_{04} - y_{00}\right) + T_{x00} \tag{2.57}$$

On the other hand, from the mass conservation equations for CV1, $\dot{m}_{02}$ is given by

$$\dot{m}_{02} = \dot{m}_{01} \frac{y_{01} - y_{04}}{x_{02} - y_{04}} \tag{2.58}$$

Finally, for the vapour in CV1, the energy balance equation is written as

$$\Sigma \dot{Q} = \dot{m}_{01} h_{01}^{v} - \dot{m}_{04} h_{04}^{v} - \dot{m}_{02} h^{v} - \dot{Q}_{vap \to int} = 0 \tag{2.59}$$

For solution, first y_{04} is calculated from Eq. (2.49) with a given η_{rec}. Then Eq. (2.50), (2.58) and Eq. (2.59) are solved together for the rest of the variables.

Once the heat transfer rate between the condensate and the heat transfer medium $\dot{Q}_{hex}$ is given by Eq. (2.52), the time derivative of heat transfer medium temperature T_{htm} is calculated by

$$\frac{dT_{htm}}{dt} = \frac{1}{M_{htm} C_{p}^{htm} + M_{hex} C_{p}^{hex}} \times \left[\dot{m}_{05} C_{p}^{htm} \left(T_{05} - T_{06}\right) + \dot{Q}_{hex} - \dot{Q}_{loss\_hex} \right] \tag{2.60}$$

where $\dot{Q}_{loss\_hex}$ is defined by Eq. (2.6).

For the liquid control volume at the bottom (CV2 in Fig. 2.17), the equations for the condenser model, Eqs. (2.28)~(2.30) apply.

2.2.10 Single-phase heat exchanger

Fig. 2.18 shows a schematic diagram of a single-phase heat exchanger.

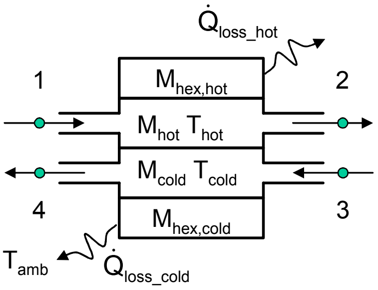

Figure 2.18 Schematic diagram of a single-phase heat exchanger

For the temperature of the hot fluid, the following equation holds

$$\frac{dT_{hot}}{dt} = \frac{1}{M_{hot}C_p^{hot} + M_{hex,hot}C_p^{hex}} \times \left[\dot{m}_{01}C_p^{hot}\left(T_{01} - T_{02}\right) - \dot{Q}_{hex} - \dot{Q}_{loss\_hot} \right] \tag{2.61}$$

And for the cold fluid,

$$\frac{dT_{cold}}{dt} = \frac{1}{M_{cold}C_p^{cold} + M_{hex,cold}C_p^{hex}} \times \left[\dot{m}_{03}C_p^{cold}\left(T_{03} - T_{04}\right) + \dot{Q}_{hex} - \dot{Q}_{loss\_cold} \right] \tag{2.62}$$

where the heat transfer rate between two fluids is defined by

$$\dot{Q}_{hex} = \left(UA\right)_{hex}\left(T_{hot} - T_{cold}\right) \tag{2.63}$$

and the heat losses are defined by

$$\dot{Q}_{loss\_hot} = \left(UA\right)_{loss\_hot}\left(T_{hot} - T_{amb}\right) \tag{2.64}$$

$$\dot{Q}_{loss\_cold} = \left(UA\right)_{loss\_cold}\left(T_{cold} - T_{amb}\right) \tag{2.65}$$

2.2.11 Solution and refrigerant tank

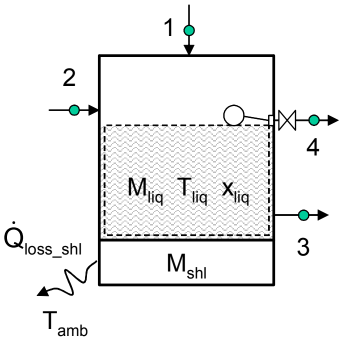

Figure 2.19 Schematic diagram of a reservoir

Solution and refrigerant tanks are reservoirs for the corresponding fluids in a system. A refrigerant tank is different from a solution tank from the fact that it has a level sensor and an overflow valve so that it can be programmed to discharge excess refrigerant to another system component, which is typically a solution tank. Both models have a single control volume for the liquid inside as shown in Fig. 2.19.

For the bulk liquid in the control volume of Fig. 2.19, the following equations are derived:

Total solution mass balance:

$$\frac{dM_{liq}}{dt} = \dot{m}_{01} + \dot{m}_{02} - \dot{m}_{03} - \dot{m}_{04} \tag{2.66}$$

Absorbent mass balance:

$$\frac{d\left(M_{liq}x_{liq}\right)}{dt} = \dot{m}_{01}x_{01} + \dot{m}_{02}x_{02} - \left(\dot{m}_{03} + \dot{m}_{04}\right)x_{03} \tag{2.67}$$

Energy balance:

$$\begin{aligned}\frac{dT_{liq}}{dt} &= \frac{1}{M_{liq}C_p^l + M_{shl}C_p^{shl}} \\ &\times\left[\dot{m}_{01}h_{01}^l + \dot{m}_{02}h_{02}^l - \left(\dot{m}_{03} + \dot{m}_{04}\right)h_{03}^l - h_{liq}^l\frac{dM_{liq}}{dt} - M_{liq}\left(\frac{\partial h_{liq}^l}{\partial x}\right)\frac{dx_{liq}}{dt} - \dot{Q}_{loss\_shl}\right]\end{aligned} \tag{2.68}$$

where $\dot{Q}_{loss\_shl}$ is the heat loss from the liquid to environment defined by

$$\dot{Q}_{loss\_shl} = \left(UA\right)_{loss\_shl}\left(T_{liq} - T_{amb}\right) \tag{2.69}$$

For simulation purposes, the solution conditions at point 3 have been set equal to those of the bulk liquid, i.e. $T_{03}=T_{liq}$, $x_{03}=x_{liq}$ and $h^l_{03}= h^l_{liq}$.

For a solution tank, the overflow $\dot{m}_{04}$ is always set to zero.

2.2.12 Expansion valve

This is a component where a throttling process takes place. Due to the high energy (enthalpy) level of the incoming liquid, which is excessive for the reduced pressure environment downstream, the excessive energy is released from the liquid in the evaporation process called flashing.

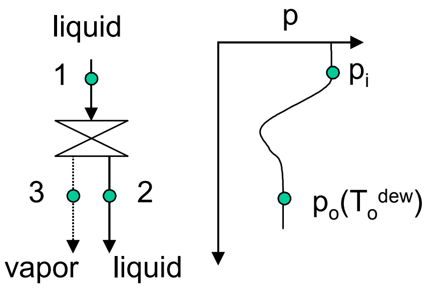

Figure 2.20 Schematic diagram of expansion valve

Adiabatic throttling process has been assumed and no thermal mass has been considered in this model. From the assumptions made, the following energy balance equation holds.

$$\Sigma \dot{Q} = h_{01}^{l} - (1-q)h_{02}^{l} - qh_{03}^{v} = 0 \tag{2.70}$$

where q is the quality at the outlet of the valve, which is defined by

$$q \equiv \frac{\dot{m}_{03}}{\dot{m}_{02} + \dot{m}_{03}} = \frac{\dot{m}_{03}}{\dot{m}_{01}} \tag{2.71}$$

For a non-azeotropic refrigerant, *q* has the following relationship with concentrations:

$$q = \frac{x_{01} - x_{02}}{y_{03} - x_{02}} \tag{2.72}$$

The vapour at point 3 can be assumed to be in equilibrium with the liquid at point 2 resulting in $T_{03}=T_{02}$ and $y_{03}=y^*(p_o, x_{02})$.

The downstream conditions are determined by solving Eqs. (2.70)~(2.72) simultaneously.

2.2.13 Mixer

This is a component where two flows of the same phase merge into a single flow.

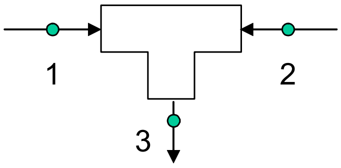

Figure 2.21 Schematic diagram of mixer

The following conservation equations were derived assuming an adiabatic homogeneous mixing.

Total mass balance;

$$\dot{m}_{03} = \dot{m}_{01} + \dot{m}_{02} \tag{2.73}$$

Absorbent mass balance;

$$\dot{m}_{03} x_{03} = \dot{m}_{01} x_{01} + \dot{m}_{02} x_{02} \tag{2.74}$$

Energy balance;

$$\dot{m}_{03} h_{03} = \dot{m}_{01} h_{01} + \dot{m}_{02} h_{02} \tag{2.75}$$

2.2.14 Splitter

In this component, a single flow is split into two flows having the same physical properties.

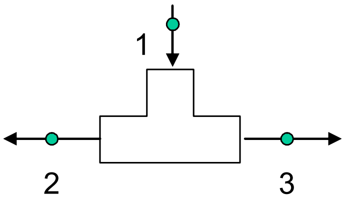

Figure 2.22 Schematic diagram of splitter

The split ratio can either be set to an arbitrary value or set dependent of the downstream condition.

Assuming no interaction with ambient, the following equations hold.

Total mass balance:

$$\dot{m}_{01} = \dot{m}_{02} + \dot{m}_{03} \tag{2.76}$$

Absorbent mass balance:

$$x_{01} = x_{02} = x_{03} \tag{2.77}$$

Energy balance:

$$T_{01} = T_{02} = T_{03} \tag{2.78}$$

2.2.15 Pressure vessel

The pressure vessel model has two vapour inlets and one outlet. The condition inside is assumed uniform and the thermal mass of the vessel has been neglected.

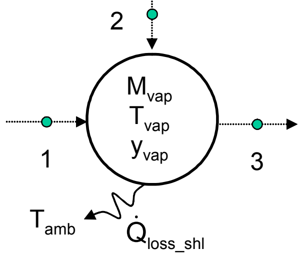

Figure 2.23 Schematic diagram of a pressure vessel

For the vapour inside the control volume, Fig. 2.23, the following equations have been derived.

Total mass balance:

$$\frac{dM_{vap}}{dt} = \dot{m}_{01} + \dot{m}_{02} - \dot{m}_{03} \tag{2.79}$$

Absorbent mass balance:

$$\frac{d\left(M_{vap}y\right)}{dt} = \dot{m}_{01}y_{01} + \dot{m}_{02}y_{02} - \dot{m}_{03}y_{03} \tag{2.80}$$

Energy balance:

$$\frac{dT_{vap}}{dt} = \frac{1}{M_{vap}C_v^v} \times \left[\dot{m}_{01}h_{01}^v + \dot{m}_{02}h_{02}^v - \dot{m}_{03}h_{03}^v - u^v\frac{dM_{vap}}{dt} - M_{vap}\left(\frac{\partial u^v}{\partial y}\right)\frac{dy_{vap}}{dt} - \dot{Q}_{loss\_shl}\right] \tag{2.81}$$

where $\dot{Q}_{loss\_shl}$ is the heat loss from the vapour to the environment, defined by

$$\dot{Q}_{loss\_shl} = \left(UA\right)_{loss\_shl}\left(T_{vap} - T_{amb}\right) \tag{2.82}$$

Note that Eq. (2.81) contains the constant volume heat capacity C^v_v and the internal energy u^v of the vapor.

2.2.16 Dry cooler

A dry cooler is basically a single-phase heat exchanger where a fluid is cooled down by air as shown in Fig. 2.24.

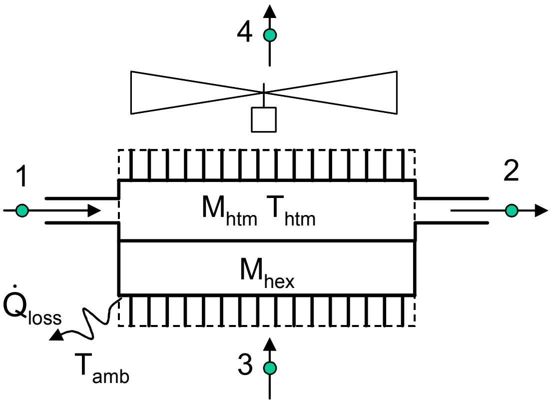

Figure 2.24 Schematic diagram of the dry cooler

Since the mass of air present in the heat exchanger is negligible compared with that of the heat transfer medium, the thermal mass of air has been neglected.

Assuming constant mass and specific heat, the following energy balance equation is derived for the heat transfer medium.

$$\frac{dT_{htm}}{dt} = \frac{1}{M_{htm}C_p^{htm} + M_{hex}C_p^{hex}} \times \left[\dot{m}_{01}C_p^{htm}\left(T_{01} - T_{02}\right) - \dot{Q}_{hex} - \dot{Q}_{loss} \right] \tag{2.83}$$

where $\dot{Q}_{hex}$ is the heat loss from the solution to the environment defined by

$$\dot{Q}_{hex} = \left(UA\right)_{hex}\left(T_{htm} - T_{air}\right)_{avg} \tag{2.84}$$

where $T_{air,avg}$ is defined by

$$T_{air,avg} = \left(1 - F\right) \times T_{03} + F \times T_{04} \tag{2.85}$$

where F is a weight factor, which has been set at 0.5.

The air temperature at the outlet T_{04} is then calculated by

$$T_{04} = T_{03} + \frac{\dot{Q}_{hex}}{\dot{m}_{03}C_p^{air}} \tag{2.86}$$

2.2.17 Wet cooling tower

A cooling tower consists of an evaporative cooler and a reservoir or sump below. Most heat and mass transfer between air and water takes place in the evaporative cooler, which is a packed structure, where the two streams are in a direct contact. As result of the direct contact, humid and warm air is rejected to the atmosphere and cooled water flows into the sump below. Compared with the mass of water in the sump, those of air and water present in the packed structure are negligibly small and therefore it has been assumed that the masses in the packed structure can be neglected and that heat and mass transfer take place instantaneously.

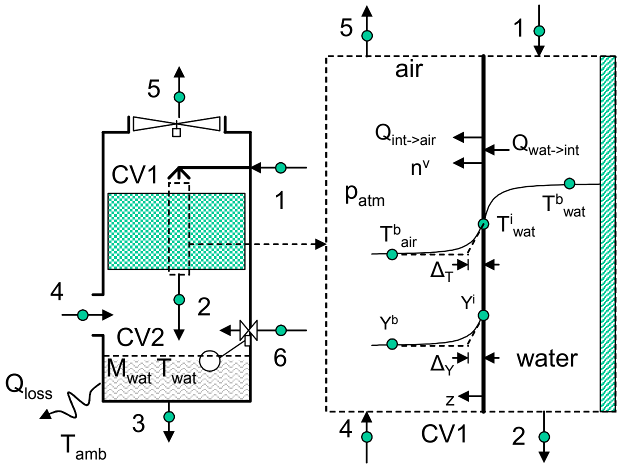

Figure 2.25 Schematic diagram of a wet cooling tower

For the control volume CV1 in Fig. 2.25 that includes air and water flows in the packed structure, the following governing equations are derived. Derivation of the following equations has been made in molar basis in order to avoid complications regarding the conversion of mass and molar fractions.

First of all, on the water side, a molar mass balance equation of water is given by

$$\Sigma\dot{N}_{water} = \dot{N}_{01} - \dot{N}_{02} - \dot{N}^v = 0 \tag{2.87}$$

where $\dot{N}^v$ is the molar flow rate of evaporated water.

On air side, the total molar mass balance is given by

$$\Sigma\dot{N}_{humid\,air} = \dot{N}_{04} - \dot{N}_{05} + \dot{N}^v = 0 \tag{2.88}$$

and the molar mass balance equation of water in the humid air is given by

$$\Sigma\dot{N}_{water\,vapor} = \dot{N}_{04}Y_{04} - \dot{N}_{05}Y_{05} + \dot{N}^v = 0 \tag{2.89}$$

where Y_{04} and Y_{05} are the mol fraction of water in the humid air flows at the inlet and outlet respectively.

The total amount of evaporated water $\dot{N}^v$ can be expressed as

$$\Sigma\dot{N} = \dot{N}^v - \int \dot{n}^v dA = 0 \tag{2.90}$$

where $\dot{n}^v$ is the molar flux at the air-water interface, which can be derived as follows considering both molecular diffusion and convection across a thin air film near the air-water interface (see Appendix D1).

Across the thin air film $0 \le z \le \Delta_Y$ in Fig. 2.25, Eq. (D1.2) in Appendix D1 gives the molar flux of water $\dot{n}^v$ as

$$\dot{n}^v = \dot{n}^v Y - D\frac{d(\rho Y)}{dz} \tag{2.91}$$

which is the same as Eq. (D1.2) except X^o_A and Y_A replaced by 1.0 and Y respectively. The first term on the right side is the convective term that would produce a different concentration profile compared with a pure diffusion case.

Assuming ideal gas, the molar density of humid air ρ is given by $\rho = p_{atm}/RT$. Then rewriting Eq. (2.91) for $\dot{n}^v$ gives:

$$\dot{n}^v = -\frac{D}{1-Y}\frac{d(\rho Y)}{dz} = -\frac{Dp_{atm}}{(1-Y)R}\frac{d}{dz}\left(\frac{Y}{T}\right) \tag{2.92}$$

Integration of Eq. (2.92) with boundary conditions of $Y=Y^i$ at z=0 and $Y=Y^b$ at z= Δ_Y gives

$$\dot{n}^v = \frac{p_{atm}}{(1-\overline{Y})R}\left(\frac{D}{\Delta_Y}\right)\left(\frac{Y^i}{T^i_{wat}} - \frac{Y^b}{T^b_{air}}\right) \tag{2.93}$$

where $\overline{Y}$ is a certain value in $Y^b \le \overline{Y} \le Y^i$ that equates Eq. (2.93) with (2.92). In the simulations, $\overline{Y}$ has been approximated as $\overline{Y} = (Y^i + Y^b)/2$

Defining mass transfer coefficient $K \equiv D/\Delta_Y$ in Eq. (2.93) and integrating it according to Eq. (2.90) gives

$$\dot{N}^v = KA\left[\frac{p_{atm}}{(1-\overline{Y}_{avg})R}\right]\left(\frac{Y^i}{T^i_{wat}} - \frac{Y^b}{T^b_{air}}\right)_{avg} \tag{2.94}$$

The mass transfer coefficient K has been calculated from heat and mass transfer analogy.

Since the humid air at the air-water interface is assumed saturated, Y^i in Eq. (2.94) is determined by

$$Y^i = \frac{p^*}{p_{atm}} \tag{2.95}$$

where p^* is the saturation pressure of water at the interface temperature T^i_{wat}.

On the other hand, the energy balance equation for the water side is written as

$$\Sigma\dot{Q} = \dot{N}_{01}H^l_{01} - \dot{N}_{02}H^l_{02} - \dot{N}^v H^v - \dot{Q}_{int\rightarrow air} = 0 \tag{2.96}$$

where H^l_{01}, H^l_{02} and H^v are the molar enthalpies of the incoming and exiting water flows and the average molar steam enthalpy respectively. $\dot{Q}_{int\rightarrow air}$ is the heat transfer rate from air-water interface to the bulk air flow.

Eq. (2.96) can be rewritten as

$$\dot{N}_{01}C_p^{wat}\left(T_{01}-T_{02}\right)-\dot{N}^v H^{fg}-\dot{Q}_{int\rightarrow air}=0 \tag{2.97}$$

where the molar latent heat of steam is defined by $H^{fg} \equiv H^v - H^l_{02}$.

For the air, an energy balance equation is derived as

$$\Sigma\dot{Q}=\dot{N}_{04}H_{04}^v-\dot{N}_{05}H_{05}^v+\dot{N}^v H^v+\dot{Q}_{int\rightarrow air}=0. \tag{2.98}$$

where H^v_{04} and H^v_{05} are molar enthalpies of the humid air flows at inlet and outlet respectively. Using an enthalpy equation for humid air assuming ideal gas mixture (see e.g. Söylemez ,1999)

$$H=\left(1-Y\right)\left(H_o^{air}+C_p^{air}T\right)+Y\left(H_o^{vap}+C_p^{vap}T\right) \tag{2.99}$$

, where H^{air}_o and H^{vap}_o are the reference enthalpies of air and water vapour respectively, and from Eq. (2.88) and (2.89), Eq.(2.98) can be rewritten as

$$\dot{N}_{04}\left[\left(1-Y_{04}\right)C_p^{air}+Y_{04}C_p^{vap}\right]\left(T_{04}-T_{05}\right)+\dot{N}^v C_p^{vap}\left(T_{wat,avg}^i-T_{05}\right)-\dot{Q}_{int\rightarrow air}=0. \tag{2.100}$$

where $T^i_{wat,avg}$ is an average temperature of air-water interface.

Finally, a relationship between interface- and bulk temperatures is given by the energy balance across the air-water interface. At the air-water interface, heat is transferred from bulk water to the interface to sustain the evaporation of water and sensible heat loss to the air as follows.

$$\Sigma Q=Q_{wat\rightarrow int}-\dot{N}^v H^{fg}-Q_{int\rightarrow air}=0 \tag{2.101}$$

where the heat transfer rates were defined as follows

$$Q_{wat\rightarrow int}=\left(\alpha A\right)_{wat\rightarrow int}\left(T_{wat}^b-T_{wat}^i\right)_{avg} \tag{2.102}$$

$$Q_{int\rightarrow air}=\left(\alpha A\right)_{int\rightarrow air}\left(T_{wat}^i-T_{air}^b\right)_{avg} \tag{2.103}$$

For solution, because some equations in the set of equations above are nonlinear, all equations were first expanded in Taylor series to the first order and the resulting Jacobian matrix system was solved using Gauss' elimination method. In simulation, iteration has been made until the difference between evaporation rates from two consecutive steps is less than 0.1kg/h. The convergence criterion was met normally after three iterations.

Using the solution of the static equations above, time derivatives of sump water mass M_{wat} and temperature T_{wat} can be calculated as follows:

The mass balance equation for the water in the sump is given by

$$\frac{dM_{wat}}{dt} = \dot{m}_{02} + \dot{m}_{06} - \dot{m}_{03} \tag{2.104}$$

where $\dot{m}_{06}$ is the make up water flow rate, which is controlled by a liquid level sensor and a valve.

Assuming a constant specific heat for the water flows involved, the time derivative of the sump water temperature is given by

$$\frac{dT_{wat}}{dt} = \frac{1}{\left(MCp\right)_{wat}} \times \left[Cp_{wat}\left(\dot{m}_{02}T_{02} + \dot{m}_{06}T_{06} - \dot{m}_{03}T_{03}\right) - \dot{Q}_{loss} - Cp_{wat}T_{wat}\frac{dM_{wat}}{dt} \right] \tag{2.105}$$

where $\dot{Q}_{loss}$ is the heat loss from water to environment.

2.3 Simulation

Using the component models developed in the previous sections, various solar absorption cooling systems have been configured according to the following sections.

First of all, Table 2.2 lists the absorption chillers that have been modeled.

Table 2.2 Dynamic absorption chiller models

Absorption cycle	Cooling medium	Working pair
Single-Effect	Air/Water	LiBr-H_2O/NH_3-$LiNO_3$/NH_3-NaSCN
Double-Effect	Water	LiBr-H_2O
Half-Effect	Air/Water	LiBr-H_2O
Generator-Absorber eXchange	Air/Water	NH_3-H_2O

Except for the double-effect LiBr-water chiller, all absorption chiller models can be configured as both air- and water-cooled systems. For a single-effect chiller, three different working pairs can be chosen but for the other three absorption chiller models, only one working pair has been implemented.

For the working fluids in Table 2.2, the thermodynamic properties from Kim and Infante Ferreira (2006), Infante Ferreira (1984) and Ziegler and Trepp (1984) have been used.

2.3.1 System configurations

As briefly mentioned at the beginning of Section 2.2, component models have been developed in such a way that they can be used in various absorption systems with different working fluids and configurations. In a simulation program, each of those component models is written in a subroutine having a proper set of parameters as arguments. System configuration is done simply by calling the necessary component subroutines, assigning consistent names to the variables and selecting proper working fluids. This modular approach enabled quick configuration of various systems.

All the systems in the following have been designed to yield a cooling capacity of about 9.2kW for a cooling medium (water) temperature at around 28°C with a wet cooling tower and 38°C with a dry cooling tower.

2.3.1.1 Single-effect systems

Fig. 2.26 shows a solar cooling system based on a single-effect absorption chiller. The system consists of in total, 14 components of 12 different modules as listed in the figure.

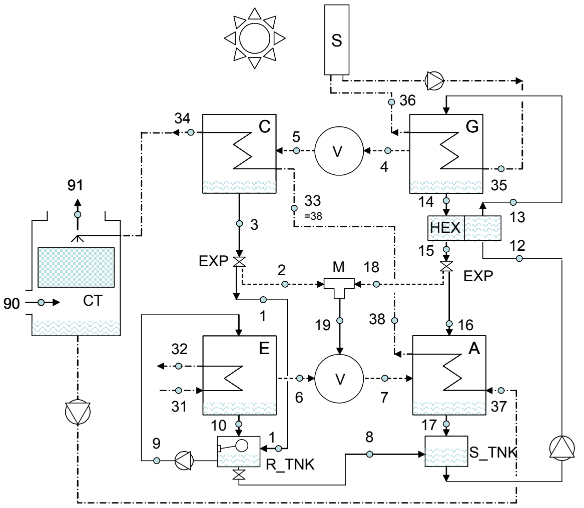

S: solar collector
CT: cooling tower
G: generator
C: condenser
E: evaporator
A: absorber
HEX: single-phase heat exchanger
S_TNK: solution tank
R_TNK: refrigerant tank
EXP: expansion valve
M: mixer
V: pressure vessel

Figure 2.26 System configuration: water-cooled single-effect system

The configuration in Fig. 2.26 has been used for all systems except for a LiBr-water system that has no heat exchanger for the refrigerant flows between condenser and evaporator.

In total, twenty five different single-effect systems have been designed. Specifications and design conditions of the systems are summarized in Table. 2.3

Table 2.3 Specifications of single-effect systems

Working pair	Cooling tower	Collector[1]		Air flow		Cool. Water[2]		Hot Water		Q_{eva} (kW)[3]	COP chiller
		€/m^2	A(m^2)	CMM	T(°C)	*lpm*	T(°C)	*lpm*	T(°C)		
LiBr-H_2O	Wet	100	48	100	32	40	27.6	40	98.4	9.2	0.75
		250	40								
		400	36								
		550	35								
		700	34								
NH_3-$LiNO_3$	Wet	100	60	120	32	50	27.9	50	100.9	9.2	0.62
		250	50								
		400	45								
		550	43								
		700	42								
NH_3-NaSCN	Wet	100	60	120	32	50	27.6	50	98.7	9.3	0.68
		250	45								
		400	40								
		550	38								
		700	38								

NH_3-$LiNO_3$	Dry	100 250 400 550 700	160 95 70 56 48	135	32	50	37.8	50	128	9.1	0.57
NH_3-NaSCN	Dry	100 250 400 550 700	135 86 62 50 43	135	32	50	37.4	50	121.2	9.1	0.62

1. Solar collector areas have been calculated by Eq. (2.2) for I_p=800W/m^2.
2. Based on dry bulb temperature 32°C, relative humidity 21.3% and atmospheric pressure 101.325kPa
3. Cooling capacity for cold water temperature of 12.5°C at evaporator inlet.

2.3.1.2 Double-effect systems

Compared with SE chiller, a double effect system has 4 more modules, namely a high-temperature generator, a high-temperature heat exchanger, an extra pressure vessel and a mixer for liquefied refrigerant after condenser, as shown in Fig. 2.27. A unique module which SE chiller does not have is the generator-condenser, i.e. steam-fired generator indicated by "GC" in the figure.

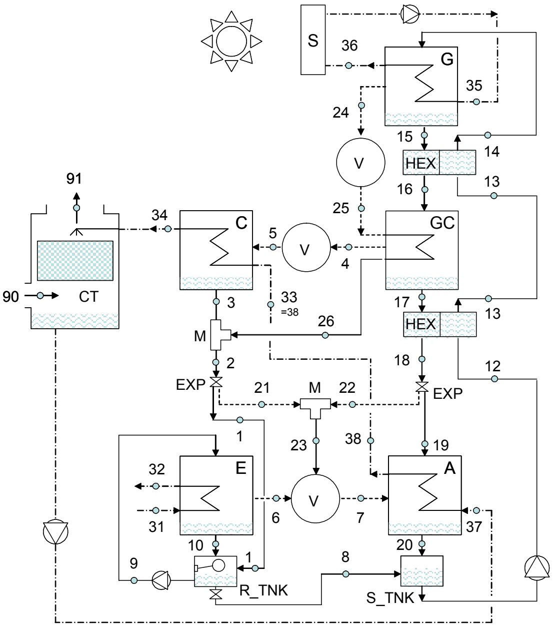

Figure 2.27 System configuration: water-cooled double-effect system

In total, three double-effect systems have been designed with the same conditions as SE chillers', specifications and design conditions of which are summarized in Table 2.4.

Table 2.4 Specifications of double-effect system

Working pair	Cooling tower	Collector[1]		Air flow		Cool. Water[2]		Hot Water		Q_{eva} (kW)[3]	COP chiller
		€/m^2	A(m^2)	CMM	T(°C)	*lpm*	T(°C)	*lpm*	T(°C)		
LiBr-H_2O	Wet	400 550 700	78 38 25	85	32	50	27.9	50	162.8	9.3	1.2

1. Solar collector areas have been calculated by Eq. (2.2) for I_p=800W/m^2.
2. Based on dry bulb temperature 32^{o}C, relative humidity 21.3% and atmospheric pressure 101.325kPa
3. Cooling capacity for cold water temperature of 12.5^{o}C at evaporator inlet.

2.3.1.3 Half-effect systems

Half-effect systems have been configured as shown in Fig. 2.28. This configuration is slightly different from the block diagram in Fig. 2.6 from the fact that an extra heat exchanger is included between the refrigerant flow from condenser (state 3→50 in Fig 2.28) and the cold solution (22→23) from mid-pressure absorber. This heat exchanger subcools the liquefied refrigerant to minimize refrigerant loss due to flashing.

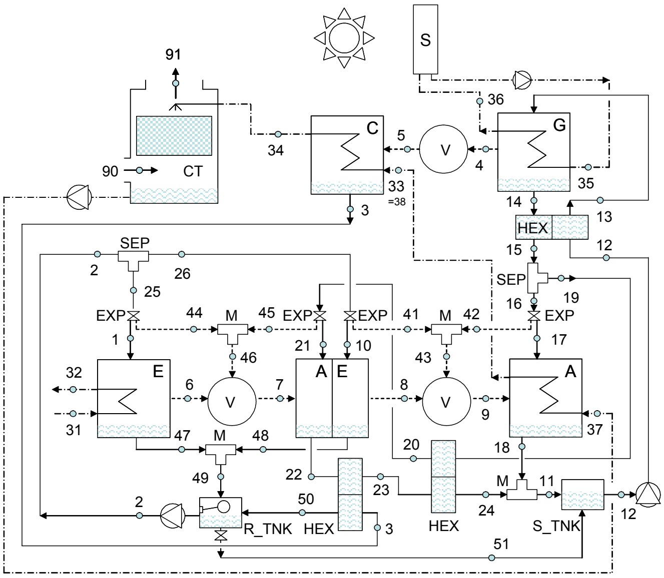

Figure 2.28 System configuration: water-cooled half-effect system

A component unique in this system is the absorber-evaporator denoted by “AE” in Fig. 2.28.

In total, ten half-effect systems have been designed and their specifications and design conditions are summarized in Table 2.5.

Table 2.5 Specifications of half-effect systems

Working pair	Cooling tower	Collector[1]		Air flow		Cool. Water[2]		Hot Water		Q_{eva} (kW)[3]	COP chiller
		€/m^2	A(m^2)	CMM	T(^{o}C)	*lpm*	T(^{o}C)	*lpm*	T(^{o}C)		
LiBr-H_2O	Wet	100	55	160	32	60	27.7	60	68.9	9.2	0.41
		250	52								
		400	52								
		550	54								
		700	61								
LiBr-H_2O	Dry	100	76	180	32	60	37.7	60	87	9.2	0.38
		250	68								
		400	64								
		550	64								
		700	66								

1. Solar collector areas have been calculated by Eq. (2.2) for I_p=800W/m^2.
2. Based on dry bulb temperature 32^{o}C, relative humidity 21.3% and atmospheric pressure 101.325kPa
3. Cooling capacity for cold water temperature of 12.5^{o}C at evaporator inlet.

2.3.1.4 GAX systems

Fig. 2.29 shows the configuration for a water-cooled GAX system. It has two components which the other systems do not have. One is the rectifier denoted by “R” and the other is the generator-absorber denoted by “GA” in the figure.

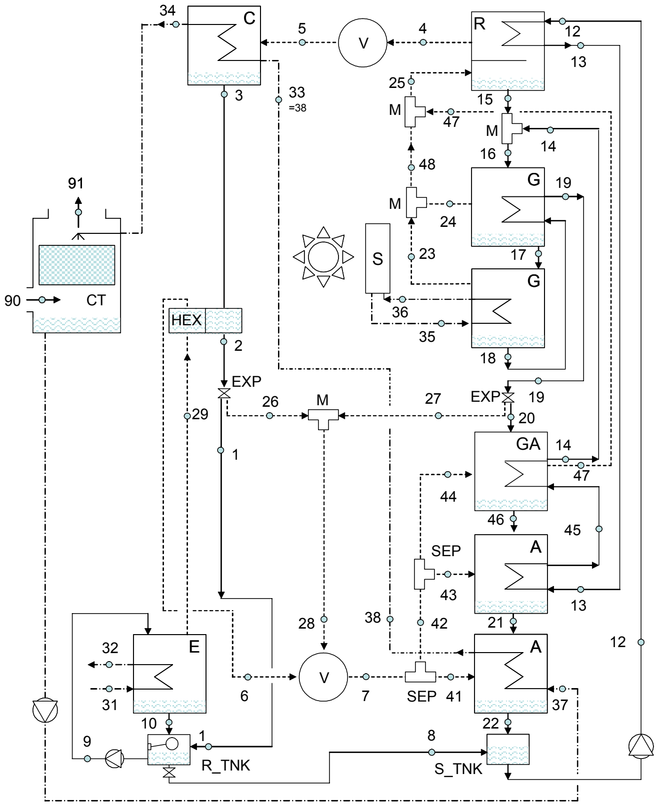

Figure 2.29 System configuration: water-cooled GAX system

In total, eight GAX systems have been designed and their specifications and design conditions are summarized in Table 2.6.

Table 2.6 Specifications of GAX systems

Working pair	Cooling tower	Collector[1]		Air flow		Cool. Water[2]		Hot Water		Q_{eva} (kW)[3]	COP chiller
		€/m²	A(m²)	CMM	T(°C)	*lpm*	T(°C)	*lpm*	T(°C)		
NH_3-H_2O	Wet	250	85	100	32	50	27.6	50	141.6	9.3	0.95
		400	50								
		550	38								
		700	30								
NH_3-H_2O	Dry	475	120	120	32	50	37.4	50	178	9.2	0.84
		550	72								
		625	50								
		700	38								

1. Solar collector areas have been calculated by Eq. (2.2) for I_p=800W/m^2.
2. Based on dry bulb temperature 32°C, relative humidity 21.3% and atmospheric pressure 101.325kPa
3. Cooling capacity for cold water temperature of 12.5°C at evaporator inlet.

2.3.2 Solution

Numerical integration of the differential equations derived in Section 2.2 has been carried out using Euler's forward-integration method (see e.g. James et al, 1985). The solution procedure is summarized in the simulation flow chart in Fig. 2.30.

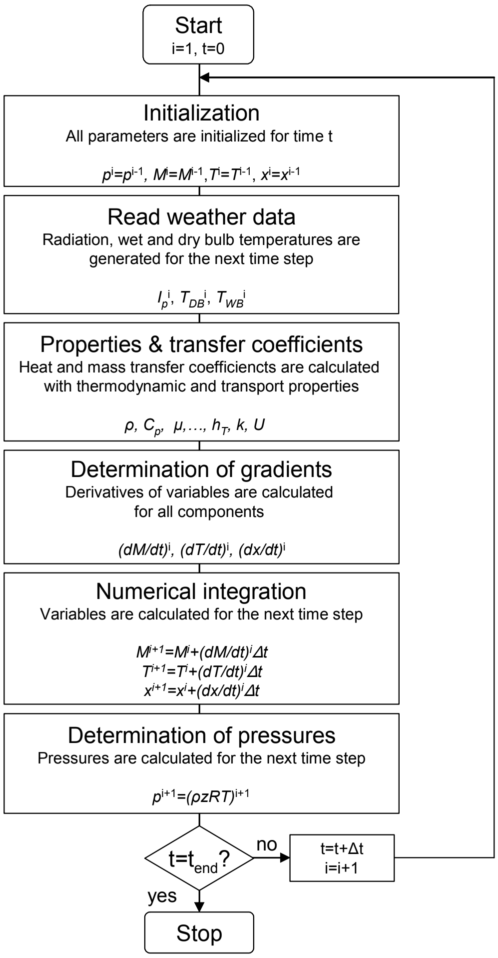

Figure 2.30 Flow chart of simulation

At the beginning, all variables are initialized with initial values or those from the previous time step. Relevant weather parameters are read from a file that contains meteorological data for the geographical location of interest. Then fluid properties and transfer coefficients are calculated for all components. All derivatives in Section 2.2 are determined and integrated. Finally system pressures are calculated for the next step. This process repeats until a preset time.

2.4 Simulation results

In this section, simulation results are presented for the various systems introduced in Section 2.3.1.

Firstly, dynamic characteristics of different systems were compared under a set of assumed working conditions that were intended to reveal their dynamic characteristics.

Secondly, the systems were simulated for two mid-summer months with actual weather data from two Italian cities. The results were compared in terms of several performance indexes including overall efficiency, specific cooling power and so on.

2.4.1 Dynamic characteristics of solar absorption cooling systems

All systems introduced in Section 2.3.1 were simulated for a 24-hour period with the following conditions:

- All temperatures in the system are initially set at 26°C.
- Chilled water temperature at evaporator inlet is kept constant at 12.5°C.
- Dry air temperature and relative humidity are constant at 32°C and 21.3%, respectively.
- The intensity of solar radiation on the surface of solar collectors is constant at 800 W/m^2 for $0 \leq t \leq 15$ hour and it is zero afterwards. (This unrealistic condition has been used because some systems do not reach their design capacities under a realistic condition.)
- Whole system is turned on at the same time when the heating medium temperature is above 40°C and turned off when it is below 30°C.

These simulation conditions were intended to show especially how quickly a system reaches its full capacity. Since one of the requirements for a solar cooling system is to deliver the maximum cooling power during a limited amount of time, a system that reaches its full capacity faster is also likely to perform better in general. Before comparing the various systems in relation to this aspect, the typical behavior of a system under the simulation conditions is explained by the following example.

Fig. 2.34 shows some simulation results for a water-cooled single-effect LiBr-water system.

Variation of heat transfer rates are shown in Fig. 2.34a for the major components. All heat transfer rates increased as the system was heated up in the beginning and eventually reached constant values. In this case, it took about 4 hours and 20 minutes to reach 90% full capacity. At 15 hour, the heat transfer rates began to decline because solar input was turned off. They fluctuated after 18 hour because a refrigerant recirculation pump operated intermittently when there was not enough refrigerant in the refrigerant tank.

Variations of liquid masses in several components are shown in Fig. 2.34b. Particularly, the mass of refrigerant in the refrigerant tank rapidly decreased in the beginning when there was not enough refrigerant generation. Then it increased to a constant level as the system approached a steady state. At 15 hour, it started to decrease and fluctuated for some time before 21 hour 30 min when the system came to a complete halt.

Finally, Fig. 2.34c and 2.34d show variations of pressure and concentration respectively.

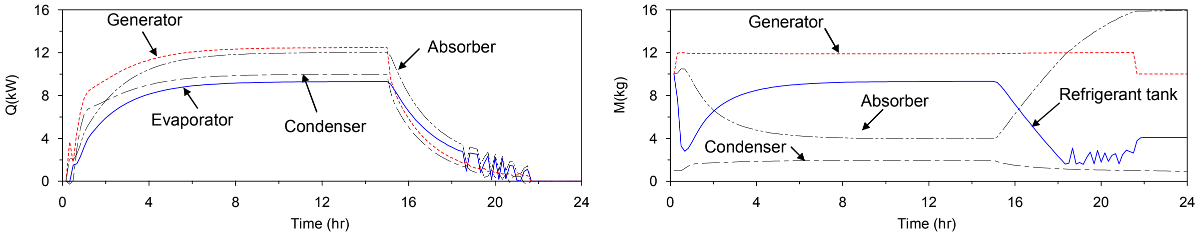

(a) Heat transfer rates

(b) Liquid masses in components

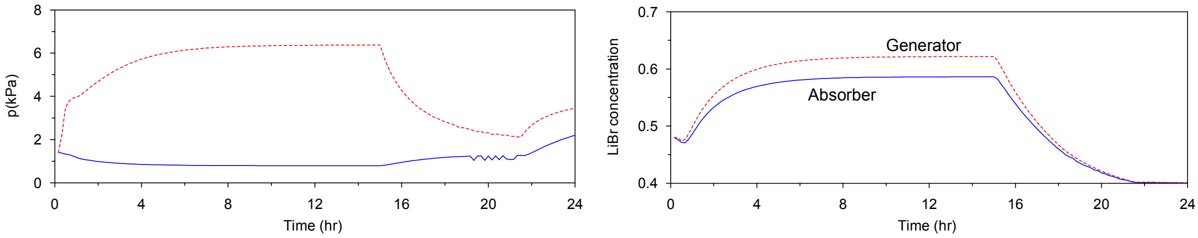

(c) Pressures

(d) Concentrations

Figure 2.34 Dynamic characteristics of a water-cooled SE LiBr-H_2O system

Behaviours of other systems are more or less the same as described above except that some of the systems have more components and thus their behaviours are more complicated.

In the following, some of the systems introduced in Section 2.3.1 are compared in terms of cooling power Q_{eva} (kW). All systems are equipped with an evacuated type solar collector [€700/m^2 in Eq. (2.2) and Fig. 2.3].

Fig. 2.35 shows the variation of cooling power for different water- and air-cooled systems. It can be seen that, the half-effect system reaches its full capacity in the shortest time both in water- and air-cooled systems.

For the water-cooled systems, while it takes 2 hours 50 minutes for the half-effect system to reach 90% of its full capacity, it takes 4 hours 20, 6 hours 40 and 7 hours 20 minutes for the single-effect, double-effect and GAX system, respectively. In general, a system with a lower driving temperature is expected to reach its full capacity earlier. But, for the double-effect and GAX systems in Fig. 2.35a, it is not the case. This is mainly because the GAX system is based on NH_3-H_2O and the double-effect system is based on LiBr-water. Ammonia solution in the operating range of a typical GAX system has roughly double the heat capacity of a LiBr solution in a double-effect system. The density of ammonia is also much larger than that of steam, all of which contributes to the slow gradient of the GAX system in Fig. 2.35a.

The two ammonia-salt systems are not shown in Fig. 2.35a because they look much similar to the single-effect LiBr-water system in the figure.

From the results in Fig. 2.35, it can be deduced that, the double-effect and GAX systems would not operate at their full capacities even for a short time unless solar radiation is extremely high.

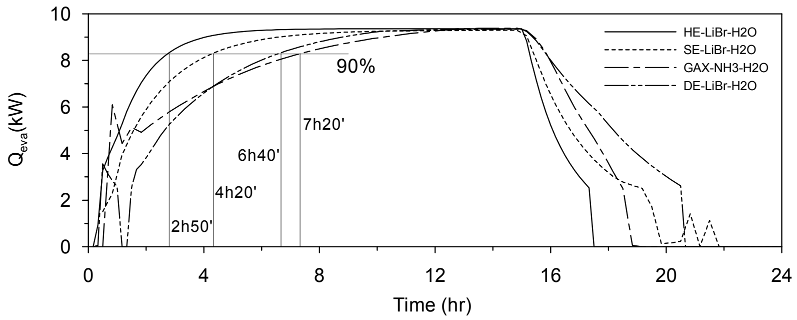

(a) Water-cooled systems

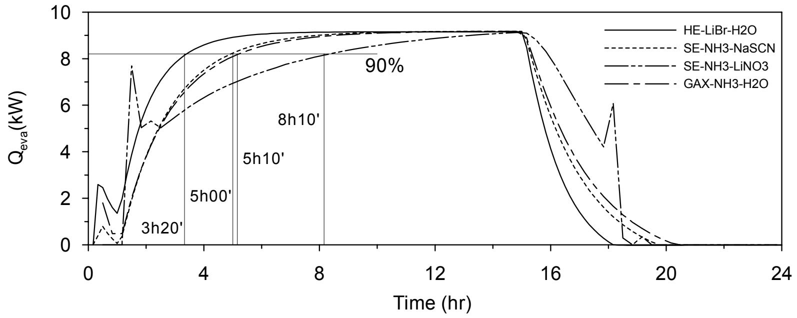

(b) Air-cooled systems

Figure 2.35 Dynamic characteristics of various systems

Similar trends can be found for air-cooled systems in Fig. 2.35b. The half-effect system is followed by two single-effect ammonia-salt systems and the GAX system. Time taken to reach full capacity is a bit longer than for its water-cooled counterpart because a higher driving temperature is required.

In the following section, it will be observed how the seasonal performance of a system is influenced by its dynamic characteristics in the simulation results carried out with actual weather data.

2.4.2 Seasonal performance of solar absorption cooling systems

The various systems introduced in Section 2.3.1 have been evaluated in terms of the seasonal performance data predicted by the simulation carried out for two summer months in two Italian cities using actual weather data.

For the two locations in Italy, Milan and Naples have been chosen.

Milan is located in the northern part of Italy (45°25'N and 9°12'E). During July and August, 20-year-average (1951-1970) meteorological data reports an average total radiation of 537.8W/m^2 (max. 1021W/m^2) on horizontal plane, average daytime dry bulb temperature of 24.4°C (max. 33.5°C) and relative humidity of 62.1% (max. 100.3%).

Naples is located down in south (40°50'N and 14°15'E) and has a typical Mediterranean climate. For the same period, the average total radiation on horizontal surface is 631.2W/m^2 (max. 1147W/m^2) and the average daytime dry bulb temperature and relative humidity are 26°C (max. 33.3°C) and 58% (max. 99.5%), respectively. Naples exhibits a hotter and drier summer than Milan.

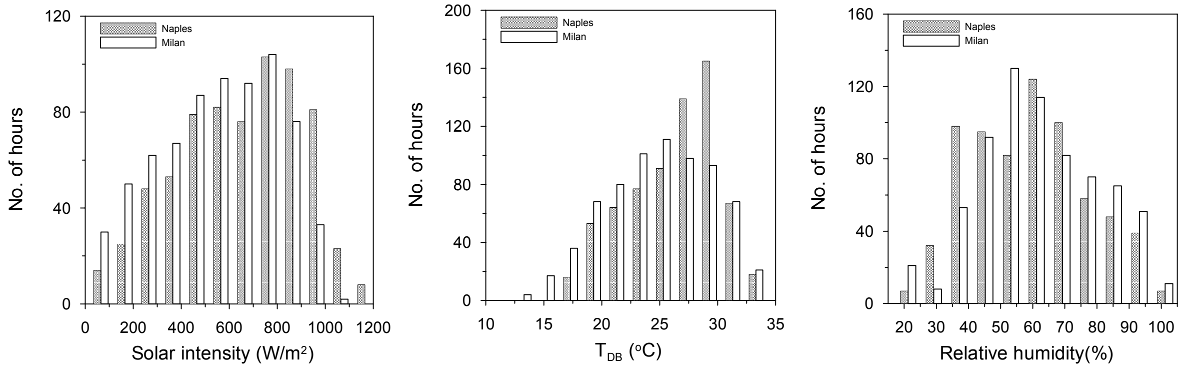

(a) Solar intensity (b) Dry bulb temperature (c) Relative humidity

Figure 2.36 Daytime weathers in Milan and Naples during July and August

For all simulation cases, the following conditions apply.

- Solar collectors are set facing south at 45^o tilt angle.
- Chilled water temperature at evaporator inlet is kept constant at 12.5^oC.
- Whole system is turned on at the same time when the heating medium temperature is above 40^oC and turned off when it is below 30^oC regardless of time of day.

By the second condition, the cooling load characteristics have been considered time independent. All systems operate as long as the third condition is met regardless of cooling demand. Some high-temperature systems were turned off only a few times in the two-month period due to this requirement. Therefore in the following, the total cooling energy production of a system is close to its theoretical maximum.

For evaluation of various systems, the following performance criteria have been used.

Average solar collector efficiency has been defined by

$$\overline{\eta}_{col} = \frac{\int \dot{Q}_{gen} dt}{A_{col} \int I_p dt} \tag{2.106}$$

, which is the ratio of total net system heat input to total solar radiation on the surface of the solar collector.

The average efficiency of an absorption chiller has been defined by

$$COP_{avg} = \frac{\int \dot{Q}_{eva} dt}{\int \dot{Q}_{gen} dt} \tag{2.107}$$

, which is the ratio of total cooling energy production to total net heat input to the chiller.

The average system efficiency has been defined by

$$\overline{\eta}_{sys} = \frac{\int \dot{Q}_{eva} dt}{A_{col} \int I_p dt} \tag{2.108}$$

, which is the product of Eq. (2.106) and (2.107)

The specific water consumption has been defined by

$$\bar{m}_{wat} = \frac{\int \dot{m}_{wat} dt}{\int \dot{Q}_{eva} dt} \tag{2.109}$$

, which is the average water consumption of a cooling tower per unit production of cooling energy.

The average cooling power has been defined by

$$\bar{Q}_{eva} = \frac{\int \dot{Q}_{eva} dt}{\int Idt / \Sigma I} \tag{2.110}$$

, which is the total cooling energy production divided by the total sum of daytime hours during the period. Total number of daytime hours during July and August is 902 hours for Milan and 914 hours for Naples. Unlike the nominal cooling capacity defined under steady state conditions, this value varies depending both on weather conditions and the dynamic characteristics of the system.

Finally, the average specific collector cost has been defined by

$$\bar{\omega} = \frac{A_{col}\omega}{\bar{Q}_{eva}} \tag{2.111}$$

, which is the total collector cost divided by the average cooling power. This value can be understood as a cost-effectiveness figure of a system in a dynamic environment. ω in Eq. (2.111) is the unit collector price (Euro/m^2 of gross surface area) also used in Eq. (2.2).

For the two summer months in Milan and Naples, 26 water-cooled and 19 air-cooled systems have been simulated. In the following, simulation results for water-cooled systems are presented followed by results for air-cooled systems.

2.4.2.1 Water-cooled systems

Simulation results for water-cooled systems in Naples are presented in Fig. 2.37 for the performance indexes defined by Eq. (2.106)~(2.111).

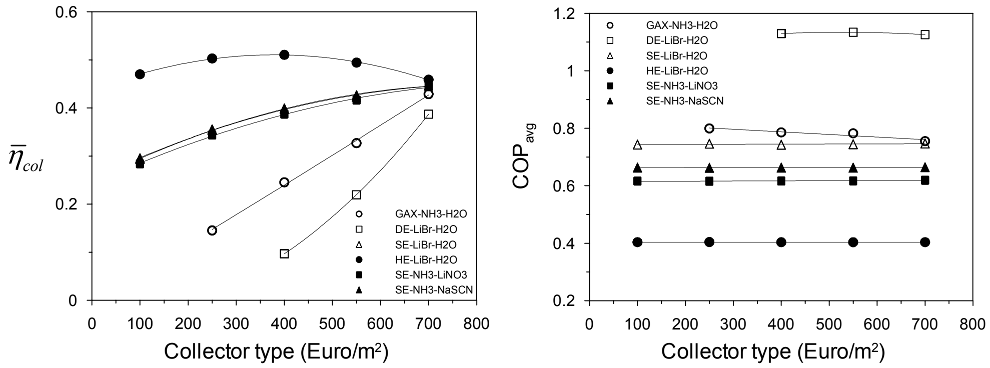

(a) Average solar collector efficiency (b) Average chiller COP

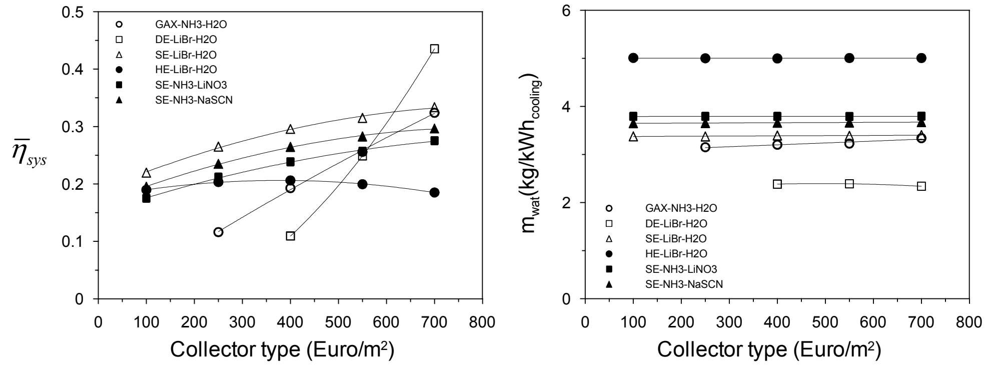

(c) Average system efficiency (d) Specific water consumption

Figure 2.37 Performance of water-cooled systems in Naples

Fig. 2.37a shows the average efficiencies of the solar collectors used in the different systems. It is clearly shown that the same type of collectors operate at different efficiencies depending on the absorption chillers because the efficiency of a solar collector is reversely proportional to the driving temperature of an absorption chiller. It can also be seen that while all the other efficiency curves have positive gradients with collector cost, that of the half-effect system shows a negative gradient in the high-cost region. This is because a low cost collector performs better than a high-cost collector in the low-temperature range where the half-effect chiller operates.

As is shown in Fig. 2.37b, the average COPs of most chillers are relatively insensitive to the collector type. But the COP of a GAX system is slightly higher with a cheaper collector. This needs some explanation.

First of all, this is due to the characteristic of GAX absorption cycle. GAX cycle COP is relatively sensitive to driving temperature as briefly mentioned with Fig. 2.9 in Section 2.1.2.4 because the cycle continuously varies from AHX to GAX cycle. Because the GAX systems in Fig. 2.37 were designed to meet the particular set of design conditions in Section 2.3.1, if operating conditions deviate from the design conditions, the COP of the GAX chiller varies accordingly. The particular case of Fig. 2.37b is understood in this line. Since the average solar radiation on the solar collector surface during the simulation period is much lower than 800W/m^2 (the reference solar radiation used for chiller design) solar collectors are operated at lower temperatures than they were originally designed for. Consequently they operate at higher efficiencies. Since this positive deviation of “actual performance” from the original design is greater for a cheaper solar collector (Efficiency of a cheap collector is more sensitive to working temperature. See Fig. 2.3), the solar system with a cheaper solar collector can provide a chiller with more heat or higher-temperature heating medium than a more expensive solar system. This is the reason why the COP of the GAX chiller in Fig. 2.37b increases with decreasing solar collector price.

Regardless of chiller type, the average COP of a chiller in Fig 2.37b is lower than its design COP because part of the solar heat is used to warm up the system and eventually lost to ambient.

Being a product of collector efficiency and chiller COP, the average system efficiency in Fig. 2.37c follows the trend of the corresponding average collector efficiency curve in Fig. 2.37a because the chiller COP is more or less constant in Fig. 2.37b. System efficiency increases with a more expensive collector except for the half-effect system.

The maximum system efficiency of 0.435 is found for the double-effect system with €700/m^2 collector. This value is about 1.3 times larger than the maximum efficiency of the single-effect LiBr-water system, which is about 0.33. But this high system efficiency is possible only when the double-effect chiller is equipped with an expensive solar collector. As is shown in Fig. 2.37c, the efficiency of double-effect system drops sharply for cheaper collectors.

The system efficiency of a single-effect LiBr-water system ranges from 0.22 to 0.33 for different solar collectors and it is higher than those of other systems in the whole range except for the double-effect system with expensive solar collectors. It is followed by the two ammonia-salt systems and the half-effect system. In terms of efficiency, the half-effect system is only marginally better than two ammonia-salt systems with the cheapest solar collector.

Specific water consumptions of the systems are shown in Fig. 2.37d. It can be seen that water consumption is relatively insensitive to collector type and it is reversely proportional to chiller COP. The double-effect system consumes the least amount of water and the half-effect system consumes the largest. Compared with 2.37 $kg_{water}/kWh_{cooling}$ of the double-effect system, that of single-effect LiBr-water system is 3.37 $kg_{water}/kWh_{cooling}$, which is 42% more. The half-effect system consumes 5 $kg_{water}/kWh_{cooling}$, which is about 48% more than that of the single-effect system. All these water consumptions are less than 5.3 $kg_{water}/kWh_{cooling}$ which is the average of European solar cooling systems published in SACE(2003). Considering that the wet cooling tower model used in the simulation did not take account of various losses in a real wet cooling tower, such deviations are regarded acceptable.

Finally, the average cooling power and specific collector costs are shown in Fig. 2.38.

As can be seen in Fig. 2.38a, the average cooling power of all systems is much smaller than their design cooling capacity, which was commonly set at around 9.2 kW in Section 2.3.1. This means that all systems operated in part-load conditions for most of the time.

Generally the average cooling power increases with solar collector price. It is interesting that the gradient is much steeper with the double-effect system and it is even close to zero for the GAX system. These different characteristics result in extremely different trends for the GAX and double-effect systems in Fig. 2.38b.

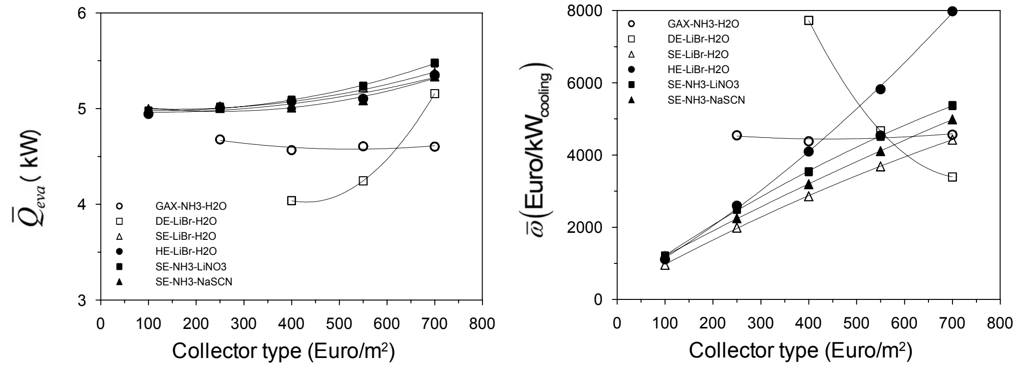

(a) Average cooling power (b) Average specific collector cost

Figure 2.38 Average cooling power and specific collector costs in Naples

Although the cooling power increases with the collector price, the gradients are different for the double-effect and the other lower-temperature systems. While it is steep for the double-effect system, it is not for the lower-temperature systems, which results in the increasing curves for them in Fig. 2.38b. On the other hand, the average cooling power of the GAX system slightly decreases with collector price because of the decreasing COP in Fig. 2.37b.

Among the systems considered, the single-effect LiBr-water chiller showed the lowest average specific collector costs. The minimum average specific collector cost for the single-effect chiller is €961/kW$_{\text{cooling}}$.

Simulation results for Milan are similar to those for Naples. Since the solar radiation in Milan is slightly lower than in Naples, the performance of a system is slightly poorer than its counter part in Naples. Nevertheless, it can be concluded that single-effect LiBr-water systems are the most cost effective for both cities. Although a double-effect system with high-temperature solar collectors can be considered as an alternative, initial investment cost will be higher than that of a single-effect system by as much as three times for solar collectors alone. And finally, the half-effect chiller does not offer any advantage over a single-effect chiller in all performance indexes considered.

2.4.2.2 Air-cooled systems

Although a water-cooled system can operate at a higher efficiency that an air-cooled system, it requires a cooling tower that consumes water and inevitably brings a couple of problems with it concerning the water usage. For this reason, a water-cooled system is not favourable for small-scale solar cooling applications. Therefore if an air-cooled system can be offered at a competitive cost, it would be helpful to promote solar cooling technology more widely into the market. In the following, simulation results for 19 air-cooled systems in Naples are discussed focussing on the performance of a half-effect absorption chiller.

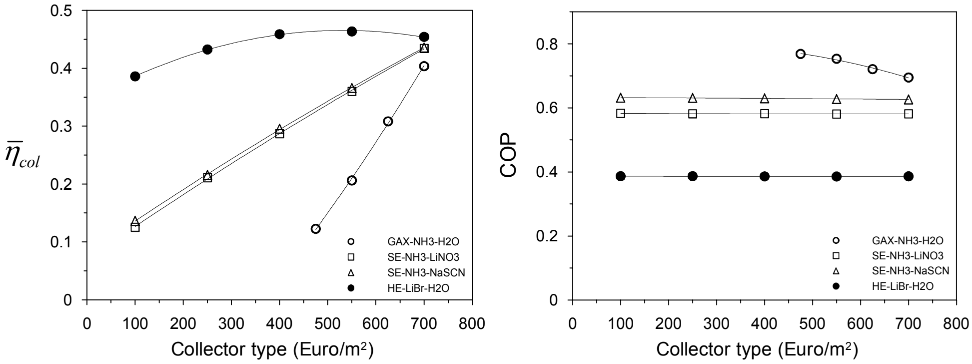

(a) Average solar collector efficiency (b) Average chiller COP

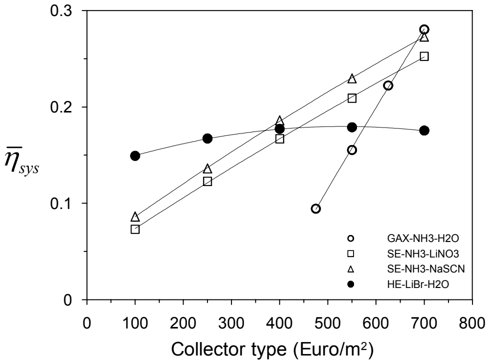

(c) Average system efficiency

Figure 2.39 Performance of air-cooled systems in Naples

Fig. 2.39a shows the average efficiencies of solar collectors operating in different systems. It can be seen that the gradient of efficiency curve for the half-effect systems is not as steep as the others. This is because differences in solar collector efficiencies are not large in the low temperature range where the half-effect chiller operates. For the single-effect and GAX systems, the average solar collector efficiency changes significantly with solar collector price.

Average COPs of different absorption chillers are shown in Fig. 2.39b. Except for the GAX chiller, the average COP is insensitive to solar collector price. The reason for the changing COP of the GAX chiller has already been explained in the previous section for water-cooled systems. Like for water-cooled chillers, the average COP of an air-cooled chiller is lower than its design value because part of the solar heat is lost to ambient.

Average system efficiency curves are shown in Fig. 2.39c. The trends are the same as those in Fig. 2.37c. Naturally, absolute efficiency of an air-cooled system is lower that that of its water-cooled counterpart. The average system efficiency of the air-cooled half-effect system is lower than that of a water-cooled half-effect system by 0.01-0.04.

Fig. 2.40 shows average cooling power and specific collector costs for the different systems shown in Fig. 2.39.

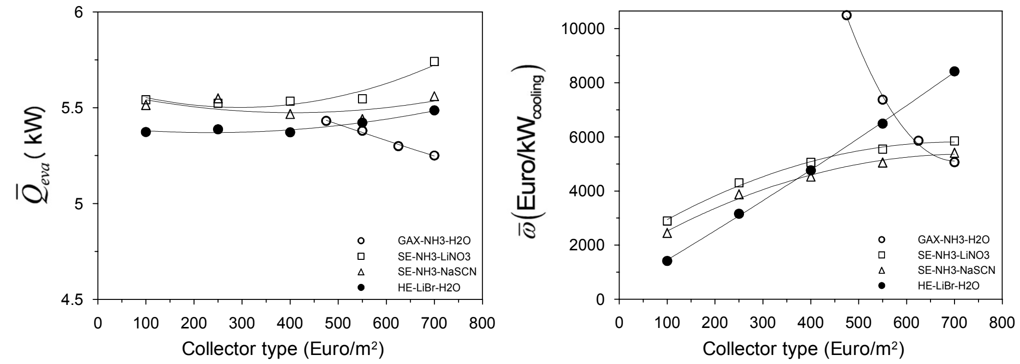

(a) Average cooling power (b) Average specific collector cost

Figure 2.40 Average cooling power and specific collector costs in Naples

Fig 2.40a shows the dependence of cooling power on solar collector price. Unlike for the other systems, the cooling power of the GAX system decreases with collector price. This is due to its decreasing chiller COP in Fig. 2.39b.

Finally, Fig. 2.40b shows average specific solar collector costs for the different systems. The average specific collector cost of the GAX system decreases with collector price. This means that the solar collectors with a price below €600/m^2 are not cost-effective for the GAX chiller. Except for the GAX systems, the average specific solar collector costs decrease with cheaper solar collectors.

The minimum average specific solar collector cost is found with the half-effect system with the cheapest solar collector, which is about €1,414/kWh$_{cooling}$. This value is 58% of the second lowest cost of the single-effect NH_3-NaSCN system. Compared with that of water-cooled single-effect LiBr-water system (€961/kWh$_{cooling}$) in the previous section, it is about 47% more expensive. This is the extra investment required to avoid a cooling tower. Most of this increased investment cost comes from the solar collector, however, it can be compensated by the elimination of the cooling tower.

As mentioned in Section 2.1.2, a cooling tower can be as expensive as €200-250 per kW$_{cooling}$ (Schweigler et al, 2005). And considering its installation, maintenance, water usage and so on, the actual increase in the initial investment for an air-cooled system may not be so large. Although it is also an interesting subject to compare water- and air-cooled systems from a financial point of view, it will not be given here because it is not the purpose of this study.

To make a conclusion, the analysis above suggested that a low-temperature chiller as the half-effect LiBr-water chiller could provide an air-cooled solar absorption cooling system with an investment cost much lower than a conventional air-cooled absorption chiller would require.

2.5 Conclusions

In this chapter, starting with an overview of the state of the art of solar absorption cooling technologies, dynamic models were developed and then simulation results were discussed for the evaluation of various systems. From the results, the following conclusions could be drawn.

For a water-cooled system:

- The single-effect LiBr/H2O chiller requires the minimum investment on solar collectors.

- The double-effect LiBr/H2O chiller can yield the highest efficiency only with an excessive solar collector cost.

- The half-effect LiBr/H2O chiller cannot compete with the single-effect LiBr/H2O chiller in terms of both initial and operating costs.

For an air-cooled system:

- The half-effect LiBr/H2O chiller requires the minimum investment on solar collectors.

- The ammonia absorption chillers can yield higher efficiencies only with excessive solar collector costs.

All in all, the single- and the half-effect LiBr/H2O chillers are advantageous for minimizing initial cost for water- and air-cooled solar air conditioning systems, respectively. In particular, the half-effect LiBr/H2O chiller considered in this study is thought to be a promising choice for the development of an economic air-cooled solar cooling system thanks to its low-temperature operability and the low risk of crystallization at an elevated heat rejection temperature.

It is recommended that a low-temperature absorption chiller based on the half-effect LiBr-water absorption cycle should be developed for a low-cost air-cooled solar absorption cooling system. Development of such an absorption chiller will help promote solar cooling technology by providing a competitive option for the applications where use of a cooling tower has been an inhibitive factor.

Nomenclature

A	area, m^2
c_1, c_2	constant
C_p	constant-pressure heat capacity, kJ/kgK
C_v	constant-volume heat capacity, kJ/kgK
D	mass diffusivity, m^2/s
F	weight factor in Eqs. (2.11) and (2.12)
f	weight factor in Eq. (2.47)
H	molar enthalpy, kJ/kmol
H^{fg}	molar latent heat, kJ/kmol K
h^{fg}	specific latent heat, kJ/kgK
h	specific enthalpy, kJ/kg
I_p	incident solar intensity, kW/m^2
K	mass transfer coefficient, m/s
M	mass, kg
$\dot{m}$	mass flow rate, kg/s
$\dot{N}$	molar flow rate, kmol/s
$\dot{n}$	molar flux, $kmol/m^2s$
p	pressure, kPa

$\dot{Q}$	heat transfer rate, kW
q	quality, $kg_{vapour}/kg_{mixture}$
R	Universal gas constant, 8.31447 kJ/kmol K
T	temperature, K
T_r	reduce temperature, see Eq. (2.1) for definition
t	time, s
U	overall heat transfer coefficient, kW/m^2K
u	internal energy, kJ/kg
Y	molar fraction of water in humid air
x	mass fraction of absorbent in liquid
y	mass fraction of absorbent in vapour

Greek symbols

α	heat transfer coefficient, kW/m^2K
ε	effectiveness
ω	specific collector price, €/m^2 gross area
η	efficiency
ρ	density, kg/m^3 or mol/m^3
γ	heat capacity ratio, C_p/C_v
Δh_{des}	heat of desorption, kJ/kg
Δt	time step, s
Δ_Y	concentration boundary layer thickness in vapor, m

Super- and subscripts

*	saturated condition
abs	absorber
atm	atmospheric
avg	average
amb	ambient
b	bulk
con	condenser
col	solar collector
dew	dew point
DB	dry bulb
eva	evaporator
gen	generator
hex	heat exchanger
htm	heat transfer medium
int, i	interface
liq, l	liquid
loss	heat loss
o	optical
ref	refrigerant
rec	rectification
shl	shell
sol	solution
sys	system
vap, v	vapour
WB	wet bulb
wat	water

Abbreviations

ABS	absorber
AHX	absorber heat exchanger
CON	condenser
COP	coefficient of performance
DE	double-effect
EVA	evaporator
GAX	generator-absorber exchange
GEN	generator
GHX	generator heat exchanger
HP	high-pressure
HT	high-temperature
LP	low-pressure
LT	low-temperature
MP	mid-pressure
SE	single-effect

References

Anand, D.K., Allen, R.W., Kumar, B., 1982, Transient simulation of absorption machines, J. of Solar Energy, Vol. 104, pp 197-203

Alvares, S.G., Trepp, C., 1987, Simulation of a solar driven aqua-ammonia absorption refrigeration system, part 1: mathematical description and system optimization, Int. J. Refrigeration, Vol. 10, pp. 40-48

Bina, J., Radermacher, R., Moran, D., 2005, Transient simulation of an absorption chiller in a CHP system, Proc. of Int. Sorption Heat Pump Conference, Denver, USA

Butz, D., Stephan, K., 1989, Dynamic behaviour of an absorption heat pump, Int. J. of Refrigeration, Vol. 12, pp. 201-212

Collector Catalogue 2004, 2004, Institut für Solartechnik SPF, Rapperswil, Switzerland

Fu, D.G., Poncia, G., Lu, Z., 2006, Implementation of an object-oriented dynamic modeling library for absorption refrigeration systems, Applied Thermal Engineering, Vol. 26, pp. 217-225

Garimella, S. , Lacya, D., Stoutb, R.E., 1997, Space-conditioning using triple-effect absorption heat pumps, Applied Thermal Engineering, pp. 1183-1197

Grossman, G, Michelson, E, 1985, A modular computer simulation of absorption systems, ASHRAE Trans., Vol. 91, pp. 1808-1827

Infante Ferreira, C.A., 1984, Thermodynamic and physical property data equations for ammonia-lithium nitrate and ammonia-sodium thiocyanate solutions, Solar Energy, Vol. 32, pp. 231-236

James, M.L., Smith, G.M., Wolford, J.C., 1985, Applied numerical methods for digital computation, 3rd ed., Harper & Row Publishers, Inc., New York

Jeong, S., 1990, Simulation des dynamischen Verhaltens einer periodisch wirkenden Absorptionswarmepumpe mit dem Stoffgernisch Ammoniak/Wasser, Dissertation, Technical University Aachen

Jeong, S., Kang, B.H., Karng, S.W., 1998, Dynamic simulation of an absorption heat pump for recovering low grade waste heat, Applied Thermal Engineering, Vol. 18, pp. 1-12

Kaushik, S.C., Sheridan, N., Lam, K., Kaul, S., 1985, Dynamic simulation of an ammonia-water absorption cycle solar heat pump with integral refrigerant storage, J. of Heat Recovery Systems, Vol. 5., pp. 101-116

Kaushik, S.C., Rao, S.K., Kumari, R., 1991, Dynamic simulation of an aqua-ammonia absorption cooling system with refrigerant storage, Energy Convers. Mgmt., Vol. 32, pp 197-206

Keizer, C., 1982, Absorption refrigeration machines, Dissertation, TU Delft

Kim, D.S, Machielsen, C.H.M., 2002a, Evaluation of air-cooled solar absorption cooling systems, Proc. of ISHPC 2002, Shanghai, China

Kim, D.S, Machielsen, C.H.M., 2002b, Comparative study on water- and air-cooled solar absorption chillers, Proc. of EuroSun 2002 ISES Conference, Bologna, Italy

Kim, D.S., Infante Ferreira, C.A., 2006, A Gibbs energy equation for LiBr aqueous solutions, Int. J. Refrigeration, Vol. 29, pp. 36-46

Kim, J.S., Ziegler, F., Lee, H., 2002, Simulation of the compressor-assisted triple-effect H2O/LiBr absorption cooling cycles, Applied Thermal Engineering, Vol. 22, pp. 295-308

Kohlenbach, P., Ziegler, F., 2006, Development of a dynamic simulation model for transient absorption chiller performance, Proc. of 7th IIR Gustav Lorentzen Conf. on Natural Working Fluids, Trondheim, Norway

McLinden, M.O., Klein, S.A., 1983, Simulation of an absorption heat pump, solar heating and cooling systems, Solar Energy, Vol. 31, pp. 473-482

Peritsch, M., 2006, Supermärkte als Energiezentralen, Publikation Energiesysteme der Zukunft, Federal Ministry of Transport, Innovation and Technology, Austria, http://www.energiesystemederzukunft.at/publikationen/, the last access on 08 Dec. 2006

SACE, 2003, Solar Air conditioning in Europe: Final Report, EC project NNE5/2001/25

Sano, J., Hihara, E., Saito, T., Nagaoka, Y., Nishyama, N., 1991, Dynamic simulation of an absorption refrigerating machine, Proc. of Absorption Heat Pump Conference, Tokyo, Japan, pp. 133-138

Schweigler, C., Hiebler, S., Kren, C., Mehling, H., 2005, Low temperature heat storage for solar heating and cooling applications, Proc. of International Conference Solar Air Conditioning, Bad Staffelstein, Germany

Söylemez, M.S., 1999, Theoretical and experimental analyses of cooling towers, ASHRAE trans., Vol. 105, pp. 330-337

Stitou, D., Spinner, B., Satzger, P., Ziegler, F., 2000, Development and comparison of advanced cascading cycles coupling a solid/gas thermochemical process and a liquid/gas absorption process, Applied Thermal Engineering, Vol. 20, pp. 1237-1269

Stuart, L., Sheridan, G.N.R., 1977, Modeling of a solar-operated absorption air conditioner system with refrigerant storage, Solar Energy, Vol. 19, pp. 691-700

Worek, W.M., Ludovisi, D., Meckler, M., 2003, Enhancement of a double-effect absorption cooling system using a vapour recompression absorber, Energy, Vol. 28pp. 1151-1163

Ziegler, B., Trepp, Ch., 1984, Equation of state for ammonia-water mixtures, Int. J. Refrigeration, Vol. 7, pp. 101-106

Zhuo, C., 1995, Absorption heat transformer with TFE-Pyr as the working pair, Dissertation, TU Delft

3 Design of a half-effect chiller set-up

Content of this Chapter is a summary of the design activities carried out in project "Solar-driven air-cooled absorption cooling systems" [2].

Water exerts sub-atmospheric pressures under the typical operating conditions of a LiBr-water chiller. Especially in an evaporator, influence of pressure is enormous on the evaporation (saturation) temperature of water. For example, at 0.87 kPa, the saturation temperature of water is about 5°C. At such a low pressure, a pressure change equivalent to 6 mm of water head increases this saturation temperature by 1K. This means that evaporation temperature can be different with location even in a small static water drop. For this reason, main components (generator, condenser, absorber and evaporator) are designed as falling film type heat exchangers in LiBr-water chillers. And in order to minimize the flow resistance in vapour path, a pair of heat exchangers, i.e. generator-condenser or evaporator-absorber, is put in a single vessel. In this way, the risk of leakage is also minimized.

Although the boundary is not clear, "Shell & Tube" type designs are dominant in large chillers and "Shell & Coil" type designs are more common in small chillers.

In a Shell & Tube type chiller, working fluids are distributed over the banks of straight tubes in horizontal position. Bottom of a shell is partitioned to separate refrigerant and solution falling from the tubes above.

In a Shell & Coil type chiller, spirally coiled tubes are used instead of horizontal tubes. Often multiple numbers of coils with different coiling diameters are arranged concentrically for compact design. A working fluid is distributed at the top of the coil normally by a doughnut-shaped liquid distributor.

In this Chapter, a half-effect chiller has been designed with Shell & Coil type heat exchangers because it allows firstly, a more compact design and secondly, presents lower risk of leakage.

In Section 3.1, beginning with the general description of a half-effect absorption cycle, several conceptual designs are discussed regarding the practical aspects in the development of an experimental chiller.

In Section 3.2, simple thermodynamic models and simulation results are presented. From the results, a set of operating conditions has been chosen for the design of the set-up.

Finally, designs of set-up components are presented in Section 3.3.

---

[2] The idea of a low temperature-driven air-cooled absorption chiller has been granted a funding by NOVEM (the Netherlands Agency for Energy and Environment) in the framework of BSE-NEO under contract number BSE-NEO 0268-02-03-04-0008 for the project "Zongedreven airconditioning met lucht gekoelde absorptiekoelsystemen (Solar-driven air-cooled absorption cooling systems)" during the period March 2003 to May 2005. The results of this project can be found in the progress- and the final reports (Kim and Infante Ferreira, 2003, 2004, 2005).

3.1 Configuration of the chiller

In this Section, several conceptual designs are presented for the development of a half-effect LiBr-H_2O absorption chiller. Various aspects related to the practical development of the components will be discussed.

To begin with, the working principle of a heat-coupled half-effect absorption chiller is described below.

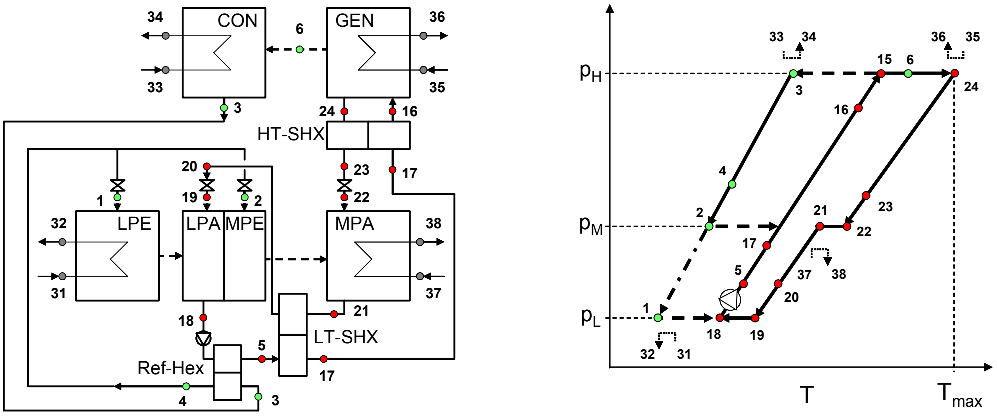

(a) Block diagram (b) p-T-x diagram

Figure 3.1 Heat-coupled serial-flow half-effect cycle

The numerical indices given in Fig. 3.1 will be used in the process description below.

The half-effect cycle given in Fig. 3.1 is a serial-flow type. As briefly mentioned in Ch. 2, a parallel-flow type cycle is only slightly different in configuration of the solution circuit, and will be explained later.

The cycle has three levels of system pressures, namely high pressure p_H, mid pressure p_M and low pressure p_L. At each pressure level, there is a pair of components. A generator and a condenser operate at p_H, MPE (Mid-Pressure Evaporator) and MPA (Mid-Pressure Absorber) at p_M, and LPE (Low-Pressure Evaporator) and LPA (Low-Pressure Absorber) at p_L.

From the outlet (point 18 in Fig. 3.1) of LPA, a solution pump lifts refrigerant-rich solution to the generator (18→24) via Ref-Hex (Refrigerant Heat eXchanger, 18→5), LT-SHX (Low-Temperature Solution Heat eXchanger, 5→17) and HT-SHX (High-Temperature Solution Heat eXchanger, 17→16). In the generator, the rich solution is boiled by a heating medium flow (35→36) fed from solar collectors and the resulting steam is supplied to the condenser (6-3).

The liquefied refrigerant from the condenser (3) is split into two flows. One is supplied to LPE (1) and the other to MPE (2). And they are absorbed by LPA (20→18) and MPA (23→21) respectively. Among these two split refrigerant flows, only the refrigerant in LPE (1) delivers cooling effect. The other refrigerant in MPE (2) only cools down LPA (20→18), which is why the maximum temperature of the cycle (T_{max} in Fig. 3.1) is significantly lower than that of a conventional single-effect cycle.

If the liquefied refrigerant from the condenser can be cooled down somehow before being supplied to the evaporators, it helps reducing flash losses. This is realized by Ref-Hex (Refrigerant Heat exchanger), between condenser and LPA so that the refrigerant from the condenser is cooled down (3→4) while the cold solution from LPA is warmed up (18→5).

On the other hand, hot and refrigerant-poor solution at the outlet of generator (24) flows to MPA (23→21) after exchanging heat (24→23) with the colder rich solution (17→16) in HT-SHX. Then the poor solution is cooled by coolant flow (37→38) and absorbs the vapour from MPE (2) in MPA (23→21).

The solution at the outlet of MPA (21) flows further to LPA after exchanging heat (21→20) again to the colder rich solution on the other side of the LT-SHX (5→17). And in LPA, it absorbs the vapour from LPE (1) while it is being cooled by the evaporating refrigerant in MPE (2). Finally, the rich solution at the outlet of LPA returns to the solution pump to make a complete cycle.

As already mentioned, the sole purpose of MPE (2) is to cool down LPA (20→18) to a temperature lower than ambient so that the maximum cycle temperature T_{max} (=T_{24}) can be significantly lowered.

A chiller design should enable all the processes described above in a physical environment. Before starting the physical design of the chiller, types of components and their arrangement in a physical dimension should be firstly decided. For this purpose, several design concepts were prepared and one particular design concept has been finally chosen for physical design of the chiller. In the following the general description is given of pre-design studies that have been carried out.

Fig. 3.2 shows one of the conceptual designs developed initially.

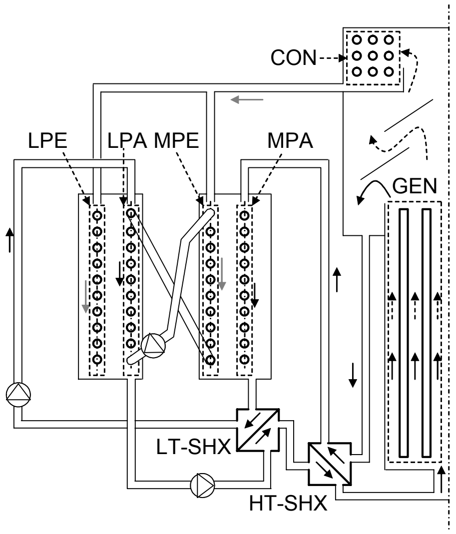

Figure 3.2 Indirect heat-coupled serial-flow half-effect chiller
with a flooded generator (Refrigerant heat exchanger not shown)

The chiller in Fig. 3.2 is based on the serial-flow cycle. For convenience, the refrigerant heat exchanger is not shown in the figure.

The generator is located in the center of the machine with a condenser on top of it surrounded by evaporators and absorbers, which are actually tubular heat exchangers coiled around the generator. The location of the generator was decided to keep its heat loss to ambient at a minimal level. And by positioning a condenser at the top of it, the flow path of vapour from the generator could be shortened.

Several problems can be found in this configuration. Firstly, the generator is configured as flooded type in Fig. 3.2. A flooded type generator is advantageous in terms of wetting of heat transfer surface. Besides when all components are physically arranged in a proper scheme, self-circulating configuration is possible as in Fig. 1.6 in Ch. 1. However the thermodynamic performance of a flooded generator is poor considering that it requires an elevated driving temperature for the extra hydraulic pressure on the heat transfer surface exerted by the flooded solution inside.

The second problem is the need of a secondary heat transfer circuit for the heat transfer between LPA and MPE. Although the secondary heat transfer circuit enables use of ordinary tube coils for both of the components, the heat transfer resistance between the components is large.

Both flooded generator and indirect heat transfer between LPA and MPE contribute to a high generator temperature, which in turn would decrease the system efficiency.

Finally, the configuration in Fig. 3.2 is shown to have three circulation pumps. Considering that the biggest advantage with an absorption chiller is minimal consumption of electricity, use of many circulation pumps is not acceptable. Among the pumps, the solution pump between MPA and LPA may be omitted if LPA is located below MPA.

In order to avoid the heat transfer resistance between LPA and MPE, tube coil type heat exchangers were abandoned for the components. Instead, a vertical plate heat exchanger has been chosen for both of the components. In a new design, solution flows on one side of the vertical plate and refrigerant flows on the other. Therefore heat is transferred directly from one side to the other through the plate and a secondary heat transfer circuit is not necessary.

For the generator, a falling film type heat exchanger has also been considered to avoid the increased boiling temperature of a flooded generator. A falling film generator would also minimize the charge of solution. Consequently, the possibility of a self-circulating configuration was also abandoned.

Although arranging MPA and LPA in a vertical plane would avoid the use of a circulation pump between them, this makes the whole design excessively complicated especially in combination with the vertical plate type LPA-MPE design. Therefore this idea has been abandoned.

Need of the solution pump between MPA and LPA in Fig. 3.2 comes from the “serial” flow configuration of the serial flow cycle in Fig. 3.1. If the solution flow is reconfigured according to a parallel flow scheme, the circulation pump would not be necessary. Fig. 3.3 shows a parallel-flow cycle.

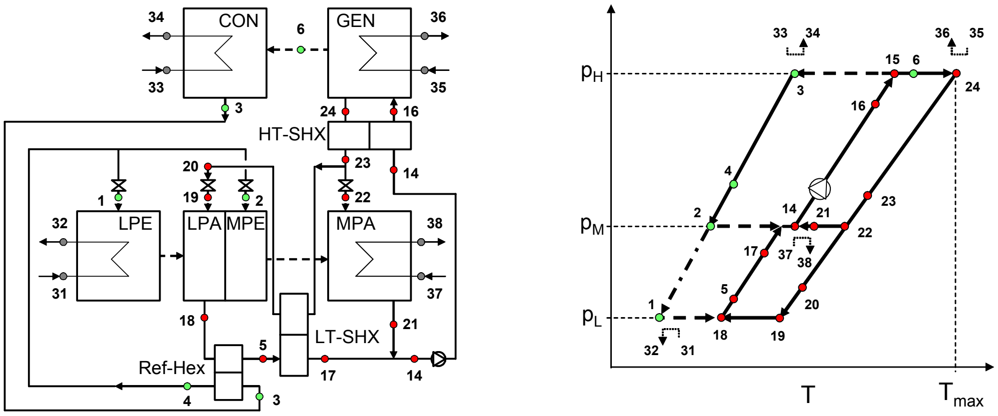

(a) Block diagram (b) p-T-x diagram

Figure 3.3 Heat-coupled parallel-flow half-effect cycle

A parallel-flow cycle is different from a serial-flow cycle in that the poor solution from a generator is split into two flows and supplied to mid- and low-pressure absorbers in parallel (see the split point 23 in Fig. 3.3a).

Serial- and parallel-flow cycles are not much different from a thermodynamic point of view except that a parallel-flow cycle has “solution split ratio” as an extra variable. When optimized, the two cycles yield practically the same COP. Design of an actual parallel-flow chiller is, however, quite different that of a serial-flow chiller in several aspects.

Firstly, arrangement of components is relatively flexible as already explained above regarding the solution pump between MPA and LPA. Secondly, absorbers in a parallel-flow cycle have to be designed with lower solution flow rates that those of a serial-flow cycle.

Although the first point is certainly an advantage, the second one brings about some difficulties to the practical designs of the absorbers. Since wetting of heat transfer surface is incomplete under a certain flow rate called minimum wetting rate (MWR, see e.g. Hartley and Murgatroyd, 1964), design of an absorber should take this limit into account especially for a parallel-flow cycle.

A new configuration has been developed taking into account the various design aspects mentioned above, which is shown in Fig. 3.4.

In this configuration, LPA and MPE is simply a vertical plate with falling film flows on both sides and also a falling film type heat exchanger is used for the generator. The poor solution from the generator is split after HT-SHX and supplied to LPA and MPA in parallel. There is only one solution pump for lifting rich solution to the generator.

Considering the simplicity and feasibility of design, the concept in Fig. 3.4 has been finally chosen for the design of a half-effect LiBr-H_2O absorption chiller.

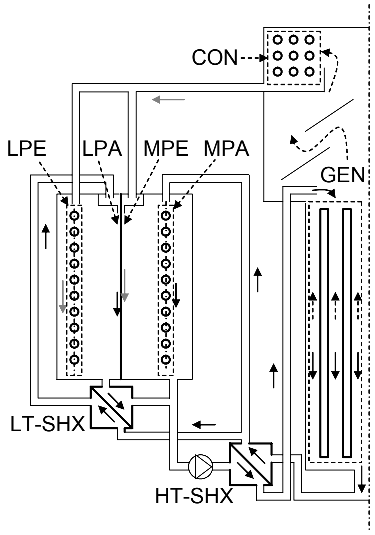

Figure 3.4 Direct heat-coupled parallel-flow half-effect chiller
with a falling film generator (Refrigerant heat exchanger not shown)

Packaging is also an important aspect in design. Because the chiller operates under vacuum, all components should be put in pressure vessels. Infiltration of air is critical to the chiller performance and the whole chiller package should be designed to minimize such a risk. In order to ensure vacuum-tightness at a minimal cost, it was decided to put most of the components in a single pressure vessel, which has three separated compartments to accommodate high-, mid- and low-pressure components. Since the pressure differences between the three pressure compartments are small, the thickness of a compartment wall does not need to be as large as that of the pressure vessel.

Positioning a generator in the center of a vertical pressure vessel with a condenser on the top of it and arranging mid- and low-pressure components around make the final configuration of the chiller as shown in Fig. 3.5.

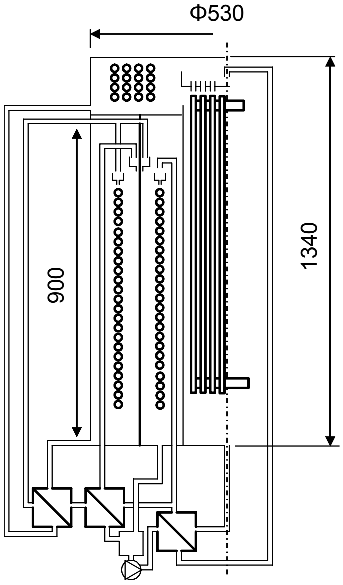

Figure 3.5 Configuration of a half-effect LiBr-H_2O chiller

The dimensions shown in Fig. 3.5 were derived from the design results that will follow in the next section.

3.2 Cycle design

Before physical design of components, a series of thermodynamic simulations were carried out to evaluate influences of various parameters including component sizes, flow rates of working fluids and so on. Based on the results, the cycle was further optimized both for high performance and for a compact overall physical dimension.

First of all, all components in the chiller were described in terms of effectiveness (see e.g. ε-NTU method in Holman, 1997). Choice of this particular modeling method was made because the effectiveness concept is very convenient when a complex thermal system consisting of many components has to be optimized taking into account the size (or performance) of each and every component.

In the following the summary of component models and the results of parametric simulations for a parallel-flow half-effect LiBr-H_2O absorption chiller are given. Numerical indexes refer to Fig. 3.3.

3.2.1 Generator (GEN)

Rich solution is supplied to a generator with ε_{GEN} under pressure $p_H=p^*(T_{03})$ at the flow rate $\dot{m}_{16}$, the concentration x_{16} and the temperature T_{16}. Heating medium enters the generator at $\dot{m}_{35}$ and T_{35}. Poor solution leaves the generator at $\dot{m}_{24}$, x_{24} and T_{24}. Superheated vapour leaves for condenser with $\dot{m}_{06}$ and T_{06}.

Governing equations are derived as follows.

Total mass balance:

$$\sum \dot{m} = \dot{m}_{16} - \dot{m}_{06} - \dot{m}_{24} = 0 \tag{3.1}$$

LiBr mass balance:

$$\sum \dot{m}_{LiBr} = \dot{m}_{16} x_{16} - \dot{m}_{24} x_{24} = 0 \tag{3.2}$$

Energy balance:

$$\sum \dot{Q} = \dot{m}_{35} C_{p35} (T_{35} - T_{36}) - (\dot{m}_{24} h_{24}^l + \dot{m}_{06} h_{06}^v - \dot{m}_{16} h_{16}^l) = 0 \tag{3.3}$$

where h^v_{06} is enthalpy of the superheated vapour that flows to the condenser and h^l_{16} and h^l_{24} are the enthalpy of the solutions at the inlet and outlet of the generator respectively.

Heat transfer model:

In case the heating medium has a larger thermal capacity, the maximum generator temperature is given by

$$T_{24} = T_{15} + \varepsilon_{\mathrm{GEN}}(T_{35} - T_{15}) \tag{3.4}$$

and the closest approach temperature (CAT), the minimum temperature difference between two heat exchanging streams, is defined by

$$CAT_{GEN} \equiv T_{35} - T_{24} = (1 - \varepsilon_{\mathrm{GEN}})(T_{35} - T_{15}) \tag{3.5}$$

where T_{15} is the equilibrium temperature of the incoming solution at its concentration and the system pressure, i.e. $T_{15}=T^*(p_H, x_{16})$. CAT expression in Eq. (3.5) is sometimes more convenient than the equivalent effectiveness expression in Eq. (3.4) and it is thus also used.

Using Eq. (3.1) and (3.2), circulation ratio "λ" is defined by

$$\lambda \equiv \dot{m}_{16} / \dot{m}_{06} = x_{24}/(x_{24}-x_{16}) \tag{3.6}$$

Physically, λ is a specific flow rate of rich solution for the generation of a unit refrigerant flow rate. The flow rate of poor solution at the outlet can also be described in terms of λ as $\dot{m}_{24} / \dot{m}_{06} = \lambda - 1$. Then, Eq. (3.3) can be rewritten as

$$\sum \dot{Q} = \dot{m}_{35} C_{p35} (T_{36} - T_{35}) - \dot{m}_{06} \left[\lambda (h^l_{24} - h^l_{16}) + h^v_{06} - h^l_{24} \right] = 0 \tag{3.7}$$

For solution, Eq. (3.7) should be solved simultaneously either with Eq. (3.4) or (3.5).

3.2.2 Condenser (CON)

The vapour condenses in a condenser with ε_{CON} under pressure $p_H=p^*(T_{03})$ at the rate of $\dot{m}_{03}$ $(= \dot{m}_{06})$. Coolant enters at $\dot{m}_{33}$ and T_{33} (^{o}C).

Governing equations for the condenser are given as follows.

Mass balance:

$$\sum \dot{m} = \dot{m}_{03} - \dot{m}_{01} - \dot{m}_{02} = 0 \tag{3.8}$$

where $\dot{m}_{01}$ and $\dot{m}_{02}$ are the refrigerant flow rates to LPE (point 1 in Fig. 3.3) and MPE (2) respectively.

Energy balance:

$$\sum \dot{Q} = \dot{m}_{03} (h^{fg}_{03} + C^v_p \Delta T^{\mathrm{sup}}) - \dot{m}_{33} C_{p33} (T_{34} - T_{33}) = 0 \tag{3.9}$$

where ΔT^{sup} is the superheating of the vapour coming into the condenser, which is defined by

$$\Delta T^{\mathrm{sup}} \equiv T_{06} - T_{03} \tag{3.10}$$

where T_{06} is the vapour temperature at the generator outlet and T_{03} is the dew temperature in the condenser.

Heat transfer model:

$$T_{34} = T_{33} + \varepsilon_{\mathrm{CON}}(T_{03} - T_{33}) \tag{3.11}$$

In order to save computing time for calling a property subroutine and to avoid an iterative process for the solution of Eq. (3.9), the latent heat of saturated steam h^{fg} has been made a 2nd-order polynomial function of T^{dew} so that h_{03}^{fg} is given by

$$h_{03}^{fg} = a_1 + a_2 T_{03} + a_3 T_{03}^2 \tag{3.12}$$

where a_1=2495.62, a_2=-2.0126 and a_3=-0.0037682 can be used within maximum 0.5% error of the steam table data from Schmidt (1979) for $0\ ^{o}C < T^{dew} < 212\ ^{o}C$.

Then Eq. (3.9), (3.11) and (3.12) can be combined to give a solution for T_{03} as

$$T_{03} = \frac{-b_2 + \sqrt{b_2^2 - 4b_1 b_3}}{2b_1} \tag{3.13}$$

where

$b_1 = a_3\ \dot{m}_{03}$
$b_2 = (a_2 - C_{p06}^{v})\ \dot{m}_{03} - \varepsilon_{CON}\ \dot{m}_{33} C_{p33}$
$b_3 = \varepsilon_{CON}\ \dot{m}_{33} C_{p33}\ T_{33} + \dot{m}_{03}\ (a_1 + C_{p06}^{v}\ T_{06})$

3.2.3 Low-Pressure Evaporator (LPE)

Refrigerant evaporates in LPE with ε_{LPE} under pressure $p_L = p^*(T_{01})$ at the flow rate of $\dot{m}_{01}$. Chilled water enters the evaporator at $\dot{m}_{31}$ and T_{31}.

LPE can be described by the following equations.

Heat balance:

$$\sum \dot{Q} = \dot{m}_{31} C_{p31}(T_{31} - T_{32}) - \dot{m}_{01}\left(h_{01}^{fg} - C_{p01}^{l} \Delta T^{sub}\right) = 0 \tag{3.14}$$

and ΔT^{sub} is the subcooling of the liquid entering the evaporator, which is defined by

$$\Delta T^{sub} \equiv T_{04} - T_{01} \tag{3.15}$$

Heat transfer model:

$$T_{32} = T_{31} - \varepsilon_{\mathrm{LPE}}(T_{31} - T_{01}) \tag{3.16}$$

Similar to the condenser model, the dew temperature T_{01} is solved as

$$T_{01}=\frac{-b_2+\sqrt{b_2^2-4b_1b_3}}{2b_1} \tag{3.17}$$

where

$b_1= a_3\, \dot{m}_{01}$
$b_2= (a_2 +C_{p01}^{\,l})\, \dot{m}_{01} + \varepsilon_{LPE}\, \dot{m}_{31}C_{p31}$
$b_3= -\varepsilon_{LPE}\, \dot{m}_{31}C_{p31}T_{31}+\dot{m}_{01}(a_1-C_{p01}^{\,l}\,T_{04})$

3.2.4 Low-Pressure Absorber/Mid-Pressure Evaporator (LPA/MPE)

Refrigerant evaporates in MPE under the pressure $p_M=p^*(T_{02})$ at the flow rate of $\dot{m}_{02}$. Poor solution enters the absorption side at $\dot{m}_{20}$, x_{20} and T_{20}. The size of this component is represented by $\varepsilon_{LPA\text{-}MPE}$.

Total mass balance on absorption side:

$$\sum \dot{m} = \dot{m}_{20}+\dot{m}_{01}-\dot{m}_{18}=0 \tag{3.18}$$

LiBr mass balance on absorption side:

$$\sum \dot{m}_{LiBr} = \dot{m}_{20}x_{20}-\dot{m}_{18}x_{18}=0 \tag{3.19}$$

Energy balance:

$$\sum \dot{Q}=(\dot{m}_{20}h_{20}^{l}+\dot{m}_{01}h_{01}^{v}-\dot{m}_{18}h_{18}^{l})-\dot{m}_{02}(h_{02}^{v}-h_{04}^{l})=0 \tag{3.20}$$

where h^v_{01} is enthalpy of the saturated steam from LPE and h^l_{20} is the enthalpy of incoming solution.

Heat transfer model:

$$T_{18}=T_{19}-\varepsilon_{\text{LPA-MPE}}(T_{19}-T_{02}) \tag{3.21}$$

where T_{19} is the equilibrium temperature of the incoming solution at its concentration and the system pressure, i.e. $T_{19}=T^*(p_L, x_{20})$.

From Eq. (3.18) and (3.19), the flow rate at the outlet of LPA is written as $\dot{m}_{18}=\dot{m}_{01}x_{20}/(x_{20}-x_{18})$. Noting that $x_{20}=x_{24}$ and using Eq. (3.6), $\dot{m}_{18}$ is rewritten as $\dot{m}_{18}=\dot{m}_{01}\lambda(x_{24}-x_{16})/(x_{24}-x_{18})$. Also noting that $\dot{m}_{20}=\dot{m}_{18}-\dot{m}_{01}$, Eq. (3.20) becomes

$$\dot{m}_{01}\left[\lambda\left(\frac{x_{24}-x_{16}}{x_{24}-x_{18}}\right)(h_{20}^{l}-h_{18}^{l})+(h_{01}^{v}-h_{20}^{l})\right]-\dot{m}_{02}(h_{02}^{v}-h_{04}^{l})=0 \tag{3.22}$$

3.2.5 Mid-Pressure Absorber (MPA)

Poor solution is supplied to MPA with ε_{MPA} at $\dot{m}_{22}$, x_{23} and T_{23}. Coolant enters the absorber at $\dot{m}_{37}$ and T_{37}. Rich solution leaves the absorber at $\dot{m}_{21}$, x_{21} and T_{21}. Saturated steam is supplied by MPE at $\dot{m}_{02}$ and T_{02}.

Total mass balance on absorption side:

$$\sum \dot{m} = \dot{m}_{22}+\dot{m}_{02}-\dot{m}_{21}=0 \tag{3.23}$$

LiBr mass balance on absorption side:

$$\sum \dot{m}_{LiBr} = \dot{m}_{22}x_{23}-\dot{m}_{21}x_{21}=0 \tag{3.24}$$

Energy balance:

$$\sum \dot{Q}=(\dot{m}_{22}h_{23}^{l}+\dot{m}_{02}h_{02}^{v}-\dot{m}_{21}h_{21}^{l})-\dot{m}_{37}C_{p37}(T_{38}-T_{37})=0 \tag{3.25}$$

where h^{v}_{02} is enthalpy of the saturated steam from MPE and h^{l}_{23} is the enthalpy of the incoming solution.

Heat transfer model:

$$T_{21}=T_{22}-\varepsilon_{\mathrm{MPA}}(T_{22}-T_{37}), \quad \text{when } T_{22}-T_{21}>T_{38}-T_{37} \tag{3.26}$$
$$T_{38}=T_{37}+\varepsilon_{\mathrm{MPA}}(T_{22}-T_{37}), \quad \text{when } T_{22}-T_{21}< T_{38}-T_{37} \tag{3.27}$$

where T_{22} is the equilibrium temperature of the incoming solution at its concentration and the system pressure, i.e. $T_{22}=T^{*}(p_M, x_{23})$.

From Eq. (3.23) and (3.24) and noting that $x_{23}=x_{24}$, the flow rate at the outlet of MPA is written as $\dot{m}_{21}=\dot{m}_{02}x_{24}/(x_{24}-x_{21})$. Then, similar to LPA model, Eq. (3.25) is rewritten as

$$\sum \dot{Q}=\dot{m}_{02}\left[\lambda\left(\frac{x_{24}-x_{16}}{x_{24}-x_{21}}\right)(h_{23}^{l}-h_{21}^{l})+(h_{02}^{v}-h_{23}^{l})\right]-\dot{m}_{37}C_{p37}(T_{38}-T_{37})=0 \tag{3.28}$$

3.2.6 Refrigerant Heat Exchanger (Ref-Hex)

Liquefied refrigerant at the flow rate $\dot{m}_{03}$ is cooled down from T_{03} to T_{04} in the hot side and rich solution with the flow rate of $\dot{m}_{18}$ is warmed up from T_{18} to T_{05}. Effectiveness of this heat exchanger is $\varepsilon_{\text{Ref-Hex.}}$

This heat exchanger is described by the following governing equations.

Energy balance:

$$\begin{aligned}\sum \dot{Q} &= \dot{m}_{18} C_{p18}(T_{05} - T_{18}) - \dot{m}_{03} C_{p03}(T_{03} - T_{04}) \\ &= \dot{m}_{01} \lambda \left(\frac{x_{24} - x_{16}}{x_{24} - x_{18}} \right) C_{p18}(T_{05} - T_{18}) - \dot{m}_{03} C_{p03}(T_{03} - T_{04}) = 0\end{aligned} \tag{3.29}$$

Heat transfer model:

$$T_{04} = T_{03} - \varepsilon_{\text{Ref-Hex}}(T_{03} - T_{18}) \tag{3.30}$$

3.2.7 Low-Temperature Solution Heat eXchanger (LT-SHX)

Rich solution at the flow rate of $\dot{m}_{18}$ is heated from T_{05} to T_{17} in the cold side and poor solution at $\dot{m}_{19}$ is cooled down from T_{23} to T_{20}. This heat exchanger has an effectiveness of $\varepsilon_{\text{LT-SHX.}}$

The governing equations are derived as follows.

Energy balance:

$$\begin{aligned}\sum \dot{Q} &= \dot{m}_{18} C_{p18}(T_{17} - T_{05}) - \dot{m}_{20} C_{p20}(T_{23} - T_{20}) = 0 \\ &= \dot{m}_{01} \lambda \left(\frac{x_{24} - x_{16}}{x_{24} - x_{18}} \right) \left[C_{p18}(T_{17} - T_{05}) - \left(\frac{x_{18}}{x_{24}} \right) C_{p20}(T_{23} - T_{20}) \right] = 0\end{aligned} \tag{3.31}$$

Heat transfer model:

$$T_{20} = T_{23} - \varepsilon_{\text{LT-SHX}}(T_{23} - T_{05}) \tag{3.32}$$

3.2.8 High-Temperature Solution Heat exchanger (HT-SHX)

Rich solution at $\dot{m}_{16}$ is heated from T_{14} to T_{16} in the cold side and poor solution at $\dot{m}_{24}$ is cooled down from T_{24} to T_{23} in the hot side. Effectiveness is $\varepsilon_{\text{HT-SHX}}$.

The governing equations are derived as follows.

Energy balance:

$$\sum\dot{Q} = \dot{m}_{16}C_{p16}(T_{16} - T_{14}) - \dot{m}_{24}C_{p24}(T_{24} - T_{23}) \\ = \dot{m}_{03}\left[\lambda C_{p16}(T_{16} - T_{14}) - (\lambda - 1)C_{p24}(T_{24} - T_{23})\right] = 0 \tag{3.33}$$

Heat transfer model:

$$T_{23} = T_{24} - \varepsilon_{\text{HT-Hex}}(T_{24} - T_{14}) \tag{3.34}$$

3.2.9 Solar collector

Heating medium enters a solar collector with an efficiency η_{col} and surface area of A_{col} at the flow rate of $\dot{m}_{35}$ and T_{36} and gets warmed up to T_{35} under the solar radiation with solar intensity of I_p.

Governing equations are given as follows.

Energy balance:

$$\sum\dot{Q} = \dot{m}_{35}C_{p35}(T_{35} - T_{36}) - \eta_{col}I_pA_{col} = 0 \tag{3.35}$$

Note that Eq. (3.35) is related to the energy balance equation for the generator in Eq. (3.3).

3.2.10 Dry cooler

Heat has to be rejected to ambient from the condenser and MPA by a dry cooling tower, i.e. a water-to-air heat exchanger. Water has been considered as the heat transfer medium circulating through the dry cooler and those components.

Three configurations may be considered in the circulation of cooling water. Cooling water returning from the dry cooler can firstly be supplied to the condenser and then to MPA or to MPA first and then condenser. Or the cooling water can be split and supplied to both components in parallel.

From a preliminary simulation result, it turned out to be the best to supply the cooling water firstly to MPA and then condenser in series. The reason was that the heat rejection of condenser was so large that the performance of MPA was significantly deteriorated when MPA was located downstream. Therefore the cooling water path was configured as such and then T_{33}=T_{38} in Fig. 3.3.

Governing equations for this component are given as follows.

Energy balance:

$$\sum \dot{Q} = \dot{m}_{37} C_{p37} (T_{34} - T_{37}) - \dot{m}_{air} C_{p,air} (T_{air,out} - T_{air,in}) = 0 \qquad (3.36)$$

Heat transfer model:

In case the cooling air has a larger thermal capacity, the minimum cooling water temperature is given by

$$T_{37} = T_{34} - \varepsilon_{\mathrm{DTower}} (T_{34} - T_{air,in}) \qquad (3.37)$$

and the closest approach temperature $\mathrm{CAT}_{\mathrm{DTower}}$ is defined by

$$CAT_{DTower} \equiv T_{37} - T_{air,in} = \left(1 - \varepsilon_{\mathrm{DTower}}\right)\left(T_{34} - T_{air,in}\right) \qquad (3.38)$$

3.2.11 Simulation results

Using the effectiveness models developed in the previous sections, first of all, simulations have been carried out to figure out the influence of design parameters on the energetic and financial characteristics. Design parameters are the circulation ratio, LiBr concentrations of solution and effectiveness of components.

Based on the simulation results, each parameter has been set at its final design value not only for system performance but also for a low investment cost and compact packaging.

During simulation, the same working conditions were applied as used in Section 2.3.1 in Ch. 2, which are

- T_{amb}=32°C ; Ambient temperature, exceeded 14 hrs in Milan and Naples in July and August
- T_{31}=12.5°C ; Chilled water return temperature
- I_p=800W/m^2 ; Solar intensity perpendicular to collector surface. $I_{p,avg}$=730 W/m^2 for Milan and $I_{p,avg}$=840 W/m^2 for Naples between 10:00-15:00 in July and August

For the estimation of investment cost on solar collectors, three flat plate collectors were considered as listed in Table 3.1.

Table 3.1 Specifications of solar collectors

Name	Type	[1]Efficiency $\eta_0/c_1/c_2$	[2]Efficiency at T^*=0.085	Unit Price (€/m^2)
Flat I	Flat plate	0.723/2.65/0.0110	0.43	200
Flat II		0.682/4.30/0.0077	0.27	150
Flat III		0.752/6.44/0.0214	0.08	100

1. $\eta = \eta_o - c_1 T_r - c_2 I_p T_r^2$, $T_r = (T_{avg} - T_{amb})/I_p$, gross efficiency with wind
2. T_r =0.085 when T_{amb}=32°C, T_{avg}=100°C and I_p=800W/m^2

The three collectors in Table 3.1 are actual collectors chosen from Collector Catalogue 2004 (2004). Among the three collectors, Flat II is close to what the efficiency-cost correlation Eq. (2.2) represents in Section 2.1.1 of Ch. 2. But Flat I has much higher efficiency and Flat III has a much lower efficiency than Eq. (2.2) gives for the prices specified in Table 3.1. Due to the uncertainties in the market price of a solar collector, unit price in Table 3.1 must be understood as rather a measure of performance than a real price in the market.

Table 3.2 lists major design parameters and the corresponding variable ranges in simulation. Some of the parameters were not varied in the simulation because either they have already been optimized or they were pre-determined by conventional design practice.

Table 3.2 Design parameters

Parameter	Standard value	Range	Remark
λ	9	8-13	Circulation ratio
x_{24}	55.5%	46-66%	Minimum LiBr concentration in LPA and MPA
x_{15}-x_{18}	0%	Fixed	Pre-determined, insensitive around the standard value
CAT_{GEN}	4K		Pre-determined for the balance between generator and collector sizes
CAT_{DTower}	5K		Pre-determined for a reasonably sized dry cooler
T_{01}	5°C		Set to prevent the refrigerant from freezing
$\dot{m}_{35}$	60 lpm		Pre-determined with CAT_{GEN}
$\dot{m}_{31}$	26 lpm		Determined with T_{31}=12.5°C and T32=7°C for 10kW
$\dot{m}_{37}$	60 lpm		Pre-determined with CAT_{DTower}
ε_{CON}	0.9	0.4-0.9	
$\varepsilon_{LPA\text{-}MPE}$	0.5		
$\varepsilon_{Ref\text{-}Hex}$	0.9		
$\varepsilon_{LT\text{-}SHX}$	0.8		
$\varepsilon_{HT\text{-}SHX}$	0.7		

In the following, all quantities are based on a cooling capacity of 10kW, which is suitable for air conditioning of 200-330m^2 of space assuming 30-50W/m^2 of cooling load.

Fig. 3.6 shows variations of chiller's COP and the required collector area against the effectiveness of individual component. While the effectiveness of a component was varied, values of the other parameters are kept constant at their standard values in Table 3.2.

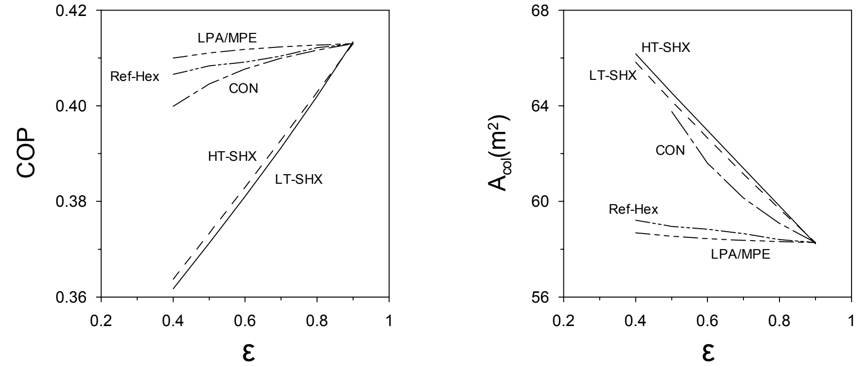

(a) COP (b) Collector area (Flat I in Table 3.1)

Figure 3.6 Influence of the effectiveness of a component

COP increases rapidly with effectiveness for the two solution heat exchangers in Fig. 3.6a. COP is relatively insensitive to the effectiveness of LPA/MPE, Ref-Hex and condenser.

As shown in Fig. 3.6b, solar collector area is also significantly dependent on the effectiveness of solution heat exchangers. This is because of the increasing chiller COP with the effectiveness in Fig. 3.6a.

The dependency of solar collector area on the condenser effectiveness has a different reason because the magnitude of the corresponding COP increase in Fig. 3.6a cannot explain such a large decrease of solar collector area as shown in Fig. 3.6b. This is due to the decrease in the generator temperature (T_{24} in Fig. 3.3) with increasing condenser performance.

From Fig. 3.6, it can be concluded that among the components considered, the two solution heat exchangers and condenser have to be given a priority in design.

In Fig. 3.7, the effect of both circulation ratio λ and maximum generator temperature T_{24} are shown together. Being an equilibrium temperature for the corresponding LiBr concentration, T_{24} is equivalent to the design parameter x_{24} in Table 3.2.

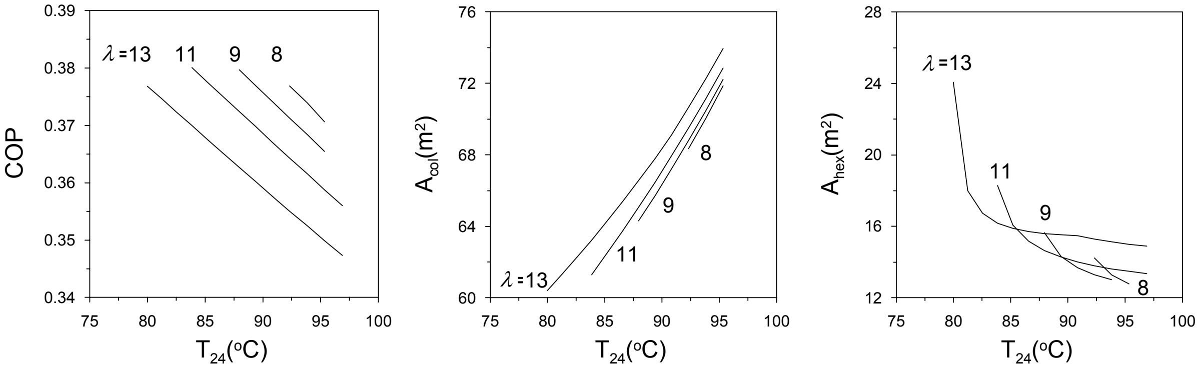

(a) COP (b) Collector area (Flat I) (c) Total heat transfer area

Figure 3.7 Influences of circulation ratio and the maximum generator temperature

In Fig. 3.7a, it is shown that COP increases with decreasing λ and with decreasing T_{24}. This results in decreasing solar collector area with decreasing λ and T_{24} in Fig. 3.7b.

Besides the COP and solar collector area, the size or cost of the chiller is also an important factor. Fig. 3.7c shows the sum of heat transfer areas for all components of the absorption chiller, which were calculated back from the effectiveness values of the components assuming a typical heat transfer coefficient for each component. Similar to the collector area, the total heat transfer area also decreases with decreasing λ. But, for a constant λ, total heat transfer area increases with decreasing T_{24} and particularly its increasing gradient becomes very large as T_{24} approaches a certain value. As will be seen later, this is mainly due to a sharp increase in the heat transfer area requirement of MPA for low T_{24}.

Then the sum of the collector and the heat transfer area in Fig. 3.7b and 3.7c can be understood as a measure of total cost for the chiller, which is shown in Fig. 3.8.

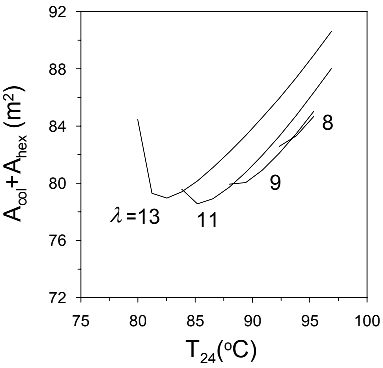

Figure 3.8 Sum of collector and heat transfer area

In Fig. 3.8, it is shown that each curve has a minimum at a certain generator temperature, which suggests that a chiller can be designed for a low cost around that generator temperature. Although Fig. 3.8 is only for the collector type Flat I in Table 3.1, the other collectors show similar trends.

In order to estimate the physical size of an individual component, the heat transfer area is presented for several components in the following.

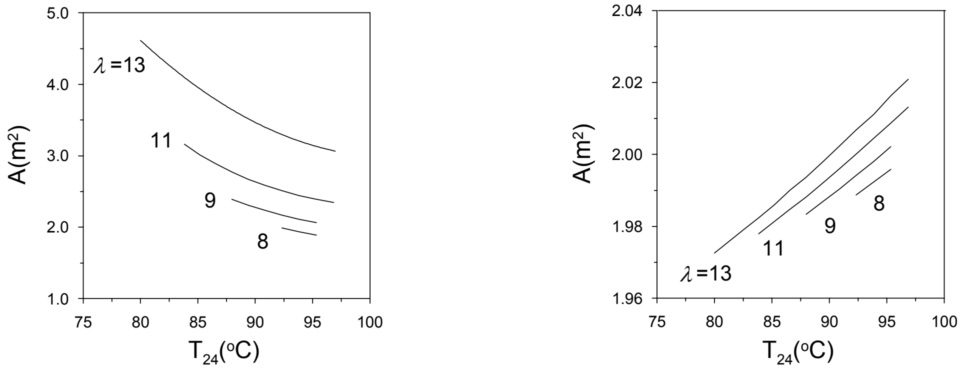

(a) Generator (b) Condenser

Figure 3.9 Heat transfer area of generator and condenser

Heat transfer area for the generator is shown in Fig. 3.9a, where it varies substantially with T_{24} and λ. The heat transfer area has been calculated assuming an overall heat transfer coefficient in the range of U=1.4-1.9kW/m^{2}K depending on λ (The heat transfer coeeficients were calculated for horizontal film generator using the correlations in Appendix B). Circulation ratio and hot water temperature have been chosen to avoid an excessively large generator. To give a sense of physical size, 1m^2 of heat transfer area is equivalent to about fifteen times that of a 1m-long Φ22mm tube.

The heat transfer area of the condenser is relatively insensitive to λ and T_{24} as shown in Fig. 3.9b. All values are within 2±0.03m^2. Overall heat transfer coefficients at around 3kW/m^{2}K were used for heat transfer area calculation using appropriate correlations in Appendix B.

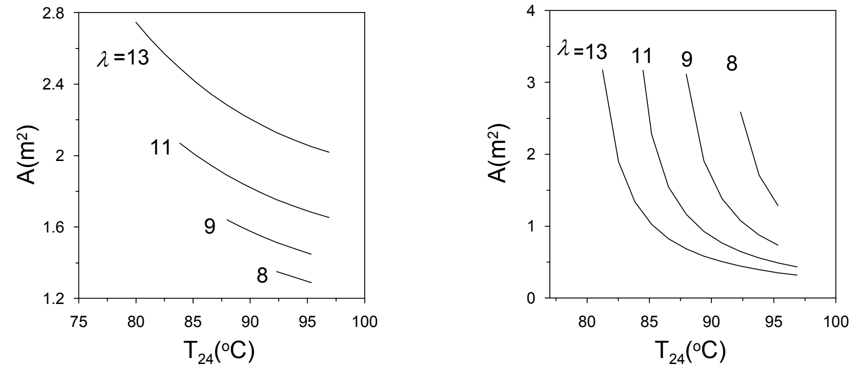

(a) LPA/MPE (b) MPA

Figure 3.10 Heat transfer area of LPA/MPE and MPA

In Fig. 3.10a, the heat transfer area of LPA/MPE is sensitive to both λ and T_{24}. To obtain a rough idea of its size, a 1m-high Φ330mm vertical tube has roughly 1m^2 of heat transfer surface. Overall heat transfer coefficients were assumed to be around 0.5kW/m^{2}K (Due to the uncertainty in empirical correlations in small flow rate range, rather arbitrary 1kW/m^{2}K of falling film heat transfer coefficient was assumed on both sides).

For a constant λ, the heat transfer area of MPA increases exponentially as T_{24} decreases as shown in Fig. 3.10b. This behavior mainly contributed to the trends of total heat transfer area curves in Fig. 3.7c. Therefore it can be understood that the minimum generator temperature T_{24} is practically limited by the size of MPA. In the calculation of heat transfer area, overall heat transfer coefficients were assumed between U=1.2-1.7kW/m^{2}K (calculate from empirical correlations in Appendix B for a horizontal falling film tube absorber) depending on the circulation ratio.

Finally the heat transfer areas of the two solution heat exchangers are shown in Fig. 3.11.

It can be seen that, in both cases, the heat transfer area is more sensitive to circulation ratio than to generator temperature. Overall heat transfer coefficients at around 0.45kW/m^{2}K were calculated from the empirical correlations in Appendix B for both heat exchangers.

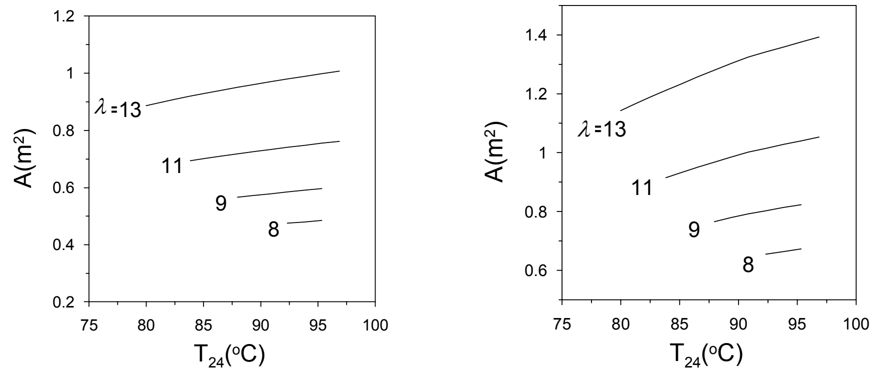

(a) LT-SHX (b) HT-SHX

Figure 3.11 Heat transfer area of solution heat exchangers

One component missing in the results shown above is the low-pressure evaporator. Since design parameters for this component were already fixed in Table 3.2, it was excluded in the simulation. The design parameters in Table 3.2 give ε_{LPE}= 0.73 and a rather arbitrary and conservative overall heat transfer coefficient of 0.5kW/m^{2}K has been assumed in the calculation of its heat transfer area due to the high uncertainty of exisiting correlations for the falling film flows in a very small flow rate range.

From the results above, it was concluded that a half-effect chiller with a driving temperature at around 90°C could be realized within a small physical dimension if some extended heat transfer surfaces could be used. Then for the physical design of the components of an experimental set-up, the cycle summarized in the following Table 3.3 has been chosen. The COP of this particular cycle is 0.38 with $\lambda \approx 12$ and $T_{24} \approx 84^oC$.

Table 3.3 Specification of target cycle

<table>
<tr><th rowspan="3"></th><th colspan="4">T (°C)</th><th colspan="4">x (LiBr%)</th><th colspan="2">p (kPa)</th><th colspan="4">$\dot{m}$ (kg/hr)</th><th rowspan="3">$\dot{Q}$ (kW)</th><th rowspan="3">A_{hex} (m^2)</th></tr>
<tr><th colspan="2">hot</th><th colspan="2">cold</th><th colspan="2">hot</th><th colspan="2">cold</th><th rowspan="2">hot</th><th rowspan="2">cold</th><th colspan="2">hot</th><th colspan="2">cold</th></tr>
<tr><th>in</th><th>out</th><th>in</th><th>out</th><th>in</th><th>out</th><th>in</th><th>out</th><th>in</th><th>out</th><th>in</th><th>out</th></tr>
<tr><td>CON</td><td>51</td><td>51</td><td>42.2</td><td>50.1</td><td>0</td><td>0</td><td>0</td><td>0</td><td>13</td><td></td><td>32.8</td><td>32.8</td><td>2407</td><td>2407</td><td>22.2</td><td>1.98</td></tr>
<tr><td>GEN</td><td>87.9</td><td>78.4</td><td>69.1</td><td>83.8</td><td>0</td><td>0</td><td>49.7</td><td>54.2</td><td></td><td>13</td><td>2407</td><td>2407</td><td>395.3</td><td>362.5</td><td>26.6</td><td>3.74</td></tr>
<tr><td>MPA</td><td>56.3</td><td>40.3</td><td>37</td><td>42.2</td><td>54.2</td><td>49.7</td><td>0</td><td>0</td><td>2.09</td><td></td><td>196.3</td><td>214.1</td><td>2407</td><td>2407</td><td>14.5</td><td>2.22</td></tr>
<tr><td>LPA/MPE</td><td>37.4</td><td>25.6</td><td>18.2</td><td>18.2</td><td>54.2</td><td>49.7</td><td>0</td><td>0</td><td>2.09</td><td>0.87</td><td>166.2</td><td>181.2</td><td>17.8</td><td>0</td><td>11.9</td><td>2.25</td></tr>
<tr><td>LPE</td><td>12.5</td><td>7</td><td>5</td><td>5</td><td>0</td><td>0</td><td>0</td><td>0</td><td></td><td>0.87</td><td>1562</td><td>1562</td><td>15</td><td>0</td><td>10.0</td><td>4.80</td></tr>
<tr><td>HT-SHX</td><td>83.8</td><td>56.3</td><td>44.5</td><td>69.1</td><td>54.2</td><td>54.2</td><td>49.7</td><td>49.7</td><td>13</td><td>13</td><td>362.5</td><td>362.5</td><td>395.3</td><td>395.3</td><td>6.6</td><td>1.05</td></tr>
<tr><td>LT-SHX</td><td>56.3</td><td>37.4</td><td>32.7</td><td>49.5</td><td>54.2</td><td>54.2</td><td>49.7</td><td>49.7</td><td>13</td><td>0.87</td><td>166.2</td><td>166.2</td><td>181.2</td><td>181.2</td><td>2.0</td><td>0.79</td></tr>
<tr><td>Ref-Hex</td><td>51</td><td>28.1</td><td>25.6</td><td>32.7</td><td>0</td><td>0</td><td>49.7</td><td>49.7</td><td>13</td><td>0.87</td><td>32.8</td><td>32.8</td><td>181.2</td><td>181.2</td><td>0.87</td><td>0.35</td></tr>
<tr><td rowspan="4">$COP_{chiller}$</td><td colspan="2" rowspan="4">0.38</td><td colspan="5">Collector type</td><td>I</td><td>II</td><td>III</td><td colspan="6">Remarks</td></tr>
<tr><td colspan="5">Collector efficiency, η_{col}</td><td>0.54</td><td>0.41</td><td>0.32</td><td colspan="6" rowspan="3">1. I_p=800W/m^2
2. T_{amb}=32°C
3. η_{col} based on gross dimension with no-wind condition.
4. Collector types from Table 3.1</td></tr>
<tr><td colspan="5">Collector area, A_{col} (m^2)</td><td>61.8</td><td>81.2</td><td>104</td></tr>
<tr><td colspan="5">System efficiency (COP×ηcol)</td><td>0.2</td><td>0.16</td><td>0.12</td></tr>
</table>

3.3 Design of components

In this section, physical designs are presented for the various components, which have been prepared according to the cycle in Table 3.3.

The specification of the cycle in Table 3.3 gives necessary information to define the UA values for each of the components. After the UA values have been calculated, the heat exchange areas were calculated using appropriate heat transfer correlations given in Appendix B. Since the heat exchanger type and location of a component have been already decided in Section 3.1 and illustrated in Fig. 3.5, component design was actually a coordination of the aspect ratios of the components.

Among the components, generator and condenser experienced some major changes from their original designs due to technical and financial limitations. In the following, design of each component is given in detail.

3.3.1 Generator

Fig. 3.12 shows two different designs for generator.

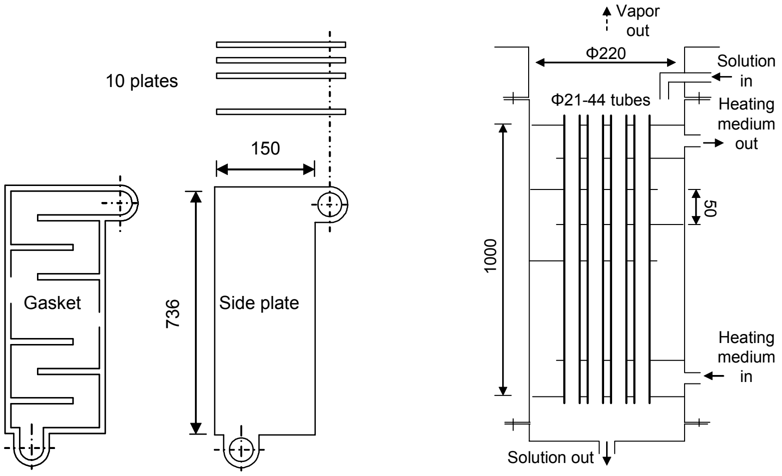

(a) Plate (b) Shell & tube

Figure 3.12 Generator designs

The generator has been originally designed in the plate type as shown in Fig. 3.12a, which consists of 10 identical vertical falling film plate heat exchangers. A single plate heat exchanger consisted of two side plates and a gasket. The gasket was designed to maintain a channel for the heating medium between the two side plates.

Total surface area of the plate design is 2.2m^2 when bare plates are used. Since the required heat transfer area is 3.74m^2 in Table 3.3, a heat transfer surface with an extended surface ratio (the ratio of extended surface to base area) of 1.7 was to be used in the original design.

As a trial, a plate heat exchanger was fabricated by brazing copper plates with nickel metal foams. But this experiment failed. The reasons were, firstly, the soldering material used for the brazing plugged the passages of the heating medium flow. Secondly, the brazing cost was prohibitively high.

Due to technical and financial limitations, the shell and tube type design in Fig. 3.12b has been chosen as the final design for the generator. It has 44 Φ21 mm stainless-steel heat transfer tubes with the total heat transfer area of 2.76m^2, which is slightly larger than that of bare plate design. But use of an extended heat transfer surface was impossible in the design. Consequently the final generator design has been given 74% of the heat transfer area in Table 3.3. As can be expected, this will result in either increase in generator temperature or reduction of cooling capacity as will be shown in Ch. 5 and 7.

3.3.2 Condenser

Since the design of the generator has been changed as discussed in the previous Section, the design of the condenser has also been changed accordingly.

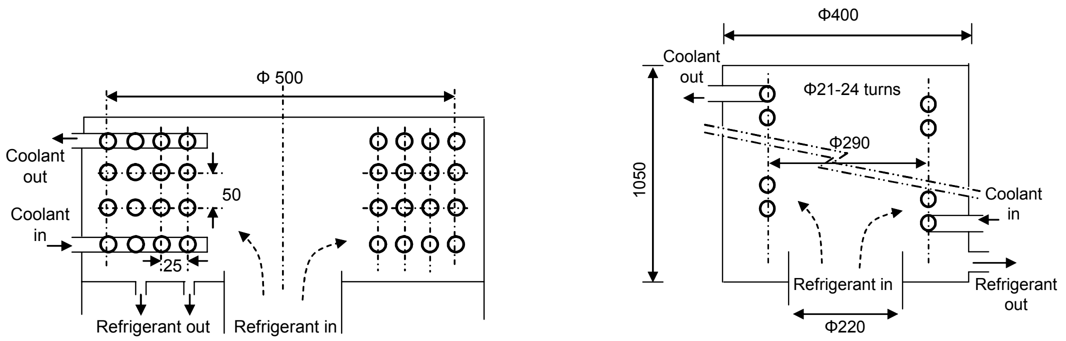

(a) Multi-path (b) Single-path

Figure 3.13 Condenser design

Fig. 3.13a shows the original design that has been made together with the plate type generator design in Fig. 3.12a. This design allowed a low height for a condenser so that the condenser could be located on the top of the chiller as shown in Fig. 3.5. For this purpose, the cooling water flow needed to be split into multiple numbers of tubes as illustrated in Fig. 3.13a.

The design in Fig. 3.13a has been abandoned because of the change in generator design. Instead, a simpler but larger condenser design in Fig. 3.13b has been chosen, which can be mounted on top of the shell and tube generator shown in Fig. 3.12b. It has a single tube coil made of a Φ21 mm stainless-steel tube having 1.5m^2 of heat transfer area, which is about 75% of the heat transfer area requirement presented in Table 3.3. Like the generator design, this reduced heat transfer area negatively influences the system performance as will be analyzed in Ch. 5 and 7.

3.3.3 Low-Pressure Absorber/Mid-Pressure Evaporator (LPA/MPE)

The final design of LPA/MPE is shown in Fig. 3.14. It is basically a large vertical copper tube with a liquid distributor on both sides. The tube was made by rolling a 3mm-thick copper plate into a 400mm diameter tube.

Inside the tube, a refrigerant distributor is located at the top designed to distribute refrigerant evenly along the perimeter. On the other side, a similar distributor is used to distribute the poor solution.

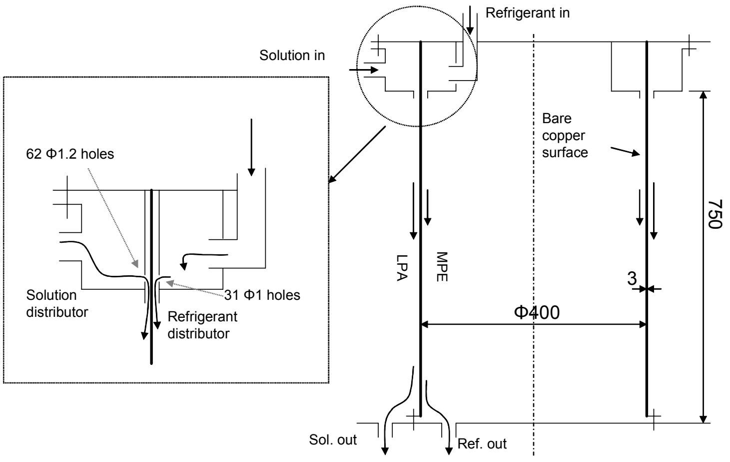

Figure 3.14 LPA/MPE design

According to Table 3.3, this component should have been designed to have $2.2 m^2$ of heat transfer surface. But the final design has only $0.94 m^2$, which is only 42% of it. The tube had to be made by rolling a plain copper plate while an enhanced heat transfer plate was originally planned to be used. Although several ideas of attaching some sorts of enhanced surfaces to the rolled tube afterwards, none was practically realizable within the given time and budget. Therefore it has been decided to use a plain copper tube as is illustrated in Fig. 3.14.

The reduction of heat transfer area by as much as 58% for this component is expected to have a serious effect on the system performance. As shown in Fig. 3.10a, the influence of this reduction on the generator temperature or system capacity will be much larger than those of generator and condenser. A quantitative analysis will be given in Ch. 5 and 7.

3.3.4 Mid-Pressure Absorber (MPA)

The mid-pressure absorber is a single tube coil having a solution distributor at the top and a receiver at the bottom as shown in Fig. 3.15. The whole assembly is located in the space inside the LPA/MPE in Fig. 3.14.

When the coil in Fig. 3.15 is made of a Φ21 mm plain stainless-steel tube, the total heat transfer area is $1.2 m^2$ which is about 54% of the heat transfer area required according to Table 3.3. Therefore the tube should have had an extended surface ratio of about 1.85. It was practically impossible to purchase such enhanced heat transfer tubes in a small quantity. For this reason, the idea of using enhanced heat transfer tubes was abandoned. As a result, the final heat transfer area is only 54% of the value required as listed in Table 3.3. A quantitative analysis of the influence of this reduction will be given in Ch. 5 and 7.

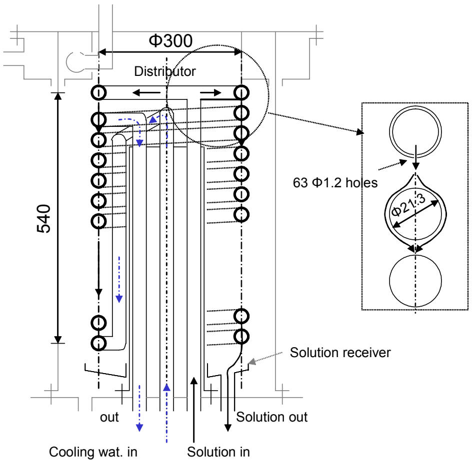

Figure 3.15 MPA design

A solution distributor is positioned at the top of the coil. It is a tube ring having 63 evenly spaced Φ1.2 mm holes at its bottom.

Below the coil is a solution receiver, which is a doughnut-shaped tray designed to collect the rich solution falling from above.

3.3.5 *Low-Pressure Evaporator*

The construction of the low-pressure evaporator is similar to the construction of the MPA. It is a single tube coil with a refrigerant distributor and receiver at its top and bottom respectively. Fig. 3.15 shows the final design of LPE.

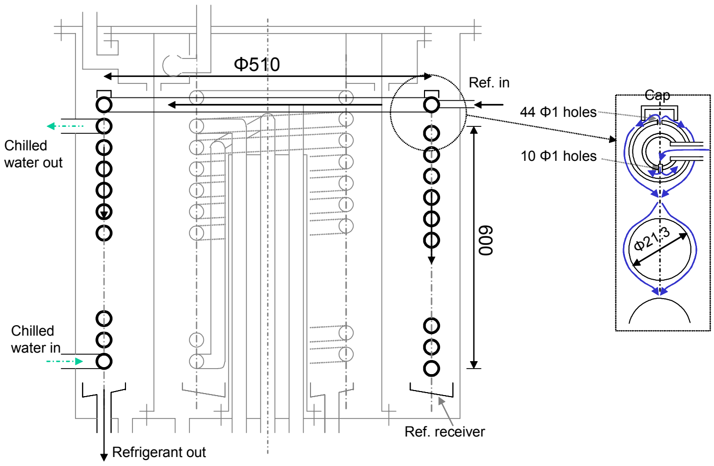

Figure 3.16 LPE design

Because no enhanced heat transfer tube was available, the coil was made of a Φ21 mm plain stainless-steel tube. The heat transfer area is 2.25m^2, which is about 47% of the required area listed in Table 3.3.

3.3.6 *Single-phase heat exchangers*

For the three single-phase heat exchangers in the chiller, the following plate heat exchangers were selected from a standard product range:

		Model	Heat transfer area
HT-SHX	:	CETEPAC 611-50	1.4m^2
LT-SHX	:	CETEPAC 617-30	1.2m^2
Ref-Hex	:	CETEPAC 400-40	0.5m^2

All of the heat exchangers above have larger heat transfer area than specified in Table 3.3. This is due to the differences between the manufacturer's heat transfer coefficients and those used in the calculation of Fig. 3.11.

3.4 Summary

Several conceptual designs have been developed for the choices of the final chiller set-up configuration. For the best system performance, falling film heat exchangers were chosen for all two-phase components and direct heat-coupling between LPA and MPE has been applied.

Components have been thermodynamically modeled and simulated in a cycle. The influence of the size of each component on the performance and cost of the chiller has been investigated. Based on the simulation results, a set of operating conditions have been chosen for design of the components.

All components have been physically designed according to the selected cycle. Due to the unavailability of enhanced heat transfer surfaces, most components were designed with less heat transfer area than required. The influence of the reduced area will be analyzed in Ch. 5 and 7.

Nomenclature

A	area, m^2
C_p	constant-pressure heat capacity, kJ/kgK
h	enthalpy, kJ/kg
h^{fg}	latent heat, kJ/kgK
I_p	incident solar intensity, kW/m^2
$\dot{m}$	mass flow rate, kg/s
p	pressure, kPa
$\dot{Q}$	heat transfer rate, kW
T	temperature, K
U	overall heat transfer coefficient, kW/m^{2}K
x	mass fraction of absorbent in liquid

Greek symbols

λ	circulation ratio, kg solution/kg refrigerant
ε	effectiveness
η	efficiency

Super- and subscripts

*	saturated condition
col	solar collector
dew	dew point
hex	heat exchanger
liq, l	liquid
ref	refrigerant
vap, v	vapour

Abbreviations

CAT	closest approach temperature
CON	condenser
COP	coefficient of performance
GEN	generator
LPA	low-pressure absorber
LPE	low-pressure evaporator
MPA	mid-pressure absorber
MPE	mid-pressure evaporator
NTU	number of transfer unit

References

Collector Catalogue 2004, 2004, Institut für Solartechnik SPF, Rapperswil, Switzerland

Hartley, D.E., Murgatroyd, W., 1964, Criteria for the break-up of thin film layers flowing isothermally over solid surfaces, Int. J. Heat Mass Transfer, Vol. 7, pp. 1003-1015

Holman, J.P., 1997, Heat transfer, McGraw-Hill, 8th ed.

Kim, D.S., Infante Ferreira, C.A., 2003, 1st progress report, Solar Absorption Cooling, Report K-332, Laboratory for Refrigeration and Indoor Climate Technology, TU Delft

Kim, D.S., Infante Ferreira, C.A., 2004, 2nd progress report, Solar Absorption Cooling, Report K-334, Engineering Thermodynamics, TU Delft

Kim, D.S., Infante Ferreira, C.A., 2005, Final report, Solar Absorption Cooling, Report K-SOLAR, Engineering Thermodynamics, TU Delft

Schmidt E., Properties of Water and steam in SI-Units. Berlin: Springer-Verlag 1979.

4 Thermodynamics of LiBr aqueous solutions[3]

This chapter presents new correlations for the thermodynamic properties of LiBr-H_2O solutions in wide concentration and temperature ranges.

4.1 Introduction

Aqueous LiBr solution is a mixture of water and lithium bromide, the brine that has been most popular in absorption refrigeration industry thanks to its outstanding thermodynamic characteristics ever since its first introduction to the industry by Carrier in mid 20th century.

Among the two ingredients, water plays two roles. First of all, water is the refrigerant that releases and absorbs heat at different pressure levels producing cooling effect. Secondly, it is the solvent. Pure lithium bromide exists as a white crystal with a very strong affinity to water. The crystal lacks fluidity and has very poor heat and mass transfer characteristics. Water provides the needed fluidity and thus facilitates transportation of the substance.

LiBr is an extremely hygroscopic white crystalline solid, which is normally synthesized from the reaction of the hydroxide and hydrobromic acids, a metallic salt with melting point 552 ^oC and boiling point 1265 ^oC. It is highly soluble in water and dissociates into Li^+ and Br^- ions when dissolved.

Matching its popularity in the industry, many studies have been carried out on the thermodynamic properties of the solution and the properties in the working domain of the conventional machines are well established. But, as more attention is given to the unconventional cycles for better use of energy [e.g. high-temperature triple effect cycles of Grossman et al (1994) and Kaita (2002), a refrigeration cycle of Kojima et al (2003) and low temperature-driven solar cycles of Kim and Machielsen (2002a,b)], need of an accurate thermodynamic study covering wide ranges of conditions has been growing. This chapter presents the results of a study that has been started from this motivation.

In the following a summary is given of literature regarding the thermodynamic studies on the solution.

Among the early thermodynamic studies, the most prominent may be Löwer (1960). It was the first complete study that presented practically all thermophysical properties of the solution. Using a Gibbs energy equation, he successfully described the thermodynamic properties of the solution based on his own experimental data. But the maximum solution temperature of 130 ^oC limits the applicable range of this study, which is rather low for the present applications.

The most famous work is, however, probably McNeely (1979). He developed a Dühring equation from the extensive collection of equilibrium vapour pressures and calculated the solution enthalpies for wide ranges of temperature and concentration using Haltenburger (1939)'s method. It has been very popular in the industry because it is easy to use and also

---

[3] Content in thic chapter has been previously published in "Kim, D.S., Infante Ferreira, C.A., 2006, A Gibbs Energy Equation for LiBr aqueous solutions, Int. J. Refrigeration, Vol. 29, pp. 36-46"

quite accurate in the working ranges of conventional absorption machines. But in the high concentration region, his dew temperatures are inconsistent with more recent measurements and his enthalpy shows a questionable trend in differential heat of dilution as the author himself mentioned.

In 1987, Herold and Moran (1987) have reproduced McNeely (1979)'s data using a Gibbs energy equation with a modified Debye-Hückel model (Pitzer, 1973). Based on a statistical method, they determined coefficients of the Gibbs energy equation using a limited amount of data known at the time.

In 1994, Feuerecker et al (1994) carried out a study based on their own pressure measurements for the solutions in the concentration range from 40 to 76 LiBr wt% and temperatures from 45 to 190 ^{o}C. They reported good agreement of equilibrium vapour pressure with McNeely (1979) for the solutions of concentration below 60 wt.%, but significant deviations above this concentration. Although this study seems quite reliable in the high temperature region, it may not be so in the low temperature region where the differential heat of dilution calculated from their Dühring equation deviates substantially from the measurement of Lange and Schwartz (1928).

In 2000, Chua et al (2000) developed a set of equations for the solutions in the concentration range from 0 to 75 wt.% and the temperature range from 0 to 190 ^{o}C. For equilibrium criteria, they collected 11 sets of equilibrium pressure data but finally chose only two data sets to develop a Dühring equation. They assumed Dühring's rule is valid in the entire range and deliberately curve-fitted the Dühring gradients and intercepts of McNeely (1979) and Feuerecker et al (1994) with high-degree polynomial equations. Although those two studies may be reliable sources for the working ranges they were chosen for, it is risky to neglect all the other experimental data measured in the other regions. Besides, the Dühring's rule may not be satisfactory in some regions as McNeely (1979) and Haltenburger (1939) mentioned potential errors due to the constant Dühring gradient in the high concentration region. The use of the extreme high-degree polynomial functions also raises a question on their choice of fitting parameter.

One year later in 2001, Kaita (2001) suggested a new set of equations for the high temperature and pressure ranges of triple-effect machines by supplementing the vapour pressure data of Feuerecker et al (1994) with that of Lenard et al (1992) for the high temperature range and McNeely (1979) for the low temperature range. His results are valid in the concentration range from 40 to 65 wt% and the temperature range from 20 ^{o}C to 210 ^{o}C. He developed a 2nd-degree dew temperature equation to cover the wide pressure range but did not use it in his enthalpy calculation. Consequently, his dew temperature equation is inconsistent with his enthalpy.

As described above, all the preceding studies were either limited to narrow working ranges or failed to provide a simple and accurate description for the solutions in wide working ranges.

The study presented in this chapter is intended to develop a Gibbs energy description for the solutions in wide ranges of temperature and concentration because, until the present moment, there is no study that accurately and consistently describes the thermodynamic properties of the solutions in wide working ranges on a sound thermodynamic basis.

The Gibbs energy concept is a very useful tool in describing thermodynamic characteristics of mixtures and solutions. The concept has been successfully applied to some working pairs in the absorption field. It provides a thermodynamically sound basis for the design and analysis of absorption systems in simple but very effective ways.

Besides Löwer (1960) and Herold and Moran (1987) on LiBr-H_2O, Schulz (1973) and Ziegler and Trepp (1984) also reported successful applications of the concept to the NH_3-H_2O pair. Schulz (1973) applied the concept to ammonia-water mixture and provided correlations valid up to 25 bar. Ziegler and Trepp (1984) modified it and extended the range of the equations to 500K and 50bar for heat pump applications.

As summarized above, all the preceding studies were either limited to narrow working ranges or failed to provide a simple and accurate description for the solutions in wide working ranges. Considering the observed need of a new description for the solutions over wide working ranges, it has been decided to develop a Gibbs energy equation that could accurately describe the properties of the solutions in wide working ranges using the latest experimental data.

4.2 Gibbs energy of LiBr-H2O solutions

The purpose of the study reported in this Chapter was to derive a Gibbs energy expression from which all the secondary properties can be derived. In the following, a Gibbs energy equation is derived based on the thermodynamic theories of electrolytes, which are well described in literature including Ruiter (1986) and Smith et al (2001).

Thermodynamic description of an electrolyte solution requires a hypothetical reference fluid called ‘infinitely dilute solution’ because the pure solute is a solid substance in the standard state. In an electrolyte system, concentration of a solute is often expressed in molality m, which is customarily defined as ‘the number of mol solute per kg solvent’. But it is redefined here as ‘the number of kmol solute per kg solvent’ for convenience and its relations with other concentrations are given in Eq. (4.1). In the following, the subscripts 1 and 2 denote LiBr and water respectively and complete dissociation of the solute is assumed (υ=2).

$$m = \frac{x_1}{(1-x_1)M_2} = \frac{x_{1w}}{(1-x_{1w})M_1} \tag{4.1}$$

x_1 and x_{1w} are the stoichiometric mole fraction and the weight fraction of LiBr respectively. Based on the thermodynamic theory of electrolyte solutions, the molar Gibbs energy of an electrolyte solution can be expressed as follows [see e.g. Ruiter (1986)].

$$G^l = x_1 G^{\infty}_{1\,(T,p)} + (1-x_1)G^l_{2(T,p)} + x_1 \upsilon RT\left[\ln\left(\frac{m}{m_\circ}\right) - 1\right] + G^E{}_{(T,p,x_1)} \tag{4.2}$$

In Eq. (4.2), the 1st term on the right side is the contribution of the infinitely dilute solution and the 2nd term is that of pure water. The 3rd term is the Gibbs energy generation in an ideal mixing process, where m_o is the standard molality (m_o = 0.001 kmol per kg solvent). The last term is the excess Gibbs energy by which a real solution differs from ideal one, which is separately given by

$$G^E = x_1 \upsilon RT\left[\ln\gamma^{\pm} + (1-\phi)\right] \tag{4.3}$$

where ϕ and $\gamma^{\pm}$ are called osmotic- and mean ionic activity coefficient respectively. Since only steam exists in the vapour phase, the osmotic coefficient ϕ can be written as Eq. (4.4) in relation to the states of pure water.

$$\phi = \frac{1}{RT\upsilon mM_2}\int_p^{p^*}(V_2^g - V_2^l)dp \tag{4.4}$$

Through Eq. (4.4), ϕ dictates the equilibrium criteria of the system. From the definition of 'partial property', the Gibbs-Duhem relation, Eq. (4.5) exists between ϕ and $\gamma^{\pm}$.

$$\ln\gamma^{\pm} = \phi - 1 + \int_0^m \frac{(\phi-1)}{m}dm \tag{4.5}$$

Therefore, once ϕ is determined as a function of concentration from Eq. (4.4), $\gamma^{\pm}$ follows from Eq. (4.5). Then the excess Gibbs energy G^E in Eq. (4.3) can be fully described.

Differentiations of Eq. (4.2) give the rest of the solution properties as follows. They also apply to the corresponding excess properties.

$$H = -RT^2\left[\frac{\partial(G/RT)}{\partial T}\right]_{p,x} \tag{4.6}$$

$$S = -\left(\frac{\partial G}{\partial T}\right)_{p,x} \tag{4.7}$$

$$V = \left(\frac{\partial G}{\partial p}\right)_{T,x} \tag{4.8}$$

$$C_p = -T\left(\frac{\partial^2 G}{\partial T^2}\right)_{p,x} \tag{4.9}$$

4.2.1 Determination of osmotic coefficient

The osmotic coefficient ϕ is a function of pressure, temperature and concentration. Regarding its pressure dependence, it may be assumed that ϕ can be expressed as

$$\phi = \phi'(T,m) + \phi''(T,p,m) \tag{4.10}$$

Below is shown how ϕ'' and ϕ' can be determined from the relevant experimental data.

4.2.1.1 Dependence on solution density

ϕ'' in Eq. (4.10) can be determined from experimental solution density. Inserting Eq. (4.2) into Eq. (4.8) gives a pressure derivative of the molar Gibbs energy of the solution, which is actually the molar volume of the solution, as follows.

$$V^l = x_1 V_1^\infty + (1 - x_1) V_2^{*l} + V^E \tag{4.11}$$

where V_1^∞ and V_2^{*l} are the molar volume of the infinitely dilute solution and that of pure water respectively. The last term V^E is the excess volume, which is the pressure derivative of G^E in Eq. (4.3).

Inserting Eq. (4.5) into Eq. (4.3) gives G^E expressed in terms of osmotic coefficient only as follows.

$$G^E = x_1 \upsilon RT \int_0^m \frac{(\phi - 1)}{m} dm \tag{4.12}$$

Differentiating Eq. (4.12) according to Eq. (4.8) gives

$$V^E = x_1 \upsilon RT \int_0^m \frac{1}{m} \left(\frac{\partial \phi}{\partial p} \right)_{T,x} dm \tag{4.13}$$

which makes the relationship between the excess volume and the pressure gradient of osmotic coefficient clear. So, once V^E is given as a function, $\partial\phi/\partial p$ can also be expressed as a function from Eq. (4.13).

Using the solution density data from International Critical Table (1928, hereafter ICT), Löwer (1960) and Lee et al (1990) for V^l and the pure water data from Schmidt (1979) for V_2^{*l} in Eq. (4.11), V_1^∞ and V^E have been correlated by

$$x_1 V_1^\infty + V^E = x_1 RT \sum_{i=0}^{2} b_i m^{i/2} \quad \text{where } b_i = \sum_{j=0}^{2} b_{ij} T^{-j} \tag{4.14}$$

The coefficients b_{ij} are given in Table A1.1 of Appendix A. Among the several fitting parameters considered, $m^{1/2}$ turned out to be the best, which is also suggested by the theory of Debye-Hückel (1923).

Since V_1^∞ is not a function of concentration, it is clear that $V_1^\infty = RTb_0$ from Eq. (4.14). And then V^E is given by

$$V^E = x_1 RT \sum_{i=1}^{2} b_i m^{i/2} \tag{4.15}$$

Equating Eq. (4.13) with (4.15) and differentiating it against m gives ϕ'' as

$$\phi'' = \frac{p}{2\upsilon} \sum_{i=1}^{2} i \cdot b_i m^{i/2} \tag{4.16}$$

Using a polynomial function developed for the volume of saturated water V_2^{*l} from Schmidt (1979), Eq. (4.11) can be rewritten as

$$V^l = x_1 RT\sum_{i=0}^{2} b_i m^{i/2} + (1-x_1)R\sum_{j=0}^{2} e_j T^j \qquad (4.17)$$

where the coefficients e_j are given in Table A1.1 of Appendix A.

Eq. (4.17) reproduces the solution density of ICT (1928), Löwer (1960) and Lee et al (1990) within the standard deviation of 0.13 %, 0.34 % and 0.38 % respectively (see Fig. 4.1 and 4.2). The overall standard deviation is 0.29%.

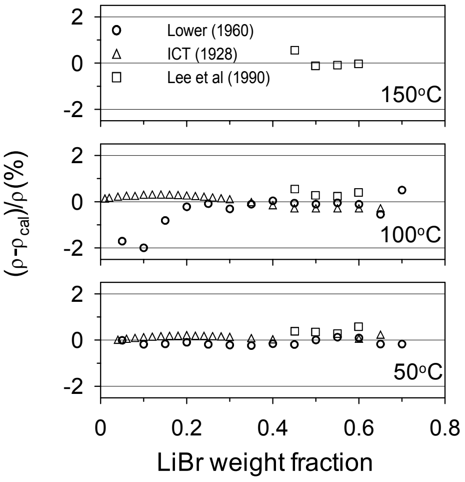

Figure 4.1 Illustration of errors in calculated solution density

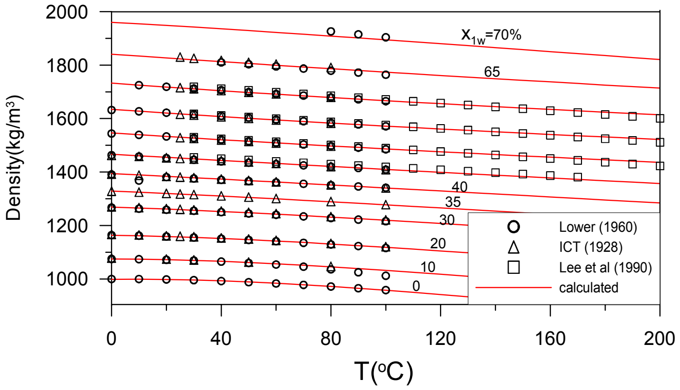

Figure 4.2 Calculated and experimental solution density

4.2.1.2 Dependence on equilibrium vapour pressure

ϕ' in Eq. (4.10) can be determined from equilibrium vapour pressure. Inserting Eq. (4.4) and (4.16) into (4.10) and rearranging it for ϕ' gives

$$\phi' = \frac{1}{RT\upsilon m M_2}\int_{p}^{p^{*s}} (V_2^{*g} - V_2^{*l})dp - \frac{p}{2\upsilon}\sum_{i=1}^{2} i \cdot b_i m^{i/2} \qquad (4.18)$$

For ease of calculation, the following equation has been developed using the steam data from Schmidt (1979).

$$V_2^{*g} - V_2^{*l} = \frac{RT}{p}\tanh\left[\alpha - \beta\ \ln(p)\right] \quad \text{where } \alpha = \sum_{j=0}^{2}\alpha_j T^{-j}\ ,\ \beta = \sum_{j=0}^{2}\beta_j T^{-j} \qquad (4.19)$$

The coefficients α_j and β_j are given in Table A1.1 of Appendix A.

Since V_2^{*l} is negligibly small, the term 'tanh[α-βln(p)]' in Eq. (4.19) can be considered as the compressibility factor with the maximum error of 0.11% in steam volume up to 1,200 kPa and 270 ^{o}C.

Using Eq. (4.19), after integration, Eq. (4.18) can be rewritten as

$$\phi' = \frac{1}{\upsilon m M_2 \beta}\ln\left\{\frac{\cosh\left[\alpha - \beta\ln\left(p\right)\right]}{\cosh\left[\alpha - \beta\ln\left(p^*\right)\right]}\right\} - \frac{p}{2\upsilon}\sum_{i=1}^{2} i\cdot b_i m^{i/2} \qquad (4.20)$$

In order to calculate ϕ' from Eq. (4.20), the saturated steam pressure data from Schmidt (1979) and Perry et al (1984) were used for p^* and 6 sets of equilibrium vapour pressures were collected from the literature for p. ϕ' in Eq. (4.20) has been calculated for each of the vapour pressures and the results were fitted by

$$\phi' = 1 + \sum_{i=1}^{6} a_i m^{i/2} \qquad \text{where } a_i = \sum_{j=0}^{2} a_{ij} T^{-j} \qquad (4.21)$$

The coefficients a_{ij} are given in Table A1.1 of Appendix A and some fitting curves are shown in Fig. 4.3.

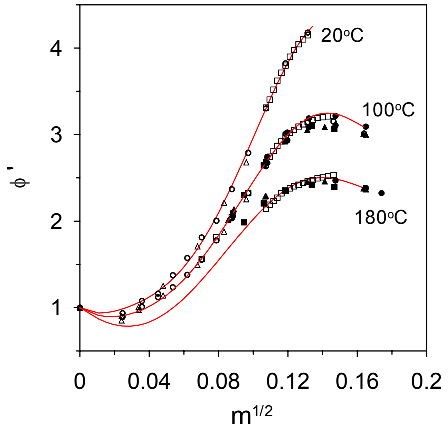

Figure 4.3 Calculated ϕ' and the fitting curves [○: Löwer (1960), △: ICT (1928), □: McNeely (1979), ●: Feuerecker et al (1994), ▲: Iyoki and Uemura (1989), ■: Lenard et al (1992)]

Inserting Eq. (4.16) and (4.21) into Eq. (4.10) completes the expression for ϕ as

$$\phi = 1 + \sum_{i=1}^{6} (a_i + \frac{ib_i}{2\upsilon} p) m^{i/2} \tag{4.22}$$

Inserting Eq. (4.22) into Eq. (4.5) and (4.3) gives the expressions for ln$\gamma^{\pm}$ and G^E respectively as

$$\ln \gamma^{\pm} = \sum_{i=1}^{6} (1 + \frac{2}{i})(a_i + \frac{ib_i}{2\upsilon} p) m^{i/2} \tag{4.23}$$

$$G^E = x_1 \upsilon RT \sum_{i=1}^{6} \left[\frac{2}{i} (a_i + \frac{ib_i p}{2\upsilon}) \right] m^{i/2} \tag{4.24}$$

Experimental values of ϕ and ln$\gamma^{\pm}$ for the solutions at 25 °C from Hamer and Wu (1972) and Robinson and McCoach (1947) are shown with the calculated values from Eq. (4.22) and (4.23) in Fig. 4.4.

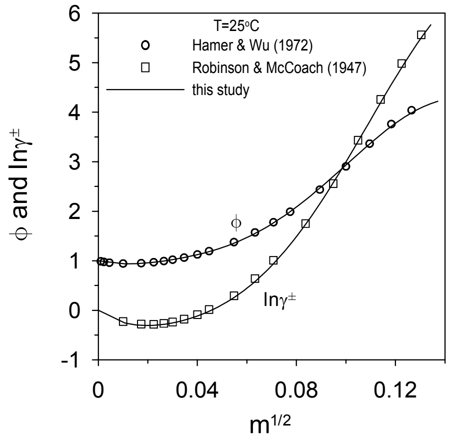

Figure 4.4 Calculated and experimental ϕ and ln$\gamma^{\pm}$ at 25 °C

The equilibrium pressure p can be calculated from ϕ by

$$p = \exp\left\{ \frac{1}{\beta} \left[\alpha - \ln(\theta + \sqrt{\theta^2 - 1}) \right] \right\} \tag{4.25}$$

where $\theta = \cosh[\alpha - \beta \ln(p^*)] \exp(\phi \upsilon m M_2 \beta)$ and the coefficients α and β are the same as given in Eq. (4.19).

Strictly speaking, calculation of p from Eq. (4.25) needs iteration because ϕ includes p as in Eq. (4.22). But, since the pressure dependence of ϕ is negligibly small, the pressure term in Eq. (4.22) can be safely neglected so that the iteration is not necessary for calculation of p from Eq. (4.25). The equilibrium pressures calculated in this way have been compared with the original vapour pressures. The results are illustrated in Fig. 4.5 and the deviations are summarized in Table 4.1.

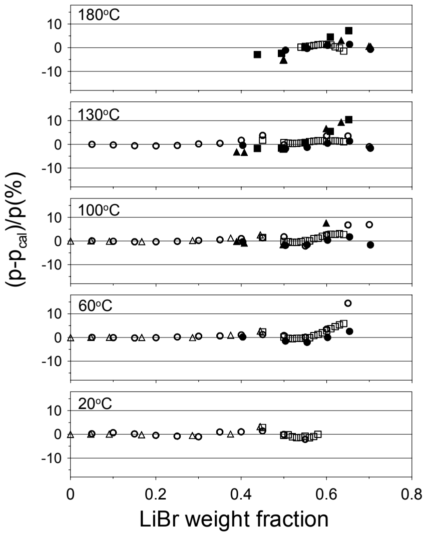

Figure 4.5 Comparison of vapour pressure [○: Löwer (1960), △: ICT (1928), □: McNeely (1979), ●: Feuerecker et al (1994), ▲: Iyoki and Uemura (1989), ■: Lenard et al (1992)]

Table 4.1 Equilibrium pressure data sources and the fitting results

Data source	LiBr wt%	T (^{o}C)	No. of data used	Standard deviation	
				p^*(%)	T^{dew}(K)
Löwer (1960)	0~70	0~130	185	3.2	0.56
ICT (1928)	0~45	0~100	36	1.2	0.22
McNeely (1979)	45~64	0~180	140	1.8	0.29
Feuerecker et al (1994)	40.4~70.3	45~190	80	1.4	0.31
Iyoki and Uemura (1989)	38.9~70.3	101~180	40	4.9	1.36
Lenard et al (1992)	43.8~65.2	125~211	24	3.5	1.17
Total	0~70.3	0~211	487	2.9	0.63

It should be noted that some of the data from the data sources were not used. The vapour pressures from ICT (1928) were found exceptionally higher than the others for the solutions above 45 wt%. They were disregarded because they are probably in error as McNeely (1979) and Koehler et al (1987) have suggested. McNeely (1979) reported that his vapour pressures might be in error above 64 wt% referring to the abnormal trends in differential heat of dilution in this region and therefore they were disregarded. Also his data below 45 wt% were also disregarded because it turned out that they are different from ICT (1928) only by the fitting errors McNeely (1979) introduced in fixing his dew temperature lines in this region.

For the concentrations below 40 wt.%, the deviations from Löwer (1960) and ICT (1928) are negligibly small as can be seen in Fig. 4.5. However, above this concentration, Löwer (1960)'s pressures are substantially higher than those obtained from Eq. (4.25). The standard deviation of 3.3 % is mainly attributed to the discrepancy between sources in this region.

Agreement with McNeely (1979) is good for the concentrations between 45 and 60 wt.%. Above 60 wt.%, the deviation becomes larger especially near crystallization limits. Standard deviation is 1.8% in pressure and 0.29 K in boiling temperature.
Standard deviation from Feuerecker et al (1994) is 1.4 % in pressure and 0.31 K in boiling temperature, the best consistency among the original data sets used in this study.

The high-pressure data of Lenard et al (1992) agree well with the calculated values from Eq. (4.25) and also with Feuerecker et al (1994)'s data up to 55 wt.%. The deviation in this region is 1.8 %. The difference becomes large above 60 wt.%, to which the overall standard deviation of 3.5% is mainly attributed.

Consistency with Iyoki and Uemura (1989) is the worst, resulting in the standard deviation of 4.9 %. This large deviation is partly due to the fact that the consistency within the data set is not much better. They reported a mean deviation of 2.33 % (3.3 % standard deviation) from the equation of Uemura and Hasaba (1964).

4.2.2 Enthalpy of solution

From Eq. (4.2) and (4.6), the molar enthalpy of solution is given by

$$H^l = x_1 H^{\infty}_{1(T,p)} + (1-x_1) H^{*l}_{2(T,p)} + H^E_{(T,p,m)} \tag{4.26}$$

Using the data for pure water from Schmidt (1979), molar enthalpy of pure water H_2^{*l} can be calculated by

$$H_2^{*l} = H_{2\circ}^{*l} + \int_{T_\circ}^{T} C_{p2}^{*l} dT + \int_{p_\circ}^{p} \left[V_2^{*l} - T\left(\frac{\partial V_2^{*l}}{\partial T}\right)_p \right] dp \tag{4.27}$$

, where $C_{p2}^{*l} = R\sum_{j=0}^{2} d_j T^j$ and $V_2^{*l} = R\sum_{j=0}^{2} e_j T^j$. The coefficients d_j and e_j are listed in Table A1.1 of Appendix A.

Differentiation of Eq. (4.12) gives the excess enthalpy H^E as follows.

$$H^E = -RT^2 \frac{\partial}{\partial T}\left(\frac{G^E}{RT}\right)_{p,x} = -x_1 \upsilon RT^2 \sum_{i=1}^{6} \frac{2}{i}\left(\frac{\partial a_i}{\partial T} + \frac{i}{2\upsilon}\frac{\partial b_i}{\partial T} p\right) m^{i/2} \tag{4.28}$$

The enthalpy of infinitely dilute solution H_1^{∞} can be determined using either experimental heat of solution or heat capacity of the solution. Since experimental heat of solution is only available for a few temperatures, the heat capacity data of a reference solution were used to determine H_1^{∞}.

For the reference solution of concentration $x_{1\text{o}}$, Eq. (4.26) can be rearranged for H_1^{∞} as

$$H_1^{\infty} = \frac{H_\circ^l - (1 - x_{1\circ}) H_2^{*l} - H_\circ^E}{x_{1\circ}} \tag{4.29}$$

where the subscript 'o' denotes the reference state.

Since H_2^{*l} and H^E are given in Eq. (4.27) and (4.28), H_1^{∞} can be determined from Eq. (4.29) if the enthalpy of the reference solution H_o^l is given. For this purpose, as recommended by Jeter et al (1992), 60 wt% solution was chosen as the reference solution. Most experimental heat capacity sources agree with each other at this concentration. The solution heat capacities from Löwer (1960), Feuerecker et al (1994), Jeter et al (1992) and Rockenfeller (1987) were fitted with a polynomial equation as illustrated in Fig. 4.6 to allow for the calculation of H_o^l.

The resulting H_1^∞ can be expressed by

$$H_1^\infty = H_{1\circ}^\infty + \int_{T_\circ}^{T} C_{p1}^\infty dT + \left[V_1^\infty - T\left(\frac{\partial V_1^\infty}{\partial T}\right)_p \right](p - p_\circ^*) \qquad (4.30)$$

where heat capacity Cp_1^∞ is defined by

$$C_{p1}^\infty = RT^{-2}\sum_{j=0}^{2} c_j T^{-j} \qquad (4.31)$$

with c_j given in Table A1.1 of Appendix A.

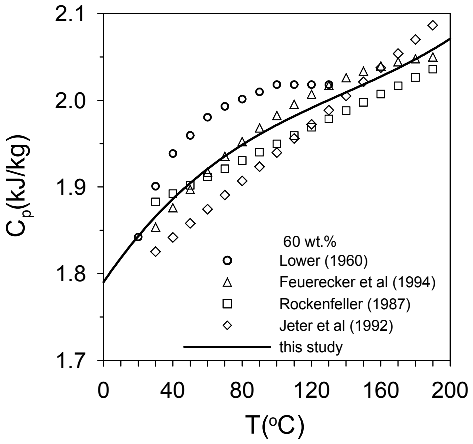

Figure 4.6 Heat capacity of 60 wt% solution

Using Eq. (4.27), (4.28) and (4.30), the enthalpy has been calculated from Eq. (4.26). The zero enthalpies were chosen for pure water and 50 wt% solution at 0 °C. Fig. 4.7 shows some of the results in comparison with literature values. The enthalpy of this study is relatively in good agreement with Feuerecker et al (1994) and Kaita (2001). The discrepancy between this study and Feuerecker et al (1994) is believed to have come from the disagreement in equilibrium vapour pressure that also caused the disagreement in the differential heat of dilution in Fig. 4.8. Seeing that the differential heat of dilution calculated from their Dühring equation deviates substantially from the experimental data of Lange and Schwartz (1928), it is questionable whether their Dühring equation can be safely extrapolated to the low temperature region.

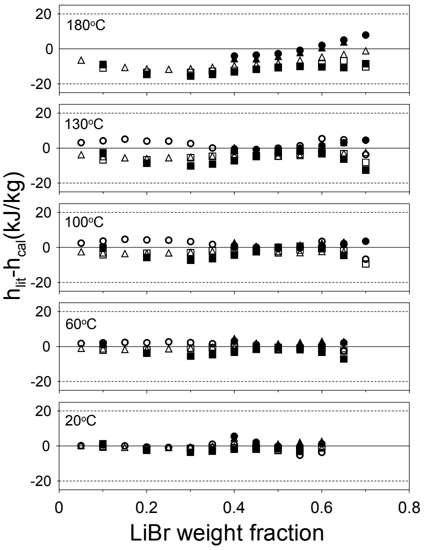

Figure 4.7 Comparison of calculated enthalpy with literature values [○: Löwer (1960), △: Chua et al (2000), □: McNeely (1979), ●: Feuerecker et al (1994), ■: Herold and Moran (1987), ▲: Kaita (2001)]

On the other hand, the deviation from Kaita (2001) has nothing to do with equilibrium vapour pressure because he did not use his equilibrium equation in enthalpy calculation. Instead, he used differential heat of dilution data from several sources and the heat capacity data from Rockenfeller (1987). The difference between the heat capacity of Rockenfeller (1987) and that of this study can be seen in Fig. 4.9. Compared to the heat capacity of this study, the average heat capacity of Rockenfeller (1987) is smaller below 60 wt% but slightly larger above this concentration, which probably caused a similar trend in enthalpy difference between this study and Kaita (2001).

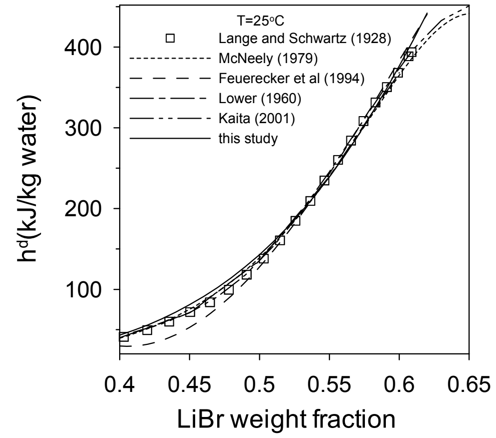

Figure 4.8 Comparison of differential heat of dilution

The enthalpy values of McNeely (1979), Herold and Moran (1987) and Chua et al (2000) show similar trends against this study for the solutions below 60 wt% as shown in Fig. 4.7. This similarity originates from that fact that all these studies were based on the dew temperatures of McNeely (1979). Chua et al (2000) deviates from the rest of the group above 60 wt% because they used the vapour pressure of Feuerecker et al (1994) in that region. In the high concentration region, McNeely (1979)'s enthalpy is smaller than the others because his dew temperature gradient is much smaller in this region. The second reason is that McNeely (1979) calculated his reference solution enthalpy using Löwer (1960)'s heat capacity for 50 wt% solution, which is constant in the high temperature region. This is contradictory to the measurements of Jeter et al (1992) and Rockenfeller (1987), which show appreciable temperature dependences throughout the whole temperature range. Consequently, the temperature gradient of McNeely (1979)'s heat capacity curve in the high temperature region is zero at around 50 wt% and becomes even negative as the concentration increases as shown in Fig. 4.9.

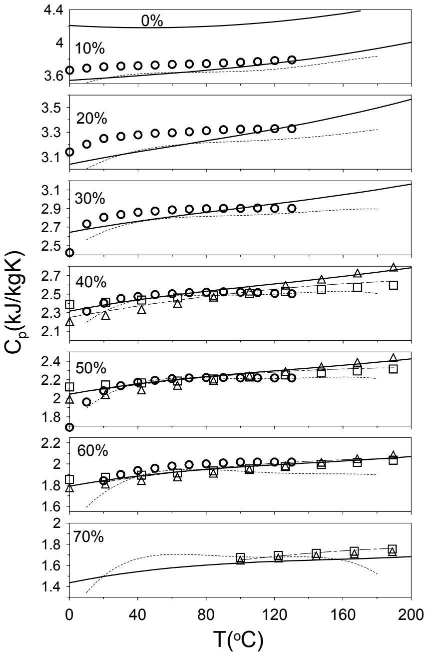

Figure 4.9. Comparison of calculated heat capacity with literature values [○: Löwer (1960), △: Jeter et al (1992), □: Rockenfeller (1987), ----: McNeely (1979), −−−: Feuerecker et al (1994), —: this study:]

Speaking of the enthalpy deviations quantitatively, this study is different from Feuerecker et al (1994) and Kaita (2001) by maximum 6 and 10 kJ/kg respectively. The maximum difference from McNeely (1979) is as large as 15 kJ/kg.

4.2.3 *Entropy of solution*

From Eqs. (4.2), (4.24) and (4.7), the molar entropy of the solution is given by

$$S^l = x_1 S^{\infty}_{1(T,p)} + (1-x_1) S^{*l}_{2(T,p)} - x_1 \upsilon R\left[\ln\left(\frac{m}{m_\circ}\right) - 1\right] + S^{E}_{(T,p,m)} \tag{4.32}$$

where $S^{\infty}{}_1$ and $S^{*l}{}_2$ are the molar entropy of the infinitely dilute solution and that of pure water respectively. The third term is the entropy generation in an ideal mixing and the last term S^E is the extra entropy generation in a real mixing process.

$S^{*l}{}_2$ can be calculated as follows using the steam table data.

$$S^{*l}_2 = S^{*l}_{2\circ} + \int_{T_\circ}^{T} \frac{C^{*l}_{p2}}{T} dT - \int_{p_\circ}^{p} \left(\frac{\partial V^{*l}_2}{\partial T}\right)_p dp \tag{4.33}$$

Using Eqs. (4.24) and (4.28), the excess enthalpy S^E is given by

$$S^E = \frac{H^E - G^E}{T} = -x_1 \upsilon R \sum_{i=1}^{6} \frac{2}{i} \left[a_i + \frac{ib_i}{2\upsilon} p + T\left(\frac{\partial a_i}{\partial T} + \frac{i}{2\upsilon}\frac{\partial b_i}{\partial T} p\right) \right] m^{i/2} \tag{4.34}$$

S_1^∞ can be calculated by the following equation using C_{p1}^∞ from Eq. (4.31) and V_1^∞ from Eq. (4.14).

$$S_1^\infty = S_{1\circ}^\infty + \int_{T_\circ}^{T} \frac{C_{p1}^\infty}{T} dT - \int_{p_\circ}^{p} \left(\frac{\partial V_1^\infty}{\partial T} \right)_p dp \tag{4.35}$$

The zero entropy states have been chosen for pure water and 50 wt% solution at 0 °C. The results are illustrated in Fig. 4.10 with those of Löwer (1960), Feuerecker et al (1994), Chua et al (2000), Kaita (2001) and Koehler et al (1987).

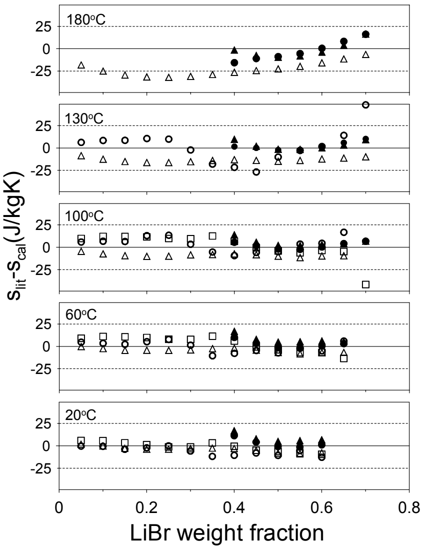

Figure 4.10 Comparison of calculated entropy with literature values [○: Löwer (1960), △: Chua et al (2000), □: Koehler et al (1987), ●: Feuerecker et al (1994), ▲: Kaita (2001)]

Except for Koehler et al (1987) that did not present enthalpy data, the other sources show similar trends in comparison with this study as for the enthalpy.

4.3 Conclusions

Thermodynamic properties of LiBr aqueous solution have been successfully described with a Gibbs energy equation for the solutions in the concentration range from 0 to 70 wt% and the temperature range from 0 to 210 °C.

The equation for osmotic coefficient developed in this study is able to reproduce the original solution density and the equilibrium vapour pressure from the literature within a standard deviation of 0.29 % and 2.9 % respectively. Solution enthalpy has been calculated using experimental heat capacity and differential heat of dilution based on the osmotic coefficient equation. The calculated enthalpy is consistent with the experimental differential heat of dilution and heat capacity data taken from the literature. This study agree relatively well with Feuerecker et al (1994) and Kaita (2001) but deviates substantially from those based on the equilibrium vapour pressures of McNeely (1979) especially in the high concentration and temperature regions.

The approach adopted in this study has proved its high flexibility and accuracy for describing electrolyte solutions over wide working ranges by allowing all relevant parameters to be systematically expressed in a single Gibbs energy equation that can be readily expandable to other thermodynamic property equations.

Being able to describe the properties of solutions from pure solvent to the highly concentrated solutions near crystallization limits at temperatures from freezing points to 210 °C, this study provides a consistent and reliable basis for simulation and analysis of LiBr absorption systems.

Nomeclature

C_p	molar heat capacity, kJ/kmol K
G	molar Gibbs energy, kJ/kmol
H	molar enthalpy, kJ/kmol
h	specific enthalpy, kJ/kg
h^d	specific differential heat of dilution, kJ/kg of solvent
M	molar mass, kg/kmol
m	molality, kmol solute /kg of solvent
p	pressure, kPa
R	universal gas constant, kJ/kmol K
S	molar entropy, kJ/kmol K
s	specific entropy, kJ/kg K
T	temperature, K
V	molar volume, m^3/kmol
x	concentration

Greek symbols

$\gamma^{\pm}$	mean ionic activity coefficient
ϕ	osmotic coefficient
υ	dissociation number (2 for LiBr)
ρ	density, kg m^{-3}

Superscripts

dew	dew point
∞	ideal fluid for solute species
*	saturation state of pure solvent
g	vapor phase
l	liquid phase
E	excess property

Subscripts

1	solute (=LiBr)
2	solvent (=water)

o reference, standard state
w weight

References

Chua HT, Toh HK, Malek A, Ng KC, Srinivasan K., 2000, Improved thermodynamic property fields of LiBr-H2O solution. Int. J. Refrigeration, Vol. 23, pp. 412-29

Debye P, Hückel E., 1923, Zur theorie der elektrlyte. Physikalische Zeitschrift Vol. 24, pp.185-208

Feuerecker G, Scharfe J, Greiter I, Frank C, Alefeld G., 1994, Measurement of thermophysical properties of aqueous LiBr-solutions at high temperatures and concentrations. In: Proceedings of International Absorption Heat Pump Conference, New Orleans, USA, 1Vol. 31, pp 493-9

Grossman, G., Wilke, M., Devault, R.C., 1994, Simulation and performance analysis of triple-effect absorption cycle, ASHRAE Trans., Vol. 100, pp. 452-462

Haltenburger W., 1939, Enthalpy-concentration charts from vapour pressure data. Industrial Engineering Chemistry, Vol. 31, pp. 783-6.

Hamer WJ, Wu Y., 1972, Osmotic coefficients and mean activity coefficients of unit-univalent electrolytes in water at 25°C. J of Physical and Chemical Reference Data, Vol. 1, pp. 1047-99.

Herold KE, Moran MJ., 1987, Thermodynamic properties of lithium bromide/water solutions, ASHRAE Transactions, Vol. 93, pp. 35-48

ICT, International Critial Table, 1928, New York: McGraw Hill

Iyoki S, Uemura T., 1989, vapour pressure of water-lithium bromide system and the water-lithium bromide-zinc bromide-lithium chloride system at high temperatures, Int. J. Refrigeration, Vol. 112, pp. 278-82

Jeter SM, Moran JP, Teja AS., 1992, Properties of Lithium Bromide-Water solutions at High Temperatures and Concentrations – III: Specific Heat. ASHRAE Transactions, Vol. 98, pp. 137-49

Kaita Y., 2001, Thermodynamic properties of lithium bromide-water solutions at high temperatures, Int. J. Refrigeration, Vol., 24, pp. 374-90

Kaita, Y., 2002, Simulation results of triple-effect absorption cycles, Int. J. Refrigeration, Vol. 25, pp. 999-1007

Kim, D.S., Machielsen, C.H.M., 2002, Evaluation of air-cooled solar absorption cooling systems, Proc. of ISHPC 2002, Shanghai, China

Kim, D.S., Machielsen, C.H.M., 2002, Comparative study on water- and air-cooled solar absorption chillers, Proc. of EuroSun 2002 ISES Conference, Bologna, Italy

Kim, D.S., Infante Ferreira, C.A., 2006, A Gibbs Energy Equation for LiBr aqueous solutions, Int. J. Refrigeration, Vol. 29, pp. 36-46

Koehler WJ, Ibele WE, Soltes J, Winter ER., 1987, Entropy calculations for lithium bromide aqueous solutions and approximation equation, ASHRAE Transactions , vol. 93, pp. 2379-88.

Kojima, M., Fujita, T., Irie, T., Inoue, N., 2003, Development of water-lithium bromide absorption machine operating below zero degrees, Proc. of 21st IIR Int. Cong. of Ref., Wash. D.C., USA

Lange E, Schwartz E., 1928, Lösungs and verdünnungswärmen von salzen von äussersten verdünnung bis zur sättigung-IV Lithiumbromid. Zeitschrift für Physikalische Chemie , Vol. 133, pp. 129-50

Lee RJ, DiGuilio RM, Jetter SM, Teja AS., 1990, Properties of lithium bromide-water solutions at high temperatures and concentrations-II: Density and Viscosity, ASHRAE Transactions, Vol. 96, pp. 709-14

Lenard JLY, Jeter SM, Teja AS., 1992, Properties of Lithium Bromide-Water solutions at High Temperatures and Concentrations – IV: vapour Pressure, ASHRAE Transactions, Vol. 98, pp. 167-72

Löwer H., 1960, Thermodynamische und physikalische Eigenschaften der wässrigen Lithiumbromid-Losung, Dissertation, Technischen Hochschule Karlsruhe

McNeely LA., 1979, Thermodynamic properties of aqueous solutions of lithium bromide, ASHRAE Transactions, Vol. 85, pp. 413-34

Perry RH, Green DW, Maloney JO., 1984, Perry's Chemical Engineers Handbook; 6th ed., New York: McGraw-Hill Book Co

Pitzer, K.S., 1973, Thermodynamics of electrolytes. I. Theoretical basis and general equations, J. Phys. Chem., Vol.77, pp.268-277

Robinson RA, McCoach HJ., 1947, Osmotic and activity coefficients of lithium bromide and calcium bromide solutions, J. of the American Chemical Society, Vol. 69, p. 2244.

Rockenfeller U., 1987, Laboratory results: solution=LiBr-H2O, properties=P-T-x, heat capacity. Unpublished data, Boulder city, NV: Rocky Research Inc. (cited from Jeter et al, 1992).

Ruiter JP., 1986, Thermodynamic description of mixtures and solutions, Arnhem: Kema Scientific & Technical Reports; Vol. 4, ISBN 90-353-0044-0.

Schmidt E., 1979, Properties of Water and steam in SI-Units. Berlin: Springer-Verlag

Schulz, S.C.G, 1973, Equations of state for the system ammonia-water for use with computers, Proceedings of 13th International Congress of Refrigeration

Smith, J.M., Van Ness, H.C., Abbott, M.M., 2001, Chemical engineering thermodynamics, 6th edition, McGraw-Hill

Uemura T, Hasaba S., 1964, Studies on the lithium bromide-water absorption refrigerant machine, Technology Report Kansai University, Vol. l6, pp. 31-55 (cited from Iyoki and Uemura, 1989).

Ziegler B., Trepp, Ch., 1984, Equation of state for ammonia-water mixtures, Int. J. Refrigeration, Vol. 7, pp. 101-106

5 Steady-state modeling and simulation

A steady-state model is developed for simulation of the proposed solar-driven absorption chiller. The present modeling work focuses primarily on modeling of the transport phenomena at the vapor-liquid interfaces of falling film flows and also on the transformation of governing equations for easy and quick solution.

Dynamic models in Ch. 2 are largely based on the models presented in this chapter. Although lumped parameters can serve the goal of Ch. 2 sufficiently well, since those lumped parameter models in Ch. 2 cannot describe the heat and mass transfer processes in the various components to local detail, steady-state distributed parameter models have been developed for more accurate prediction of components and system behaviour.

Motivation and ideas of the present modeling approach are briefly described in Section 5.1 and modeling details and simulation results follow in the following sections.

5.1 Modeling strategy

A schematic diagram of the chiller is given in Fig. 5.1 with major state points numbered for system modeling purposes.

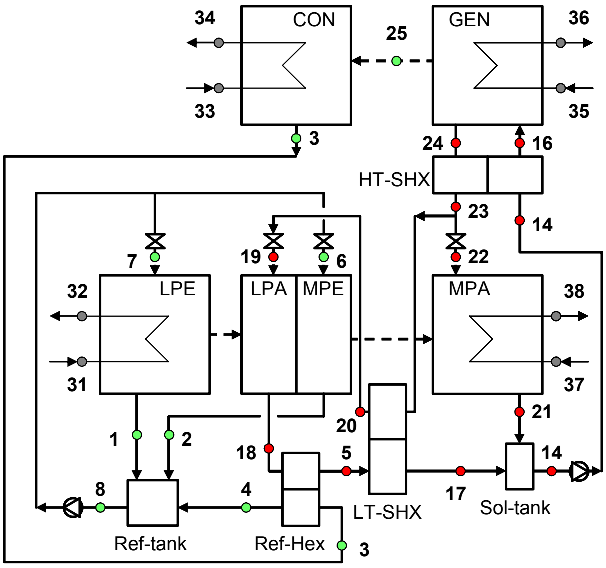

Figure 5.1 Schematic diagram of the system

Note that the system in Fig. 5.1 has a refrigerant tank and a pump for recirculation of refrigerant through the evaporators. Inclusion of the recirculation circuit was decided for the experimental chiller setup and thus in the system model because it has been thought impossible to wet the evaporators' heat transfer surface with the flow rate of refrigerant given in Ch. 3.

The chiller in Fig. 5.1 has six two-phase heat & mass exchangers, three single-phase heat exchangers and two mixing tanks. Because many components are coupled to each other and thus there are many interactive parameters to be included in the system model, it is important to develop governing equations that are easy and quick to solve.

Since the governing equations for absorption and desorption processes in general are highly non-linear, various iterative methods have been used for solution, which requires extra procedures other than solving the original equations themselves. For example, the modified Newton-Raphson method by Powell (1970) requires determination of a Jacobian matrix to correct intermediate solutions at every step until the solution converges [e.g. Grossman and Michelson (1994) and Zhuo (1995)]. And because there are always possibilities of physically unrealistic solutions, enough care should be given also to the initial and intermediate solutions. In many cases, these extra measures impose excessive complications and inefficiencies in the solution process.

Generally, much of the non-linearity in an absorption system originates from the non-linear nature of the working fluids' properties. Enthalpy of solution, for example, is often treated as an implicit function of independent variables because of its high non-linearity. Consequently, energy balance equations that inevitably include solution enthalpies cannot be solved explicitly and thus property functions should be called in every time to update the enthalpy terms for an improved intermediate solution.

One way to avoid all these problems regarding the solution of non-linear equations is to develop linear governing equations in the first place or to transform the non-linear equations into some equivalent linear forms for a simple and quick solution. This approach is adopted here and a great deal of effort is given to the derivation of linear or quasi-linear equations in the following sections.

Lumped parameter models are probably most commonly used in simulation of absorption systems. Because an absorption system model has to be capable of describing complex thermal processes in many components involving a large number of variables, lumped parameter model may be a practical choice. But, since it describes driving potentials in heat or mass transfer process with an average term, which is typically a logarithmic mean, lumped parameter model cannot accurately describe those highly nonlinear temperature and concentration profiles encountered in simultaneous heat and mass transfer processes. For example, when a subcooled solution is supplied to the generator, the solution first absorbs vapour and starts generating vapour somewhere downstream only after that the bulk solution becomes hot enough. In this case, bulk and interface temperature and thus concentration profiles cross at the point where the vapour generation starts. Lumped parameter models simply cannot describe this phenomenon.

A two-dimensional numerical falling film model proposed by Yang and Wood (1992), Wassenaar (1994) or others could be an option but it is not thought practical for a system simulation because it would require excessive memory and computing time.

A practical alternative may be a one-dimensional differential model based on empirical heat and mass transfer correlations. Although the number of variables increases in proportion to that of differential control volumes used and so does the computing time, the solution would be quicker than for two-dimensional numerical models and as accurate as the empirical heat and mass correlations used. Details of the modeling results are given in the following sections.

5.2 Generator

The generator produces refrigerant vapour by heating refrigerant-rich solution interface with a heating medium. For a LiBr-water absorption chiller, a falling film type generator is preferred because the pressure drop in the vapour flow is relatively small. A schematic diagram of a falling film type generator is given in Fig. 5.2.

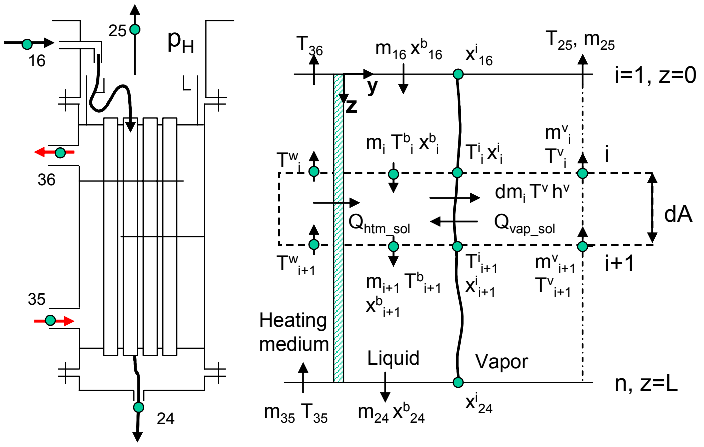

Figure 5.2 Schematic diagrams of generator and control volume

The generator in Fig. 5.2 is a shell & tube type heat exchanger where the heating medium flows through the shell side in an upward cross flow configuration and refrigerant vapour is generated from the solution that flows downward inside the vertical tubes.

Several assumptions were made to simplify the model, which are

- The same working conditions are applied to all the tubes regardless of the position
- Heating medium flow is counter-current to the solution flow
- Pressure drop along the vapour flow is negligible

For the ith liquid control volume shown in Fig. 5.2, the following governing equations can be derived.

Total mass balance for liquid film:

$$\sum \dot{m} = \dot{m}_i - d\dot{m}_i - \dot{m}_{i+1} = 0 \tag{5.1}$$

LiBr mass balance for liquid film:

$$\sum \dot{m}_{LiBr} = \dot{m}_i x_i^b - \dot{m}_{i+1} x_{i+1}^b = 0 \tag{5.2}$$

Energy balance for liquid film:

$$\begin{aligned}\sum \dot{Q} &= \dot{Q}_i - \dot{Q}_{htm\_sol} - \dot{Q}_{vap\_sol} \\ &= \dot{Q}_i - \dot{m}_{35} C_{p35} (T_{i+1}^w - T_i^w) - \alpha^v dA \Delta T_{avg}^v = 0\end{aligned} \tag{5.3}$$

where $\dot{Q}_{htm\_sol}$ and $\dot{Q}_{vap\_sol}$ are the heat transfer rate from hot water to bulk solution and that from bulk vapour to vapor-solution interface respectively. α^v is the heat transfer coefficient between bulk vapour and the interface and $\dot{Q}_i$ is the desorption heat defined by

$$\dot{Q}_i = \dot{m}_{i+1}h_{i+1} + d\dot{m}_i h^v - \dot{m}_i h_i \tag{5.4}$$

and the average temperature difference between the vapour and the solution is defined by

$$\Delta T^v_{avg} \equiv \frac{1}{2}\left(T^v_i + T^v_{i+1} - T^i_i - T^i_{i+1}\right) \tag{5.5}$$

Overall heat transfer:

$$\sum \dot{Q} = \dot{m}_{35}C_{p35}(T^w_{i+1} - T^w_i) - UdA\Delta T^l_{avg} = 0 \tag{5.6}$$

where ΔT^l_{avg} denotes the mean temperature difference between the heating medium and the solution defined by

$$\Delta T^l_{avg} \equiv \frac{1}{2}\left(T^w_i + T^w_{i+1} - T^b_i - T^b_{i+1}\right) \tag{5.7}$$

Mass transfer in liquid film:

$$\sum \dot{m}_{H_2O} = d\dot{m}_i - \rho K dA \Delta x_{avg} = 0 \tag{5.8}$$

where K denotes the mass transfer coefficient and Δx_{avg} the mean concentration difference, which is defined between bulk and interface concentrations by

$$\Delta x_{avg} \equiv \frac{1}{2}\left(x^i_i + x^i_{i+1} - x^b_i - x^b_{i+1}\right) \tag{5.9}$$

For the ith vapour control volume shown in Fig. 5.2, the following governing equations can be derived.

Total mass balance for vapour flow:

$$\sum \dot{m} = \dot{m}^v_i - d\dot{m}_i - \dot{m}^v_{i+1} = 0 \tag{5.10}$$

Energy balance for vapour flow:

$$\sum \dot{Q} = \left(\dot{m}^v_i h^v_i - d\dot{m}_i h^v - \dot{m}^v_{i+1} h^v_{i+1}\right) + \alpha^v dA \Delta T^v_{avg} = 0 \tag{5.11}$$

All equations above will be expressed in terms of the primary variables including mass flow rate $\dot{m}$, temperature T and concentration x and transformed into appropriate forms for easy and quick solution.

Note that the arithmetic means are used for the driving potentials in Eq. (5.5), (5.7) and (5.9) instead of logarithmic means. This is valid for infinitesimal differential control volumes and would provide acceptable accuracy for reasonably sized differential elements. It is advantageous that they are all expressed linearly in T and x. But it is not certain at this moment whether Eq. (5.8) is linear in independent variables because the interface concentration x^i is not fully described yet.

On the other hand, Eq. (5.2) and (5.3) are nonlinear. Especially Eq. (5.3) is complicated because the desorption heat $\dot{Q}_i$ in Eq. (5.4) contains the solution enthalpies that are highly non-linear in T and x. If the enthalpy terms in Eq. (5.4) are not to be expressed explicitly in terms of the primary variables, the desorption heat $\dot{Q}_i$, being an implicit function of the variables, presents extra difficulties in the solution process. This is a significant disadvantage especially for a differential model where many of such equations should be solved simultaneously.

In the following, these non-linear equations are transformed to appropriate forms for quick and simple solution using some thermodynamic and heat and mass transfer theories.

5.2.1 Simultaneous heat and mass transfer

Solution of Eq. (5.8) requires knowledge of the interface concentrations. The goal of this section is to express the interface concentration explicitly in terms of the bulk properties of the falling film, preferably with a linear equation. For this purpose, two famous studies of Nakoryakov and Grigoreva (1980) and Yüksel and Schlünder (1987) are used as presented in the following.

5.2.1.1 Developing flow

Nakoryakov and Grigoreva (1980) analyzed the entrance region of a laminar film flow over a vertical wall and considered two thermal boundary layers, one of which grows from the wall and the other from vapor-liquid interface. The two layers eventually meet somewhere down stream. The idea is illustrated in Fig. 5.3.

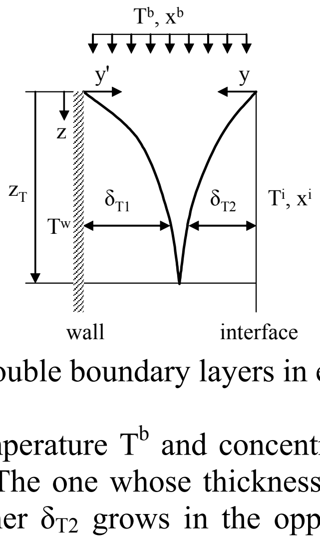

Figure 5.3 Double boundary layers in entrance region

At z=0, a solution with bulk temperature T^b and concentration x^b is supplied. Soon the two boundary layers begin to grow. The one whose thickness is denoted by δ_{T1} grows from the wall to the interface and the other δ_{T2} grows in the opposite direction. The two boundary layers meet downstream at $z=z_T$. The authors assumed a constant velocity $\bar{u}$ in the layer δ_{T2} and solved the conduction and diffusion equations for temperature and concentration.

The governing equation is given for temperature by

$$\bar{u}\frac{\partial T}{\partial z}=\frac{k}{\rho C_p}\frac{\partial^2 T}{\partial y^2} \tag{5.12}$$

with boundary conditions : $T(z,0)=T^i$ and $T(z,\infty)= T(0,y)=T^b$.

And for concentration, it is given by

$$\bar{u}\frac{\partial x}{\partial z}=D\frac{\partial^2 x}{\partial y^2} \tag{5.13}$$

with boundary conditions : $x(z,0)=x^i$ and $x(z,\infty)= x(0,y)=x^b$.

The solution of Eq. (5.12) is given by

$$\frac{T-T^i}{T^b-T^i}=erf(\eta_1) \quad \eta_1=\frac{1}{2}\sqrt{\frac{\rho C_p\bar{u}}{k}}\frac{y}{\sqrt{z}} \tag{5.14}$$

where erf(η) is the error function. And the solution of Eq. (5.13) is given similarly by

$$\frac{x-x^i}{x^b-x^i}=erf(\eta_2) \quad \eta_2=\frac{1}{2}\sqrt{\frac{\bar{u}}{D}}\frac{y}{\sqrt{z}} \tag{5.15}$$

Since the heat transfer rate at the interface should be equal to the heat involved in absorption or desorption, inserting T and x in Eq. (5.14) and (5.15) into a heat balance equation at the interface, i.e. $k\partial T/\partial y=-\Delta h\cdot\rho D\partial x/\partial y$ where Δh is heat of ab(de)sorption (see Appendix C2), and rearranging it gives

$$x^b-x^i=\frac{C_p\sqrt{Le}}{\Delta h}\left(T^i-T^b\right) \tag{5.16}$$

where Le is lewis number defined by $Le\equiv(k/\rho Cp)/D$.

From Eq. (C1.7) in Appendix C1, T^i in Eq. (5.16) can be expressed on Celsius scale as

$$T^i=\left[A_1\left(x^i-x^b\right)+A_2\right]\left(T^{dew}+273.15\right)-273.15 \tag{5.17}$$

Inserting Eq. (5.17) into Eq. (5.16) and rearranging it for x^i gives

$$x^i=x^b+C_1T^b+C_2T^{dew}+C_3 \tag{5.18}$$

where $C_1 \equiv \left[A_1 \left(T^{dew} + 273.15 \right) + \frac{\Delta h}{C_p Le^{0.5}} \right]^{-1}$, $C_2 \equiv -C_1 A_2$ and $C_3 \equiv 273.15(C_1 + C_2)$.

Eq. (5.16) and thus Eq. (5.18) is valid in the entrance region where the two boundary layers in Fig. 5.3 are still developing, i.e. $0<z<z_T$. Nakoryakov and Grigoreva (1980) also gave the entrance length z_T as

$$2\left(\frac{9\mathrm{Fr}}{\mathrm{Pr}\,\mathrm{Re}^2}\frac{z_T}{\delta}\right)^{1/3} + 4\left(\frac{2}{3\,\mathrm{Re}\,\mathrm{Pr}}\frac{z_T}{\delta}\right)^{1/2} = 1 \tag{5.19}$$

The entrance length z_T has been calculated for a falling film flow of 50 % solution at 53 °C. The result is illustrated against Reynolds number in Fig. 5.4.

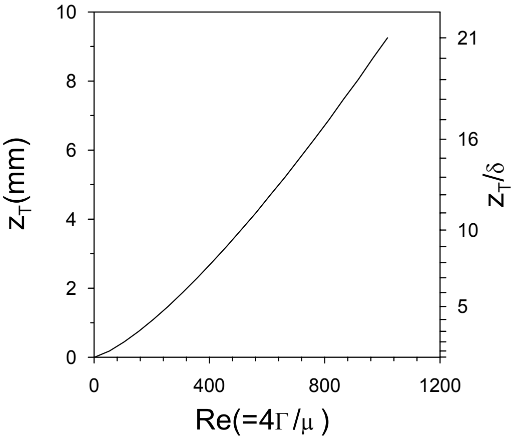

Figure 5.4 Thermal entrance length in falling film flow (x=0.5 and T=53°C)

According to Fig. 5.4, z_T is only 2 mm for Re=320, which corresponds to the flow rate of Γ=0.16 kg/ms. Considering that this Reynolds number is well beyond typical design flow rates for falling film heat exchangers in absorption machines, Eq. (5.18) would be applicable only to the 1st differential control volume if its size is not selected smaller than 2 mm.

5.2.1.2 Fully developed flow

Yüksel and Schulünder (1987) suggested a method to determine interface conditions based on heat and mass transfer analogy. Average Sherwood numbers determined from the calculated interface concentrations were in good agreement with those determined from their infrared measurement technique.

They have derived an interface model for fully developed falling film flows from the heat and mass transfer analogy [see e.g. Holman (1997)] given by

$$\frac{\alpha}{K} = \rho_{sol} C_{psol} Le^{1-n} \tag{5.20}$$

where α and K denote the liquid-side heat transfer coefficient at the interface and the mass transfer coefficient respectively.

Yüksel and Schulünder (1987) suggested that the exponent ‘n’ should be a value between 0.4 and 0.5 according to the Schmidt number exponents in correlations for isothermal falling film absorption from several studies (see Yüksel and Schulünder, 1987 for references).

Their study is based on the stagnant film model (see e.g. Bird et al, 1965 or Baehr and Stephan, 1998), which assumes a thin stagnant film adjacent to the phase-changing surface. The thickness of a stagnant film is shown as Δ in Fig. 5.5.

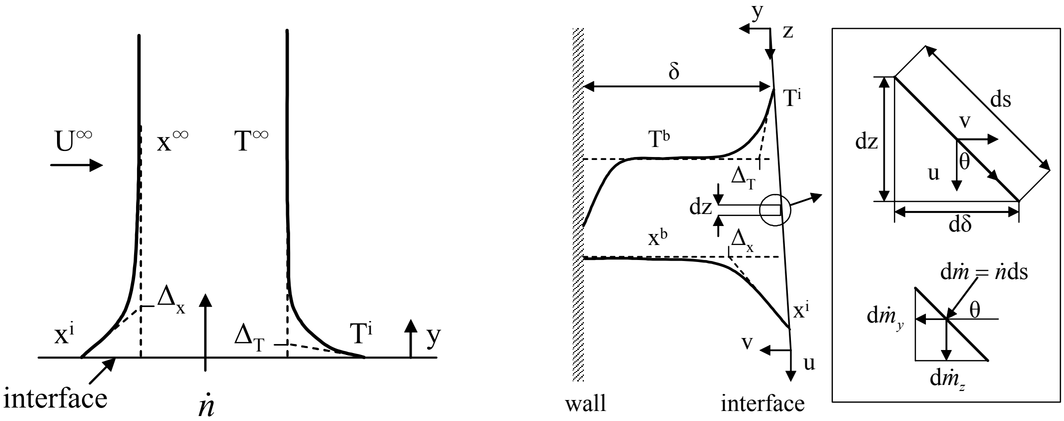

(a) Stagnant film model (b) Falling film flow

Figure 5.5 Stagnant film model and falling film flow

The basic ideas of the stagnant film theory are introduced in the following. Although Yüksel and Schulünder (1987) described the same ideas on molar basis, mass based expressions are used in the following to be consistent with the rest of this chapter.

Over the stagnant concentration layer $0 \le y \le \Delta_x$ in Fig. 5.5a, the mass balance equation is given for the mass flux $\dot{n}$ by

$$\dot{n} = \rho_{sol} D \frac{dx}{dy} + (1-x)\dot{n} \tag{5.21}$$

with boundary conditions $x=x^i$ at $y=0$ and $x=x^{\infty}$ at $y=\Delta_x$ (see e.g. Bird et al, 1965).

And over temperature layer $0 \le y \le \Delta_T$, the energy balance equations is given by

$$k\frac{d^2T}{dy^2} - \dot{n}C_{p,H_2O}\frac{dT}{dy} = 0 \tag{5.22}$$

with boundary conditions, $T=T^i$ at $y=0$, $T=T^{\infty}$ at $y=\Delta_T$ (see e.g. Bird et al, 1965).

Eq. (5.21) and the boundary conditions give

$$\dot{n} = \rho_{sol}\left(\frac{D}{\Delta_x}\right)\ln\left(\frac{x^{\infty}}{x^i}\right) \tag{5.23}$$

from which the mass transfer coefficient is defined by

$$K \equiv \frac{D}{\Delta_x} = \frac{\dot{n}}{\rho_{sol} \ln\left(x^{\infty} / x^{i}\right)} \tag{5.24}$$

Eq. (5.22) and the boundary conditions give the heat flux at y=0 as

$$\dot{q}_{y=0} = \frac{\dot{n} C_{p,H_2O}\left(T^{\infty} - T^{i}\right)}{1 - \exp\left(\dot{n} C_{p,H_2O} \Delta_T / k\right)} \tag{5.25}$$

Replacing $\dot{q}_{y=0} = \dot{n}\,\Delta h$ in Eq. (5.25) gives the heat transfer coefficient at the interface α as

$$\alpha \equiv \frac{k}{\Delta_T} = \frac{\dot{n} C_{p,H_2O}}{\ln\left[1 + C_{p,H_2O}\left(T^{i} - T^{\infty}\right) / \Delta h\right]} \tag{5.26}$$

Yüksel and Schulünder (1987) used these stagnant film models for the falling film flows replacing x^{∞} and T^{∞} with x^b and T^b respectively.

Inserting Eq. (5.24) and (5.26) into Eq. (5.20) and rearranging it finally gives the equation of Yüksel and Schulünder (1987) as follows.

$$\left(\frac{x^b}{x^i}\right)^{\frac{C_{pH_2O}}{C_{psol} Le^{1-n}}} = \frac{C_{pH_2O}}{\Delta h}(T^i - T^b) + 1 \tag{5.27}$$

As shown above, Yüksel and Schulünder (1987)'s model is based on the assumption that the original stagnant film model is valid for the falling film flows. But it is questionable if it is true.

For this stagnant film model to be applicable to the falling film flows, first of all, the convective mass flux in the transverse direction in the falling film should be equal to the total mass flux at the interface. The following proves that this is not true.

Assuming that the total mass of the vapour being absorbed at the interface Fig.6.5b is $d\dot{m}$, then the mass flow in the transverse direction $d\dot{m}_y$ in Fig. 5.5b may be expressed in terms of film thickness δ and the velocity at the interface u_i as

$$d\dot{m}_y = d\dot{m} - \rho u_i d\delta \tag{5.28}$$

where, for the film thickness δ, the following general correlation can be used

$$\delta = a\left(\frac{\nu^2}{g}\right)^{1/3} \mathrm{Re}^b \tag{5.29}$$

in which the constant *a* and the exponent b depend on the pattern of the flow.

Dividing Eq. (5.28) with $d\dot{m}$ gives

$$\frac{d\dot{m}_y}{d\dot{m}} = 1 - \rho u_i \frac{d\delta}{d\dot{m}} \tag{5.30}$$

Expressing in Reynolds number, Eq. (5.30) becomes

$$\frac{d\dot{m}_y}{d\dot{m}} = 1 - \frac{u_i}{u_{avg}} \frac{\mathrm{Re}}{\delta} \frac{d\delta}{d\left(\mathrm{Re}\right)} \tag{5.31}$$

Inserting Eq. (5.29) into Eq. (5.31) gives

$$\frac{d\dot{m}_y}{d\dot{m}} = 1 - b\left(\frac{u_i}{u_{avg}}\right) \equiv F_y \tag{5.32}$$

where the ratio defined by F_y is the portion of the transverse mass flux out of total mass flux at the interface. It is found from Eq. (5.32) that $F_y = 0.5$ for laminar flows assuming $b=1/3$ and $u_i/u_{avg}=1.5$ from Nusselt (1916). Therefore the original film model overestimates the transverse mass flux.

Considering this ratio of transverse and total mass flux in Eq. (5.32), the mass transfer coefficient can be redefined as

$$K \equiv \frac{\dot{n}}{\rho_{sol} F_y \ln\left(x^b / x^i\right)} \tag{5.33}$$

Then, Eq. (5.27) should be modified as

$$\left(\frac{x^b}{x^i}\right)^{\frac{C_{pH_2O} F_y^2}{C_{psol} Le^{1-n}}} = F_y \left(\frac{C_{pH_2O}}{\Delta h}\right)(T^i - T^b) + 1 \tag{5.34}$$

In order to make Eq. (5.34) more suitable for the present application, expanding the left-hand side in Taylor series and taking only the first two terms gives

$$x^b - x^i = \left(\frac{C_{psol} Le^{1-n}}{\Delta h}\right)(T^i - T^b) + \Pi \tag{5.35}$$

where $\Pi \equiv \left(\frac{x^b}{F_y} - 1\right)\left(\frac{C_{psol} Le^{1-n}}{\Delta h}\right)(T^i - T^b)$.

Note that if the exponent n is 0.5, Eq. (5.35) is analogous to Eq. (5.16) except for the last term Π on the right-hand side, which can be treated as a residual in the solution process because it is relatively small.

In the same way as Eq. (5.16) is treated, Eq. (5.35) is rearranged for x^i as

$$x^i = x^b + D_1 T^b + D_2 T^{dew} + D_3 \tag{5.36}$$

where $D_1 \equiv \left[A_1 \left(T^{dew} + 273.15 \right) + \frac{\Delta h}{C_p Le^{1-n}} \right]^{-1}$, $D_2 \equiv -D_1 A_2$ and $D_3 \equiv 273.15(D_1+D_2) - D_1 \frac{\Delta h}{C_p Le^{1-n}} \Pi$.

Using Eq. (5.18) and (5.36) for the interface concentrations, Eq. (5.8) can now be expressed as follows.

$$\dot{m}_i - \dot{m}_{i+1} - \frac{\rho K dA}{2} \left[\Phi_i T_i^b + \Phi_{i+1} T_{i+1}^b + \left(\Theta_i + \Theta_{i+1} \right) T^{dew} + \left(\Omega_i + \Omega_{i+1} \right) \right] = 0 \tag{5.37}$$

where $\Phi_i = C_1$, $\Theta_i = C_2$ and $\Omega_i = C_3$ in Eq. (5.18) if the ith node is in the thermal entrance region or $\Phi_i = D_1$, $\Theta_i = D_2$ and $\Omega_i = D_3$ in Eq. (5.36) if it is not.

5.2.2 Energy balance for liquid film

Eq. (5.3) includes the desorption heat $\dot{Q}_i$, which is a highly non-linear function of several independent variables. Since this non-linearity is the main source of the inefficiency in the solution process, Eq. (5.3) will be transformed to allow a simple and quick solution.

From the thermodynamic study presented in Ch. 4, it is shown in Appendix C2 that the desorption heat can be excellently approximated by Eq. (C2.16).

For the ith differential control volume of liquid in Fig. 5.2, Eq. (C2.16) is rewritten as

$$\dot{Q}_i = \dot{m}_i C_{p,i}^l (T_{i+1}^s - T_i^s) + d\dot{m}_i \left[a_{x=x_i} h^{fg} + C_p^{\mathrm{v}} (T^v - T_i^s) \right] \tag{5.38}$$

where $a_{x=xi}$ is the gradient $\partial(1/T^{dew})/\partial(1/T)$ at $x=x_i$ and T^v and T^s denote vapour temperature and equilibrium temperature at the corresponding bulk concentration and the working pressure respectively.

Since Eq. (5.38) was derived for saturated solutions, taking account of the non-equilibrium temperatures of bulk solutions at the inlet and outlet of the differential volume, $\dot{Q}_i$ can be written as

$$\begin{aligned} \dot{Q}_i = {} & \dot{m}_i C_{p,i}^l (T_{i+1}^s - T_i^s) + \left[a_{x=x_i} h^{fg} + C_p^{\mathrm{v}} (T^v - T_i^s) \right] d\dot{m}_i \\ & - \dot{m}_{i+1} C_{p,i+1}^l (T_{i+1}^s - T_{i+1}^b) + \dot{m}_i C_{p,i}^l (T_i^s - T_i^b) \end{aligned} \tag{5.39}$$

Assuming $C^l_{p,i+1} = C^l_{p,i}$ in Eq. (5.39) and replacing $d\dot{m}_i = \dot{m}_i - \dot{m}_{i+1}$ from Eq. (5.1) gives

$$Q_i = \left(\dot{m}_{i+1} C_{p,i}^l \right) T_{i+1}^b - \left(\dot{m}_i C_{p,i}^l \right) T_i^b + \left[a_{x=x_i} h^{fg} + C_p^{\mathrm{v}} (T^v - T_i^s) + C_{p,i}^l T_{i+1}^s \right] \left(\dot{m}_i - \dot{m}_{i+1} \right) \tag{5.40}$$

Inserting Eq. (5.40) into Eq. (5.3) and rearranging it gives

$$
\begin{aligned}
&\left(\dot{m}_{i+1}C^{l}_{p,i}\right)T^{b}_{i+1}-\left(\dot{m}_{i}C^{l}_{p,i}\right)T^{b}_{i}+\left[a_{x=x_i}h^{fg}+C^{\mathrm{v}}_{p}(T^{v}-T^{s}_{i})+C^{l}_{p,i}T^{s}_{i+1}\right]\left(\dot{m}_{i}-\dot{m}_{i+1}\right)\\
&\qquad-\left(\dot{m}_{35}C_{p35}\right)\left(T^{w}_{i+1}-T^{w}_{i}\right)-\frac{\alpha^{v}dA}{2}\left(T^{v}_{i}+T^{v}_{i+1}-T^{i}_{i}-T^{i}_{i+1}\right)=0
\end{aligned}
\tag{5.41}
$$

The last term on the left-hand side of Eq. (5.41) is the heat transfer rate from the vapour flow. The interface temperatures T^{i}_{i} and T^{i}_{i+1} should be expressed in a similar way to the case of interface concentrations.

From Eq. (5.17) and (5.18), the interface temperature T^{i} is written for the developing region as

$$
T^{i}=C_4T^{b}+C_5T^{dew}+C_6 \tag{5.42}
$$

where $C_4 \equiv A_1(273.15+T^{dew})C_1$, $C_5 \equiv A_1(273.15+T^{dew})C_2+A_1C_3+A_2$ and $C_6 \equiv 273.15(A_1C_3+A_2-1)$.

And similarly for fully developed region, from Eq. (5.17) and (5.36), it is

$$
T^{i}=D_4T^{b}+D_5T^{dew}+D_6 \tag{5.43}
$$

where $D_4 \equiv A_1(273.15+T^{dew})D_1$, $D_5 \equiv A_1(273.15+T^{dew})D_2+A_1D_3+A_2$ and $D_6 \equiv 273.15(A_1D_3+A_2-1)$.

Then Eq. (5.41) can now be expressed as follows.

$$
\begin{aligned}
&-\left(\dot{m}_{i}C^{l}_{p,i}-\frac{\alpha^{v}dA}{2}\Phi'_{i}\right)T^{b}_{i}+\left(\dot{m}_{i+1}C^{l}_{p,i}+\frac{\alpha^{v}dA}{2}\Phi'_{i+1}\right)T^{b}_{i+1}+\left[a_{x=x_i}h^{fg}+C^{v}_{p}(T^{v}-T^{s}_{i})+C^{l}_{p,i}T^{s}_{i+1}\right]\left(\dot{m}_{i}-\dot{m}_{i+1}\right)\\
&-\left(\dot{m}_{35}C_{p35}\right)\left(T^{w}_{i+1}-T^{w}_{i}\right)-\frac{\alpha^{v}dA}{2}\left[T^{v}_{i}+T^{v}_{i+1}-\left(\Theta'_{i}+\Theta'_{i+1}\right)T^{dew}-\left(\Omega'_{i}+\Omega'_{i+1}\right)\right]=0
\end{aligned}
\tag{5.44}
$$

where $\Phi'_i=C_4$, $\Theta'_i=C_5$ and $\Omega'_i=C_6$ in Eq. (5.42) if the ith node is in the thermal entrance region or $\Phi'_i=D_4$, $\Theta'_i=D_5$ and $\Omega'_i=D_6$ in Eq. (5.43) if it is not.

5.2.3 Energy balance for vapour flow

Using Eq. (5.10), Eq. (5.11) can be rewritten as

$$
\begin{aligned}
\sum\dot{Q}&=\dot{m}^{v}_{i}\left(h^{v}_{i}-h^{v}_{i+1}\right)-d\dot{m}_{i}\left(h^{v}-h^{v}_{i+1}\right)+\alpha^{v}dA\Delta T^{v}_{avg}\\
&=\dot{m}^{v}_{i}C^{v}_{p}\left(T^{v}_{i}-T^{v}_{i+1}\right)-d\dot{m}_{i}C^{v}_{p}\left(T^{v}-T^{v}_{i+1}\right)+\frac{\alpha^{v}dA}{2}\left(T^{v}_{i}+T^{v}_{i+1}-T^{i}_{i}-T^{i}_{i+1}\right)=0
\end{aligned}
\tag{5.45}
$$

The temperature of the vapour being generated in the ith control volume can be assumed as $T^{v}=(T^{i}_{i}+T^{i}_{i+1})/2$. Then Eq. (5.45) becomes

$$\left(\dot{m}_i^v C_p^v + \frac{\alpha^v dA}{2}\right) T_i^v - \left(\dot{m}_{i+1}^v C_p^v - \frac{\alpha^v dA}{2}\right) T_{i+1}^v - \left[\frac{\left(\dot{m}_i - \dot{m}_{i+1}\right) C_p^v + \alpha^v dA}{2}\right]\left(T_i^i + T_{i+1}^i\right) = 0 \quad (5.46)$$

The interface temperatures in Eq. (5.46) are given in Eq. (5.42) and (5.43). Then Eq. (5.46) can be rewritten as

$$\begin{aligned}&\left(\dot{m}_i^v C_p^v + \frac{\alpha^v dA}{2}\right) T_i^v - \left(\dot{m}_{i+1}^v C_p^v - \frac{\alpha^v dA}{2}\right) T_{i+1}^v \\ &- \left[\frac{\left(\dot{m}_i - \dot{m}_{i+1}\right) C_p^v + \alpha^v dA}{2}\right]\left[\Phi_i' T_i^b + \Phi_i' T_{i+1}^b + \left(\Theta_i' + \Theta_{i+1}'\right) T^{dew} + \left(\Omega_i' + \Omega_{i+1}'\right)\right] = 0\end{aligned} \quad (5.47)$$

where Φ'$_i$=C$_4$, Θ'$_i$=C$_5$ and Ω'$_i$=C$_6$ in Eq. (5.42) if the ith node is in the thermal entrance region or Φ'$_i$=D$_4$, Θ'$_i$=D$_5$ and Ω'$_i$=D$_6$ in Eq. (5.43) if it is not.

5.2.4 Implementation of the generator model

In the previous sections, five governing equations were derived as summarized in Table 5.1 for each differential element. For a generator with *n* differential elements, the total number of equations is thus 5*n*.

Table 5.1 Summary of the final equations for generator

Equations	Reference
LiBr mass balance for liquid film: $\dot{m}_{i+1}\boldsymbol{x}_{\boldsymbol{i+1}}^{\boldsymbol{b}} = \dot{m}_i x_i^b$	Eq. (5.2)
Energy balance for liquid film: $-\left(\dot{m}_i C_{p,i}^l - \frac{\alpha^v dA}{2}\Phi_i'\right)\boldsymbol{T}_{\boldsymbol{i}}^{\boldsymbol{b}} + \left(\dot{m}_{i+1} C_{p,i}^l + \frac{\alpha^v dA}{2}\Phi_{i+1}'\right)\boldsymbol{T}_{\boldsymbol{i+1}}^{\boldsymbol{b}} + \left[a_{x=x_i} h^{fg} + C_p^v (T^v - T_i^s) + C_{p,i}^l T_{i+1}^s\right]\left(\boldsymbol{\dot{m}}_{\boldsymbol{i}} - \boldsymbol{\dot{m}}_{\boldsymbol{i+1}}\right)$ $-\left(\dot{m}_{35} C_{p35}\right)\left(\boldsymbol{T}_{\boldsymbol{i+1}}^{\boldsymbol{w}} - \boldsymbol{T}_{\boldsymbol{i}}^{\boldsymbol{w}}\right) - \frac{\alpha^v dA}{2}\left[\boldsymbol{T}_{\boldsymbol{i}}^{\boldsymbol{v}} + \boldsymbol{T}_{\boldsymbol{i+1}}^{\boldsymbol{v}} - \left(\Theta_i' + \Theta_{i+1}'\right)\boldsymbol{T}^{\boldsymbol{dew}}\right] = -\frac{\alpha^v dA}{2}\left(\Omega_i' + \Omega_{i+1}'\right)$	Eq. (5.44)
Overall heat transfer: $\dot{m}_{35} C_{p35}(\boldsymbol{T}_{\boldsymbol{i+1}}^{\boldsymbol{w}} - \boldsymbol{T}_{\boldsymbol{i}}^{\boldsymbol{w}}) - \frac{UdA}{2}\left(\boldsymbol{T}_{\boldsymbol{i}}^{\boldsymbol{w}} + \boldsymbol{T}_{\boldsymbol{i+1}}^{\boldsymbol{w}} - \boldsymbol{T}_{\boldsymbol{i}}^{\boldsymbol{b}} - \boldsymbol{T}_{\boldsymbol{i+1}}^{\boldsymbol{b}}\right) = 0$	Eq. (5.6)
Mass transfer in liquid film: $\boldsymbol{\dot{m}}_{\boldsymbol{i}} - \boldsymbol{\dot{m}}_{\boldsymbol{i+1}} - \frac{\rho K dA}{2}\left[\Phi_i \boldsymbol{T}_{\boldsymbol{i}}^{\boldsymbol{b}} + \Phi_{i+1}\boldsymbol{T}_{\boldsymbol{i+1}}^{\boldsymbol{b}} + \left(\Theta_i + \Theta_{i+1}\right)\boldsymbol{T}^{\boldsymbol{dew}}\right] = \frac{\rho K dA}{2}\left(\Omega_i + \Omega_{i+1}\right)$	Eq. (5.37)
Energy balance for vapour flow: $\left(\dot{m}_i^v C_p^v + \frac{\alpha^v dA}{2}\right)\boldsymbol{T}_{\boldsymbol{i}}^{\boldsymbol{v}} - \left(\dot{m}_{i+1}^v C_p^v - \frac{\alpha^v dA}{2}\right)\boldsymbol{T}_{\boldsymbol{i+1}}^{\boldsymbol{v}}$ $-\left[\frac{\left(\dot{m}_i - \dot{m}_{i+1}\right) C_p^v + \alpha^v dA}{2}\right]\left[\Phi_i'\boldsymbol{T}_{\boldsymbol{i}}^{\boldsymbol{b}} + \Phi_i'\boldsymbol{T}_{\boldsymbol{i+1}}^{\boldsymbol{b}} + \left(\Theta_i' + \Theta_{i+1}'\right)\boldsymbol{T}^{\boldsymbol{dew}}\right] = \left[\frac{\left(\dot{m}_i - \dot{m}_{i+1}\right) C_p^v + \alpha^v dA}{2}\right]\left(\Omega_i' + \Omega_{i+1}'\right)$	Eq. (5.47)

* Only the bold characters are treated as independent variables in the solution process.

On the other hand, six primary variables, namely T^w, T^b, x^b, $\dot{m}$, T^v and T^{dew}, were identified. Given the working pressure or corresponding dew temperature, T^{dew}, the total number of unknowns is thus 5(*n*+1) for the generator with *n* differential elements. Therefore, the generator can be solved only when the boundary conditions are given for the rest of the variables. In a system simulation, these boundary conditions and even the working pressure are determined in the relations with other components but they are arbitrarily given in this section for illustration of the solution process. The solution method is briefly introduced in the following.

Given the working pressure, for a generator with n differential elements, $5n$ equations and 5 boundary conditions form the following matrix equation.

$$[A][B]=[C] \tag{5.48}$$

where [A] is a $5(n+1)\times5(n+1)$ coefficient matrix, [B] is a $5(n+1)\times1$ column matrix for the unknowns (solution vector) and [C] a $5(n+1)\times1$ column matrix for the residuals and boundary conditions. Although no special matrix solver is required to solve Eq. (5.48), Cholesky's method has been chosen for its good computational economics (James et al, 1985).

The components of [B] are defined for i=1 to n+1 by

$$B_{k(n+1)+i} = \begin{array}{ll} T^{w}_{i} & \text{for k=0} \\ T^{b}_{i} & \text{for k=1} \\ x^{b}_{i} & \text{for k=2} \\ \dot{m}_{i} & \text{for k=3} \\ T^{v}_{i} & \text{for k=4} \end{array} \tag{5.49}$$

An augmented coefficient matrix, which is the matrix [A] added with an extra column for the components c_i from [C], is formed using the governing equations and boundary conditions as follows.

$$\tilde{A} = \left[\begin{array}{ccc|c} a_{1,1} & \cdot & a_{1,5(n+1)} & c_1 \\ \cdot & \cdot & \cdot & \cdot \\ a_{5(n+1),1} & \cdot & a_{5(n+1),5(n+1)} & c_{5(n+1)} \end{array}\right] \tag{5.50}$$

Once matrix $\tilde{A}$ is complete, a matrix solver subroutine is called and determines the $5n$ unknowns.

Iteration of Eq. (5.48) is necessary because some of the components in [A] include the primary variables. Consequently, the matrix [A] should be updated from the previous intermediate solution and Eq. (5.48) should be solved repeatedly until the convergence criteria are met. A relaxation factor can be used between intermediate solutions to stabilize the solution process as in

$$b^{j}_{i}=R\cdot b^{j}_{i}+(1-R)b^{j-1}_{i} \tag{5.51}$$

where the 'b^j_i' denotes the i^th^ component of the solution vector [B] from the j^th^ iteration step and 'R' is the relaxation factor between 0 to 1.

The number of differential control volumes n should be decided considering the accuracy of the solution and the required memory size and computing time. Near the entrance where temperature and concentration profiles are developing, finer elements would be necessary to follow the rapid changes. But such a small element is not necessary downstream, where profiles are already developed and it would only waste computer memory and would delay the solution process. Non-uniform grid would be desirable in this situation.

In order to provide a reference, solution has been obtained using 200 evenly sized differential elements for a 1 m-long generator, i.e. the length of each control volume is 5 mm. A strongly subcooled 50 wt% solution with 66°C (T^S=74.3°C at 11.5kPa) was supplied at the top so that rapid changes of temperature and concentration profiles can be clearly seen. The solution is shown in Fig. 5.6.

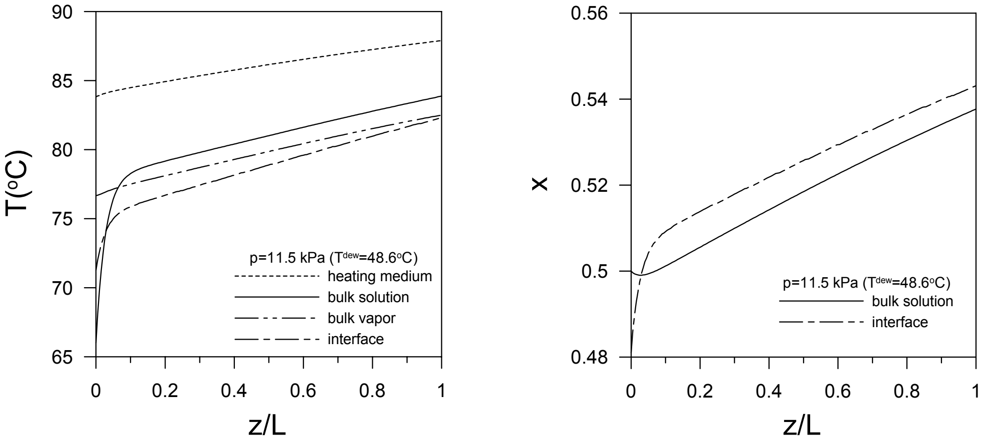

(a) Temperature profiles (b) Concentration profiles

Figure 5.6 Uniform grid solution for generator

Note that the bulk and the interface temperature profiles cross at around z/L=0.03. This profile crossover means that absorption takes place in the entrance region due to the subcooling of the supplied solution.

Note also that the profiles change rapidly until z/L=0.2 and become almost linear after that. It suggests that the fine grids are not necessary downstream. In order to save memory and computing time, several non-uniform grid systems have been considered. It was found that an exponential grid could provide economic and accurate solutions. Position of the i^{th} node in such an exponential grid system is given by

$$\frac{z_i}{L} = \frac{\exp\left[F\left(i-1\right)\right]-1}{\exp\left(Fn\right)-1} \tag{5.52}$$

where 'n' is the total number of control volumes and 'F' is an adjustable constant for varying grid sizes. Fig. 5.7 compares an exponential grid solution and the uniform grid solution from Fig. 5.6 on a logarithmic scale.

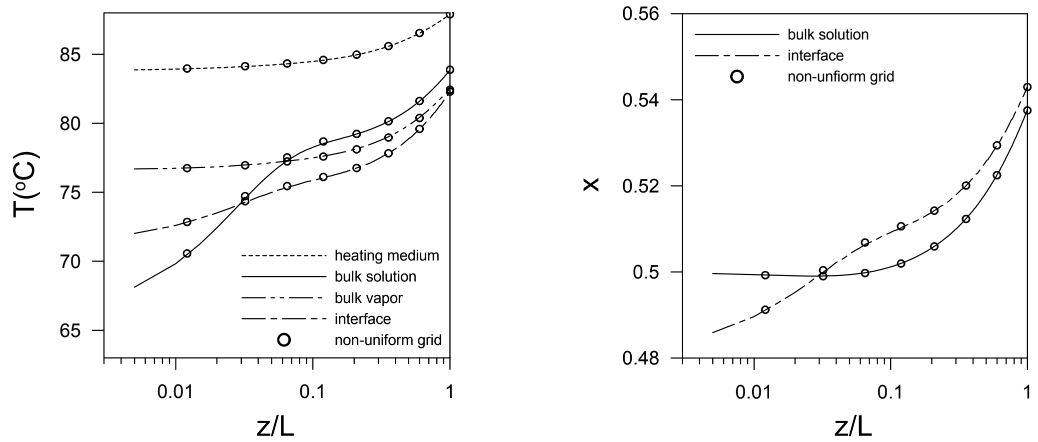

(a) Temperature profiles (b) Concentration profiles

Figure 5.7 Uniform and non-uniform grid solutions for generator

Grid sizes were chosen from Eq. (5.52) with F=0.5 and n=8 for the non-uniform grid solution in Fig. 5.7. The same convergence criterion was applied to both solutions, which requires that the two consecutive solutions for the bulk concentration at the generator outlet should be within the absolute difference of 10^{-6} (i.e. 0.0001 LiBr weight %).

The uniform solution converged after 16 iterations and non-uniform did after 13. The computing time was 226.31 sec for the uniform solution and 0.11 sec for the non-uniform solution on an Intel Pentium 4 PC (CPU clock speed 2.4GHz). This particular uniform grid solution cost 22.3 times more memory and 2057 times more computing time than the non-uniform grid solution. On the other hand, the differences between the two solutions are 3×10^{-3}K and 0.017 wt% respectively in the bulk temperature and concentration at the generator outlet, which are negligible in the present application.

Although convergence of a solution is influenced by many factors, advantage of using a non-uniform grid is clear in the example above. In order to save memory and computing time, a properly selected non-uniform grid will be used in the simulations.

5.3 Mid-Pressure Absorber

The MPA (Mid-Pressure Absorber) is a water-cooled absorber that takes the refrigerant vapour from the MPE (Mid-Pressure Evaporator) at the middle system pressure. A schematic diagram is given in Fig. 5.8 for the MPA.

Note that in Fig. 5.8, the direction of the vapour flow in the i^{th} liquid control volume is drawn opposite to the actual direction to be consistent with the sign convention used for the generator.

The MPA is a coiled tube at the top of which a solution distributor is mounted. Solution flows downward along the outer surface of the coil while cooling water flows spirally upwards inside the tube coil.

The source of refrigerant vapor, MPE is built around MPA to minimize the distance that the vapour must travel. Since the bulk vapour flows horizontally into the solution in this arrangement, the heat transfer between vapour and the solution can be neglected.

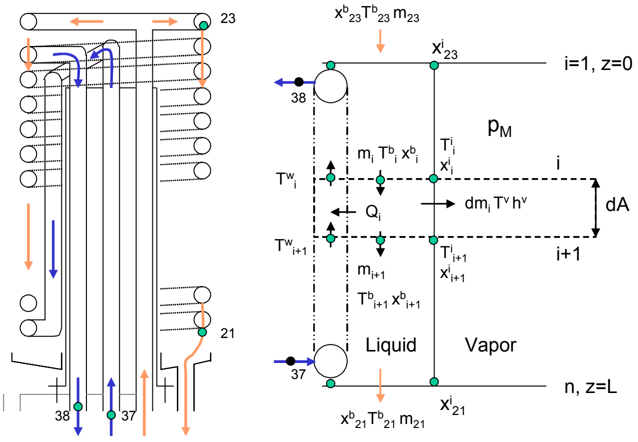

Figure 5.8 Schematic diagram of MPA and the control volume

Several assumptions were made to simplify the model, which are

- The geometry can be approximated to a vertical plate with equivalent capacity
- Cooling water flow is counter-current to the solution flow
- Pressure drop along the vapour flow is negligible
- Heat transfer between solution and vapour is negligible

From these assumptions, the governing equations of MPA become identical to those of the generator except for the negligible liquid-vapor heat transfer.

For the ith liquid control volume shown in Fig. 5.8, the following governing equations can be derived.

Total mass balance for liquid film:

$$\sum \dot{m} = \dot{m}_i - d\dot{m}_i - \dot{m}_{i+1} = 0 \tag{5.53}$$

LiBr mass balance for liquid film:

$$\sum \dot{m}_{LiBr} = \dot{m}_i x_i^b - \dot{m}_{i+1} x_{i+1}^b = 0 \tag{5.54}$$

Energy balance for liquid film:

$$\sum \dot{Q} = \dot{Q}_i - \dot{m}_{37} C_{p37} (T_{i+1}^w - T_i^w) = 0 \tag{5.55}$$

where the absorption heat $\dot{Q}_i$ is defined by

$$\dot{Q}_i = \dot{m}_{i+1} h_{i+1} + d\dot{m}_i h^v - \dot{m}_i h_i \tag{5.56}$$

Overall heat transfer:

$$\sum \dot{Q} = \dot{m}_{37} C_{p37} (T_{i+1}^w - T_i^w) - U dA \Delta T_{avg} = 0 \tag{5.57}$$

where ΔT_{avg} denotes the mean temperature difference between the two flows defined by

$$\Delta T_{avg} \equiv \frac{1}{2}\left(T_i^w + T_{i+1}^w - T_i^b - T_{i+1}^b\right) \tag{5.58}$$

Mass transfer in liquid film:

$$\sum \dot{m}_{H_2O} = d\dot{m}_i - \rho K dA \Delta x_{avg} = 0 \tag{5.59}$$

where Δx_{avg} denotes the mean concentration difference between bulk and interface defined by

$$\Delta x_{avg} \equiv \frac{1}{2}\left(x_i^i + x_{i+1}^i - x_i^b - x_{i+1}^b\right) \tag{5.60}$$

Note that the governing equations are the same as those for the generator except that the heat transfer term between liquid and vapour is neglected in Eq. (5.55).

Except for Eq. (5.55), all the other equations are identical to those of the generator and therefore the final equations will not be repeated.

5.3.1 Energy balance for liquid film

Eq. (5.55) is transformed in a way similar to the case of the desorption heat in section 5.2.2.

From Eq. (C2.17) in Appendix C2, for the ith liquid control volume in Fig. 5.8, the absorption heat $\dot{Q}_i$ can be written as

$$\dot{Q}_i = \dot{m}_{i+1} C_{p,i+1}^l (T_{i+1}^s - T_i^s) + d\dot{m}_i \left[a_{x=x_{i+1}} h^{fg} + C_p^{\mathrm{v}} (T^v - T_{i+1}^s) \right] \tag{5.61}$$

where T^s denotes equilibrium temperature at the corresponding bulk concentration and the working pressure. Note that the interface temperature in the last bracket on right-hand side is T^s_{i+1}, not T^s_i as in Eq. (5.38). It is because, in Appendix C2, while the point “1” in Eq. (C2.16) and Fig. C2.1 is the starting point of desorption process, that of Eq. (C2.17) and Fig. C2.3 is the end point of absorption process.

Since Eq. (5.61) is only valid for saturated solutions, taking account of the non-equilibrium solution temperatures at the inlet and the outlet and replacing $C^l_{p,i+1}=C^l_{p,i}$ and $d\dot{m}_i = \dot{m}_i - \dot{m}_{i+1}$, $\dot{Q}_i$ becomes

$$\begin{aligned} \dot{Q}_i &= \dot{m}_{i+1} C_{p,i+1}^l (T_{i+1}^s - T_i^s) + d\dot{m}_i \left[a_{x=x_{i+1}} h^{fg} + C_p^{\mathrm{v}} (T^v - T_{i+1}^s) \right] \\ &\qquad - \dot{m}_{i+1} C_{p,i+1}^l (T_{i+1}^s - T_{i+1}^b) + \dot{m}_i C_{p,i}^l (T_i^s - T_i^b) \\ &= \left(\dot{m}_{i+1} C_{p,i}^l\right) T_{i+1}^b - \left(\dot{m}_i C_{p,i}^l\right) T_i^b + \left(\dot{m}_i - \dot{m}_{i+1}\right)\left[a_{x=x_{i+1}} h^{fg} + C_{p,i}^l T_i^s + C_p^{\mathrm{v}} (T^v - T_{i+1}^s) \right] \end{aligned} \tag{5.62}$$

Finally, inserting Eq. (5.62) into Eq. (5.55) gives

$$\left(\dot{m}_{i+1}C^{l}_{p,i}\right)T^{b}_{i+1}-\left(\dot{m}_{i}C^{l}_{p,i}\right)T^{b}_{i}-\dot{m}_{37}C_{p37}(T^{w}_{i+1}-T^{w}_{i})$$
$$+\left(\dot{m}_{i}-\dot{m}_{i+1}\right)\left[a_{x=x_{i+1}}h^{fg}+C^{l}_{p,i}T^{s}_{i}+C^{\mathrm{v}}_{p}(T^{v}-T^{s}_{i+1})\right]=0 \qquad (5.63)$$

5.3.2 *Implementation of the MPA model*

The solution process is the same as for the generator except that there are now 5 primary variables, namely T^{w}, T^{b}, x^{b}, $\dot{m}$ and T^{dew}. The governing equations in their final forms are summarized in Table 5.2.

Table 5.2 Summary of the final equations for the MPA

Equations	Reference
LiBr mass balance for liquid film: $\dot{m}_{i+1}\boldsymbol{x^{b}_{i+1}}=\dot{m}_{i}x^{b}_{i}$	Eq. (5.54)
Energy balance for liquid film: $\left(\dot{m}_{i+1}C^{l}_{p,i}\right)\boldsymbol{T^{b}_{i+1}}-\left(\dot{m}_{i}C^{l}_{p,i}\right)\boldsymbol{T^{b}_{i}}-\dot{m}_{37}C_{p37}(\boldsymbol{T^{w}_{i+1}}-\boldsymbol{T^{w}_{i}})$ $+\left[a_{x=x_{i+1}}h^{fg}+C^{l}_{p,i}T^{s}_{i}+C^{\mathrm{v}}_{p}(T^{v}-T^{s}_{i+1})\right]\left(\boldsymbol{\dot{m}_{i}}-\boldsymbol{\dot{m}_{i+1}}\right)=0$	Eq. (5.63)
Overall heat transfer: $\dot{m}_{37}C_{p37}(\boldsymbol{T^{w}_{i+1}}-\boldsymbol{T^{w}_{i}})-\frac{UdA}{2}\left(\boldsymbol{T^{w}_{i}}+\boldsymbol{T^{w}_{i+1}}-\boldsymbol{T^{b}_{i}}-\boldsymbol{T^{b}_{i+1}}\right)=0$	Eq. (5.57)
Mass transfer in liquid film: $\boldsymbol{\dot{m}_{i}}-\boldsymbol{\dot{m}_{i+1}}-\frac{\rho KdA}{2}\left[\Phi_{i}\boldsymbol{T^{b}_{i}}+\Phi_{i+1}\boldsymbol{T^{b}_{i+1}}+\left(\Theta_{i}+\Theta_{i+1}\right)\boldsymbol{T^{dew}}\right]=\frac{\rho KdA}{2}\left(\Omega_{i}+\Omega_{i+1}\right)$	Eq. (5.37) Eq. (5.59)

* Only the bold characters are treated as independent variables in the solution process.

With a given working pressure or the corresponding saturation temperature, T^{dew}, there are 4(*n*+1) unknowns and 4*n* equations for *n* control volumes in the MPA. Given 4 boundary conditions, Eq. (5.48) is solved with a 4(*n*+1)×4(*n*+1) coefficient matrix [A], a 4(*n*+1)×1 column matrix for residuals and a 4(*n*+1)×1 column matrix [B] for the variables that is defined for i=1 to *n*+1 by

$$B_{k(n+1)+i}=\begin{array}{ll} T^{w}_{i} & \text{for k=0} \\ T^{b}_{i} & \text{for k=1} \\ x^{b}_{i} & \text{for k=2} \\ \dot{m}_{i} & \text{for k=3} \end{array} \qquad (5.64)$$

The MPA has been solved for illustration purposes and the result is given in Fig. 5.9.

Like the generator's case, 200 evenly sized grids were used for this case. A superheated 53.0 wt% solution (T^{s}=45.3 ^{o}C at 2.08 kPa) was assumed at the top of MPA and 37 ^{o}C of coolant inlet temperature was assumed at the bottom.

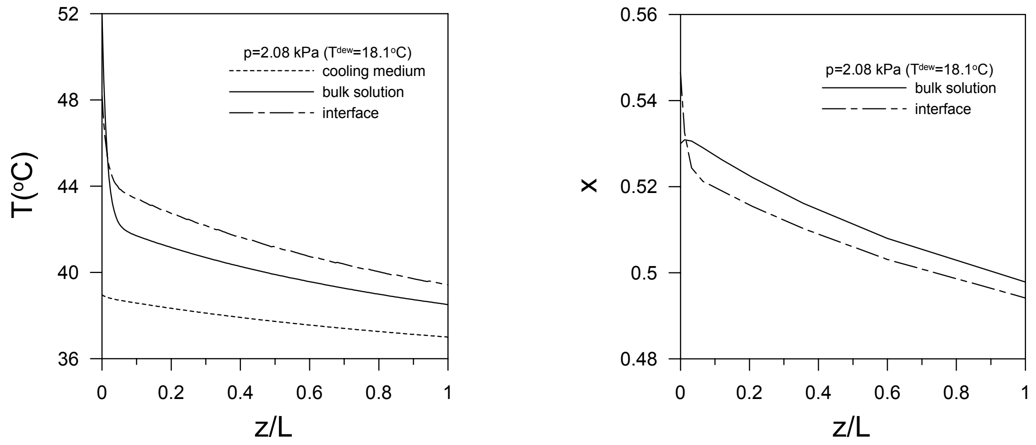

(a) Temperature profiles (b) Concentration profiles

Figure 5.9 Uniform grid solutions for MPA

Supply of the superheated solution resulted in sharp profile changes near the top. As is the case for the generator, prediction of these rapid changes requires fine grids only in the entrance region. A non-uniform grid system similar to that of the generator can also provide practically identical results as shown in Fig. 5.10.

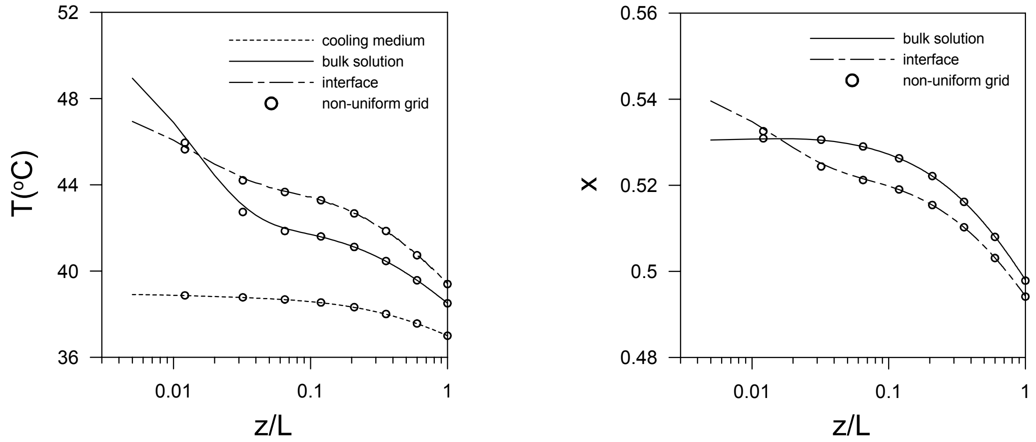

(a) Temperature profiles (b) Concentration profiles

Figure 5.10 Uniform and non-uniform grid solutions for MPA

Comparison of the uniform- and non-uniform solution showed results that are comparable to the case of the generator. The uniform grid solution cost 22.3 times more memory and 1150 times more computing time than the non-uniform grid solution. The differences between the two solutions are 5×10^{-3}K and 1.6×10^{-4} (0.016 wt%) respectively in the bulk temperature and concentration at the MPA outlet.

5.4 Low-Pressure Absorber/Mid-Pressure Evaporator

The LPA/MPE unit is a heat exchanger that has an evaporator on one side and an absorber on the other side. Since the pressure drop must be minimized on both sides, both sides were designed as falling film type. As shown in Fig. 5.11, this component is basically a large vertical tube with two circular liquid distributors mounted at the top to develop falling film flows on both sides of the tube wall.

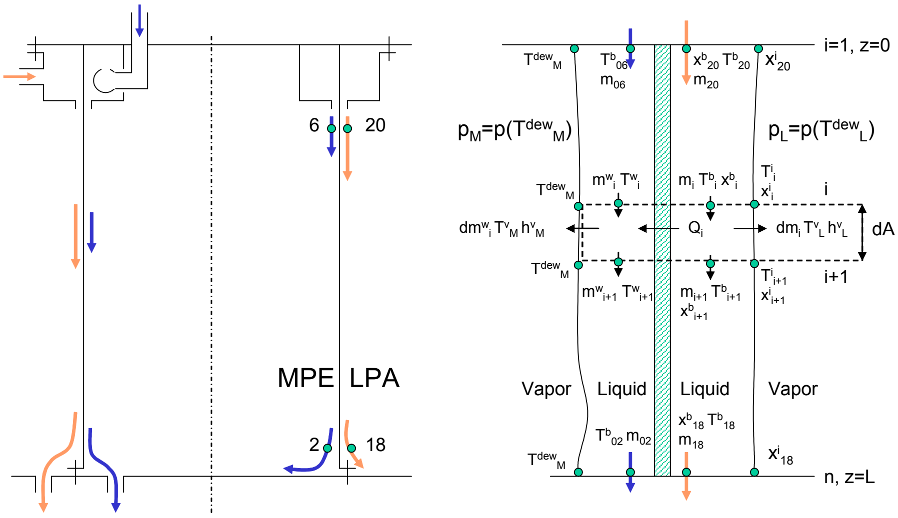

Figure 5.11 Schematic diagram of LPA/MPE unit and the control volume

The two vertical falling film flows and the control volumes are shown in Fig. 5.11. Although this component is different from the generator and the MPA by the fact that both fluids experience phase change, the modeling is essentially the same. The flow in the MPE is a special case of the falling film flow in the generator and the LPA is the same as the falling film of the MPA. Modeling of this subject is only as complicated as combining the two falling film models.

Since the MPA is mounted inside the MPE and the LPE around the LPA, the pressure drops in the vapour flows and the heat transfer to or from the vapour can be neglected.

For the ith liquid control volumes shown in Fig. 5.11, the following governing equations can be derived.

Total mass balance for liquid film on the LPA side:

$$\sum \dot{m} = \dot{m}_i - d\dot{m}_i - \dot{m}_{i+1} = 0 \tag{5.65}$$

Total mass balance for liquid film on the MPE side:

$$\sum \dot{m} = \dot{m}_i^w - d\dot{m}_i^w - \dot{m}_{i+1}^w = 0 \tag{5.66}$$

LiBr mass balance for liquid film on the LPA side:

$$\sum \dot{m}_{LiBr} = \dot{m}_i x_i^b - \dot{m}_{i+1} x_{i+1}^b = 0 \tag{5.67}$$

Energy balance for liquid film on the LPA side:

$$\sum \dot{Q} = (\dot{m}_{i+1} h_{i+1} + d\dot{m}_i h_L^v - \dot{m}_i h_i) + \dot{Q}_i = 0 \tag{5.68}$$

where $\dot{Q}_i$ is the heat transfer rate from the LPA to the MPE.

Energy balance for liquid film on the MPE side:

$$\sum \dot{Q} = (\dot{m}_{i+1}^{w} h_{i+1}^{w} + d\dot{m}_{i}^{w} h_{M}^{v} - \dot{m}_{i}^{w} h_{i}^{w}) - \dot{Q}_{i} = 0 \tag{5.69}$$

Overall heat transfer:

$$\sum \dot{Q} = \dot{Q}_{i} - UdA\Delta T_{avg} = 0 \tag{5.70}$$

where ΔT_{avg} denotes the mean temperature difference between the two flows defined by

$$\Delta T_{avg} \equiv \frac{1}{2}\left(T_{i}^{b} + T_{i+1}^{b} - T_{i}^{w} - T_{i+1}^{w}\right) \tag{5.71}$$

Mass transfer in liquid film on the LPA side:

$$\sum \dot{m}_{H_2O} = d\dot{m}_{i} - \rho K dA \Delta x_{avg} = 0 \tag{5.72}$$

where Δx_{avg} denotes the mean concentration difference between bulk and interface defined by

$$\Delta x_{avg} \equiv \frac{1}{2}\left(x_{i}^{i} + x_{i+1}^{i} - x_{i}^{b} - x_{i+1}^{b}\right) \tag{5.73}$$

Heat transfer at the vapor-liquid interface on the MPE side:

$$\sum \dot{Q} = d\dot{m}_{i}^{w} h^{fg} - \alpha^{w} dA \Delta T_{avg}^{w} = 0 \tag{5.74}$$

where α^w denotes the liquid-side heat transfer coefficient near the vapor-liquid interface and ΔT_{avg}^{w} denotes the mean temperature difference between bulk and interface defined by

$$\Delta T_{avg}^{w} \equiv \frac{1}{2}\left(T_{i}^{w} + T_{i+1}^{w} - 2T_{M}^{dew}\right) \tag{5.75}$$

where, in turn, the $T^{dew}{}_{M}$ denotes the interface temperature, i.e. the dew temperature of the steam at the working pressure of the MPE.

Note that a new heat transfer expression, Eq. (5.74) is added to define the relationship between bulk and interface temperatures in the MPE. This is equivalent to Eq. (5.72), the mass transfer equation of LPA, in respect that it defines the conditions at the vapor-liquid interface in LPA.

Since all the other equations are analogous to those counterparts in the previous sections or need no more treatment, the following sections will deal with only the energy balance and overall heat transfer equation, i.e. Eq. (5.68)~(5.70).

5.4.1 Energy balance for liquid film on the LPA side

Combining Eq. (5.68) and (5.70) gives

$$(\dot{m}_{i+1}h_{i+1} + d\dot{m}_i h_L^{\mathrm{v}} - \dot{m}_i h_i) + \frac{UdA}{2}\left(T_i^b + T_{i+1}^b - T_i^w - T_{i+1}^w\right) = 0 \tag{5.76}$$

Recalling that the terms in the 1st bracket on the left-hand side of Eq. (5.76) represents the absorption heat given by Eq. (5.62), Eq. (5.76) becomes

$$\begin{aligned}&\left(\dot{m}_{i+1}C_{p,i}^l + \frac{UdA}{2}\right)T_{i+1}^b - \left(\dot{m}_i C_{p,i}^l - \frac{UdA}{2}\right)T_i^b - \frac{UdA}{2}\left(T_i^w + T_{i+1}^w\right)\\ &\qquad + \left[a_{x=x_{i+1}} h_L^{fg} + C_{p,i}^l T_i^s + C_p^{\mathrm{v}}(T_L^v - T_{i+1}^s)\right]\left(\dot{m}_i - \dot{m}_{i+1}\right) = 0\end{aligned} \tag{5.77}$$

5.4.2 Energy balance for liquid film on the MPE side

From Eq. (5.66) and (5.69), the evaporation heat $\dot{Q}_i$ is given by

$$\begin{aligned}\dot{Q}_i &= \dot{m}_i^w\left(h_{i+1}^w - h_i^w\right) + d\dot{m}_i^w\left(h_M^{\mathrm{v}} - h_{i+1}^w\right)\\ &= \left(\dot{m}_{i+1}^w C_{p,i}^l\right)T_{i+1}^w - \left(\dot{m}_i^w C_{p,i}^l\right)T_i^w + \left(h_M^{fg} + C_{p,i}^l T_M^{dew}\right)\left(\dot{m}_i^w - \dot{m}_{i+1}^w\right)\end{aligned} \tag{5.78}$$

Note that Eq. (5.78) is identical to the expression for the desorption heat Eq. (5.40) with $T^b = T^w$, $a_{x=xi} = 1.0$, $T^v = T^s_i$ and $T^s_{i+1} = T^{dew}_M$.

Combining Eq. (5.70) and (5.78) and rearranging it gives

$$\begin{aligned}&\left(\dot{m}_{i+1}^w C_{p,i}^l + \frac{UdA}{2}\right)T_{i+1}^w - \left(\dot{m}_i^w C_{p,i}^l - \frac{UdA}{2}\right)T_i^w\\ &\qquad + \left(h_M^{fg} + C_{p,i}^l T_M^{dew}\right)\left(\dot{m}_i^w - \dot{m}_{i+1}^w\right) - \frac{UdA}{2}\left(T_i^b + T_{i+1}^b\right) = 0\end{aligned} \tag{5.79}$$

5.4.3 Implementation of the LPA/MPE model

Governing equations of the final forms are summarized in Table 5.3 below.

Table 5.3 Summary of the final equations for LPA/MPE

Equations	Reference
LiBr mass balance for liquid film on LPA side: $\dot{m}_{i+1}\boldsymbol{x_{i+1}^b} = \dot{m}_i x_i^b$	Eq. (5.67)
Energy balance for liquid film on LPA side: $\left(\dot{m}_{i+1}C_{p,i}^l + \frac{UdA}{2}\right)\boldsymbol{T_{i+1}^b} - \left(\dot{m}_i C_{p,i}^l - \frac{UdA}{2}\right)\boldsymbol{T_i^b} - \frac{UdA}{2}\left(\boldsymbol{T_i^w} + \boldsymbol{T_{i+1}^w}\right)$ $+ \left[a_{x=x_{i+1}} h_L^{fg} + C_{p,i}^l T_i^s + C_p^{\mathrm{v}}(T_L^v - T_{i+1}^s)\right]\left(\boldsymbol{\dot{m}_i} - \boldsymbol{\dot{m}_{i+1}}\right) = 0$	Eq. (5.77)
Energy balance for liquid film on MPE side:	Eq. (5.79)

$\left(\dot{m}_{i+1}^{w}C_{p,i}^{l}+\frac{UdA}{2}\right)\boldsymbol{T_{i+1}^{w}}-\left(\dot{m}_{i}^{w}C_{p,i}^{l}-\frac{UdA}{2}\right)\boldsymbol{T_{i}^{w}}+\left(h_{M}^{fg}+C_{p,i}^{l}T_{M}^{dew}\right)\left(\boldsymbol{\dot{m}_{i}^{w}}-\boldsymbol{\dot{m}_{i+1}^{w}}\right)-\frac{UdA}{2}\left(\boldsymbol{T_{i}^{b}}+\boldsymbol{T_{i+1}^{b}}\right)=0$	
Mass transfer in liquid film on LPA side: $\boldsymbol{\dot{m}_{i}}-\boldsymbol{\dot{m}_{i+1}}-\frac{\rho KdA}{2}\left[\Phi_{i}\boldsymbol{T_{i}^{b}}+\Phi_{i+1}\boldsymbol{T_{i+1}^{b}}+\left(\Theta_{i}+\Theta_{i+1}\right)\boldsymbol{T_{L}^{dew}}\right]=\frac{\rho KdA}{2}\left(\Omega_{i}+\Omega_{i+1}\right)$	Eq. (5.37) Eq. (5.72)
Heat transfer at the vapor-liquid interface on MPE side: $h_{M}^{fg}\left(\boldsymbol{\dot{m}_{i}^{w}}-\boldsymbol{\dot{m}_{i+1}^{w}}\right)-\frac{\alpha^{w}dA}{2}\left(\boldsymbol{T_{i}^{w}}+\boldsymbol{T_{i+1}^{w}}-2\boldsymbol{T_{M}^{dew}}\right)=0$	Eq. (5.74)

[*] Only the bold characters are treated as independent variables in the solution process.

In Table 5.3, 7 primary variables, namely T^w, T^b, x^b, $\dot{m}$, $\dot{m}_i^w$, $T^{dew}{}_L$ and $T^{dew}{}_M$ can be identified. Excluding the two dew temperatures associated with the working pressures, the solution vector [B] in Eq. (5.48) becomes a 5(*n*+1)×1 column matrix defined for i=1 to *n*+1 by

$$B_{k(n+1)+i} = \begin{array}{ll} T^{w}{}_{i} & \text{for k=0} \\ T^{b}{}_{i} & \text{for k=1} \\ x^{b}{}_{i} & \text{for k=2} \\ \dot{m}_{i} & \text{for k=3} \\ \dot{m}_{i}^{w} & \text{for k=4} \end{array} \qquad (5.80)$$

Given 5 boundary conditions and the two working pressures, Eq. (5.48) can be solved with a 5(*n*+1)×5(*n*+1) coefficient matrix [A] and a 5(*n*+1)×1 residual matrix [C].

The LPA/MPE unit has been solved for 200 evenly sized grids for an example and the result is given in Fig. 5.12.

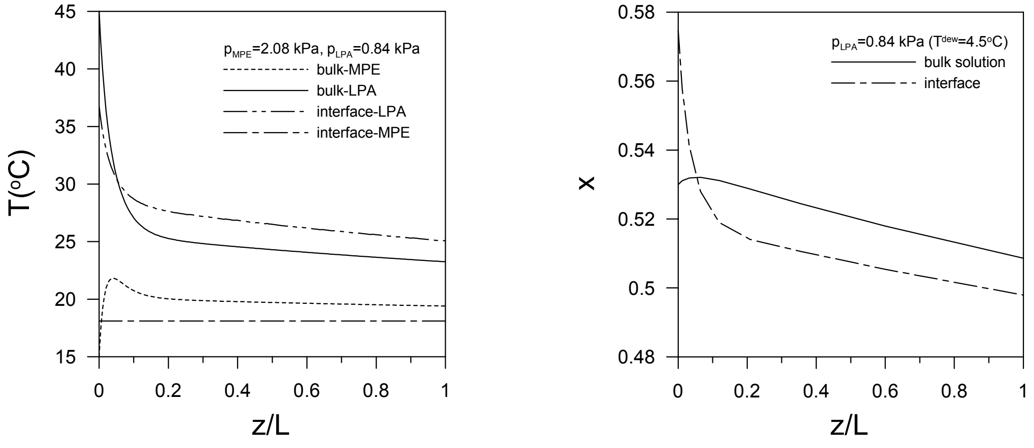

(a) Temperature profiles (b) Concentration profiles in LPA

Figure 5.12 Uniform grid solutions for LPA/MPE

In Fig. 5.12, while a superheated 53 wt% solution with 45 °C (T^s=29.9 °C at 0.84 kPa) is supplied to the LPA, a subcooled refrigerant with 15 °C is supplied to the MPE at 2.08 kPa (T^{dew}=18.1 °C). Consequently, there is a large temperature difference between the two fluids near the top and the profiles change very rapidly in that region. Profiles crossovers are observed on both sides near the top, which means that desorption takes place on the LPA side and condensation takes place on the MPE side.

It was found that the sizes of grids must be chosen with care around the inversion point of the bulk refrigerant temperature profile (z/L=0.04 in Fig. 5.12a). Coarse grids around this point can yield unrealistic solutions or cause the solution to diverge.

A non-uniform grid system that is similar to those used in the previous sections can give practically identical results as shown in Fig. 5.13.

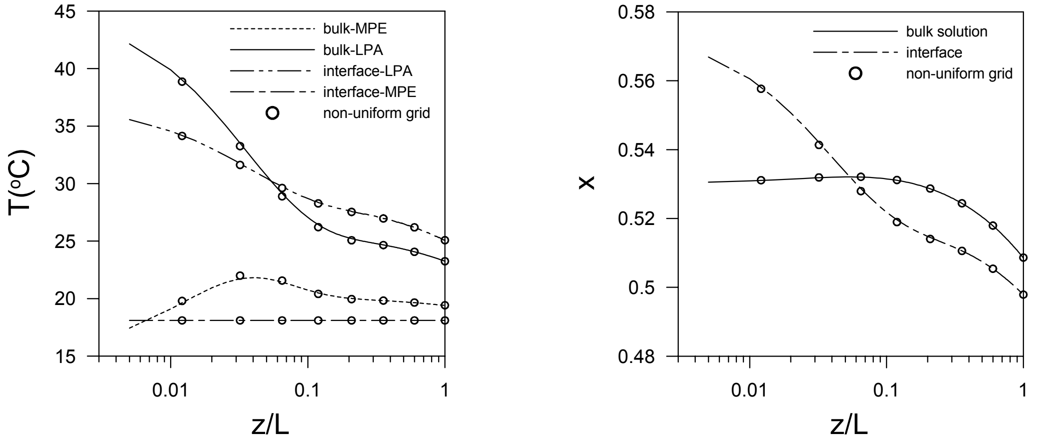

(a) Temperature profiles (b) Concentration profiles in LPA

Figure 5.13 Uniform and non-uniform grid solutions for LPA/MPE

The uniform grid solution cost 22.3 times more memory and 2061 times more computing time than the non-uniform grid solution. The differences between the two solutions are 3×10^{-3}K and 1.0×10^{-4} (0.01 wt%) respectively in the bulk temperature and concentration at the LPA outlet.

5.5 Condenser

A schematic diagram of the condenser is given in Fig. 5.14, which shows a single tube coil in a pressure vessel. Cooling water flows upwards inside the coil and refrigerant vapour condenses outside the coil to be collected at the bottom.

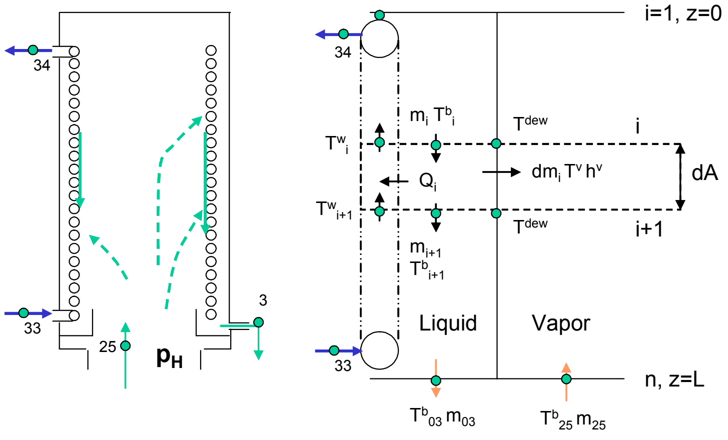

Figure 5.14 Schematic diagram of condenser and the control volume

Several assumptions were made to simplify the model, which are

- The geometry can be approximated to a vertical plate with equivalent capacity
- Cooling water flow is counter-current to the condensate flow
- Pressure drop along the vapour flow is negligible
- Heat transfer between the condensate and the vapour is negligible

By assuming condensation on a vertical plate, such effects as the mixing and transversal flows, which are likely to be present in a tube coil condenser, are all lumped into the average heat transfer coefficient to be used.

For the ith liquid control volume shown in Fig. 5.14, the following governing equations can be derived.

Total mass balance for liquid film:

$$\sum \dot{m} = \dot{m}_i - d\dot{m}_i - \dot{m}_{i+1} = 0 \tag{5.81}$$

Energy balance for liquid film:

$$\sum \dot{Q} = (\dot{m}_{i+1}h_{i+1} + d\dot{m}_i h^v - \dot{m}_i h_i) - \dot{m}_{33}C_{p33}(T_{i+1}^w - T_i^w) = 0 \tag{5.82}$$

Overall heat transfer:

$$\sum \dot{Q} = \dot{m}_{33}C_{p33}(T_{i+1}^w - T_i^w) - UdA\Delta T_{avg} = 0 \tag{5.83}$$

where ΔT_{avg} denotes the mean temperature difference between the two flows defined by

$$\Delta T_{avg} \equiv \frac{1}{2}\left(T_i^w + T_{i+1}^w\right) - T^{dew} \tag{5.84}$$

5.5.1 Overall heat transfer

Note that the temperature difference is defined between the bulk cooling water temperature and the interface temperature, i.e. T^{dew}, in Eq. (5.84). This is only to follow the definition of condensation heat transfer coefficient to be used.

Inserting Eq. (5.84) into Eq. (5.83) and rearranging it gives the overall heat transfer equation as

$$\left(\dot{m}_{33}C_{p33} - \frac{UdA}{2}\right)T_{i+1}^w - \left(\dot{m}_{33}C_{p33} + \frac{UdA}{2}\right)T_i^w + UdAT^{dew} = 0 \tag{5.85}$$

5.5.2 Energy balance for condensate film

Considering the superheating of the vapour and Eq. (5.81), Eq. (5.82) can be rewritten as

$$\begin{aligned}&\dot{m}_{i+1}C_p^l T_{i+1}^b - \dot{m}_i C_p^l T_i^b - \dot{m}_{33}C_{p33}(T_{i+1}^w - T_i^w)\\&\qquad + \left(\dot{m}_i - \dot{m}_{i+1}\right)\left[h^{fg} + C_p^v\left(T^v - T^{dew}\right) + C_p^l T^{dew}\right] = 0\end{aligned} \tag{5.86}$$

On the other hand, the bulk condensate temperature T^b can be expressed in terms of the wall temperature and the saturation temperature as

$$T^b = F_1 T^{wal} + \left(1 - F_1\right)T^{dew} \tag{5.87}$$

where the constant F_1=0.68 for laminar vertical film condensation given by Rohsenow (1973) may be used. The wall temperature, in turn, can be expressed as follows from the definitions of the heat transfer coefficients.

$$T^{wal} = F_2 T^{dew} + \left(1 - F_2\right)T^w \tag{5.88}$$

where the constant F_2 is defined as $F_2 \equiv (1/\ \alpha^l + 1/\ \alpha^w + \Delta t/k)^{-1}(1/\ \alpha^w + \Delta t/k)$ with α^l, α^w and $k/\Delta t$ denoting the heat transfer coefficient for condensation, cooling water and the wall conduction respectively.

Inserting Eq. (5.88) into Eq. (5.87) gives T^b as

$$T^b = \left(F_1 F_2 + 1 - F_1\right)T^{dew} + F_1\left(1 - F_2\right)T^w \tag{5.89}$$

Replacing T^b in Eq. (5.86) with Eq. (5.89) and rearranging it gives

$$\begin{aligned}&\left[\dot{m}_{i+1}C_p^l F_1\left(1 - F_2\right) - \dot{m}_{33}C_{p33}\right]T_{i+1}^w - \left[\dot{m}_i C_p^l F_1\left(1 - F_2\right) - \dot{m}_{33}C_{p33}\right]T_i^w\\&-\left(\dot{m}_i - \dot{m}_{i+1}\right)\left[C_p^v + C_p^l\left(F_1F_2 - F_1\right)\right]T^{dew} + \left(\dot{m}_i - \dot{m}_{i+1}\right)\left[h^{fg} + C_p^v T^v\right] = 0\end{aligned} \tag{5.90}$$

5.5.3 *Implementation of the condenser model*

As summarized in Table 5.4, three primary variables, i.e. T^w, $\dot{m}$ and T^{dew}, were used in Eq. (5.85) and (5.90) to describe each control volume in the condenser.

Table 5.4 Summary of the final equations for condenser

Equations	Reference
Overall heat transfer: $\left(\dot{m}_{33}C_{p33} - \frac{UdA}{2}\right)\boldsymbol{T_{i+1}^w} - \left(\dot{m}_{33}C_{p33} + \frac{UdA}{2}\right)\boldsymbol{T_i^w} + UdA\,\boldsymbol{T^{dew}} = 0$	Eq. (5.85)
Energy balance for condensate film: $\left[\dot{m}_{i+1}C_p^l F_1\left(1 - F_2\right) - \dot{m}_{33}C_{p33}\right]\boldsymbol{T_{i+1}^w} - \left[\dot{m}_i C_p^l F_1\left(1 - F_2\right) - \dot{m}_{33}C_{p33}\right]\boldsymbol{T_i^w}$ $-\left(\dot{m}_i - \dot{m}_{i+1}\right)\left[C_p^v + C_p^l\left(F_1F_2 - F_1\right)\right]\boldsymbol{T^{dew}} + \left[h^{fg} + C_p^v T^v\right]\left(\boldsymbol{\dot{m}_i} - \boldsymbol{\dot{m}_{i+1}}\right) = 0$	Eq. (5.90)

* Only the bold characters are treated as independent variables in the solution process.

Therefore, for *n* control volumes, there are 2*n* equations for the total number of unknowns of 2(*n*+1)+1. Besides the two boundary conditions, i.e. $\dot{m}_1 = 0.$ and $T^{W}{}_{n+1}=T_{33}$, one more restriction is required. This extra restriction is given either in terms of the dew temperature T^{dew} or the total condensation rate $\dot{m}_{n+1}$. When T^{dew} is given, $\dot{m}_{n+1}$ is calculated under the given T^{dew}. But in a system simulation, T^{dew} is calculated to keep the mass balance between the condenser and the generator, i.e. equality of the total mass condensed and generated $\left(\dot{m}_{n+1}\right)_{CON} = \left(\dot{m}_1 - \dot{m}_{n+1}\right)_{GEN}$. Fig. 5.15 shows an example of such a calculation.

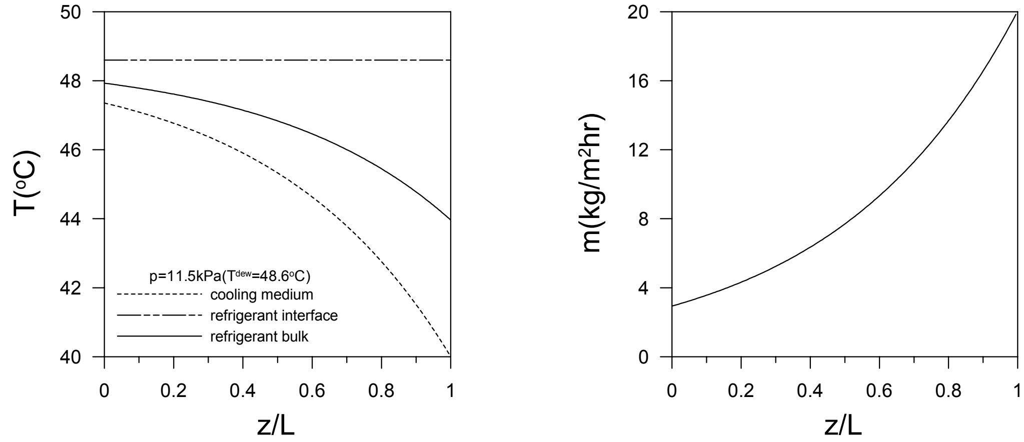

(a) Temperature profiles (b) Local mass flux

Figure 5.15 Uniform grid solutions (200 even grids) for condenser

In Fig. 5.15a, the bulk condensate temperature has been calculated from Eq. (5.87). In Fig. 5.15b, the mass flux downstream is larger due to the larger temperature difference between the coolant and the dew temperature because the coolant flows upwards.

Use of non-uniform grid is not particularly advantageous for the condenser because the temperature profiles are monotonous.

5.6 Low-Pressure Evaporator

A schematic diagram of the LPE is given in Fig. 5.16, which shows a single tube coil with a refrigerant distributor mounted at the top. Chilled water flows upwards inside the coil and refrigerant vapour evaporates outside. A tray collects unevaporated refrigerant at the bottom.

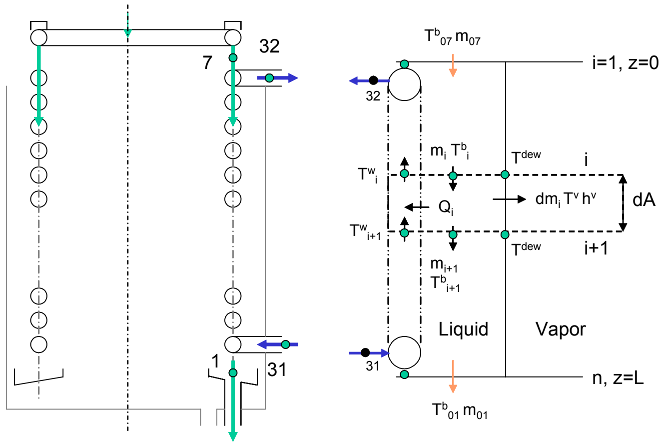

Figure 5.16 Schematic diagram of the LPE and the control volume

Several assumptions were made to simplify the model, which are

- The geometry can be approximated by a vertical plate with equivalent capacity
- Chilled water flow is counter-current to the refrigerant flow
- Pressure drop along the vapour flow is negligible
- Heat transfer between liquid and vapour is negligible

For the ith control volume in Fig. 5.16, the following governing equations are derived.

Total mass balance for liquid film:

$$\sum \dot{m} = \dot{m}_i - d\dot{m}_i - \dot{m}_{i+1} = 0 \tag{5.91}$$

Energy balance for liquid film:

$$\sum \dot{Q} = \dot{Q}_i - \dot{m}_{31} C_{p31} (T_{i+1}^w - T_i^w) = 0 \tag{5.92}$$

where evaporation heat $\dot{Q}_i$ is defined by

$$\dot{Q}_i = \dot{m}_{i+1} h_{i+1} + d\dot{m}_i h^v - \dot{m}_i h_i \tag{5.93}$$

Overall heat transfer:

$$\sum \dot{Q} = \dot{m}_{31} C_{p31} (T_{i+1}^w - T_i^w) - UdA\Delta T_{avg}^b = 0 \tag{5.94}$$

where ΔT_{avg}^b denotes the mean temperature difference between chilled water and refrigerant defined by

$$\Delta T_{avg}^b \equiv \frac{1}{2}\left(T_i^w + T_{i+1}^w - T_i^b - T_{i+1}^b\right) \tag{5.95}$$

Heat transfer in liquid film:

$$\sum \dot{Q} = d\dot{m}_i h^{fg} - \alpha^l dA\Delta T_{avg}^i = 0 \tag{5.96}$$

where α^1 the liquid-side heat transfer coefficient near the vapor-liquid interface and ΔT_{avg}^i denotes the mean temperature difference between bulk and interface defined by

$$\Delta T_{avg}^i \equiv \frac{1}{2}\left(T_i^b + T_{i+1}^b - 2T^{dew}\right) \tag{5.97}$$

Since analogous equations have been derived in the previous sections for all the equations above, only the final equations are given in Table 5.5 of Section 5.6.1.

5.6.1 Implementation of the LPE model

Three primary variables, i.e. T^w, T^b, $\dot{m}$ and T^{dew}, were used to describe this evaporator model. For each control volume, Eq. (5.92), (5.94) and (5.96) should be solved. Therefore, for n control volumes, $3n$ equations are available for the total number of unknowns of $3(n+1)+1$.

Table 5.5 Summary of the final equations for the LPE

Equations	Reference
Energy balance for refrigerant film: $\dot{m}_{i+1}C^l_{p,i}\boldsymbol{T^b_{i+1}} - \dot{m}_i C^l_{p,i}\boldsymbol{T^b_i} + \left(h^{fg} + C^l_{p,i}T^{dew}\right)\left(\boldsymbol{\dot{m}_i} - \boldsymbol{\dot{m}_{i+1}}\right) - \dot{m}_{31}C_{p31}(\boldsymbol{T^w_{i+1}} - \boldsymbol{T^w_i}) = 0$	Eq. (5.92)
Overall heat transfer: $\left(\dot{m}_{31}C_{p31} - \frac{UdA}{2}\right)\boldsymbol{T^w_{i+1}} - \left(\dot{m}_{31}C_{p31} + \frac{UdA}{2}\right)\boldsymbol{T^w_i} + \frac{UdA}{2}\left(\boldsymbol{T^b_i} + \boldsymbol{T^b_{i+1}}\right) = 0$	Eq. (5.94)
Heat transfer in liquid film: $h^{fg}\left(\boldsymbol{\dot{m}_i} - \boldsymbol{\dot{m}_{i+1}}\right) - \frac{\alpha^l dA}{2}\left(\boldsymbol{T^b_i} + \boldsymbol{T^b_{i+1}} - 2\boldsymbol{T^{dew}}\right) = 0$	Eq. (5.96)

* Only the bold characters are treated as independent variables in the solution process.

Given the working pressure T^{dew}, the system can be solved with three boundary conditions, e.g. T^w_{n+1}, T^b_1, $\dot{m}_1$. But in a system simulation, T^{dew} should be determined to keep the mass balance between the LPE and LPA, i.e. equality of the total mass evaporated and absorbed $\left(\dot{m}_1 - \dot{m}_{n+1}\right)_{LPE} = \left(\dot{m}_{n+1} - \dot{m}_1\right)_{LPA}$.

For the purpose of illustration, LPE is solved assuming that superheated liquid refrigerant is supplied at the top with 15 °C and a working pressure of 0.84 kPa (T^{dew}=4.5 °C). Fig. 5.17 shows the result.

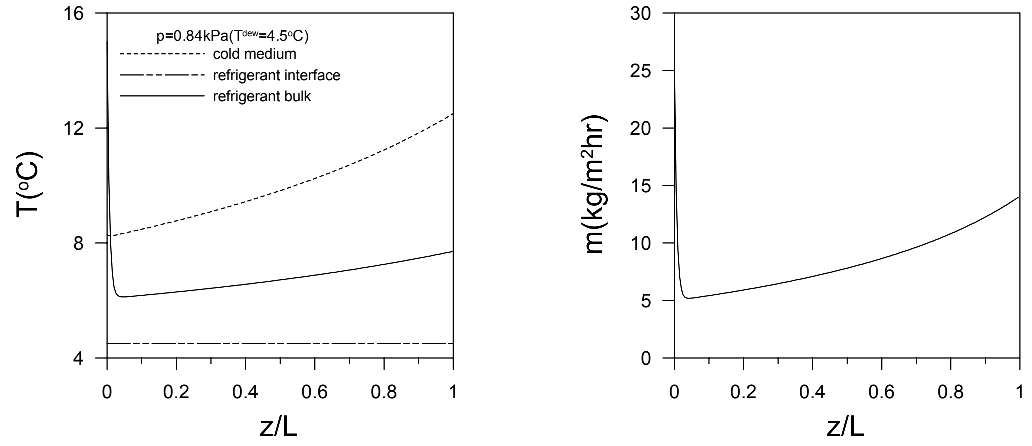

(a) Temperature profiles (b) Local mass flux

Figure 5.17 Uniform grid solutions (200 evenly sized) for LPE

Because the supplied refrigerant is significantly superheated, evaporation takes place very quickly near the top. This is why the mass flux is excessively high in this region in Fig. 5.17b.

Very fine grids are required to predict such rapid profile changes as in Fig. 5.17. Profiles downstream are, however, smooth and do not require such fine grids. Non-uniform grids such as used in the other components would effectively improve the solver performance. Fig. 5.18 shows an example of such a non-uniform grid solution.

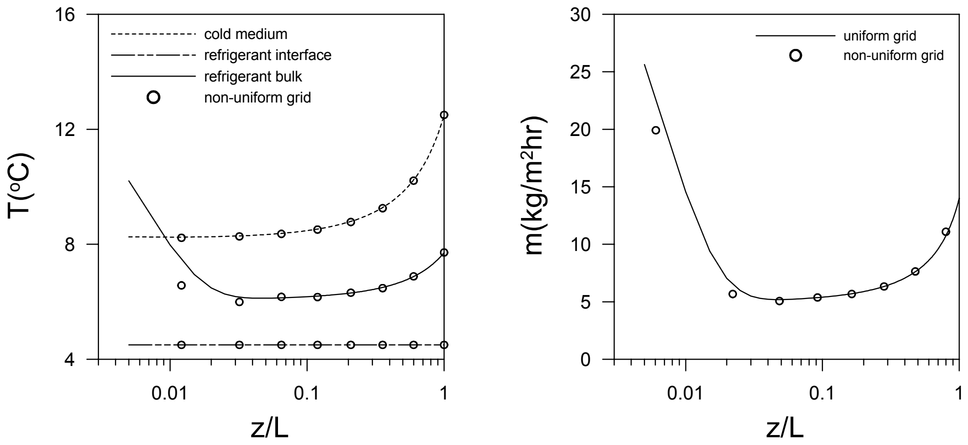

(a) Temperature profiles (b) Local mass flux

Figure 5.18 Uniform and non-uniform grid solutions for LPE

This particular non-uniform grid solution is different from the uniform grid solution by 0.44 % (e.g. 44W for 10kW cooling) in capacity. However it was absolutely advantageous in the memory and the computing time requirements. The total number of variables was 603 for the uniform solution and it was 27 for the non-uniform solution. While the uniform solution took 49.56 sec to converge, the non-uniform solution took only 0.0625 sec.

5.7 Heat exchangers and mixing tanks

There are three single-phase heat exchangers and two mixing tanks in the system. This section summarizes the governing equations derived for these components. Fig. 5.19 shows a schematic diagram showing the flow network between these components.

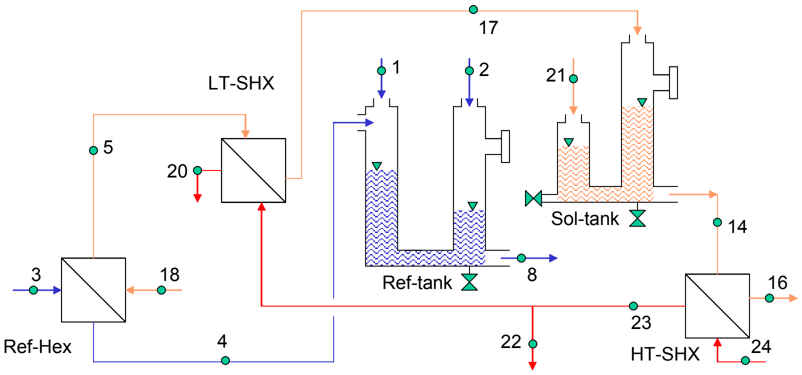

Figure 5.19 Flows between heat exchangers and mixing tanks

5.7.1 *Heat exchangers*

The ε-NTU model is used for all single-phase heat exchangers. Fig. 5.20 shows a schematic diagram of a heat exchanger.

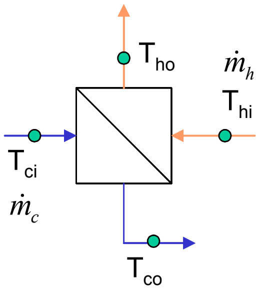

Figure 5.20 Schematic diagram of heat exchanger

For the case of minimum capacity fluid on hot side, the heat exchanger in Fig. 5.21 can be described by

$$T_{hi} - T_{ho} - \varepsilon\left(T_{hi} - T_{ci}\right) = 0 \qquad (5.98)$$

where ε is given, for the type of heat exchanger, as a function of NTU, which is in turn function of thermal capacities of the heat exchanging fluids and UA of the heat exchanger [see e.g. Holman (1997)].

Considering that hot-side fluid is minimum capacity fluid for all three heat exchangers, using the notations in Fig. 5.20, the following equations can be derived.

HT-SHX : $$T_{24} - T_{23} - \varepsilon_{\text{HT-Hex}}\left(T_{24} - T_{14}\right) = 0 \qquad (5.99)$$

LT-SHX : $$T_{23} - T_{20} - \varepsilon_{\text{LT-Hex}}\left(T_{23} - T_{05}\right) = 0 \qquad (5.100)$$

Ref-Hex : $$T_{18} - T_{05} - \varepsilon_{\text{Ref-Hex}}\left(T_{18} - T_{03}\right) = 0 \qquad (5.101)$$

5.7.2 Mixing tanks

The solution tank in Fig. 5.19 receives two solution flows at different temperatures and concentrations from the absorbers above. For the solution tank, the following equations can be derived.

Total mass balance for mixing solution:

$$\Sigma\dot{m} = \dot{m}_{18} + \dot{m}_{21} - \dot{m}_{16} = 0 \qquad (5.102)$$

LiBr mass balance for mixing solution:

$$\Sigma\dot{m}_{LiBr} = \dot{m}_{18}x_{18}^{b} + \dot{m}_{21}x_{21}^{b} - \dot{m}_{16}x_{16}^{b} = 0 \qquad (5.103)$$

Energy balance for mixing solution:

$$\Sigma\dot{Q} = \dot{m}_{18}h_{17} + \dot{m}_{21}h_{21} - \dot{m}_{14}h_{14} = 0 \qquad (5.104)$$

In the mixing process, since the concentration difference between the mixing solutions is rather small, the heat of mixing can be neglected. Then Eq. (5.104) can be approximated by

$$\dot{m}_{17}T_{17} + \dot{m}_{21}T_{21}^{b} - \dot{m}_{14}T_{14} = 0 \tag{5.105}$$

And for the refrigerant tank in Fig. 5.19, the following equations are derived.

Total mass balance for mixing refrigerant:

$$\Sigma\dot{m} = \dot{m}_{01} + \dot{m}_{02} + \dot{m}_{04} - \dot{m}_{08} = 0 \tag{5.106}$$

Energy balance for mixing refrigerant:

Neglecting the flashing of refrigerant entering the refrigerant tank at point 4 in Fig. 5.19, the energy balance equation can be written as

$$\Sigma\dot{Q} = \dot{m}_{01}T_{01}^{b} + \dot{m}_{02}T_{02}^{b} + \dot{m}_{04}T_{04} - \dot{m}_{08}T_{08} = 0 \tag{5.107}$$

5.8 Simulation results

The system in Fig. 5.1 has been simulated using the component models developed in the previous sections. Relations between different components have been specified by properly defining the boundary conditions of each component. For example, outlet conditions of the generator have to be expressed in terms of the inlet conditions of LPA and MPA, which are actually defined by the governing equations of the single-phase heat exchangers and the other components in between. The same applies for the outlet conditions of the absorbers in relation to the inlet conditions of the generator.

With the component models described above, the number of variables needed to describe the system in Fig. 5.1 is equal to the sum of the governing equations of all components, boundary conditions and three system pressures. For example, as explained in Section 5.2, the generator model has five equations for each discrete control volume as given in Table 5.1 and also five boundary conditions. Since the boundary conditions are also given in terms of equations (heat exchangers, solution tank and so on), the total number of equations to describe the generator is $5\times(n_{GEN}+1)$, where n_{GEN} is number of the discrete control volumes. And thus it is $4\times(n_{MPA}+1)$ for MPA and likewise for the other components.

Therefore including three system pressures (dew temperatures), the number of equations to describe the system in Fig. 5.1 is N:

$$N=5\times(n_{GEN}+1)+ 4\times(n_{MPA}+1) +5\times(n_{LPA\text{-}MPE}+1)+2\times(n_{CON}+1) +3\times(n_{LPE}+1)+3 \tag{5.108}$$

The resulting N governing equations could be solved in the same way as explained for the generator in Section 5.2. A N×(N+1) augmented matrix was solved by Cholesky’s method and the coefficients were renewed after each iteration until the convergence criteria were met. Some simulation results are presented in the following sections.

5.8.1 Prediction of chiller performance

First of all, the performance of the chiller designed in Ch. 3 is predicted using the models developed in the previous sections. As described in Ch. 3, most components were manufactured with less heat transfer area than demanded by the chosen refrigeration cycle in Table 3.3. The effect of these area reductions will be shown in terms of the change in system performance.

Table 5.6 summarizes the heat transfer areas in the original and the final component designs in Ch. 3.

Table 5.6 Heat transfer area in the original and final designs

Component	Original design area (m^2, Table 3.3)	Final design area (m^2)	Original/Final (-)
CON	1.98	1.50	1.33
GEN	3.74	2.76	1.36
MPA	2.22	1.20	1.85
LPA/MPE	2.25	0.94	2.39
LPE	4.80	2.25	2.13
HT-SHX	1.05	1.40	0.75
LT-SHX	0.79	1.20	0.66
Ref-Hex	0.35	0.50	0.70

As can be seen in Table 5.6, except for the three single-phase heat exchangers, all components were manufactured with less heat transfer area than required. In the following, simulation results based on the original and the final design area are compared to show influences of the changes in heat transfer area.

The accuracy of the simulation results depends on the capability to predict the transfer coefficients for the components listed in Table 5.6 in a realistic way. Among others, the prediction of heat transfer coefficients for the evaporating falling film flows in the evaporators is most important. This is because recirculation of refrigerant became essential to achieve a reasonable cooling capacity since there is no special geometry or treatment to promote wetting on the heat transfer surface in the final evaporator designs. Therefore, before anything else, an optimal refrigerant recirculation rate had to be chosen and therefore accurate description of the evaporating water films was needed.

Among the two evaporators, MPE brings bigger uncertainty to simulation because a reliable empirical correlation is hard to find for the evaporating water films on a vertical plate in the low Reynolds number range.

Without recirculation, the refrigerant flow rate per unit width (Γ, kg/ms) is 0.004 kg/ms in MPE, which is equivalent to a Reynolds number of 15.7 ($Re \equiv 4\Gamma/\mu$). For such low Reynolds numbers, only a few experimental studies are available and they show contradictory results. This is probably due to incomplete wetting of the heat transfer surface, which is often encountered when a falling film heat exchanger operates in low Reynolds number ranges. Some discussion on wetting is also given in Ch. 6 where the results of an experimental investigation on falling film flows are presented.

An overview and analysis of the experimental studies on falling film flows in the past are also given in Ch. 6. In this section, only brief description of the empirical correlations used for the simulation of falling film flows in the chiller is given. Table 5.7 lists the empirical correlations chosen.

Table 5.7 Empirical correlations used for falling film flows

Component	Correlation	Flow types	Surface wetness
CON	Nusselt (1916)	Filmwise water condensation on a horizontal tube	Complete
GEN	Wilke (1962)	Subcooled water-glycol film flows on a vertical tube	Complete
LPA			
MPA	Rogers (1981)	Subcooled water film on horizontal tubes	All
LPE			
MPE	Kim & Infante Ferreira (2006)	Subcooled water film on a vertical plate	All

Wilke (1962) has measured heat transfer coefficients for the falling film flows of water-glycol solutions on the outer surface of a 2.4m-long Φ42mm vertical tube within the Prandtl number range from 5.4 to 210. His laminar heat transfer correlation is not applicable for the flows on an incompletely wet surface because the tube surface was completely wet when he used the highly-concentrated glycol-water solution (95% glycol, Pr=210) within the low Reynolds number range (Re≈9~32). Since the kinematic viscosity of a 95% glycol-water solution is $16.8\times10^{-6}m^2/s$ at 30^oC, which is about 21 times larger than that of water, the volumetric flow rate of this solution should also be larger than that of water by the same factor to obtain the same Reynolds number. Therefore the correlation of Wilke (1962) was used only for the generator and the LPA but not for the MPE.

For water film flows on the partially wet surface of MPE, the heat transfer correlation of Kim & Infante Ferreira (2006) has been used, which is described in detail in Ch. 6.

For the falling film flows on horizontal tubes, Rogers (1981) and Armbruster and Mitrovic (1998) agree excellently with each other, which suggests that use of either study would ensure high reliability. For heat transfer coefficients of the bulk liquid films in MPA and LPE, Rogers (1981) has been chosen.

Using these empirical correlations, the COP and the cooling capacity of the chiller have been calculated changing the refrigerant recirculation flow rate. The results are shown in Fig. 5.21.

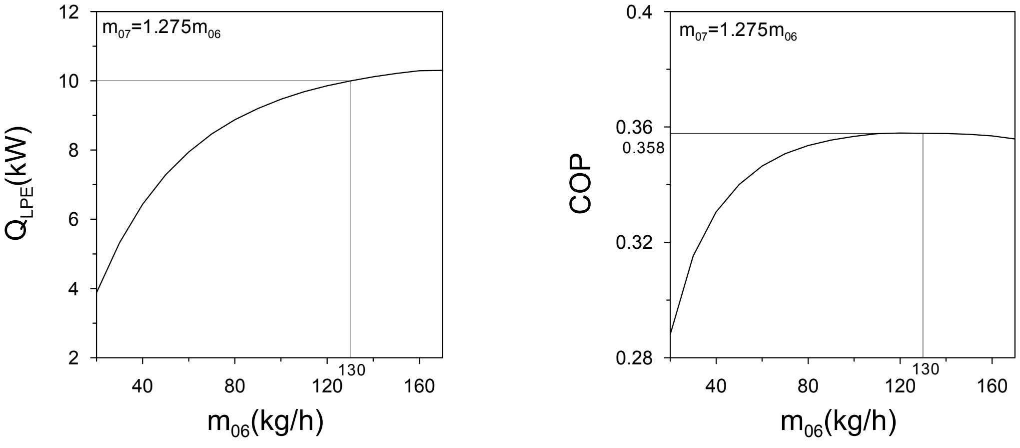

(a) Cooling capacity (b) COP

Figure 5.21 Influence of refrigerant recirculation on system performance

In Fig. 5.21, $\dot{m}_{06}$ is the refrigerant flow rate at the top of MPE. When $\dot{m}_{06}$ is changed, its equivalent in LPE, i.e. $\dot{m}_{07}$, is also changed so that both evaporators can have the same peripheral flow rate Γ (kg/ms). Considering that the perimeter of LPE is 1.275 times that of MPE, it is set that $\dot{m}_{07}=1.275\times\dot{m}_{06}$.

Fig. 5.21a shows that cooling capacity increases rapidly with the recirculation rate in the beginning but later approaches a certain limit. The COP shows a similar trend in the beginning but slightly decreases after a maximum.

It is clearly shown in Fig. 5.21 how important it is to have good heat transfer performance in the evaporators. Without recirculation, COP and cooling capacity would be less than 0.29 and 4kW respectively. This will be seen again in the next Section where the influence on the system performance of heat and mass transfer performance in each component is examined.

For 10kW cooling capacity, it is predicted that in total, about 300kg/h of refrigerant recirculation would be needed. The COP is predicted to be 0.358.

In order to evaluate the influence of the design changes from the original and the final design as listed in Table 5.6, the cooling capacity and the COP have been calculated for both designs. The results are presented in Fig. 5.22 for different heating (T_{35}) and cooling water temperatures (T_{37}).

The solution flow at the generator inlet and all secondary heat transfer media were maintained at the flow rates listed in Table 3.3 of Ch. 3.

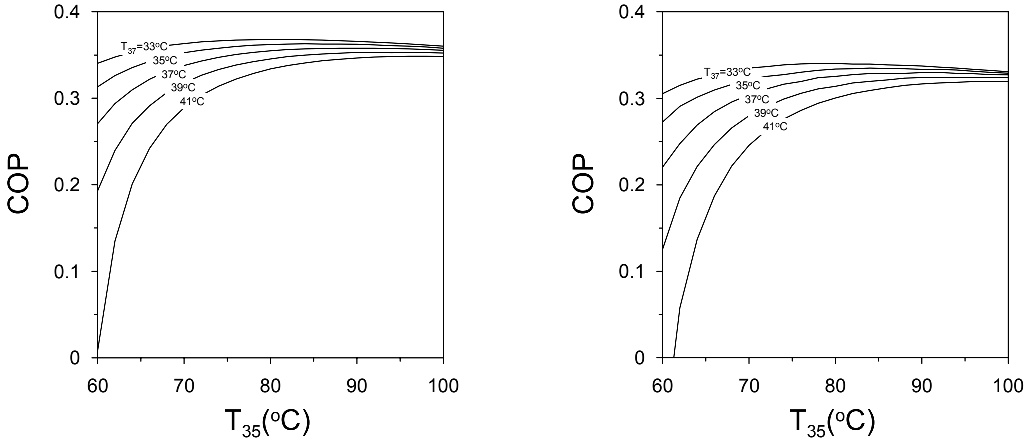

(a) Original design (b) Final design

Figure 5.22 Predicted COPs for various heat transfer medium temperatures

Fig. 5.22a shows the COP of the chiller with the original component designs. For a certain cooling medium temperature, the COP firstly increases rapidly and then levels or slightly decreases with increasing heating medium temperature. The same trend is found in Fig. 5.22b for the chiller with the final component designs. At the design cooling- and heating medium temperatures, i.e. T_{35}=88°C and T_{37}=37°C, COPs in Fig. 5.22a and 5.22b are 0.358 and 0.329 respectively.

Compared with the decrease in COP, reduction of cooling capacity is substantial as shown in Fig. 5.23. At the design point, while cooling capacity of the originally designed chiller is

10kW, that of the final design is predicted to be 5.73kW. In average, the cooling capacity in Fig. 5.23b is about 56% of that in Fig. 5.23a.

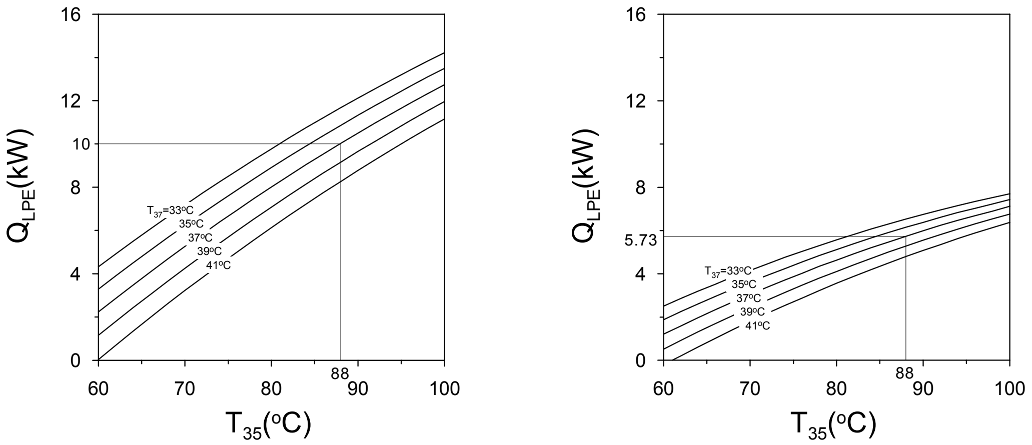

(a) Original design (b) Final design

Figure 5.23 Predicted cooling capacities for various heat transfer medium temperatures

In the following section, the influence on the system performance of each design parameter will be examined. Differences between the original and the final designs will also be evaluated.

5.8.2 Influence of heat transfer area

Each change in the component designs in Table 5.6 contributes to the discrepancies in the system performance illustrated in Figs. 5.22 and 5.23. In this section, the influence of each component design is quantitatively examined.

In the following analysis the influence of the heat and mass transfer performance of each component on the cooling capacity of chiller is quantitatively examined by multiplying the corresponding transfer area by an arbitrary factor. The factor, in practice, may also be understood as an enhancement in the transfer process itself.

Fig. 5.24a shows the variation of the cooling capacity against the heat transfer areas in generator, i.e. heat transfer area on heating medium side and that on solution side. The mass transfer area on solution side has been assumed equal to the heat transfer area. This assumption applies to all components.

Enhancement of the transfer process on the solution side is more effective to increase the cooling capacity than that on the heating medium side. But the influence of the size on performance of the generator is not large. Simultaneous augmentation of heat transfer surfaces on both sides by 1.36 times, i.e. restoring the heat transfer area to the original design value (see Table 5.6), would only increase the cooling capacity from 5.73 to 5.90kW, which is an increase of about 3%.

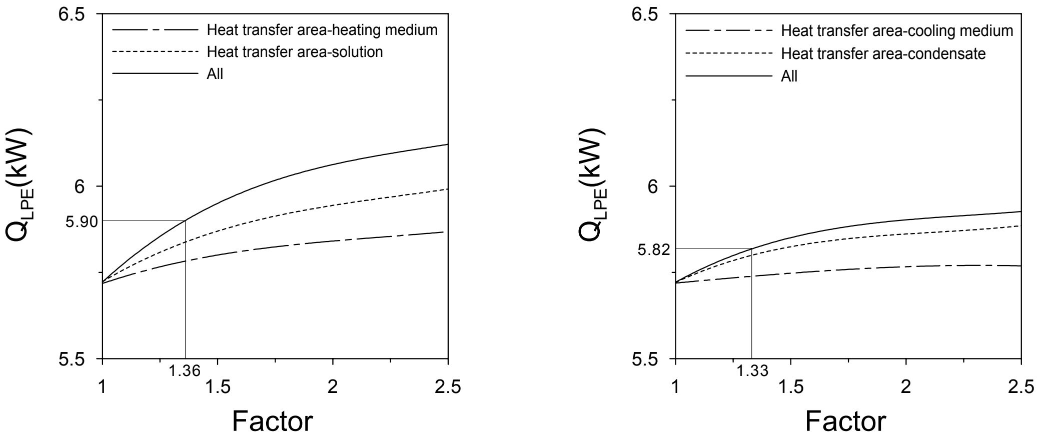

(a) Generator (b) Condenser

Figure 5.24 Influence of heat transfer areas in generator and condenser

Compared with the generator, enhancement of the condenser performance has even less influence on the system performance. Simultaneous augmentation of the heat transfer areas on both sides by 1.33 times would only increase the cooling capacity from 5.73 to 5.82kW, which is an increase of about 1.6%.

Fig. 5.25 shows the influences of MPA and LPA/MPE on system performance.

In Fig. 5.25a, it is shown that MPA has a larger influence than the generator and the condenser. For an increase of 1.85 times of the heat transfer areas on both solution and cooling medium sides, the cooling capacity is predicted to increase by 0.3kW, which is an increase of 5.2%.

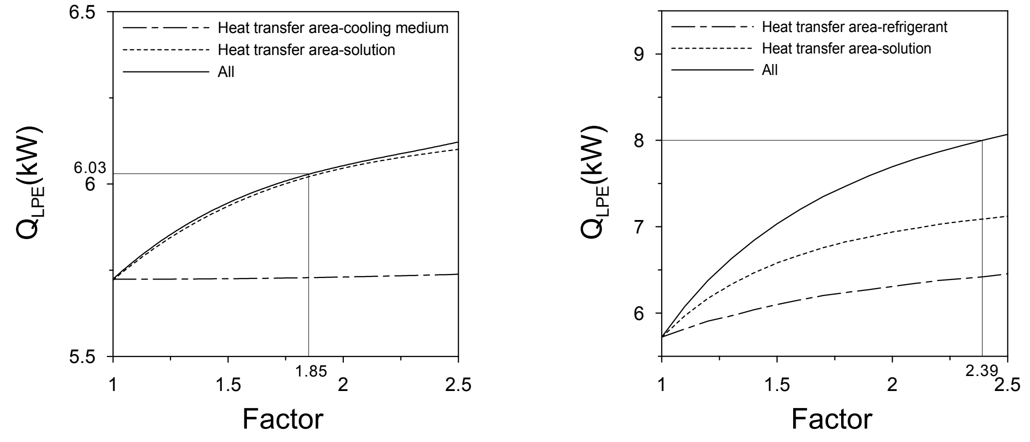

(a) MPA (b) LPA/MPE

Figure 5.25 Influence of heat transfer areas in MPA and LPA/MPE

Fig. 5.25b shows that LPA/MPE is the most critical component for the achievement of a reasonably large cooling capacity. Enhancement on the solution side is predicted to be more effective to increase the cooling capacity. Note that this is true only because the heat transfer performance on the refrigerant side has already been optimized by refrigerant recirculation as illustrated in Fig. 5.21. Enhancement on the refrigerant side would be much more effective if recirculation was not assumed.

Simultaneous augmentation of the heat transfer areas by 2.39 times on both sides would increase the cooling capacity from 5.73 to 8kW, an increase of 39.6%.

Influence of heat transfer enhancement in LPE is marginal as shown in Fig. 5.26. Increase in cooling capacity is comparable to that of MPA. This is also because the heat transfer performance on refrigerant side has already been enhanced by recirculation.

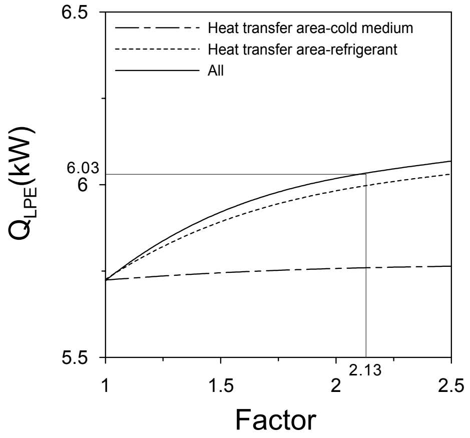

Figure 5.26 Influence of heat transfer areas in LPE

5.8.3 Influence of operating parameters

In this section, the influence of some operating parameters on system performance is investigated.

Fig. 5.27 shows variation of the COP and the cooling capacity with the solution flow rate entering the generator, which can be controlled by modulating the solution pump located downstream of the two absorbers in Fig. 5.1. While the solution flow rate entering the generator was changed, the solution leaving the generator was evenly distributed into MPA and LPA.

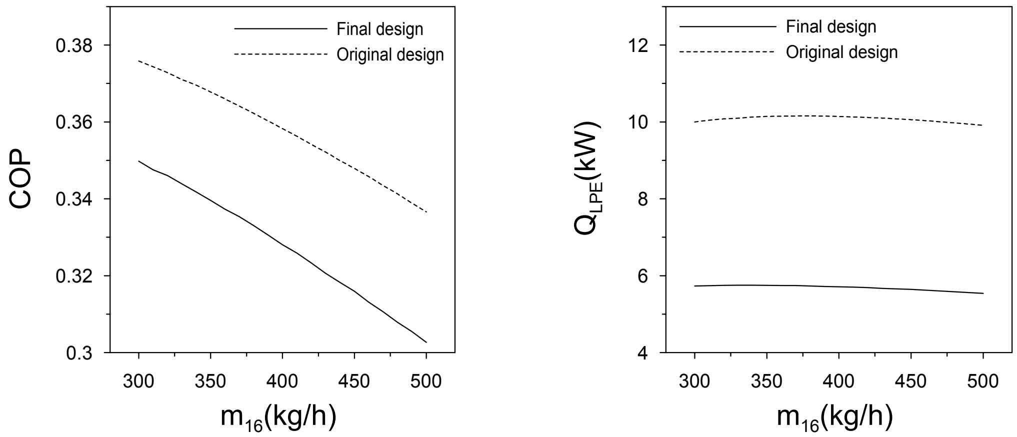

(a) COP (b) Cooling capacity

Figure 5.27 Influence of the solution flow rate to generator

The COP is predicted higher with smaller solution flow rate in Fig. 5.27a. This is mainly because effectiveness is increased for the two solution heat exchangers with smaller solution flow rate. Cooling capacity is relatively insensitive to the solution flow rate. Although it is hard to see in Fig. 5.27b, there is a maximum cooling capacity at a certain flow rate. There is a solution flow rate below which both cooling capacity and COP would decrease sharply. This would be the point when a liquid film breaks into rivulets to expose dry heat transfer surface in LPA or generator. This point could not be predicted with the empirical correlation (Wilke, 1962) used for these components.

Fig. 5.28 shows the influence of solution distribution between MPA and LPA. COP and cooling capacity were calculated varying the distribution ratio while solution flow rate was maintained at 395.3kg/h at the generator inlet.

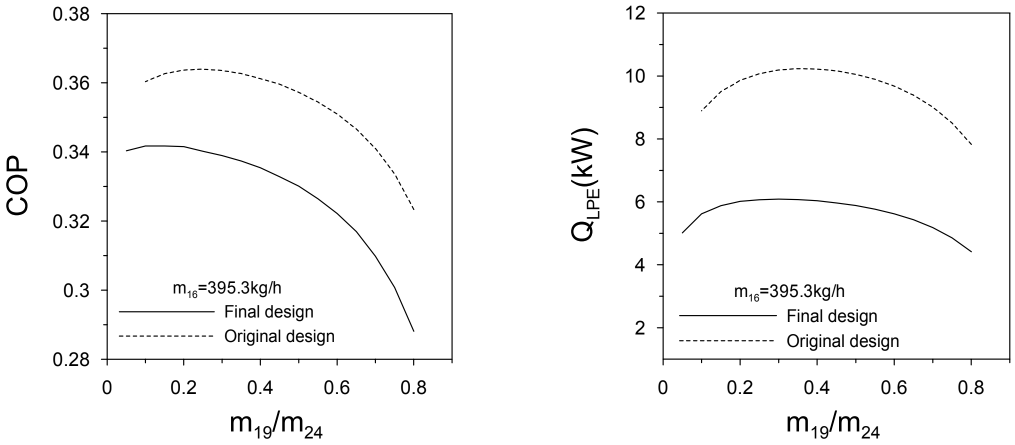

(a) COP (b) Cooling capacity

Figure 5.28 Influence of the solution distribution ratio

In Fig. 5.28, $\dot{m}_{19} / \dot{m}_{24}$ is the fraction of solution supplied to LPA of the solution flow rate from generator. Therefore as the ratio increases, less solution is supplied to MPA. In practice, the ratio can be controlled by valves or a properly designed manifold.

In Fig. 5.28a, each COP curve has a maximum point. Maximum COP is reached at $\dot{m}_{19} / \dot{m}_{24}$=0.25 and 0.1 for the original and the final design respectively. Cooling capacity also shows a similar trend. Maximum cooling capacity is achieved at $\dot{m}_{19} / \dot{m}_{24}$=0.35 and 0.3 for the original and the final design respectively.

The maxima predicted in Fig. 5.28 are, however, uncertain because, again, Wilke (1962)'s correlation used for LPA cannot describe the falling film flows under an incompletely wet condition, which is expected as $\dot{m}_{19} / \dot{m}_{24}$ approaches 0. This is demonstrated by Fig. 5.29, where Rogers (1981) has been used for LPA instead of Wilke (1962) for the calculation of COP and cooling capacity for the final design. Although Rogers (1981) may not be able to accurately predict the absolute magnitude of the heat transfer coefficient in LPA, it would produce a realistic trend because it takes account of incomplete surface wetting conditions.

COP predicted by Rogers (1981) shows clearly a maximum value at $\dot{m}_{19} / \dot{m}_{24}$=0.25 in contrast with that of Wilke (1962) in Fig. 5.29. This is because while Rogers (1981) gives a decreasing Nusselt number with decreasing Reynolds number in low Reynolds number range, Wilke (1962)'s correlation predicts the opposite approaching Nusselt's theoretical solution. Cooling capacity predicted by Rogers (1981) starts to decrease from $\dot{m}_{19} / \dot{m}_{24}$ =0.35.

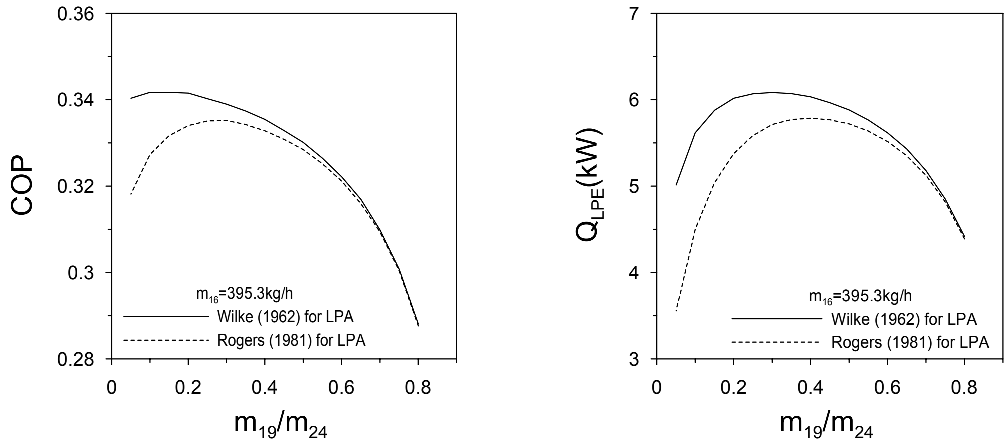

(a) COP (b) Cooling capacity

Figure 5.29 Influence of the empirical correlations used for LPA

From Fig. 5.28 and 5.29, optimum solution distribution ratio is expected to be between 0.2 and 0.4. In the original cycle design, it was 0.4 (see Table 3.3).

Fig. 5.30 shows the influence of distribution ratio of refrigerant between LPE and MPE. COP and cooling capacity are shown against the fraction of refrigerant supplied to LPE ($\dot{m}_{07}$) out of total refrigerant circulation rate ($\dot{m}_{08}$).

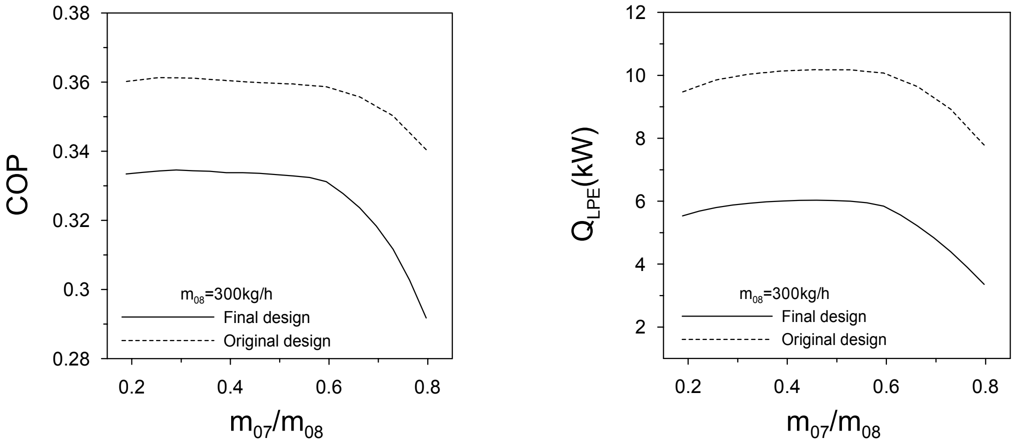

(a) COP (b) Cooling capacity

Figure 5.30 Influence of the refrigerant distribution ratio

While $\dot{m}_{07}$ was changed, $\dot{m}_{08}$ was maintained at 300kg/h. Therefore as $\dot{m}_{07}$ was increased, the refrigerant flow rate in MPE, i.e. $\dot{m}_{06}$, was decreased.

Both COP and cooling capacity are more or less stable in the range of $0.2 < \dot{m}_{07} / \dot{m}_{08} < 0.6$ and rapidly decrease there beyond. Notice that for the ratio 0.4 complete wetting has experimentally identified by Kim and Infante Ferreira (2006)'s correlation for subcooled water film. This is approximately the condition ($\dot{m}_{06}$=130kg/h) for maximum COP in Fig. 5.21.

5.9 Summary and conclusions

A one-dimensional steady-state differential model has been developed for a parallel-flow half-effect LiBr-H_2O absorption chiller. Governing equations for falling film flows were derived using the latest thermodynamic and transport theories available. The model is able to accurately predict both overall system performance and detailed local transfer processes in individual components.

The behaviour of the chiller designed in Ch. 3 has been simulated using the model. COP and cooling capacity of the chiller are predicted to be less than the original targets by 13% and 43% respectively due to the reduction of heat transfer areas in components. The reduced heat transfer areas in LPA/MPE turned out to be the main reason for this reduced performance.

The biggest uncertainty in the simulation results lies in the accuracy of the empirical correlation for the falling film flows on incompletely wet surfaces. Some efforts will be made in Ch. 6 to provide theoretical and experimental analysis on this subject.

The model developed in this chapter will also be used to analyze the experimental data from the experimental chiller setup in Ch. 7.

Nomenclature

A	area, m^2
Cp	heat capacity, kJ/kg K
D	mass diffusivity, m^2/s
Fr	Froude number
g	gravity constant, m/s^2
h	specific enthalpy, kJ/kg
h^{fg}	specific latent heat, kJ/kg
K	mass transfer coefficient, m/s
k	thermal conductivity, kW/m K
L	length, m
Le	Lewis number, (k/ρCp)/D
$\dot{m}$	mass fllow rate, kg/s
NTU	Number of transfer unit
Nu	Nusselt number
$\dot{n}$	mass flux, kg/m^2 s
p	pressure, kPa
Pr	Prandtl number
$\dot{Q}$	heat transfer rate, kW
$\dot{q}$	heat flux, kW/m^2
R	relaxation factor
Re	Reynolds number
T	temperature, K
U	overall heat transfer coefficient, kW/m^2 K
u	longitudinal velocity, m/s
v	lateral velocity, m/s
x	LiBr mass fraction

y	lateral distance, m
z	longitudinal distance, m

Greek symbols

α	heat transfer coefficient, kW/m^2 K
λ	specific mass flow rate or circulation ratio, kg solution/kg refrigerant
ν	kinematic viscosity, m^2/s
ρ	density, kg/m^3
μ	dynamic viscosity, Pa s
δ	film thickness, m
Γ	flow rate per unit length, kg/m s
ε	effectiveness
Δh	heat of ab(de)sorption, kJ/kg
Δt	wall thickness, m

Super- and subscripts

avg	average
b	bulk flow
dew	dew point
htm	heat transfer medium
i	phase interface, control volume index
L	low pressure
l	liquid
M	mid pressure
o	reference state
s	saturation
sol	solution
v, vap	vapor
w	heat transfer medium or refrigerant
wal	wall
∞	infinity

Abbreviations

CON	condenser
GEN	generator
HT-Hex	high-temperature heat exchanger
LPA	low-pressure absorber
LPE	low-pressure evaporator
LT-Hex	low-temperature heat exchanger
MPA	mid-pressure absorber
MPE	mid-pressure evaporator
Ref-Hex	refrigerant heat exchanger

References

Armbruster, R., Mitrovic, J., 1998, Evaporative cooling of a falling film on horizontal tubes, Experimental Thermal and Fluid Science, Vol. 18, pp. 183-194

Baehr, H.D., Stephan, K., 1998, Wärme- und Stoffübertragung, 3rd ed., Springer-Verlag, Berlin

Bird, R.B., Stewart, W.E., Lightfoot, E.N., 1965, Transport phenomena, Wiley, New York

Grossman, G., Michelson, E., 1985, A modular computer simulation of absorption systems, ASHRAE Trans., Vol. 91, pp. 1808-1827

Holman, J.P., 1997, Heat transfer, 6th ed., McGraw-Hill

James, M.L., Smith, G.M., Wolford, J.C., 1985, Applied numerical methods for digital computation, Harper & Row publishers

Kim, D.S., Infante Ferreira, C.A., 2006, Effect of surface geometry and surfactants on the performance of falling films, Proc. 7th Gustav-Lorentzen Conference on Natural Working Fluids, Trondheim, Norway

Nakoryakov, V.E., Grigoreva, N.I., 1980, Calculation of Heat and Mass Transfer in Nonisothermal Absorption on the Initial Portion of a Downflowing Film, translated from Teoreticheskie Osnovy Khimicheskoi Tekhnologii, Vol.14, pp. 483-488

Nusselt, W., 1916, Die oberflachenkondnesation des wasserdampfes, VDI Z., Vol. 60, p. 541

Powell, M.J.D, 1970, A hybrid method for nonlinear equations, Numerical Methods for Nonlinear Algebraic Equation, Gordon and Breach Science Publisher, London, UK, pp. 87-113

Rogers, J.T., 1981, Laminar falling film flow and heat transfer characteristics on horizontal tubes, Can. J. Chem. Eng., Vol. 59, pp. 213-222

Rohsenow, W.M., 1973, Film condensation, Ch. 12 in Handbook of Heat Transfer, McGraw-Hill Book company, New York

Wassenaar, R., 1994, Simultaneous heat and mass transfer in a horizontal tube absorber, Dissertation, TU Delft

Wilke, W., 1962, Wärmeübergang in Rieselfilm, VDI-Forschungsheft 490, Issue B, Vol. 28

Yang, R., Wood, D., 1992, A numerical modeling of an absorption process on a liquid falling film, Solar Energy, Vol. 48, pp. 195-198

Yüksel, M.L., Schlünder, E.U., 1987, Heat and Mass Transfer in Non-isothermal Absorption of Gases in Falling Liquid Films Part I: Experimental Determination of Heat and Mass Transfer Coefficients, Chem. Eng. Process, Vol. 22, pp. 193-202

Zhuo, C., 1995, Absorption heat transformer with TFE-Pyr as the working pair, Dissertation, TU Delft

6 Heat and mass transfer in falling film flows[4]

As was confirmed by the simulation results in Ch. 5, performance of the half-effect absorption chiller is heavily dependent on the performance of LPA-MPE, which is a vertical tube having falling films flows on both sides. This component has been designed to operate with very small flow rates of working fluids near minimum wetting rates. Lack of experimental data on the falling film flows in this low flow rate range was the biggest uncertainty in the design and simulation of this component, which motivated the experiments introduced in Section 6.2.

In the following, publications of experimental studies on several types of falling film heat exchangers are reviewed in Section 6.1 and the experimental study carried out with the falling film flows on vertical plates is introduced with an experimental setup, methods and results in Section 6.2 and 6.3.

6.1 Literature survey

Due to the significant influence of pressure drop on its performance, a LiBr-H_2O absorption machine is normally designed with falling film type heat exchangers. Tubular falling film heat exchangers are most common and they are classified further into two groups according to the posture of heat transfer tubes, i.e. horizontal and vertical. The horizontal type has been popular for many years, while the vertical type has been recently applied to air-cooled machines (Ogawa et al, 1991; Medrano et al, 2002). Although rare, use of plate type falling film heat exchangers can also be found in a few absorption systems (Becker, 1989; Flamensbeck et al, 1998).

Numerous experimental and theoretical studies are found regarding the transport phenomena in liquid film flows. Not to mention the field of absorption refrigeration, wide variety of applications can be found for liquid film equipments in various fields. Particularly, the subjects of minimum wetting rate and stability of falling film flows are of special interest in, for example, gas processing (Bond and Donald, 1957), cooling of nuclear reactors (Fujita and Ueda, 1978a), film coating (Ruschak and Weinstein, 2003). In the following, the literature is reviewed focusing on the experimental studies on the heat and mass transfers in falling film flows particularly in the low flow rate range.

6.1.1 Falling film flows on horizontal tubes

Horizontal tube evaporators have been intensively investigated for their popular uses in refrigeration, chemical, petroleum refining, desalination, food industries and so on. Since flow behavior has a significant impact on the sensible and latent heat transfer to a liquid flowing over a horizontal tube, flow patterns (transition mode) have been studied by many researchers including Yung et al (1980), Mitrovic (1986), Armbruster and Mitrovic (1994), Hu and Jacobi (1996a, 1998) and Roques and Thome (2002). Reynolds numbers were given in function of

---

[4] A part of this chapter has been published in "Kim, D.S., Infante Ferreira, C.A., 2006, Effect of surface geometry and surfactants on the performance of falling films, Proc. 7th Gustav-Lorentzen Conference on Natural Working Fluids, Trondheim, Norway"

Kapitza number (or modified Galileo number) for transitions between different flow regimes, i.e. droplet, jet (or column) and sheet mode, in Armbruster and Mitrovic (1994), Hu and Jacobi (1996a) in Roques and Thome (2002).

Many studies are found also about the heat transfer in subcooled falling films on horizontal tubes including Rogers (1981), Mitrovic (1990) and Hu and Jacobi (1996b). Hu and Jacobi (1996b) measured local temperatures on the tube surface and presented average sensible heat transfer correlations for water-ethylene glycol solution flows in droplet, jet and sheet mode. Armbruster and Mitrovic (1998) introduced empirical heat transfer correlations of Rogers (1981) and Mitrovic (1990) for subcooled water flows in a wide flow rate range (Γ=0.02-0.3kg/ms) and recommended either of the two correlations as a benchmark for experiments pointing out their excellent agreement.

It is notable that, in evaporative cooling conditions, the heat transfer enhancement induced by upward air stream was observed in the water flows not on the tube surface but mostly between adjacent tubes (Armbruster and Mitrovic, 1998), which suggests that the flow between tubes should also play a similar important role in horizontal tube absorbers.

Some experimental studies are found about horizontal tube absorbers including Nagaoka et al (1987), Wassenaar (1994), Consenza and Vliet (1990), Greiter et al (1993), Hoffmann et al (1996), Remec et al (1996), Kyung and Herold (2002), Yoon et al (2002) and Park et al (2003). In these studies, influences of operating conditions such as solution flow rate, temperature and solution composition (absorbent and additives concentrations) on the performance of heat exchanger tubes were investigated. Some of them are briefly summarized in the following.

Nagaoka et al (1987) carried out a series of experiments to investigate the performance of tubes with different surface geometries focusing on the role of an additive (1-octanol) in surface convection. They reported heat and mass transfer coefficients for bare, finned, cross-grooved and fluted tubes and pointed out that the heat transfer coefficient increased with the surface area of tubes but the mass transfer coefficient did not follow the trend. They observed that heat transfer coefficients were almost doubled and mass transfer coefficients were increased even more with the presence of surface convection. They suggested that surface geometry should be such that it would not obstruct the fluid motion on film surface.

Wassenar (1994) measured the absorption of methanol into the falling film flows of $LiBr/ZnBr_2$ solutions over 10 vertically aligned horizontal tubes (ϕ12 mm, 340 mm long) with different inter-tube gaps at 0, 3, 15 and 24 mm. The solution flow rate was varied between 0.002-0.05 kg/ms with the solution concentration maintained approximately at 30 wt%. The measurements were used to validate his flow models. It was reported that the mixing effect in the flows between tubes enhanced the transfer process with increasing inter-tube gap up to 15 mm.

Hoffmann et al (1996) carried out a series of tests with 24 vertically aligned plain and knurled copper tubes varying flow rate, LiBr and additive (max. 640ppm of 1-octanol and 2-ethyl-1-hexanol) concentrations. The authors reported that for both tubes, heat transfer coefficient increased sharply with increasing flow rate ($\Gamma=\dot{m}/2L$) below 0.015kg/ms due to increasing wetted surface area and it leveled off at around 0.03 kg/ms approaching an asymptotic value. They observed mixing and splashing of the flows between tubes and concluded that laminar-film models were not valid to describe the systems. They also reported improvement of heat transfer coefficient by 20-40% with the knurled surface and 60-140% with the additive (2-

ethyl-1-hexanol) in comparison with that of plain tubes without an additive. Addition of the additive was reported to have no further effect in heat transfer enhancement above 40 ppm.

Kyung and Herold (2002) carried out experiments on bare copper tubes with 57 and 60 wt% aqueous LiBr solutions in the same flow rate range as Hoffmann et al (1996). Experimental data showed a “plateau” heat transfer coefficient above solution flow rate of 0.04 kg/ms commonly in both cases with and without an additive (2-ethyl-1-hexanol). It was reported that heat transfer coefficients were increased by 1.7 times with the additive and the effect was saturated above 80ppm in the test range (max. 500ppm). They also claimed that heat flux played a strong role in the additive’s enhancement mechanism and “solution slinging” (solution drops ejected from tubes due to slinging motion of flows between tubes) decreased the heat transfer coefficients.

Yoon et al (2002) reported experimental results using 60 wt% aqueous LiBr solution and three different types of stainless steel tubes, i.e. bare, floral and hydrophilic (plasma-treated) tubes, in a commercial size absorber setup focusing on the determination of an optimum additive concentration (max. 5,000ppm of 1-octanol tested). They visualized wetted surface area of the tubes at a solution flow rate of 0.027kg/ms and reported that the hydrophilic and floral tubes had larger wetted surface area than the bare tube by 30-110% and 20-70% respectively. It is notable that heat transfer coefficients increased with increasing additive concentration up to 3,500ppm.

Park et al (2003) measured absorption rates of water vapour into the falling film flows of aqueous LiBr solutions (55, 58 and 61 wt%) over 24 vertically aligned copper tubes in the Reynolds number range of 10-60. Three different types of tubes, i.e. bare (zero roughness assumed) and two sandpapered tubes (roughness 6.968×10^{-6}m with sandpaper #24 and 0.386×10^{-6}m with #600), were tested. Increased Nusselt numbers were reported by a factor between 2 and 3 in comparison with that of the bare tube. The enhancement was attributed to improved wettability by the surface roughness.

Complex flow patterns of the falling film flows in horizontal tube banks with different geometries seem to make it difficult to describe this type of absorber with a single general model. It is also believed to be a reason for the discrepancies found among the experimental data in the literature.

Pise et al (2003) pointed out the discrepancies between the experimental data in the literature. Hoffmann et al (1996) tested 24 copper tubes (ϕ16mm, 400mm long) with 6mm apart from each other [the dimensions were not given in Hoffmann et al (1996) but in Beutler et al (1996)]. Kyung and Herold (2002) used two copper tube bundles (4 tubes of 360mm and 8 tubes of 460mm long, common ϕ19.1mm) with 25.4mm spacing between tube walls. The absorber of Yoon et al (2002) consisted of 48 stainless steel tubes (ϕ15.88mm, 400mm long) arranged in a staggered array (6 columns and 8 rows) with unmentioned tube spacing. The test setup of Park et al (2003) was much similar to that of Hoffmann et al (1996) consisting of the same number of tubes with the same diameter only different in tube length and the spacing between tubes (500mm, 10 mm). Considering these differences between the experimental setups, it is no wonder that the experimental data from these studies are not in good agreement.

It is also not surprising that there is yet no general model for describing horizontal absorbers (Killion and Garimella, 2002) considering that fundamental studies on the flow patterns in horizontal absorbers were initiated only recently (Cavallini et al, 2002; Killion and Garimella, 2002) and the enhancement mechanisms of additives are still not clearly understood

(Kashiwagi et al, 1985; Hihara and Saito, 1993; Kulankara and Herold, 2000; Koenig et al, 2003)

6.1.2 Falling film flows on vertical tubes

Compared with the horizontal falling film heat exchangers, applications of vertical falling film heat exchangers are relatively rare in industries. Nevertheless a large number of experimental studies are found on the falling film flows on vertical surfaces, which represents the importance of this subject in understanding the fundamental characteristics of falling film flows.

Heat transfer in subcooled or evaporating falling film flows on plain vertical tubes was investigated by many researchers including Wilke (1962), Chun and Seban (1971) and Fujita and Ueda (1978a, 1978b) and Krupiczka et al (2002) .

Wilke (1962) measured heat transfer coefficients of subcooled water-glycol solution flows on the outer surface of a 2.4 m-long ϕ42 mm vertical tube with Prandtl numbers ranging from 5.4 to 210 and film Reynolds numbers ($Re_f=4\Gamma/\mu$) ranging from 9 to 12,000. He gave empirical Nusselt number correlations for laminar, transient (or wavy laminar) and turbulent regions. By use of a high Prandtl number fluid, complete wetting of surface was ensured even for the lowest Reynolds number.

Chun and Seban (1971) investigated evaporating falling film flows of saturated water on the exterior of a 610 mm-long (electrically heated section 292 mm) ϕ28.6 mm vertical tube. The minimum flow rate was limited by the occurrence of circumferentially non-uniform wetting and the maximum flow rate was limited by “overshooting” of the feed at a distributor mounted at the top of the tube. Two empirical heat transfer correlations were given for wavy laminar and turbulent regions covering film Reynolds numbers from 320 to 21,000 under low heat flux conditions without nucleate boiling.

Fujita and Ueda (1978a) investigated subcooled water falling films on the exterior of electrically heated 600 mm- and 1000mm-long ϕ16 mm vertical tubes focusing on the film distortion and breakdown that occurred at high heat flux conditions. Flow rates were kept above minimum wetting rate so that the distortion or breakdown of a film was caused solely by heat flux. They observed that their low heat flux data approached the correlation of Wilke (1962) and the deviation became larger with increasing heat flux, which was attributed to the film distortion caused by high heat flux. They developed a model for the film distortion taking into account the variation of surface tension due to non-uniform temperature distribution along the tube circumference. They further carried out experiments on nucleate boiling in falling film flows with saturated water (Fujita and Ueda, 1978b) and reported that their low-heat-flux ($30<\dot{q}<70$ kW/m^2) heat transfer coefficients agreed with Chun and Seban (1971) within 10%.

Krupiczka et al (2002) measured heat transfer coefficients of evaporating falling film flows inside an electrically heated 700 mm-long ϕ24 mm vertical tube with water, methanol and isopropanol for film Reynolds numbers in the range from 745 to 3,315 and heat fluxes from 2.2 to 31 kW/m^2. The authors separated the heat flux into convective and nucleate boiling fluxes and presented empirical Nusselt number correlations in function of boiling number

($\mathrm{Bo}=\dot{q}/\dot{n}\,h^{fg}$). Their correlations were identical to Chun and Seban (1971) for small boiling numbers ($\mathrm{Bo}<10^{-5}$).

Absorption processes in the falling film flows on vertical surfaces have been intensively studied in the chemical engineering field regarding gas absorption in wetted-wall columns. Among many, only a few studies are briefly introduced in the following.

Bond and Donald (1957) carried out experiments on the absorption of ammonia from humid air-ammonia mixtures into falling water film flows inside a 1.2 m-long ϕ25.4 mm vertical glass tube for determination of the minimum water flow rate to maintain a continuous water film on the surface. They correlated the experimental data with the difference between the surface tensions of (subcooled) bulk and saturated solutions. Great care was taken for even distribution of the water and a continuous film was maintained at water flow rates down to 0.005kg/ms when it was without absorption. The authors stressed the important role of ripples at film surface on the film breakdown pointing out that a surface active agent could suppress the ripples and prevent the breakdown of the water film even for an extremely low flow rate.

Yih and Chen (1982) measured the absorption rates of carbon dioxide and oxygen into the falling water film flows on the exterior of a 2.12 m-long ϕ27.2 mm vertical tube in the film Reynolds number range from 129 to 10,500. The authors compared their experimental data with those of 10 other studies and developed empirical Sherwood number correlations in wavy laminar, transition and turbulent regions covering film Reynolds numbers in the range from 49 to 10,500 and Schmidt numbers from 148 to 981. The authors mentioned that surface tension effects were important in low flow rate region including wavy-laminar flows.

In the field of absorption refrigeration, a number of experimental studies were carried out on the absorption processes in vertical falling film flows on the exterior of vertical tubes (Yüksel and Schlünder, 1987; Matsuda et al, 1994; Kim et al, 1995; Miller and Keyhani, 1999, 2001) and also on the interior of vertical tubes (Medrano et al, 2002; Takamatsu et al, 2003; Bourouis et al, 2005).

Yüksel and Schlünder (1987) measured local heat and mass transfer coefficients in falling aqueous LiBr film flows with a single Prandtl number of 7.4 for film Reynolds numbers ($\mathrm{Re_f}=4\Gamma/\mu$) from 600 to 4,800. Heat and mass transfer coefficients were determined independently from each other by measuring the film surface temperatures with an infrared pyrometer. They proved that turbulence was damped not only near the wall but also in the vicinity of the film surface and therefore the assumption that the bulk and surface temperatures were equal in turbulent flows was not correct. They separately defined heat transfer coefficients for near interface and near wall and showed that the Sherwood number calculated from heat and mass transfer analogy at the interface agreed very well with the one determined by the infrared measurements. It was reported that their Sherwood numbers agreed well with those of the isothermal absorption, i.e. absorption with no heat generation, of carbon dioxide in falling water films including that of Yih and Chen (1982).

Matsuda et al (1994) measured absorption and desorption rates in falling film flows of aqueous LiBr solutions (40, 55 and 60 Libr wt %) along a 580 mm-long ϕ15.7 mm vertical stainless steel tube for film Reynolds numbers in the range from 24 to 259 for absorption and from 3.4 to 297 for desorption. They did not report heat and mass transfer coefficients but showed that the experimental mass transfer rates agreed well with the simulation results based on several empirical correlations. Chun and Seban (1971) was used for the heat transfer coefficients for heat transfer in both absorption and desorption and the empirical Sherwood number correlations for carbon dioxide absorption into water film have been used for mass transfer. The flow rates were limited by the occurrence of a dry patch and the minimum flow rates were 0.022 and 0.004 kg/ms for absorption and desorption respectively.

Kim et al (1995) reported experimental Sherwood numbers for the absorption of water vapour into falling film flows of 60 wt % aqueous LiBr solution on the exterior of a 1.83 m-long (variable absorber length between 400-850 mm) ϕ38.1mm vertical stainless steel tube for film Reynolds numbers in the range from 15 to 150. They achieved uniform wetting down to a very small Reynolds number in the order of unity without absorption and with absorption, down to 16. Wave inception was reported between 100 to 200 mm downstream from the top for the flows in the film Reynolds number range between 30 and 90. Experimental data showed that Sherwood number increased linearly with film Reynolds number up to 50 and then leveled off. The bulk LiBr concentration profiles were found linear against absorber length. Presence of a non-absorbable gas (air, less than 2% in volume) in the setup imposed a certain uncertainty on the absolute values of their Sherwood numbers.

Miller and Keyhani (1999) measured temperature profiles of the falling film flows on the exterior of a 1.524 m-long ϕ19.05 mm vertical stainless steel tube during the absorption of water vapour into 60 wt% aqueous LiBr solution at the film Reynolds number of 290. Coolant temperatures were measured by thermocouples installed 0.15 m apart along the 1.8 m-long probe inserted inside the tube and wall temperatures were measured by RTDs (Resistance Temperature Detector). Saturated 60% aqueous LiBr solution was supplied and film surface temperatures were measured along the length by a visualization technique based on thermographic phosphors. The phosphor (La_2O_2S:EU) seeded in the LiBr solution was excited by a pulsed nitrogen laser focused on the film surface and the florescent decay emitted by the phosphor was measured and converted into temperature. The authors concluded that firstly, temperature and concentration profiles were roughly linear with the absorber length and therefore the heat load and the mass absorption rate could be calculated with a constant flux approximation and secondly, the convective effect of the waves on the film surface was not significant and therefore the absorption process was largely heat-transfer dominated for the film Reynolds numbers below 400. The authors also developed empirical Nusselt and Sherwood number correlations based on the measurements with 62 and 64 wt% aqueous LiBr solutions in the film Reynolds number range from 100 to 400 and reported agreement with the Sherwood numbers of Kim et al (1995) within an absolute error of 7% (Miller and Keyhani, 2001).

Medrano et al (2002) carried out measurements of falling film flows of 57.9 and 60 wt% aqueous LiBr solutions inside of a 1.5 m-long ϕ22.1 mm (internal diameter) vertical stainless steel tube in the film Reynolds number range of 50 to 300. The flow rate was limited by the film breakdown observed at a film Reynolds number of about 40. They compared their absorption rates with those of Kim et al (1996) and Miller and Keyhani (1999), which were for the falling film flows outside tubes, and reported no significant differences. They recommended use of shorter tubes to reduce subcooling at the absorber exit and higher salt concentrations in the solution for larger driving potentials for heat and mass transfer.

Takamatsu et al (2003) presented experimental data for the absorption of water vapour into the falling film flows of 53 wt% LiBr solution inside of 400 and 1,200 mm-long ϕ19.05 mm (inside diameter 16.05 mm) copper tubes in the film Reynolds number range of 50 to 550. Incomplete wetting was observed by an endoscope for the Reynolds numbers below 130. They compared their results with those of Kim and Kang (1995) and pointed out that Nusselt and Sherwood numbers were strongly dependent on the subcooling of inlet solution and the length of a tube. It is notable that the Reynolds number for minimum wetting was three times that of Medrano et al (2002).

Bourouis et al (2005) used the same experimental setup as Medrano et al (2002) to determine the heat and mass transfer coefficients for the absorption of water vapour into the falling film flows of aqueous mixed-salts (LiBr+LiI+$LiNO_3$+LiCl) solutions and compared the results with those of LiBr solutions of Medrano et al (2002). The heat and mass transfer coefficients of the fluid were in the range of 0.2-0.4 kW/m^2K and $2\text{-}4.4\times10^{-5}$ m/s respectively in the film Reynolds number range of 50 to 200. While the mixed-salt solution had slightly lower heat and mass transfer coefficients than those of LiBr solutions, they enabled higher heat and mass fluxes under air-cooled conditions with a considerably lower risk of crystallization.

6.1.3 Falling film flows on plates and helical coils

Although many theoretical and experimental studies are found in the literature for the hydrodynamic characteristics of wavy and turbulent falling film flows on vertical surfaces (see Ambrosini et al, 2002), just a few articles were found to report experimental heat and mass transfer data.

Brauner and Maron (1982) measured the mass transfer coefficients from solid surface to bulk liquid for the falling film flows of 1 mol NaOH solution on a nickel-plated inclined cooper plate (63 ×120 mm^2) using an electrochemical technique. The plate surface was electrically separated into anode and cathode and formed a closed electrical circuit when electrolyte solution flowed on it. Local mass transfer rates were estimated by measuring the voltage drops between electrodes in the circuit. They also measured film thickness using a capacitance method and demonstrated the relation between surface waves and the mass transfer rates. However no quantitative information was given regarding the mass transfer measurements.

Al-Sibai et al (2002) measured heat transfer coefficients from the falling film flows of three different silicon oils (Pr=10, 25, 45) on an electrically heated constantan foil (700×240×0.025 mm^3) in the Reynolds number range of 40-516. The falling film flows were perturbed by a loud speaker located above a liquid distributor to investigate the influence of surface waves on heat transfer rate. Experimental Nusselt numbers showed enhancements of heat transfer in comparison with the Nusselt solution (by factors up to 1.3) and substantial dependence on Prandlt number.

Use of a plate type falling film absorber is an attractive idea for small capacity machines considering that it can be made more compact and cheaper than tubular heat exchangers (Flamensbeck et al, 1998). But just a few experimental studies were found on this type of absorbers, which are briefly summarized in the following.

Becker (1989) developed a single-effect alcohol-salt (CH_3OH-LiBr/$ZnBr_2$) absorption heat pump using a plate fin type compact heat exchanger (trapezium offset strip fins made of Inconel 600 brazed on 700mm×240mm×1mm stainless steel plates) as an absorber. From 35 sets of experimental data, he derived correlations of the correction factors for the theoretical heat and mass transfer coefficients of the absorber. He mentioned that the theoretical heat transfer coefficients on film side were 2.5-6 times larger than the measured values (0.15-

0.25kW/m^{2}K for 4<Re_f<24 and 75<Pr<120) and suspected incomplete wetting of the absorber surface as one of the reasons.

Chen and Sun (1997) investigated heat and mass transfer in a combined absorber-evaporator for application in a so-called CDE (Concentration Difference Energy) engine. This absorber-evaporator heat exchanger was a 300 mm-wide 1,000 mm-long 2 mm-thick vertical copper plate, where aqueous $CaCl_2$ solution flowed on one side and pure water flowed on the other side. Steam was generated from the water flow that was heated by the $CaCl_2$ solution that absorbed the steam generated on the other side of the plate. Pressure difference was maintained by a valve in a ϕ50.8 mm steam tube connecting the two sides, which was supposed to be an engine in a real CDE power system. Film Reynolds numbers were varied between 100 and 1,300 for the solution (35 and 40 wt%, Pr=20-30) and between 250 and 1,300 for water (15 ^{o}C, Pr=8). Experimental data were processed according to Yüksel and Schlünder (1987) and empirical correlations for Nusselt and Sherwood numbers were derived. Substantial deviations were found in comparison with the data of Yih and Chen (1982) and Yüksel and Schlünder (1987), which were attributed to the differences in heat exchanger geometry and the Prandtl number of the working fluids.

Flamensbeck et al (1998) developed a double-effect water-hydroxides (H_2O-NaOH/KOH) absorption chiller employing plate heat exchangers for a condenser (four normal brazed plate heat exchangers connected in parallel) and a high-pressure condenser/mid-pressure generator [a plate fin heat exchanger which is similar to that of Becker (1989)]. Plate heat exchangers were avoided for low-pressure components due to the excessive pressure drop on vapour side and instead, liquid-liquid heat exchangers and adiabatic evaporator and absorber were used. The choice of the particular hydroxide mixture has been preferred for its high-lift operability in spite of its high corrosiveness. No data was given for the performance of a falling film plate heat exchanger.

Helical tube coils are frequently used in small absorption chillers (e.g. Yazaki, 2005; Safarik et al, 2005) in favor of easy and cheap manufacturability. The behavior of a falling film flow on a helical coil would deviate substantially from that of a horizontal tube when the helix angle (inclination of helix to horizon) is large and a large portion of the liquid flows down along the tube in the helical path.

Kwon and Jeong (2003) investigated the falling film flows on a small helical coil (ϕ12.7 tube, coiling diameter 82.7 mm, number of windings 30, estimated helix angle 2.8^o) for steam condensation into subcooled water and for ammonia absorption into an ammonia-water solution. Average Nusselt numbers were measured for co- and counter-current vapor-liquid flow configurations in the Reynolds number ranges 60-600 for water condensation and 60-400 for ammonia absorption. Nusselt numbers were smaller with the counter-current configuration for both condensation and absorption cases, which was attributed to uneven liquid distribution or stagnation due to the disturbance of the vapour flowing in adverse direction.

Yoon et al (2005) measured heat and mass transfer coefficients in the falling films flows of some aqueous salt solutions (50/60wt% LiBr and 58/61/64wt% LiBr+LiI+$LiNO_3$+LiCl) on a helical absorber (ϕ15.9 tube, coiling diameter 236 mm, estimated number of windings 10, estimated helix angle 2.5^o). Measured heat and mass transfer coefficients were given for 60 wt% solutions in the flow range from 0.01 to 0.04 kg/ms.

6.1.4 Summary

In Table 6.1, some of the studies reviewed in the previous sections are summarized. Those studies not listed in the table are either insufficient in experimental data or less relevant to the present topics.

Table 6.1 Experimental heat and mass transfer data in the literature

	type	Working fluid	Γ(kg/ms) or Re_f	Correlation
Horizontal tubes				
Rogers (1981)	Sensible	Subcooled water	0.020-0.300	yes
Mitrovic (1990)				
Hoffmann et al (1996)	Absorption	LiBr-H_2O, 46/51/57 wt%	0.006-0.045	
Kyung & Herold (2002)	Absorption	LiBr-H_2O, 57/60 wt%	0.014-0.050	
Yoon et al (2002)	Absorption	LiBr-H_2O, 60 wt%	0.010-0.035	
Park et al (2003)	Absorption	LiBr-H_2O, 55/61 wt%	0.010-0.080	
Vertical tubes-outside				
Wilke (1962)	Sensible	Subcooled water	$9<Re_f<12,000$	yes
Chun & Seban (1971)	Evaporation	Saturated water	$320< Re_f <21,000$	yes
Yih & Chen (1982)	Absorption	CO_2, O_2, H_2, He in water	$49< Re_f <10,500$	yes
Yüksel & Schlünder (1987)	Absorption	LiBr-H_2O, Pr=7.4	$600< Re_f <4,800$	
Kim et al (1995)	Absorption	LiBr-H_2O, 50/60 wt%	$15< Re_f <150$	
Miller & Keyhani (2001)	Absorption	LiBr-H_2O, 62/64 wt%	0.014-0.026	yes
Vertical tubes-inside				
Medrano et al (2002)	Absorption	LiBr-H_2O, 58/60 wt%	0.007-0.022	
Takamatsu et al (2003)	Absorption	LiBr-H_2O, 53 wt%	0.013-0.025	
Bourouis et al (2005)	Absorption	(LiBr+LiI+LiNO3+LiCl)-H_2O, 61/64 wt%	$50< Re_f <200$	
Vertical plates				
Chen & Sun (1997)	Absorption	$CaCl_2$-H2O, 35/40 wt%	$100< Re_f <1,300$	yes
Helical coils				
Kwon & Jeong (2003)	Condensation Absorption	- Steam condensation into subcooled water - NH_3-H_2O, 30 wt%	0.006-0.042 0.008-0.040	
Yoon et al (2005)	Absorption	LiBr-H_2O, 60 wt% (LiBr+LiI+LiNO3+LiCl)-H_2O, 60 wt%	0.010-0.040	

Although the number of studies listed in Table 6.1 does not necessarily represent the intensity of R&D efforts on the particular type of heat exchanger, as far as in absorption refrigeration field, horizontal falling film heat exchangers have been more intensively investigated than the others. Vertical falling film heat exchangers, on the other hand, seem to have been investigated more for understanding of fundamental physics in falling film flows.

Experimental data on the sensible heat transfer to subcooled water flows on horizontal tube banks were found in many studies. Among them, the correlations of Rogers (1981) and Mitrovic (1990) take account of the geometry parameters of a tube bank (tube diameter and spacing) and cover the entire flow range from drop to sheet flow mode. Since these correlations agree very well with each other, either of them can be used for prediction of the heat transfer coefficient between bulk film and wall in a horizontal tube evaporator or absorber. It may also be used for a helical tube coil heat exchanger when helix angle is small.

Experimental data on horizontal absorbers were found rather scattered and fragmented. All the studies on horizontal absorbers in Table 6.1 tested different designs of absorbers in terms of tube diameter, length and spacing and tests were mostly done with only a few absorbent concentrations of practical interest.

Wilke (1962) and Chun and Seban (1971) on the subcooled and saturated water films on vertical tubes are widely accepted and frequently cited in the literature. Yih and Chen (1982) is also noteworthy regarding its comprehensive collection of experimental data on the absorption of sparingly soluble gases into water. However, unlike horizontal falling film heat exchangers, these studies did not deal with the flow region below the minimum wetting rate where tube surface is not completely wet. Wilke (1962) used a highly viscous water-glycol solution (Pr=210) to reach the minimum film Reynolds number of 9 without having a dry patch. The minimum Reynolds number of Chun and Seban (1971) was 320, which was intentionally controlled to avoid the occurrence of dry patches. Yih and Chen (1982) limited their experiments to Reynolds numbers higher than 129 to avoid incomplete wetting at film Reynolds numbers below 100. Although they added some experimental data from other sources (Emmert and Pigford, 1954; Kamei and Oishi, 1955; Hikita et al, 1959), the correlation they developed for the Reynolds number in the range from 49 to 300 was not so satisfactory because surface tension effects have been neglected.

The studies of water absorption with vertical absorbers in Table 6.1 carried out experiments within narrow operating ranges of their own interest and rarely referred to other works for a comprehensive analysis. Even worse is that the incompatible definitions of heat and mass transfer coefficients used in some studies (this will be discussed in Section 6.2.2) do not allow a direct comparison of the experimental data.

Studies on plate and helical absorbers are rare in the literature. The experimental data of Chen and Sun (1997) showed substantial deviations from those of Yüksel & Schlünder (1987). The authors attributed this to the differences in geometry and working fluid and did no further effort to explain it. The two studies of helical coil absorbers may be comparable to those of horizontal absorbers considering the small helix angles of the coils used.

As mentioned in Section 5.8.1 in Ch. 5, the correlation of Rogers (1981) has been used for prediction of the heat transfer between tube wall and bulk falling liquid film in both LPE and MPA. Since the correlation takes account of surface tension effects in form of Kapitza ($Ka \equiv \rho\sigma^3/g\mu^4$) number, it is also used when an additive (surface active agent) is added to the solution. The correlation of Rogers (1981) and the experimental data of horizontal and helical falling film absorbers in Table 6.1 will be compared in Section 6.3.

The correlation of Chun and Seban (1971) cannot be used for any of the models developed in Ch. 5 because it includes both heat transfer resistances near wall and interface. Instead, the correlation of Wilke (1962) has been used in the simulation of the generator and LPA in Ch. 5. Although use of this correlation for LPA may be justified by the observation of the completely wetted surface during the chiller test (after addition of an additive) in Ch. 7, it may not be so accurate for the generator where even distribution of solution to 44 vertical tubes (see Section 3.3.1 in Ch. 3) cannot be expected when the flow rate is small. Although Wilke (1962)'s correlation can also be used for MPE, its use should be limited strictly to complete wetting conditions.

As was reviewed above, there is no experimental data available for LPA or MPE that will operate under incomplete wetting conditions. The experiments presented in the next section have been carried out to fill this gap.

6.2 Falling film flows on vertical plates

This study has been intended to provide heat and mass transfer coefficients for the simulation of LPA/MPE in Section 5.8 in Ch. 5. Since LPA/MPE is a large-diameter tube (ϕ400 mm) and thus its curvature is small, a plate heat exchanger has been chosen for the experiments instead of a vertical tube. In the following, the setup, methods and results are described.

6.2.1 Experimental setup

Fig. 6.1 shows a schematic diagram of the experimental setup used in this study. Measurement points for different variables are marked with appropriate symbols in the legend. Components were arranged at appropriate vertical positions for the circulation of working fluids and the maximum circulation rate was limited by the liquid column height between components.

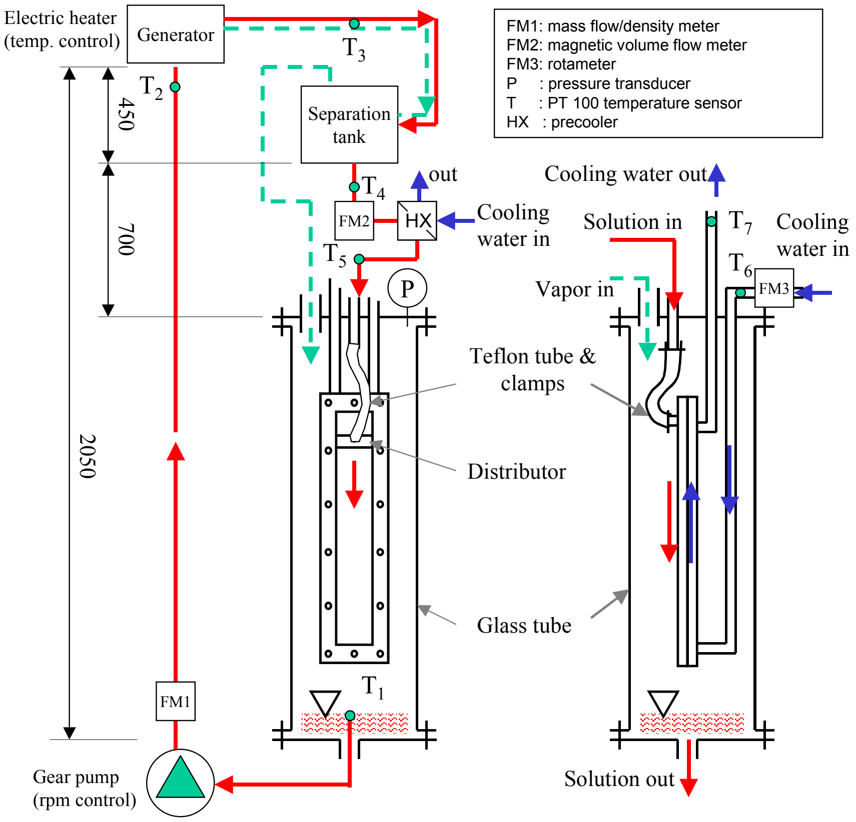

Figure 6.1 Falling film flow setup

The setup mainly consists of a generator, a separator, a precooler and an absorber.

The generator has four 1.5 kW electric heating elements and one of them is temperature-controlled, all together giving a continuous heat input range from 0 to 6.0 kW.

The separator is an empty vessel with three connections. When a two-phase flow from the generator enters the separator from the side, the liquid is separated from the vapour and flows down through the tube at the bottom while the vapour goes out through the tube at the top. The flow rate of the separated liquid is measured before it enters the absorber below.

The precooler is installed right above the absorber to cool down the incoming solution with tap water when needed.

The absorber consists of a copper plate heat exchanger in a 900mm-long ϕ150 mm glass tube. The heat exchanger is attached to a circular steel plate that seals the glass tube at the top with a silicon o-ring. The heat exchanger consists of flange-tightened copper (front) and steel plates (back) with a rubber gasket in between. On the copper plate, liquid is designed to flow in a thin film. Through the rectangular channel formed by the rubber gasket between the two plates (when tightened, the rubber gasket is compressed to 1.5 mm making hydraulic diameter d_h of the water channel to be about 3 mm), cooling water can be supplied to cool down the thin film flow on the copper plate.

Design details of the heat exchanger are given in Fig. 6.2.

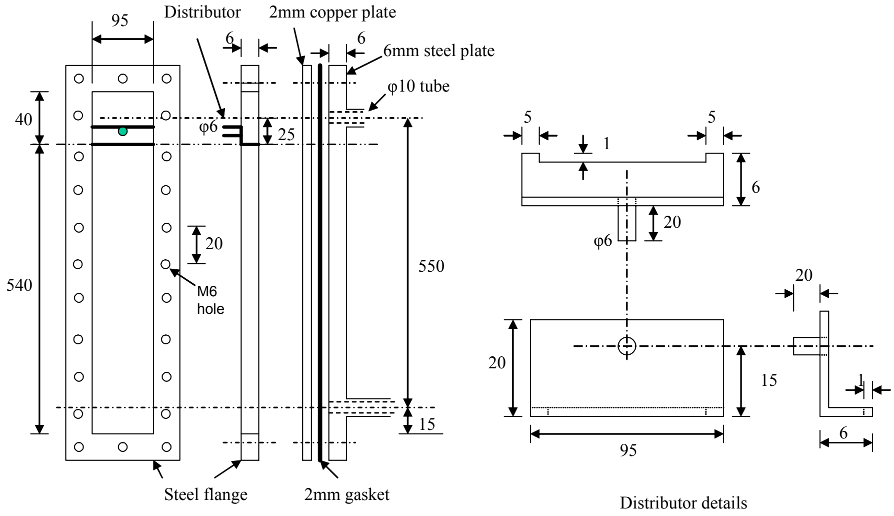

Figure 6.2 Plate falling film heat exchanger

The distributor in Fig. 6.2 is attached to the steel flange and distributes liquid over the copper plate through a narrow slot of 85×1 mm^2. In order to minimize the effect of incoming liquid velocity, a piece of wire mesh was rolled and inserted into the space between the distributor and the copper plate.

6.2.2 Definition of transfer coefficients

Unlike single-phase heat transfer, absorption process involves phase change at the vapor-liquid interface accompanying the variation of liquid composition providing somewhat complex boundary conditions to the system. Determination of the interface condition is important for the design and analysis of an absorber in this aspect. Because there is no device to measure any quantities at the interface in the present experimental setup, interface conditions will be determined by the heat and mass transfer models used in Ch. 5.

Because the local states cannot be measured, the results will be presented in terms of average heat and mass transfer coefficients. Then, the first step is to define the heat and mass transfer coefficients.

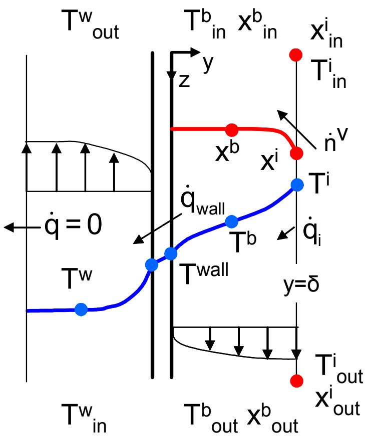

Figure 6.3 Concentration and temperature profiles in absorber

In the control volume in Fig. 6.3, heat flux at the wall can be expressed as

$$\dot{q}_{wall} = k\left(\frac{\partial T}{\partial y}\right)_{y=0} \equiv \alpha_{bulk}(T^b - T^{wall}) \tag{6.1}$$

, where α_{bulk} is the heat transfer coefficient from bulk liquid to the plate wall based on the bulk liquid temperature T^b and the wall temperature T^{wall}.

The total heat rejection to coolant can be expressed in terms of overall heat transfer coefficient U and an average temperature difference ΔT_{avg} as

$$\dot{Q} = \int U(T^b - T^w)dA \equiv \bar{U}A\Delta T_{avg} \tag{6.2}$$

, where ΔT_{avg} is defined by

$$\Delta T_{avg} \equiv \frac{(T^b_{in} - T^w_{out}) - (T^b_{out} - T^w_{in})}{\ln\left[(T^b_{in} - T^w_{out})/(T^b_{out} - T^w_{in})\right]} \tag{6.3}$$

, which is a logarithmic mean temperature difference between the bulk liquid and the cooling water.

Since the necessary bulk temperatures in Eq. (6.3) are measured, the average bulk film heat transfer coefficient $\bar{\alpha}_{bulk}$ can be calculated back from the definition of overall heat transfer coefficient $\bar{U}$ as

$$\bar{\alpha}_{bulk} = \left[\frac{1}{\bar{U}} - \frac{1}{\bar{\alpha}_{cool}} - \left(\frac{\Delta t}{k}\right)_{wall}\right]^{-1} \tag{6.4}$$

, where $\bar{\alpha}_{cool}$ and $(\Delta t/k)_{wall}$ are the heat transfer coefficient of cooling water and the plate wall respectively.

As mentioned in Section 6.1.4, different definitions of ΔT_{avg} have been used in Eq. (6.2) in some of the studies in Table 6.1.

Yüksel & Schlünder (1987) calculated local heat transfer coefficients with measured local temperatures from energy balance and averaged the local transfer coefficients.

Hoffmann et al (1996), Kyung and Herold (2002) and Yoon et al (2002) used the same logarithmic mean temperature as Eq. (6.3) but, instead of measured bulk temperature T^b, equilibrium bulk solution temperatures calculated from bulk concentration and pressure, i.e. $T^*(p,x^b)$, were used. On the other hand, Chen and Sun (1997) used T^i instead of T^b in Eq. (6.3) using the model of Yüksel & Schlünder (1987) for determination of T^i.

Takamatsu et al (2003) measured local wall temperatures and calculated average heat transfer coefficients with arithmetic mean temperatures.

Miller and Keyhani (2001) used $\Delta T_{avg}=T^i_{in}-T^w_{in}$, which is the maximum temperature difference in the system. Medrano et al (2002) and Bourouis et al (2005) adopted a similar approach but used $\Delta T_{avg}=T^*(p,x^b_{in})-T^w_{in}$.

Park et al (2003) and Kwon and Jeong (2003) used the same ΔT_{avg} as in Eq. (6.3).

Regarding the use of a logarithmic mean temperature for an absorber, Fujita and Hihara (2005) questioned its justification. The authors showed the inadequateness of a logarithmic mean temperature as a driving potential by comparing it with the solution of a differential model and pointed out that the error of the logarithmic method is large when the inlet solution temperature deviates from the corresponding equilibrium temperature.

Use of equilibrium temperatures instead of the measured bulk temperature in Eq. (6.3) gives an “overall” heat transfer resistance from vapor-liquid interface and wall. For determination of this overall resistance, some researchers assumed $T^i=T^*(p,x^b)$ and others measured or calculated T^i using a model such as Yüksel & Schlünder’s (1987).

Heat transfer process between bulk liquid and the wall is not different from that of a sensible heat transfer except that the interface conditions are applied as boundary conditions (Imagine that the liquid film flows through a channel bounded by a stationary wall and a moving interface). Therefore if the boundary conditions allow, a logarithmic mean temperature based on bulk temperatures can be used as a driving potential. This is also implied by Miller and Keyhani (1999) who measured local interface and coolant temperatures in a vertical tube absorber with a saturated LiBr solution supplied at the inlet. They reported slightly exponential (approximately linear) interface and coolant temperature profiles along the tube, which suggests that a logarithmic mean temperature could be used as an average driving temperature.

But still one question remains. The solution temperature measured at the outlet of an absorber may be assumed reasonably close to the “true” value because the temperature is measured right after the heat exchanger. But it is not the case with inlet solution temperature. Since the inlet temperature is measured before the absorber, if solution enters the absorber and experiences substantial changes, it cannot be regarded as a true value. This is probably why some researchers reported strong dependence of their heat transfer coefficients on the subcooling of inlet solutions (Kyung and Herold, 2002; Takamatsu et al, 2003). The best way to avoid this uncertainty is to supply only saturated solution to an absorber so that the solution may not change substantially in temperature before it reaches the heat transfer surface. For this, during the heat transfer tests in this study, care was taken to minimize the heat loss between the separation tank and the absorber.

Similar to the heat flux in Eq. (6.1), the mass flux at the vapor-liquid interface can be expressed as

$$\dot{n}^v = \rho D \left(\frac{\partial x}{\partial y} \right)_{y=\delta} \equiv \rho K (x^b - x^i) \tag{6.5}$$

, where K is the mass transfer coefficient based on bulk and interface concentrations.

The total mass absorbed into the film can be expressed in terms of an average mass transfer coefficient and a logarithmic mean concentration difference as follows (see eg. 5-78 and 5-79 in Perry et al, 1984).

$$\dot{m}^v = \int \rho K (x^b - x^i) dA \equiv \rho \bar{K} A \Delta x_{avg} \tag{6.6}$$

, where Δx_{avg} has been defined by

$$\Delta x_{avg} \equiv \frac{(x^b_{in} - x^i_{in}) - (x^b_{out} - x^i_{out})}{\ln\left[(x^b_{in} - x^i_{in}) / (x^b_{out} - x^i_{out}) \right]} \tag{6.7}$$

The biggest uncertainty in determination of $\bar{K}$ comes from the difficulty in measuring the interface concentrations, i.e. x^i_{in} and x^i_{out}.

Like heat transfer coefficients, definition of the driving potential for mass transfer also differs among the studies in Table 6.1.

Yih and Chen (1982) used an average logarithmic concentration difference derived from mass balance equations, which is a special case of Eq. (6.7) assuming $x^i_{in}=x^i_{out}$, which is valid for dilute isothermal systems such as the absorption of CO_2 in water.

Yüksel and Schulünder (1987) calculated an average concentration difference by integrating a local logarithmic concentration difference along the length of an absorber.

Kim et al (1995) gave overall mass transfer coefficients from vapour to bulk LiBr solution using a logarithmic (partial water) pressure difference considering the effect of non-absorbable gas (air max. 2% in volume) in the vapour phase.

Chen and Sun (1997) used Eq. (6.7) with calculated x^i using the model of Yüksel & Schlünder (1987) and Yoon et al (2002) used $x^*(p,T^b)$ instead of x^i in Eq. (6.7). Bourouis et al (2005) also reported mass transfer coefficients based on a logarithmic concentration difference but did not mention clearly whether interface concentrations, i.e. x^i, or equilibrium concentration, i.e. $x^*(p,T^b)$, were used.

Takamatsu et al (2003) defined the driving potential as $\Delta x_{avg} \equiv (x^b - x^i)/x^i$ and mentioned it yielded similar results to Yüksel and Schlünder (1987).

Miller and Keyhani (2001) used the difference between the bulk concentrations at the inlet and outlet, i.e. $\Delta x_{avg} \equiv x^b_{in} - x^b_{out}$, to avoid using the interface concentrations which they did not measure.

For the interface concentrations and temperatures in Eq. (6.7), the models of Nakoryakov and Grigoreva (1980) and Yüksel and Schlünder (1987) summarized in Ch. 5 will be used. This approach has been experimentally proved for its accuracy by Yüksel and Schlünder (1987) and has been adopted also by several other researchers including Chen and Sun (1997) and Takamatsu et al (2003).

6.2.3 Determination of coolant-side heat transfer coefficient

For the determination of coolant-side heat transfer coefficient $\overline{\alpha}_{cool}$ in Eq. (6.4), the plate heat exchanger was tested firstly in a condensation mode, i.e. with only pure water charged in the system.

During the tests, from the bottom of the setup in Fig. 6.1, water was fed to the generator by a gear pump. It was heated by the electric heaters in the generator to supply a two-phase flow to the separation tank below, where steam was separated from water. And then the steam condensed on the surface of the copper plate while it was cooled by cooling water. The water separated at the separation tank directly returned to the bottom of the glass tube bypassing the test section.

For each of three levels of generator power (1.5, 3 and 4.5 kW nominal), the cooling water flow rate was varied in the range of 1.5-7.4 lpm, which corresponded to Reynolds numbers in the range of 400-2,200 (cooling water temperature 9.8-13.9 ^oC at the inlet). The water flow rate to the generator was varied within the range of $5.56\text{-}12.8\times10^{-3}$ kg/s depending on the generator power.

In total, three sets of tests were carried out and 41 data points were obtained. Pressures (dew temperatures) and condensation heat transfer rates were measured during the tests as shown in Fig. 6.4.

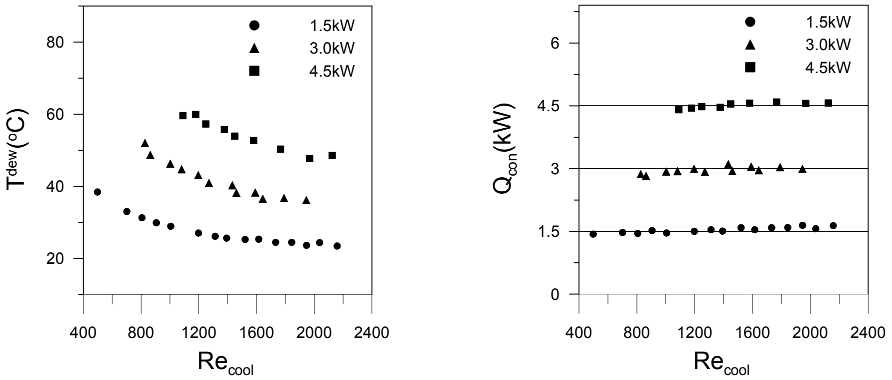

(a) Dew temperature vs. coolant Re no. (b) Condensation heat vs. coolant Re no.

Figure 6.4 Dew temperature and heat transfer rate for condensation tests

Dew temperature (pressure) increased with decreasing cooling water Reynolds numbers in Fig. 6.4a. This is because cooling water flow rate was decreased while heat input to the generator was maintained at a constant value.

On the other hand, the condensation heat transfer rate $\dot{Q}_{con}$ in Fig. 6.4b decreased only slightly with decreasing Reynolds number. Since heat input was constant in each set of tests, the condensation heat transfer rate should have been constant too. This is believed to be the influence of heat loss which increased with increasing dew temperature in Fig. 6.4a.

Except for the test surface, the whole absorber heat exchanger was insulated with three layers of a 0.3 mm-thick paper masking tape. Foam insulators could not be used because of "out-gassing" in vacuum environment. Although paper is a good insulator (thermal conductivity ~0.05W/mK), condensation took place on its surface. The paper surface has been observed wet during the condensation tests and this has been taken into account in the following analysis.

Taking into account the condensation on the paper surface, $\dot{Q}_{con}$ can be written as

$$\dot{Q}_{con} = \dot{Q}_{front} + \dot{Q}_{back} \tag{6.8}$$

, where $\dot{Q}_{front}$ denotes the heat transferred through the test surface and $\dot{Q}_{back}$ through rest of the surface, which is mostly the backside of the heat exchanger.

Since $\dot{Q}_{front}$ transfers through a 2mm-thick copper plate to cooling water flow, it can be written as

$$\begin{aligned}\dot{Q}_{front} &= \bar{U}_{front} A_{front} \Delta T_{con} \\ &= \left[\frac{1}{\bar{\alpha}_{con,front}} + \left(\frac{\Delta t}{k} \right)_{copper} + \frac{1}{\bar{\alpha}_{cool}} \right]^{-1} A_{front} \Delta T_{con}\end{aligned} \tag{6.9}$$

, where mean temperature difference ΔT_{con} is defined by

$$\Delta T_{con} \equiv \frac{T_{out}^{w} - T_{in}^{w}}{\ln\left[(T^{dew} - T_{in}^{w}) / (T^{dew} - T_{out}^{w}) \right]} \tag{6.10}$$

And since $\dot{Q}_{back}$ transfers through firstly, three layers of paper tape, then 6mm-thick steel plate to cooling water flow, it can be written as

$$\begin{aligned}\dot{Q}_{back} &= \bar{U}_{back} A_{back} \Delta T_{con} \\ &= \left[\frac{1}{\bar{\alpha}_{con,back}} + \left(\frac{\Delta t}{k} \right)_{paper} + \left(\frac{\Delta t}{k} \right)_{steel} + \frac{1}{\bar{\alpha}_{cool}} \right] A_{back} \Delta T_{con}\end{aligned} \tag{6.11}$$

In order to determine the cooling water-side heat transfer coefficient $\bar{\alpha}_{cool}$, one should solve Eq. (6.8), (6.9) and (6.11) simultaneously. What makes this process more complex is that the observed condensation mode on the test surface was a combination of drop- and film-wise condensation, for which no reliable correlation exists.

Since heat transfer coefficient of drop-wise condensation generally reports dozens of times higher than that of film-wise condensation and the condensation observed on the test surface seemed somewhere between the two condensation regimes, any estimation using an empirical correlation was thought highly unreliable. Therefore instead of using an empirical correlation, the Wilson plot method (Wilson, 1915) has been chosen as an alternative.

The idea of Wilson plot method originated from the fact that overall heat transfer coefficients in condensation experiments appeared as a linear line in so-called Wilson plot when the heat transfer coefficient on condensation side was maintained constant while cooling water flow rate was varied. Then, in the Wilson plot, the condensation heat transfer coefficient is the intercept of the linear line at the y-axis. This is explained briefly in the following.

Overall heat transfer coefficient $\bar{U}_{con}$ can be written as

$$\frac{1}{\bar{U}_{con}} = \frac{1}{\bar{\alpha}_{con}} + \left(\frac{\Delta t}{k}\right)_{wall} + \frac{1}{\bar{\alpha}_{cool}} \tag{6.12}$$

, where $\bar{\alpha}_{con}$ is an average condensation heat transfer coefficient. If $\bar{\alpha}_{con}$ is constant and $\bar{U}$ is determined from experimental data, Eq. (6.12) is a function of $\bar{\alpha}_{cool}$ only. Since $\bar{\alpha}_{cool}$ can be written as

$$\bar{\alpha}_{cool} = C \,\mathrm{Re}^m \,\mathrm{Pr}^n \left(\frac{k}{d_h}\right)_{cool} \tag{6.13}$$

, where C is a constant and d_h is a hydraulic diameter of the cooling water channel, Eq. (6.12) becomes

$$\frac{1}{\bar{U}_{con}} = \frac{1}{C}\left(\frac{d_h}{k}\right)_{cool}\left(\frac{1}{\mathrm{Re}^m \,\mathrm{Pr}^n}\right) + \frac{1}{\bar{\alpha}_{con}} + \left(\frac{\Delta t}{k}\right)_{wall} \tag{6.14}$$

, which is a linear function in $1/\bar{U}$ -$1/(\mathrm{Re}^m\mathrm{Pr}^n)$ plane.

When Reynolds number increases infinitely, Eq. (6.14) becomes

$$\left(\frac{1}{\bar{U}}\right)_{\mathrm{Re}\to\infty} = \frac{1}{\bar{\alpha}_{con}} + \left(\frac{\Delta t}{k}\right)_{wall} \tag{6.15}$$

and therefore $\bar{\alpha}_{con}$ can be obtained from the intercept of the Eq. (6.14) at y-axis.

This Wilson plot method is useful when the heat transfer coefficient should be determined for a heat exchanger with a complex geometry or there is no empirical correlation available as in the present case.

Application of the Wilson plot method in the present case is a little complicated because firstly, the steam condensed not only on the test section but also on the insulated part of the heat exchanger and secondly, the condensation heat transfer coefficients could not be maintained at a constant value in this study. Nevertheless, Eq. (6.8), (6.9) and (6.11) should be solved simultaneously using Eq. (6.13). The solution has been obtained as described below.

First of all, for $\bar{\alpha}_{con,back}$ in Eq. (6.11), the Nusselt solution for film-wise condensation (see B1 in Appendix B) has been used based on the observation that the insulated surface was completely wet during the tests.

Regarding the condensation heat transfer coefficients on the front, although heat flux was almost constant as shown in Fig. 6.4b, because the dew temperature changed as in Fig. 6.4a, it cannot be expected that condensation heat transfer coefficient remained constant during the tests. Constant pressure could have been achieved if the inlet temperature of cooling water had been controlled.

In order to minimize errors caused by the varied dew temperature, only data in the range 1,200<Re<2000 have been used. Data below Re=1,200 have been neglected because the dew temperatures were much higher than the others and the data above Re=2,000 have been rejected because the cooling water flows might belong to a different flow (non-laminar) regime.

Whether it was because of the inconstant condensation heat transfer coefficients or because of insufficient number of the data points, "best fit" of each set of the data (i.e. 1.5, 3 and 4.5 kW cases in Fig. 6.4) gave different values for the exponent m of the Reynolds number in Eq. (6.13). Therefore it has been decided that m should be varied arbitrarily to find a value that could give best agreement between the different sets of experiments. The Wilson plots in Fig. 6.5 show this process in graphs.

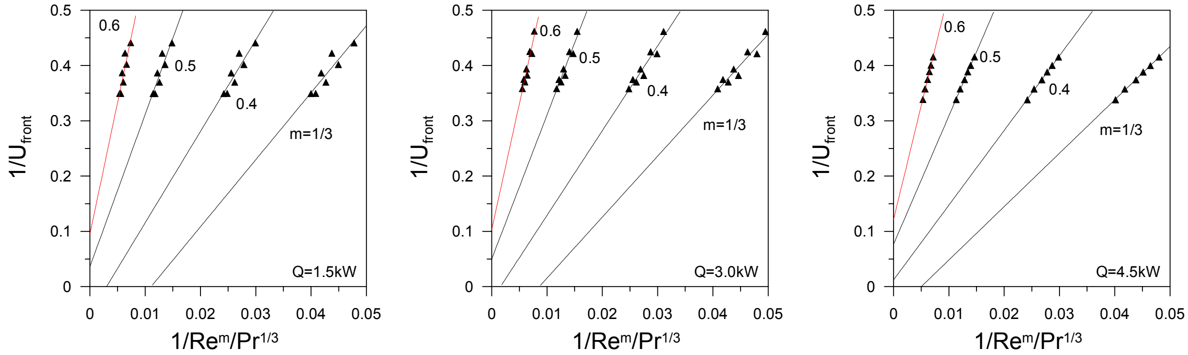

(a) 1.5 kW (b) 3 kW (c) 4.5 kW

Figure 6.5 Wilson plots

Firstly, each set of the data was fitted by a linear function with an arbitrary exponent in the range of 1/3 to 0.6 as shown in Fig. 6.5. For forced convection in a smooth tube, the exponent of Reynolds number in empirical correlations is 0.8 for turbulent flows and about 1/3 for laminar flows. On the other hand, for convective heat transfer on a flat plate, Reynolds-Colburn analogy suggests again 0.8 for turbulent flows and 0.5 for laminar flows (see e.g. Holman, 1997). Since the cooling water channel of the heat exchanger in Fig. 6.2 has a wide and thin rectangular cross section, the exponent is expected to be between 1/3 and 0.5. Exponent of Prandtl number is commonly set at 1/3 for all cases.

Note that the intercept on y-axis increases from Fig. 6.5a to 6.5c for a same exponent. Since condensation heat transfer coefficient is inversely proportional to the intercept, this means that condensation heat transfer coefficient decreased with increasing condensation rate.

And secondly, in Fig. 6.5a, the lines for exponents 0.4 and 1/3 have negative intercepts on y-axis. This suggests that the exponent should be bigger than 0.4 so that condensation heat transfer coefficient can be positive in all cases.

It turned out that smaller exponent gives better agreement between the three sets of test results, which narrows it between 0.4 and 0.5. The exponent *m* was finally set to 0.45.

The resulting Nusselt number correlation is given by

$$Nu = 0.241\,\mathrm{Re}^{0.45}\,\mathrm{Pr}^{1/3}\left(\frac{\mu}{\mu_{wall}}\right)^{0.14} \tag{6.16}$$

, where viscosity ratio $(\mu/\mu_{\mathrm{wall}})^{0.14}$ has been added to take account of the difference between bulk and wall temperatures. Experimental data and Eq. (6.16) are shown in Fig. 6.6a.

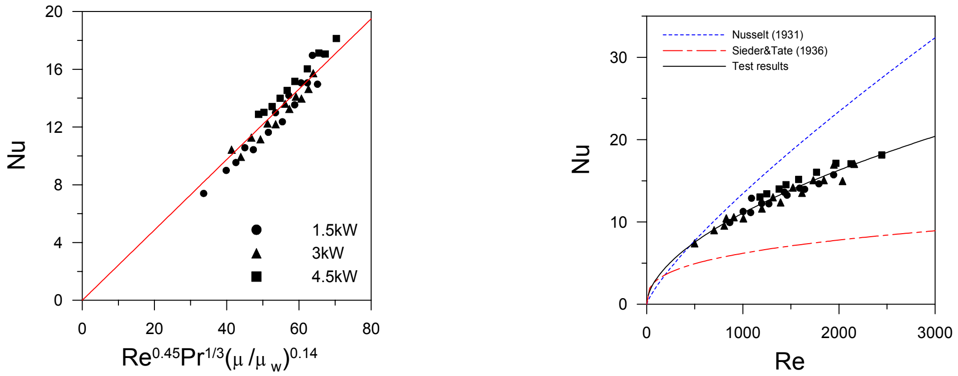

(a) Coolant-side Nu number (b) Comparison with empirical correlations

Figure 6.6 Coolant-side Nu number

The results were compared with some empirical correlations for developing laminar and turbulent flows in Fig. 6.6b. It turned out that the heat transfer coefficient was larger than predicted by the laminar correlation of Sieder and Tate (1936) and smaller than the turbulent correlation of Nusselt (1931).

Eq. (6.16) reproduces heat transfer coefficients within ±9.5% of the test results as shown in Fig. 6.7.

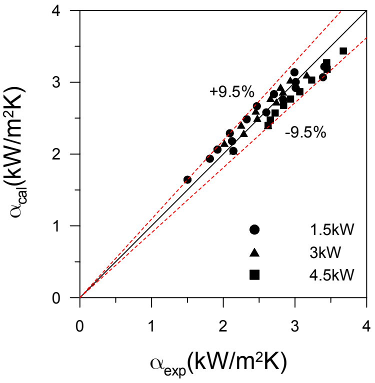

Figure 6.7 Error range of Eq. (6.16)

6.2.4 *Falling film experiments and results*

After condensation tests have been finished, the system was drained and charged with 10.26kg of 50 wt% LiBr-water solution. Due to incomplete drainage, the concentration of the solution inside the system was found slightly lower than the original charging concentration.

During preliminary tests, the amount of solution charged was found too large because the solution overflowed into the absorber through the vapour line from the top of the separation tank. For this reason, 1.3 kg of solution has been extracted leaving 8.96 kg of the solution in the system. It was also observed that the wet area on the test surface changed with time and history of the flow variation, i.e. the wet areas were different for the same flow rate when the desired flow rate was reached from a larger flow rate or from a smaller flow rate. For this reason, experimental data were recorded during the stable operation preceded by the circulation of a flow rate larger than the desired value.

Tests were carried out varying solution flow rate for different working fluids (LiBr-water solution and water with or without an additive) and different heat transfer surfaces (bare and screened copper surface). During each set of tests, the cooling water flow rate and the outlet temperature of the generator were kept constant. The conditions for the experiments are summarized in Table 6.2.

Table 6.2 Experimental conditions

	Working fluid	Surface	Avg. Re_{cool}	Remark	Constants in Eqs. (6.23) & (6.24)			
					a	b	c	d
1	solution	bare	1395		0.0312	0		
2	solution	screen	1403		9.62×10^{-3}	0.293		
3	solution	bare	no cooling	subcooled solution			6.92×10^{-4}	0.866
4	solution	screen	no cooling				1.00×10^{-3}	0.806
5	solution+ octanol*	bare	1371		0.0773	-0.0591		
6	solution+ octanol	screen	1375		0.0531	+0.0369		
7	solution+ octanol	bare	no cooling	subcooled solution			8.67×10^{-4}	0.951
8	solution+ octanol	screen	no cooling				7.45×10^{-4}	0.981
9	water	bare	1378	open to atmosphere	4.50×10^{-4}	1		
10	water+ octanol	bare	1390		8.15×10^{-3}	0		

* A synonym of 2-Ethyl-1-hexanol ($C_8H_{18}O$). In all cases, the concentration is 100ppm based on mass.

Experiments 1 to 8 in Table 6.2 were intended to determine the influence of different surface geometries and of the presence of octanol in aqueous LiBr solution on heat and mass transfer during the absorption process.

Experiments 1, 2, 5 and 6 were intended to determine the heat transfer coefficient between bulk solution and test surface. The solution at the inlet of absorber was not controlled, i.e. the precooler in Fig. 6.1 was not in operation. For this reason, condition of the solution was close to its equilibrium state.

On the other hand, experiments 3, 4, 7 and 8 were performed without circulation of cooling water to simulate an adiabatic condition at the test surface. During these tests, the cooling water channel was kept dry and the ends of cooling water tubes were taped to stop possible air circulation. These tests were intended to determine the solution-side mass transfer coefficient at vapor-liquid interface of the falling film flows. The precooler in Fig. 6.1 was operated at its full capacity to subcool the solution at the absorber inlet.

Finally, for experiments 9 and 10, the system was open to atmosphere to prevent steam generation so that only the sensible heat transfer in subcooled water falling film flows could be investigated with or without the presence of octanol.

Two different surfaces have been tested. One is a bare surface of copper plate and the other is the same copper plate covered with a copper wire screen. The screen is a standard product woven with 0.38mm copper wires having 22 meshes per inch. It was not mechanically bonded onto the surface but inserted between the steel flange and the copper plate in Fig. 6.2 and tightly bolted while it was stretched sideways. Because complete contact between the screen and the plate was impossible, some portion of the screened test section had void space between the screen and the plate surface.

For all cases, absorption rate $\dot{m}^v$ can be calculated by

$$\dot{m}^v = \dot{m}^l_{out} - \dot{m}^l_{in} \tag{6.17}$$

, where $\dot{m}^l_{out}$ is measured by the mass flow meter FM1 in Fig. 6.1 after the absorber and the inlet mass flow rate $\dot{m}^l_{in}$ can be calculated by

$$\dot{m}^l_{in} = \rho_{in}\dot{V}^l_{in} \tag{6.18}$$

, where the volumetric flow rate $\dot{V}^l_{in}$ is measured by the magnetic volume flow meter FM2 at the absorber inlet in Fig. 6.1. Note that the density of solution ρ_{in} is a function of temperature and concentration, i.e. $\rho_{in}=\rho(T^b_{in}, x^b_{in})$. Because the density of the solution at the absorber inlet was not measured, ρ_{in} in Eq. (6.18) had to be determined indirectly.

Since the mass of LiBr is constant anywhere along the solution flow, mass conservation for LiBr is written as

$$\Sigma\dot{m}_{LiBr} = \dot{m}^l_{out}x^b_{out} - \dot{m}^l_{in}x^b_{in} = \dot{m}^l_{out}x^b_{out} - \rho_{in}\dot{V}^l_{in}x^b_{in} = 0 \tag{6.19}$$

, where the solution concentration x^b_{out} was determined by the density signal from the mass flow meter at the absorber outlet. Since the temperature of the solution at the inlet, T^b_{in}, was measured right before the volumetric flow meter (T_4 in Fig. 6.1), Eq. (6.19) is a function of x^b_{in} only. By solving Eq. (6.19) for x^b_{in} using a proper density correlation, the mass flow rate at the absorber inlet was determined by Eq. (6.18) and the absorption rate could be calculated from Eq. (6.17).

Alternative way to determine mass flow rate at the inlet is to solve an energy balance equation over the absorber, which is given by

$$\dot{m}_{in}^{l} h_{in}^{l} + \dot{m}^{v} h^{v} - \dot{m}_{out}^{l} h_{out}^{l} - \dot{Q}_{cool} = 0 \tag{6.20}$$

, where the heat transfer rate from bulk liquid to cooling water $\dot{Q}_{cool}$ is determined by

$$\dot{Q}_{cool} = \dot{m}^{w} C_{p}^{w} \left(T_{out}^{w} - T_{in}^{w} \right) \tag{6.21}$$

Using Eq. (6.17) and (6.19), Eq. (6.20) can be rewritten as

$$\dot{m}_{out}^{l} \left[\frac{x_{out}^{b}}{x_{in}^{b}} h_{in}^{l} + \left(1 - \frac{x_{out}^{b}}{x_{in}^{b}} \right) h^{v} - h_{out}^{l} \right] - \dot{Q}_{cool} = 0 \tag{6.22}$$

, where the measured volumetric flow rate $\dot{V}_{in}^{l}$ and the density $\rho_{in}=\rho(T^{b}_{in}, x^{b}_{in})$ at the absorber inlet do not appear. Eq. (6.22) is also a function of x^{b}_{in}, which is shown explicitly and also implicitly in $h^{l}_{in}=h^{l}(T^{b}_{in}, x^{b}_{in})$. Using a proper enthalpy correlation for h^{l}_{in}, Eq. (6.22) can be easily solved.

Solutions of Eq. (6.19) and (6.22) were used to crosscheck the mass flow rate at the absorber inlet $\dot{m}_{in}^{l}$. For all cases, the thermodynamic correlations introduced in Ch. 4 have been used.

The difference in $\dot{m}_{in}^{l}$ determined in the two different ways was found less than 6 % for the cases where the absorber was cooled by cooling water and less than 2 % for the adiabatic cases. It was found that Eq. (6.19) tends to give a smaller $\dot{m}_{in}^{l}$, i.e. larger $\dot{m}^{v}$, than Eq. (6.22).

Although the discrepancy between the solutions of Eq. (6.19) and (6.22) did not significantly influence heat transfer coefficients, it made big differences in mass transfer coefficients. Mass transfer coefficients determined with Eq. (6.19) were larger that those with (6.22) and showed erratic trends. This is because the solution of Eq. (6.19) is very much sensitive to the measurement errors in flow rates, i.e. $\dot{m}_{in}^{l}$ and $\dot{V}_{in}^{l}$, and the magnitudes of the errors were in the same order of $\dot{m}^{v}$ values in adiabatic absorption tests (see Appendix D2 for calibration results of flow meters). For this reason, Eq. (6.22) was used for the analysis of all experiments.

In total, 134 experiments were carried out and finally 60 data points were selected and processed to give the following results. The other data points were discarded because of several reasons including the condensation on test section and poor heat balance. To give a quick overview of the experimental conditions for the selected data, ranges of some parameters are summarized in Table 6.3. Original measured data are given in Appendix D3.

Note that heat input to the generator was not constant as in the condensation tests in the previous section. Instead, only one of the heaters inside the generator was automatically controlled to maintain the outlet temperature, i.e. T_3 in Fig. 6.1, at preset temperatures. For the water-cooled experiments (i.e. experiments 1, 2, 5, 6, 9 and 10), T_3 was set to 40 °C and for the adiabatic tests (i.e. experiments 3, 4, 7 and 8), it was set to 50 ^oC. Experimental data with higher temperature settings have been discarded because the system pressures were so high that condensation on the test section or on the inner surface of the glass tube has been observed.

Table 6.3 Experimental ranges of some parameters

	x^b_{in} (LiBr wt%)[1]	T^b_{in} (^oC)	m^l_{in} (kg/h)	p (kPa)	T^w_{in} (^oC)	m^w (kg/h)[2]
1	49.34±0.03	27.4±1.0	14.5-19.9	1.06-1.08	8.6±0.01	310.6±0.7
2	49.86±1.30	26.4±0.3	11.7-19.2	1.01-1.07	9.1±0.17	311.0±0.3
3	48.94±0.13	12.0±0.23	11.3-24.9	2.48-2.79	-	0
4	50.07±0.37	11.6±0.7	12.0-24.3	2.84-3.00	-	0
5	50.61±0.93	26.7±0.7	11.9-23.3	0.73-0.81	8.0±0.02	311.7±1.6
6	49.00±0.16	26.3±0.7	11.9-24.3	0.82-0.90	8.3±0.28	309.8±1.0
7	50.47±0.37	11.2±1.1	11.5-29.3	2.65-2.89	-	0
8	50.19±0.1	11.2±1.1	12.1-31.4	2.62-2.93	-	0
9	0	34.2±2.2	2.3-32.2	-	8.9±0.91	311.6±1.7
10	0	33.9±1.1	2.2-32.2	-	9.0±0.66	314.5±3.5

1. Converted from the density and temperature of solution
2. Water density is multiplied by the measured volume flow rate

In the following, the experimental data are presented in various forms and discussed regarding the different heat and mass transfer characteristics of the falling film flows.

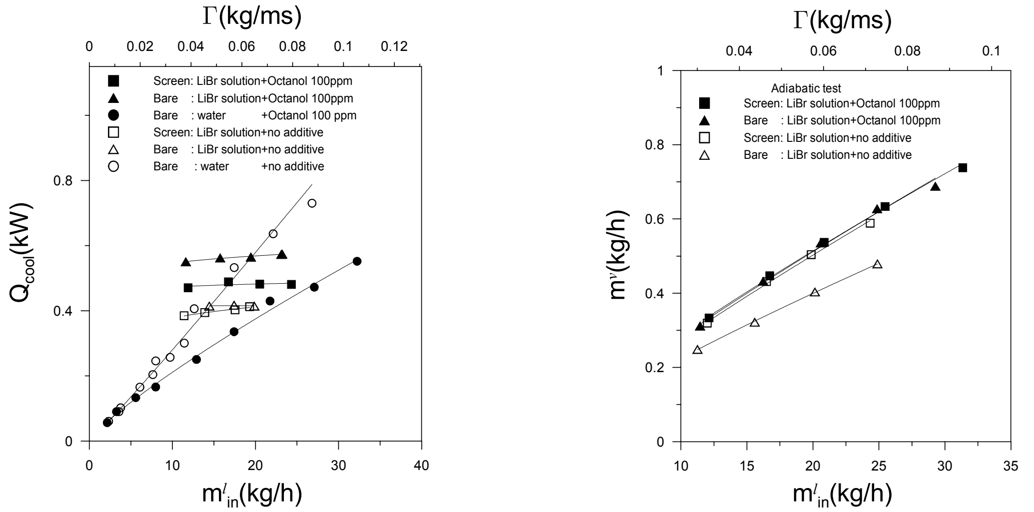

(a) Heat transfer rates in water-cooled tests (b) absorption rates in adiabatic tests

Figure 6.8 Experimental heat and mass transfer rates

Fig. 6.8a shows the heat transfer rates from falling film flows to cooling water. For the absorption cases, heat transfer rate increased slowly with increasing film flow rate. It increased however much more rapidly with increasing flow rate for the two cases of sensible heat transfer in water.

Fig. 6.8b shows vapour absorption rates from the adiabatic absorption tests. The absorption rates increased linearly with film flow rate.

Heat and mass transfer coefficients were calculated using the definitions given in Section 6.2.2 and are presented in Fig. 6.9.

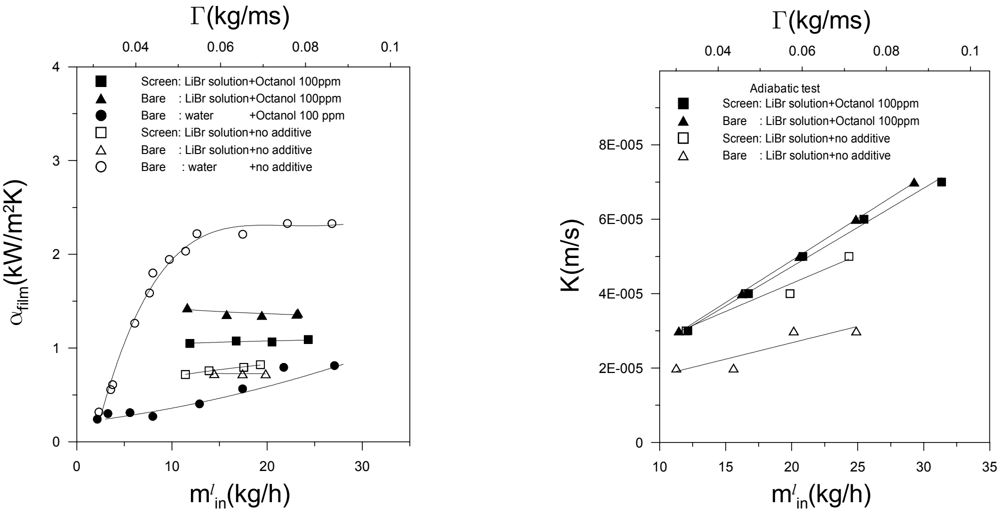

(a) Bulk film heat transfer coefficients (b) mass transfer coefficients

Figure 6.9 Experimental heat and mass transfer coefficients

Firstly, regarding the absorbing films in Fig. 6.9a, the heat transfer coefficient was increased substantially by the addition of additive. It was roughly doubled for the bared surface and increased by about 60% for the screened surface.

The effect of the additive on water film was found opposite. Water with octanol showed much smaller heat transfer coefficient than that of pure water in the entire flow rate range tested. In the case of pure water, it seems that a sort of transition took place near the flow rates around $\dot{m}_{in}^{l}$=12 kg/h. This point coincides with the point when the test section was fully wet with water, which will be discussed in Section 6.3.

Mass transfer coefficients increased linearly with flow rate as shown in Fig. 6.9b. Octanol almost doubled the mass transfer coefficient for the bare surface. But it had a little effect on the screened surface.

In Fig. 6.10, the heat and mass transfer coefficients in Fig. 6.9 are shown in terms of Nusselt and Sherwood numbers against film Reynolds number. In order to minimize the influence of property variation, Nusselt and Sherwood numbers were divided by $Pr^{1/2}$ and $Sc^{1/2}$, respectively.

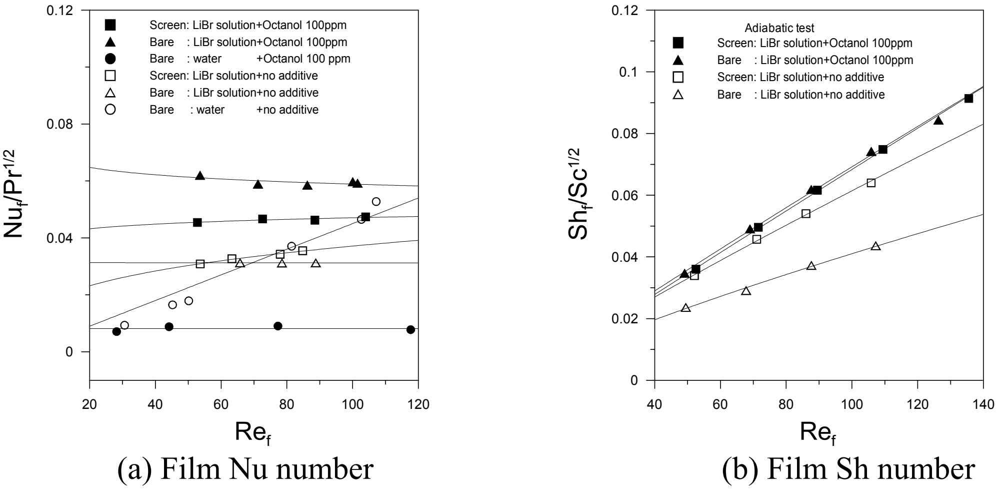

(a) Film Nu number (b) Film Sh number

Figure 6.10 Non-dimensional numbers

First of all, in Fig. 6.10a, the Nusselt number of pure water increases linearly with the Reynolds number (not shown in Fig. 6.10a but up to $Re_f \approx 170$, $\Gamma \approx 0.04$ kg/ms) while the others are more or less constant. Besides it is remarkable that addition of octanol in pure water changed its behavior completely (○ and ●in Fig. 6.10a).

It is obvious that octanol suppressed heat transfer performance when mixed with water. During the tests, water flows with octanol were observed smoother on the film surface and also narrower in flow width than those of pure water. It seems that octanol suppressed the waves on the surface and also decreased the wet surface area.

The water-cooled absorption tests with pure LiBr solution indicate that the screened surface only slightly increases the heat transfer (□ and Δ in Fig. 6.10a). It is thought that the screen mainly improves wetting of the heat transfer surface. On the other hand, the screen seems to have a negative influence when octanol is mixed (■ and ▲ in Fig. 6.10a). During the water-cooled absorption tests of LiBr solution with octanol, highly intensive local convections were observed on the 'free' surface of the falling film on the bare surface, which must have enhanced the transfer process. The screen is thought to have suppressed these local convections. Nusselt numbers of the bare and screened surfaces are a factor of 2 and 0.4 larger than for the additive free case, respectively.

Similar trends are found with the screen on the mass transfer results from adiabatic absorption tests in Fig. 6.10b.

Firstly, the screen also enhanced mass transfer when octanol was not added to solution. Its influence is, however, stronger than the case of heat transfer. With the screen, the Sherwood number was improved by a factor of 1.6 (□ and Δ in Fig. 6.10b). But the screen did not change the Sherwood number when octanol was added (■ and ▲ in Fig. 6.10b). Octanol increased the Nusselt number by a factor of 1.8 and 1.1 for the bare and screened surface, respectively.

The results in Fig. 6.10 can be represented by the following correlations for $40 < Re_f < 110$ with the coefficients a, b, c and d as indicated in Table 6.2.

$$Nu_f = a\,Re_f^b\,Pr^{1/2} \tag{6.23}$$

$$Sh_f = c\,Re_f^d\,Sc^{1/2} \tag{6.24}$$

All the fluid properties were calculated for the average inlet and outlet bulk conditions.

In the next section, the results obtained above will further be analyzed with help of the observations made during the tests. Comparison will also be made with other experimental data from literature.

6.3 Analysis of the experimental results

6.3.1 *Flow patterns – wetted area*

During the tests, falling film flows of one experimental case were clearly discernable from those of other cases even with naked eyes. In the following, some observations made during the tests are discussed in relation to the heat and mass transfer coefficients reported in the previous section.

Fig. 6.11 shows typical flow patterns observed on the bare copper surface for the corresponding experimental cases.

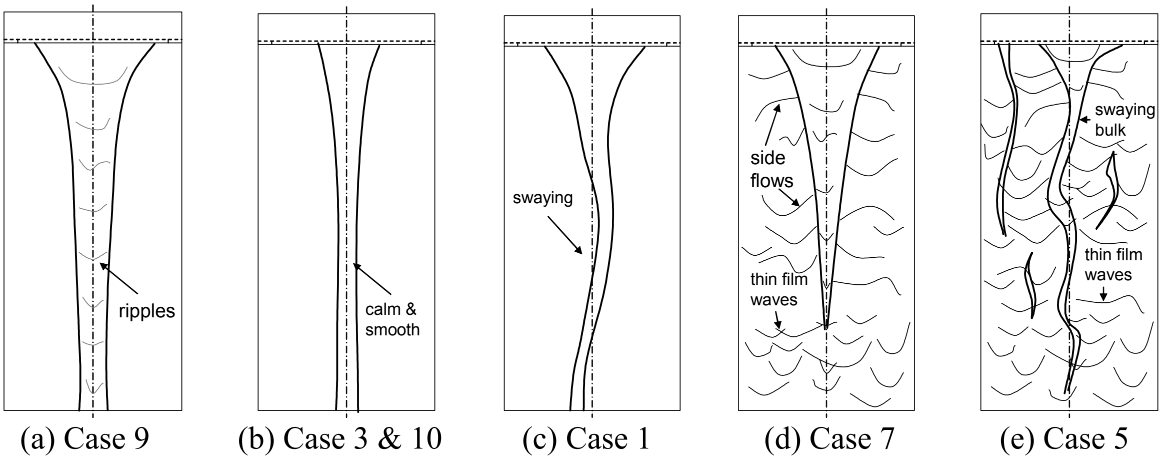

(a) Case 9 :water (b) Case 3 & 10 :adiabatic sol. (c) Case 1 :wat-cooled sol. (d) Case 7 :adiabatic sol.+oct. (e) Case 5 :wat-cooled sol.+oct.

Figure 6.11 Flow patterns on the bare surface

Fig. 6.11a shows the flow pattern of a pure water flow for Case 9. The flow was wide at the top and narrowed as it flowed down. Ripples were observed on the surface in all cases. Wet surface area was observed to increase clearly with flow rate.

Fig. 6.11b shows a solution flow without octanol in adiabatic condition. It was steady and very calm on the surface. Although wet surface area increased with flow rate, it was hard to estimate the change quantitatively within the solution flow range tested. The water flows with octanol looked very similar to Fig. 6.11b. Wet surface area increased very slowly with flow rate.

Fig. 6.11c shows a solution flow without octanol when it was cooled by cooling water. The bulk solution stream swayed sideways. Due to its rapid movement, it was impossible to make out surface condition and wet surface area.

Fig. 6.11d shows a typical flow pattern of the solution flows with octanol in adiabatic condition. Tiny filament-like side streams came out from the main bulk stream at its sides. The side streams were thin and chaotic in movement but the main bulk stream was relatively calm and steady. When flow rate was small, boundary of the main stream could not be clearly seen downstream. Instead, the space seemed to be covered with waves of very thin films.

When the flow in Fig. 6.11d was cooled, the main bulk stream moved rapidly sideways and the chaotic movement of the filament-like side streams was enhanced as in Fig. 6.11e. A few minor streams also appeared intermittently next to the main stream. The surface seemed full of large and small local convections and it was impossible to estimate wet surface area.

These local convections on the surface in Fig. 6.11d and 6.11e, which were induced by octanol and intensified by the cooling of the plate with water, are attributed to the instability originated from the uneven distribution of surface tension at vapour-liquid interface, i.e. Marangoni effect. Particularly for the case in Fig. 6.11e, there must be strong surface tension gradients on the surface so that even the bulk liquid film flow was moved sideways. Among researchers, it is generally accepted that the enhancement mechanism of additives is based on Marangoni convection (Beutler et al, 1996; Ziegler and Grossman, 1996). But thorough description of this enhancement mechanism is still not available particularly regarding the behaviour of additives in the film of absorbent solution (see e.g. Koenig et al, 2003).

Flow patterns observed on the screened surface are shown in Fig. 6.12.

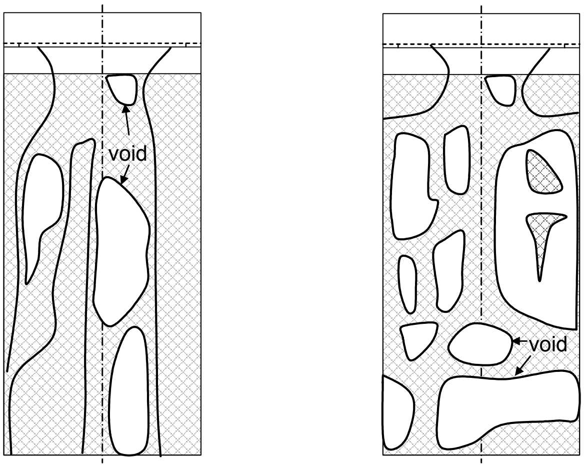

(a) Case 4 (b) Case 6

Figure 6.12 Flow patterns on the screened surface

The screen made it hard to observe any characteristic movement of the flows on the surface other than the occurrence of void regions. Although impossible to estimate it quantitatively, the screened surface provided a larger wet surface area than the bare surface without octanol in case of adiabatic absorption (Case 4 & Case 8). But it was impossible to tell whether the screen provided a larger surface when water cooling was applied (Case 2 & Case 6).

The observations above confirmed, first of all, that variation of wet surface area significantly influenced the transfer processes. The wet surface area did not only change with flow rate and liquid composition but also with heat flux. Although no quantitative estimation was made, when an absorbing flow was cooled, the bulk stream of solution moved sideways increasing average effective wet surface area, whether it was added with octanol or not.

For water flows, however, wet surface area could be estimated by observation. Although this estimation is likely to be in large error, it may help understand the experimental results. Fig. 6.13 shows the wet surface fraction and Nusselt numbers for the case of pure water and that of water with octanol.

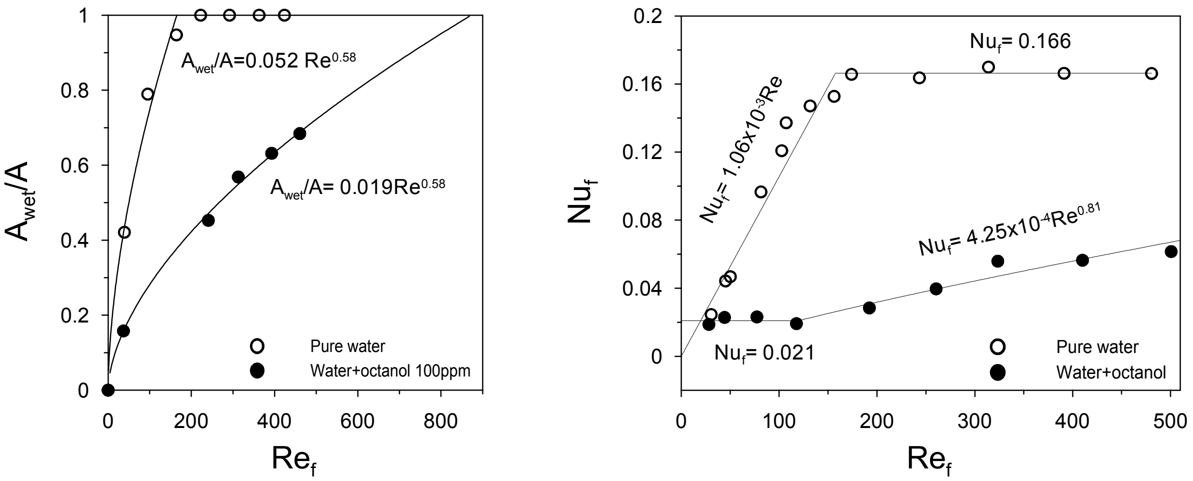

(a) Wet surface fraction (b) Film Nu number

Figure 6.13 Experimental data for water film flows ($T^{b}_{in}\approx 30^{o}C$)

Fig. 6.13a shows that the heat transfer surface was not completely wet with pure water below Re_f =200 and it was never completely wet with water+octanol flows in the entire Reynolds number range tested.

In Fig. 6.13b, Nusselt number of pure water starts to decrease at around the same Reynolds number as that of the wet fraction. The Nusselt number of water+octanol decreases with decreasing Reynolds number down to Re_f=120 but remains constant with further decrease of the Reynolds number.

It is believed that the behavior of the Nusselt numbers in Fig. 6.13b was due to incomplete wetting of the heat transfer surface. Actually, complete wetting of the surface was only observed in the pure water flows at large Reynolds numbers. Although the surface looked wet in Case 5 and 7 (Fig. 6.11d and e), it was not completely covered by bulk solution film. Prediction of dry patch formation and estimation of wetted surface area are closely related to the minimum wetting rate (MWR), i.e. the minimum flow rate that is required to make or maintain a completely wet surface. It may be helpful at this moment to introduce previous studies regarding MWR.

MWR of a liquid on a solid surface is dependent on properties of the liquid, material and condition of the solid surface. This subject has been addressed by many researchers taking consideration of balances between inertial and surface forces (and/or energies) including Hartley and Murgatroyd (1964), Bankoff (1971), Mikielewicz and Moszynski (1976), Doniec (1988), Tang et al (1991), El-Genk and Saber (2001).

Hartley and Murgatroyd (1964), being recognized as a pioneering work by the subsequent investigations, presented two criteria for the break up of liquid films over isothermal solid surfaces based on the “force” and “energy” balances in the liquid films shown in Fig. 6.14.

For the “force” criterion, they assumed that surface tension force must balance the fluid pressure along the film curvature at the stagnation point in a stable dry patch in Fig. 6.14a.

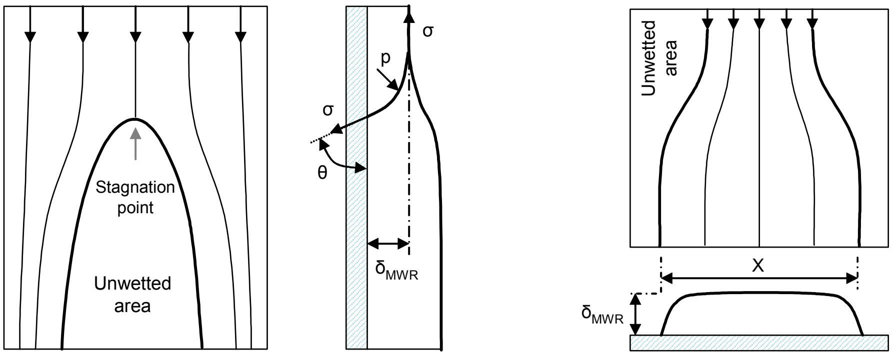

(a) Dry patch formation in liquid film (b) Laterally unstrained liquid film

Figure 6.14 Liquid film flows below MWR (Hartley & Murgatroyd, 1964)

Using the parabolic velocity profile in a uniform laminar falling film, Hartley and Murgatroyd (1964) gave the minimum film thickness as

$$\delta_{MWR} = 1.72\left[\sigma\left(1-\cos\theta\right)/\rho\right]^{1/5}\left(\mu/\rho g\right)^{2/5} \tag{6.25}$$

, where θ is the contact angle of a liquid on a solid surface.

For the "energy" criterion, they assumed that the sum of kinetic and surface energy should be minimum for a stable liquid film and derived

$$\delta_{MWR} = 1.34\left[\sigma/\rho\right]^{1/5}\left(\mu/\rho g\right)^{2/5} \tag{6.26}$$

, where the contact angle θ is missing because they assumed the film thickness was constant across the flow width X as in Fig. 6.14b.

Hartley and Murgatroyd (1964) gave flow rate for the minimum thickness, i.e. MWR, as follows using the Nusselt theory.

$$\Gamma_{MWR} = \frac{\rho^2 g}{3\mu}\delta_{MWR}^3 \tag{6.27}$$

Many of subsequent studies suggested different models based on the minimum energy theory of Hartley and Murgatroyd (1964).

Bankoff (1971) derived a minimum energy criterion for a stable rivulet whose cross-section was a segment of a circle using the parabolic velocity profile of a uniform laminar falling film. Different from Eq. (6.26) of Hartley and Murgatroyd (1964), his equation included contact angle terms.

Mikielewicz and Moszynski (1976) developed another energy criterion for a stable rivulet adopting the approach of Bankoff (1971) and taking account of the width of the original unbroken film.

Doniec (1988) derived a second-order ordinary differential equation for the rivulet profile that had a minimum total energy for a given flow rate and presented the minimum film thickness which was different from the force criterion of Hartley and Murgatroyd (1964) only in constant, i.e. the constant 1.72 in Eq. (6.25) replaced by 1.45.

Tang et al (1991) developed an energy criterion assuming a parabolic velocity profile in a laminar film with a uniform thickness, which agreed best with Eq. (6.25) among the models compared in the study. They also carried out experiments to determine the minimum wetting rates of water and LiBr-water solutions on horizontal tube bundles. Minimum wetting rates ($\Gamma_{\min}=\dot{m}_{\min}/2L$) were reported to be 0.129 and 0.143 kg/ms for water and 50 wt% LiBr-water solution on copper tubes respectively. They calculated contact angles back from the minimum flow rates and reported 35.4° for water and 29.7° for the LiBr solution.

El-Genk and Saber (2001) presented another minimum energy criterion based on a two-dimensional velocity profile and a rivulet profile that was derived assuming a force balance between pressure and surface tension across film surface. The minimum thickness of El-Genk and Saber (2001) can be represented by

$$\delta_{MWR}=1.72\left[\sigma\left(1-\cos\theta\right)/\rho\right]^{1/5}\left(\mu/\rho g\right)^{2/5}\times\left(1-\cos\theta\right)^{0.02} \qquad (6.28)$$

, which is very close to Eq. (6.25), i.e. the force criterion of Hartley and Murgatroyd (1964).

Extensive comparison of Eq. (6.28) with the experimental data from the literature and the correspondence of Eq. (6.25) and (6.28) given by El-Genk and Saber (2001) validate the use of either Eq. (6.25) or (6.28) for estimation of MWR.

Eq. (6.25) and (6.27) give $\Gamma_{MWR}\approx0.039$ kg/ms for 30°C pure water on a copper plate using the contact angle $\theta=20^{\circ}$ given in Hartley and Murgatroyd (1964), which is equivalent to $Re_f=193$ agreeing surprisingly well with the observation in Fig. 6.13. On the other hand, the same equations give $\Gamma_{MWR}\approx0.099$ kg/ms ($Re_f=134$) for 30°C, 50 wt% LiBr-water solution on a copper plate using the contact angle of $\theta=29.7^{\circ}$ given by Tang et al (1991). All data obtained for the LiBr solution cases have mass flow rates lower than the MWR. This indicates that for most experiments incomplete wetting is to be expected.

For the case of water with octanol in Fig. 6.13, it is impossible to estimate MWR in the same way due to absence of contact angle data. However it may be interesting to indirectly estimate how much the contact angle changed from that of pure water. Since octanol in a low concentration hardly changes bulk properties of liquid (viscosity changes 2.5% with 100ppm 2-ethyl-1-hexanol, Beutler et al, 1996), from Eq. (6.25) and (6.27), the relation between MWRs of pure water and water+octanol mixture may be written as

$$\left(\frac{\mathrm{Re}_{\mathrm{wat+oct}}}{\mathrm{Re}_{\mathrm{wat}}}\right)_{MWR}=\left(\frac{\sigma_{\mathrm{wat+oct}}}{\sigma_{\mathrm{wat}}}\right)^{3/5}\left(\frac{1-\cos\theta_{\mathrm{wat+oct}}}{1-\cos\theta_{\mathrm{wat}}}\right)^{3/5} \qquad (6.29)$$

For 30°C water, $Re_{f,MWR\_wat}\approx193$, $\sigma_{wat}=71\times10^{-3}$ N/m and $\theta_{wat}=20^{\circ}$ can be used in Eq. (6.29). Extrapolation of the fitting line for the water+octanol data in Fig. 6.13 gives approximately $Re_{f,MWR\_wat+oct}\approx900$. And for the purpose of a rough approximation, the surface tension data of the water and n-octanol mixture given by Fujita (1993) may be used in Eq. (6.29): $\sigma_{wat+oct}=58\times10^{-3}$ N/m. With these inputs, Eq. (6.29) gives $\theta_{wat+oct}=87.8^{\circ}$, which suggest that octanol increases the contact angle of water on copper surface.

This increase of contact angle may be understood as follows.

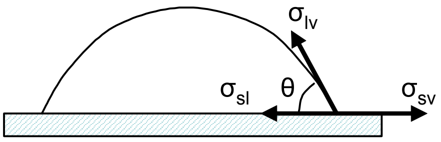

Figure 6.15 Balance of surface tensions at phase boundary

Fig. 6.15 shows a liquid drop on a solid surface and the forces acting on its vapor-liquid-solid phase boundary. Then the contact angle θ can be expressed by

$$\cos\theta = \frac{\sigma_{\mathrm{sv}} - \sigma_{\mathrm{sl}}}{\sigma_{\mathrm{lv}}} \tag{6.30}$$

, which is known as Young-Dupre equation. σ_{sv} denotes the surface tension acting on solid-vapor interface, σ_{sl} on solid-liquid interface and σ_{lv} on liquid-vapor interface. Since octanol does not only reduce σ_{lv} but also σ_{sv} and σ_{sl}, if octanol reduced (σ_{sv}-σ_{sl}) more than σ_{lv}, the contact angle should increase to satisfy Eq. (6.30). This is believed to be what happens when octanol is added in the water.

It is interesting that the fitting curves in Fig. 6.13a have the same exponent of Reynolds number of 0.58. According to the Bankoff (1971), the flow rate of a stable rivulet whose cross-section is a segment of a circle is given by

$$\dot{m} = \frac{2\rho^2 g}{3\mu}\Phi(\theta)R^4 \tag{6.31}$$

and its maximum film thickness is given by

$$\delta_{\max} = R\left[\frac{\Phi(\theta)}{\sin\theta}\right]^{1/3} \tag{6.32}$$

, where R is the radius of the circle and Φ(θ) is a function of the contact angle θ that arose from integration of the parabolic velocity profile of a uniform laminar flow he used.

Eq. (6.31) suggests that flow width of the rivulet X (=2Rsinθ), thus the wet surface area, should be proportional to $Re_f^{0.33}$ ($Re_f \sim \dot{m}/R$). And an empirical MWR equation of El-Genk and Saber (2001), who used a more realistic velocity profile, suggests that it is proportional to $Re_f^{0.3}$. Therefore 0.58 of the Reynolds number's exponent in Fig. 6.13 seems excessively large. However it should be noted that the flows observed on the test section were not fully developed but were still developing to rivulets as indicated by the funnel-like flow boundaries in Fig. 6.11a and b. This may be the reason for the large discrepancy in the exponent of Reynolds number.

Assuming that the aspect ratio of a rivulet, i.e. the ratio of flow width X to film thickness δ, is constant as is suggested in Eq. (6.32), Nusselt number is expected to be constant for a fully developed rivulet because heat transfer coefficient α is proportional to X but inversely proportional to δ_{max}, i.e. $\alpha \sim X/\delta_{max}$. This seems reasonably in agreement with the results in Fig. 6.10a except for the pure water. The different behavior of pure water flow may be explained by the observations that firstly, pure water flow had ripples on its surface and secondly, it experienced a slow but large change in flow width than the other flows (see e.g. Fig. 11a and

11b), both of which cannot be described by Eq. (6.31) and (6.32). Note that the analysis above is only approximately valid for fully developed laminar flows on plane surfaces.

6.3.2 Comparison with other studies

In this section, the experimental data reported in the previous section are compared with those of some studies listed in Table 6.1. Because no experimental data were gathered for the falling film flows on vertical plates, all of the experimental data quoted below are for tubular absorbers. Therefore the following content should be taken as a qualitative review of the present experimental results in relation to those of previous investigations.

In Fig. 6.16, Nusselt numbers of this study and Kwon and Jeong (2003) are shown for falling water film flows. Kwon and Jeong (2003) measured heat transfer coefficients of falling water films over a small helical tube coil while steam was condensed on the film surface. The coil was located in a narrow annulus between two concentric cylinders and the steam was supplied from top to bottom or in the opposite direction so that co-current or countercurrent vapor-liquid flow configurations could be realized.

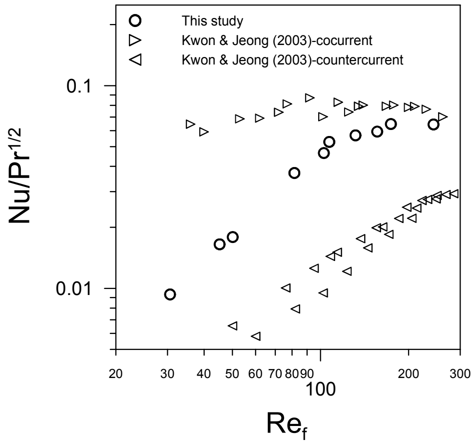

Figure 6.16 Nu numbers for pure water flows

Measured Nusselt numbers were much larger with co-current configuration and the authors concluded that the co-current steam flow helped water to evenly distribute over the coil surface and the countercurrent flow caused poor distribution and eventually flooding under high flow rate conditions. As is shown in the figure, Nusselt numbers of the present study are positioned between the two sets of data of Kwon and Jeong (2003). Although the vapor-liquid configuration in the absorber used in this study is co-current (see Fig. 6.1), the area for steam flow is so large that influence of velocity of steam is not likely to have influenced the results. Nevertheless it is notable that Nusselt number from this study approaches that of the co-current flow from Kwon and Jeong (2003) in high Reynolds number region.

For comparison of the Nusselt numbers of absorbing solution flows in this study, some experimental data were gathered from several studies on horizontal tube absorbers (Hoffmann et al, 1996; Kyung and Herold, 2002; Park et al, 2003; Yoon et al, 2002), a helical coil absorber (Yoon et al, 2005) and vertical tube absorbers (Yüksel & Schlünder, 1987; Takamatsu et al, 2003). The rest of the studies in Table 6.1 were inadequate for comparison because of the incompatible definitions of transfer coefficients used in those studies.

Fig. 6.17 shows Nusselt numbers of this study and those of the others against Reynolds number in logarithmic scales. All horizontal tube absorber data are in the low Reynolds number region below Re_f =100 while all vertical tube absorber data belong to the region above Re_f =100. Since some studies quoted here gave only average heat transfer coefficients without measured temperatures, Prandtl numbers used for the calculation of $Nu_f/Pr^{1/2}$ in Fig. 6.17 are not accurate because a rather arbitrary but typical temperature of 35 °C was used in those cases. The errors involved are, however, not so significant as to change the following overview.

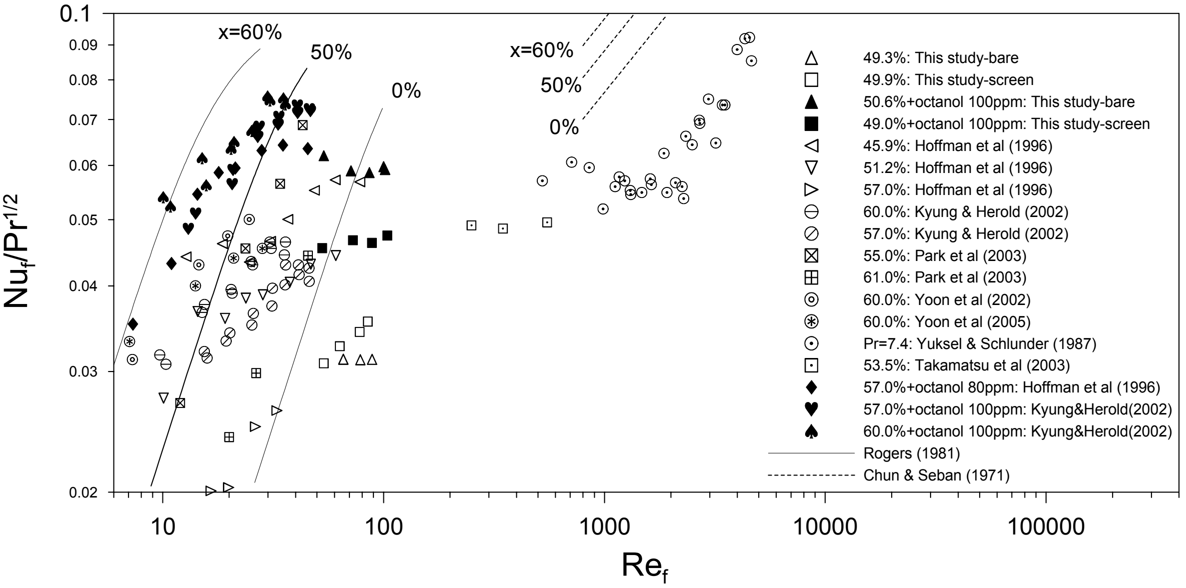

Figure 6.17 Comparison of Nu numbers

Solid lines in Fig. 6.17 are the correlation of Rogers (1981) for 50, 60 wt% LiBr-water solutions and pure water at 35 °C. Tube diameter and spacing were assumed commonly at ϕ16 mm and 0, i.e. no gap between tubes. Dashed lines are the correlation of Chun and Seban (1971) for the same working fluids for a comparison with the data in high Reynolds number region (⊙ in Fig. 6.17, Yüksel and Schlünder, 1987).

First of all, it is readily seen that the horizontal absorber data are scattered in a wide area. But, looking closely into it, one can see that the data for the solutions with additives (♦, ♥ and ♠ in Fig. 6.17, all 2-ethyl-1-hexanol) are closely gathered. Since an additive lessens the influence of surface tension effects, the agreement of those data with additives suggests that, besides Prandtl number, addition of an extra parameter for surface tension effect might improve the consistency between the scattered non-additive data.

The Nusselt numbers for pure LiBr solutions from this study (□ and △ in Fig. 6.17) are smaller than those of horizontal absorbers with a comparable LiBr concentration. For example, 51wt% data of Hoffmann et al (1996) (▽ in Fig. 6.17) is about 50% larger that this study (△ in Fig. 6.17) at Ref ≈65.

Regarding the horizontal tube data with additives (♦, ♥ and ♠ in Fig. 6.17), the discrepancy from this study (▲ in Fig. 6.17) is smaller. It is interesting that these horizontal tube data tend to flatten beyond $Re_f \approx 30$. This flattening or asymptotic trend can also be seen in the non-additive data (◁ and ▽ in Fig. 6.17) of Hoffmann et al (1996).

Rogers (1981)'s correlation, indicated by solid lines in Fig. 6.17, seems able to predict the heat transfer coefficient of a horizontal tube absorber with a reasonable accuracy. The accuracy is expected to be higher for solutions with additives because the correlation cannot take account of surface condition, i.e. material and roughness, which is less influential with the presence of an additive.

Regarding the Nusselt numbers in turbulent region beyond $Re_f \approx 1{,}300$, a large deviation is found of the experimental data of Yüksel & Schlünder (1987) from the correlation of Chun and Seban (1971). But it is notable that the correlation of Chun and Seban (1971) and the experimental data of Yüksel & Schlünder (1987) have a similar trend against Reynolds number.

As can be seen in Fig. 6.17, there are only a few data available in the range of $100 < Re_f < 1000$. Therefore it is hard to say whether the data of this study are consistent with those studies on vertical tube absorbers. Nusselt numbers of Yüksel & Schlünder (1987) and Takamatsu et al (2003) in this region seem to be insensitive to Reynolds number.

Sherwood numbers of this study are shown in Fig. 6.18 with those reported by several previous studies.

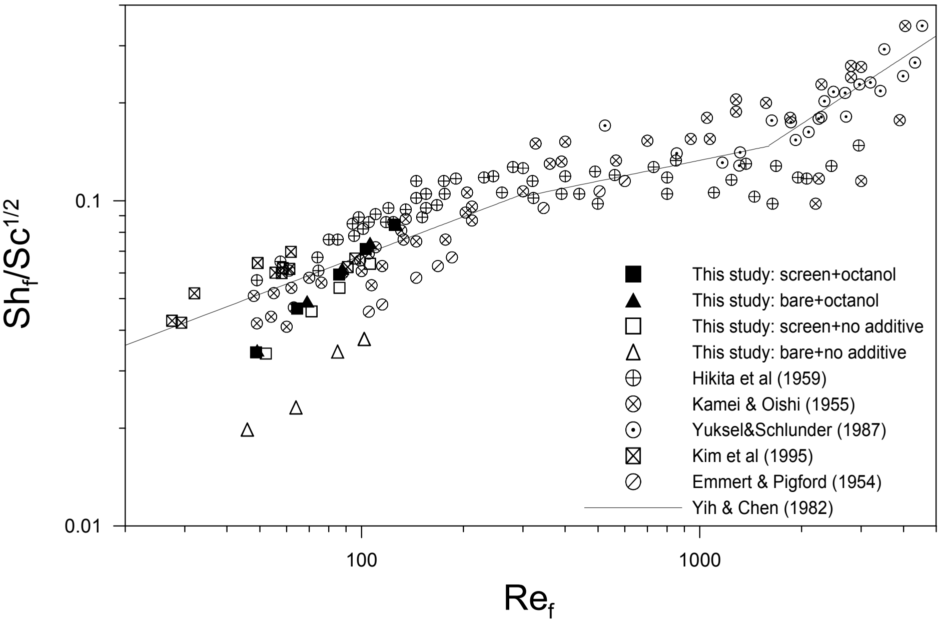

Figure 6.18 Comparison of Sh numbers

Among the data quoted, Emmert and Pigford (1954), Kamei and Oishi (1955) and Hikita et al (1959) were obtained for the absorption of carbon dioxide into falling water films. The solid lines in Fig. 6.18 are the correlations developed by Yih and Chen (1982).

The data of Kim et al (1995) and Yüksel & Schlünder (1987) were obtained for the absorption of steam into aqueous LiBr solutions on vertical tubes and seem consistent with the water-carbon dioxide data and the correlation of Yih and Chen (1982).

Sherwood numbers for the case of pure solution on bare surface (Δ in Fig. 6.18) are smaller than for Kim et al (1995), Hikita et al (1959) and Kamei and Oishi (1955). These small

Sherwood numbers are believed to be the result of incompletely wetted surface considering that those of other studies were obtained with fully wetted surface. Kim et al (1995) mentioned that their test tube was uniformly wet even at a Reynolds number down to 16.

Fitting curves of the Sherwood numbers in this study have a similar Reynolds number exponent at around 0.9 [see Eq. (6.24) and Table 6.2] while it is approximately 0.5 for the other data in Fig. 6.18. This discrepancy may also be due to the incomplete surface wetness.

6.4 Summary and conclusions

Due to the lack of experimental data, experiments have been carried out to measure heat and mass transfer coefficients of the falling film flows on vertical plates. An experimental setup has been designed and constructed for observation of the flow patterns as well as the measurement of all necessary parameters.

Pure water and aqueous LiBr solutions with or without octanol have been tested on a bare copper plate with or without a wire screen for a range of flow rates. The results are summarized in the following.

Nusselt number of pure water increased almost linearly with Reynolds number up to a Reynolds number at about 180 on the bare copper plate, at which point the test surface was observed completely wet. From visualization, this linear relationship appears to be closely related to the wet surface area. Beyond the previously mentioned Reynolds number, the Nusselt number remained more or less constant within the tested range.

LiBr solutions flowed in narrow rivulets on the bare copper plate. Nusselt number was observed insensitive to flow rate. Wet surface area was small and changed little with flow rate.

On the screen-covered copper plate, Nusselt number of LiBr solution was slightly larger than those of the bare surface and increased slowly with flow rate. Larger wet surface areas were also observed during these experiments.

When octanol was added, Nusselt number of LiBr solution was increased by a factor 2 on the bare surface and by 0.4 on the screened surface respectively. Marangoni convection was observed on the bare surface during the experiments. Heat transfer enhancement of octanol was less with the screened surface and the screen is believed to suppress Marangoni convection to some degree.

Octanol had a negative influence on water flows. Nusselt numbers of the octanol-added water flows were much lower than those of pure water flows at a same flow rate. Although octanol should have decreased the surface tension of water, it is believed to have increased the contact angle of water on the copper surface leading to poor wetting of the surface.

Sherwood numbers of LiBr solutions increased linearly with flow rate regardless of surface type within the tested range.

The wire screen was found to greatly improve the mass transfer in LiBr solution flows without octanol. However when octanol was added, no improvement was observed with the wire screen. It is believed that the wire screen suppressed Magangoni convection. Octanol improved mass transfer by a factor of 1.8 and 1.1 for the bare and screened surface respectively.

Observations made during the tests strongly suggest that octanol enhances heat and mass transfer firstly, by improving wettability of surface and secondly, by promoting Magangoni convection. Therefore such a surface structure as the fine-mesh wire screen used in this study should be avoided because it could obstruct Magangoni convection.

Finally, comparison with other studies showed that some of the experimental data obtained in this study were within and some were below the lower boundary of existing experimental data of tubular absorbers.

The results obtained in the present experimental study have been used for the simulation of the chiller model in Ch. 5 and will also be used to analyze the behavior of the chiller setup in the next chapter.

Nomenclature

A	area, m^2
Bo	boiling number, Bo≡$\dot{q}/\dot{n}\, h^{fg}$
Cp	heat capacity, kJ/kg K
D	mass diffusivity, m^2/s
d_h	hydraulic diameter, m
g	gravity constant, m^2/s
h	enthalpy, kJ/kg
h^{fg}	latent heat, kJ/kg
k	thermal conductivity, kW/mK
K	mass transfer coefficient, m/s
Ka	Kapitza number, $Ka \equiv \rho\sigma^3/g\mu^4$
L	length, m
$\dot{m}$	mass flow rate, kg/s
$\dot{n}$	mass flux, kg/m^2s
Nu	Nusselt number, $Nu \equiv \alpha_{cool} d_h/k$
Nu_f	film Nusselt number, $Nu_f \equiv \alpha_{bulk} \delta^+/k$
p	pressure, kPa
Pr	Prandtl number
$\dot{Q}$	heat transfer rate, kW
$\dot{q}$	heat flux, kW/m^2
Re	Reynolds number, $Re \equiv \rho v d_h/\mu$
Re_f	film Reynolds number, $Re_f \equiv 4\Gamma/\mu$
R	radius, m
Sc	Schmidt number
Sh_f	film Sherwood number, $Sh_f \equiv K\delta^+/D$
T	temperature, K
U	overall heat transfer coefficient, kW/m^2K
v	velocity, m/s
$\dot{V}$	volumetric flow rate, m^3/s
X	flow width, m

x	absorbent concentration in liquid
y	distance through film, m

Greek symbols

α	heat transfer coefficient , kW/m^{2}K
ΔT	temperature difference, K
Δt	thickness, m
Δx	concentration difference
δ	film thickness, m
δ^+	theoretical film thickness , $\delta^+ \equiv (\nu^2/g)^{1/3}$
Γ	mass flow rate per unit perimeter, kg/ms
θ	contact angle, degree
μ	dynamic viscosity, Pa s
ν	kinematic viscosity, m^2/s
ρ	density, kg/m^3
σ	surface tension, N/m

Super- and Subscripts

*	equilibrium or saturated
avg	average
b, bulk	bulk falling film
back	back side
con	condensation
cool	cooling water
dew	dew point
film	film
front	front (process) side
i	interface
in	inlet
l	liquid
max	maximum
min	minimum
out	outlet
oct	octanol (2-ethyl-1-hexanol)
s	solid
sol	solution
v	vapor
w, wat	water
wet	wet surface
wall	wall

Abbreviation

MWR	minimum wetting rate
LPA	low-pressure absorber
MPE	mid-pressure evaporator
MPA	mid-pressure absorber
RTD	Resistance temperature detector

References

Al-Sibai, F., Leefken, A., Renz, U., 2002, Local and instantaneous distribution of heat transfer rates through wavy films, Int. J. Thermal Science, Vol. 41, pp. 658-663

Ambrosini, W., Forgione, N., Oriolo, F., 2002, Statistical characteristics of a water film falling down a flat plate at different inclinations and temperatures, Int. J. Multiphase flow, Vol. 28, pp. 1521-1540

Armbruster, R., Mitrovic, J., 1994, Patterns of falling film flow over horizontal smooth tubes, Proc. of 10th International Heat Transfer Conference, Vol. 3, pp. 275-280, Brighton, UK

Armbruster, R., Mitrovic, J., 1998, Evaporative cooling of a falling water film on horizontal tubes, Experimental Thermal and Fluid Science, Vol. 18, pp. 183-194

Bankoff, S.G., 1971, Minimum thickness of a draining liquid film, Int. J. Heat Mass Transfer, Vol. 14, pp. 2143-2146

Becker, H., 1989, Compact heat and mass exchangers of the plate fin type in thermal sorption systems, Dissertation, TU Delft

Beutler, A., Greiter, I., Wagner, A., Hoffmann, L., Schreier, S., Alefeld, G., 1996, Surfactants and fluid properties, Int. J. Refrigeration, Vol. 19, pp. 342-346

Bond, J., Donald, M.B., 1957, The effect of absorption on the wetted area of absorption towers, Chemical Engineering Science, Vol. 6, pp. 237-244

Bourouis, M., Vallès, M., Medrano, M., Coronas, A., 2005, Absorption of water vapour in the falling film of water-(LiBr+LiI+$LiNO_3$+LiCl) in a vertical tube at air-cooling thermal conditions, Int. J. Thermal Sciences, Vol. 44, pp. 491-498

Brauner, N., Maron, D.M., 1982, Characteristics of inclined thin films, waviness and the associated mass transfer, Int. J. Heat Mass Transfer, Vol. 25, pp. 99-110

Cavallini, A., Doretti, L., Fornasieri, E., Longo, G.A., Zilio, C., 2002, Patterns of LiBr+water falling film in presence of surfactants, Proc. of Int. Sorption Heat Pump Conference, Shanghai, China

Chen, Y.M., Sun, C.Y., 1997, Experimental study on the heat and mass transfer of a combined absorber-evaporator exchanger, Int. J. Heat Mass Transfer, Vol. 40, pp. 961-971

Chun, K.R., Seban, R.A., 1971, Heat transfer to evaporating liquid films, J. Heat Transfer, Vol. 93, pp. 391-396

Consenza, F, Vliet, G., 1990, Absorption in falling water/LiBr films on horizontal tubes, ASHRAE Trans., Vol. 96, pp. 693-701

Doniec, A., 1988, Flow of a laminar liquid film down a vertical surface, Chem. Eng. Science, Vol. 43, pp. 847-854

El-Genk, M.S., Saber, H.H., 2001, Minimum thickness of a flowing down liquid film on a vertical surface, Int. J. Heat Mass Transfer, Vol. 44, pp. 2809-2825

Emmert, R.E., Pigford, R.L., 1954, A study of gas absorption in falling liquid films, Chem. Eng. Progr., Vol. 50, p. 87 (cited from Yih and Chen, 1982)

Flamensbeck, M., Summerer, F., Riesch, P., Ziegler, F., Alefeld, G., 1998, A cost effective absorption chiller with plate heat exchangers using water and hydroxides, Applied Thermal Engineering, Vol. 18, pp.413-425

Fujita, T., Ueda, T., 1978a, Heat transfer to falling liquid films and film breakdown – I. Subcooled liquid films, Int. J. Heat Mass Transfer, Vol. 21, pp. 97-108

Fujita, T., Ueda, T., 1978b, Heat transfer to falling liquid films and film breakdown – II. Saturated liquid films with nucleate boiling, Int. J. Heat Mass Transfer, Vol. 21, pp. 109-118

Fujita, T., 1993, Falling liquid films in absorption machines, Int. J. Refrigeration, Vol. 16, pp. 2-294

Fujita, I., Hihara, E., 2005, Heat and mass transfer coefficients of falling-film absorption process, Int. J. Heat Mass Transfer, Vol. 48, pp. 2779-2786

Greiter, I., Wagner, A., Weiss, V., Alefeld, G., 1993, Experimental investigation of heat and mass transfer in a horizontal-tube falling film absorber with aqueous solutions, Proc. of Int. Absorption Heat Pump conf., ASME, New Orleans, USA, AES Vol. 31., pp. 225-232

Hartley, D.E., Murgatroyd, W., 1964, Criteria for the break-up of thin liquid layers flowing isothermally over solid surfaces, Int. J. Heat Mass Transfer, Vol. 7, pp. 1003-1015

Hihara, E., Saito, T., 1993, Effect of surfactant on falling film absorption, Int. J. Refrigeration, Vol. 16, pp. 339-346

Hikita, H., Nakanishi, K., Kataoka, T., 1959, Liquid phase mass transfer in wetted-wall columns, Chem. Eng. Tokyo, Vol. 23, p. 459 (cited from Yih and Chen, 1982)

Hoffmann, L., Greiter, I., Wagner, A., Weiss, V., Alefeld, G., 1996, Experimental investigation of heat and mass transfer in a horizontal-tube falling-film absorber with aqueous solutions of LiBr with and without surfactants, Int. J. Refrigeration, Vol. 19, pp. 331-341

Holman, J.P., 1997, Heat transfer, 6th ed., McGraw-Hill

Hu, X., Jacobi, A.M., 1996a, The intertube falling film: Part 1- Flow characteristics, mode transitions, and hysteresis, Trans. ASME, Vol. 118, pp. 616-625

Hu, X., Jacobi, A.M., 1996b, The intertube falling film: Part 2- Mode effects on sensible heat transfer to a falling liquid film, Trans. ASME, Vol. 118, pp. 626-633

Hu, X., Jacobi, A.M., 1998, Departure-site spacing for liquid droplets and jets falling between horizontal circular tubes, Experimental Thermal and Fluid Science, Vol. 16, pp. 322-331

Kamei, S., Oishi, J., 1955, Mass and heat transfer in a falling liquid film of wetted-wall tower, Mem. Fac. Kyoto Univ. Vol. 17, p. 277 (cited from Yih and Chen, 1982)

Kashiwagi, T., Kurosaki, Y., Shishido, H., 1985, Enhancement of vapour absorption into a solution using the Marangoni effect, Trans. JSME, Vol. B51, pp. 1002-1009 (cited from Ziegler and Grossman, 1996)

Killion, J., Garimella, S., 2002, Visual documentation of departures from idealized falling films over horizontal tube banks, Proc. Int. Sorption Heat Pump Conference, Shanghai, China

Kim, B.J., Kang, I.S., 1995, Absorption of water-vapor into wavy-laminar falling film of aqueous lithium bromide, KSME Int. J., Vol. 9, pp. 115-22 (cited from Takamatsu et al, 2003)

Kim, D.S., Infante Ferreira, C.A., 2006, Effect of surface geometry and surfactants on the performance of falling films, Proc. 7th Gustav-Lorentzen Conference on Natural Working Fluids, Trondheim, Norway

Kim, K.J., Berman, N.S., Chau, D.S.C., Wood, B.D., 1995, Absorption of water vapour into aqueous lithium-bromide, Int. J. Refrigeration, Vol. 18, pp. 486-494

Kim, K.J., Berman, N.S., Wood, B.D., 1996, The interfacial turbulence in falling film absorption: effects of additives, Int. J. Refrigeration, Vol. 19, pp. 322-330

Koenig, M.S., Grossman, G., Gommed, K., 2003, The role of surfactant adsorption rate in heat and mass transfer enhancement in absorption heat pumps, International Journal of Refrigeration , Vol. 26, pp. 129-139

Krupiczka, R., Rotkegel, A., Ziobrowski, Z., 2002, Heat transfer to evaporating liquid films within a vertical tube, Chemical Engineering and Processing, Vol. 41, pp. 23-28

Kulankara, S., Herold, K.E., 2000, Theory of heat/mass transfer additives in absorption chillers, International J. Heating, Ventilating, Air-Conditioning and Refrigeration, Vol. 6, pp. 369-380

Kwon, K., Jeong, S., 2003, Effect of vapour flow on the falling-film heat transfer of a helical coil, Proc. of International Congress of Refrigeration, Washington D.C., USA

Kyung, I.S., Herold, K.E., 2002, Performance of horizontal smooth tube absorber with and without 2-ethyl-hexanol, Journal of Heat Transfer, Trans. of ASME, Vol. 124, pp.177-183

Matsuda, A., Choi, K.H., Hada, K., Kawamura, T., 1994, Effect of pressure and concentration on performance of a vertical falling-film type of absorber and generator using lithium bromide aqueous solutions, Int. J. Refrigeration, Vol. 17, pp. 538-542

Medrano, M., Bourouis, M., Coronas, A., 2002, Absorption of water vapour in the falling film of water-lithium bromide inside a vertical tube at air-cooling thermal conditions, Int. J. Thermal Sciences, Vol. 41, pp. 891-898

Mikielewicz, J., Moszynski, J.R., 1976, Minimum thickness of a liquid film flowing vertically down a solid surface, Int. J. Heat Mass Transfer, Vol. 19, pp. 771-776

Miller, W.A., Keyhani, M, 1999, The experimental analysis of local heat and mass transfer data for vertical falling film absorption, Proc. of International Mechanical Engineering Congress and Exposition, Nashville, USA

Miller, W.A., Keyhani, M, 2001, The correlation of simultaneous heat and mass transfer experimental data for aqueous lithium bromide vertical falling film absorption, Journal of Solar Energy Engineering, Vol. 123, pp. 30-42

Mitrovic, J., 1986, Influence of tube spacing and flow rate on heat transfer from a horizontal tube to a falling liquid film, Proc. of 8th International Heat Transfer conference, Vol. 4, pp. 1949-1956, San Francisco, USA

Mitrovic, J., 1990, Wärmeübergang in Rieselfilmen an waagrechten Rohren, VDI Fortschtirr-Ber. 3 (211) (cited from Armbruster and Mitrovic, 1998)

Nagaoka, Y., Nishiyama, N., Ajisaka, K., Nakamura, M., 1987, Absorber of absorption refrigerating machine: Enhancement of heat and mass transfer in falling film absorbers by surface configuration, Proc. of 17th Int. Congress of Refrigeration, IIR, Vienna, Austria, pp. 990-995 [cited from Fujita (1993)]

Nakoryakov, V.E., Grigoreva, N.I., 1980, Calculation of Heat and Mass Transfer in Nonisothermal Absorption on the Initial Portion of a Downflowing Film, translated from Teoreticheskie Osnovy Khimicheskoi Tekhnologii, Vol.14, pp. 483-488

Nusselt, W., 1931, Der Warmeaustausch zwischen Wand und Wasser im Rohr, forsch. Geb. Ingenieurwes., Vol.2, p.309

Ogawa, M., Hoshida, T., Oda, Y., 1991, Study on heat transfer analysis for the vertical condenser/absorber of an air-cooling absorption chiller/heater, Proc. of Absorption Heat Pump Conf., Tokyo, Japan, pp. 225-230

Park, C.W., Kim, S.S., Cho, H.C., Kang, Y.T., 2003, Experimental correlation of falling film absorption heat transfer on micro-scale hatched tubes, Int. J. Refrigeration, Vol. 26, pp. 758-763

Perry RH, Green DW, Maloney JO., 1984, Perry's Chemical Engineers Handbook; 6th ed., New York: McGraw-Hill Book Co

Pise, A.T., Devotta, S., Kant, K., 2003, Heat and mass transfer studies in a horizontal tube fallino film absorber, Prc. of Int. Congress of Refrigeration, Washington D.C., USA

Remec, J., Gjerkes, H., Gaspersic, B., 1996, Absorption of vapour into liquid film on horizontal tubes, ASHRAE Trans., Vol. 102, pp. 973-979

Rogers, J.T., 1981, Laminar falling film flow and heat transfer characteristics on horizontal tubes, Can. J. Chem.. Eng., Vol. 59, pp. 213-222 (cited from Armbruster and Mitrovic, 1998)

Roques, J.-F., Thome, J.R., 2002, Falling film transitions between droplets, column and sheet flow modes on a vertical array of horizontal 19 FPI and 40 FPI low finned tubes, Proc. of 1st International Conference on Heat Transfer, Fluid Mechanics and Thermodynamics, pp. 523-528, Kruger Park, South Africa

Ruschak, K.J., Weinstein, S.J., 2003, Laminar, gravitationally driven flow of a thin film on a curved wall, Journal of Fluids Engineering, Trans. of the ASME, Vol. 125, pp. 10-17

Safarik, M., Richter, L., Mockel, F., Kretschmar, S., 2005, Performance data of a small capacity absorption chiller, Proc. of International Conference Solar Air-conditioning, Bad Staffelstein, Germany

Sieder, E.N., Tate, C.E., 1936 Heat transfer and pressure drop of liquids in tubes, Ind. Eng. Chem., Vol.28, p.1429

Takamatsu, H., Yamashiro, H., Takata, N., Honda, H., 2003, vapour absorption by LiBr aqueous solution in vertical smooth tubes, Int. J. Refrigeration, Vol. 26, pp. 659-666

Tang, J., Lu, Z., Yu-chi, B., 1991, Minimum wetting area of film flow on solid surface, Proc. of the 18th International Congress of Refrigeration, Montreal, Vol. II, pp. 519-523

Wassenaar, R., 1994, Simultaneous heat and mass transfer in a horizontal tube absorber, Dissertation, TU Delft

Wilke, W., 1962, Wärmeübergang in Rieselfilm, VDI-Forschungsheft 490, Issue B, Vol. 28

Wilson, E.E., 1915, A basis for rational design of heat transfer apparatus, J. Heat Transfer, Vol. 37, pp. 47-82

Yazaki Energy Systems Inc., 2005, Specifications of water-fired chillers and chiller-heaters at http://www.yazakienergy.com/waterfiredspecifications.htm, the last access on 06 Dec. 2006

Yih, S.M., Chen, K.Y., 1982, Gas absorption into wavy and turbulent falling liquid films in a wetted-wall column, Chem. Eng. Commun., Vol. 17, pp. 123-136

Yoon, J.I., Kim, E., Choi, K.H., Seol, W.S., 2002, Heat transfer enhancement with a surfactant on horizontal bundle tubes of an absorber, Int. J. Heat Mass Transfer, Vol. 45, pp. 735-741

Yoon, J.I., Kwon, O.K., Moon, C.G., Lee, H.S., Pradeep, B., 2005, Heat and mass transfer characteristics of a helical absorber using LiBr and LiBr+LiI+LiNO$_3$+LiVl solutions, Int. J. Heat Mass Transfer, Vol. 48, pp. 2102-2109

Yung, D., Lorentz, J.J., Ganic, E.N., 1980, Vapor/liquid interaction and enhancement in falling film evaporators, ASME J. of Heat Transfer, Vol. 102, pp. 20-25

Yüksel, M.L., Schlünder, E.U., 1987, Heat and mass transfer in non-isothermal absorption of gases in falling liquid films part I: experimental determination of heat and mass transfer coefficients, Chem. Eng. Process, Vol. 22, pp. 193-202

Ziegler, F., Grossman, G., 1996, Heat-transfer enhancement by additives, Int. J. Refrigeration, Vol. 19, pp. 301-309

7 Test and analysis of a chiller setup

An experimental chiller setup has been constructed with the components designed in Ch. 3. Firstly, the setup has gone through a series of preliminary tests for troubleshooting before it was tested under various operating conditions in full scale tests. In the following sections, the test results and analysis are presented for each of the operating parameters. The behavior of the setup could be well understood in connection with the performance of various components. At the end of this chapter, several conclusions and recommendations are made regarding the present test results and the need of further work.

7.1 Chiller setup

Fig. 7.1 shows a schematic diagram of the chiller setup that has been assembled with the components designed in Ch. 3. Photographs of the setup are also available in Appendix B2.

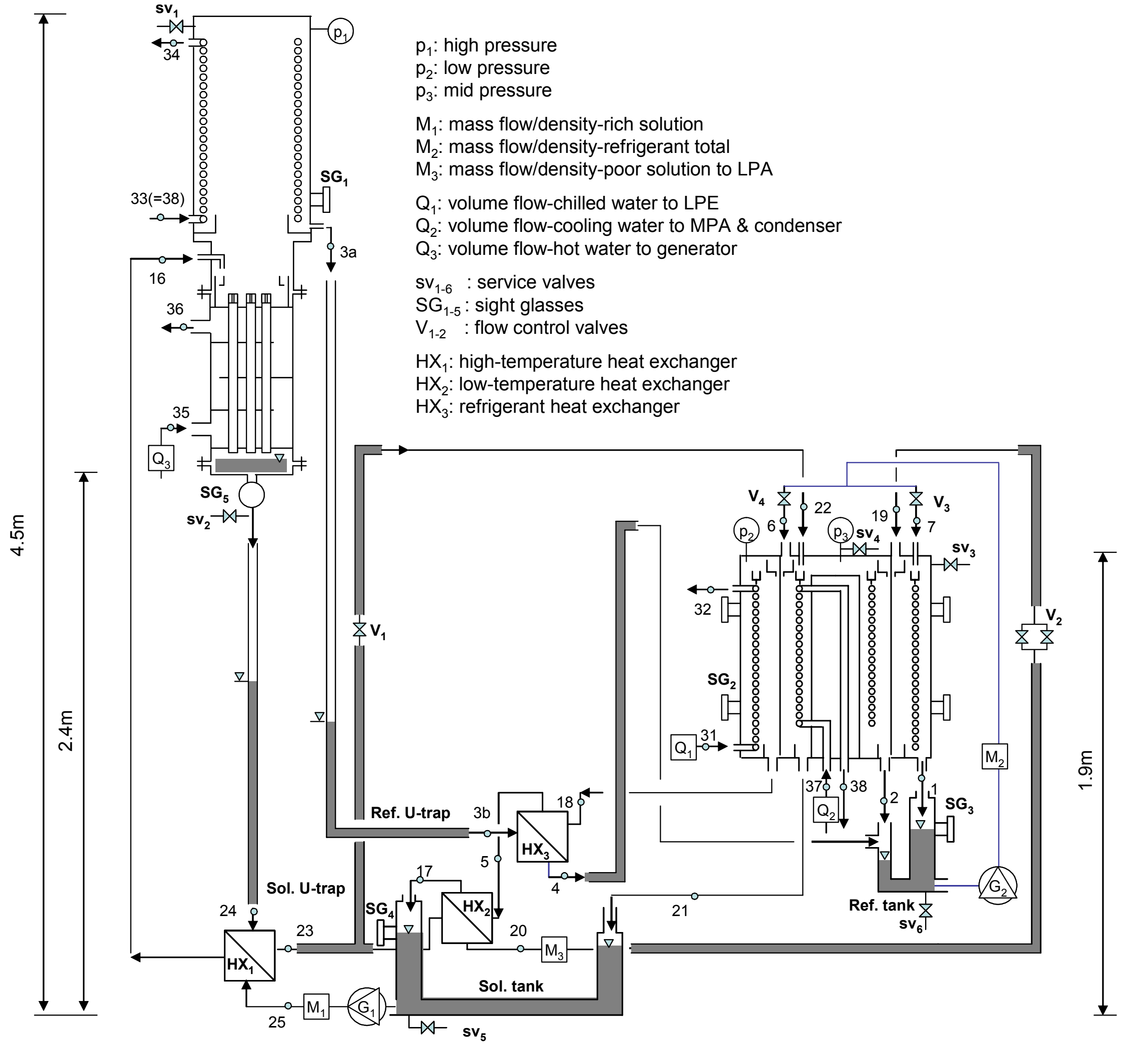

Figure 7.1 Schematic diagram of a chiller setup

First of all, as shown in the figure, the condenser-generator column on the left is located at a high position above the absorber-evaporator shell on the right in order to ensure a large amount of solution to flow from the generator to the absorbers overcoming the flow resistances in the heat exchangers and measuring equipment installed in the connecting lines. Bottom of the generator is about 2.4 m above ground, which is 0.5 m higher than the top of the absorbers. Although the condenser-generator column could have been lowered considering the pressure differences between the generator and absorbers, it has been decided not to take any risk. During preliminary tests, it was confirmed that the solution flow rate from the generator could be increased to a much higher flow rate than originally designed.

From the generator, hot and concentrated solution flows through firstly, the sight glass SG_5 in Fig. 7.1, where the flow can be visually confirmed. It is cooled in the high-temperature heat exchanger HX_1 (point 24→23 in Fig. 7.1) and then split into two streams at a certain ratio by the flow valves V_1 and V_2. One stream goes to MPA (23→22) and the other goes to LPA through the low-temperature heat exchanger HX_2 and flow meter M_3 (23→19).

As shown in Fig. 7.1, the pipeline between the generator and the absorbers and that between the condenser and the refrigerant tank are in a “U” shape and thus act as vapour traps that separate the pressures in those components.

The solution supplied to MPA is cooled down while absorbing vapour (22→21) by cooling water (37→38) and collected in a solution tank. On the other hand, the solution in LPA (19→18) is cooled by refrigerant (6→2) and also collected by the same solution tank through firstly, the refrigerant heat exchanger HX_3 (18→5) and then the low-temperature heat exchanger HX_2 (5→17). These collected solutions are mixed in the tank and pumped back to the generator by pump G_1 through mass flow meter M_1 and high temperature heat exchanger HX_1 (25→16). In the generator, the solution is heated by hot water (35→36) and repeats the cycle from the generator bottom.

In the condenser, the vapour generated in the generator is condensed cooled by cooling water (33→34) and the condensed refrigerant is further cooled in the refrigerant heat exchanger HX_3 (3→4) before reaching the refrigerant tank.

The refrigerant in the refrigerant tank is pumped by the refrigerant pump G2 through mass flow meter M_2 to the top of evaporators. The refrigerant flow is then split into two, one for LPE and the other for MPE. Even distribution of the refrigerant is intended by the identical capillary tubes denoted by V_3 and V_4 in the figure. The refrigerant in LPE is heated (7→1) by chilled water (31→32) and that in MPE is heated (6→2) by warm solution (19→18). From the bottom of evaporators, remaining refrigerant is collected again in the refrigerant tank.

For observation of the flows inside the setup, several sight glasses have been installed. Sight glass SG_1 is located near the bottom of the condenser so that the last few turns of the condenser tube coil inside can be observed. The absorber-evaporator shell has eight sight glasses in total (SG_2), where 4 sight glasses are arranged 90^o apart near the top and the bottom of the shell so that a few turns of LPE coil and parts of LPA surface can be observed. The solution and refrigerant tanks have one sight glass each (SG_3 and SG_4) so that the level of fluid inside can be observed. And finally, the sight glass below the generator (SG_5) allows the observation of solution flow.

Besides there are service valves available at several locations in the system for various purposes including evacuation of inert gases, charging or sampling of working fluids.

7.2 Preliminary tests and troubleshooting

Before a full scale test was started, the chiller setup has been tested for its proper functions. During preliminary tests, several problems have been detected and some corrective measures were taken as described in the following.

7.2.1 Vacuum tightness

After the setup was assembled, several leaks have been detected and sealed. Unfortunately, however, one major leak could not be sealed properly, which was found in the flange that connects the condenser and the generator. After several attempts, it was concluded that replacement of the damaged surface in the flange could only guarantee a satisfactory vacuum level. However the option was rejected because it was practically impossible at the moment. In a leakage test, system pressure was observed to increase linearly with time at a speed of 3.19×10^{-2} Pa/s. Assuming 0.3 m^3 for the total system volume, it is equivalent to a leakage rate of approximately 1 cc/s at 10 kPa and 20^{o}C. This is quite a large leak considering that the total system pressure could be about 1 kPa higher than the partial pressure of water in 10 hours after the system has been evacuated. Fortunately, however, this leak did not influence the pressures of the absorbers and evaporators during the tests because they were separated from the condenser-generator column by the U-traps described previously. It has been observed that those pressures remained constant even when the condenser pressure increased with time.

7.2.2 Refrigerant recirculation in evaporators

To improve the wetting of the evaporator surfaces, the chiller setup is equipped with a refrigerant tank and a gear pump for the recirculation of refrigerant.

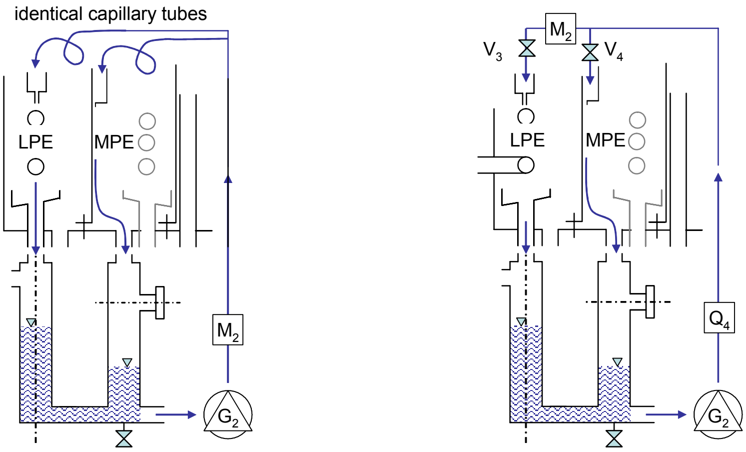

(a) Original circuit (b) Final circuit

Figure 7.2 Refrigerant recirculation circuits

In a preliminary test, the refrigerant tank in Fig. 7.2a was filled with water under atmospheric pressure and the pump was turned on to measure the water flow rate with mass flow meter M_2.

After the preliminary test, the recirculation circuit has been modified from Fig. 7.2a to Fig. 7.2b to correct the following problem.

Originally, two identical capillary tubes were used to distribute the refrigerant evenly to the evaporators as in Fig. 7.2a. However it was found that the flow resistances in the capillary tubes and the mass flow meter M_2 were too high. For this reason, the capillary tubes were replaced by two identical small flow control valves and flow meter M_2 was replaced by a magnetic flow meter with a smaller pressure drop. Instead M_2 was used to measure the flow rate to LPE as shown in Fig. 7.2b. By these modifications, the recirculation rates could be increased to a much larger flow rate.

Another problem was found in the structure of LPE. During the preliminary test, it was found that some water escaped the refrigerant tray below as shown in Fig. 7.3.

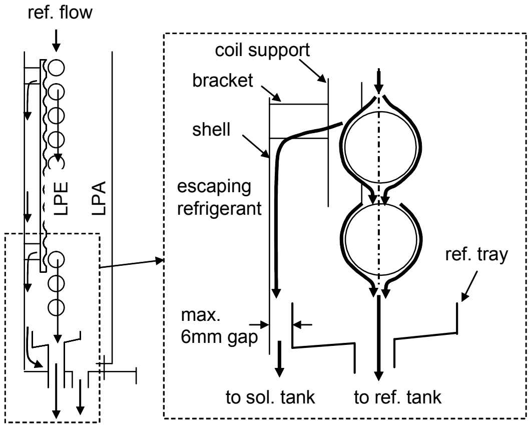

Figure 7.3 Escaping refrigerant from LPE

In its design, alignment of the LPE coil was ensured by vertical supports that fixed the coil to the shell as in Fig. 7.3. Some of the refrigerant must have deviated from the coil and flowed along the shell as illustrated in the figure. Since the refrigerant tray down at the bottom did not completely contact the inner wall of the shell, the refrigerant escaped the refrigerant tray through the gap between the tray and the wall. According to the manufacturing drawing of the tray, the gap varied from 0 to 6mm along the shell perimeter. It would have been possible to prevent this from happening if either the tray had been designed to firmly fit the inner diameter of the shell or properly designed supports had been used.

Influence of the escaping refrigerant turned out to be significant on the chiller performance. The refrigerant returned directly to the solution tank without any contribution for refrigeration only to waste the heat input to the generator. Although its influence on heat capacity might be small, COP of the chiller has been greatly decreased.

Another problem that was not detected during the preliminary test but found later was cavitation within recirculation pump G_2 in Fig. 7.2. The problem was not detected earlier because the preliminary test was carried out under atmospheric pressure only to check the water flow rate in the circuit. Later it was found that cavitation took place in the pump under the vacuum pressures tested and the pump speed had to be limited to max. 25 Hz. As will be described later, this was one of the major problems that had compromised the chiller performance. For this reason, the maximum recirculation flow rate was limited to approximately 1.2 lit/s, which was only 25% of the original plan. Unfortunately replacement of the pump was not possible.

In conclusion, the problems of the escaping refrigerant and cavitation were not resolved. Influences of these problems will be discussed later with test results.

7.2.3 Solution flows in absorbers

After the modification of the refrigerant circuit, the solution tank in Fig. 7.4a was filled with LiBr solution and pump G_l was turned on. A problem was detected when the solution returned to the solution tank. During the test, the refrigerant density measured by M_2 in Fig. 7.2 was exceptionally high and increasing liquid level was observed in the refrigerant tank even when there was no generation of refrigerant. It was found that the flow resistance in the return line of MPA was so large that solution overflowed from the solution tray of MPA to the refrigerant tank.

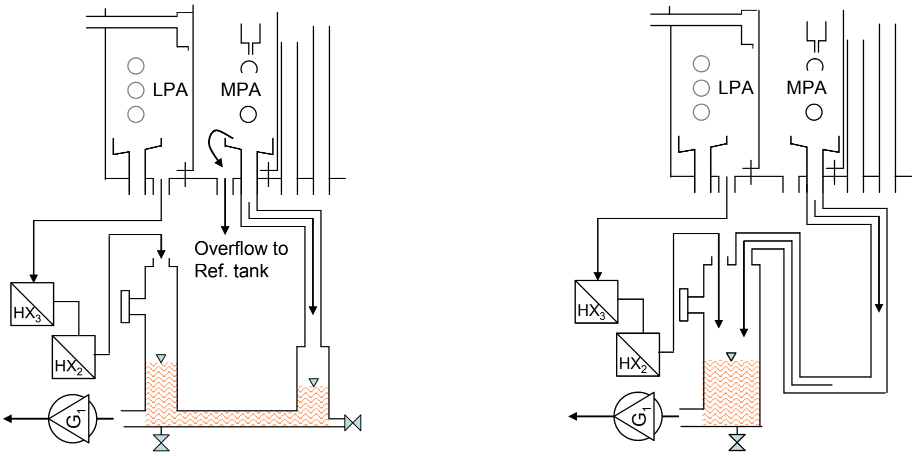

(a) Original circuit (b) Final circuit

Figure 7.4 Overflow from MPA

This problem has been resolved by modifying the solution tank and the suction line as in Fig. 7.4b. In the final circuit in Fig. 7.4b, the suction pressure created by the pump G_l drew the solution flow from MPA without overflow.

After the modification, the chiller setup was evacuated and put to a test run. The refrigerant and solution pumps were turned on and controlled to the desired flow rates. Also all secondary water flows were circulated at desired flow rates and temperatures. However the abnormally high density of refrigerant did not disappear even after the overflowing problem was gone. The density measurement of M_2 suggested the existence of a heavy substance in the refrigerant in spite of repeated cleaning of the refrigerant tank. Another source of solution was suspected, which must have contaminated the refrigerant.

After some time, a hot narrow patch was found on the shell surface as shown in Fig. 7.5, which was supposed to be coldest in the whole setup because it was closest to LPE. And by no accident, the patch was located right below the solution supply tube to LPA as in the figure.

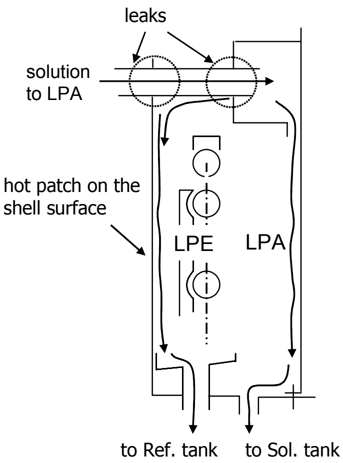

Figure 7.5 Leaking solution from LPA

It was suspected that one of the connections marked with circles in Fig. 7.5 was not completely sealed. Solution must have escaped from somewhere in this pipe line and flowed down along the inner wall of the shell forming the hot patch while it absorbed some vapour from LPE. Some of this leaked solution must have fallen into the tray below LPE to contaminate the refrigerant.

Locating the exact leaking point and sealing it was impossible meaning that tests could only be done with contaminated refrigerant. Instead, it has been decided to install a "blow down" tube to remove contaminated refrigerant frequently as in Fig. 7.6.

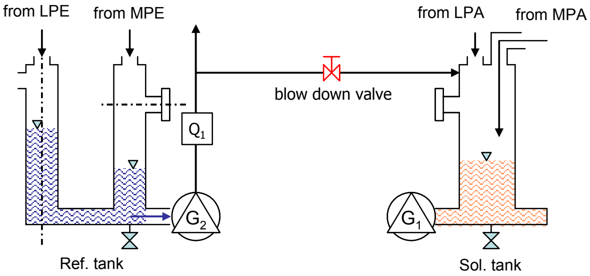

Figure 7.6 Blow down tube

By empting the refrigerant tank before operating the setup, the refrigerant contaminated during the previous operation could be removed so that a reasonably low LiBr concentration could be maintained in the refrigerant tank. Blow down has been carried out whenever it was thought necessary even while the setup was in operation.

7.3 Test results – 1st charging condition

After all necessary measures were taken to cope with the problems found in the preliminary tests but before the originally planned tests were carried out in full scale, several attempts were made to properly charge the setup with LiBr solution. Charging volume and concentration were changed several times until the setup ran properly. The criteria for the 'proper charge' were firstly, how steadily the solution flowed at the design flow rates and secondly, how close the concentrations were to the design values. The setup was finally ready with 28kg of 50 wt% solution. It should be mentioned that this is a rough estimation because the solution and refrigerant charged during the preliminary tests could not be drained completely.

Octanol had already been added to the charged solution at 100 ppm by mass (3.35 cc in 28kg). Although this first charging condition was by no means an optimum, several sets of tests were carried out according to Table 7.1.

Table 7.1 Parameters and values- 1st charging (28kg of 50 wt% solution + 100ppm octanol)

Parameters	Step1	Step2	Step3	Step4	Step5	Step6	Remark
T_{31} (°C)	13	15	20	24			chilled water temperature
T_{35} (°C)	65	70	75	79	84	89	heating water temperature
T_{33} (°C)	33	37	40				cooling water temperature
$\dot{m}_{35}$ (kg/h)	1200	1500	1800	2100	2400		heating water flow rate
$\dot{m}_{33}$ (kg/h)	1200	1500	1800	2100	2400		cooling water flow rate
$\dot{m}_{31}$ (kg/h)	900	1050	1200	1350	1500		chilled water flow rate
$\dot{m}_{07}$ (kg/h)	12	17	22	27	32	37	refrigerant flow rate to LPE
$\dot{m}_{19}$ (kg/h)	130	140	150	160	170	180	solution flow rate to LPA

1. Standard values are in gray cells.
2. Numerical indices should be referred to Fig. 7.1
3. No standard value for $\dot{m}_{19}$. The solution from generator was distributed to two absorbers as evenly as possible.

Tests were carried out to determine influences of the chosen parameters on system performance. Standard values (in gray cells of Table 7.1) were chosen for the parameters as close to the corresponding design values as possible. For each series of tests, only the single parameter of interest was changed according to the steps in Table 7.1 while the other parameters were set to the corresponding standard values. Among the standard values, T_{31}, i.e. the chilled water temperature at LPE's inlet, has been set to 24°C, which is far higher than the original design of 12.5°C. This was to compensate for the deteriorated performance of the evaporators, which will be explained in the next section.

It should be mentioned that analysis of the components in the system is limited only to heat transfer for several reasons. For determination of an average mass transfer coefficient, accurate temperature and concentration measurements are required at the inlet and outlet of a component. Unfortunately, this was impossible for some components. The outlet temperature of LPA, for example, was not reliable because of the mixing of refrigerant at its bottom as explained in Section 7.2.2. Besides, "crossover" of bulk and interface concentration (temperature) profiles (see Ch. 5) has been observed particularly in the generator and MPA, which makes it impossible to define an average driving potential for mass transfer such as Eq. (6.7) in Ch. 6. For these reasons, it has been concluded that involved uncertainty was too high and no mass transfer analysis was attempted.

In the following sections, test and analysis results are presented for each parameter.

7.3.1 Chilled water temperature

In this set of tests, the setup was tested varying chilled water temperature from 13 to 24.5°C. Influence of this parameter has become of particular concern in relation to the identification of the contaminated refrigerant by leaking solution and cavitation of the recirculation pump as described in Section 7.2.

Fig. 7.7 shows the measured cooling capacity and COP against chilled water temperature.

The cooling capacity sharply decreases from 3.3 to 0.7 kW while the chilled water temperature (T_{31} in Fig. 7.1) decreases from 24.5 to 13°C. COP also shows a similar trend decreasing linearly from 0.21 to 0.067.

As will be explained later, this poor performance is largely due to the low heat transfer coefficients in some components. The small cooling capacity at a low chilled water temperature forced the use of a high chilled water temperature as a standard value because otherwise, relatively large measurement errors would seriously undermine the reliability of the analysis especially of the evaporators and absorbers. This was the reason why 24°C has been chosen as a standard value for chilled water temperature in Table 7.1.

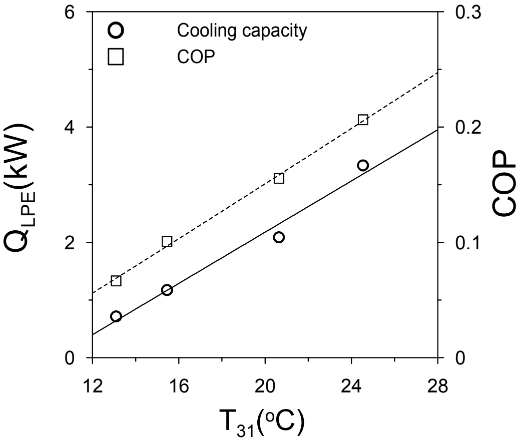

Figure 7.7 Cooling capacity and COP vs. chilled water temperature

The data shown in Fig. 7.7 are the results of combined effects of several parameters. During the test, the chilled water temperature could not be varied alone keeping the other parameters unchanged. The behavior of the setup may be understood in the following discussion.

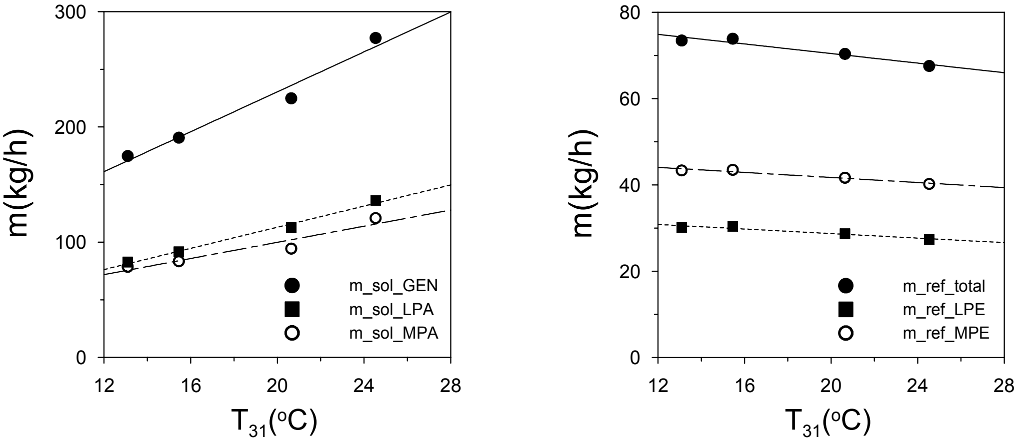

(a) Solution flow rates (b) Refrigerant recirculation

Figure 7.8 Solution and refrigerant recirculation rates vs. chilled water temperature

Fig. 7.8 shows the measured solution and refrigerant flow rates in the setup. While Fig. 7.8a shows that the solution flow rates to the generator and absorbers increase with the chilled water temperature, Fig. 7.8b shows those of evaporators decrease. Since pumps were running at constant speeds and flow control valves were untouched during the test, the variation of flow rates was mainly due to changes of the liquid levels in solution and refrigerant tank. The liquid level in the refrigerant tank was observed to decrease with increasing chilled water temperature, which is thought to have caused the decreasing refrigerant flow rates in Fig. 7.8b. On the contrary, this it thought to have caused the increasing solution flow rates to the generator and the absorbers in Fig. 7.8a.

System pressures and concentrations varied as also shown in Fig. 7.9. Fig. 7.9a shows that all three system pressures have increased with chilled water temperature. Fig. 7.9b, on the other hand, shows that concentrations decreased.

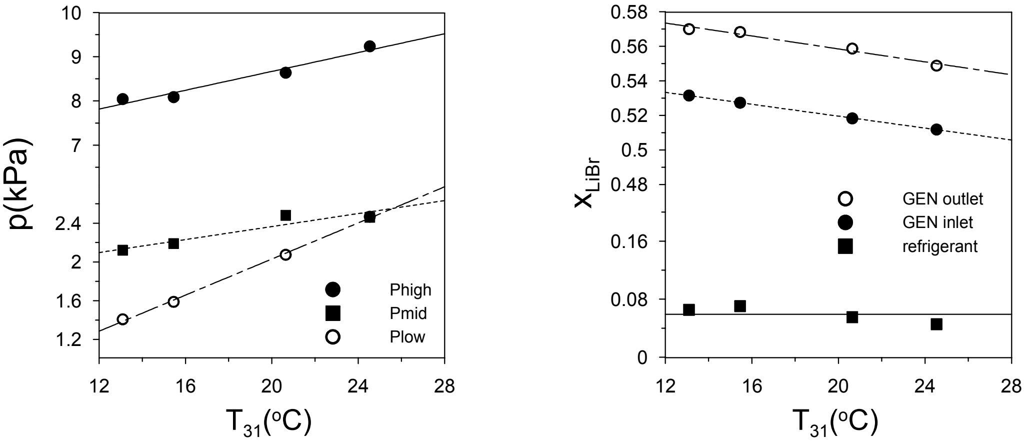

(a) Pressures (b) LiBr concentrations

Figure 7.9 Pressures and concentrations vs. chilled water temperature

The increasing pressures in Fig. 7.9a were due to the increased heat and mass transfer rates in the components as suggested by the increasing condensation and evaporation (absorption) rates in Fig. 7.10, which were calculated from the energy balance equations for the condenser and the two evaporators.

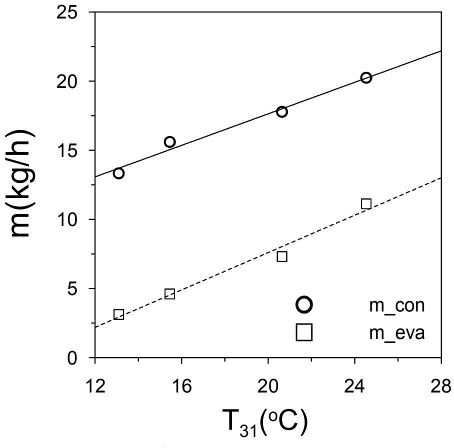

Figure 7.10 Condensation & evaporation rates (LPE+MPE) vs. chilled water temperature

It is notable that the condensation rate is much larger than the evaporation rate in Fig. 7.10. It suggests that only 24 to 56 % of the refrigerant condensed in the condenser was effectively used and the rest was lost, most likely because of the faulty design of LPE described in Section 7.2.2. This is the main reason of the low COP in Fig. 7.7.

The decreasing solution concentrations in Fig. 7.9b are related to the liquid level in the refrigerant tank. As the chilled water temperature increased, liquid level decreased in the refrigerant tank and therefore the solution in the generator and absorbers were diluted instead.

Regarding the LiBr concentration in the refrigerant, it is hard to say anything in relation with chilled water temperature because it increased with time. Nevertheless the concentration slightly decreased with high chilled water temperature in Fig. 7.9b, which must have brought positive effects to the evaporators. It turned out that the presence of LiBr in the refrigerant did not significantly change the evaporation temperature. During all tests, LiBr concentration in the refrigerant varied between 0 and 16.5 wt% and an analysis suggests that the temperature change in an evaporation process, i.e. temperature glide, was only 2.6K in maximum and 0.2 K in average for LPE and it was 2.9K in maximum and 0.2 K in average for MPE.

However, the impurity of refrigerant may have lowered the heat transfer coefficients in evaporators. Since octanol has been added to the LiBr solution, the contaminated refrigerant had not only LiBr but also octanol which, in Ch. 6, has been shown to significantly lower the heat transfer coefficient of water.

Fig. 7.11 shows film heat transfer coefficients of the components determined from the experimental data.

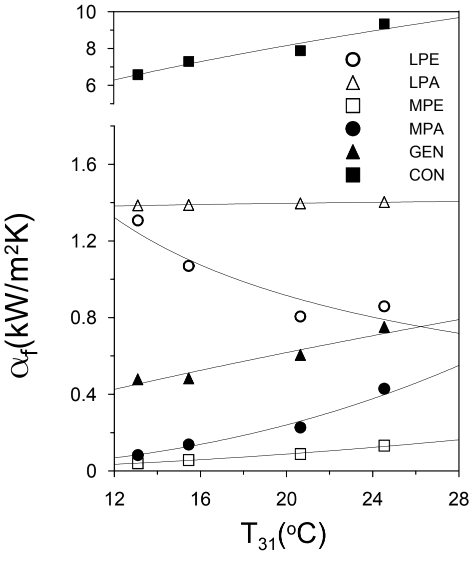

Figure 7.11 Heat transfer coefficients vs. chilled water temperature

There are a few points to be made clear regarding the determination of the heat transfer coefficients in the system.

Firstly, for the film-side temperatures in the logarithmic mean temperature difference, equilibrium temperatures have been used with the corresponding pressure and bulk concentrations. This was inevitable because "temperature crossover" has been observed in many cases. The "temperature crossover" can be encountered when a generator is supplied with a subcooled solution or reversely when an absorber is supplied with a superheated solution. In the worst case, the temperature profile of the bulk solution and that of the heat transfer medium cross each other somewhere downstream as has already been described in Ch. 5. In such a case, no logarithmic mean temperature difference can be defined. This phenomenon has been constantly observed in LPE and MPA.

In LPE, measured refrigerant temperature was almost always higher than that of chilled water at the top, which has been expected from the simulations in Ch. 5. Beside this temperature inversion, however, the measured refrigerant temperature at its bottom could not be used with a high reliability because the leaked solution from LPA must have increased the temperature.

In MPA, on the other hand, temperature inversion has been observed at its bottom. Solution temperature was measured lower than that of cooling water at the bottom for an unknown reason, which also made it impossible to use the measured bulk temperature in a logarithmic mean temperature difference.

Secondly, the heat transfer coefficient of MPE has been determined using the experimental results from Ch. 6, i.e. Eq. (6.23) for the LiBr solution+octanol 100ppm film flows, for LPA. Its reverse, i.e. to determine the heat transfer coefficient of LPA by using the heat transfer coefficient of water flows from Ch. 6 for MPE, has also been attempted. However the heat transfer coefficients of LPA determined in this way were unrealistically small. The heat transfer rate between LPA and MPE has been calculated from the energy balance equation of LPA using the measured solution flow rate and temperature in LPA and the evaporation rate calculated from the energy balance of LPE. The use of Eq. (6.23) for LPA may be justified as follows. Since the surface of LPA has been observed completely wet during all experiments through the eight sight glasses around the absorber-evaporator shell (SG2 in fig. 7.1), it is reasonable to assume that the heat transfer coefficient of LPA is in the order of magnitude of Eq. (6.23). Besides, it turned out that the heat transfer coefficient of LPA practically did not influence the heat transfer coefficient of MPE unless it was significantly smaller than given by Eq. (6.23) because the overall heat transfer coefficients measured for LPA-MPE were so small.

In Fig. 7.11, it is notable that the heat transfer coefficients of MPE and MPA are quite small. That of MPE, in particular, is in the range between 0.04 and 0.13kW/m^{2}K. Even considering the high uncertainties involved in its determination, it is smaller than the value used in the design of Ch. 4 (c.a. 1kW/m^{2}K) by an order of magnitude. MPA also shows much smaller heat transfer coefficients (0.08-0.43kW/m^{2}K) than used in the design (c.a. 1.5kW/m^{2}K).

All in all, heat transfer coefficients are much smaller than the design values except for the condenser, LPE and LPA. Especially the poor performance of MPE and MPA must have caused the poor performance of the setup in Fig. 7.7.

The trends of heat transfer coefficients against chilled water temperature in Fig. 7.11 should be understood in relation with the variation of other parameters in Fig. 7.8-7.10, which is not so simple. Because the purpose of the discussion given in this section is to determine the reasons for the poor performance of the setup, the behavior of components will be discussed later in Section 7.5. However the primary reason for the poor performance of MPE and MPA seem to be the very small flow rates in Fig. 7.8. Since the refrigerant flow rate to MPE was limited by the cavitation problem described in Section 7.2.2, the performance of MPE could not be substantially improved by increasing the refrigerant flow rate. However the performance of MPA was clearly observed to improve with the increasing solution flow rate as will be discussed in the following sections.

7.3.2 Heating and cooling water temperatures

The influence of heating and cooling water temperatures on the performance of the setup are analyzed in this section.

The influence of heating water temperature is the most interesting for solar absorption cooling because it decides not only the performance of a chiller but also that of solar collector.

Since the generator temperature is a very strong function of cooling water temperature, the influence of heating and cooling water temperatures are presented together in the following.

Fig. 7.12 shows the influence of hot (heating) water temperature on the system performance at different cooling water temperatures.

In Fig. 7.12, T_{35} is the hot water temperature measured at the generator inlet and T_{33} is the cooling water temperature measured at the inlet of MPA which is the lowest in the system because the cooling water is supplied to MPA first and then to the condenser in series.

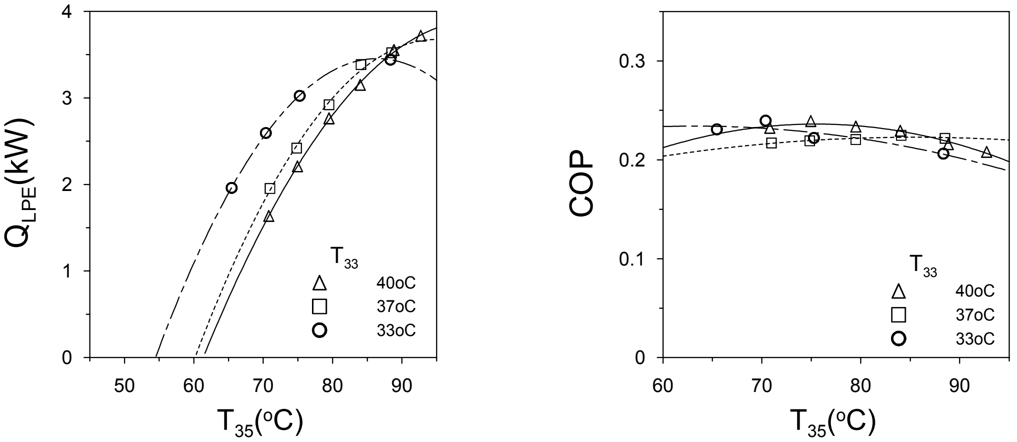

(a) Cooling capacity (b) COP

Figure 7.12 Cooling capacity and COP vs. hot water temperature

In Fig. 7.12a, it seems that the cooling capacity approaches a certain limit value for a cooling water temperature as the hot water temperature increases. Gradients of the capacity curves are steep in the low temperature region and become slow as hot water temperature increases.

At a constant heating temperature, the cooling capacity increases as cooling water temperature decreases in the low hot water temperature region. The increase of cooling capacity is greater when T_{33} is decreased from 37 to 33^{o}C than from 40 to 37^{o}C. In the high hot water temperature region, the cooling capacity seems less influenced by cooling water temperature.

COP in Fig. 7.12b seems relatively insensitive to both hot and cooling water temperatures. All COP values are in the range between 0.21 and 0.24.

Fig. 7.13 shows variation of the system pressures during the tests.

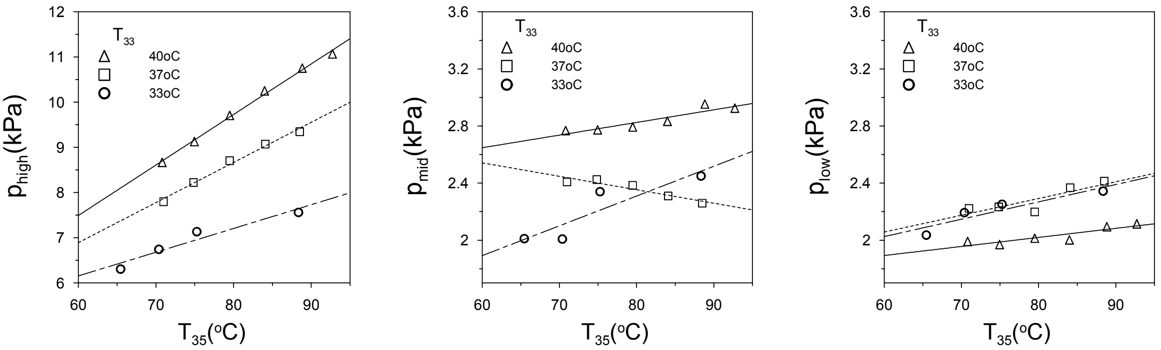

(a) High pressure (b) Mid pressure (c) Low pressure

Figure 7.13 System pressures vs. hot water temperature

For all cooling water temperatures, system pressures increase with increasing hot water temperature in Fig. 7.13 except for the mid pressure of 37^{o}C cooling water temperature in Fig. 7.13b. Regarding the decreasing mid pressure in Fig. 7.13b, although it is not certain exactly how, the capacity of MPA must have been increased more rapidly than MPE with increasing hot water temperature.

It is notable from Fig. 7.13b and 7.13c that mid system pressure is almost the same as or even lower than low system pressure for the 33 and 37 ^{o}C cooling water cases. Since mid and low system pressures are more or less decided by the performance of MPA and LPA respectively, this suggests that the performance of LPA is relatively poor in comparison with MPA. On the other hand, considering that LPA is cooled by MPE, MPE may be blamed for the “pressure inversion”. This is believed to be the case as will be explained later with Fig. 7.18.

Fig. 7.14 shows the variation of some flow rates measured during the tests. Firstly, the condensation rate in Fig. 7.14a increases with increasing hot water temperature, which explains the increasing trends in Fig. 7.13a.

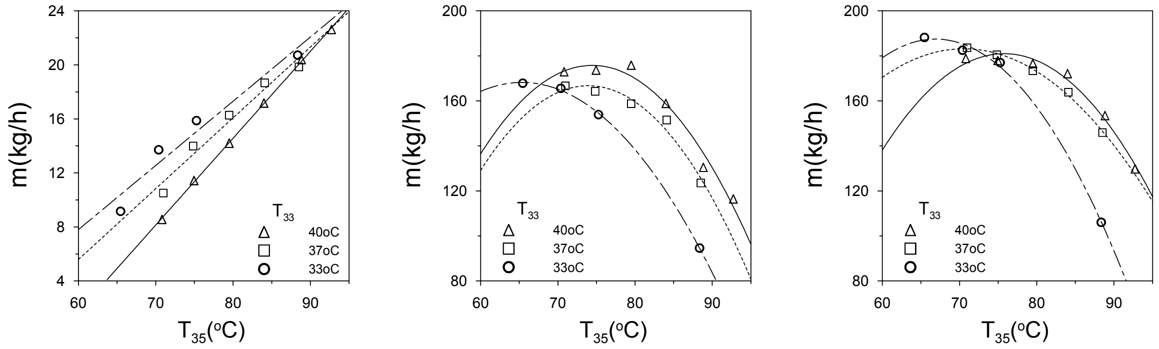

(a) Condensation rate (b) Solution flow to MPA (c) Solution flow to LPA

Figure 7.14 Flow rates of working fluids vs. hot water temperature

Solution flow rate, however, decreases in both absorbers as hot water temperature increases in Fig. 7.14b and 7.14c. This is because more refrigerant was moved to the refrigerant tank as more refrigerant was generated with increasing hot water temperature and consequently less hydraulic pressure was available in solution pipes to push the solution from the generator back to the absorbers. This is supported by the increasing refrigerant recirculation rates into the two evaporators in Fig. 7.15.

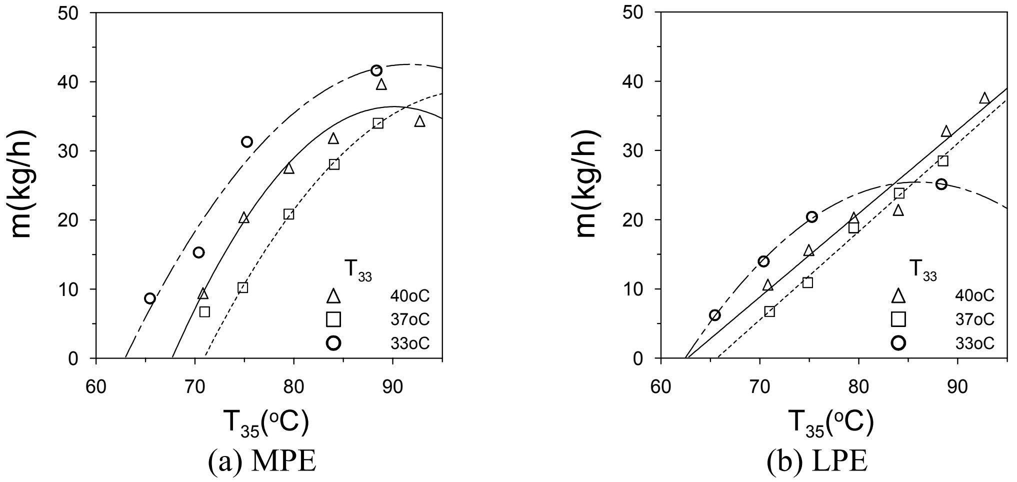

(a) MPE (b) LPE

Figure 7.15 Refrigerant recirculation rates vs. hot water temperature

Fig. 7.15 shows the recirculation rates into the two evaporators. As can be seen in the figure, recirculation rates commonly increased with increasing hot water temperature, which is attributed to the increased liquid level in the refrigerant tank due to the increasing condensation rate in Fig. 7.14a.

LiBr concentrations measured during the tests are shown in Fig. 7.16. LiBr concentration increases with hot water temperature at the generator inlet and outlet. From Fig. 7.16a and 7.16b, it can be seen that the concentration difference between generator inlet and outlet is inversely proportional to cooling water temperature, which suggests that in general, more refrigerant was generated with lower cooling water temperature.

In Fig. 7.16c it is shown that the average LiBr concentration in the refrigerant was 11.8 wt% for 40°C, 1.4 wt% for 37oC and 7.2 wt% for 33°C of cooling water temperature.

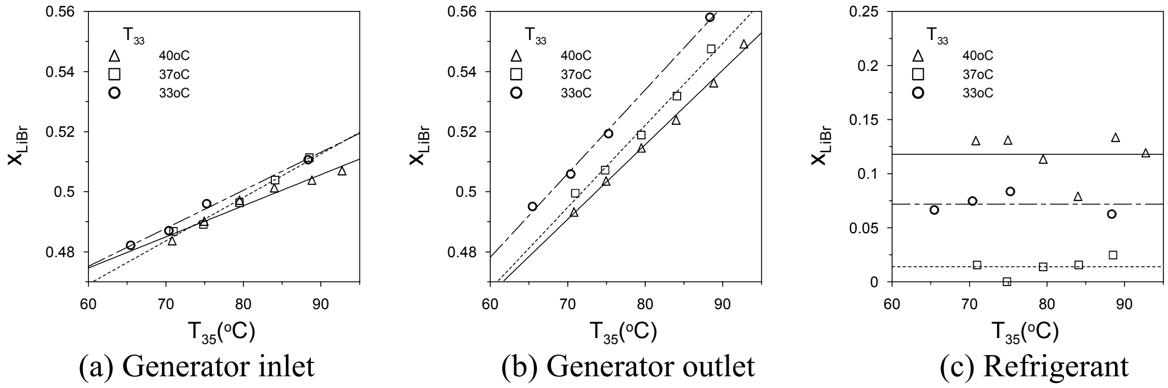

(a) Generator inlet (b) Generator outlet (c) Refrigerant

Figure 7.16 Concentrations vs. hot water temperature

In the following, heat transfer coefficients determined from the experimental data are presented.

Fig. 7.17 shows the heat transfer coefficients of the absorbers. Firstly, in Fig. 7.17a, it is notable that a heat transfer coefficient curve of MPA seems to have a maximum point. Comparing Fig. 7.17a and Fig. 7.14b, it can be seen that this maximum heat transfer coefficient point in Fig. 7.17a is slightly to the right of the corresponding maximum solution flow rates shown in Fig. 7.14b. Absolute magnitudes of the heat transfer coefficients are much larger than those of Fig. 7.11 in the entire range.

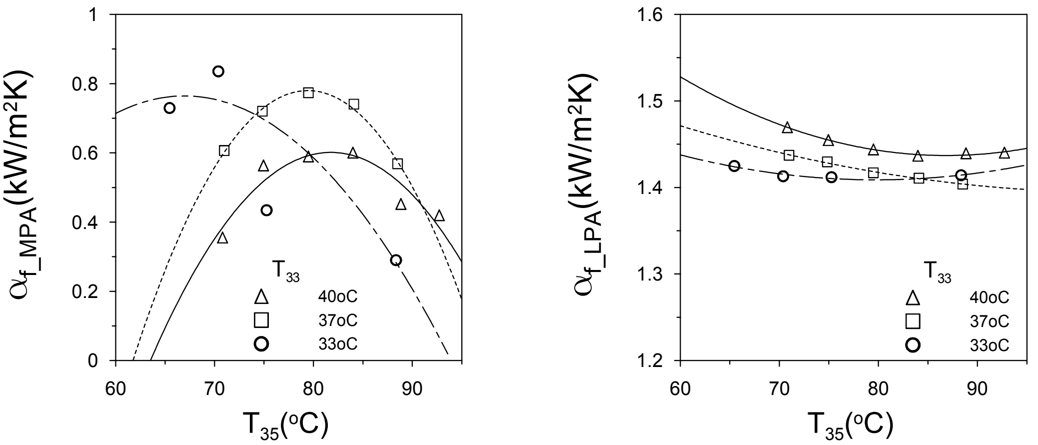

(a) MPA (b) LPA

Figure 7.17 Heat transfer coefficients in absorbers vs. hot water temperature

As in the previous section, the heat transfer coefficients of LPA in Fig. 7.17b have been calculated by Eq. (6.23) using the flow rates shown in Fig. 7.14c.

Fig. 7.18 shows the heat transfer coefficients of the evaporators. For MPE, heat transfer coefficient increases with hot water temperature to a maximum point and then decreases in Fig. 7.18a. This trend is comparable to that of recirculation rate in Fig. 7.15a. All heat transfer coefficients in Fig. 7.18a are in the range from 0.1 to 0.22 kW/m^{2}K. Note that the heat transfer coefficients of 33 and 37 °C cooling water cases are much smaller than that of 40 °C. These low heat transfer coefficients of 33 and 37 °C cooling water cases are believed to be the reason for the pressure inversion observed in Fig. 7.13b and 7.13c.

Heat transfer coefficient of LPE also increases with hot water temperature as shown in Fig. 7.18b, which seems also closely related with the recirculation rate in 7.15b.

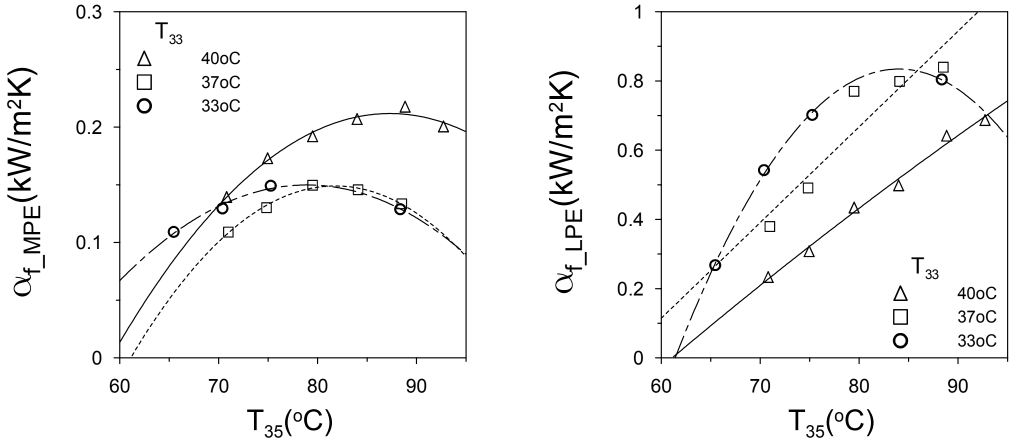

(a) MPE (b) LPE

Figure 7.18 Heat transfer coefficients in evaporators vs. hot water temperature

It can be understood that the steep gradient of a heat transfer coefficient curve in Fig. 7.18b is directly related with that of the corresponding cooling capacity curve in Fig. 7.12.

It is uncertain why the heat transfer coefficient of 40°C cooling water case is the largest in Fig. 7.18a but is the smallest in Fig. 7.18b. It is hard to associate this behavior with the refrigerant flow rates and the LiBr concentrations in Fig. 7.15 and 7.16c (Note that the LiBr concentrations in Fig. 7.16c not large enough to change fluid- and thermodynamic properties of solution noticeably). There may be another parameter involved in this behavior such as the refrigerant loss and the influence of octanol. Considering the complexity, heat transfer coefficients of the evaporators will be discussed separately in Section 7.5.

Finally, the heat transfer coefficients of the condenser and generator are shown in Fig. 7.19.

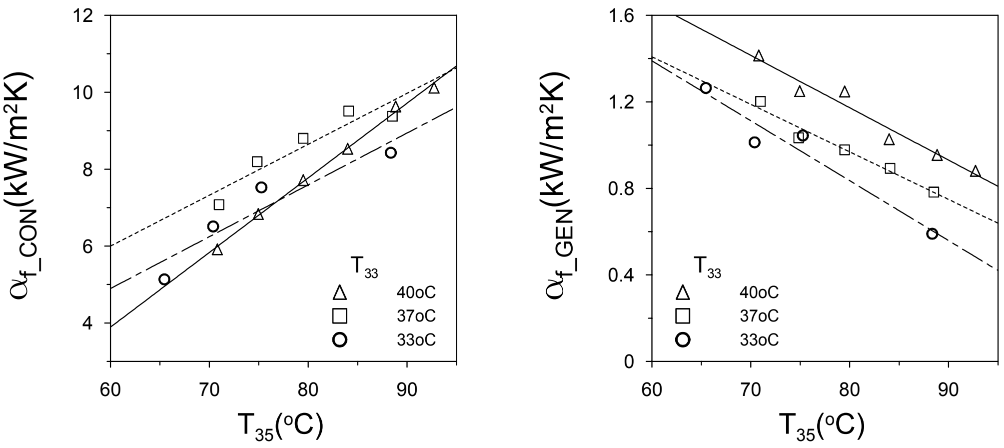

(a) Condenser (b) Generator

Figure 7.19 Heat transfer coefficients of high-pressure components

Condensation heat transfer coefficient increases with hot water temperature in Fig. 7.19a, which is very similar to the trend of condensation rate in Fig. 7.14a.

On the other hand, heat transfer coefficients of the generator decrease with increasing hot water temperature. This is believed to be due to the decreasing solution flow rates through the generator. Note that the sum of the flow rates in Fig. 7.14 b and 7.14c is the flow rate at the generator outlet.

From the analysis above, the cooling capacity in Fig. 7.12a is believed to have been influenced mainly by the performance of the two evaporators, which were in turn heavily dependent on the refrigerant recirculation rates.

The low COP values in Fig. 7.12b are, however, thought to be due to the refrigerant that leaked from LPE into LPA as shown in Fig. 7.20.

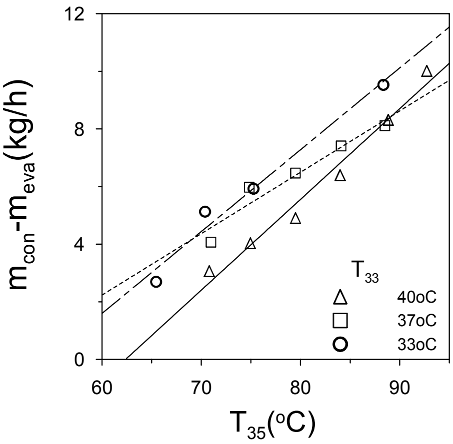

Figure 7.20 Estimated refrigerant loss vs. hot water temperature

7.3.3 Secondary water flow rates

In this section, the influences of chilled water and cooling water flow rates are briefly discussed. Unfortunately, the experiments with hot water flow rate as parameter were carried out with constant generator power instead of constant hot water temperature and they will not be presented here.

Fig. 7.21 shows cooling capacity and COP against the chilled and cooling water flow rates.

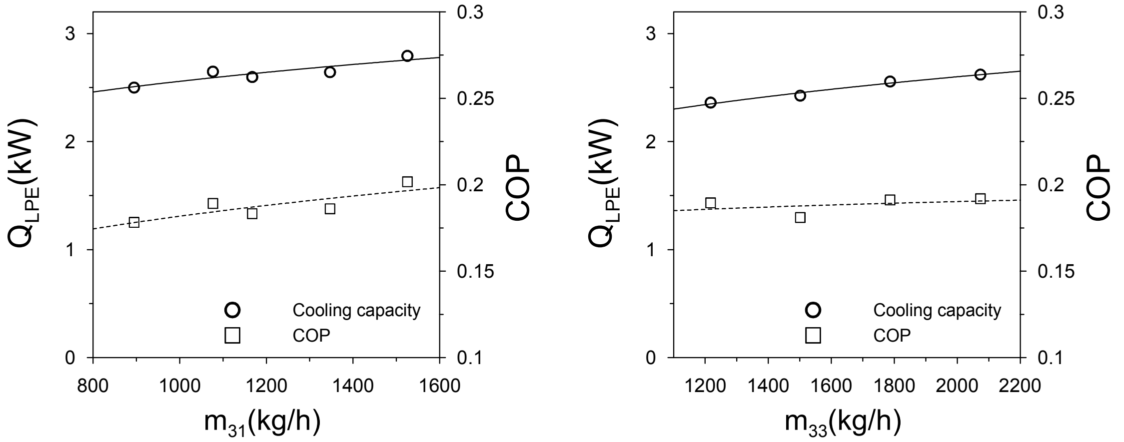

(a) Chilled water flow rate (b) cooling water flow rate

Figure 7.21 Influence of secondary water flow rates

In Fig. 7.21a, both cooling capacity and COP increase slightly with increasing chilled water flow rate. During the test, most of operating parameters were observed almost constant except for the condensation rate and the refrigerant recirculation rates, which slightly increased with chilled water flow rate. It seems that the trends in Fig. 7.21a are mainly due to the increasing heat transfer coefficient of LPE in Fig. 7.22a, where the other heat transfer coefficients are practically constant.

In Fig. 7.21b, the cooling capacity slightly increases with increasing cooling water flow rate but COP remains practically constant. Heat transfer coefficients in Fig. 7.22b are, however, not as clearly associated with the trends.

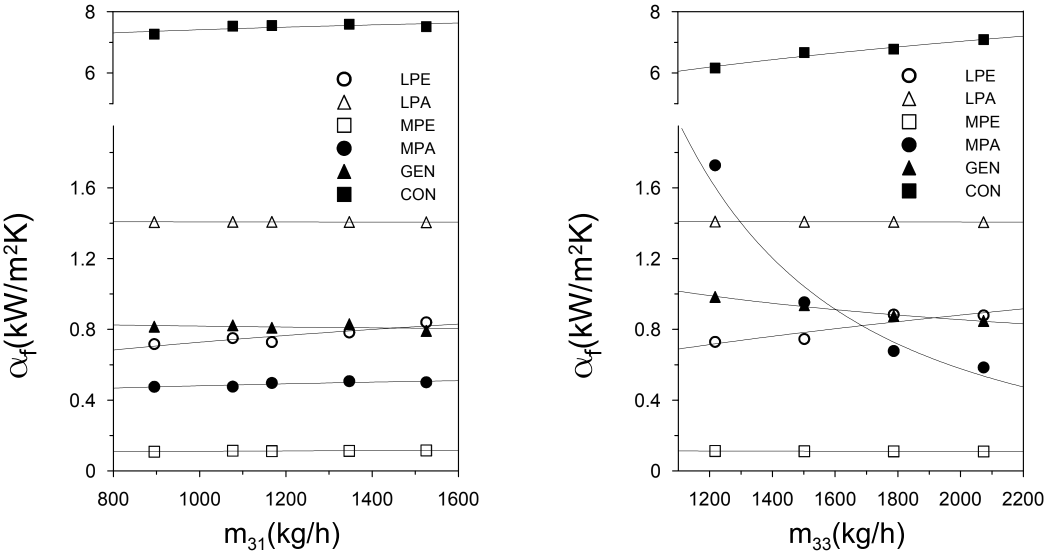

(a) Chilled water flow rate (b) Cooling water flow rate

Figure 7.22 Heat transfer coefficients vs. chilled water flow rate

In Fig. 7.22b, heat transfer coefficient appears to increase with cooling water flow rate in the condenser and LPE but decreases in MPA and the generator. The heat transfer coefficients of LPA and MPE are practically constant. Different trends in heat transfer coefficients are mainly due to the corresponding internal flow rates which were varied during the test as in Fig. 7.23.

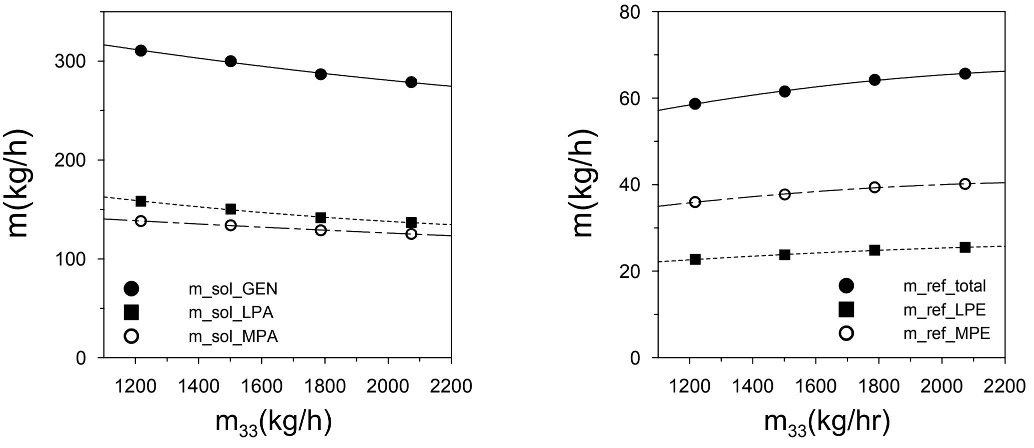

(a) Solution flow rate (b) Refrigerant recirculation

Figure 7.23 Solution and refrigerant flow rates vs. cooling water flow rate

For example, the solution flow rates to the absorbers, and consequently to the generator, decreased with increasing cooling water flow rate as the pressure differences between the generator and absorbers decreased with increasing cooling water flow rate as shown in Fig. 7.24a. This is thought to be the main reason for the decreasing heat transfer coefficients in the generator and MPA in Fig. 7.22b. However the heat transfer coefficient of LPA was not influenced by the decreased solution flow rate because it is not sensitive to the solution flow rate as was already observed in Ch. 6.

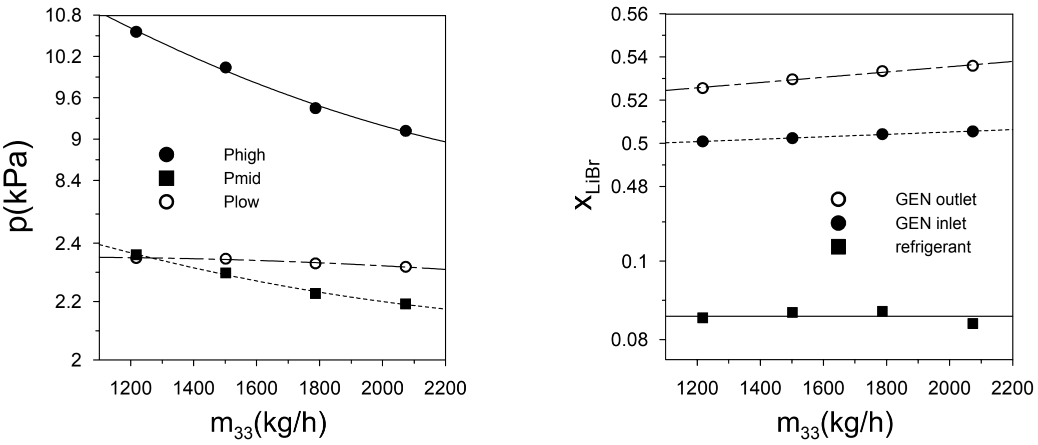

(a) Pressures (b) Concentrations

Figure 7.24 Pressures and concentrations vs. cooling water flow rate

It is notable in Fig. 7.24a that the mid pressure is lower than the low pressure in most of the cooling water flow rate range and the difference becomes larger with increasing cooling water flow rate. This suggests that the increase in cooling water flow rate improved MPA's performance more than that of LPA/MPE.

The increasing trends of cooling capacity in Fig. 7.21b in spite of the decreasing heat transfer coefficients of MPA and the generator in Fig. 7.22b suggests that the cooling capacity of the setup was more strongly influenced by other parameters including the increasing heat transfer coefficients of LPE in Fig. 7.22b, the increasing refrigerant recirculation rate in Fig. 7.23b and also the increasing LiBr concentration at the generator outlet and therefore in the absorbers in Fig. 7.24b.

7.3.4 Distribution of refrigerant between two evaporators

It was possible to vary the distribution of refrigerant between the two evaporators. In this section, the system performance is investigated for different refrigerant distribution conditions in the evaporators.

For each experiment, the flow control valves V_3 and V_4 in Fig. 7.1 were manipulated so that different flow rates of refrigerant were supplied to the two evaporators. Fig. 7.25 shows the changes in the flow rates measured during the tests.

Fig. 7.25a shows the refrigerant recirculation rates to the two evaporators and the total recirculation rate, i.e. the sum of the two recirculation rates. Because the flow rates are shown against $\dot{m}_{07}$, the recirculation rate to LPE, which is $\dot{m}_{07}$ itself, is shown as a straight line.

During the tests, the refrigerant recirculation rate to MPE, i.e. $\dot{m}_{06}$, was observed to decrease with increasing $\dot{m}_{07}$. $\dot{m}_{06}$ was decreased more rapidly than the increase of $\dot{m}_{07}$ so that the total recirculation was decreased as shown in the figure. As previously mentioned, the total recirculation rate was not controllable but dependent primarily on the liquid level in the refrigerant tank. All attempts to maintain a constant total recirculation rate failed because of cavitation in the refrigerant pump.

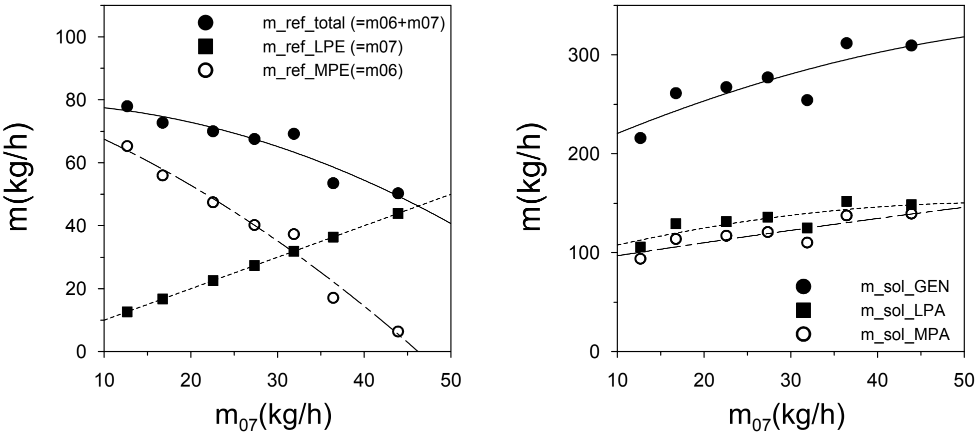

(a) Refrigerant recirculation rates (b) Solution flow rates

Figure 7.25 Solution and refrigerant flow rates vs. recirculation rate in LPE

As $\dot{m}_{07}$ was increased, solution flow rates increased in the generator and absorbers as given in Fig. 7.25b.

Fig. 7.26 shows the corresponding changes in cooling capacity and COP.

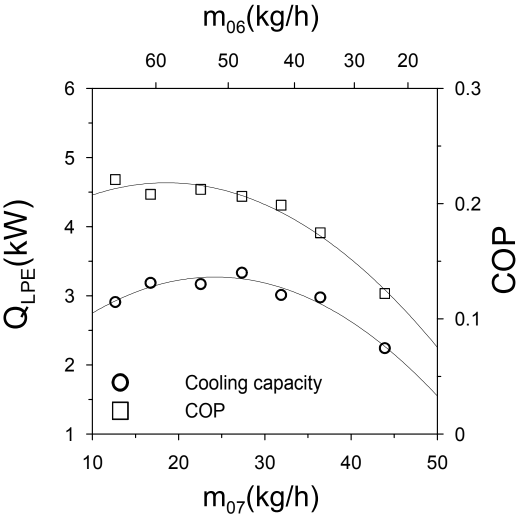

Figure 7.26 Cooling capacity and COP vs. refrigerant recirculation rates

In Fig. 7.26, the optimum operating point seems different for cooling capacity and COP. While the cooling capacity it the maximum at $\dot{m}_{07}$=27 kg/h ($\dot{m}_{06}$=40 kg/h), COP is more or less constant at its maximum value in the range $\dot{m}_{07}$=12~22 kg/h ($\dot{m}_{06}$=47~65 kg/h).

The trend of COP may be explained by Fig. 7.27. Fig. 7.27 compares the condensation rate calculated from the heat transfer rate in the condenser and the evaporation rate calculated from the heat transfer rates of the two evaporators. The difference between the two flow rates is the refrigerant lost somewhere between the condenser and the evaporators (see e.g. Fig. 7.3). It can be seen that the difference becomes almost constant as less refrigerant is supplied to LPE, i.e. as $\dot{m}_{07}$ decreases. This is thought to be the main reason for the trends of cooling capacity and COP in Fig. 7.26.

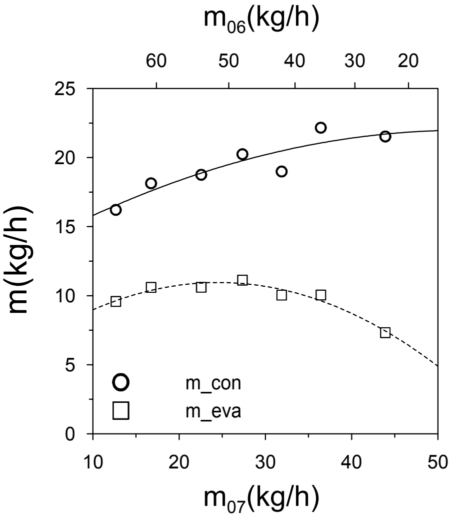

Figure 7.27 Condensation and evaporation rates vs. refrigerant distribution

Finally, Fig. 7.28 shows heat transfer coefficients of the various components in the setup. First of all, it can be seen that heat transfer coefficient of LPE increases with increasing $\dot{m}_{07}$.

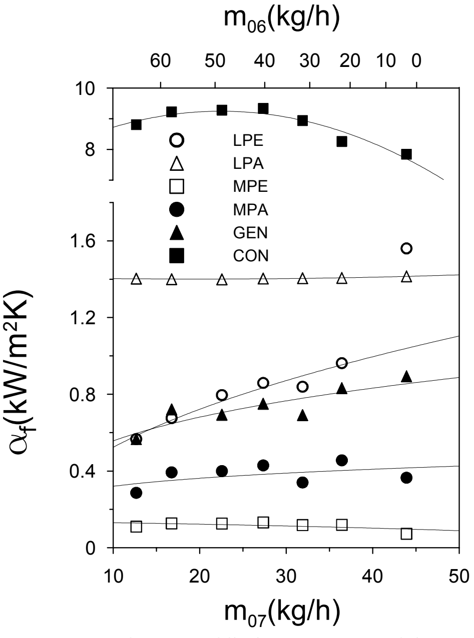

Figure 7.28 Heat transfer coefficients vs. refrigerant distribution

Those of MPA and the generator also increase with increasing $\dot{m}_{07}$ mainly due to the increasing solution flow rates in Fig. 7.25b.

On the other hand, heat transfer coefficient of MPE slightly decreases as can be expected from the decreasing refrigerant flow rate in Fig. 7.25a. This is believed to be another reason for the decreasing trend of the cooling capacity in the high flow rate region in Fig. 7.26.

7.3.5 Distribution of solution between two absorbers

In this section, the system performance is investigated for different solution distributions between the absorbers. During the tests, the flow control valves V_1 and V_2 in Fig. 7.1 were manipulated so that the solution is supplied to the two absorbers at different flow rates.

Fig.7.29 shows the solution and refrigerant flow rates measured during the tests.

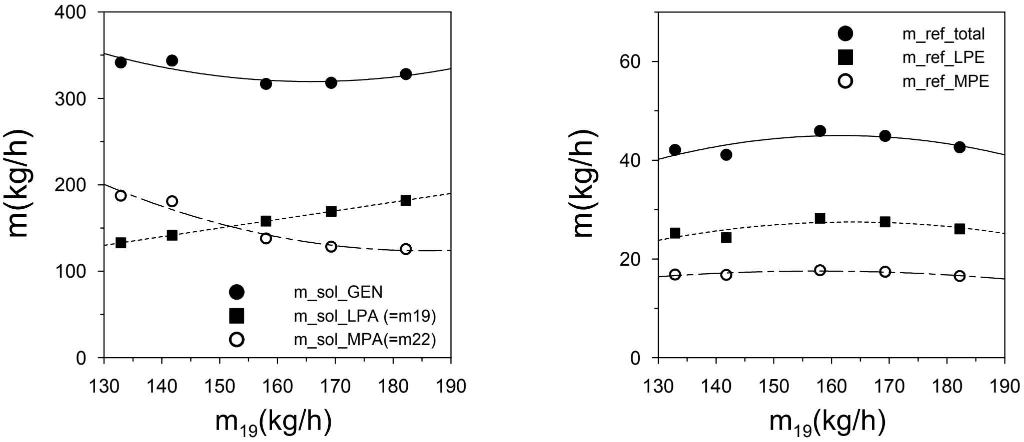

(a) Solution flow rates (b) Refrigerant recirculation rates

Figure 7.29 Solution and refrigerant flow rates vs. solution flow rate in LPA

During the tests, the solution flow rate to LPA, i.e. $\dot{m}_{19}$, was varied from 130 to 190 kg/h, which was between 40 and 60% of the solution from the generator. While $\dot{m}_{19}$ was increased, that of MPA, i.e. $\dot{m}_{22}$, was decreased as shown in Fig. 7.29a. On the other hand, the flow rate to the generator was decreased at the beginning to reach its minimum in the range $157 < \dot{m}_{19} < 170$ kg/h and then slightly increased for higher LPA flows. The refrigerant recirculation rates in Fig. 7.29b commonly show maximum values at $\dot{m}_{19} = 157$ kg/h.

Fig. 7.30 shows the corresponding cooling capacity and COP of the setup.

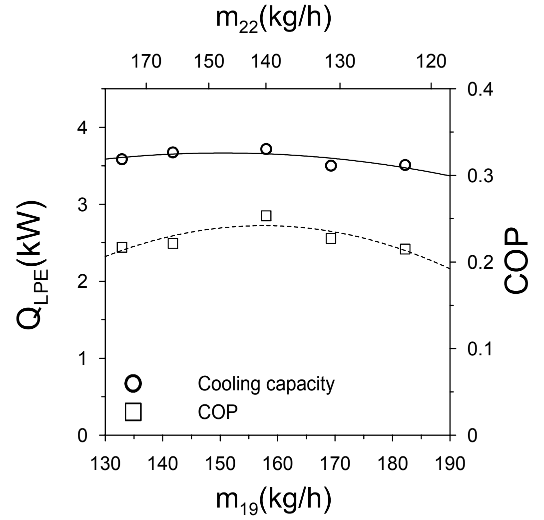

Figure 7.30 Cooling capacity and COP vs. solution flow rates

It seems that both cooling capacity and COP reached the maximum values at $\dot{m}_{19}$=157 kg/h, where the refrigerant recirculation rates were also maximum as shown in Fig. 7.29b.

Fig. 7.31 shows the corresponding variation of the heat transfer coefficients in the setup.

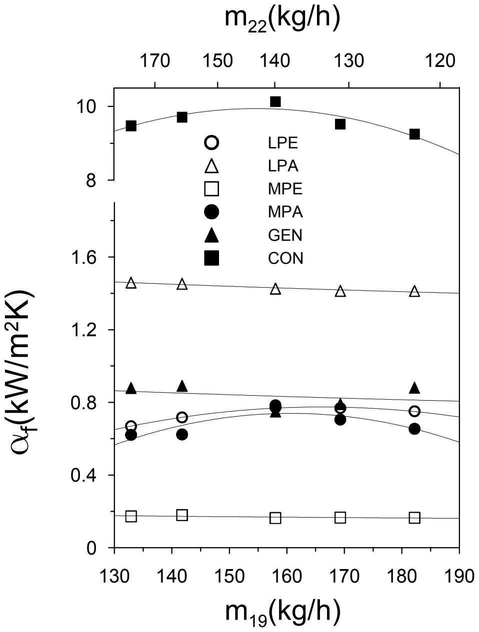

Figure 7.31 Heat transfer coefficients vs. solution distribution

Again, some of the heat transfer coefficients exhibit the maximum values at the same flow rate while others are more or less constant.

The experimental data above shows that even distribution of solution is desirable between the two absorbers.

7.4 Test results – 2nd charging condition

After the tests listed in Table 7.1 were completed, 2 kg of 50 wt% LiBr solution was added into the setup. 3.83 ml of octanol was also added to make its average concentration to be 200 ppm in the solution.

It has been decided to charge 2 extra kg kg of solution so that the solution flow rates could be increased especially for high heating temperature conditions because the maximum solution flow rate to the generator has been less than 300 kg/h at the design hot water temperature (T_{35}≈88°C) under the previous charging condition. The addition of octanol was intended to increase the heat transfer performance in the absorbers.

The second set of tests was done by varying only the secondary water temperatures shown in Table 7.2.

Table 7.2 Parameters and values- 2nd charging (30kg of 50% solution+200ppm octanol)

Parameters	Step1	Step2	Step3	Step4	Step5	Step6	Remark
T_{31} (°C)	13	16	19	24			chilled water temperature
T_{35} (°C)	65	70	75	79	84	89	heating water temperature
T_{33} (°C)	28	34	37	42			cooling water temperature

1. Standard values are in gray cells.
2. Numerical indices should be referred to Fig. 7.1

It was observed that the extra charge of solution greatly improved the system performance as is described in the following.

7.4.1 *Chilled water temperature*

Fig. 7.32 shows the cooling capacity and COP measured with the new charging condition in comparison with the previous test results.

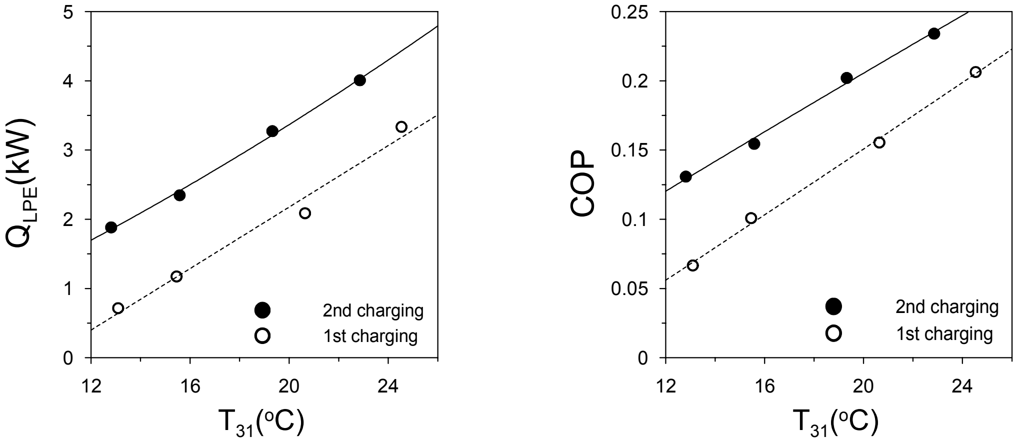

(a) Cooling capacity (b) COP

Figure 7.32 Cooling capacity and COP vs. chilled water temperature

Compared with the results of the 1st charging condition, the cooling capacity has increased with 1.3 kW and the COP has increased approximately with 0.06 in the tested range.

This improvement of performance has been mainly due to the increased solution flow rates in the setup, which was in turn attributed to the extra solution charge into the setup. As will be presented in Section 7.5, the influence of the additional octanol turned out to be marginal if there was any.

The flow rates of solution in the setup are mainly dependent on the hydraulic head exerted by the solution inside the vertical pipe right after the generator in Fig. 7.1, which pushes the solution to pass through the U-trap between the generator and absorbers. Under the 1st charging condition, there was not enough solution to form a large hydraulic head especially when the generator was heated at a high temperature and thus more refrigerant was generated. For this reason, the sight glass at the generator outlet, i.e. SG_5 in Fig. 7.1, was partly void in all cases. After charging of the extra solution, it was completely filled with solution, which suggested that solution level was somewhere at the bottom of the generator.

Due to the increased hydraulic head, the solution flow rates in the setup have been greatly increased in comparison to those of the 1st charging condition as shown in Fig. 7.33.

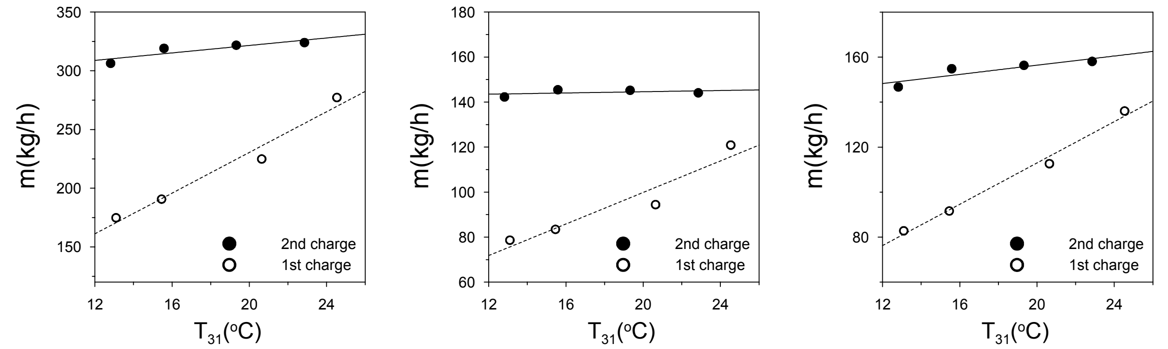

(a) Generator inlet (b) MPA inlet (c) LPA inlet

Figure 7.33 Solution flow rates vs. chilled water temperature

The solution flow rates of the 2nd charging in Fig. 7.33 are also influenced by chilled water temperature but much less significantly than those of the 1st charging condition.

Condensation rate in Fig. 7.34a also shows an increase of 16~35% from those of the 1st charging condition.

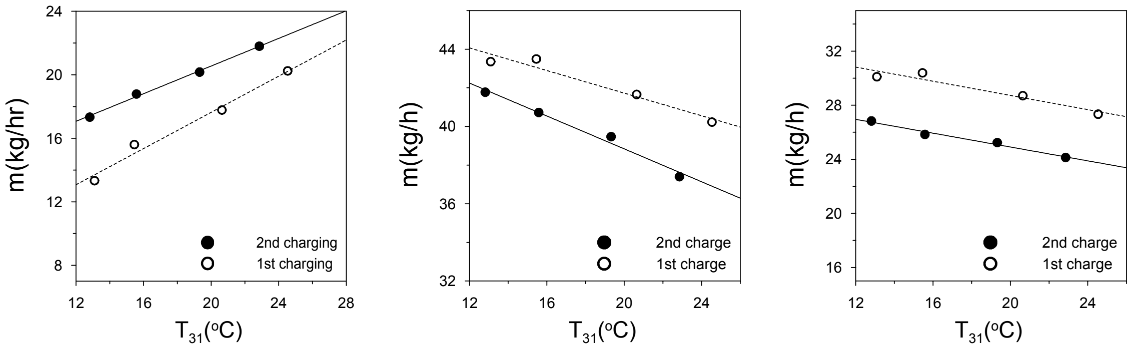

(a) Condensation rate (b) MPE inlet (c) LPE inlet

Figure 7.34 Refrigerant flow rates vs. chilled water temperature

On the other hand, Fig. 7.34b and 7.34c show decrease of the refrigerant recirculation rates in the evaporators. This is probably because of the observed decrease of LiBr concentration in the refrigerant. Average LiBr concentration in the refrigerant was about 6 wt% for the 1st charging condition and it was 2.5 wt% for the 2nd in this case. This low LiBr concentration has probably worsened the pump cavitation resulting in the decreased flow rates shown in Fig. 7.34b and 7.34c.

With the 2nd charging condition, heat transfer coefficients of some components have changed significantly from those of the 1st as shown in the following.

Fig. 7.35 shows the heat transfer coefficients of the generator and the condenser. The generator heat transfer coefficient of the 2nd charging condition is much larger that that of the 1st charging and it increases very slowly with increasing chilled water temperature in Fig. 7.35a. This is due to the slowly increasing solution flow rate in Fig. 7.33a. Note that the heat transfer coefficient curves in Fig. 7.35a are very similar to those of solution flow rates in Fig. 7.33a.

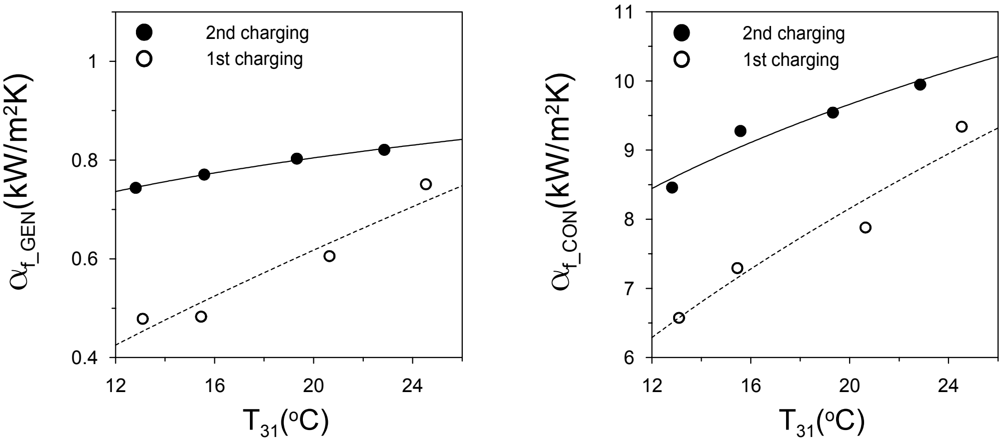

(a) Generator (b) Condenser

Figure 7.35 Heat transfer coefficients of high-pressure components

Heat transfer coefficient is also larger for the condenser of the 2nd charging cases as shown in Fig. 7.35b. Heat transfer coefficient of the condenser has been consistently observed to be proportional to the condensation rate, which needs an explanation. This subject will be discussed in Section 7.5.

Fig. 7.36 compares heat transfer coefficients of the absorbers for the two charging conditions.

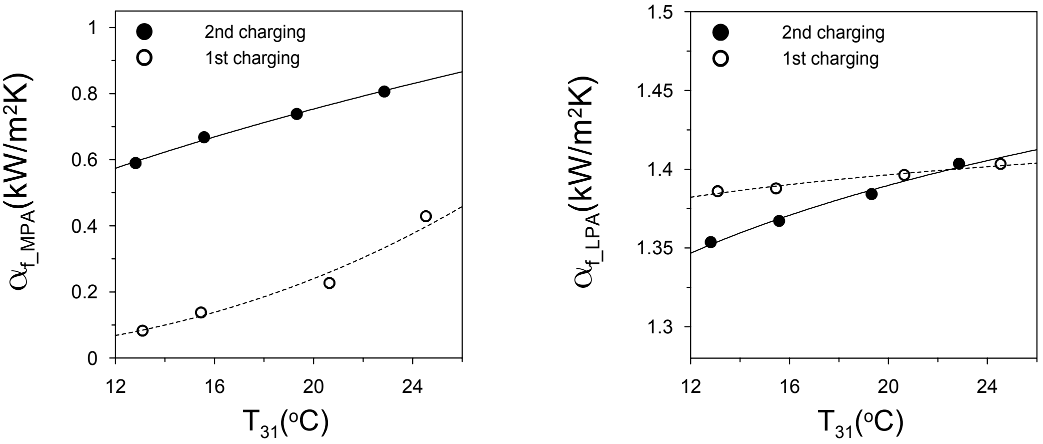

(a) MPA (b) LPA

Figure 7.36 Heat transfer coefficients of absorbers

First of all, it is notable that the heat transfer coefficient of MPA has been increased remarkably for the 2nd charging condition in Fig. 7.36a. Comparing Fig. 7.36a and Fig. 7.33b, it can be said that the performance of MPA is very sensitive to solution flow rate in the tested range.

The heat transfer coefficients of LPA in Fig. 7.36b are not measured but calculated values using Eq. (6.23) for the LiBr solution+octanol 100ppm film flows. Therefore the heat transfer coefficients of the 2nd charging condition, where octanol concentration is 200 ppm, may be inaccurate. This will be discussed in Section 7.5. Nevertheless the heat transfer coefficient of LPA is expected much less sensitive to solution flow rate as has been confirmed by the experiment in Ch. 6 (see Fig. 6.10a).

Fig. 7.37 shows heat transfer coefficients of the evaporators.

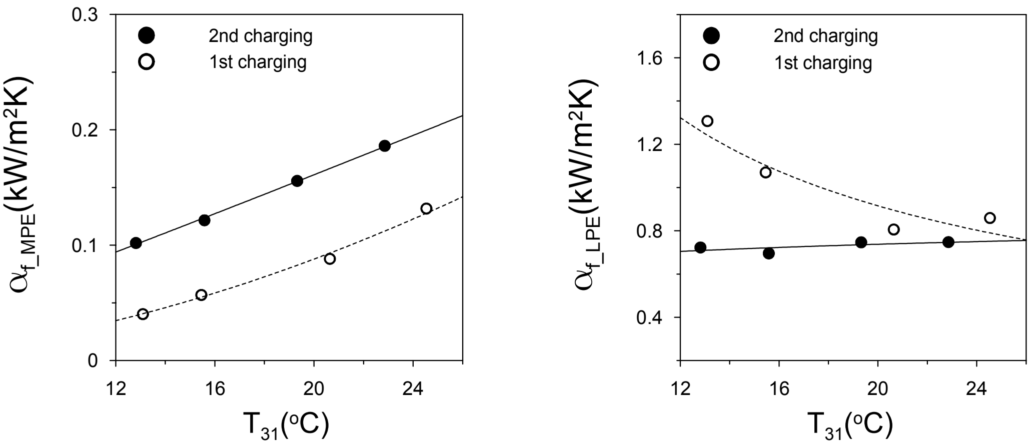

(a) MPE (b) LPE

Figure 7.37 Heat transfer coefficients of evaporators

Fig. 7.37a shows that heat transfer coefficient of MPE has been increased in the 2nd charging condition. But this is not due to the increased refrigerant flow rate in this component. On the contrary, Fig. 7.34b indicates that the flow rate has been decreased. One of the possible reasons for this improvement is the smaller LiBr concentration measured in the refrigerant (average 2.5 wt% in comparison to 6 wt% in the 1st charging condition).

Heat transfer coefficient of LPE is larger for the cases in the 1st charging condition in Fig. 7.37. The heat transfer coefficients of the 1st and 2nd charging conditions show different trends against chilled water temperature in the figure. While that of the 1st charging condition shows a trend similar to the corresponding refrigerant flow rate in Fig. 7.34c, that of 2nd charging condition is more or less constant.

Consistency in heat transfer coefficient data seems poor for the two evaporators. Trends in Fig. 7.37 cannot be clearly associated with the corresponding refrigerant flow rates in Fig. 7.34b and 7.34c. This subject will be further discussed in Section 7.5.

7.4.2 Heating water temperature

In this section, the influence of hot water temperature is investigated for the 2nd charging condition.

Fig. 7.38 shows cooling capacity and COP against hot water temperature.

Cooling capacity increases with increasing hot water temperature as shown in Fig. 7.38a. The trend of cooling capacity for the 2nd charging condition appears somewhat similar to that of the 1st charging condition.

On the other hand, the trend of COP is quite different for the two conditions. While COP of the 2nd charging condition decreases linearly with increasing hot water temperature, that of the 1st charging condition barely changes.

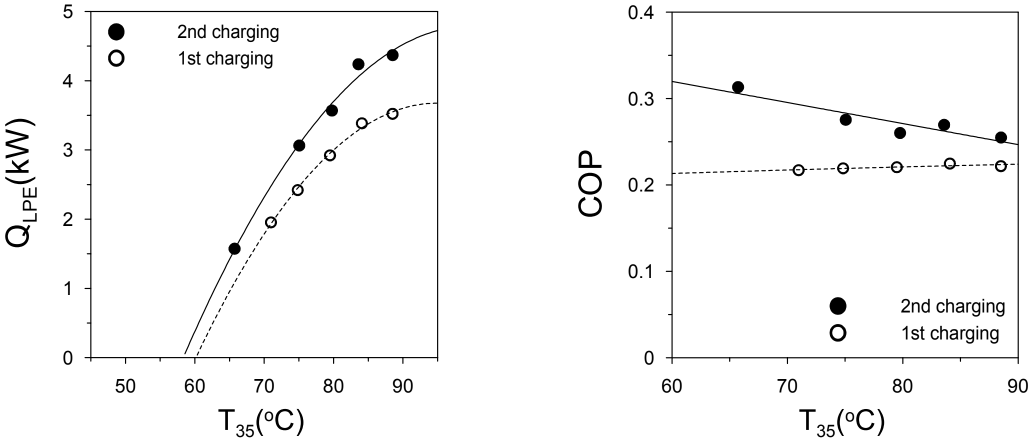

(a) Cooling capacity (b) COP

Figure 7.38 Cooling capacity and COP vs. hot water temperature

Cooling capacity has been increased by 24 % from 3.52 to 4.37 kW and COP has been increased by 15% from 0.222 to 0.255 at the design point 88.5°C. The improvement of performance was mainly due to the different characteristics of the solution flow rates given in Fig. 7.39.

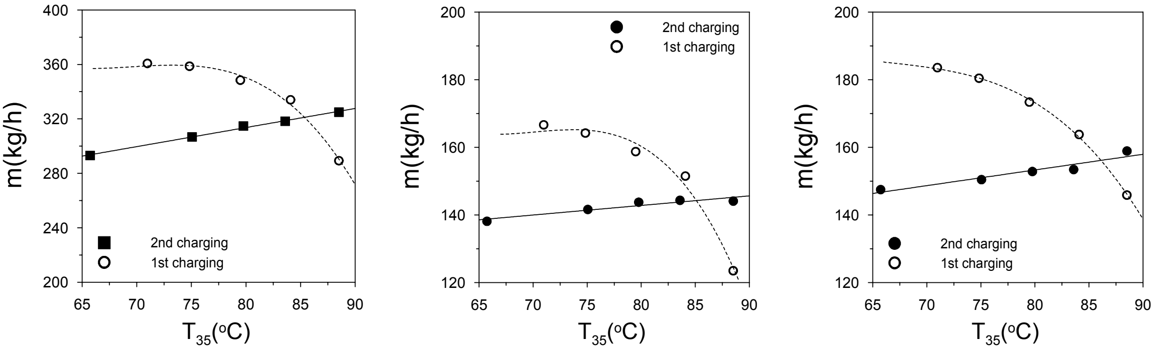

(a) Generator inlet (b) MPA inlet (c) LPA inlet

Figure 7.39 Solution flow rates vs. hot water temperature

In Fig. 7.39, the differences are obvious between the solution flow rates of the 1st and 2nd charging conditions. While the solution flow rates of the 1st charging condition decrease with increasing hot water temperature, those of the 2nd charging condition linearly increase.

Fig. 7.40 shows the corresponding variation of the three system pressures.

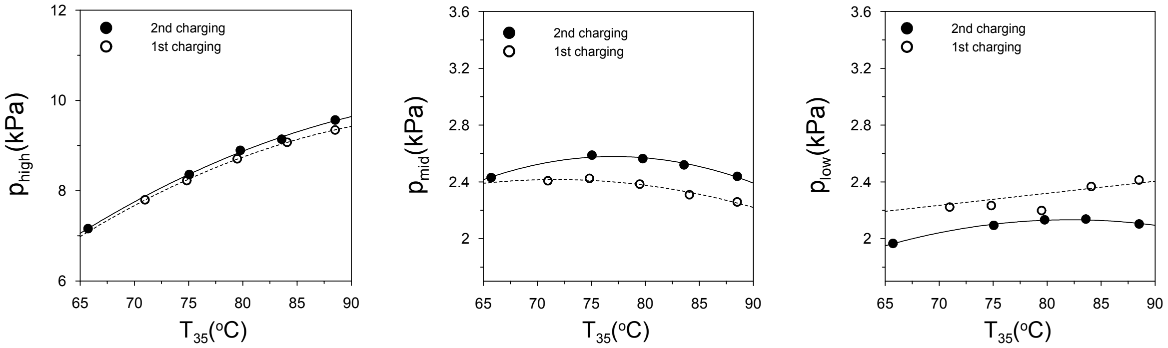

(a) High pressure (b) Mid pressure (c) Low pressure

Figure 7.40 System pressures vs. hot water temperature

It is notable that high and mid system pressures have been increased in comparison with those of the 1st charging condition in Fig. 7.40a and 7.40b but the low system pressure has been decreased in Fig. 7.40c.

However the different solution flow rates of the 2nd charging condition did not significantly change the heat transfer coefficients of the generator and the absorbers as shown in Fig. 7.41.

Heat transfer coefficient of the generator was actually lower than that of the 1st charging condition in low temperature region as shown in Fig. 7.41a. That of MPA is slightly larger only in high temperature region in Fig. 7.41b. Although LPA's heat transfer coefficient of the 2nd charging condition is larger than that of the 1st in the entire range of Fig. 7.41c, the difference is not significant.

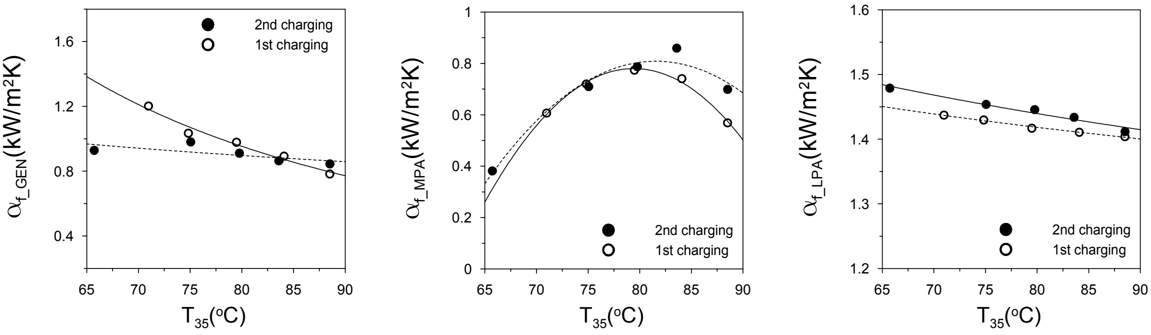

(a) Generator (b) MPA (c) LPA

Figure 7.41 Heat transfer coefficients in the generator and the absorbers

Condensation rate was larger for the 2nd charging condition as shown in Fig. 7.42a and the heat transfer coefficient of MPE was also larger for the 2nd charging condition, Fig. 7.42b. The cooling capacity increase in Fig. 7.38a seems largely due to these improvements. LPE seems to have experienced no significant change in heat transfer coefficient according to Fig. 7.42c.

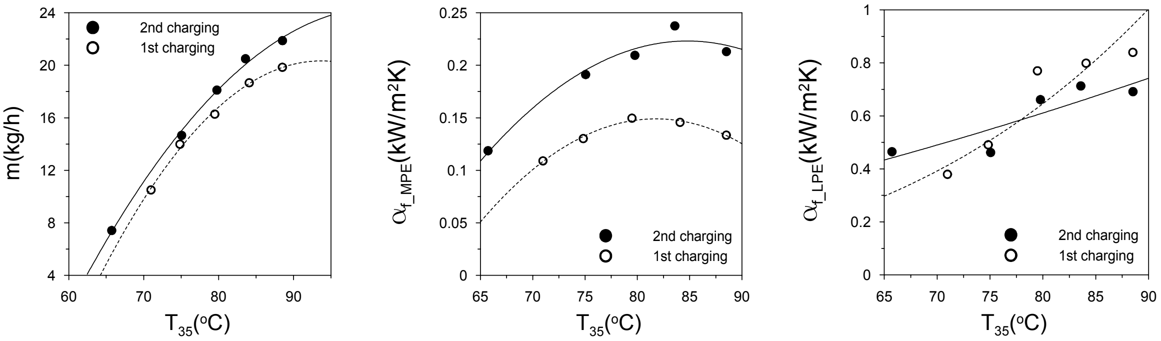

(a) Condensation rate (b) Heat transfer coeff. MPE (c) Heat transfer coeff. LPE

Figure 7.42 Condensation rate and evaporator heat transfer coefficients

The COP increase in Fig. 7.38b may, however, be explained by the comparison of solution circulation ratios of the two charging conditions in Fig. 7.43.

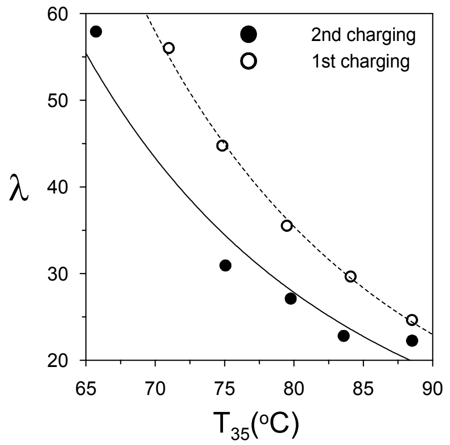

Figure 7.43 Solution circulation ratio vs. hot water temperature

The circulation ratio in Fig. 7.43 has been defined as the solution flow rate at the generator inlet divided by the sum of the evaporation rates in MPE and LPE. As shown in Fig. 3.7a in Ch. 3, COP is inversely proportional to the circulation ratio. It is clearly shown in Fig. 7.43 that the circulation ratio of the 2nd charging condition was smaller than that of the 1st in the entire test range.

7.4.3 Cooling water temperature

This section describes the influence of the inlet cooling water temperature on the system performance for different hot water temperatures. The tests were carried out varying the cooling water temperature while hot water inlet temperature was maintained at three different levels.

Fig. 7.44 shows variation of the cooling capacity and COP against the coolant temperature for different heating medium temperatures.

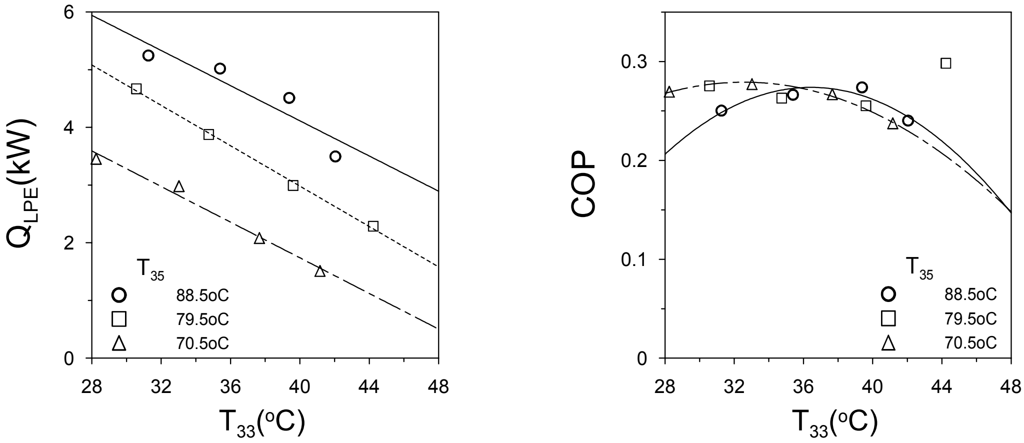

(a) Cooling capacity (b) COP

Figure 7.44 Cooling capacity and COP vs. cooling water temperature

Fig. 7.44a shows that cooling capacity decreases with increasing cooling water temperature. The maximum cooling capacity of 5.3 kW was achieved with cooling and heating water temperature 31 and 88.5°C respectively.

COP ranges from 0.24 to 0.3 in Fig. 7.44b. Although it is hard to draw a common trend, COP tends to decrease with increasing cooling water temperature. Since the COP in the low cooling water temperature region is greatly influenced by the refrigerant loss from LPE, it is impossible to explain the COP trend without considering this influence.

Fig. 7.45 shows the corresponding variation of system pressures. For all hot water temperatures, system pressures commonly increase with increasing cooling water temperature. However, the influence of hot water temperature is not the same for the system pressures.

In Fig. 7.45a, high system pressure is proportional to hot water temperature for a constant cooling water temperature. However in Fig. 7.45b, the mid system pressure of 88.5 ^{o}C hot water case is lower than that of 79.5 ^{o}C hot water in the high cooling water temperature region. Also in Fig. 7.45c, the low system pressure of 88.5 ^{o}C hot water is the lowest in the low cooling water temperature range and those of 79.5 and 70.5 ^{o}C hot water cases are hardly discernable from each other.

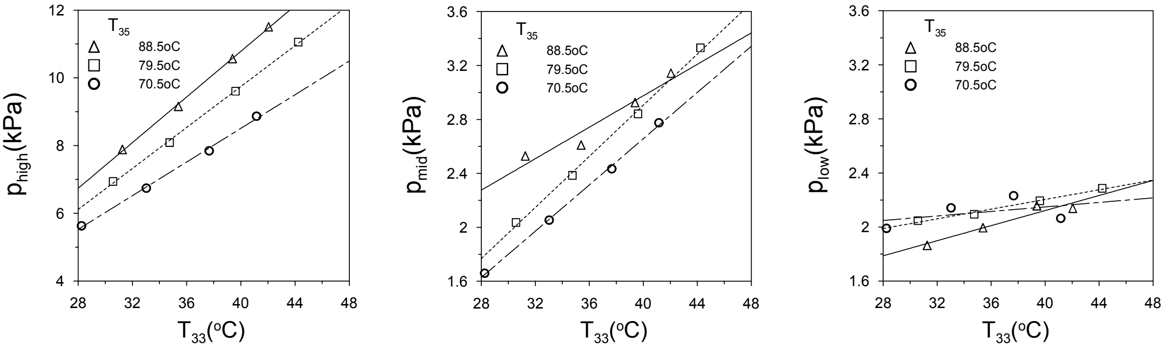

(a) High pressure (b) Mid pressure (c) Low pressure

Figure 7.45 System pressures vs. cooling water temperature

A notable fact in Fig. 7.45 is that the pressure inversion between mid and low system pressures observed in the 1st charging condition (see Fig. 7.13b and 7.13c) is not observed in most of the operating conditions. Fig. 7.45b and 7.45c show that mid system pressure is always higher than low system pressure except for the low cooling water temperature range.

Fig. 7.46 shows the difference between the condensation rate calculated from the overall energy balance equation of the condenser and the evaporation rate calculated from the overall energy balance equations of the two evaporators. It is clear that the difference, i.e. the amount of refrigerant lost somewhere between the condenser and the evaporators, is larger with lower cooling water temperature and higher hot water temperature. This trend agrees with that of the condensation rate in Fig. 7.47b suggesting that the refrigerant loss was proportional to the cooling capacity. Therefore COP would have been much higher than is shown in the low cooling temperature region of Fig. 7.44b if there had been no refrigerant loss.

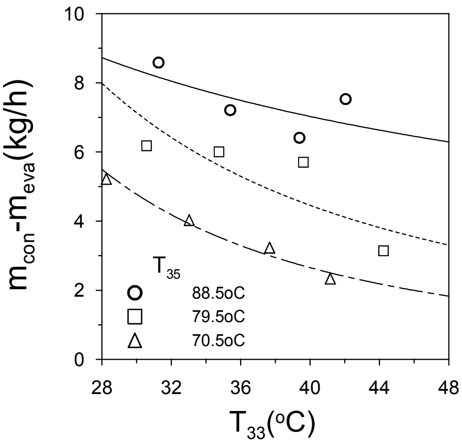

Figure 7.46 Refrigerant loss vs. cooling water temperature

Fig. 7.47 shows the solution flow rates in the generator and the refrigerant flow rates in the condenser during the tests. In Fig. 7.47a, the solution flow rate increases with increasing cooling water and hot water temperatures. On the other hand, the condensation rate in Fig. 7.47b increases with increasing hot water temperature but decreases with increasing cooling water temperature.

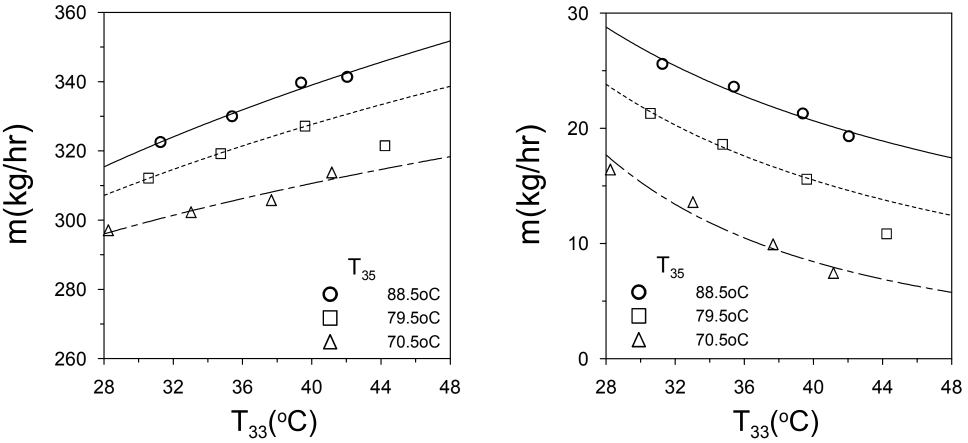

(a) Solution flow rate in generator (b) Condensation rate

Figure 7.47 Flow rates in high-pressure components

Fig. 7.48 shows the corresponding heat transfer coefficients of the generator and the condenser.

In Fig. 7.48a, the heat transfer coefficient of the generator increases with increasing cooling water temperature, which is similar to the corresponding solution flow rate in Fig. 7.47a. However the magnitudes of the heat transfer coefficients are in the reverse order of the solution flow rates in Fig. 7.47a. This is thought to be the influence of the temperature and LiBr concentration of the solution.

Fig. 7.48b shows the variation of condensation heat transfer coefficient against cooling water temperature for different hot water temperatures. It increases with increasing cooling water temperature. This trend may be explained by the decreasing condensation rate with increasing cooling water temperature in Fig. 7.47b. However the influence of hot water temperature in Fig. 7.48b cannot be explained in the same way. Since the condensation rate is proportional to hot water temperature in Fig. 7.47b, the heat transfer coefficient should be reversely proportional to hot water temperature, which is not the case in Fig. 7.48b. Therefore the influence of condensation rate alone cannot explain the data in Fig. 7.48. Behavior of the condenser will be further discussed in Section 7.5.

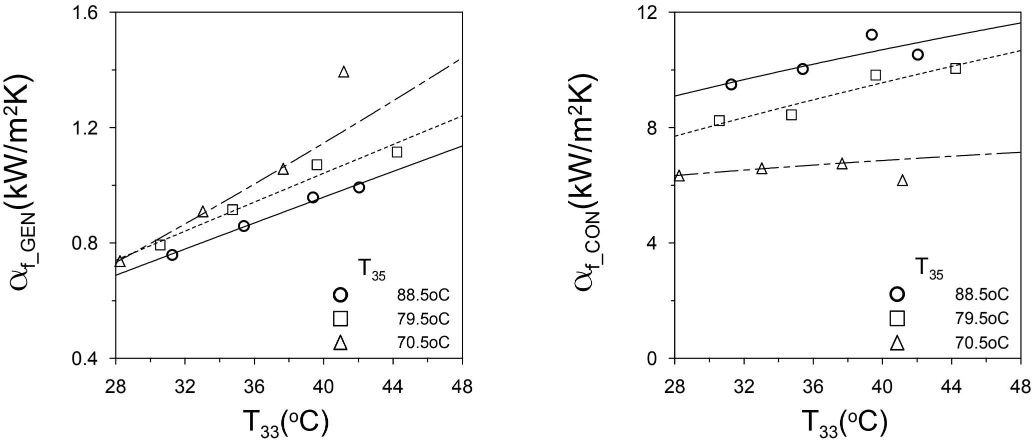

(a) Generator (b) Condenser

Figure 7.48 Heat transfer coefficients of high-pressure components

Fig. 7.49 shows the solution flow rate and the heat transfer coefficient of MPA.

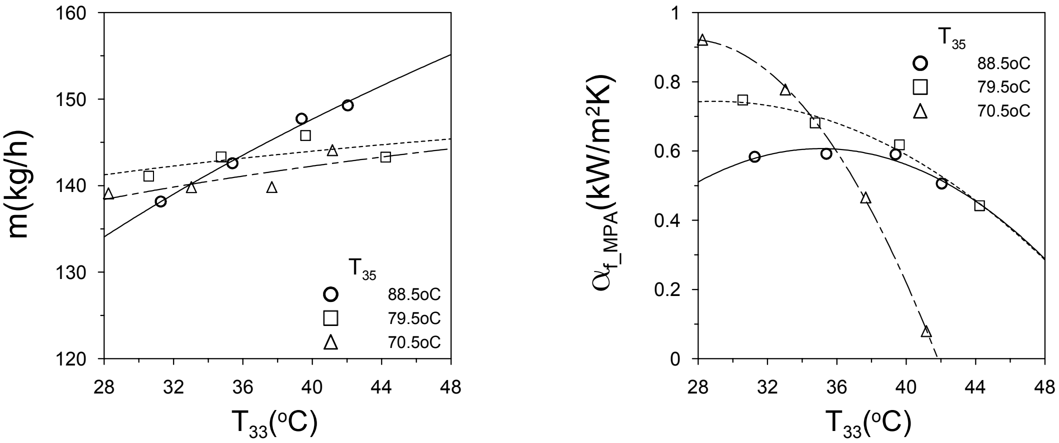

(a) Solution flow rate (b) Heat transfer coefficient

Figure 7.49 Solution flow rate and heat transfer coefficient of MPA

For all hot water temperatures, the solution flow rate increases with increasing cooling water temperature in Fig. 7.49a. Its increasing gradient is particularly steep for 88.5 ^{o}C hot water temperature. However the heat transfer coefficients in Fig. 7.49b commonly decrease with increasing cooling water temperature, which cannot be explained only by the variation of properties. There seem to be extra parameters involved in the heat transfer coefficient other than the solution flow rate.

Fig. 7.50 shows the solution flow rates in LPA and the corresponding heat transfer coefficients calculated with Eq. (6.23) from Ch. 6. The equation predicts that the heat transfer coefficient increases slightly with increasing cooling water temperature because of the increasing solution flow rate in Fig. 7.50a. Heat transfer coefficient is smaller for higher hot water temperature because of the decrease in Pr number.

It should be noted that use of Eq. (6.23) for the heat transfer coefficients of LPA assumes that the influence of the increased octanol concentration in the 2nd charging condition is negligible. This will further be discussed in Section 7.5.

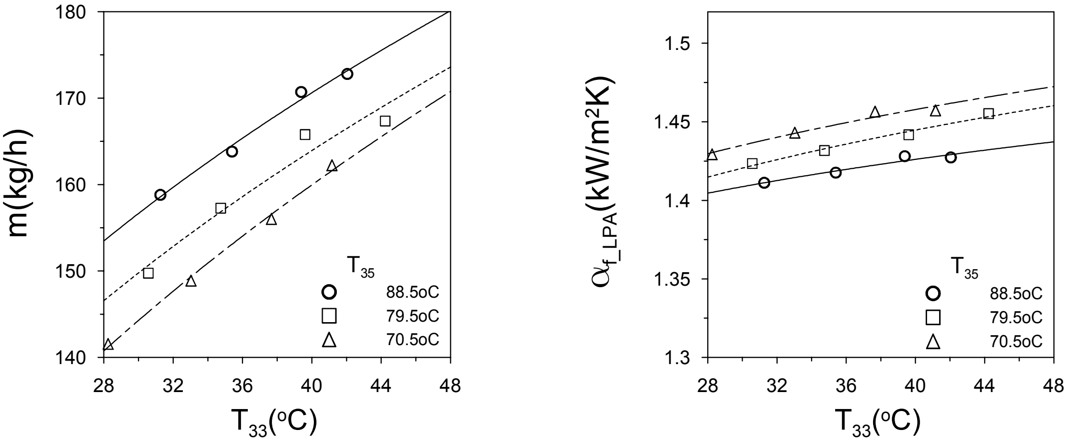

(a) Solution flow rate (b) Heat transfer coefficient

Figure 7.50 Solution flow rate and heat transfer coefficient of LPA

Fig. 7.51 shows the refrigerant recirculation rate in MPE and the corresponding heat transfer coefficients. The trends of the heat transfer coefficient and the refrigerant flow rates agree. However, the gradient of a heat transfer coefficient curve in Fig. 7.51b seems slower than that of a refrigerant flow rate curve in Fig. 7.51a especially for the low hot water temperatures.

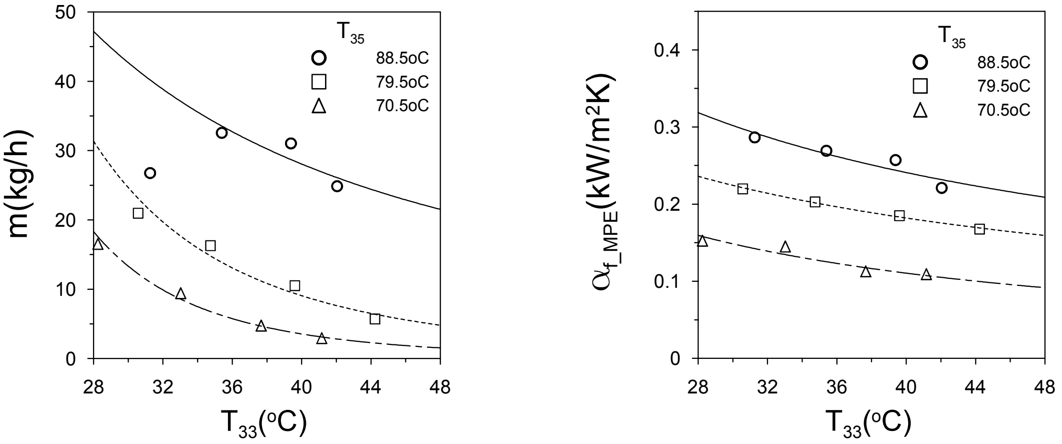

(a) Refrigerant flow rate (b) Heat transfer coefficient

Figure 7.51 Refrigerant flow rate and heat transfer coefficient of MPE

Fig. 7.52 shows the refrigerant recirculation rate in LPE and the corresponding heat transfer coefficients. The flow rate curves in Fig. 7.52a and the heat transfer curves in Fig. 7.52b look very much similar suggesting a strong relation between the two.

All in all, the trend of cooling capacity in Fig. 7.44a may be understood in relation with the condensation rate in Fig. 7.47b and the evaporator heat transfer coefficients in Fig 7.51b and Fig. 7.52b.

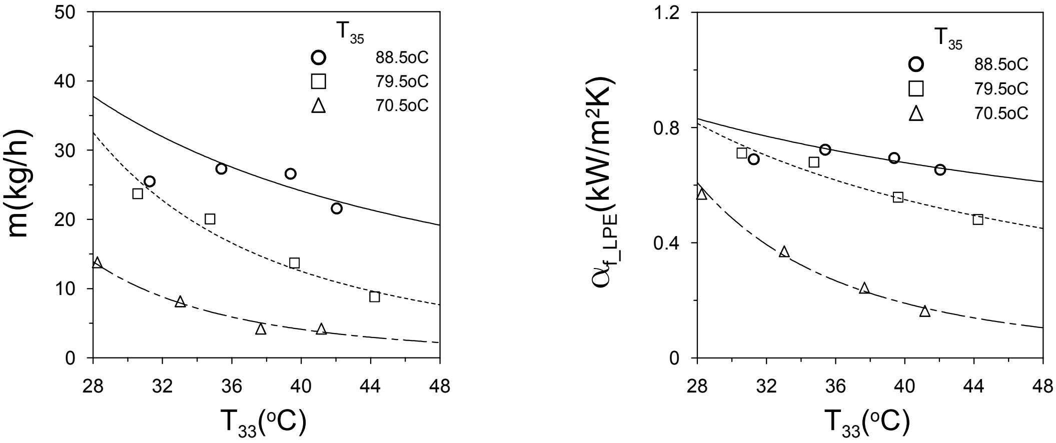

(a) Refrigerant flow rate (b) Heat transfer coefficient

Figure 7.52 Refrigerant flow rate and heat transfer coefficient of LPE

7.5 Analysis of the components

In total, the experimental results of the 78 sets of experiments have been investigated for the analysis of the various components in the setup. Firstly, the falling film heat transfer coefficients presented in the previous sections were converted to Nusselt numbers for an analysis in the following.

Fig. 7.53 shows the film Nusselt numbers of the generator against film Reynolds number. The Nusselt numbers are highly consistent and can be excellently correlated by the Reynolds number.

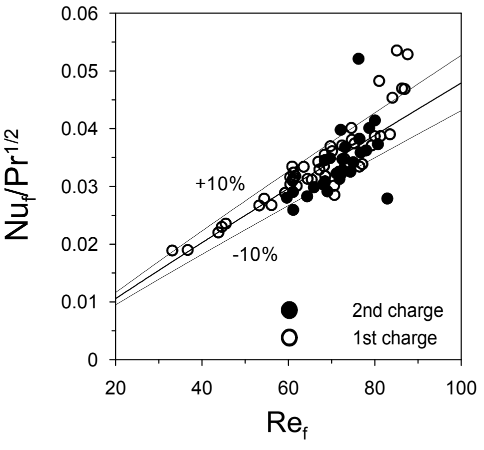

Fig. 7.53 Film Nusselt number of the generator

It can be seen that the Nusselt number increases almost linearly with Reynolds number in most of the range. This may have a close relation with the wetting of the tubes. Besides, no clear deviation can be found of the Nusselt numbers of the 2nd charging condition from those of the 1st suggesting that the increased octanol concentration had no effect on the generator.

Eq. (7.1) can represent the Nusselt numbers within a standard deviation of ±10%.

$$Nu_f=6.33\times10^{-4}Re_f^{0.94}Pr^{1/2} \qquad (7.1)$$

Considering the arbitrariness of the non-condensable gas concentration in the generator-condenser column, the high consistency indicates that the data were little influenced by the presence of non-condensable gas. It may be such that the non-condensable gas might be driven out of the generator tubes by the high velocity of steam flow so that the partial pressure of water was almost equal to the total pressure inside the generator.

Fig. 7.54 shows the film Nusselt number of the condenser against the film Reynolds number calculated with the condensation rate.

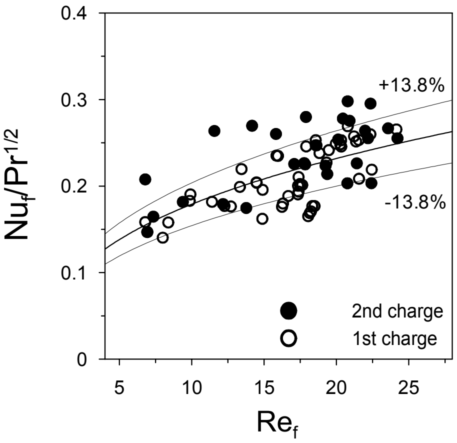

Fig. 7.54 Film Nusselt number of the condenser

Compared with the generator, the consistency among the data is not too bad. Eq. (7.2) can represent the data within a standard deviation of ±13.8%.

$$Nu_f = 7.58 \times 10^{-2} Re_f^{0.37} Pr^{1/2} \quad (7.2)$$

From the high consistency, it may be said also for the condenser that the influence of arbitrariness of the non-condensable gas concentration is not significant. However, the trend of the Nusselt number in Fig. 7.54 is not what is normally expected. Nusselt number is expected to decrease with the increasing condensation rate, i.e. film Reynolds number. Since the transport properties of refrigerant are already taken into account in terms of Prandtl number, this trend is not the influence of different working conditions. This may be explained as follows.

Assuming that the mass of non-condensable gas inside the condenser was constant throughout the tests, its influence on the condensation heat transfer coefficient should have been larger when total pressure was low. That is, the condensation heat transfer coefficient might have been significantly underestimated for the low pressures. This may be the case for the Nusselt numbers in the low Reynolds number region, where most of the tests were done with low pressures.

Alternative explanation may be possible with regards to the variation in “wetted (film condensation)” area in the condenser. As condensation rate increases, more condensate drops fell directly onto the adjacent tube below so that the condensate film was broken and therefore larger heat transfer surface might be exposed directly to vapor. If the net effect of the increase in the “dry” heat transfer surface and the increase in the condensate film thickness had been positive, the increasing trend of Nusselt number in Fig. 7.54 may be acceptable.

Fig. 7.55 shows the Nusselt numbers of LPA. Note that Nusselt numbers for this component have been "calculated" using Eq. (6.23) for the measured solution flow rate and conditions.

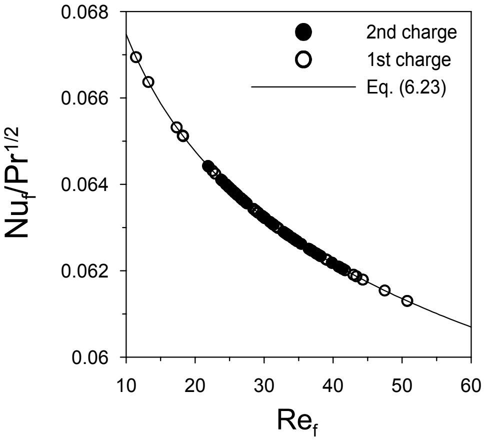

Fig. 7.55 Film Nusselt number of LPA

As explained in Section 7.3.1, the data in Fig. 7.55 have been used to determine the heat transfer coefficients of MPE. The uncertainty involved in using Eq. (6.23) for LPA is small because the magnitude of overall heat transfer coefficients measured for LPA/MPE unit are far smaller than the heat transfer coefficient predicted from Eq. (6.23) so that the influence of the heat transfer coefficient on LPA side is negligible. Fig. 7.56 show shows the resulting Nusselt numbers for MPE.

Fig. 7.56 shows the Nusselt numbers of MPE presented in two different ways. Fig. 7.56a takes account of only the Prandtl number but Fig. 7.56b includes also the Boiling number.

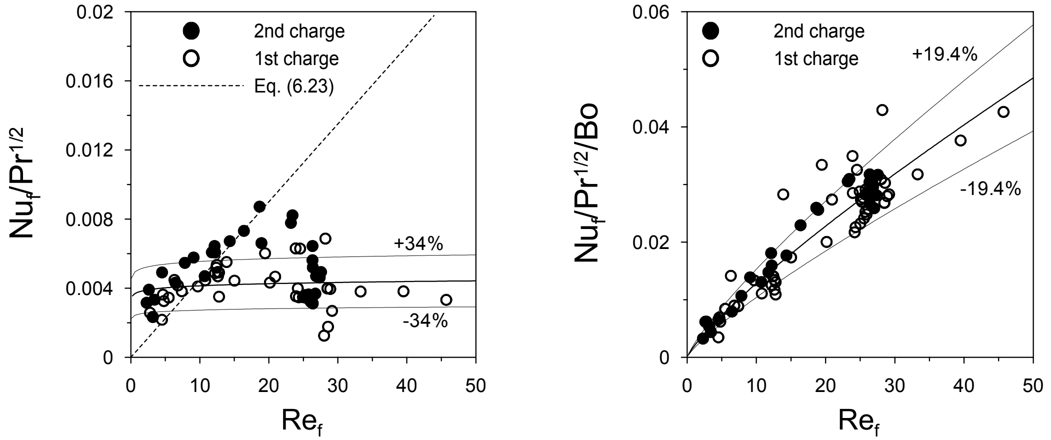

(a) $Nu_f/Pr^{1/2}$ vs. Re_f (b) $Nu_f/Pr^{1/2}/Bo$ vs. Re_f

Fig. 7.56 Film Nusselt number of MPE

As can be seen in Fig. 7.56a, the data are highly inconsistent especially in the range of Reynolds number from 20 to 30, which shows no relation to Reynolds number. For comparison with the experimental data from Ch. 6, Eq. (6.23) for the sensible heat transfer in pure water is shown as the dashed line. It can be seen that the experimental data are reasonably in good agreement with Eq. (6.23) below Reynolds number 20. Inclusion of Boiling number improved the consistency among the data as shown in Fig. 7.56b.

From Fig. 7.56b, it is thought that nucleate boiling might take place in some cases. Depending on the operating condition, heat flux in MPE ranged from 1 to 5 kW/m^2 based on the total surface area. But considering that the wet surface area on MPE side must have been much smaller, the actual heat flux might be larger by several times.

From Fig. 7.56b, the Nusselt number of MPE can be represented within a standard deviation of ±19.4% by

$$\mathrm{Nu_f} = 1.92\times10^{-3}\mathrm{Re_f^{0.825}Pr^{1/2}Bo} \tag{7.3}$$

where Boiling number has been defined by $\mathrm{Bo} \equiv \dot{q}/\left(\Gamma/L\right)h^{fg}$. The characteristic length L used in the definition of Boiling number is the height of MPE.

It has been already mentioned in the previous sections that the low heat transfer coefficient of MPE was the main reason for the poor performance of the setup. The maximum Nusselt number from Fig. 7.56 is only 0.022 with the corresponding heat transfer coefficient of 0.28 kW/m^{2}K. This low heat transfer coefficient is believed to be the combined result of the poor wettability of the contaminated refrigerant and the small flow rate of the cavitating pump.

Heat transfer coefficient of MPA appears also influenced by heat flux as shown in Fig. 7.57.

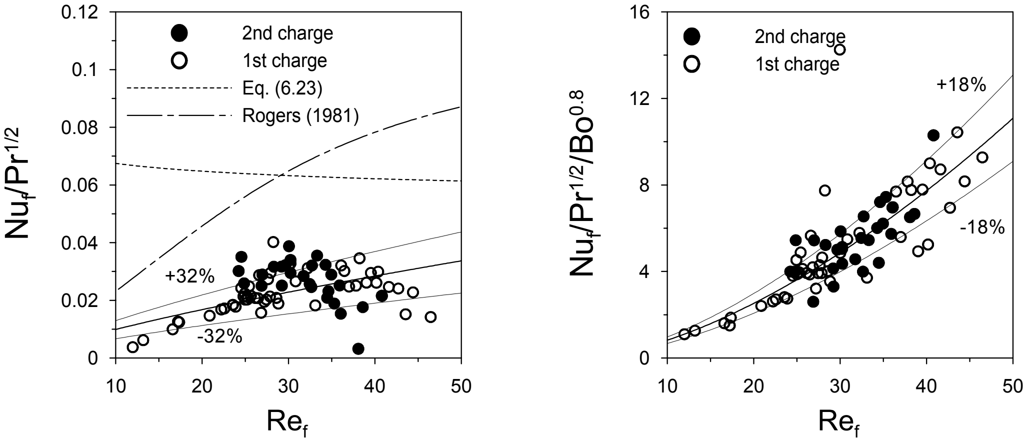

(a) Nu$_f$/Pr$^{1/2}$ vs. Re$_f$ (b) Nu$_f$/Pr$^{1/2}$/Bo$^{0.8}$ vs. Re$_f$

Fig. 7.57 Film Nusselt number of MPA

Fig. 7.57a shows a scatter of the data, which seem to have no relation with Reynolds number beyond the Reynolds number of 30. However, when taking account of heat flux in terms of Boiling number, the consistency between the data significantly improves as shown in Fig. 7.57b. Boiling number used in Fig. 7.57 is the same as MPE except the tube diameter of MPA has been used as the characteristics length.

The dashed and dash-dot lines in Fig. 7.57a represent Eq. (6.23) in Ch. 6 (experiment 5 in Table 6.2) and the correlation of Rogers (1981) for 50 wt% LiBr solution (see Ch. 5 and Ch. 6), respectively. First of all, the negative slope of Eq. (6.23) against Re$_f$ is clearly observable in contrast with the experimental data. On the other hand, the correlation of Rogers (1981) predicts a similar trend to the experimental data in the low film Reynolds region. Nevertheless, the maximum experimental Nu_f is only about half the magnitude of Eq. (6.23) and Rogers (1981). This low Nu_f is suspected to originate mainly from the poor fabrication of MPA.

Eq. (7.4) can represent the data in Fig. 7.57b within a standard deviation of ±18%.

$$Nu_f = 2.01 \times 10^{-2} Re_f^{1.61} Pr^{1/2} Bo^{0.8} \quad (7.4)$$

It is notable that no systematic deviation of the 2nd charging data is found from the 1st charging data in Fig. 7.57. This suggests that the additional charge of octanol over 100 ppm had little effect on MPA, which also agrees with other studies including Hoffmann et al (1996) and Kyung and Herold (2002).

Regarding the influence of heat flux on the Nusselt numbers, a short discussion may be necessary. It is generally agreed that the heat and mass transfer enhancement of a surfactant is attributed to the Marangoni effect induced by the variation of local surface tension during absorption processes (Fujita, 1993; Hihara and Saito, 1993; Ziegler and Grossman, 1996). And it has been reported that the intensity of surface convection or flow instability coincided with the absorption rate (Hoffmann et al, 1996), which was also observed during the falling film tests in Ch. 6. Therefore it is natural to include the effect of heat flux in correlating experimental data. Although no empirical correlation has been presented, the dependence on heat (or mass) flux of the transfer coefficients has also been reported in a few studies (Kim et al, 1996; Kyung and Herold, 2002).

Although it served as a good correlating parameter in Eq. (7.4), unlike in nucleate boiling, the Boiling number does not represent any physical parameter involved in an absorbing film flow and therefore it is not desirable to use. However, all attempts have failed to replace it with other non-dimensional numbers that include surface tension including Marangoni number [$Ma \equiv (\sigma^i - \sigma^b)\delta/\mu D$]. The main reason for the failure of using Marangoni number is that there is neither measurement nor a model available for the surface tension at interface. Actually this is currently one of the new research subjects in the field (Koenig et al, 2003).

Fig. 7.58 shows film Nusselt numbers of LPE. Compared with that of MPE in Fig. 7.56a, Nusselt number of LPE can be correlated without any other parameter than Reynolds and Prandtl numbers.

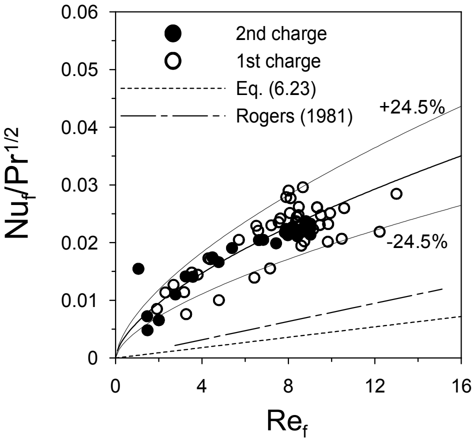

Fig. 7.58 Film Nusselt number of LPE

The dashed and dash-dot lines in Fig. 7.58 are Eq. (6.23) and the correlation of Rogers (1981) for pure water, respectively. In this case, the experimental data are larger than both correlations by several times. Such a discrepancy is not too surprising considering the peculiarities of LPE design and the high uncertainty in the composition of refrigerant.

The Nusselt numbers in Fig. 7.58 can be represented by

$$Nu_f = 6.16 \times 10^{-3} Re_f^{0.63} Pr^{1/2} \qquad (7.5)$$

within a standard deviation of ±24.5%, which is relatively large in comparison with the other components. However, inclusion of a Boiling number only worsened the correlation in this case, which suggests that heat flux barely influenced this component. The relatively large scatter in Fig. 7.58 may be due to the refrigerant loss and contamination.

Finally, Fig. 7.59 shows the effectiveness of the three single-phase heat exchangers in the setup. Effectiveness and UA values of the heat exchangers have been determined from the test results and are expressed to show the ε-NTU relations in the figure. Solid lines are theoretical ε-NTU curves for different thermal capacity ratios, i.e. $(\dot{m}\,Cp)_{min}/(\dot{m}\,Cp)_{max}$.

It can be seen that the behavior of the heat exchangers agree reasonably well with the theoretical values. Especially, the effectiveness of the refrigerant heat exchanger exactly follows the sharply changing theoretical curves in Fig. 7.59c.

As show in Fig. 7.59a, the effectiveness of the high-temperature solution heat exchanger was varied during the tests within the range from 0.7 to 0.8, which satisfied the original design of 0.7.

On the other hand, in Fig. 7.59b, the effectiveness of the low-temperature solution heat exchanger was varied between 0.88 and 1.0 satisfying the original design of 0.8.

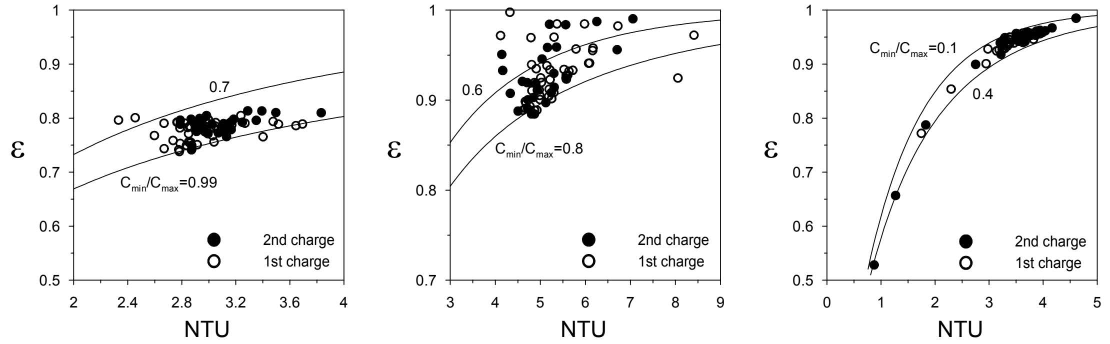

(a) High-Temp. Sol. Hex (b) Low-Temp. Sol. Hex (c) Refrigerant Hex

Figure 7.59 Effectiveness of single-phase heat exchangers

7.6 Comparison with the simulation model

In order to understand the test results better, some test conditions have been simulated with the chiller model from Ch. 5. In the following, the test results presented in Section 7.4.3 are compared with the corresponding simulation results.

Before simulation, the original chiller model in Ch. 5 has been modified as follows.

- Incorporation of a refrigerant loss model
  The test results suggested that some refrigerant was lost from LPE to the solution tank. This loss has been modeled by the discharge of a specific amount of refrigerant from the refrigerant tank to the solution tank. The amount of lost refrigerant has been assumed equal to the difference between the condensation and the evaporation rate (see. Fig. 7.46).

- Use of the experimental solution and refrigerant flow rates
  For the solution flow rate at the generator inlet, the flow rates in Fig. 7.47a have been used. The solution flow rates at the generator outlet were distributed to the absorbers according to the ratio between those shown in Fig. 7.49a and Fig. 7.50a. The refrigerant flow rates in Fig. 7.51a and 7.52a were used for the evaporators.

- Use of the experimental heat transfer coefficients
  For all components except the condenser and LPA, the correlations developed in Section 7.5 have been used. Nusselt (1916) and Eq. (6.23) have been used for the condenser and LPA respectively. The effectiveness values in Fig. 7.58 were used for the single-phase heat exchangers.

- Assumption of infinitely large mass transfer coefficients
  The experimental heat transfer coefficients used in the simulation were determined actually assuming saturated conditions for the solutions (Recall that equilibrium temperatures have been used in logarithmic temperature difference). To be compatible with this assumption, mass transfer coefficient has been assumed infinitely large and consequently the simulation has been reduced to a heat transfer-dominant problem. In practice, mass transfer coefficients were set to arbitrary large values at around $Sh/Sc^{1/2} \approx 3$ (see experimental data in Fig. 6.18 for comparison).

Regarding the refrigerant contamination, it has been decided not to modify the evaporators. It is because firstly, its influence on evaporation temperature is not too large and secondly, its influence on the heat transfer coefficient has already been reflected by the use of experimental heat transfer coefficients.

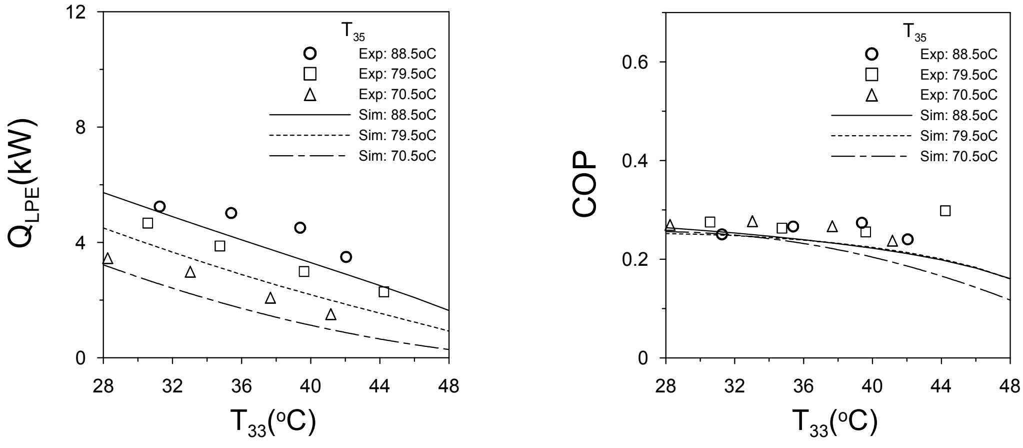

(a) Cooling capacity (b) COP

Figure 7.60 Measured and simulated system performance

Fig. 7.60 shows the simulated cooling capacity and COP against cooling water temperature for different hot water temperatures. The experimental data from Fig. 7.44 are also shown together.

Simulation results agree reasonably well with the experimental results. Although the chiller model slightly under-predicts both cooling capacity and COP, it produces very similar trends.

During the simulation, it was confirmed again that MPE was the key component that decided the behavior of the setup. A slight change in its refrigerant flow rate caused substantial differences in the simulation results.

It is interesting to see how the performance of MPE and the refrigerant loss have influenced the system performance. The performance of MPE might have been greatly improved either by increasing the refrigerant recirculation rate or by improving the surface condition for better wetting. Assuming that the refrigerant recirculation rate in MPE had been maintained constantly at 50 kg/h (see Fig. 7.51a for the actual values) and there had been no refrigerant loss, the chiller model predicts the following.

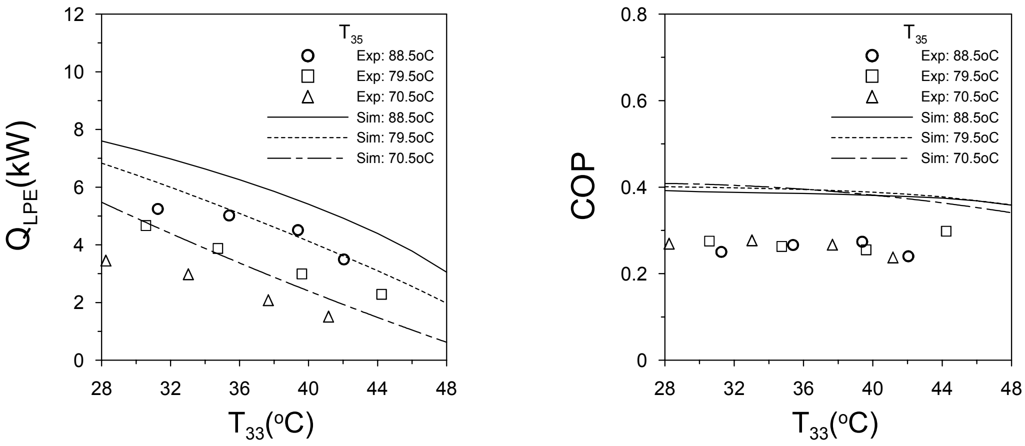

(a) Cooling capacity (b) COP

Figure 7.61 Simulation results for the chiller with an improved MPE and no refrigerant loss

Fig. 7.61 shows that both cooling capacity and COP significantly would improve by increasing the refrigerant recirculation rate and stopping the refrigerant loss. The cooling capacity in Fig. 7.61a is 0.8-2.3kW larger than that of Fig. 7.60a and the COP in Fig. 7.61b is 0.13-0.2 larger than that of Fig. 7.60b.

From the simulation results above, it is now clear that the low COP of the setup is due to the refrigerant loss and the small cooling capacity is mainly attributable to the poor performance of MPE. The comparison with the experimental results also validated the accuracy of the chiller model.

7.7 Conclusions

A half-effect chiller setup has been tested with various parameters including the charging conditions. The following conclusions were derived based on the test results.

Regarding the design and fabrication of the setup, the following problems were detected;

- Air leaked constantly into the setup through the flange between the condenser and the generator, which forced regular evacuation of the setup to maintain an acceptable vacuum level.

- Cavitation of the refrigerant recirculation pump significantly limited the recirculation flow rates through the evaporators resulting in a small cooling capacity.

- Unknown amount of solution that escaped from a leaking solution tube contaminated the refrigerant, which very likely lowered the heat transfer coefficients in the evaporators.

- Due to the faulty design of LPE, a substantial amount of refrigerant escaped from LPE into the solution tank leading to a low COP.

From the analysis of test results, the following conclusions were derived;

- By optimizing the charging conditions in the setup, the performance could be improved significantly.

- The influence of increased octanol concentration from 100 to 200 ppm was negligible, which agrees with the results of Hoffmann et al (1996) and Kyung and Herold (2002).

- Cooling capacity was 2 kW and COP was 0.13 at the original design conditions. When tested with chilled water temperature of 24°C, they were 4.4 kW and 0.25 respectively. This poor performance is mainly due to the small capacities of the components as summarized in Table 7.3.

  Table 7.3 Design and actual UA values for the components

Component	UA_{design} (kW/K)[1]	UA_{actual} (kW/K)[2]	UA_{actual}/UA_{design}
Generator	4.0	2.0	0.50
Condenser	6.4	6.2	0.97
LPA/MPE	1.0	0.23	0.23
MPA	2.0	0.8	0.40
LPE	2.4	1.6	0.67

  1. Calculated from the design results in Table 3.3 of Ch. 3
  2. Estimated at the operating points near the original deign conditions.

  The performance of the chiller setup was dominated by LPA/MPE, which is shown to have the smallest capacity of all in Table 7.3. This small capacity, in turn, was due to the poor heat transfer coefficient of MPE.

- The heat transfer coefficients of all major components were analyzed and expressed in empirical Nusselt number correlations. The simulation results based on these experimental heat transfer coefficients agreed well with the test results.

- Simulation results suggest that both cooling capacity and COP significantly would improve by increasing the refrigerant recirculation rate and stopping the refrigerant loss.

A half-effect LiBr-H_2O chiller setup has been tested and the test results were fully analyzed. Although the system performance was not close to what had been originally designed, the reasons for the deviation were identified and discussed. The results of the present work will be helpful for further development of the chiller.

7.8 Recommendations

Regarding the various problems detected, the following is recommended.

- For the LPA/MPE unit, measures should be taken to improve the evaporator-side heat transfer coefficient. This can be done either by recirculating enough refrigerant or by using a special heat transfer surface.

- The generator should be redesigned to enhance its film-side heat transfer coefficient or to accommodate more heat transfer area.

- Design parameters for the tube coil heat exchangers, i.e. LPE and MPA, should be optimized to improve the performance and also to avoid loss of refrigerant or solution. This includes the liquid distributors, tube spacing and the method of coil alignment.

- Solution and refrigerant trays at the bottom of the absorbers and evaporators should be designed to prevent overflow or escaping of the working fluids.

- The refrigerant recirculation circuit around the evaporators should be carefully redesigned to prevent refrigerant loss and cavitation of the recirculation pump.

As for the need of future research, the following subjects need to be considered.

- Enhanced heat and mass transfer surface and its wetting

  It is necessary to use an extended surface for some components in order to achieve the original design capacity. Since the surface has to be fully wetted with a very small amount of liquid, the physical dimension of any surface structure would better be comparable to the reach of the liquid's capillary action. For this reason, some macro-scale surface structures of a few hundreds micrometers may be considered. Application of some hygroscopic coating techniques may also be beneficial.

- Heat and mass transfer enhancement with a surfactant

  It is well known that a surfactant can significantly promote heat and mass transfer in an absorption process. It is generally agreed that the enhancement is caused by the flow instability induced by the surfactant. This subject needs to be studied so that the behavior of a surfactant in an absorbing liquid film can be unraveled.

Nomenclature

A	area, m^2
Bo	boiling number

	$Bo \equiv \dot{q} / (\Gamma/L) h^{fg}$ for a vertical plate
	$Bo \equiv \dot{q} / (\Gamma/d) h^{fg}$ for a horizontal tube
Cp	heat capacity, kJ/kg K
D	mass diffusivity, m^2/s
d	tube diameter, m
g	gravity constant, m^2/s
h^{fg}	latent heat, kJ/kg
k	thermal conductivity, kW/mK
L	length, m
$\dot{m}$	mass flow rate, kg/s
Ma	Marangoni number, $Ma \equiv (\sigma^i - \sigma^b)\delta/\mu D$
Nu_f	film Nusselt number, $Nu_f \equiv \alpha\delta^+/k$
P	perimeter, m
p	pressure, kPa
Pr	Prandtl number
$\dot{Q}$	heat transfer rate, kW
$\dot{q}$	heat flux, kW/m^2
Re_f	film Reynolds number, $Re_f \equiv 4\Gamma/\mu$
T	temperature, K
U	overall heat transfer coefficient, kW/m^2K
x	absorbent concentration in liquid

Greek symbols

α	heat transfer coefficient, kW/m^2K
δ	film thickness, m
δ^+	theoretical film thickness, $\delta^+ \equiv (\nu^2/g)^{1/3}$, m
Γ	mass flow rate per unit perimeter
	$\Gamma \equiv \dot{m}/P$ for a vertical tube or plate
	$\Gamma \equiv \dot{m}/2L$ for a horizontal tube, kg/ms
μ	dynamic viscosity, Pa s
ν	kinetic viscosity, m^2/s
ρ	density, kg/m^3
σ	surface tension, N/m
λ	circulation ratio

Super- and Subscripts

*	equilibrium or saturation
con	condensation
eva	evaporation
f	film
i	interface
b	bulk

References

Fujita, T., 1993, Falling liquid films in absorption machines, Int. J. Refrigeration, Vol. 16, pp. 2-294

Hihara, E., Saito, T., 1993, Effects of surfactant on falling film absorption, Int. J. Refrigeration, Vol. 16, pp. 339-346

Hoffmann, L., Greiter, I., Wagner, A., Weiss, V., Alefeld, G., 1996, Experimental investigation of heat and mass transfer in a horizontal-tube falling-film absorber with aqueous solutions of LiBr with and without surfactants, Int. J. Refrigeration, Vol. 19, pp. 331-341

Kim, K.J., Berman, N.S., Wood, B.D., 1996, The interfacial turbulence in falling film absorption: effects of additives, Int. J. Refrigeration, Vol. 19, pp. 322-330

Koenig, M.S., Grossman, G., Gommed, K., 2003, The role of surfactant adsorption rate in heat and mass transfer enhancement in absorption heat pumps, Int. J. refrigeration, Vol. 26, pp. 129-139

Kyung, I.S., Herold, K.E., 2002, Performance of horizontal smooth tube absorber with and without 2-ethyl-hexanol, Journal of Heat Transfer, Trans. of ASME, Vol. 124, pp.177-183

Nusselt, W., 1916, Die oberflachenkondnesation des wasserdampfes, VDI Z., Vol. 60, p. 541

Rogers, J.T., 1981, Laminar falling film flow and heat transfer characteristics on horizontal tubes, Can. J. Chem.. Eng., Vol. 59, pp. 213-222 (cited from Armbruster and Mitrovic, 1998)

Ziegler, F., Grossman, G., 1996, Heat transfer enhancement by additives, Int. J. Refrigeration, Vol. 19, pp. 301-309

8 Conclusions and recommendations

At present, thermally driven refrigeration technologies are regarded to have high potential of rendering more economic solar air conditioning systems. Solar electric and thermo-mechanical technologies are limited only to special applications because of the excessive investment cost for solar electric panels and heat engines. However, even the cost of a thermally driven solar cooling technology is still prohibitively high for its wide promotion. Although economics of a thermally driven solar cooling system varies widely depending on many parameters, financial benefit is often only marginal. In many cases, it is the high capital cost associated with initial investment that negates all the benefit from the free solar energy. Therefore solar cooling should be hardly attractive to an individual person, if there were no incentives for it. In this respect, political and financial supports from the government play an important role for the promotion of solar cooling technologies in the private sector. In the mean time, much effort should be made both from research community and industry to cut down the cost of solar cooling technology to make it viable in the market.

Among many thermally driven refrigeration technologies, absorption cooling has the largest share of the current solar cooling market. Besides its other technical and economical merits, the well-developed absorption cooling industry in conventional refrigeration market strongly supports its leading status in the solar cooling market. To date, most solar absorption air conditioning systems have been based on LiBr-water absorption chillers. Popularity of this type of machine originates from its simplicity and cost-effectiveness, which has also been justified by the simulation study in Chapter 2. Considering the excellent properties of LiBr as absorbent, it is not likely that another water-absorbing absorbent would take its place in the market any time soon. However, crystallization of LiBr prohibits its use in a high-lift heat pump or air-cooled chiller. Although there have been efforts to replace LiBr with some alternatives, no solution has been successfully introduced in the market. For this reason, ammonia absorption chillers have been considered for almost all air-cooled solar cooling systems. The simulation study in Chapter 2 showed, however, that a new LiBr-water chiller based on a low temperature-driven half-effect cycle would render a cost-effective air-cooled solar cooling system. The proposed LiBr-water chiller operates far away from the crystallization limit of LiBr and performs better with low-temperature flat plate solar collectors. It was shown in Chapter 2 that the initial investment for an air-cooled half-effect LiBr-water solar air conditioning system could be lower than that of the cheapest ammonia system by as much as 58%. This new air-cooled solar air conditioning system is regarded as a promising solution for the small-scale solar cooling applications particularly in hot and arid regions where use of wet cooling towers should be avoided.

The simulation and design results for the chiller in Chapter 3 showed that most of the components in the chiller should be constructed with enhanced heat transfer surfaces to realize the design targets within a reasonably small physical space. However, the original chiller design with extended heat transfer surfaces has been abandoned for its excessive demand in development cost and time. As an alternative, the final chiller design has been prepared with a simpler configuration and plain heat transfer surfaces sacrificing the compactness and high power density of the original design. Besides the system configurations considered in Chapter 3, there was one option that was overlooked in the design process. Although it was not mentioned in Chapter 3, it might have been possible to design a direct air-cooled system so that the secondary cooling water loop could be avoided. Such a system design would have allowed low auxiliary power consumption and improved performance. However, it would probably have required several new types of heat exchangers and the corresponding R&D effort. Nevertheless, a direct air-cooled system would be definitely advantageous and it is recommended to consider this possibility in the future.

Currently, LiBr is the most popular water-absorbent in absorption air conditioning industry. It has been subjects of so many studies that it would be redundant to repeat its excellent thermodynamic properties here. However, most of the previous approaches to describe this popular absorbent have been fragmental and empirical. In this respect, the study presented in Chapter 4 differentiates itself with the comprehensive collection of experimental data and the firm thermodynamic basis it is based on. It should be noted that there have been continuous effort to replace LiBr with an alternative to avoid crystallization at an elevated heat rejection temperature. The methodology developed in the study is generally applicable to any electrolyte system with a single volatile component and therefore it would also serve well for development of a complete thermodynamic database for such an alternative.

Understanding of heat and mass transfer mechanisms in falling film flows plays a critical role in the design and analysis of an absorption system. The heat and mass transfer models developed in this thesis are largely based on the film theory that assumes hypothetical stagnant layers at vapor-liquid interface. In Chapter 5, various falling film flows have been modeled with these (temperature and concentration) layers and bulk flows using proper boundary conditions to connect them. In this approach, a falling film model has one more degree of freedom for describing interface conditions than the conventional lumped models which are based on logarithmic mean temperature and concentration differences. As a result, the models developed in this thesis are able to predict the temperature and concentration profiles in falling film flows more accurately. Besides, a numerical technique has been developed to facilitate the simulation of individual components and their combinations, i.e. system model, using non-uniform grids and explicit quasi-linear governing equations. The weakest point of the falling film flow models in this thesis is that they are fully dependant on experimental heat and mass transfer coefficients. Therefore when the experimental data used in the simulation are unreliable, which was the case for some of the components in the chiller, so are the results. Nevertheless, the whole system has been simulated for different operating parameters using some experimental data available from literature. The results showed that the chiller setup would yield a cooling power of 5.7 kW and a COP of 0.33 at the design condition, which are 43 and 13 % smaller that the corresponding design values. And it was found that the cooling power of the chiller is the most sensitive to the performance of LPA/MPE, which is a large-diameter tube with falling film flows on both sides. Observing the high uncertainty of the LPA/MPE model in the low film Reynolds number range, a series of experiments has been carried out with a plate-type falling film heat exchanger and the results were presented in Chapter 6.

It is always tempting to design a falling film heat exchanger with a small flow rate so as to form a film on the heat transfer surface as thinly as possible to minimize heat and mass transfer resistances in the liquid film. However, such an attempt is often confronted with a frustrating result that originates mainly from incomplete wetting of the heat transfer surface. In the literature survey in Chapter 6, the experimental heat and mass transfer data of falling film flows are observed highly inconsistent in the small flow rate range below the critical flow rate called minimum wetting rate. In this small flow rate range, a falling film flow is characterized by the existence of dry patches that are apparently in arbitrary shapes and sizes and consequently by low heat and mass transfer coefficients. Therefore design of a falling film heat exchanger in this region cannot be successful without taking account of the fact. Also for the purpose of simulations, it is important to understand the characteristics of the falling film flows in this region for accurate modeling of absorption chillers. For this reason, Chapter 6 has been dedicated mainly to the experimental investigation of the falling film flows on a vertical plate heat exchanger in the small flow rate range. Experiments were carried out with four different working fluids namely, water and LiBr-water solution with and without octanol (100 ppm mass) and two different heat transfer surfaces namely, plain copper surface with and without a copper wire-mesh screen (mesh #22). From the results, it was concluded that;

- Nusselt number of pure water increased almost linearly with Reynolds number up to a Reynolds number at about 180 on the bare copper plate, at which point the test surface was observed completely wet, and beyond the Reynolds number, the Nusselt number remained more or less constant within the tested range. From visualization, this linear relationship appears to be closely related to the wet surface area. LiBr solutions without octanol flowed in narrow rivulets on the bare copper plate. Nusselt number was observed insensitive to flow rate. Wet surface area was small and changed little with flow rate. On the screen-covered copper plate, Nusselt number of LiBr solution without octanol was slightly larger than those of the bare surface and increased slowly with flow rate. Larger wet surface areas were also observed during these experiments.

- When octanol was added, Nusselt number of LiBr solution was increased by a factor 2 on the bare surface and by 0.4 on the screened surface respectively. Marangoni convection was observed on the bare surface during the experiments. Heat transfer enhancement of octanol was less with the screened surface and the screen is believed to suppress the intensive local convections to some degree. Octanol had a negative influence on water flows. Nusselt numbers of the octanol-added water flows were much lower than those of pure water flows at a same flow rate. Although octanol should have decreased the surface tension of water, it is believed to have increased the contact angle of water on the copper surface leading to poor wetting of the surface.

- Sherwood numbers of LiBr solutions increased linearly with flow rate within the tested range regardless of surface type and the presence of octanol. The wire screen was found to greatly improve the mass transfer in LiBr solution flows without octanol. However when octanol was added, no improvement was observed with the wire screen. It is believed that the wire screen suppressed the film surface convection. Octanol improved mass transfer by a factor of 1.8 and 1.1 for the bare and screened surface respectively. Observations made during the tests strongly suggest that octanol enhances heat and mass transfer firstly, by improving wettability of surface and secondly, by promoting the local convections on the film surface. Therefore such a surface structure as the fine-mesh wire screen used in this study should be avoided in absorber design because it could obstruct the local convections on film surface.

From the experimental and analysis results in Chapter 6, it is thought that enhancement of heat and mass transfers in a plate-type falling film heat exchanger in the small flow rate range may be realized firstly, by promoting wetting of heat transfer surface and secondly by incorporating some micro-structures which would provide extra heat and mass transfer surfaces without suppressing Marangoni convection. The first idea may be realized by applying a hydrophilic coating technique and the second idea by developing specially designed micro-scale patterns on the heat transfer surface. Realization of such an enhanced heat transfer plate would enable novel designs of various absorption systems in general as well as the compact half-effect LiBr-water chiller originally designed in Chapter 3.

As regards to the basic enhancement mechanism of a surfactant, it should be noted that there is still no general theory. More specifically, no previous study has succeeded in completely describing the behavior of a surfactant in falling film flows. This implies a great problem in understanding and thus modeling of the heat and mass transfer enhancement by a surfactant. To make matters worse, experimental surface tension and contact angle data are rare, which are indispensable for the study of the falling film flows in small flow rate range. All in all, this lack of fundamental knowledge forces empirical and often case-by-case approach in the design of a falling film heat exchanger. A strong need of research is observed regarding the behavior of falling film flows in incompletely wet conditions with a special focus on the characterization of surfactants at liquid-solid and vapor-liquid interfaces and the mechanism of heat and mass transfer enhancement.

A half-effect LiBr-water chiller setup has been constructed according to the final design in Chapter 3 and tested with various parameters including the charging conditions. Chapter 7 of this thesis has been dedicated to the description of the results. The following is a summary of the conclusions drawn from the test results.

Preliminary test of the setup revealed several problems in the setup as follows;

- Air leaked constantly into the setup through the flange between the condenser and the generator, which forced regular evacuation of the setup to maintain an acceptable vacuum level at the high pressure side of the system.

- Cavitation of the refrigerant recirculation pump significantly limited the recirculation flow rates in the evaporators resulting in a small cooling capacity.

- Unknown amount of solution that escaped from a leaking solution tube contaminated the refrigerant, which very likely lowered the heat transfer coefficients in the evaporators.

- Due to the faulty design of LPE, substantial amount of the refrigerant escaped from LPE into the solution tank leading to a low COP.

Other than evacuating the setup regularly for the air leakage, no measure has been taken to fix the problems because of the limited available resources at the time. After the preliminary tests, a series of tests have been carried out to investigate the influences of various parameters. From the analysis of test results, the following conclusions were derived:

- By optimizing the charging conditions (mass and concentration of LiBr-water solution) in the setup, the performance could be improved significantly. However, the influence of increased octanol concentration from 100 to 200 ppm was negligible.

- Cooling capacity was 2 kW and COP was 0.13 at the original design conditions. When tested with 24 ^{o}C of chilled water temperature, they were 4.4 kW and 0.25 respectively. This poor performance is mainly due to the small capacities of the components as summarized in Table 7.3 in Chapter 7.

- The performance of the chiller setup was dominated by LPA/MPE, which has been found to have the smallest capacity of all components. This small capacity, in turn, was due to the poor heat transfer coefficient in MPE, which is in turn due to the small refrigerant recirculation rate limited by cavitation of the refrigerant pump.

- The heat transfer coefficients of all major components were analyzed and expressed in empirical Nusselt number correlations. The simulation results based on these experimental heat transfer coefficients agreed well with the test results.

- Simulation results suggest that both cooling capacity and COP significantly would improve by increasing the refrigerant recirculation rate in MPE and stopping the refrigerant loss in LPE.

Although the system performance was not close to what had been originally designed, the reasons for the deviation were identified and discussed in Chapter 7. To summarize the results, it can be said that the poor system performance was attributable mainly to the small capacity of MPE rather than other faulty designs and fabrication errors in the setup.

Although direct heat transfer between LPA and MPE may also be realized by other types of heat exchangers, the LPA/MPE in the chiller setup is believed the most practical, straightforward design. In this component, with octanol added in LiBr-water solution, LPA was believed to operate with acceptable performance. However, the heat transfer coefficient in MPE was smaller than the corresponding design value by an order of magnitude. The reasons were firstly, the absolutely small refrigerant rate limited by cavitation of the recirculation pump and secondly, poor wetting characteristics of the contaminated refrigerant. These problems may be resolved relatively easily by redesigning the refrigerant recirculation circuit and fixing the leaking solution line. However, recalling the simulation result in Chapter 5, the overall system performance would have not met the original goals even if all the problems detected in the setup had been resolved. The test results in Chapter 7 also showed it clearly that the original goals would not be achievable without, at least, doubling the heat transfer coefficient in most of the components. It is believed that achievement of such level of enhancement is not possible without using enhanced or augmented heat transfer surfaces. This is the reason why R&D on enhanced heat transfer surfaces is strongly recommended for the further development of the chiller. Any new development of an enhanced heat transfer surface should start from considering firstly, the “lack of knowledge” about the falling film flows especially in incompletely wetting conditions and secondly, the feasibility of realizing a “direct-air cooled” chiller design.

Appendix A Properties of working fluids

A1. Summary of Gibbs energy equation for LiBr-Water solution

The Gibbs energy equation developed in Ch. 4 is summarized in the following.

Molar Gibbs energy of LiBr aqueous solutions in the concentration range of 0 to 70 wt% and the temperature range of 0 to 210 ^{o}C is given by

$$G^l = x_1 G_1^\infty + (1-x_1) G_2^l + x_1 \upsilon RT\left[\ln\left(1000m\right) - 1\right] + G^E \qquad \text{(A1.1)}$$

where

$$G_1^\infty = H_{1\circ}^\infty - TS_{1\circ}^\infty + \int_{T_\circ}^{T} C_{p1}^\infty dT - T\int_{T_\circ}^{T} \frac{C_{p1}^\infty}{T} + V_1^\infty (p - p_\circ^*) \qquad \text{(A1.2)}$$

$$C_{p1}^\infty = RT^{-2}\sum_{j=0}^{2}\frac{c_j}{T^j} \qquad \text{(A1.3)}$$

$$V_1^\infty = RT\sum_{j=0}^{2}\frac{b_{0j}}{T^j} \qquad \text{(A1.4)}$$

$$G_2^l = H_{2\circ}^l - TS_{2\circ}^l + \int_{T_\circ}^{T} C_{p2}^l - T\int_{T_\circ}^{T}\frac{C_{p2}^l}{T} dT + V_2^l (p - p_\circ^*) \qquad \text{(A1.5)}$$

$$C_{p2}^l = R\sum_{j=0}^{2} d_j T^j \qquad \text{(A1.6)}$$

$$V_2^l = R\sum_{j=0}^{2} e_j T^j$$

(A1.7)

$$G^E = x_1 \upsilon RT\left[\ln\gamma^\pm + (1-\phi)\right] \qquad \text{(A1.8)}$$

$$\phi = 1 + \sum_{i=1}^{6}(a_i + \frac{ib_i}{2\upsilon} p) m^{i/2} \qquad \text{(A1.9)}$$

$$\ln\gamma^\pm = \sum_{i=1}^{6}(1+\frac{2}{i})(a_i + \frac{ib_i}{2\upsilon} p) m^{i/2} \qquad \text{(A1.10)}$$

$$p = \exp\left\{\left[\alpha - \ln(\theta + \sqrt{\theta^2 - 1})\right]/\beta\right\} \qquad \text{(A1.11)}$$

$$\theta = \cosh\left[\alpha - \beta\ln(p^*)\right]\exp\left[\phi\upsilon m \mathrm{M}_2 \beta\right] \qquad \text{(A1.12)}$$

$$\alpha = \sum_{j=0}^{2}\alpha_j T^{-j} \qquad \text{(A1.13)}$$

$$\beta = \sum_{j=0}^{2} \beta_j T^{-j} \tag{A1.14}$$

For maximum error of ±0.15K in T^{dew} within –15~110 °C from McNeely (1979)

$$\log(p^*) = 7.05 - \frac{1603.54}{T} - \frac{104095.5}{T^2} \tag{A1.15}$$

For maximum error of ±0.05K in T^{dew} within –15~200 °C from Schmidt (1979) and Perry et al (1984)

$$\log(p^*) = 7.137 - \frac{1820.06}{T} + \frac{53309.16}{T^2} - \frac{45431991.41}{T^3} + \frac{4602051824.}{T^4} \tag{A1.16}$$

Table A1.1 Summary of constants

	0	1	2
a_{1j}	-2.1963155×10^{1}	$+4.9372316\times10^{3}$	-6.5548406×10^{5}
a_{2j}	-3.8104752×10^{3}	$+2.6115345\times10^{6}$	-3.6699691×10^{8}
a_{3j}	$+1.2280854\times10^{5}$	-7.7187923×10^{7}	$+1.0398560\times10^{10}$
a_{4j}	-1.4716737×10^{6}	$+9.1952848\times10^{8}$	-1.1894502×10^{11}
a_{5j}	$+7.7658213\times10^{6}$	-4.9375666×10^{9}	$+6.3175547\times10^{11}$
a_{6j}	-1.5118922×10^{7}	$+9.8399744\times10^{9}$	-1.2737898×10^{12}
b_{0j}	-4.4178654×10^{-5}	$+3.1148992\times10^{-2}$	-4.3611226
b_{1j}	$+3.0793992\times10^{-4}$	-1.8632098×10^{-1}	$+2.7387137\times10^{1}$
b_{2j}	-4.0807943×10^{-4}	$+2.1607955\times10^{-1}$	-2.5175971×10^{1}
c_j	-9.4401336×10^{5}	-5.8423257×10^{8}	0
d_j	$+1.1971933\times10^{1}$	-1.8305511×10^{-2}	$+2.8709378\times10^{-5}$
e_j	$+2.6629961\times10^{-3}$	-3.8651891×10^{-6}	$+7.4648411\times10^{-9}$
α_j	$+1.1375\times10^{1}$	-3.8590×10^{3}	$+5.1319\times10^{5}$
β_j	$+8.6010\times10^{-1}$	-1.9575×10^{2}	$+2.3136\times10^{4}$
H_{1o}^{∞}	-57.1521	H_{2o}^{l}	0
S_{1o}^{∞}	+47.5562	S_{2o}^{l}	0
T_o	273.15	P_o^*	0.6108

References

McNeely, L.A., 1979, Thermodynamic properties of aqueous solutions of lithium bromide, ASHRAE Transactions, Vol.85, pp.413–434

Perry, R.H., Green, D.W., Maloney ,J.O., 1984, Perry's Chemical Engineers Handbook; 6th ed., New York: McGraw-Hill Book Co.

Schmidt E., 1979, Properties of Water and steam in SI-Units. Berlin: Springer-Verlag

A2 Transport properties

Transport properties of working fluids were collected from various sources. For LiBr-water solution, in most cases, experimental data or original correlations have been extended to fit entire concentration range.

A2.1 Thermal conductivity of solution, ksol (kW/mK)

The thermal conductivity of solution by Diguilio et al (1990) has been extended down to pure water as shown in the Fig. A2.1.

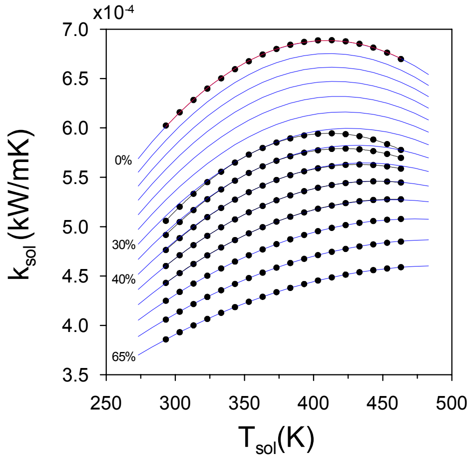

Figure A2.1 Thermal conductivity of aqueous lithium bromide solution

$$k_{sol} = \sum_{i=1}^{3}\sum_{j=1}^{4} a_{ij} x^{j-1} T^{i-1}$$

(A2.1)

where x in LiBr mole fraction and T in K.

Table A2.1 a_{ij} in Eq. (A2.1)

i\j	1	2	3	4
1	-0.386E-03	-0.312E-03	+1.776E-02	-4.162E-2
2	+5.245E-06	-6.413E-06	-8.010E-05	+2.130E-4
3	-6.399E-09	+1.014E-08	+1.003E-07	-2.814E-7

The difference of Eq. (A2.1) from the original correlation of Diguilio et al (1990) is substantial for 30~40% solutions at high temperatures. The gradients of the original correlation in the region were impossible to follow with a 3rd-order polynomial function. It is unclear if this trend is natural. Eq. (A2.1) is, however, safe to use for this project because the working range of the system is far from the region where large deviations exist.

A2.2 Dynamic viscosity of solution, μsol(Pa s)

The dynamic viscosity data from Diguilio et al (1990) have also been used. The values from the original correlation were correlated between pure water and 65% as shown in Fig. A2.2.

$$\ln \mu_{sol} = \sum_{i=1}^{4}\sum_{j=1}^{4} a_{ij} x^{j-1} T^{i-1} \qquad (A2.2)$$

where x in LiBr mole fraction and T in K.

Table A2.2 a_{ij} in Eq. (A2.2)

i\j	1	2	3	4
1	+15.434	-1.796	-454.0	+1645.
2	-1.497E-01	+8.581E-02	+3.187	-11.190
3	+3.211E-04	-4.050E-04	-6.116E-03	+2.286E-02
4	-2.398E-07	+6.025E-07	+2.699E-06	-1.336E-05

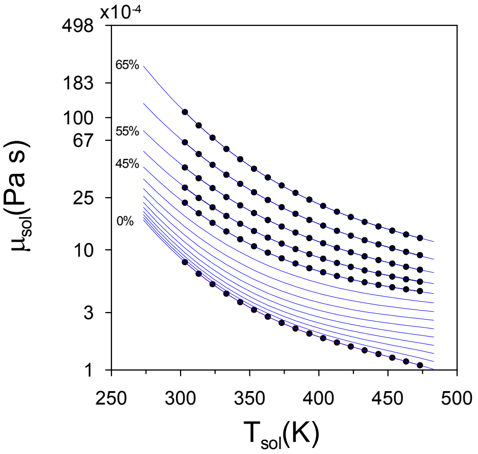

Figure A2.2 Dynamic viscosity of aqueous lithium bromide solution

A2.3 Surface tension of solution, σ (mN/m)

Surface tension is important for falling film flows. The falling film flows are more susceptible to capillary forces when flow rates are small. Since the influence of surface tension on the transfer characteristics of falling film flows were proven very strong, much interest has been given to additives (surface active agents). But, no general theory is available for quantitative description of additive's influence and only incomplete experimental data are available.

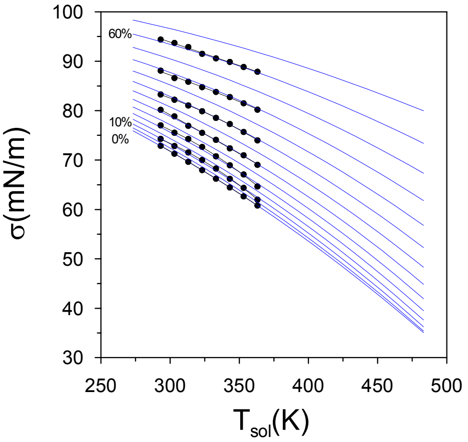

Figure A2.3 Surface tension of aqueous lithium bromide solution

The surface tension data of pure solution from Yao et al (1991) have been curve-fitted by Eq. (A2.3).

$$\sigma_{sol} = \sum_{i=1}^{3}\sum_{j=1}^{3} a_{ij} (x_w \times 100)^{j-1} T^{i-1} \qquad \text{(A2.3)}$$

where x_w is in LiBr mass fraction and T in K.

Table A2.3 a_{ij} in Eq. (A2.3)

i\j	1	2	3
1	+100.06	-38.325	+72.416
2	-2.832E-02	+2.992E-01	-3.764E-01
3	- 2.198E-04	-4.492E-04	+9.149E-04

A2.4 Thermal conductivity of saturated steam, kvap (kW/m K)

Data from Schmidt (1979) were curve-fitted by

$$\ln k_{vap} = \text{-4.891E-03} + \frac{\text{2.282E-06}}{T} + \frac{\text{2.501E-09}}{T^2} \qquad \text{(A2.4)}$$

where T is in K.

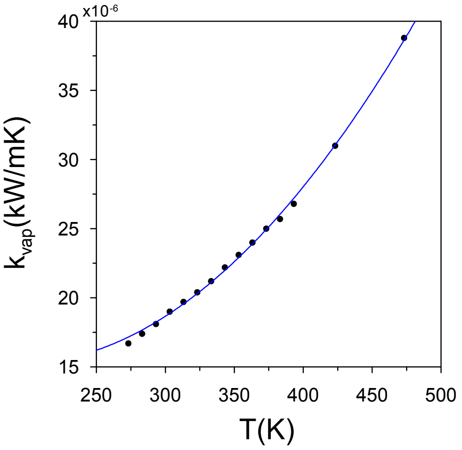

Figure A2.4 Thermal conductivity of saturated steam

A2.5 Dynamic viscosity of saturated steam, μvap (Pa s)

Viscosity data of saturated steam were also collected from Schmidt (1979).

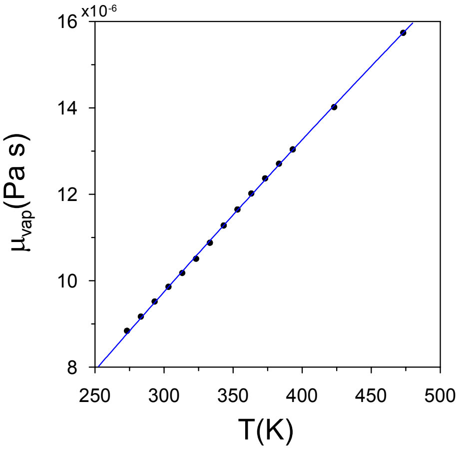

Figure A2.5 Dynamic viscosity of saturated steam

$$\ln \mu_{vap} = -13.029 + \frac{6.364\text{E-}03}{T} - \frac{4.659\text{E-}06}{T^2} \quad \text{(A2.5)}$$

where T is in K.

A2.6 Mass diffusivity of LiBr, D (m2/s)

Mass diffusivity data were collected from Gierow et al (1993).

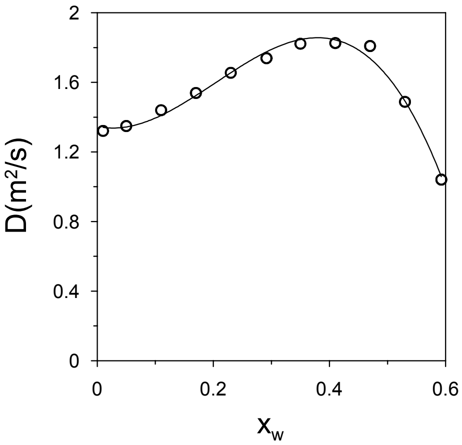

Figure A2.6 Mass diffusivity of LiBr in 25 °C solutions

$$D = \left(1.231 + 189.319\text{m} - 17275.827\text{m}^2 + 327172.786\text{m}^3\right) \times 10^{-9} \times \left(\frac{\mu_\circ}{\mu}\right)\left(\frac{T}{T_\circ}\right) \quad \text{(A2.6)}$$

where m is in molality and T is in K. The last terms is a correction factor for temperature where μ and μ_o are dynamic viscosities of the solutions at T_o (=298.15K) and T, respectively.

A2.7 Solubility of LiBr in water

The crystallization data from Boryta (1970) were fitted with polynomial functions for the regions as shown in Fig. A2.7.

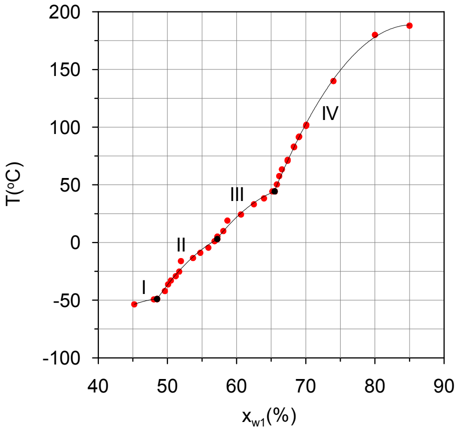

Figure A2.7 Solubility of LiBr in water (Boryta, 1970)

For the region I, where $x_w < 0.485$

$$T=-398.3+25.107\times(100\ x_w)-0.253\times(100\ x_w)^2 \qquad \text{(A2.7a)}$$

For the region II, where $0.485< x_w < 0.572$

$$T=-919.4+38.51957477\times(100\ x_w)-0.3080928653\times(100\ x_w)^2 \qquad \text{(A2.7b)}$$

For the region III, where $0.572< x_w < 0.655$

$$T=-1159.4+42.7386184\times(100\ x_w)-0.308288545\times(100\ x_w)^2 \qquad \text{(A2.7c)}$$

For the region IV, where $x_w > 0.655$

$$T=-4486.9+130.3204838\times(100\ x_w)-0.8697209191\times(100\ x_w)^2 \qquad \text{(A2.7d)}$$

where T in K and x_w in LiBr mass fraction.

A2.8 Freezing points

Freezing line from Duvall et al (2001) was fitted graphically as shown in Fig. A2.8.

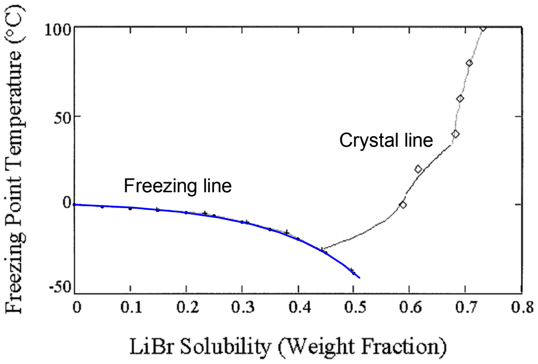

Figure A2.8 Freezing line (Duvall et al, 2001)

The freezing line in Fig. A2.7 can be approximated by

$$T=273.15-969.28*m-2.0435E-05*m^2 \quad \text{(A2.8)}$$

where T in K and m in molality.

References

Boryta, D.A., 1970, Solubility of lithium bromide in water between –50°C and +100°C (45 to 70% lithium bromide). , J. Chem. Eng. Data, vol.15, pp.142-144

DiGuilio, R.M., Lee, R.J., Jeter, S.M., Teja, A.S., 1990, Properties of Lithium Bromide-Water solutions at High Temperatures and Concentrations – I. Thermal Conductivity, ASHRAE Transactions, Vol.96, pp.702-708

Duvall, K.N., Dirksen, J.A., Ring, T.A., 2001, Ostwald-Meyers Meta-stable Region in LiBr Crystallization, J. Colloid Interface Science, Vol. 239, pp. 391-398

Gierow, M., Jerqvist, A., Measurement of mass diffusivity with holographic interferometry for H2O/NaOH and H2O/LiBr working pairs, Proceddings of the International Heat Pump conference, AES. Vol. 31, pp. 525-532

Schmidt E., 1979, Properties of Water and steam in SI-Units. Berlin: Springer-Verlag

Yao, W., Bjustrom, H., Setterwall, F., 1991, Surface tension of lithium bromide solutions with heat transfer additives, J. Chem. Eng. Data, Vol.36, pp.96-98

Appendix B System Design

B1. Empirical correlations

Single-phase convective heat transfer

$$Nu = 0.036 Re^{0.8} Pr^{0.33} \left(\frac{\mu}{\mu_w} \right)^{0.14} \left(\frac{D}{l} \right)^{0.054} \tag{B1.1}$$

for a developing flow where $10 < l/D_h < 400$ by Nusselt (1931).

$$Nu = 1.86 \left(RePr \right)^{1/3} \left(\frac{D}{l} \right)^{1/3} \left(\frac{\mu}{\mu_w} \right)^{0.14} \tag{B1.2}$$

for a developing laminar flow where $RePrD_h/l > 10$ by Sieder & Tate (1936).

Condensation on horizontal tubes

$$h = 0.725 \left[\frac{\rho(\rho - \rho_v) g h^{fg} k_l^3}{\mu_l (nD)(T - T_w)} \right]^{1/4} \tag{B1.3}$$

for laminar film condensation by Nusselt (1916).

Falling film flow on horizontal tubes

$$h = Nu \times k \left(\frac{\rho^2 g}{\mu^2} \right)^{1/3} \tag{B1.4}$$

where,

$$Nu = 0.948 \frac{RePr}{2Ga^{1/3}} \left[1. - \exp\left(-2 \frac{Ga^{1/3} Nu_m}{RePr} \right) \right] \left(\frac{s}{D} \right)^m$$

$Nu_m = 0.938 Re^{1/9} Pr^{1/3} Ga^{-1/9}$ for t<0.089

$$\begin{aligned} Nu_m = {} & 1.043 \frac{Re^{1/9} Pr^{1/3}}{Ga^{1/9}} \frac{0.463 t^{1/3} + 0.00139 t^{-2/3}}{1 - 0.7625 \exp(\xi)} \\ & + \frac{1.727}{Re^{1/3}} \left(0.824 - \frac{0.0732}{t} \right) \left[1 - \frac{0.2375}{1 - 0.7625 \exp(\xi)} \right] \left(1 - \frac{0.2711}{\xi} \right) \end{aligned} \quad \text{for t>0.089}$$

where $t = 2.5871\frac{2}{\pi(2/3)^{4/3}}\frac{Ga^{1/3}}{Re^{4/3}Pr}$, $\xi = 0.2623 - 2.95t$, $m = 0.16\frac{ReKa^{0.025} - 5.25}{ReKa^{0.025} + 1}$,

$Ga = \left(\frac{\pi D}{2}\right)^3 \frac{\rho^2 g}{\mu^2}$, $Re = \frac{\Gamma}{\mu}$ and $Ka = \frac{\rho\sigma^3}{g\mu^4}$ by Rogers (1981).

Falling film flow on vertical tube

$$h = Nu \times k\left(\frac{\rho^2 g}{\mu^2}\right)^{1/3} \tag{B1.5}$$

$Nu = 1.76Re^{-1/3}$ for $Re<Re_{tr}$

$Nu = 0.0323Re^{1/5}Pr^{0.344}$ for $Re_{tr} < Re<1600$

$Nu = 0.00102Re^{2/3}Pr^{0.344}$ for $1600<Re<3200$

$Nu = 0.00871Re^{2/5}Pr^{0.344}$ for $Re>3200$

, where $Re = \frac{4\Gamma}{\mu}$ and $Re_{tr}=2460/Pr^{0.646}$ by Wilke (1962).

Shell-side flows of a shell and tube heat exchanger

See Bell-Delaware method in Sinnott (1999).

References

Nusselt, W., 1916, Die Oberflachenkondensation des Wasserdampfes, VDI Z., Vol. 60, p.541

Nusselt, W., 1931, Der Warmeaustausch zwischen Wand und Wasser im Rohr, forsch. Geb. Ingenieurwes., Vol.2, p.309

Sieder, E.N., Tate, C.E., 1936 Heat transfer and pressure drop of liquids in tubes, Ind. Eng. Chem., Vol.28, p.1429

Sinnott, R.K., 1999, Coulson and Richardson's Chemical Engineering, Vol. 6 chemical engineering design, 4th ed., Elsevier Butterworth-Heinemann

Rogers, J.T., 1981, Laminar falling film flow and heat transfer characteristics on horizontal tubes, Can. J. Chem. Eng., vol.59, pp213-222

Wilke, W., 1962, Warmeubergang an rieselfilm, VDI-Forschungsheft 490, Issue B, Vol. 28

B2. Drawings and photographs

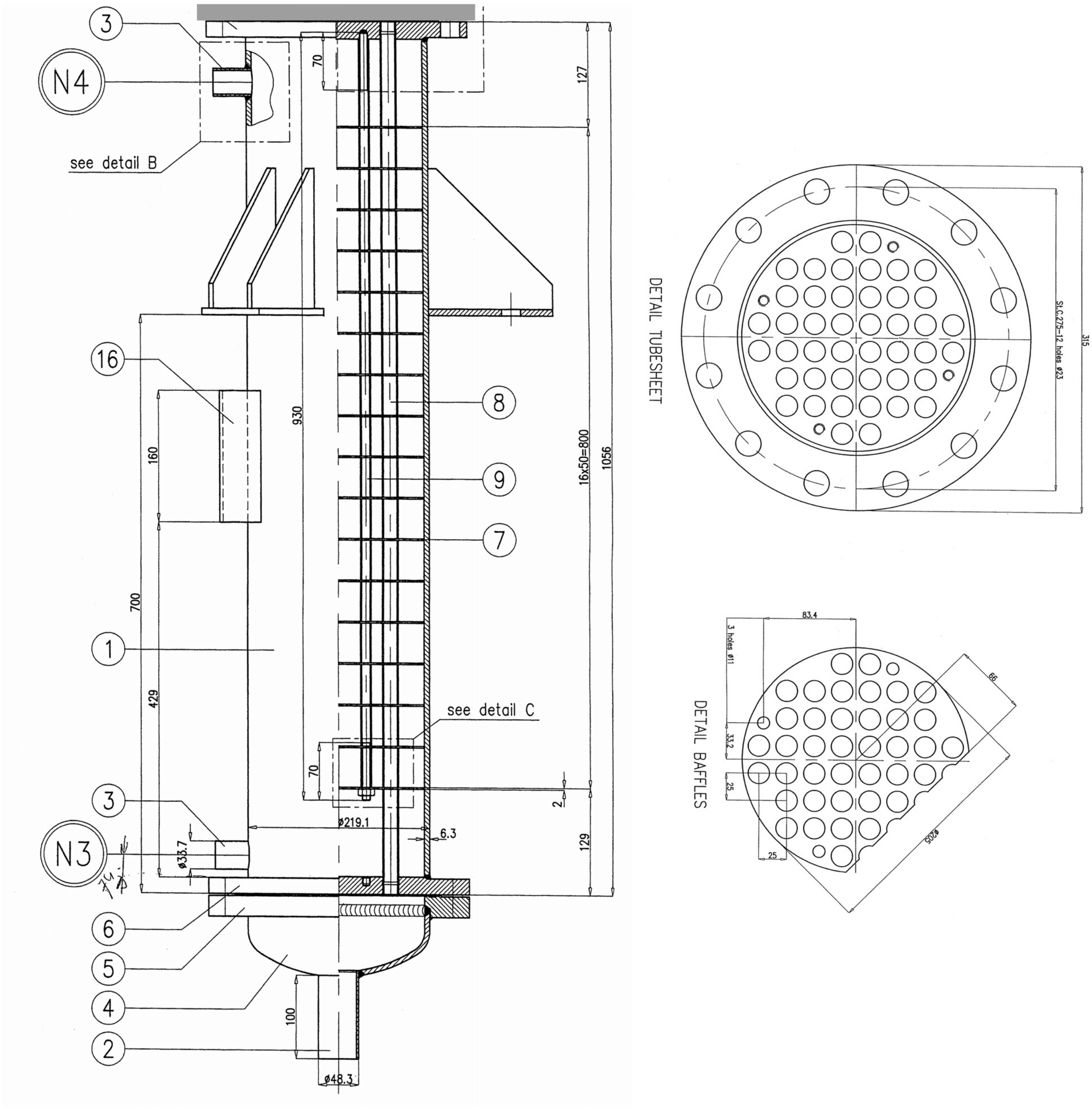

Figure B2.1. Shell & Tube generator

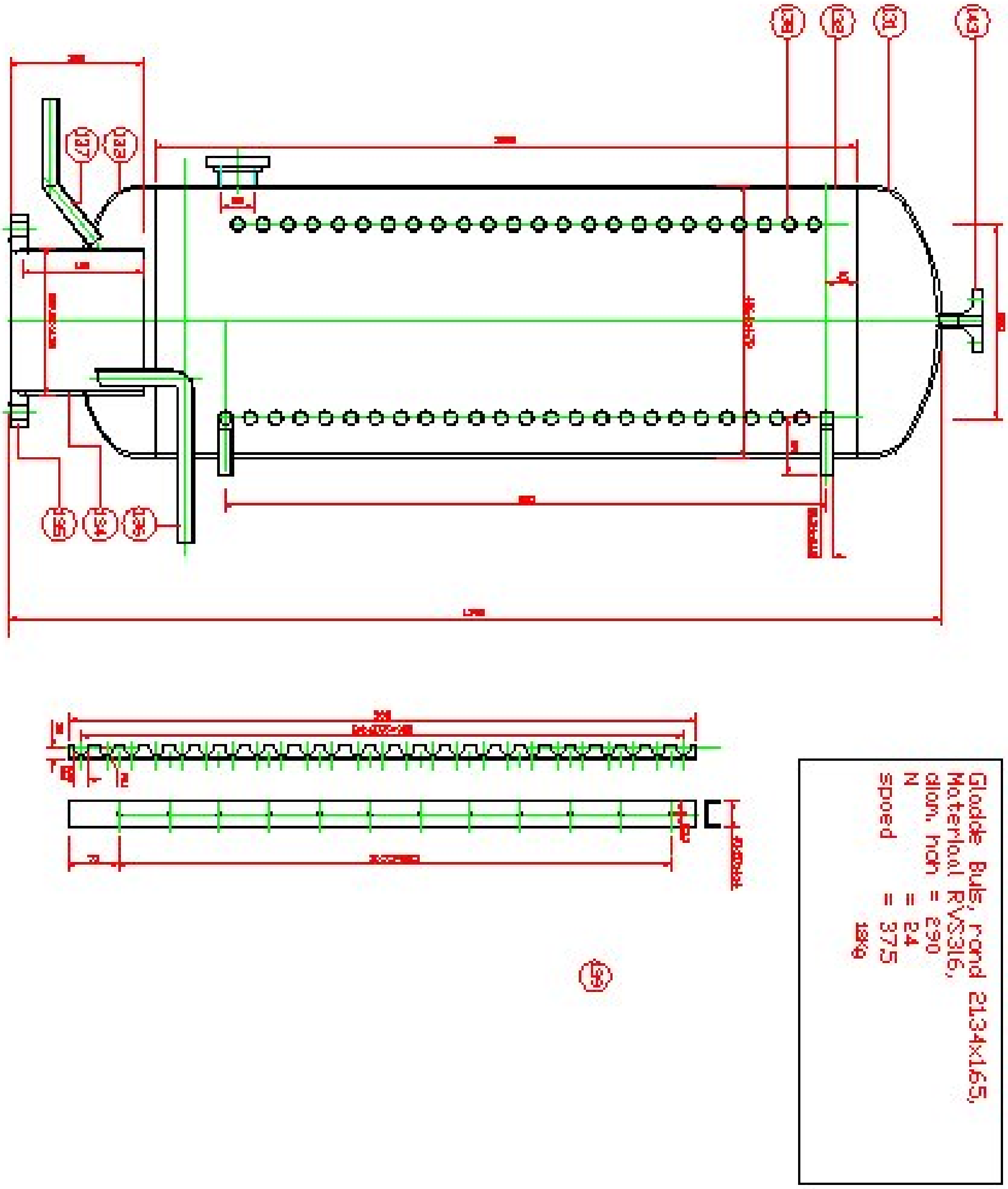

Figure B2.2. Shell & coil condenser

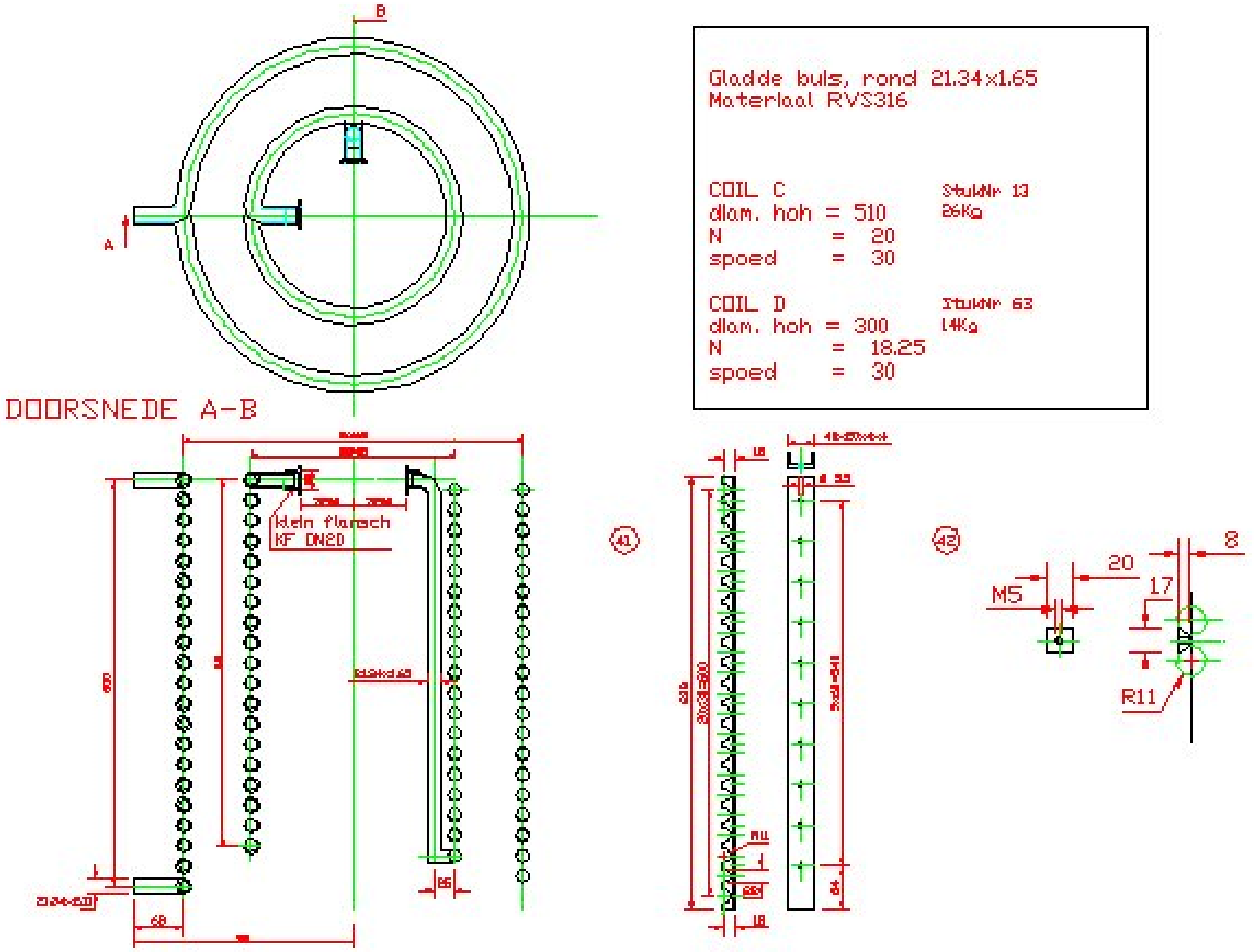

Figure B2.3. Coils for MPA and LPE

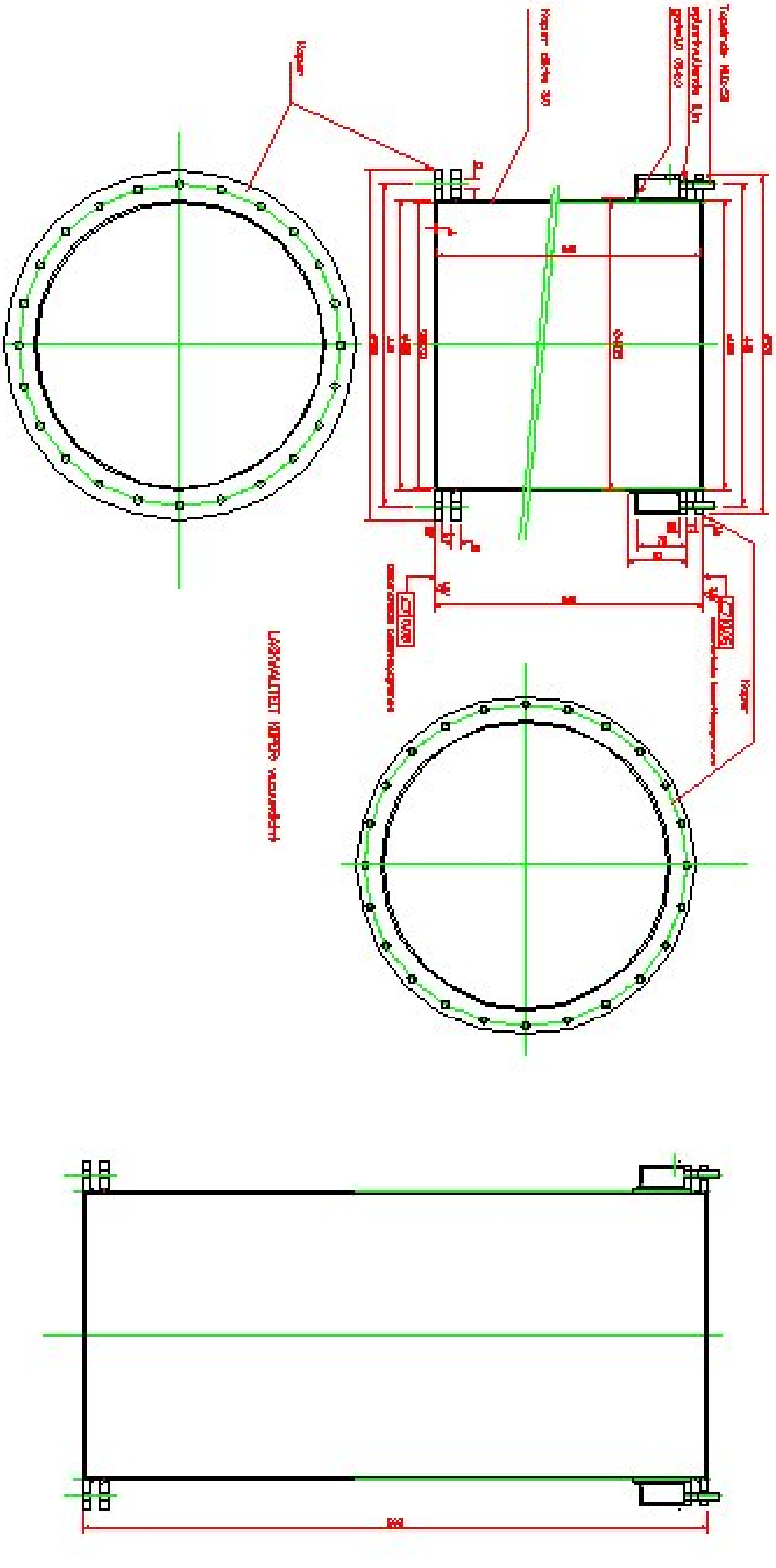

Figure B2.4. LPA/MPE

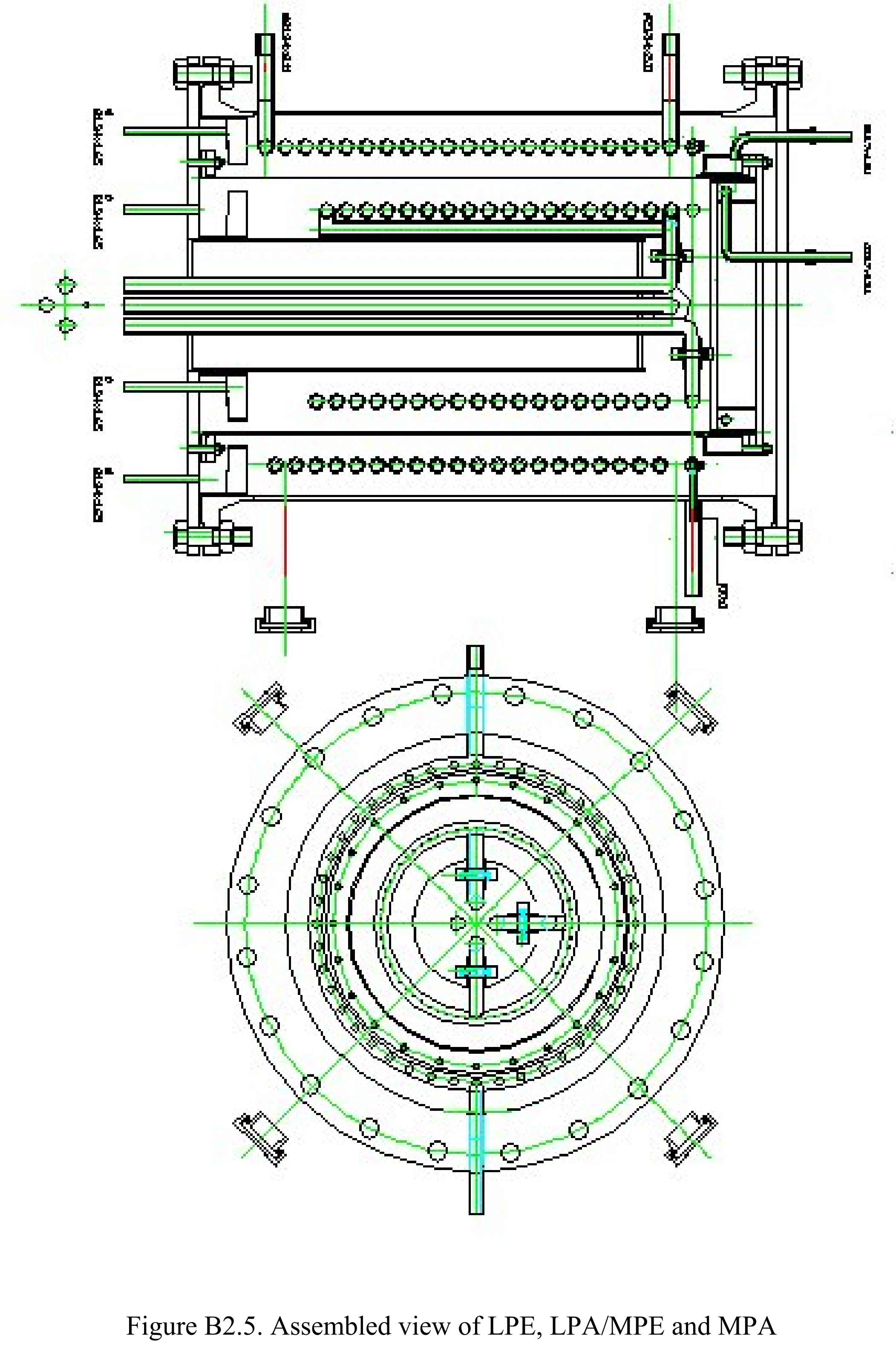

Figure B2.5. Assembled view of LPE, LPA/MPE and MPA

(a) Condenser-generator column(top-right) & absorber-evaporator shell(bottom-middle)

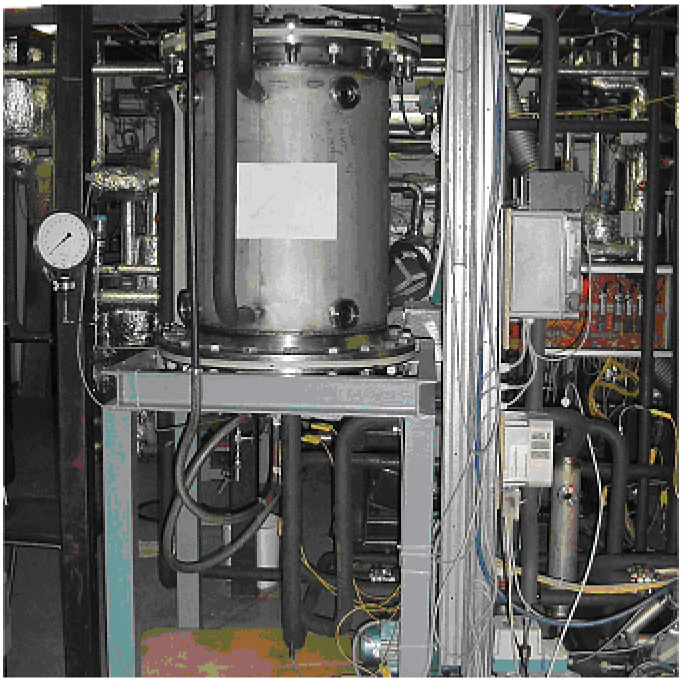

(b) absorber-evaporator shell and the tubing

Figure B2.6 Photographs of the chiller setup

Appendix C Approximation of the thermodynamic processes in LiBr-Water solution

C1. Phase equilibrium

Although the equilibrium conditions for LiBr-Water system has been completely described by osmotic coefficient ϕ in Ch. 4, the equation is not convenient to use in modeling transfer processes. For this reason, an approximate equilibrium equation has been derived from the original osmotic coefficient equation as follows.

Assuming that steam is ideal gas for low pressures and neglecting the specific volume of water in Eq. (4.4) in Ch. 4, the osmotic coefficient ϕ can be approximated by

$$\phi = \frac{1}{\upsilon m M_{H2O}} \ln\left(\frac{p^*}{p}\right) \qquad \text{(C1.1)}$$

Since the saturated steam pressure p^* and the equilibrium pressure p can be approximated by $\ln p^* = c_1 + c_2/T$ and $\ln p = c_1 + c_2/T^{dew}$ within a narrow pressure range, Eq. (C1.1) can be rewritten as

$$\frac{1}{T^{dew}} = \frac{1}{T} - \phi c_2^{-1} \upsilon m M_{H2O} \qquad \text{(C1.2)}$$

Since ϕ in Eq. (4.22) in Ch. 4 can be approximated by the following linear equation of 1/T within a narrow temperature range

$$\phi = \left(\frac{\partial \phi}{\partial 1/T}\right)_{T_\circ} \left(\frac{1}{T} - \frac{1}{T_\circ}\right) + \phi_\circ \qquad \text{(C1.3)}$$

, Eq. (C1.2) can be written as

$$\frac{1}{T^{dew}} = \frac{a}{T} + b \qquad \text{(C1.4)}$$

where '*a*' and '*b*' are functions of concentration only. For the purpose of illustration, the constants *a* and *b* determined from the correlation of Kim and Infante Ferreira (2006) are shown in Fig. C1.1 against LiBr mass fraction x_w.

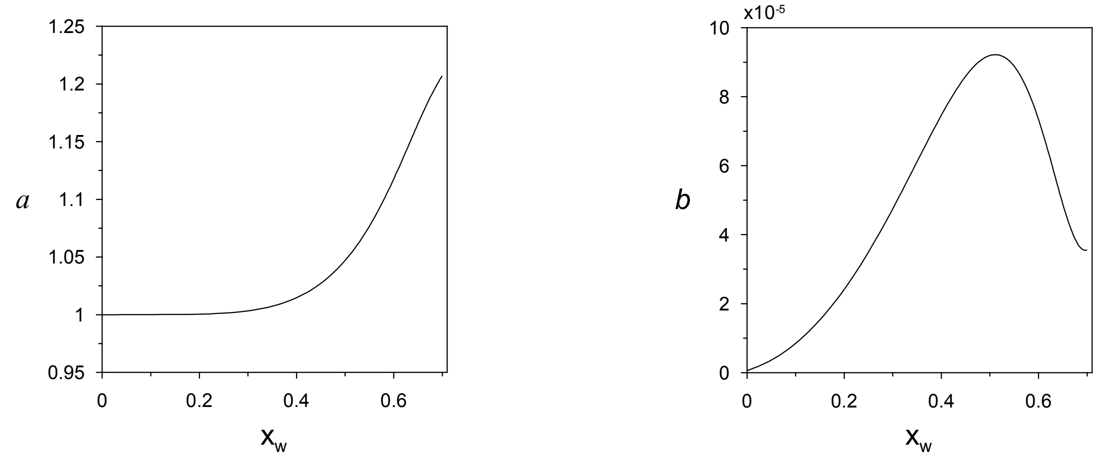

Figure C1.1 *a* and *b* of Eq. (C1.4)

As it is clear in Fig. C1.1, both *a* and *b* are non-linear functions of concentration. These functions can also be approximated by a linear equation for a narrow concentration range as follows.

Rearranging Eq. (C1.4) for T gives

$$T = \left(\frac{a}{1 - bT^{dew}} \right) T^{dew} \tag{C1.5}$$

Expanding Eq. (C1.5) in Taylor series against concentration and taking only the first two terms gives

$$T = \left(\frac{\partial T}{\partial x} \right)_{x_\circ} x + T_{x00} \tag{C1.6}$$

where $\left(\frac{\partial T}{\partial x} \right)_{x_\circ} = \frac{\left[\left(\frac{da}{dx} \right)_{x_\circ} \left(1 - bT^{dew} \right) + a_{x_\circ} \left(\frac{db}{dx} \right)_{x_\circ} \right] T^{dew}}{\left(1 - b_{x_\circ} T^{dew} \right)^2}$ and $T_{x00} \equiv T_{x_\circ} - x_\circ \left(\frac{\partial T}{\partial x} \right)_{x_\circ}$

for a reference concentration x_o.

It is sometimes convenient to have T^{dew} explicitly in Eq. (C1.6) for solving some non-linear equations in Ch. 5. In this case, another form of Eq. (C1.6) is used as follows.

$$T = \left[A_1 \left(x - x_\circ \right) + A_2 \right] T^{dew} \tag{C1.7}$$

where $A_1 \equiv \frac{1}{T^{dew}} \left(\frac{\partial T}{\partial x} \right)_{x_\circ}$ and $A_2 \equiv \left(\frac{a_{x_\circ}}{1 - b_{x_\circ} T^{dew}} \right)$ for a reference concentration x_o.

Eq. (C1.5) can also be linearized for T^{dew}. Expanding Eq. (C1.5) in Taylor series against T^{dew} and taking only the first two terms gives

$$T = \left(\frac{\partial T}{\partial T^{dew}}\right)_{T_\circ^{dew}} T^{dew} + T_{p00} \qquad \text{(C1.8)}$$

where $\left(\frac{\partial T}{\partial T^{dew}}\right)_{T_\circ^{dew}} = \frac{a}{\left(1 - bT_\circ^{dew}\right)^2}$ and $T_{p00} \equiv T_{T_\circ^{dew}} - T_\circ^{dew}\left(\frac{\partial T}{\partial T^{dew}}\right)_{T_\circ^{dew}}$ or a reference dew temperature T^{dew}_o.

Eq. (C1.5)-(C1.8) are useful in the modeling of desorption and absorption processes. Applications of the equations can be found in Ch. 2. and Ch. 5.

C2. Process heats in desorption and absorption processes

The enthalpy of a LiBr solution is a complicated function of the temperature, concentration and pressure and so is process heat involved in absorption and desorption processes. For the purposes of modeling the absorption and desorption processes, it would be convenient if the process heat could be expressed explicitly in terms of primary variables. In the following, such a simplified expression is developed based on the contents of Ch. 4.

Desorption is a general term for the regeneration of gaseous species out of a liquid or solid mixture regardless of how it is done. But in the field of absorption cooling, it means generally boiling of a solution. Boiling of a solution is different from that of a pure substance by the fact that the compositions of species vary during the process. Fig. C2.1 shows the desorption process in the p-T-x domain. Several state points are numbered for reference.

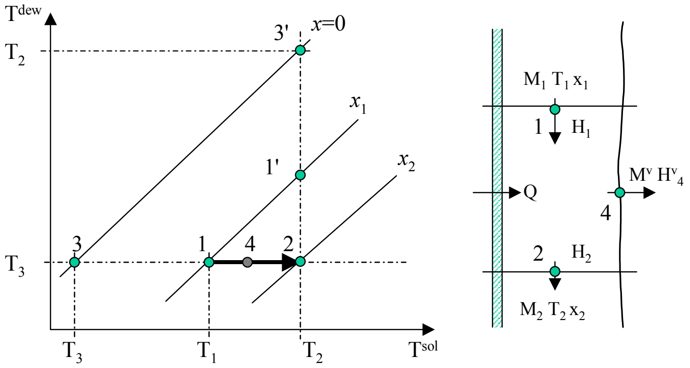

Figure C2.1. Desorption process in p-T-x domain

In Fig. C2.1, a solution is supplied at point 1 and leaves at point 2 while vapour is generated at point 4. This process takes place at the pressure of dew temperature T_3. It is assumed that the solution is saturated.

To begin with, recall from Ch.4 that the molar enthalpy H of a saturated electrolyte solution at molar concentration x and temperature T can be expressed in relation to the molar enthalpy of the reference solution H_o at x_o and T as follows [H^{∞}_1 is removed to combine H(T, x) and H_o(T, x_o) from Eq. (4.26) and H^E is expressed in terms of molality using Eq. (4.6) and (4.12)].

$$H = \left(\frac{x}{x_\circ}\right)H_\circ + \left(1-\frac{x}{x_\circ}\right)H_{H_2O} - x\upsilon RT^2\left[\int_{m_\circ}^{m}\frac{1}{m}\left(\frac{\partial\phi}{\partial T}\right)dm\right]_T \tag{C2.1}$$

Note that Eq. (C2.1) is equivalent to the equation of Haltenberger (1939), which has been derived considering the isothermal evaporation of water from dilute solution.

In order to use Eq. (C2.1) directly, the desorption heat $\dot{Q}$ is expressed on molar basis as

$$\dot{Q} = \dot{M}_2 H_2 + \dot{M}^v H_4^v - \dot{M}_1 H_1 \tag{C2.2}$$

The goal is to transform Eq. (C2.2) into a simple explicit equation of independent variables.

Dividing Eq. (C2.2) with the rate of vapour generation $\dot{M}^v$ to get the desorption heat per unit vapour generation gives

$$\dot{q} = (\lambda - 1)\left(H_2 - H_1\right) + \left(H_4^v - H_1\right) \tag{C2.3}$$

where '$\dot{q}$' and 'λ' are the desorption heat and the inlet solution flow rate per unit vapour generation. The flow rate λ has the following relation with the bulk concentrations from the total- and LiBr mass balances between point 1 and 2.

$$\lambda \equiv \frac{\dot{M}_1}{\dot{M}^v} = \frac{x_2}{x_2 - x_1} \tag{C2.4}$$

For the isotherm T_2 in Fig. C2.1, letting $x=x_2$ and $x_\circ= x_1$ in Eq. (C2.1) gives

$$H_2 = \left(\frac{x_2}{x_1}\right)H_{1'} - \left(\frac{x_2 - x_1}{x_1}\right)H_{3'} - x_2\upsilon RT_2^2\left[\int_{m_1}^{m_2}\frac{1}{m}\left(\frac{\partial\phi}{\partial T}\right)dm\right]_{T=T_2} \tag{C2.5}$$

Inserting Eq. (C2.4) and Eq. (C2.5) into Eq. (C2.3) and rearranging it gives

$$\dot{q} = \left(\frac{x_2}{x_2 - x_1}\right)\left(H_{1'} - H_1\right) + \left(H_4^v - H_{3'}\right) - \left(\frac{x_1 x_2}{x_2 - x_1}\right)\upsilon RT_2^2\left[\int_{m_1}^{m_2}\frac{1}{m}\left(\frac{\partial\phi}{\partial T}\right)dm\right]_{T=T_2} \tag{C2.6}$$

The enthalpy difference $H_{1'}$-H_1 of the 1st term on the right-hand side of Eq. (C2.6) can be approximated as

$$H_{1'} - H_1 = C_{p1}^l\left(T_2 - T_1\right) \tag{C2.7}$$

From Eq. (C2.4) and (C2.7), Eq. (C2.6) becomes

$$\dot{q} = \lambda C_{p1}^l\left(T_2 - T_1\right) + \left(H_4^v - H_{3'}\right) - \left(\frac{x_1 x_2}{x_2 - x_1}\right)\upsilon RT_2^2\left[\int_{m_1}^{m_2}\frac{1}{m}\left(\frac{\partial\phi}{\partial T}\right)dm\right]_{T=T_2} \tag{C2.8}$$

Now, the last term on the right-hand side of Eq. (C2.8) should be simplified. Replacing ϕ with Eq. (C1.1) and recalling $m=x/(1-x)/M_{H2O}$, the last term can be rewritten as

$$\left(\frac{x_1x_2}{x_2-x_1}\right)\upsilon RT_2^2\left[\int_{m_1}^{m_2}\frac{1}{m}\left(\frac{\partial\phi}{\partial T}\right)dm\right]_{T=T_2}=\left(\frac{1}{m_1}-\frac{1}{m_2}\right)^{-1}R\left[\int_{m_1}^{m_2}\frac{\partial}{\partial 1/T}\left(\ln\frac{p^*}{p}\right)d\left(\frac{1}{m}\right)\right]_{T=T_2} \quad \text{(C2.9)}$$

And the gradient inside the integral on the right-hand side of Eq. (C2.9) can be rewritten as

$$\begin{aligned}\frac{\partial}{\partial 1/T}\left[\ln\left(\frac{p^*}{p}\right)\right]_{T=T_2}&=\left(\frac{\partial\ln p^*}{\partial 1/T}\right)_{T=T_2}-\left[\left(\frac{\partial\ln p}{\partial 1/T^{dew}}\right)\left(\frac{\partial 1/T^{dew}}{\partial 1/T}\right)\right]_{T=T_2}\\&=-(H_{3'}^{fg}-H^{fg}a)/R\end{aligned} \quad \text{(C2.10)}$$

where and $a=\partial(1/T^{dew})/\partial(1/T)$ from Eq. (C1.4) and $H^{fg}_{3'}\equiv H^{*fg}[p^*(T_2)]$, $H^{fg}\equiv H^{*fg}[p^*(T_2, x)]$ from the following Clausius-Clapeyron equation

$$H^{fg}=\Delta VT\frac{dp^*}{dT}\approx\frac{RT^2}{p}\frac{dp^*}{dT}=-R\frac{d\ln p^*}{d1/T} \quad \text{(C2.11)}$$

Using Eq. (C2.10), Eq. (C2.9) can be written as

$$\begin{aligned}\left(\frac{x_1x_2}{x_2-x_1}\right)\upsilon RT_2^2\left[\int_{m_1}^{m_2}\frac{1}{m}\left(\frac{\partial\phi}{\partial T}\right)dm\right]_{T=T_2}&=\left(\frac{1}{m_2}-\frac{1}{m_1}\right)^{-1}\left[\int_{m_1}^{m_2}(H_{3'}^{fg}-H^{fg}a)d\left(\frac{1}{m}\right)\right]_{T=T_2}\\&=H_{3'}^{fg}-\left(H^{fg}a\right)_{avg}\end{aligned} \quad \text{(C2.12)}$$

where $(H^{fg}a)_{avg}$ is is defined by

$$\left(H^{fg}a\right)_{avg}=\left(\frac{1}{m_2}-\frac{1}{m_1}\right)^{-1}\int_{m_1}^{m_2}H^{fg}a\,d\left(\frac{1}{m}\right) \quad \text{(C2.13)}$$

Inserting Eq. (C2.12) into Eq. (C2.8) gives

$$\begin{aligned}\dot{q}&=\lambda C_{p1}^{l}\left(T_2-T_1\right)+\left(H_4^{v}-H_{3'}\right)-H_{3'}^{fg}+\left(H^{fg}a\right)_{avg}\\&=\lambda C_{p1}^{l}\left(T_2-T_1\right)+C_p^{v}\left(T_4-T_2\right)+(H^{fg}a)_{avg}\end{aligned} \quad \text{(C2.14)}$$

In the limiting case of λ→∞, i.e. $x_2 \to x_1$, $\dot{q}$ in Eq. (A7) approaches a_2H^{fg}, which is the heat quantity known as "latent heat of solution" or "heat of desorption" defined as the amount of heat per unit mass of vapour desorbed from an infinitely large mass of solution. Therefore the last term $(H^{fg}a)_{avg}$ is the average heat of desorption for the concentration range between x_1 and x_2. Although it should be calculated by Eq. (C2.13), it can be approximated by $H^{fg}_3a_1$, where H^{fg}_3 is the latent heat of saturated steam at the system pressure $p^*(T_3)$ and a_1 is the gradient $\partial(1/T^{dew})/\partial(1/T)$ at $x=x_1$.

Eq. (2.14) finally becomes

$$\dot{q} = \lambda C_{p1}^{l}(T_2 - T_1) + C_p^{v}(T_4 - T_1) + a_{x=x_1} H_3^{fg} \qquad \text{(C2.15)}$$

Eq. (C2.15) has been compared with the values of Eq. (C2.3) based on the enthalpy correlation developed in Ch. 4. The results are illustrated in Fig. A2.2 for the typical working ranges of generator.

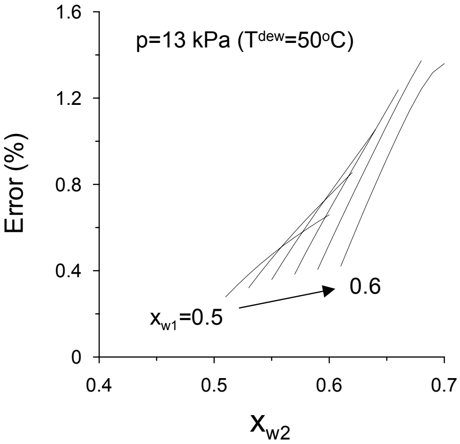

Figure C2.2 Error of Eq. (C2.15)

Error of Eq. (C2.15) increases with the concentration change during the process, i.e. $\Delta x = x_{w2} - x_{w1}$. The maximum error is less than 1.6 % for $\Delta x = 0.1$.

Multiplying Eq. (C2.15) by $\dot{M}^{v}$ and expressing it on mass basis gives the desorption heat $\dot{Q}$ finally as

$$\dot{Q} = \dot{m}_1 C_{p1}^{l}(T_2 - T_1) + \dot{m}^{v}\left[a_{x=x_1} h_3^{fg} + C_p^{v}(T_4 - T_1)\right] \qquad \text{(C2.16)}$$

Likewise, it is possible to express absorption heat in a similar way.

From the thermodynamic point of view, absorption is only the reverse process of desorption except for the vapour condition in the process. Therefore the results of the section 5.2.2 can be used for absorption process with a few minor modifications to take account of the different vapour condition.

Reversing the desorption process, the point 2 in Fig. C2.1 now becomes the inlet and the point 1 becomes outlet of the absorption process. Fig. C2.3 shows the absorption process in a p-T-x domain.

A solution is supplied at point 2 and leaves at point 1 after absorbing the vapour coming from point 3.

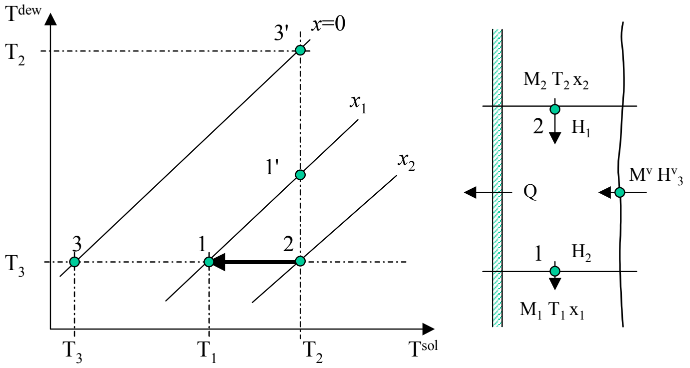

Figure C2.3 Absorption process in p-T-x domain

For the absorption process in Fig. C2.3, the absorption heat can be expressed also by Eq. (C2.2) with H^v_4 replaced by H^v_3. Then, analogous to Eq. (C2.16), the absorption heat $\dot{Q}$ for the process in Fig. C2.3 can be written as

$$\dot{Q} = \dot{m}_1 C^l_{p1}(T_2 - T_1) + \dot{m}^v \left[a_{x=x_1} h_3^{fg} + C_p^v (T_3 - T_1) \right] \qquad \text{(C2.17)}$$

Error of the Eq. (C2.17) is shown in Fig. C2.4 for typical working ranges of absorber, which is comparable to that of generator in Fig. C2.2.

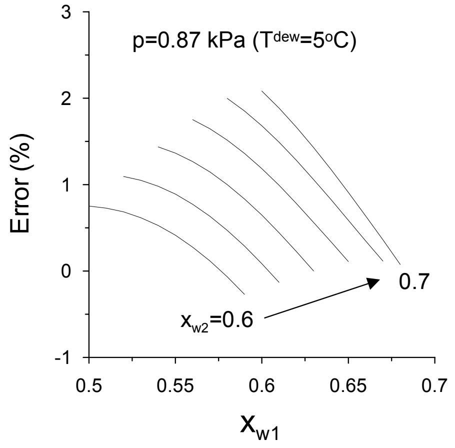

Figure C2.4 Error of Eq. (C2.17)

Applications of Eq. (C2.16) and (C2.17) can be found in Ch. 2 and 5.

References

Haltenburger W., 1939, Enthalpy-concentration charts from vapour pressure data. Industrial Engineering Chemistry, Vol. 31, pp. 783-6.

Kim, D.S., Infante Ferreira, C.A., 2006, A Gibbs Energy Equation for LiBr aqueous solutions, Int. J. Refrigeration, Vol. 29, pp. 36-46

Appendix D Heat and mass transfer in falling film flows

D1. Mass transfer at vapor-liquid interface in film theory

The following analysis is based on the original work of Lewis and Whitman (1924) [see e.g. the film theory in Bird et al (1965) or Baehr and Stephan (1998)].

Some of the following equations were used in several places of the main text including the modeling of generator, absorber, cooling tower and so on.

In the following, mass transfer equations have been derived for a binary system of substance A and B, of which A is less volatile than B. Therefore, in an NH_3-H_2O for example, the substance A corresponds to H_2O and B to NH_3.

The film theory postulates that mass is transferred across a very thin film only in the perpendicular direction to the phase boundary.

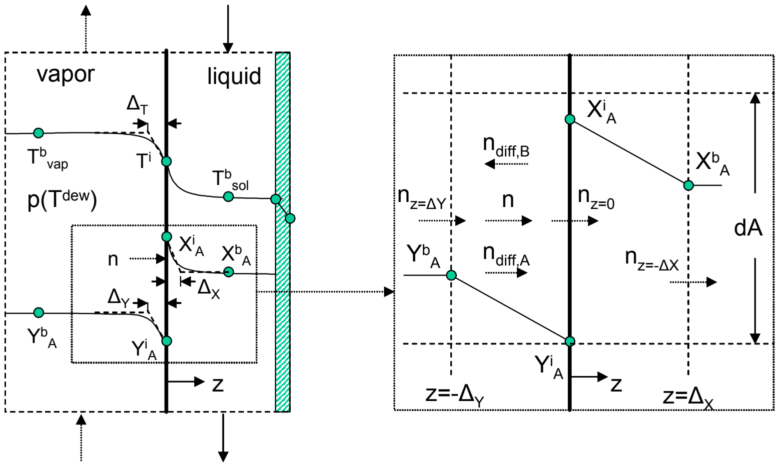

Figure D1.1 Temperature and concentration profiles in vapour and liquid flows

Considering the vapour control volume near the vapor-liquid interface in Fig. D1.1, mass transfer in vapour phase can be described as follows.

Assume that there is a net molar mass flux from vapour to the interface namely, $\dot{n}^v$. The film theory dictates that mass transfer rate $\dot{n}$ is equal everywhere across the thin film Δ_Y in Fig. D1.1. That is, for $-\Delta_Y \le z \le 0$,

$$\frac{d\dot{n}}{dz} = 0 \tag{D1.1}$$

which means $\dot{n} = \dot{n}_{z=0} = \dot{n}_{z=\Delta_Y} = \dot{n}^v$.

Then the following absorbent mass balance equation holds for $-\Delta_Y \le z \le 0$.

$$\dot{n}^v X_A^\circ = \dot{n}^v Y_A - D_{v,A} \frac{d\left(\rho_v Y_A\right)}{dz} \tag{D1.2}$$

where X°_A is the mole fraction of substance A in the mass that is transferred through vapor-liquid interface.

Treatment of density ρ_v in Eq. (D1.2) depends on Lewis number. Since the ratio of thermal boundary layer thickness to that of concentration is proportional to Lewis number, i.e. $\Delta_T/\Delta_Y \sim Le$, the temperature within the concentration film can be assumed constant at its bulk vapour temperature if Lewis number is very small, i.e. $\Delta_T \ll \Delta_Y$. This is the case in NH_3-H_2O systems, where Lewis number of vapour is in the order of 10^{-2}. Then, ρ_v can be considered constant and the following equations hold. However, when Le is close to unity, the influence of temperature on vapour density should also be taken into account as is done, for example, in air-water systems.

If the vapour temperature can be assumed constant across the thin vapour film, because density of the vapour is also considered constant, Eq. (D1.2) can be rewritten for $\dot{n}^v$ as

$$\dot{n}^v = \rho_v D_{v,A} \frac{d}{dz} \ln\left(X^\circ_A - Y_A\right) \tag{D1.3}$$

Integrating Eq. (D1.3) for $-\Delta_Y \le z \le 0$ with boundary conditions of $Y_A = Y^b_A$ at $z = -\Delta_Y$ and $Y_A = Y^i_A$ at $z=0$ gives

$$\dot{n}^v = \rho_v \left(\frac{D_{v,A}}{\Delta_Y}\right) \ln\left(\frac{X^\circ_A - Y^i_A}{X^\circ_A - Y^b_A}\right) = \rho_v K_v \ln\left(\frac{X^\circ_A - Y^i_A}{X^\circ_A - Y^b_A}\right) \tag{D1.4}$$

where mass transfer coefficient $K_v \equiv D_{v,A}/\Delta_Y$ has been introduced.

In a similar manner, $\dot{n}^v$ can be derived for the liquid as

$$\dot{n}^v = \rho_l K_l \ln\left(\frac{X^i_A - X^\circ_A}{X^b_A - X^\circ_A}\right) \tag{D1.5}$$

where mass transfer coefficient $K_l \equiv D_{l,A}/\Delta_X$ has been introduced.

Equating Eq. (D1.4) and (D1.5) gives an equation for X°_A as follows.

$$\left(\frac{X^i_A - X^\circ_A}{X^b_A - X^\circ_A}\right) = \left(\frac{X^\circ_A - Y^i_A}{X^\circ_A - Y^b_A}\right)^\beta \tag{D1.6}$$

where the exponent β on the right side is defined by $\beta \equiv (\rho K)_v/(\rho K)_l$.

Eq. (D1.6) dictates that the value of X°_A should be in the range of $Y^b_A \le X^\circ_A \le X^b_A$ and it approaches Y^b_A for $\beta \to \infty$ and X^b_A for $\beta \to 0$. This suggests an interesting point in the design of a rectifier. Because the purpose of a rectifier is to remove less volatile component, which is substance A in this case, Eq. (D1.6) suggests it be designed for a smaller β, thus for a larger X°_A. That means mass transfer should be promoted on liquid side, not on vapour side. This may be realized physically by, for example, using micro- or macro-scale turbulence promoters on the surface of heat exchanger.

References

Baehr, H.T., Stephan, K., 1998, Wärme- und Stoffübertragung, 3rd ed., Springer-Verlag, Berlin

Bird, R.B., Stewart, W.E., Lightfoot, W.E., 1965, Transport phenomena, Wiley, New York

Lewis, W.K., Whitman, W.G., 1924, Principles of gas absorption, Ind. Eng. Chem., Vol. 116, pp. 1215-1220

D2. Calibration data for falling film test setup

In the following, calibration results are presented for the measurement devices used in the falling film test setup in Ch. 6.

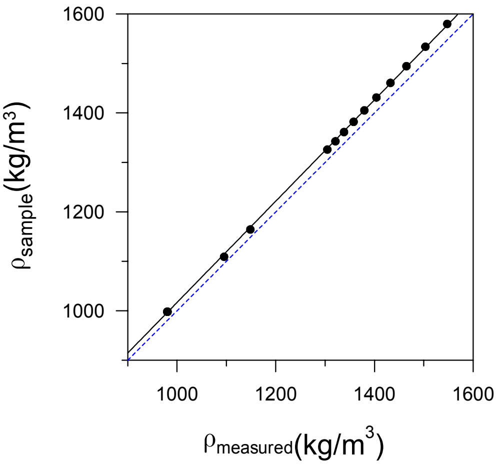

Figure D2.1 Calibration of a mass flow meter for density measurement

Fig. D2.1 shows the densities of 13 sample solutions with different LiBr concentrations from 0 to 53 wt% against the density signals of a mass flow meter (Micro Motion DL65, density accuracy ±1kg/m^3 in catalog). Error was found quite large (mean deviation ca. 24 kg/m^3, equivalent to error of ca. 1.5 wt% in LiBr concentration) as shown in the figure. For this reason, a calibration curve given in Eq. (D2.1) has been used.

$$\rho_{sample} = 1.024 \times \rho_{measured} - 6.752 \qquad \text{(D2.1)}$$

Eq. (D2.1) reproduces the densities of the samples within a standard deviation of 2.6 kg/m^3.

Fig. D2.2 shows the water flow rates weighed with a balance and a stopwatch against the signals of a mass flow meter (Micro Motion DL65, flow accuracy ±0.15% in catalog) and a magnetic volume flow meter (Krohne, flow accuracy <0.3% in catalog).

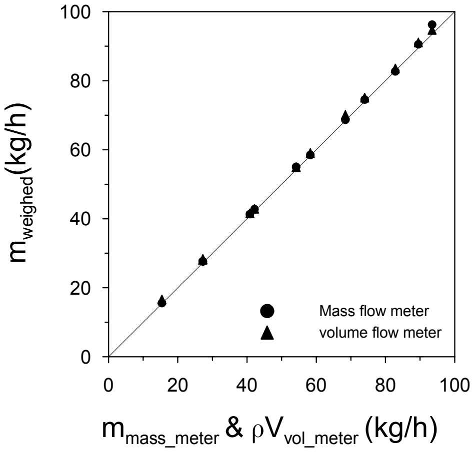

Figure D2.2 Calibration of flow rates for mass and volume flow meters

In Fig. D2.2, water density has been multiplied to the volume flow rate measurements.

The weighed flow rates agreed with the mass flow meter within a standard deviation of 0.32 kg/h and with the volume flow meter within a standard deviation of 0.28 kg/h. Since the discrepancies between weighed flow rates and the signals of flow meters were well within the uncertainty range of the weighing method, those flow rate signals were directly used in the analysis.

A rotameter used to measure cooling water flow rate had a good linear characteristic as shown in Fig. D2.3.

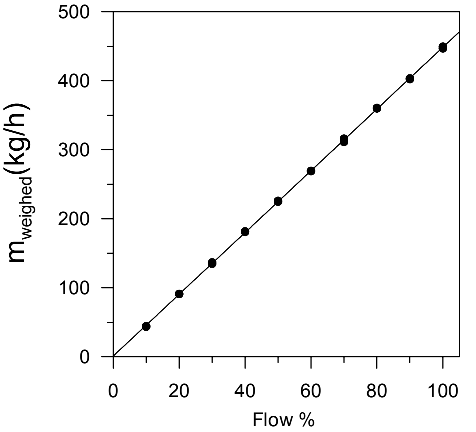

Figure D2.3 Calibration of a rotameter for cooling water (8~10 ^{o}C)

Measured water flow rates can be represented by

$$\dot{m}_{water} = 4.475\times \text{Flow\%}+1.042 \qquad \text{(D2.2)}$$

where Flow% is indicated by a floating weight in the rotameter. Eq. (D2.2) reproduces the measured flow rates within a standard deviation of 1.37 kg/h.

D3. Experimental data of the falling film tests

The original data measured during the falling film tests in Ch. 6 are summarized below. Names of the parameters and experiment number can be referred to Fig. 6.1 and Table 6.2 in Ch. 6, respectively.

Exp. #1

FM3	T1	T3	T2	T4	T5	T6	T7	FM1-mass flow	FM1-density	FM2	p	date/ser. no.
%	deg.C	deg.C	deg.C	deg.C	deg.C	deg.C	deg.C	kg/h	kg/m3	l/h	kPa	DDMM/#
69.2	22.97	33.45	24.86	29.89	27.32	8.58	9.73	20.54	1468.29	13.59	1.062	2802/07
69.2	22.96	33.64	25.10	30.46	27.50	8.56	9.71	18.05	1465.42	11.93	1.067	2802/08
68.9	22.87	34.05	25.95	30.68	27.32	8.56	9.71	15.09	1460.84	9.90	1.076	2802/09

Exp. #2

FM3	T1	T3	T2	T4	T5	T6	T7	FM1-mass flow	FM1-density	FM2	p	date/ser. no.
%	deg.C	deg.C	deg.C	deg.C	deg.C	deg.C	deg.C	kg/h	kg/m3	l/h	kPa	DDMM/#
69.2	21.72	32.75	22.45	29.56	26.74	9.19	10.33	19.61	1466.44	13.23	1.013	2802/01
69.1	21.87	32.91	22.78	29.59	26.46	9.11	10.22	18.23	1465.39	12.02	1.022	2802/02
69.2	22.41	33.36	24.36	29.75	26.25	9.10	10.19	14.90	1461.03	9.52	1.054	2802/03
69.1	22.38	33.51	26.02	29.88	26.22	8.81	9.87	12.75	1456.21	7.82	1.074	2802/04

Exp. #3

FM3	T1	T3	T2	T4	T5	T6	T7	FM1-mass flow	FM1-density	FM2	p	date/ser. no.
%	deg.C	deg.C	deg.C	deg.C	deg.C	deg.C	deg.C	kg/h	kg/m3	l/h	kPa	DDMM/#
0	28.25	39.87	29.03	34.80	13.47	19.05	19.06	24.90	1464.73	16.96	1.677	2102/01
0	30.54	41.06	31.69	36.59	12.48	19.18	19.27	20.63	1464.23	14.07	1.921	2102/02
0	28.51	41.44	30.25	35.41	12.10	18.90	19.14	15.86	1465.43	10.86	1.810	2102/03
0	30.08	45.35	33.26	35.33	12.04	18.21	18.48	11.26	1464.03	7.66	1.813	2102/04

Exp. #4

FM3	T1	T3	T2	T4	T5	T6	T7	FM1-mass flow	FM1-density	FM2	p	date/ser. no.
%	deg.C	deg.C	deg.C	deg.C	deg.C	deg.C	deg.C	kg/h	kg/m3	l/h	kPa	DDMM/#
0	40.92	46.63	40.94	43.82	12.56	20.34	20.28	24.72	1470.13	16.60	2.837	2302/01
0	41.33	46.60	41.20	43.71	11.58	20.34	20.26	20.38	1470.58	13.55	2.878	2302/02
0	41.73	46.58	41.80	43.52	11.03	20.35	20.28	16.97	1471.32	11.23	2.922	2302/03
0	42.39	46.61	42.01	43.26	11.16	20.44	20.37	12.45	1471.78	8.17	2.998	2302/04

Exp. #5

FM3	T1	T3	T2	T4	T5	T6	T7	FM1-mass flow	FM1-density	FM2	p	date/ser. no.
%	deg.C	deg.C	deg.C	deg.C	deg.C	deg.C	deg.C	kg/h	kg/m3	l/h	kPa	DDMM/#
69	18.78	33.61	20.34	30.01	27.28	8.03	9.62	23.97	1469.16	15.89	0.733	0403/09
69.8	18.77	33.57	20.62	30.08	27.28	7.99	9.56	24.76	1469.49	15.81	0.740	0403/10
69.2	18.94	34.07	20.85	30.37	26.90	8.03	9.58	21.05	1465.67	13.31	0.765	0403/11
69	19.03	34.43	23.59	30.60	26.46	8.02	9.57	17.47	1459.86	10.78	0.789	0403/12
69.5	18.43	34.67	31.40	30.81	25.57	8.05	9.56	13.25	1450.03	7.95	0.807	0403/13

Exp. #6

FM3	T1	T3	T2	T4	T5	T6	T7	FM1-mass flow	FM1-density	FM2	p	date/ser. no.
%	deg.C	deg.C	deg.C	deg.C	deg.C	deg.C	deg.C	kg/h	kg/m3	l/h	kPa	DDMM/#
69	19.19	31.82	20.21	28.88	26.87	8.47	9.80	24.89	1472.08	16.65	0.820	0203/09
69.1	19.72	32.67	20.78	29.51	26.86	8.53	9.86	21.07	1468.97	14.04	0.871	0203/10
68.6	19.90	34.20	21.24	28.66	25.54	7.91	9.27	17.23	1461.49	11.47	0.883	0203/07
68.8	19.65	33.72	24.85	30.26	26.05	8.30	9.61	12.49	1454.15	8.14	0.904	0203/08

Exp. #7

FM3	T1	T3	T2	T4	T5	T6	T7	FM1-mass flow	FM1-density	FM2	p	date/ser. no.
%	deg.C	deg.C	deg.C	deg.C	deg.C	deg.C	deg.C	kg/h	kg/m3	l/h	kPa	DDMM/#
0	40.76	46.67	39.69	43.89	13.03	19.80	19.64	30.00	1474.41	19.90	2.648	0303/01
0	41.03	46.58	40.06	43.77	11.28	20.02	19.84	25.52	1473.65	16.91	2.692	0303/02
0	41.40	46.51	40.44	43.65	10.78	20.18	20.02	21.21	1473.40	14.00	2.754	0303/03
0	41.81	46.41	40.94	43.38	10.42	20.32	20.13	16.80	1473.90	11.04	2.810	0303/04
0	42.38	46.39	42.01	43.05	10.35	20.43	20.14	12.02	1474.31	7.79	2.894	0303/05

Exp. #8

FM3	T1	T3	T2	T4	T5	T6	T7	FM1-mass flow	FM1-density	FM2	p	date/ser. no.
%	deg.C	deg.C	deg.C	deg.C	deg.C	deg.C	deg.C	kg/h	kg/m3	l/h	kPa	DDMM/#
0	33.28	40.22	33.19	37.00	12.35	17.92	17.95	31.56	1475.55	20.88	1.734	0103/01
0	33.94	40.11	33.83	37.10	11.30	17.88	17.95	26.12	1475.08	17.22	1.811	0103/02
0	34.60	40.15	34.24	37.09	10.89	18.02	18.06	21.87	1474.73	14.28	1.888	0103/03
0	35.32	40.01	34.91	37.03	9.70	17.98	18.02	16.46	1473.57	10.83	1.973	0103/04
0	35.76	39.82	36.15	36.83	9.82	18.18	18.22	12.35	1473.04	8.13	2.044	0103/05

Exp. #9

FM3	T1	T3	T2	T4	T5	T6	T7	FM1-mass flow	FM1-density	FM2	p	date/ser. no.
%	deg.C	deg.C	deg.C	deg.C	deg.C	deg.C	deg.C	kg/h	kg/m3	l/h	kPa	DDMM/#
69.6	15.64	38.19	16.33	37.87	36.76	9.18	11.50	32.07	970.02	33.40		0803/01
69.5	13.45	39.54	14.37	38.16	36.91	8.39	10.59	27.43	969.11	27.83		0803/02
69.6	11.53	40.10	12.55	38.07	36.30	8.07	10.03	21.74	965.87	23.00		0803/03
69	10.03	40.02	11.25	39.41	36.33	7.91	9.62	17.29	964.54	18.14		0803/04
69	8.77	40.28	10.29	38.91	36.48	8.00	9.34	13.22	967.15	13.15		0803/05
68.7	8.17	18.35	10.33	37.24	34.68	8.01	8.90	7.79	967.15	8.33		0803/06
68.6	8.15	42.09	11.25	31.19	29.89	8.00	8.42	3.16	967.75	3.71		0803/07
69.8	10.94	39.68	13.68	38.41	33.58	10.42	11.53	11.46	967.94	11.90		1003/07
69.6	10.49	41.13	12.62	38.54	33.24	10.19	11.19	8.73	967.67	10.12		1003/08
69	10.01	41.37	12.38	39.01	32.99	9.84	10.68	7.39	967.66	7.96		1003/09
69.5	9.62	42.02	12.32	39.05	33.01	9.51	10.21	5.82	967.43	6.34		1003/10
69.3	9.40	41.79	12.51	38.61	32.70	9.25	9.77	3.22	967.68	3.93		1003/11
69.4	9.41	41.24	13.15	37.98	31.82	9.21	9.57	1.36	968.08	2.43		1003/12

Exp. #10

FM3	T1	T3	T2	T4	T5	T6	T7	FM1-mass flow	FM1-density	FM2	p	date/ser. no.
%	deg.C	deg.C	deg.C	deg.C	deg.C	deg.C	deg.C	kg/h	kg/m3	l/h	kPa	DDMM/#
70	20.68	37.83	20.44	37.64	35.43	8.47	10.29	32.54	973.78	33.40		0903/01
70	19.36	37.86	18.78	36.53	34.38	8.54	10.21	27.85	972.67	28.09		0903/02
70	17.54	39.58	17.45	38.06	34.56	8.63	10.14	22.52	972.09	22.58		0903/03
71	17.98	43.55	17.49	38.73	34.57	8.69	9.93	18.32	972.31	18.11		0903/04
70.8	17.79	40.52	17.59	40.22	34.50	8.77	9.76	12.86	971.59	13.42		0903/05
70.9	16.67	41.57	17.19	39.95	34.56	8.88	9.60	7.92	971.10	8.32		0903/06
70.9	9.88	41.64	16.59	39.10	33.65	8.89	9.33	3.21	970.05	3.41		0903/07
69.1	20.66	40.67	20.33	39.25	34.24	10.90	11.73	11.88	972.66	12.39		1003/01
69	19.04	41.04	19.63	39.14	33.97	9.82	10.61	9.41	972.12	10.11		1003/02
69.2	16.48	41.37	18.51	39.07	33.19	9.16	9.86	7.54	971.41	7.97		1003/03
69.2	12.53	41.26	17.35	38.84	33.06	9.04	9.65	5.55	970.65	5.82		1003/04
69	10.49	41.03	16.30	38.46	32.61	8.93	9.45	4.11	969.94	4.24		1003/05
70	9.10	40.97	15.73	37.54	31.64	8.67	9.04	2.07	969.76	2.25		1003/06

Curriculum Vitae

Dong-Seon Kim was born January 1st 1969 in Yesan, South Korea. He completed his ME in mechanical engineering, thermal and fluid engineering at the Korea University, Seoul, South Korea with a thesis “A Simulation Study on A Small-capacity Air-cooled Double-effect LiBr/H_2O Absorption chiller” in 1993. After his graduation, from 1993 to 1999, he joined the HVAC Group, LSR Lab., LG Electronics, Seoul, Korea where he worked as a research engineer. From 2001 to 2005 he was appointed as Ph. D. student at the Delft University of Technology first in the former section of Refrigeration and Indoor Climate Control and later in section Engineering Thermodynamics. From 2005 he is employed by arsenal research, Vienna, Austria, where he works as research associate in the Business Unit Sustainable Energy Systems.

Publications

Kim, D.S., Infante Ferreira, C.A., 2007, Dynamic simulation of solar cooling systems, submitted for publication in Solar Energy

Kim, D.S., Infante Ferreira, C.A., 2007, Analytic modelling of absorption systems: static single-effect, submitted for publication in International Journal of Refrigeration

Kim, D.S., Infante Ferreira, C.A., 2007, Analytic modeling of a falling film absorber and determination of experimental transfer coefficients, submitted for publication in International Journal of Heat and Mass Transfer

Kim, D.S., Infante Ferreira, C.A., 2007, Solar refrigeration options – a state-of-the-art review, accepted for publication in International Journal of Refrigeration on 23 July 2007

Kim, D.S., Infante Ferreira, C.A., 2006, A Gibbs energy equation for LiBr aqueous solutions, Int. J. Refrigeration, Vol. 29, pp. 36-46

Kim, D.S., Infante Ferreira, C.A., 2006, Effect of surface geometry and surfactants on the performance of falling films, Proc. 7th Gustav-Lorentzen Conference on Natural Working Fluids, Trondheim, Norway

Kim, D.S., Infante Ferreira, C.A., Tanda, G.T., Pronk, P., 2005, Optimization of a solar ammonia-water absorption chiller, Proceedings of the IIR Conference on Thermophysical Properties and Transfer Processes of Refrigerants, Vicenza, Italy, pp. 741-748

Kim, D.S., Infante Ferreira, C.A., 2004, A Gibbs energy equation for LiBr/H2O solutions, Proc. 6th Gustav-Lorentzen Conference on Natural Working Fluids, Glasgow, U.K.

Kim, D.S, Wang. L., Machielsen, C.H.M., 2003, Dynamic modelling of a small-scale NH3/H2O absorption chiller, Proc. of 21st IIR international congress of refrigeration: "Serving the needs of mankind", Washington, USA

Kim, D.S, Machielsen, C.H.M., 2002, Evaluation of air-cooled solar absorption cooling systems, Proc. of ISHPC 2002, Shanghai, China

Kim, D.S, Machielsen, C.H.M., 2002, Comparative study on water- and air-cooled solar absorption chillers, Proc. of EuroSun 2002 ISES Conference, Bologna, Italy

Kim, D.S., Cho, H.C., Ko, C.S., 1998, A Study on the Rectification Characteristics of Packing Materials for Ammonia Absorption Heat Pump, Winter Meeting of Korean HVAC Society, 1998

Kim, D.S., Hwang, D.K., Lee, D.J., 1998, Development of Ammonia Absorption Heat Pump for Residential Use in LG Electronics, IEA Annex 24 Meeting, Tokyo

Kim, D.S., Choi, Y.D., 1993, A Simulation Study on A Small-capacity Air-cooled Double-effect LiBr/H_2O Absorption chiller, Fall Meeting of Korean HVAC Society